Stellar halos of massive galaxies: morphology, kinematics, and cosmological origin

Claudia Pulsoni

München 2021

Stellar halos of massive galaxies: morphology, kinematics, and cosmological origin

Claudia Pulsoni

Dissertation
an der Fakultät für Physik
der Ludwig–Maximilians–Universität
München

vorgelegt von
Claudia Pulsoni
aus Vizzolo Predabissi (MI), Italy

München, den 14. Mai 2021

Erstgutachter: PD. Dr. Ortwin Gerhard
Zweitgutachter: Prof. Dr. Volker Springel
Tag der mündlichen Prüfung: 5 July 2021

Ad Alessandro e Rosalia

Artist's impression of a cluster of galaxies projected "sunny side up".

A. Hofmann

Contents

List of Figures

List of Tables

Zusammenfassung

Diese Arbeit untersucht die Kinematik, die Photometrie und die intrinsischen Formen massereicher "early type" Galaxien (ETGs) bis hin zu großen Radien, wobei sowohl Beobachtungen als auch kosmologische Simulationen verwendet werden. Ziel ist die Charakterisierung der strukturellen Eigenschaften dieser Galaxien, ihrer Variation mit dem Radius und ihrer Abhängigkeit von historischen Verschmelzungen mit anderen Galaxien. Es ist seit langem bekannt, dass die hellen zentralen Bereiche ($\sim 1R_e$) von ETGs eine bimodale Verteilung der physikalischen Eigenschaften aufweisen, so dass sie in "fast rotators" (FRs) und "slow rotators" (SRs) unterschieden werden. Andererseits ist viel weniger über die dynamische Struktur von ETGs bei größeren Radien bekannt.

Stellare kinematische Messungen am lichtschwachen Rand der ETGs sind beobachtungsbedingt herausfordernd, da sie auf Absorptionslinienspektroskopie beruhen, die auf den zentralen Bereich $\sim 2R_e$ beschränkt ist. In dieser Studie wurde dieses Problem durch die Verwendung von Planetaren Nebeln (PNe) als Indikator der stellaren Halokinematik überwunden. Im Rahmen der ePN.S-Studie führte ich eine kinematische Analyse von 33 nahe gelegenen ETG-Halos bsi zu einem typischen Radius von $6R_e$ durch. Diese Arbeit zeigt, dass ETGs in den Halos eine größere Vielfalt kinematischer Verhaltensweisen aufweisen als in ihren zentralen Regionen: Ein beträchtlicher Teil der ePN.S-FRs zeigt bei großen Radien eine verringerte Rotationsunterstützung, und fast die Hälfte der FR-Probe zeigt Indikationen für eine Variation ihrer inneren Form, von oblat in der Mitte bis triaxial im Galaxienhalo. Stattdessen wurde festgestellt, dass SRs bei großen Radien eine erhöhte, aber immer noch relativ geringe Rotation aufweisen.

Diese Ergebnisse wurden mit simulierten Galaxien aus den kosmologischen magnetohydrodynamischen IllustrisTNG-Simulationen verglichen und interpretiert. Kinematik und intrinsische Formen sind eng miteinander verbunden: Übergänge zu einer niedrigeren Rotationsunterstützung in den Halos von FRs gehen mit Änderungen von abgeflachten und oblaten zu sphäroidalen Formen mit einem höheren Grad an Triaxialität einher. SRs weisen stattdessen homogenere strukturelle Eigenschaften mit dem Radius auf, mit insgesamt hoher Triaxialität und geringer Rotationsunterstützung. Die Eigenschaften von simulierten ETG-Sternhalos werden weitgehend durch das Gleichgewicht zwischen der In-situ-Komponente und den durch Verschmelzungen gewonnenen Sternen bestimmt, welche stark von der Sternmasse abhängen. In Systemen mit geringer Masse bestimmen die In-situ-Sterne spitze Rotationsprofile und nahezu oblate Formen, wobei die Abflachung mit dem Radius abnimmt. In Systemen mit höherer Masse modifizieren Verschmelzungen sowohl Rotations- als auch Formprofile, wodurch lokale Korrelationen zwischen Rotationsunterstützung, Formen und Ex-situ-Anteilen erzeugt werden,

und koppeln die Sternkomponente dynamisch an den Halo der dunklen Materie. Diese Ergebnisse legen nahe, dass die große Vielfalt der kinematischen und photometrischen Eigenschaften von Sternhalos die direkte Folge der Entwicklung von ETGs in einem kosmologischen Kontext ist: Bei großen Radien bricht die FR/SR-Dichotomie der Galaxienkerne teilweise und wird durch eine glatte Kontinuität der Halo-Eigenschaften ersetz. In diesem Bild würden ETG-Halos die Verbindung zwischen den bimodalen Kernregionen der Galaxien und dem akkretionsdominierten, stochastischen Regime der Strukturbildung in den größeren Strukturen des Universums dar.

Abstract

This thesis studies the kinematics, the photometry, and the intrinsic shapes of massive early type galaxies (ETGs) out to large radii, using both observations and cosmological simulations. The goal is the characterisation of the structural properties of these galaxies, their variation with radius, and their dependence on the merger history. The bright central regions ($\sim 1R_e$) of ETGs have long been known to display a bimodal distribution of physical properties, so that they are distinguished in fast (FRs) and slow rotators (SRs). On the other hand, much less is known about the dynamical structure of ETGs at larger radii.

Stellar kinematic measurements in the ETG faint outskirts are observationally challenging as they rely on absorption line spectroscopy, which is limited to the central $\sim 2R_e$. In this study, this issue is overcome by using planetary nebulae (PNe) as tracers of the stellar halo kinematics. As part of the ePN.S survey, I performed a kinematic analysis of 33 nearby ETG halos out to typically $6R_e$. This work revealed that ETGs have a larger diversity of kinematic behaviors in the halos than they do in their central regions: a considerable fraction of the ePN.S FRs shows reduced rotational support at large radii, and almost half of the FR sample shows indications for a variation of their intrinsic shape, from oblate in the center to triaxial in the halo. SRs instead are found to have increased but still modest rotation at large radii.

These results were compared and interpreted using simulated galaxies from the IllustrisTNG cosmological magneto-hydrodynamical simulations. Kinematics and intrinsic shapes are found to be deeply connected: transitions to lower rotational support in the halos of FRs are accompanied by changes from flattened and oblate to more spheroidal shapes, with a higher degree of triaxiality. SRs have more homogeneous structural properties with radius, with overall high triaxiality and modest rotational support. The properties of simulated ETG stellar halos are largely determined by the balance between the in-situ component and the stars accreted through mergers, which strongly depends on stellar mass. In low mass systems, the in-situ stars determine peaked rotation profiles and near-oblate shapes with flattening decreasing with radius. In higher mass systems, mergers modify both rotation and shape profiles, generating local correlations between rotational support, shapes, and ex-situ fractions, and dynamically couple the stellar component to the dark matter halo. These results suggest that the large variety of kinematic and photometric properties of stellar halos is the direct consequence of the evolution of ETGs in a cosmological context: at large radii the FR/SR dichotomy of the cores partially breaks and is substituted by a smooth continuity of halo properties. In this picture, ETG halos would represent the connection between the bimodal core regions and the accretion dominated stochastic regime of large scale structure formation.

Chapter 1

Introduction

Our modern theory of cosmology is based on the assumption that the Universe is homogeneous and isotropic on large enough scales, and that the structure and evolution of the space-time is determined by the mass and energy content of the Universe. Observations tightly constrain the cosmological parameters and point towards a flat Universe, mostly composed of dark energy ($\sim$ 68.5%) and dark matter ($\sim$ 26.5%, Planck Collaboration et al. 2018). The baryonic matter, that is protons, neutrons, and electrons, is what we can directly observe in the form of stars, stellar remnants, gas, dust, and planets, and makes up for only $\sim$ 5% of the energy density of the universe.

The dark matter is electromagnetically neutral, hence it does not emit or absorb radiation, but can be detected through the gravitational pull that it exerts on stars and galaxies (Zwicky 1937; Rubin et al. 1980). In the ΛCDM model the dark matter is cold and collision-less. Finally the dark energy component has been introduced to explain the observed accelerated expansion of the universe (Riess et al. 1998; Perlmutter et al. 1999). While several candidates have been proposed for the dark matter, the nature of the driving force behind the expansion of the universe is currently unknown.

Since the mass content of the universe is large, gravity is the dominant force on the macroscopic scales. Stars, gas, dust, and dark matter tend to cluster together in galaxies, gravitationally bound structures which range from a total mass of $10^{6-7} M_\odot$ for the dwarf galaxies to $10^{14} M_\odot$ for the most massive galaxies. Galaxies in turn tend to organize in groups and clusters, which are distributed in large scale structures.

1.1 Galaxy morphology

Galaxies are observed to have a wide range of morphologies. Elliptical galaxies are smooth, featureless stellar systems with no apparent stellar disks. Disk galaxies, instead, range from bulge[1]-less to bulge-dominated and often contain spiral arms and bar structures. Therefore, the first attempt of a galaxy classification was based on their visual appearance. The Hubble classification system, still widely in use today and schematically represented in Fig. 1.1, sorted galaxies

[1]The bulge is a bright mass concentration in the center.

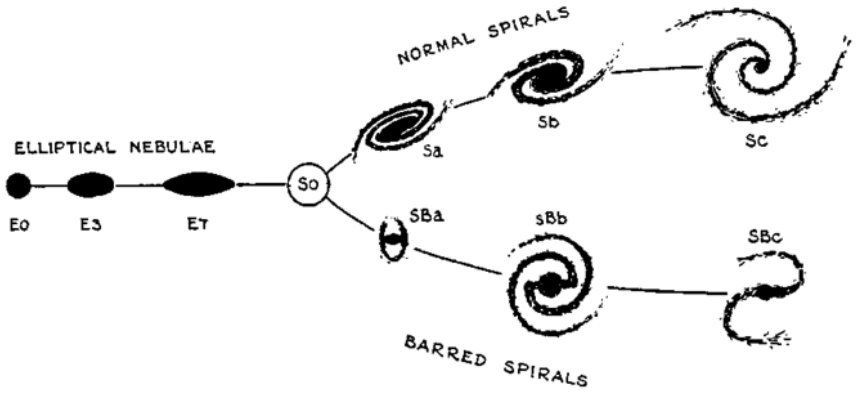

Figure 1.1: Hubble classification of galaxy morphologies (from Hubble 1936). On the left side, ellipticals and S0s are denoted as "early type galaxies"; on the right, spiral galaxies are "late type galaxies".

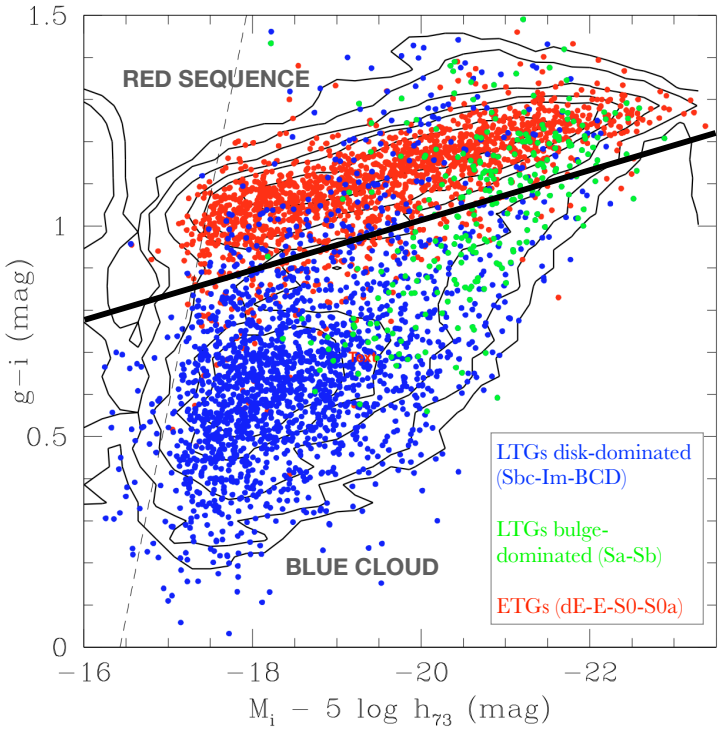

Figure 1.2: $g - i$ color versus i-band absolute magnitude relation of 4132 galaxies in the Coma supercluster from SDSS (figure adapted from Gavazzi et al. 2010). The solid line shows the empirical separation between red-sequence and blue-cloud. Galaxies are color-coded according to their Hubble type as in the legend: early type galaxies populate preferentially the red sequence while late types distribute in the blue cloud.

into a sequence with growing flattening from ellipticals to spirals (Hubble 1936). On the left side of the diagram, ellipticals are ordered according to their apparent projected ellipticity (*En*, with $n = 10 \times \varepsilon$ where ε is the ellipticity); on the right side, spirals are subdivided according to the prominence of the bulge, how tightly the spiral arms are wound and their degree of resolution, and the presence of a bar component. The lenticular or S0 galaxies are characterised by a bulge and a disk component but no spiral arms. They appear smooth and featureless, and are therefore placed as transition objects between the ellipticals and the spirals (Binney & Merrifield 1998).

Ellipticals and S0 galaxies are characterized by old stellar populations. They contain little or no dust and little or no cold interstellar gas to form new stars. These galaxies have predominantly red colors (de Vaucouleurs 1961) and are commonly denoted as "early type galaxies" (ETGs). From the S0 and Sa towards "later types" colors become progressively bluer, as the galaxies become more gas rich and the spiral arms are more and more dominated by complexes of young blue stars (e.g., Buta et al. 1994). It is now clear that galaxies display a color bimodality that tightly correlates with morphological types (Strateva et al. 2001). In a color-magnitude diagram, ETGs follow a narrow "red sequence", while the mostly star-forming late types distribute in a "blue cloud" (Fig. 1.2). Bell et al. (2004) and Faber et al. (2007) showed that color bimodality is already in place at $z \sim 1$ and, since then, the number and total stellar mass of blue galaxies have been substantially constant, while stellar mass on the red sequence grew by a factor of ~ 2. Therefore, galaxies are thought to evolve from the blue to the red sequence as they quench their star formation (e.g., Martin et al. 2007).

The Hubble sequence also correlates with stellar mass or luminosity, as the fraction of spheroid-dominated galaxies increases strongly with mass (Bernardi et al. 2010). Galaxy morphology, as well as galaxy mass, has been found to depend on environment. Dressler (1980) found a morphology-density relation in which the fraction of ellipticals and S0 increases with increasing number density of galaxies and, correspondingly, the fraction of spirals decreases. This trend has been found to persist in a wide range of densities (Postman & Geller 1984) and it is a signature of the environmental dependence of the relative importance of the different processes regulating galaxy formation and evolution (Sect. 1.6).

1.2 Early type galaxy classification and bimodality

The Hubble classification of ETGs based on their apparent flattening correlates primarily with inclination and not with any fundamental physical parameter (Tremaine 1987). This is because a sequence of increasing flattening is not directly translatable in a sequence of increasing rotation (e.g., Illingworth 1977), since ellipticals can have anisotropic velocity distributions and triaxial shapes (see also Sects. 1.3.6 and 1.5 below). The tensor virial theorem in fact predicts that non-rotating triaxial galaxies can be quite flat and supported by anisotropy (Eq. 1.21). Besides, a clear separation between ellipticals and S0s based on the presence or not of a stellar disk is not straightforward when the disk is faint or seen close to face-on, and it is complicated by the fact that many elliptical galaxies do harbour a disk-like component (e.g., Scorza & Bender 1995).

The "disky ellipticals" are identifiable through the observation of isophotes that are more elongated along the major axis than the best fitting ellipse (Bender & Moellenhoff 1987, see the

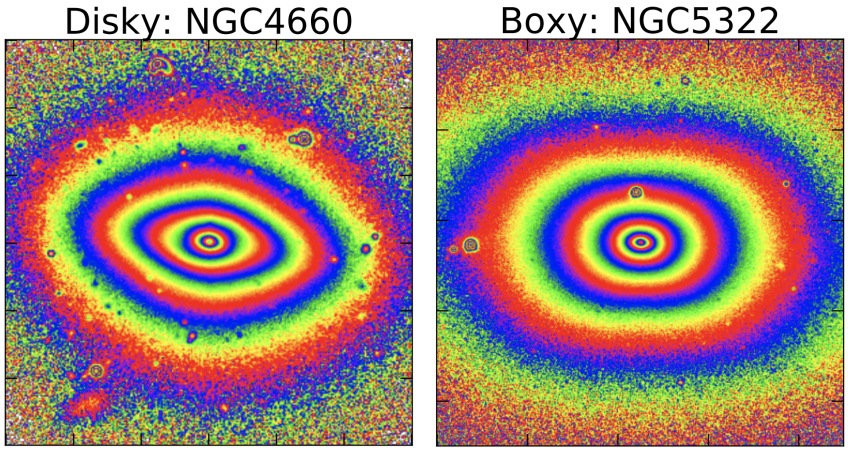

Figure 1.3: An example of elliptical galaxies with disky-distorted isophotes (on the left) and with boxy-distorted isophotes (on the right, figure from Cappellari 2016).

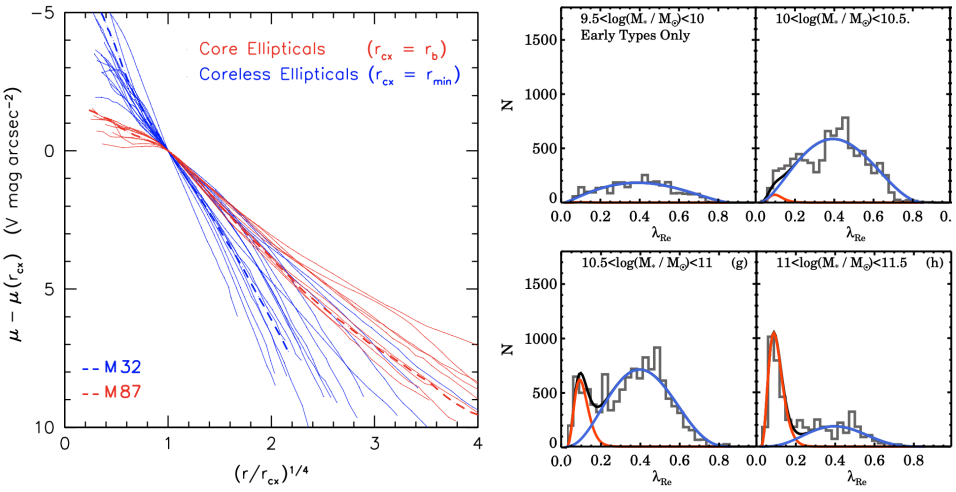

Figure 1.4: The ETG bimodality. **Left**: Major axis surface brightness profiles of elliptical galaxies in the Virgo cluster, scaled to illustrate the dichotomy between core and core-less ellipticals (figure from Kormendy et al. 2009). **Right:** Distribution of the λ_e parameter for the volume-corrected SAMI ETGs, divided in stellar mass bins. The λ_e distribution can be described by a double beta distribution highlighting the bimodality ETG kinematic properties and the presence of two populations, i.e. the fast (in blue) and the slow rotators (in red, figure from van de Sande et al. 2020).

galaxy on the left in Fig. 1.3). These galaxies show significant rotation (e.g., Bender 1987; Nieto et al. 1988) and, in a V/σ-ellipticity diagram, they distribute close to the prediction for isotropic oblate-spheroidal models given by Eq. 1.19 (e.g., Davies et al. 1983; Bender et al. 1994, see also Sect. 1.4). Most of the normal and low-luminosity ellipticals ($M_V \gtrsim -21.5$) have been found to share these properties and have therefore been connected to S0s and spiral galaxies in a sequence of increasing disk dominance or decreasing velocity anisotropy (Kormendy & Bender 1996). Giant ellipticals ($M_V < -21.5$) instead have boxy-distorted isophotes (i.e., with shapes that are more rectangular than ellipses, as the galaxy on the right in Fig. 1.3) and are less flat than normal ellipticals. They do not rotate, therefore their flattening can be explained by triaxial shapes supported by anisotropy (Binney 1976, 1978; Bender 1987).

Another distinction among elliptical galaxies comes from the observation of their surface brightness profiles. Ellipticals have outer surface brightness radial profiles that are well described by the Sérsic $R^{1/n}$ power-law (Eq. 1.2), with the index n increasing with the total luminosity (Caon et al. 1993). Low luminosity ellipticals tend to have $n < 4$ and as low as 2, close to the exponential ($n = 1$) surface brightness profiles of pure disk galaxies. Their nuclear regions can be found to contain "extra light", showing profiles that become steeper towards the center with respect to a global the Sérsic fit to the outer profiles (Faber et al. 1997, Fig. 1.4, left panel, blue profiles). Giant ellipticals generally have large Sérsic indices ($n > 4$) and nuclear regions often containing a core, that is a center characterized by a break and a much shallower profile compared to the global the Sérsic fit (Ferrarese et al. 1994; Lauer et al. 1995, Fig. 1.4, left panel, red profiles). These differences in the light distribution in the nuclear regions are thought to be related to the galaxy merger history (see Sect. 1.6).

Ferrarese et al. (1994) and Faber et al. (1997) found that cores are typically found in boxy, slowly rotating ellipticals, while power-law galaxies are generally disky ellipticals and S0s. These systematic variations of properties with galaxy luminosity, which also correlate with other global quantities such as, for example, the galaxy radio and Xray emission (Bender et al. 1989), has opened a debate about the possibility of a bimodality/dichotomy between giant boxy ellipticals with cored profiles and normal to low-luminosity disky ellipticals with power-law profiles (Ferrarese et al. 1994; Lauer et al. 1995; Kormendy & Bender 1996), although some studies find a smooth continuity of properties among two classes (e.g., Ferrarese et al. 2006; Côté et al. 2007; Krajnović et al. 2013b). This issue is still relevant today, as the advent of the integral field spectroscopy (IFS) in the last decade has shifted the classification of ETGs to a kinematics-based division, more robust with respect to inclination effects compared to the classic division based on photometry (Cappellari 2016).

Before IFS, long slit measurement along the projected major and minor axes of the galaxies could only provide an approximation of the global kinematics. In the last years, a flourishing of IFS surveys (e.g., Atlas3D - Cappellari et al. 2011, MASSIVE - Ma et al. 2014, MANGA - Bundy et al. 2015, CALIFA - Sánchez et al. 2012, SAMI - Bryant et al. 2015) is providing a large wealth of two-dimensional data mapping the stellar kinematics, as well as the distribution of the stellar populations and of the ionized gas, in galaxies with different morphology, mass, and in a wide range of environments.

The two-dimensional kinematic information unveiled that the photometrically smooth and featureless ETGs exhibit different kinematic morphologies (Krajnović et al. 2011) and that ETGs

can be divided into two physically distinct classes, the fast and the slow rotators, according to their distribution in the λ_e-ellipticity plane, where λ_e is the angular momentum parameter measured within 1 effective radius R_e (Emsellem et al. 2007, 2011, see the next Section). Slow rotators are generally bright and roughly consistent with the class of cored ellipticals, while most fast rotating ellipticals and S0s have power-law nuclear profiles, although a significant population of power-law slow rotators and of cored fast rotators exists (Krajnović et al. 2013b). With the growth in size of the ETG samples with IF kinematics, together with the number of massive galaxies probed, the existence of a kinematic bimodality has become more and more established (e.g., Graham et al. 2018). Above stellar masses $M_* > 10^{10.5} M_\odot$, the λ_e distribution of ETGs has been found to be described by a double beta distribution, indicating the presence of at least two stellar kinematic populations with non-negligible overlap (Fig. 1.4, right panel, van de Sande et al. 2020).

The interpretation of both morphology and kinematics can be clarified through the study of the galaxy dynamical structure.

1.3 Galaxy dynamics

1.3.1 The dark matter component in galaxies

In the ΛCDM paradigm, dark matter forms the backbone structure in which galaxies form, evolve, and merge (e.g., Davis et al. 1985). Dark matter halos can be thought as basic units of gravitationally bound regions of matter generated from primordial over-densities in the expanding Universe, which decoupled from the expansion, and collapsed. The mass of virialized halos is given by $M_{\rm vir} = \frac{4\pi}{3} R_{\rm vir}^3 \Delta \rho_m$, where $\Delta \sim 200 - 300$ is the virial over-density parameter relative to the background matter density. The value of $M_{\rm vir}$ depends on the definition of the halo outer edge ($R_{\rm vir}$), whose definition varies in the literature and depends on the choice of Δ (see Sect. 1.3.1 in Bullock & Boylan-Kolchin 2017).

Even though at early times gas and dark matter were mixed together, as the Universe evolved and formed the first structures, gas efficiently dissipated energy by emitting radiation and quickly fell at the center of the dark matter halos, where it eventually formed stars and galaxies. Therefore the mass distribution of gas-poor ETGs is expected to be dominated by mostly stars in the central regions (out to $1 - 3R_e$, see Gerhard 2013 for a review) and by dark matter in the outskirts. Observations suggest a tendency for more luminous galaxies to be more dark matter dominated with higher dark matter fractions in the central regions (Napolitano et al. 2005; Deason et al. 2012).

The density profiles of dark matter halos in dark-matter-only simulations converge to NFW density profiles (Navarro et al. 1996, 1997)

$$\rho(r) = \frac{\rho_s}{(r/r_s)\,[1 + (r/r_s)]^2}, \tag{1.1}$$

where ρ_s and r_s are characteristic density and radius, such that the larger the mass of a halo, the lower its characteristic density. In these simulations, dark matter halos have strongly flattened,

triaxial-prolate shapes due to anisotropy (e.g., Dubinski & Carlberg 1991; Allgood et al. 2006, see also Sect. 1.3.6). The inclusion of baryonic physics has the effect of increasing the concentration of the dark matter halos and changing their density profiles towards the isothermal model $\rho \propto 1/r^2$ (Gnedin et al. 2004). The baryonic component is also responsible for making dark matter halo shapes more spheroidal-oblate at all radii but mostly in the inner parts (Kazantzidis et al. 2004; Chua et al. 2019).

1.3.2 Dynamical modelling

The dark matter distribution in real galaxies can be derived from dynamical modelling, which yields the total mass distribution and that of the dark matter once the contribution from the baryons is subtracted. The stellar surface brightness profile with radius $I(R)$ are well described by Sérsic profiles

$$I(R) = I_e \mathrm{dex}\left\{-b(n)\left[\left(\frac{R}{R_e}\right)^{1/n} - 1\right]\right\} \tag{1.2}$$

where I_e is the surface brightness at $R = R_e$, and $b(n)$ is chosen in such a way so that R_e is the effective radius[2] of the galaxy: $b(n) \sim 0.868n - 0.142$ (Caon et al. 1993). From $I(R)$, the stellar density distribution can be derived knowing the stellar mass-to-light ratio profile (see Courteau et al. 2014, for a review).

It is now established that many galaxies host super-massive black holes in their centers with masses 10^6 to $10^{10} M_\odot$. The only way to unambiguously detect them and measure their masses is by modelling the dynamics of the galaxy central regions using high resolution kinematic and photometric data (e.g., Houghton et al. 2006). In addition to the mass distribution, dynamical models constrain the distribution of orbits that are stable in the gravitational potential of the galaxy.

1.3.3 Dynamics of a collisionless stellar system

Galaxies can be well approximated as collisionless systems of stars where two-body interactions can be neglected. This is because the typical stellar density is of the order of 1 pc^{-3} and the relaxation times are long ($\sim 10^7$ Gyr)[3]. In this formalism, the stellar system (or a tracer of the galaxy gravitational potential) is described by a distribution function f, which gives the probability density of the system in the six-dimensional phase space of coordinates $(\mathbf{x}, \mathbf{v})$ at a time t, $f(\mathbf{x}, \mathbf{v}, t) d^3\mathbf{x} d^3\mathbf{v}$. The evolution of f is set by the collisionless Boltzmann equation stating the conservation of probability, $\frac{\mathrm{d}f}{\mathrm{d}t} = 0$, which can be rewritten as

$$\frac{\mathrm{d}f}{\mathrm{d}t} \equiv \frac{\partial f}{\partial t} + \mathbf{v} \cdot \boldsymbol{\nabla} f - \boldsymbol{\nabla}\Phi \cdot \frac{\partial f}{\partial \mathbf{v}} = 0, \tag{1.3}$$

[2]The effective radius is the radius of an aperture centered on the galaxy containing half of the total emitted light.

[3]By assuming a typical number of 10^{11} stars populating a galaxy of 10 kpc radius with velocities of the order 100 km/s.

where Φ is the gravitational potential. Solving the Boltzmann equation coupled with the Poisson equation for the gravitational potential,

$$\nabla^2\Phi = 4\pi G\rho_{tot}, \tag{1.4}$$

where ρ_{tot} is the total mass density, is challenging even for a stationary system (for which $\frac{\partial f}{\partial t} = 0$), as f is a function of 6 variables, and ρ_{tot} is unknown.

Different methods for modelling galaxies include:

- **Schwarzschild modelling** - Assuming a galaxy gravitational potential, this method superposes the allowed orbits using a combination of weights to reproduce the density distribution and the kinematics of the stars (Schwarzschild 1979). The Schwarzschild modelling has been applied using the assumption of spherical symmetry or axisymmetry (e.g., Thomas et al. 2005b; Cappellari et al. 2007) and has provided most of the mass determinations of supermassive black holes at the center of galaxies (e.g., Mehrgan et al. 2019).

- **N-body models** - The galaxy phase-space is sampled by a set massive particles, whose motion is determined by their self-consistent gravitational field. Generally the N-body models require an initial model to evolve from; different initial conditions are explored in order to search for the model that best compares to the data (e.g., Blaña Díaz et al. 2017).

- **N-body made-to-measure models** - Made-to-measure models (Syer & Tremaine 1996) start from an initial N-body model, which is evolved in time by slowly adjusting some weights attributed to the particles in order to obtain a self-consistent dynamical model that reproduces the data. This method has been applied to external galaxies (e.g., de Lorenzi et al. 2008, 2009) as well as to the Milky Way (e.g., Portail et al. 2017).

1.3.4 Jeans analysis

The Jeans analysis is a simplified method which does not attempt to recover the full distribution function f but limits itself to its first two moments. This method applies the equations of the stellar hydrodynamics, or Jeans (1922) equations, to a dissipationless tracer (e.g., the stars, globular cluster, planetary nebulae), relating its density and kinematics to the gravitational potential assuming a time independent system. The Jeans equations in fact relate the information on the orbital properties given by the moments of f to the potential, and therefore to the total galaxy mass distribution. The latter can therefore be determined from the observed tracer kinematics once some symmetry is assumed (e.g., spherical symmetry or axisymmetry), and only if the anisotropy of the pressure tensor is constrained (the *mass-anisotropy degeneracy*, see below).

The zero-th moment of Eq. (1.3) delivers

$$\frac{\partial \nu}{\partial t} + \boldsymbol{\nabla} \cdot (\nu \overline{\mathbf{v}}) = 0, \tag{1.5}$$

where ν is the spatial density of the tracer and $\overline{\mathbf{v}}$ its the mean velocity

$$\overline{\mathbf{v}} \equiv \frac{1}{\nu} \int \mathbf{v} f(\mathbf{x}, \mathbf{v}) d^3\mathbf{v}. \tag{1.6}$$

The first velocity moment gives

$$\nu\frac{\partial\overline{\mathbf{v}}}{\partial t}+\nu(\overline{\mathbf{v}}\cdot\boldsymbol{\nabla})\overline{\mathbf{v}}+\boldsymbol{\nabla}\cdot(\nu\boldsymbol{\sigma}^2)=-\nu\boldsymbol{\nabla}\Phi, \tag{1.7}$$

where $\boldsymbol{\sigma}^2$ is the velocity dispersion tensor, whose elements $\sigma_{ij}^2=\overline{v_iv_j}-\overline{v_i}\,\overline{v_j}$ and

$$\overline{v_iv_j}\equiv\frac{1}{\nu}\int v_iv_jf(\mathbf{x},\mathbf{v})d^3\mathbf{v}. \tag{1.8}$$

The Jeans equations Eq. (1.5) and (1.7) are formally similar to the equations of hydrodynamics, with the difference that the pressure in the Euler equation is here substituted by a stress tensor $\nu\boldsymbol{\sigma}^2$ describing an anisotropic pressure. For a time independent system, all the derivatives of time $\frac{\partial}{\partial t}$ are zero. Assuming that ν and Φ are known, this set of four equations contains nine unknown variables, i.e. the three components of $\overline{\mathbf{v}}$ and six independent components of $\boldsymbol{\sigma}^2$. However, some of these quantities, such as the line-of-sight mean velocity and velocity dispersion, can be directly observed. By assuming some symmetry property for the galaxy, the system of equations can be closed and solved.

For a spherical stellar system, with coordinates (r,θ,ϕ) centered on the galaxy, and non-rotating, the velocity dispersion tensor is diagonal with components $\sigma_r^2\equiv\overline{v_r^2}$, $\sigma_\theta^2\equiv\overline{v_\theta^2}$, and $\sigma_\phi^2=\sigma_\theta^2$. For a time independent system, the spherical Jeans equation is

$$\frac{\mathrm{d}(\nu\sigma_r^2)}{\mathrm{d}r}+2\frac{\beta}{r}\nu\sigma_r^2=-\nu\frac{\mathrm{d}\Phi}{\mathrm{d}r}, \tag{1.9}$$

where $\beta\equiv1-\frac{\sigma_\theta^2+\sigma_\phi^2}{2\sigma_r^2}=1-\frac{\sigma_\theta^2}{\sigma_r^2}$ is the *anisotropy* of the orbital distribution. A system with $\beta<0$ has tangentially biased orbits, one with $\beta>0$ has radially biased orbits. By measuring the surface density of the tracer and the line-of-sight velocity dispersion, one can derive the gravitational potential once β is constrained (the mass-anisotropy degeneracy, Binney & Mamon 1982). The study of the shape of the line-of-sight velocity distribution can deliver additional information on the orbital anisotropy (e.g., van der Marel & Franx 1993; Gerhard 1993). The spherical Jeans equation (Eq 1.9) yields a good estimate of the mass distribution in slowly evolving round or mildly triaxial systems such as, for example, massive ellipticals (see Courteau et al. 2014 and Binney & Tremaine 2008 for more details).

For a time-independent axisymmetric galaxy, we can define a cylindrical coordinate system (R,ϕ,z) centered the galaxy and with the z axis oriented along its symmetry axis. By assuming a velocity ellipsoid approximately aligned with the cylindrical coordinates, the two non trivial Jeans equations are

$$\nu\frac{\sigma_R^2-\overline{v_\phi^2}}{R}+\frac{\partial(\nu\sigma_R^2)}{\partial R}=-\nu\frac{\partial\Phi}{\partial R} \tag{1.10}$$

and

$$\frac{\partial(\nu\sigma_z^2)}{\partial z}=-\nu\frac{\partial\Phi}{\partial z}. \tag{1.11}$$

By projecting Eq. (1.10) and (1.11) on the sky plane, and by measuring the surface density of the tracer and the line-of-sight velocity dispersion and rotation, we can obtain a unique solution as a function of σ_R^2/σ_z^2 and the galaxy inclination. Commonly employed extra assumptions on the velocity ellipsoid include

- the *semi-isotropic ellipsoid*: $\sigma_R^2 = \sigma_z^2$. This assumption is sufficient to close the set of Jeans equations to provide a unique solution (e.g., Nagai & Miyamoto 1976; Satoh 1980; Binney et al. 1990; van der Marel et al. 1990; Emsellem et al. 1994)

- the *isotropic rotator*: $\sigma_\phi = \sigma_R = \sigma_z$, as in Binney 1978.

- the *oblate velocity ellipsoid*: $\sigma_\phi = \sigma_R > \sigma_z$, as in Cappellari (2008).

The assumption of axisymmetry and cylindrically aligned velocity ellipsoid is a reasonable approximation for the mass distribution of disk galaxies and fast rotating ETGs (Cappellari 2008, but see Dehnen & Gerhard 1993).

1.3.5 The tensor virial theorem

By multiplying the first moment of the collisionless Boltzmann equation (Eq. 1.7) with Mx_k, where M is the total mass of the tracer, and integrating over all positions, we convert the differential equation in a tensor equation known as *tensor virial theorem*:

$$\frac{1}{2}\frac{\mathrm{d}^2 I_{jk}}{\mathrm{d}t^2} = 2T_{jk} + \Pi_{jk} + W_{jk}, \tag{1.12}$$

where we defined the mass density of the tracer $\rho(\mathbf{x}) = M\nu(\mathbf{x})$, the inertia tensor

$$I_{jk} = \int d^3\mathbf{x}\rho x_j x_k, \tag{1.13}$$

the potential-energy tensor

$$W_{jk} = -\int d^3\mathbf{x}\rho x_j \frac{\partial\Phi}{\partial x_k}, \tag{1.14}$$

and the kinetic-energy tensor, split into the contributions from ordered and random motion $K_{jk} = T_{jk} + \frac{1}{2}\Pi_{jk}$, where

$$T_{jk} = \frac{1}{2}\int d^3\mathbf{x}\rho\overline{v_j}\,\overline{v_k} \qquad \text{and} \qquad \Pi_{jk} = \int d^3\mathbf{x}\rho\sigma_{jk}^2. \tag{1.15}$$

If the system is time-independent, the left side of Eq. (1.12) is zero. Applied to the stars, Eq. (1.12) relates the gross kinematic and morphological properties of galaxies (Binney 1978).

1.3.6 Flattening of oblate and triaxial galaxies

An application of the virial theorem relates the flattening of ellipsoidal galaxies to their kinematics. In the case of an oblate galaxy rotating around its symmetry axis and seen edge-on, we can consider a coordinate system (x, y, z) with the z-axis aligned with the galaxy rotation axis and the x-axis aligned with the line-of-sight (LOS). In these coordinates the tensors in Eq. (1.12) are diagonal, $T_{xx} = T_{yy}$, $T_{zz} = 0$, and $K_{xx} = \frac{1}{2}M\left(\left\langle\sigma^2_{LOS}\right\rangle + \left\langle\overline{v}^2_{LOS}\right\rangle\right)$, where the brackets $\langle\cdot\rangle$ denote column-density weighted averages over the sky. As described in Sect. 4.1.2 of (Binney & Tremaine 2008) the line-of-sight velocity dispersion σ_{LOS} is the sum of two components, one arising from the velocity-dispersion tensor $\boldsymbol{\sigma}$, and one from the variation of the mean velocity $\overline{\mathbf{v}}$ along the line-of-sight.

We obtain the two non-trivial equations,

$$2K_{xx} + W_{xx} = 0 \qquad\qquad 2K_{zz} + W_{zz} = 0, \tag{1.16}$$

which give

$$\frac{M\left(\left\langle\sigma^2_{LOS}\right\rangle + \left\langle\overline{v}^2_{LOS}\right\rangle\right)}{\Pi_{zz}} = \frac{W_{xx}}{W_{zz}}. \tag{1.17}$$

By defining the global anisotropy parameter $\delta = 1 - \frac{\Pi_{zz}}{\Pi_{RR}}$ and by expressing Π_{xx} in terms of the LOS velocity dispersion $\left\langle\sigma^2_{LOS}\right\rangle$, as in Eq. 4.264 of Binney & Tremaine (2008), we obtain the relation

$$\frac{\left\langle\overline{v}^2_{LOS}\right\rangle}{\left\langle\sigma^2_{LOS}\right\rangle} = \frac{(1-\delta)W_{xx}/W_{zz} - 1}{\alpha(1-\delta)W_{xx}/W_{zz} + 1}, \tag{1.18}$$

where α is a dimensionless parameter depending only on how the stellar density and the streaming velocity vary within the (R, z) plane. Cappellari et al. (2007) quantified that $\alpha \sim 0.15$ and that the galaxy to galaxy variations are small.

The ratio W_{xx}/W_{zz} for ellipsoidal bodies depends only on the ellipticity of the galaxy and are entirely independent on the density profile so long as the equal-density surfaces are similar ellipsoids of semi-major axes $a \geq b \geq c$: $W_{xx}/W_{zz} = A(a/c)$ (Roberts 1962). Similarly, the ratio $W_{xx}/W_{yy} = B(b/a)$ with y aligned with the intermediate axis of the ellipsoid. The exact functions $A(a/c)$ and $B(b/a)$ are given by Binney & Tremaine (2008). Therefore, Eq. (1.18) provides a relation between the flattening, the rotational support, and the anisotropy δ in an oblate galaxy.

In the case of an oblate ellipsoid, $W_{xx}/W_{yy} = 1$, and for W_{xx}/W_{zz} we can consider the simple Eq. 14 and 16 in Cappellari et al. (2007) written for the intrinsic ellipticity $\varepsilon_{intr} = 1 - c/a$. For an isotropic rotator $\delta = 0$ and

$$\frac{\left\langle\overline{v}^2_{LOS}\right\rangle}{\left\langle\sigma^2_{LOS}\right\rangle} \sim 0.831\sqrt{\frac{\varepsilon_{intr}}{1 - 0.896\varepsilon_{intr}}}. \tag{1.19}$$

Schwarzschild modelling of the central regions ($\sim 1R_e$) of fast rotating ETGs has revealed that their anisotropy is limited by the relation (Cappellari et al. 2007)

$$\delta \lesssim 0.7\varepsilon_{intr}. \tag{1.20}$$

In the case of a (non-rotating) triaxial spheroid, we choose a coordinate system aligned with the principal axes of the galaxy, with the z-axis aligned with the minor axis and the x-axis aligned with the major axis. In this system, the tensors in Eq. (1.12) are diagonal so that, for each axis j we can write $\Pi_{jj} + W_{jj} = 0$, as the components $T_{jj} = 0$. Each component $\Pi_{jj} = M \left\langle \sigma_{jj}^2 \right\rangle$, and the ratio

$$\frac{\left\langle \sigma_{jj}^2 \right\rangle}{\left\langle \sigma_{xx}^2 \right\rangle} = \frac{W_{jj}}{W_{xx}} \tag{1.21}$$

relates the anisotropy of the system to its flattening through the ratio W_{jj}/W_{xx}. By using the power-law approximation $W_{xx}/W_{zz} \sim (a/c)^{0.9}$ (Gerhard 1994), we note that a flattening $c/a = 0.7$ can be supported by little anisotropy, $\left\langle \sigma_{zz}^2 \right\rangle / \left\langle \sigma_{xx}^2 \right\rangle \sim 0.85$.

1.4 Kinematic properties of fast and slow rotators within 1Re

IF kinematics revealed that the large majority ($> 80\%$) of ETGs are "regular rotators", that is galaxies with velocity fields similar to that of inclined rotating disks, without any additional features, and approximately described by a cosine law

$$V(\phi) = V_0 + V_{rot} \cos(\phi - \mathrm{PA_{kin}}), \tag{1.22}$$

where V_0 is a constant systemic velocity, V_{rot} is the amplitude of the projected rotation, ϕ is the azimuthal angle in a polar coordinate system centered on the galaxy, and $\mathrm{PA_{kin}}$ is the angle describing the orientation of the mean rotation. Only a small fraction of the ETGs are "non-regular rotators", a group including non rotating galaxies, irregular asymmetric rotators, kinematically decoupled cores, and galaxies with two counterrotating disks (Krajnović et al. 2011).

In order to quantify the "amount of rotation" contained in the central $1R_e$ of the galaxies, Emsellem et al. (2007) introduced an angular momentum parameter λ. Analogously to V/σ, λ measures the ratio between ordered rotation versus disordered motions, but in addition it includes the spatial information from the kinematic maps:

$$\lambda(\leq R) = \frac{\sum_{n=1}^{N} F_n R_n \left| V_n \right|}{\sum_{n=1}^{N} F_n R_n \sqrt{V_n^2 + \sigma_n^2}}, \tag{1.23}$$

where the summation is carried on the spatial bins of the kinematic maps contained in an elliptical aperture of semi-major axis R, each bin measuring a flux F_n, a mean stellar velocity V_n, and a velocity dispersion σ_n.

The first classification of ETGs in fast (FRs) and slow rotators (SRs) separates the galaxies at the threshold

$$\lambda_e = 0.31 \sqrt{\epsilon} \tag{1.24}$$

(Emsellem et al. 2011), shown in Fig. 1.5 with a dotted green curve. Fast rotators are mostly regular rotators, make up for $\sim 86\%$ of the ETGs, including the lenticular galaxies and 66% of all the ellipticals (Emsellem et al. 2011). Slow rotators tend to be massive and dominate the high mass end of the ETG stellar mass function, at $M_* > 10^{11.2-11.3} M_\odot$ (Veale et al. 2017a).

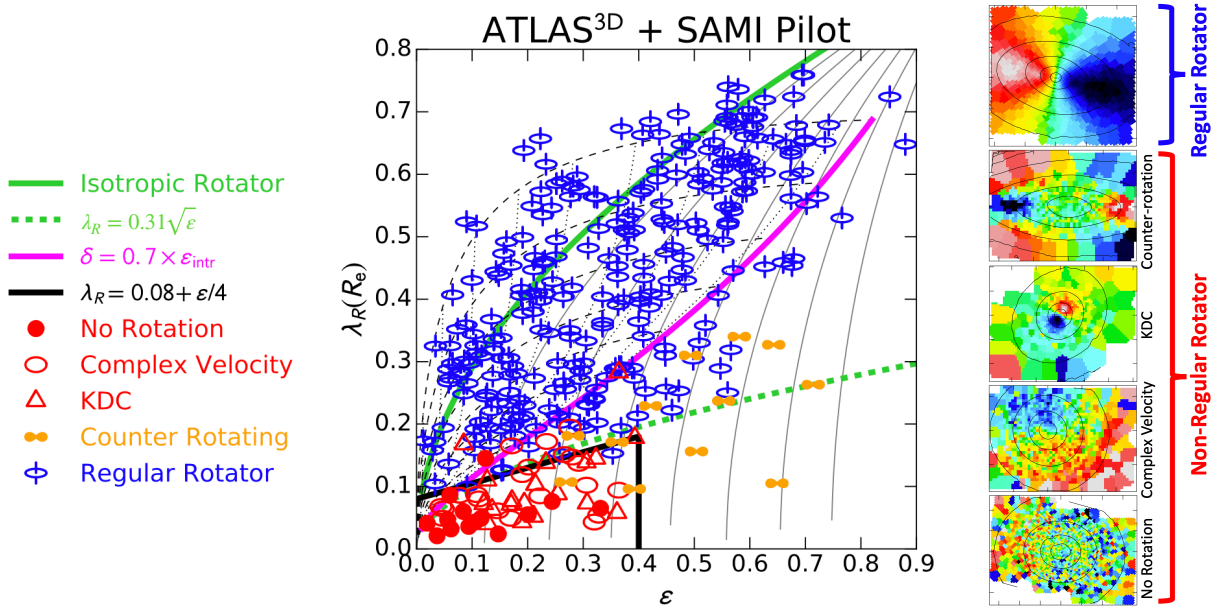

Figure 1.5: **Left**: The λ_e-ellipticity diagram (modified from Cappellari 2016) for 340 ETGs from Emsellem et al. (2011) and Fogarty et al. (2015). The green solid line is the prediction for an edge-on isotropic oblate rotator, the thin black lines show the prediction at increasing anisotropy (Eq. 1.18) by $\Delta\delta = 0.1$ each (Binney 2005). The magenta line shows the edge-on relation $\delta = 0.7\epsilon_{intr}$, where ϵ_{intr} is the intrinsic ellipticity, while the dashed black lines indicate how this relation transforms at different inclinations. The dotted green line and the solid black polygon mark the threshold for the separation of ETGs in fast and slow rotators according to the definitions of Emsellem et al. (2011) and of Cappellari (2016), respectively. **Right:** The kinematic morphology of the ETG velocity fields (modified from Cappellari 2016).

The distribution of ETGs in a diagram relating the angular momentum parameter measured within $1R_e$, λ_e, and the projected ellipticity at $1R_e$ is shown in Fig. 1.5. Regular rotators distribute in the region of the diagram outlined by the prediction for edge-on axisymmetric galaxies with oblate velocity ellipsoids and anisotropy $\delta = 0.7\epsilon_{intr}$ (magenta line, see Sect. 1.3.6) and its projections (dashed black curves), indicating that these galaxies are broadly consistent with a population of randomly oriented axisymmetric galaxies with $\delta \lesssim 0.7\epsilon_{intr}$ (Cappellari et al. 2007; Cappellari 2016). Therefore, regular rotators are not necessarily isotropic but often fall close to the prediction for isotropic rotators (given by Eq. 1.19 rewritten for the λ_e parameters using Eq. B1 in Emsellem et al. 2007, and shown in Fig. 1.5 with a solid green line) because of projection effects. Non-regular rotators distribute below the magenta line, displaying lower rotational support than the expectation for mildly anisotropic oblate rotators. The round, massive, non-rotating galaxies show growing β anisotropy profiles with radius, from tangentially biased in the core regions to radially anisotropic with $\beta \sim 0.5$ at $\sim 1R_{\rm e}$ (e.g., Thomas et al. 2014).

1.5 ETG intrinsic shapes

The three-dimensional light distributions of galaxies, or their "intrinsic shapes", contain information about their formation histories and the accretion processes that dominated their evolution. In the case of ETGs, the shape determination is complicated by the fact that they are thought to be triaxial spheroids (with axes ratios $1 \geq p \geq q \geq 0$), for which the deprojection of the surface brightness is generally non-unique (Stark 1977), even in the case of axisymmetry (Rybicki 1987; Gerhard & Binney 1996).

Intrinsic shapes of individual ETGs can only sometimes be derived from dynamical modelling of detailed photometric and kinematic data (e.g., van den Bosch & van de Ven 2009). Therefore many studies tried to infer the intrinsic shape distribution of a particular, morphologically selected galaxy population using statistical methods. The first attempts were based uniquely on photometry and performed a statistical analysis of the observed distribution of projected ellipticities, assuming a random distribution of the viewing angles (e.g. Sandage et al. 1970; Lambas et al. 1992; Padilla & Strauss 2008) In this case, strong assumptions on the intrinsic shape distributions are necessary, as the reconstruction of a triaxial shape distribution (a 2-dimensional function $f(p, q)$) from the distribution of the observed apparent ellipticity (a 1-dimensional function) is degenerate (e.g., Binggeli 1980; Ryden 1992; Weijmans et al. 2014).

Direct evidence for triaxiality comes from the observation of photometric twists, that is variations with radius of the projected major-axis position angle ($PA_{\rm phot}$). By approximating the galaxy constant luminosity surfaces with coaxial triaxial ellipsoids, it can be shown that their projection on the sky can result in elliptical isophotes with twisting $PA_{\rm phot}$ if their axial ratios varies with radius (Stark 1977; Benacchio & Galletta 1980). Isophote twists are often observed in ellipticals galaxies (e.g., Leach 1981) suggesting that these galaxies are indeed triaxial. On the other hand, the effects of triaxiality on the variation of $PA_{\rm phot}$ are model-dependent (e.g., Benacchio & Galletta 1980; Franx 1988; Madejsky & Moellenhoff 1990), and considerable twists (> 10 degrees) can be produced also in galaxies that are close to axisymmetry if viewed close to face-on (e.g., Pulsoni et al. 2018).

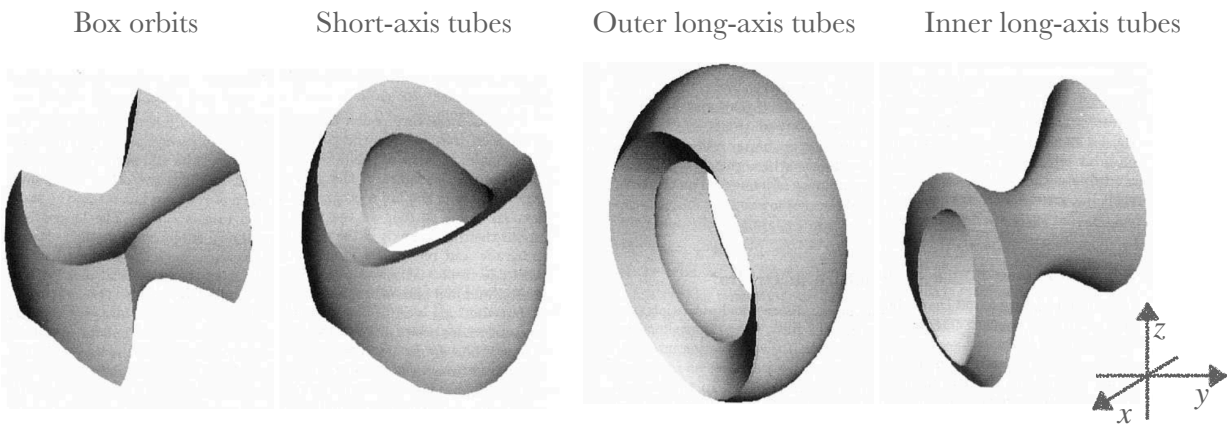

Figure 1.6: Main orbital families in a non-rotating triaxial potential, oriented as the coordinate system of coordinates sketched on the right where the x-axis is the major axis of the potential and the z-axis the minor axis (modified from Statler 1987).

The kinematic information is essential to limit the range of acceptable models as it provides insight into the internal structure of galaxies. This is because in a perfect triaxial mass distribution only three type of orbits are stable (Fig. 1.6): the box orbits, which do not contribute to the total angular momentum, the short-axis tube orbits, circulating around the potential's shortest axis, and the long-axis tube orbits, which circulate around the longest axis of the potential (de Zeeuw 1985; Binney & Tremaine 2008). Therefore, in a triaxial system, the angular momentum vector lies in the plane containing the short and the long axis, pointing in a direction determined by the relative importance of the two families of tube orbits. On the other hand, in an axisymmetric system the angular momentum is aligned with the symmetry axis of the system, which coincides with the short axis in the case of an oblate galaxy. This means that the observation of minor axis rotation, kinematic twists, and misalignments of the kinematic position angle $PA_{\rm kin}$ with the photometric $PA_{\rm phot}$ are generally considered as signatures of galaxy triaxiality (see e.g. Binney 1985; Franx et al. 1991).

IFS kinematics showed that most of the FRs are regular rotators with kinematic axes $PA_{\rm kin}$ (measured at $R \sim 1R_e$) essentially aligned with $PA_{\rm phot}$ (measured at $R \sim 2.5 - 3R_e$ Krajnović et al. 2011; Fogarty et al. 2015; Cappellari 2016, Fig. 1.7; see also Graham et al. 2018). This indicates that the family of FRs have shapes close to oblate, at least within $1R_e$. A large fraction of the non-regular rotators are instead kinematically misaligned, showing that these galaxies are generally triaxial (Krajnović et al. 2011).

By assuming oblate axisymmetric shapes (i.e., $p = 1$), the shape distribution $f(q)$ can be uniquely retrieved from the observed distribution of ellipticities. Weijmans et al. (2014) found that, for FR galaxies, $f(q)$ can be approximated by a gaussian with mean $\mu_q = 0.26$ and standard deviation $\sigma_q = 0.13$, while the slow rotators are much rounder, with $\mu_q = 0.63$ and $\sigma_q = 0.09$. By relaxing the assumption of oblateness, the intrinsic shape distribution can be only reconstructed by imposing some functional form for $f(q, p)$, and by incorporating the kinematic information by fitting both the observed ellipticity and kinematic misalignment distributions for random inclina-

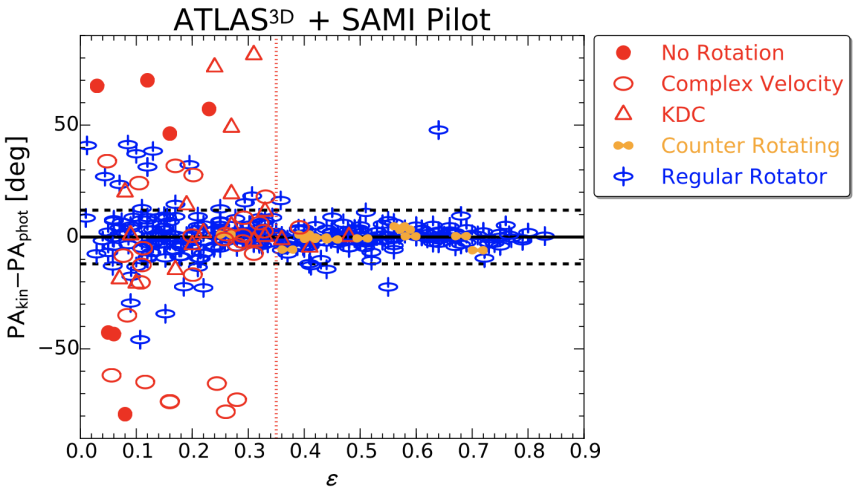

Figure 1.7: Difference between the kinematic, $PA_{\rm kin}(1R_e)$ and the photometric position angle, $PA_{\rm phot}(3R_e)$ as a function of the ellipticity in ETGs, distinguished according to their kinematic morphology as described in the legend (figure from Cappellari 2016). Most of the regular rotators are kinematically aligned, while a large fraction of the non-regular rotators are misaligned.

tions. A frequent assumption is that the intrinsic misalignment between the angular momentum and the intrinsic minor axis depends uniquely on the triaxiality of the systems (as defined in Eq. (5.3), Franx et al. 1991, but see also Bassett & Foster 2019). In this case, FRs are still found to have shapes close to oblate (Weijmans et al. 2014), with higher λ_e galaxies being flatter and axisymmetric, while lower λ_e systems have a higher occurrence of triaxiality (Foster et al. 2017). Massive SRs are instead consistent with being mildly triaxial (Ene et al. 2018; Li et al. 2018).

1.6 ETG formation and evolution

As described in the previous sections, the ETG family encompasses both ellipticals and lenticular galaxies, linked by their quenched star formation and by the similarity of their kinematic properties in the centers ($R \sim 1R_e$). Massive ETGs are mostly elliptical galaxies, they can reach total masses up to $10^{13} M_\odot$, and they are the oldest systems in the Universe. They form at high redshift ($z > 2$) and evolve through cosmic time by accreting mass hierarchically, so that more massive systems form through the accretion of less massive objects (White & Rees 1978; Peebles 1980). Therefore massive ETGs trace the star formation in the early Universe and represent the most evolved systems in the galaxy mass assembly process. On the other hand many of the low mass ETGs are lenticulars. Lenticular galaxies are relatively younger objects which are thought to be evolved from spirals (e.g., Laurikainen et al. 2010; Bellstedt et al. 2017a). For example, environmental interactions that depleted the gas content of the galaxy and effectively truncated the star formation (Gunn & Gott 1972; Moore et al. 1996; Larson et al. 1980) can be at the origin of S0s. However, the presence of field lenticulars, like NGC 3115, indicates that some of these galaxies are the results of internal effects (for example gas ejection by active nuclei, AGN, van den Bergh

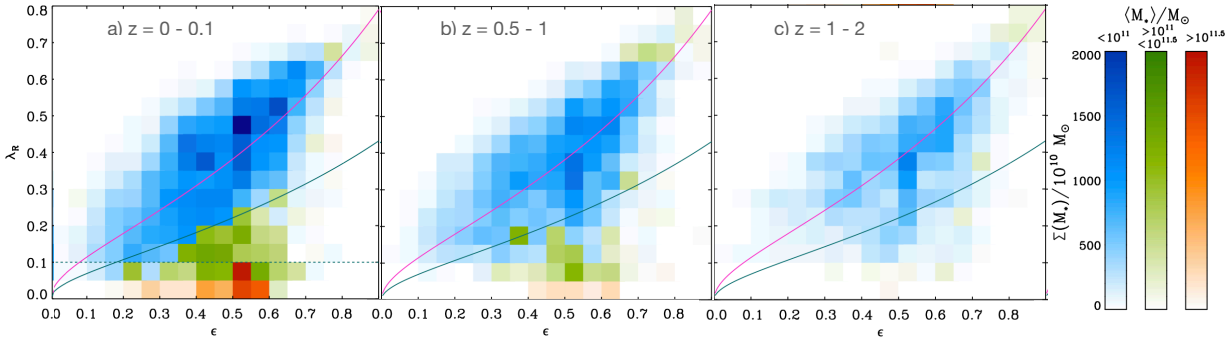

Figure 1.8: The evolution of the lambda-ellipticity diagram with redshift z in the Illustris simulation for the edge-on projections (adapted from Penoyre et al. 2017). The colour of pixels is defined by the average mass of the galaxies contained and its colour saturation by the total mass of the galaxies contained, normalized by the highest total pixel mass. At high z, the progenitors of present-day FRs and SRs are all fast rotating. The sequence of the SRs in the lambda-ellipticity appears only after $z = 1$ in the Illustris simulation.

2009) or even minor mergers of satellites (e.g., Wilman et al. 2009; Cortesi et al. 2013b).

The FR class therefore clearly includes very different objects, from lenticulars, to most of the low and intermediate mass ellipticals, as well as very massive galaxies. SRs instead are mostly massive galaxies and are generally found in the densest regions of clusters (Brough et al. 2017).

1.6.1 The two phase formation scenario

Observations and simulations indicate a rather unified formation scenario for both FRs and SRs in which stellar mass plays an essential role. This develops in two phases (e.g., Oser et al. 2010; Hilz et al. 2013; Rodriguez-Gomez et al. 2016).

In the first assembly phase, galaxies form from gas collapsing into dark matter halos producing turbulent rotating disk-like systems (e.g., Förster Schreiber et al. 2006; Genzel et al. 2006). At $z \gtrsim 1$ the progenitors of FRs and SRs are in fact indistinguishable (Penoyre et al. 2017; Lagos et al. 2017; Schulze et al. 2018, with Illustris, Eagle, and Magneticum, respectively, see Fig. 1.8). More massive galaxies rapidly assemble at higher z in the largest and densest dark matter halos (Gerhard et al. 2001; Thomas et al. 2009b), forming stars in intense bursts that produce highly compact systems which quickly quench their star formation (Daddi et al. 2005; Buitrago et al. 2008; van Dokkum et al. 2008; Damjanov et al. 2009). Lower mass galaxies tend to form later in less dense halos, where they acquire gas and form stars more gradually and slowly (e.g., Neistein et al. 2006; Cimatti et al. 2006).

The second phase of galaxy formation ($z \lesssim 1$) is characterized by a series of merger episodes, which enrich the galaxies with accreted stars (also called *ex-situ* stars, to contrast with the *in-situ* stars which instead are formed within the host, Abadi et al. 2006), and make them grow efficiently in size (Oser et al. 2010; Gabor & Davé 2012; Lackner et al. 2012; Buitrago et al. 2017). Early works showed that this was mainly driven by gas poor (dry) minor mergers (e.g Naab et al. 2009), but recent studies suggest that also major mergers are important (Rodriguez-Gomez et al.

2016, see also Chapter 6 of this thesis). The contribution of accretion to the galaxy stellar mass budget is a strong function of stellar mass. More massive galaxies can have accreted fractions larger than 80%, while lower mass systems are mostly made of in-situ stars and their accreted component is mainly deposited in the outskirts (e.g Cooper et al. 2013; Rodriguez-Gomez et al. 2016; Pillepich et al. 2018a; Tacchella et al. 2019; Davison et al. 2020).

1.6.2 How ETG stars acquire and loose specific angular momentum - the origin of the ETG bimodality

Galaxies acquire angular momentum primordially by gravitational torques induced by the large scale tidal field (Hoyle 1951; Peebles 1969). Then, by approximate conservation of the angular momentum, the collapsing star-forming gas builds up the galaxy rotation (Fall 1979; Fall & Efstathiou 1980). Therefore the high-z progenitors of present-day ETGs are mainly fast rotating systems (Penoyre et al. 2017; Lagos et al. 2017; Schulze et al. 2018).

During their evolution, galaxies undergo several physical processes that can lead to a gain or loss of rotational support. Since $z \sim 1$ ETGs tend, on average, to decrease rotation. The general picture emerging from different studies is that, in more massive galaxies galaxies ($M_* > 10^{10.5} M_\odot$), the decrease in specific angular momentum is mainly driven by the effects of major and minor mergers (e.g., Jesseit et al. 2009; Naab et al. 2014; Lagos et al. 2017, 2018b). Gas poor mergers in fact have the effect of increasing the mass and the velocity dispersion of the stars, while destroying ordered rotation (e.g., Jesseit et al. 2009) and redistributing angular momentum to stars at larger radii by dynamical friction (e.g., Hernquist 1992). Lower mass galaxies instead loose spin from environmental effects, such as interactions among galaxies and with the tidal field of the group or cluster (Choi & Yi 2017), unless they are able to continuously accrete gas and form stars. In that case they are able to sustain high rotation (Walo-Martín et al. 2020).

The family of SRs is found to evolve from the FRs between $z = 1$ and 0 through mergers events (Penoyre et al. 2017; Lagos et al. 2017; Schulze et al. 2018). Gas poor (dry) mergers are the most efficient in decreasing λ_e, although major mergers in circular orbits preferentially produce fast rotators (Naab et al. 2014; Lagos et al. 2018a,b). On the other hand, the cumulative effect of dry minor mergers rarely results in an increase of λ_e in the host (e.g., Qu et al. 2010). In general the presence of gas, either in the satellite or in the host galaxy, leads to a net spin-up (wet mergers, e.g., Naab et al. 2014; Penoyre et al. 2017).

Dry and wet mergers have a distinct impact on the shape of nuclear surface brightness profiles. The power-law profiles of low-mass ETGs are consistent with being produced by dissipative gas rich mergers. The subsequent nuclear starburst is likely responsible for the "extra light" often observed above the Sérsic profiles (e.g., Mihos & Hernquist 1994). Cores in massive ETGs are produced in dry major mergers, scoured by the orbital decay of the super-massive black holes binary which flings stars away while the two black holes merge (Faber et al. 1997; Thomas et al. 2014). The same should happen also in wet major mergers but, in that case, the core scouring can be compensated by the starbursts that produce the extra-light depending on the relative duration of the two processes (Kormendy et al. 2009; Krajnović et al. 2013b). Therefore the power-law galaxies are consistent with FRs, while the cores are hosted mainly by SRs and by some massive

FRs (Krajnović et al. 2013b).

The accretion of cold gas can, in principle, rebuild a disk component in a non-rotating merger remnant, therefore the SR progenitors need to undergo some quenching either prior or during the kinematic transformation (Lagos et al. 2020). In fact SRs are often found to be radio-loud and to have bright X-ray emission, indicating the presence of hot gas as well as AGN activity (e.g., Bender et al. 1989; Pellegrini 2005). The hot gas is thought to originate from the infalling gas into the massive dark matter halos, shock heated by the gravitational potential (e.g., White & Frenk 1991; Anderson et al. 2013). The energy output from the AGN is likely the heating mechanism that balances the cooling of the gas and keeps it hot (see Werner et al. 2019, for a review). On the other hand, AGN is considered the principal source of feedback limiting star formation in massive galaxies (e.g., Somerville et al. 2008; Lagos et al. 2020). The presence of an X-ray halo in massive systems protects the galaxies from accreting cold gas and from wet mergers (Kereš et al. 2005; Dekel & Birnboim 2006), therefore promoting the formation of SRs.

It is unclear whether the key ingredient in determining the different fate of FR and SR progenitors is only their stellar mass, or whether also the environment has an impact on λ_e. The density of the environment can influence the abundance and the geometry of the accreting gas as well as the merger history of the galaxies which, in turn, can impact the stellar rotation. The galaxy mass function does depend on the environment (e.g., Binggeli et al. 1988; Tempel et al. 2011; McNaught-Roberts et al. 2014) but, once stellar mass is fixed, the effect of environment alone on the evolution of the specific angular momentum, as well as of the role of major and minor mergers in shaping λ_e, is still debated (e.g., Brough et al. 2017; Greene et al. 2017; Wang et al. 2020).

1.7 The external regions of galaxies: the dark matter and the stellar halos

1.7.1 Dark matter halos

The first evidences of the presence of dark matter halos in galaxies come from the observations of the rotation curves in spiral galaxies (Rubin et al. 1962; Rubin & Ford 1970; Freeman 1970; Roberts & Whitehurst 1975). From extended measurements of emission-lines from cold HI gas, spiral rotation curves were found to remain flat out to tens of kpc without Keplerian drop off, while the exponential surface brightness profiles of the stars in the disk have typical scale radii of a few kpc, indicating the presence of additional mass at large radii (Bosma 1978). It is now common wisdom that the stellar components of galaxies are embedded in massive dark matter halos, with total masses roughly ten times that of the galaxies and extending out to hundreds of kpc (Macciò et al. 2008). These halos dominate the galaxy mass beyond $1 - 3R_e$ and therefore drive the dynamical properties of the galaxy external regions (e.g., Gerhard et al. 2001; Cappellari et al. 2006; Deason et al. 2012).

Techniques to measure halo masses include weak galaxy-galaxy lensing (e.g., Mandelbaum et al. 2006), which can also be used to measure the outer halo intrinsic shapes and generally indicate triaxiality (e.g., van Uitert et al. 2012), and strong lensing (Treu 2010). In massive

enough systems (above stellar masses $M_* > 10^{11} M_\odot$, where the X-ray luminosity is dominated by the gas emission and not from the X-ray binaries, e.g. Anderson et al. 2015), the X-ray hot gas can be used as an independent tracer of the dark-matter halo under the assumption of hydrostatic equilibrium (e.g., Fukazawa et al. 2006; Humphrey et al. 2012). Finally dynamical modelling of galaxies can constrain their total mass distribution and that of their dark matter halo, once the contribution from the baryons is subtracted (see Gerhard 2013 for a review of the different techniques listed above).

However, the study of the dark matter component in ETGs is observationally challenging compared to spirals, as ETGs generally lack of gas dynamical tracers (Courteau et al. 2014). At large radii, beyond $2-3R_e$, as the surface density of stars decreases quickly with radius ($\propto 1/R^2 - 1/R^3$), the stellar absorption lines become too faint to reliably deliver kinematic measurements. In addition, intermediate to high mass ETGs have surface brightness profiles with large Sérsic indices ($n \sim 4$ in Eq. 1.2, e.g. Kormendy et al. 2009), meaning that their stellar halos can span several degrees on the sky, while traditional IFU field-of-views cover only a few tens of arcsec. This makes imperative the use of alternative kinematic tracers such as, for example, planetary nebulae (PNe) and globular clusters (GCs) to overcome these limit and provide a two-dimensional mapping of the kinematics (more in Chapter 2). By modelling the kinematics and spatial distribution of these tracers, the galaxy total mass distribution and three dimensional shapes of the halos can be derived (e.g., Arnaboldi et al. 1998; Zhu et al. 2014; Alabi et al. 2016).

Constraining the orbital distribution in the anisotropic dispersion-supported elliptical galaxies is essential to relate their observed projected properties to their intrinsic structure. A notable example is the unexpected discovery of steeply decreasing outer velocity dispersion profiles in the intermediate-luminosity ellipticals NGC 4697 (Méndez et al. 2001), NGC 0821, NGC 3379, and NGC 4494 (Romanowsky et al. 2003) using PN observations. These quasi-Keplerian profiles were interpreted as indicating a lack of dark matter halos in ordinary ellipticals, thus posing a challenge to the current galaxy formation theories. However, the mass-anisotropy degeneracy (see Sect. 1.3.4) can easily reconcile the decreasing dispersion profiles with the presence of dark matter halos if the orbits are radially biased, as demonstrated later by the dynamical models from de Lorenzi et al. (2008, 2009) and Morganti et al. (2013).

Therefore, the complex dynamics of gas poor ETGs requires detailed kinematic and photometric mapping from their central regions out to their outskirts. To this end, halo kinematic measurements from stellar tracers are essential for dynamical modelling of the galaxy orbital distribution and the three dimensional mass content.

1.7.2 Stellar halos

The luminous central regions of galaxies are surrounded by diffuse stellar envelopes called stellar halos (e.g., Schombert 1986, 1988). These are often observed as additional light to the extrapolations of the inner luminosity profiles out to large radii (e.g., Huang et al. 2013b; Spavone et al. 2017; Kluge et al. 2021). The fact that halos typically contain a small fraction of the stellar mass of the galaxies, combined with the observational challenges of studying low surface brightness regions, has delayed the scientific exploration in this component to relatively recent

times (e.g., Zheng et al. 1999; Forbes et al. 2003). The investigation of stellar halos is today a hot topic of research in both observational and theoretical studies, as they provide unique insight into the galaxy assembly histories as well as information on the nature of dark matter and on the properties of the dark matter halos.

The current understanding for the origin of the stellar halos is that they mainly assemble in the second phase of the galaxy formation through the hierarchical merging of smaller satellites (Bullock & Johnston 2005; Abadi et al. 2006). Extended low-surface brightness features in the form of streams, shells, and ripples (e.g., Malin & Carter 1983; Janowiecki et al. 2010; Iodice et al. 2017; Mancillas et al. 2019), which often stand out as kinematic substructures (e.g., Longobardi et al. 2015b), are commonly observed in the outskirts of galaxies. These tidal debris that are stripped away from infalling satellites contain information on the most recent dynamical phase of the galaxy mass assembly history.

Another evidence for the ex-situ nature of the stellar halos comes from the observation of variations with radius of stellar population properties in massive ETGs. Halos are typically less rich in α-elements and more metal-poor than the galaxies (e.g., Coccato et al. 2010b; Johnston et al. 2018), indicating that, while the central regions are formed rapidly at early times, the halo components are made of stars formed in low-mass satellite galaxies with more extended star formation. The spatial segregation of the in-situ stars in the central regions and of the ex-situ component in the outskirts is predicted by cosmological simulations and is a direct consequence of the two-phase formation scenario (Bullock & Johnston 2005; Cooper et al. 2013; Rodriguez-Gomez et al. 2016).

Because of the long relaxation times in the galaxy outskirts, stellar halos maintain memory of the details of the accretion events even after the full disruption and the phase mixing of the accreted stars (Eggen et al. 1962; Binney & Tremaine 2008). The spatial distribution and the kinematic of the accreted stars depends on the mass and the internal structure of the accreted satellite, as well as on its infall time and orbit (e.g. Amorisco 2017). Satellites infall on loosely bound orbits (e.g., Benson 2005; Wetzel 2011) and progressively loose energy by dynamical friction, which drags them towards the center. More massive and denser satellites can sink deeper into the gravitational potential of the host, while stars from less massive galaxies are more easily stripped and are mainly deposited in the outskirts (Rodriguez-Gomez et al. 2016; Amorisco 2017). In major mergers, violent relaxation (Lynden-Bell 1967) efficiently mixes in-situ and accreted stars and rearranges the distributions of dark and luminous matter in the energy space yielding higher dark matter fractions in the central regions (e.g., Hilz et al. 2012). Therefore galaxies can be though as layered structures where different stellar populations are overlapped and mixed together by mergers: minor mergers tend to enhance population gradients, while major mergers act in the opposite direction.

Investigating the spatial distribution of stars and their kinematics out to very large radii can shed light into the mechanisms that regulate the buildup of galaxy mass and their evolution.

1.8 This thesis

The past decade was characterized by an important progress in our understanding of the dynamical structure of the central regions of ETGs thanks to the work of IFS surveys. This imposed a new paradigm for the ETGs that distinguishes between FRs and SRs based on the kinematic properties in the central regions ($\sim$ 1 Re, Emsellem et al. 2011; Graham et al. 2018; van de Sande et al. 2020). The structural properties of ETGs at large radii, however, remained poorly explored. This investigation is in fact hampered by the observational difficulties that characterize the study of low surface brightness components, which are particularly severe for stellar spectroscopic measurements. Kinematic studies of ETGs from integrated-light spectra out to large radii using long slit spectroscopy or IFS are available for individual objects or small samples (e.g., Kelson et al. 2002; Weijmans et al. 2009; Coccato et al. 2010a; Murphy et al. 2011; Boardman et al. 2017; Barbosa et al. 2018), and only recently the the SLUGGS (Arnold et al. 2014; Foster et al. 2016) and the MASSIVE surveys (Raskutti et al. 2014; Veale et al. 2017b) generated two-dimensional kinematic maps for larger samples of ETGs. These studies never reach beyond $3-4R_{\rm e}$ and their results are often conflicting, with no definite picture on whether or not galaxies display kinematic changes with radius (see for example the results of Foster et al. 2016 against those of Raskutti et al. 2014 and Boardman et al. 2017). In particular it is unclear whether the FR/SR classification is limited to the central regions or whether also the halos of FRs and SRs have systematically different properties (as argued by, e.g., Cappellari 2016). The fact that the outer regions of galaxies are dark matter dominated indeed does not guarantee that the dynamical properties measured in the central $\sim 1R_{\rm e}$ extrapolate to larger radii.

In addition, the class of FRs includes a variety of objects with a large range of stellar masses and that most likely formed and evolved in very different circumstances, as predicted by cosmological simulations (e.g., Naab et al. 2014). Then the natural question is whether a kinematic classification based uniquely on measurements confined to the central $\sim$ 1 Re are enough to fully represent the properties of these objects. The question is even more compelling when considering the fact that the outer regions of galaxies are expected to be mostly accreted and that the prominence of this accreted component is a function of stellar mass (e.g., Rodriguez-Gomez et al. 2016). In particular, a consequence of the two phase formation scenario is the presence of gradients with radius of stellar population properties. Because of the different origin of central and halo regions, corresponding trends in the structural properties of galaxies are in principle expected. For example, kinematic transitions from rotating central regions to dispersion dominated halos have been interpreted as signatures of transitions from in-situ dominated to ex-situ dominated components (e.g., Coccato et al. 2009; Arnold et al. 2014; Foster et al. 2016). From the theoretical side, unfortunately, most of the work on simulated ETGs from cosmological simulations is focused on the kinematic properties of the central regions (e.g., Naab et al. 2014; Penoyre et al. 2017; Schulze et al. 2018). The only notable exception is the work of Wu et al. (2014), who presented a detailed photometric and kinematic analysis of simulated ETGs out to their halos. However, the properties of these galaxies do not adequately reproduce the observed properties of the FRs (e.g., see Chapter 4).

This thesis is a study of the photometry, intrinsic shape, kinematics, and angular momentum of ETGs out to large radii, in both observations and simulations, and of their origin. The goal is

to characterize the structural properties of the stellar halos of these galaxies and relate them to their accretion history. To this aim, I am collaborating with the ePN.S survey (Arnaboldi et al. 2017) to investigate the kinematics of 33 nearby ETGs at large radii, using planetary nebulae (PNe) as tracers of the halo stellar population. This study builds upon the work of Coccato et al. (2009) and extends the analysis to more than twice the previous sample size. This allows to characterize the kinematic behavior of stellar halos in a statistically significant sample of ETGs with homogeneously validated data, to establish the presence of radial trends, and to draw conclusions for the properties of the FR and SR galaxies at large radii.

Then, using the state-of-the-art IllustrisTNG cosmological magneto-hydrodynamical simulations, I am comparing and explaining the observational results from PN observations in terms of the galaxy merger histories. To this end, I am selecting a sample of ETGs with properties consistent with real galaxies, deriving their photometry and kinematics, and modelling them to appropriately compare with the observations. I am relating the structural properties of the simulated ETG stellar halos to their accretion history by studying the impact of different mass-ratio mergers, of the fraction of accreted cold gas, and of the recent in-situ star formation.

This thesis is organized as follows:

- Chapter 2 introduces the PNe as kinematic tracers of ETGs at large radii, describing how well PNe trace the galaxy stellar population and the main techniques used for PN detection. It presents the ePN.S survey and its scientific goals.

- Chapter 3 introduces the cosmological hydrodynamical simulations as a tool for understanding galaxy evolution in a cosmological context. It describes the physical processes included and the main observables that are reproduced. Then it focuses on the IllustrisTNG project, detailing the modelling of the astrophysics, the calibration, and the first results on galaxy properties that are relevant for our work.

- Chapter 4 reports the kinematic results from the ePN.S survey published as Pulsoni et al. (2018). These revealed that ETGs have a larger variety of kinematic behaviors in the halos than they do in their central regions. The observed properties suggest that at large radii FRs and SRs have more similar structures.

- Chapter 5 extends the kinematic and photometric investigation to simulated ETGs from the IllustrisTNG simulation, which are found to reproduce the diversity of kinematic properties measured in ETG halos: the kinematic trends with radius found in observations are connected to changes in the intrinsic shape of galaxies. At large radii, FRs and SRs do not exhibit clear qualitative differences in their structural properties. These results were published in Pulsoni et al. (2020).

- Chapter 6 shows how galaxy accretion history modifies the structure of stellar halos and determines the observed variety of properties. The properties of ETG stellar halos are largely determined by the balance between the in-situ and ex-situ components, which depends on stellar mass. In low mass systems, the in-situ stars determine peaked rotation

profiles and near-oblate shapes with flattening decreasing with radius. In high mass systems, accretion generates local correlations between rotational support, shapes, and ex-situ fractions, and dynamically couple the stellar to the dark matter halo. These results were published in Pulsoni et al. (2021).

- Chapter 7 summarizes the main results of the thesis and discusses their implications.

Chapter 2

PNe as kinematic tracers in ETGs at large radii

Kinematic measurements of ETG stellar halos are observationally challenging. ETGs contain little amounts of cold gas, therefore kinematic measurements typically rely on integrated-light absorption-line spectroscopy. At increasing distance from the center, as the surface density of stars decreases as $1/R^2 - 1/R^3$ (depending on the galaxy) and drops below the sky background level, the signal-to-noise ratio of the absorption-lines deteriorates quickly. This limits the kinematic measurements from traditional long-slit spectroscopy to the central $1 - 2R_e$. Other techniques include the use of integral field units (IFU) to scan along the galaxy major axis (e.g., Weijmans et al. 2009) which, coupled with long exposure times, are able to achieve enough signal-to-noise for extracting kinematic information out to $3 - 4R_{\rm e}$. This approach, however, is strongly limited by the small field of view of the IFU, with typical diameters of a few tens of arcsec, which hampers a complete spatial coverage of the stellar halos in nearby galaxies[1] and hence miss any off-axis rotation. Wide-field spectrographs sampling the two-dimensional kinematics using multiple slits are able to overcome this problem at the cost of a lower signal-to-noise ratio which effectively reduces the probed radial distances to $2 - 3R_{\rm e}$ (e.g., Arnold et al. 2014; Foster et al. 2016). The only possibility to achieve a two-dimensional kinematic mapping out to the very outskirts of a large sample of galaxies is through alternative tracers of the stellar kinematics that overcome the limit of the decreasing surface brightness. Planetary nebulae (PNe, e.g., Coccato et al. 2009) and globular clusters (GCs, e.g., Schuberth et al. 2010; Strader et al. 2011) are the most commonly used.

Low mass stars ($1 - 8M_{\odot}$) at the end of their life generate a PN when they reach the end of the asymptotic giant branch phase and become unstable, characterized by pulsations and strong winds. These disrupt and expel the outer layers of the stars exposing their hot cores. The expanding outer shells, ionized by the UV photons from the cores, glow by emitting several emission lines from the UV to the near-infrared. The brightest is the [OIII] line at 5007 Å, which has been shown to contain up to 15% of the energy emitted by the central star (Dopita et al. 1992, see

[1] A diameter of $2 \times 4R_{\rm e}$ for a galaxy at 20 Mpc distance and with a typical $R_{\rm e}$ = 3 kpc corresponds to a diameter of 500 arcsec on the sky.

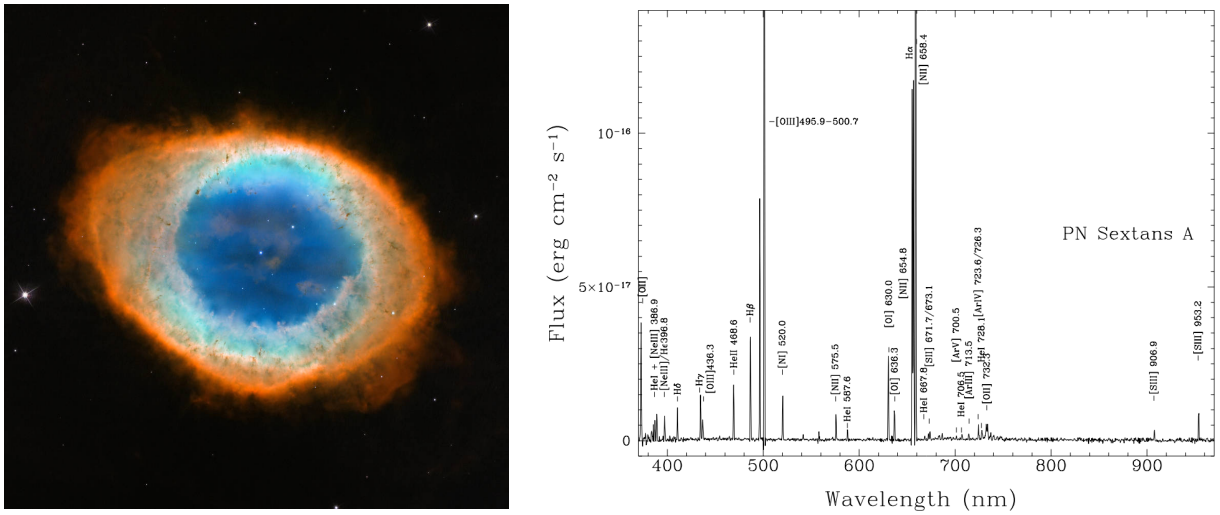

Figure 2.1: **Left**: M57 (the Ring Nubula) is an example of planetary nebula. The image is colored to illustrate the PN composition: the deep blue color shows the helium emission, the light blue color of the inner ring is that of the hydrogen and the oxygen. The red color of the outer ring is from nitrogen and sulfur emission. At the center of the nebula, the white dwarf is visible as a tiny white dot (credits: NASA, ESA and the Hubble Heritage (STScI/AURA)-ESA/Hubble Collaboration). **Right**: VLT spectrum of a planetary nebula in Sextans A (from (Magrini et al. 2005)).

Fig. 2.1). This bright line stands out against the faint galaxy background and it is detectable for kinematic measurements up to distances of $\sim$ 100 Mpc (in the Coma cluster as in Gerhard et al. 2007).

Since the PNe are drawn from the main stellar population of the ETGs, their number density is proportional to the galaxy surface brightness and their kinematic directly traces that of the stars (see Sect. 2.2). Even though GCs are generally more abundant than PNe, their relation to the underlying stellar population is less straightforward. For example, accreted low-mass systems can contribute to a larger fraction of GCs than PNe and light, meaning that the GC kinematics is more likely to follow the accreted stars than the overall stellar population (Coccato et al. 2013). Recent works, however, suggest that the red, metal-rich GCs are tracers of the host galaxy properties (Fahrion et al. 2020; Dolfi et al. 2020).

The observational work presented in this thesis is based on PNe measurements. Therefore in this chapter I focus only on PN detections and on their properties as kinematic tracers.

2.1 Detecting planetary nebulae

PNe are detected through their [OIII] emission line. This is easily identifiable in the outer regions of galaxies where the stellar continuum is faint. In the central regions, where the galaxy is bright and absorption-line spectroscopy is possible, only the brightest PNe can be observed. There, the kinematic information from PNe is naturally incomplete and needs to be integrated

with observations from integrated light for a full picture of the galaxy properties. In this sense, absorption-line spectroscopy and PN kinematic measurements are complementary to each other.

2.1.1 Detection techniques

Extra-galactic PNe can be detected through the one of following techniques.

- **On-off technique** - PNe can be revealed as point-like objects in narrow-band images centered on the [OIII] line (at the redshift of the target) that do not appear in a broad-band or off-band image (Jacoby et al. 1990). The PN line-of-sight velocity is then measured through a spectroscopic follow-up of the detected point-like sources.

- **Counter-dispersed imaging** - This technique allows the simultaneous measurement of the PN positions and line-of-sight velocities (Douglas & Taylor 1999). The field of interest is images through a slit-less spectrograph tuned to the [OIII] line at the redshift of the galaxy. Objects with a continuum emission appear as strikes on the counter-dispersed image, while the mono-chromatic PNe appear as dots. The PN velocity can be measured when a second image is taken after rotating the spectrograph by 180°: the PN velocity is in fact proportional to the difference in the PN position between the two images (see Fig. 2.2). The double counter-dispersed imaging is done either in two consecutive, reversed exposures or simultaneously, using duplicate spectrograph arms as in the Planetary Nebula Spectrograph (see Sect. 2.3.1). A similar approach is the one utilised by Méndez et al. (2001), which uses an on-off technique to detect PNe plus a slitless dispersed image. The PN line-of-sight velocities are in this case measured from the shift in positions in the dispersed image compared to the undispersed on-band image.

- **Multi-slit imaging** - This technique is used for observing distant faint PNe with flux comparable to the sky background noise. It combines a mask of parallel multiple slits with a narrow-band filter, centered around the [OIII] line at the redshift of the target (Arnaboldi et al. 2007). The monochromatic PN emission is collected in a small number of pixels in the two-dimensional spectrum, while the sky emission is dispersed in wavelength. This reduces the sky-noise by a factor of 5-10 (Gerhard et al. 2005).

- **IFS** - IFS observations can be also be used to detect PNe. However, compared to the methods described above, the PN detection is limited by the small field of view of the IFU, as already commented above. This effectively restricts the use of this technique only to the bright central regions of galaxies. There, the PNe emission lines are isolated in the observed spectrum after modelling and subtracting the contribution from the galaxy integrated stellar spectrum (Sarzi et al. 2011).

2.1.2 Contaminants

The highest source of contamination in PN detections are from unresolved, point-like, background [OII] emitters at $z \sim 0.34$ and from Lyman alpha (Ly-α) galaxies at $z \sim 3.12$ (Kudritzki

et al. 2000). These emission lines, once red-shifted, fall in the range of wavelength typically measured for the PNe. In the PN.S counter-dispersed images, the resolution of the PN.S allows to recognize and reject detections of [OII] emitters, as their oxygen doublet at 3726 − 3729 Å is resolved in wavelength. A fraction of the Ly-α galaxies can be identified as spatially resolved sources. Those that are unresolved can be in part identified and removed by comparing their measured velocities to the galaxy line-of-sight velocity distribution, as the Ly-α approximately distribute uniformly in velocity range selected by the band-pass of the narrow-band filter. The amount of contamination can be evaluated by using background emission galaxy surveys (as Gronwall et al. 2007, see Longobardi et al. 2013 for more details), or with additional observations with a Hα narrow band filter. Arnaboldi et al. (2003) demonstrated that a combination of [OIII] and Hα imaging is an efficient tool to distinguish PNe from high-redshift emission-line galaxies.

2.2 PNe as tracers of the stellar populations

Numerous studies demonstrate that the properties of the galaxy PN population trace those of the bulk of its stars in both elliptical (Coccato et al. 2009) and lenticular galaxies (Cortesi et al. 2013b). Their logarithmic number density profiles with radius are proportional to the surface brightness profiles of the hosts, and their kinematics agrees, within errors, with the kinematics of stars in the regions of overlap. These characteristics make PNe the ideal probes for stellar kinematics in ETG halos.

The relation between the total number of PNe, N_{TOT}, and the total bolometric luminosity of the galaxy, L_{bol}, is parametrized by the so-called α parameter: $N_{TOT} = \alpha L_{bol}$. Observationally, the value of the α parameter is found to be linked to the metallicity and star formation history of the parent stellar populations (e.g., Hui et al. 1993). For example, an empirical relation between α and color suggests a systematic change of the α-parameter with the morphological type of the host galaxy (e.g., Buzzoni et al. 2006). For the red and old stellar populations in ETG halos, typical values of $\log \alpha$ range from -6.5 to -7.

Extended PN studies that investigated the ETG outermost halos, at several tens of kpc distant from the center (Longobardi et al. 2013; Hartke et al. 2018, 2020), revealed variations of the α parameter with radius caused by the increased contribution of intra-cluster or intra-group light at large radii. This blue, metal-poor component (with metallicity -0.5 to -0.1 solar) is associated with a higher α than the halo, meaning that it contributes to a larger number of PNe than the halo stellar population (with solar metallicity or higher) for the same bolometric luminosity. In these cases, where strong variations of stellar populations are observed, care must be taken to statistically separate the PN populations (see e.g., Longobardi et al. 2015a; Hartke et al. 2018).

2.3 The extended PN.S ETG survey

Starting from the first observations of Nolthenius & Ford (1987), PNe have been used to trace the kinematics and dynamics in ETGs. Early results showed that the outer regions of ETGs can

contain some angular momentum even though the cores are non-rotating (Arnaboldi et al. 1994) and that minor axis rotation can be important at large radii, where halos can become triaxial (Peng et al. 2004). The finding of decreasing outer velocity dispersion profiles (Romanowsky et al. 2003) has emphasized the presence of orbital anisotropy at large radii, with increasing contribution from radial orbits (e.g., de Lorenzi et al. 2008).

The extended Planetary Nebula Spectrograph (ePN.S) survey (PI: Magda Arnaboldi) investigates the kinematics, the dynamics, the angular momentum, and the mass distribution in the halos of 33 nearby ETGs (distance $\leq$ 25 Mpc) using PNe as tracers (Arnaboldi et al. 2017). The survey is mainly based on PN observations from the Planetary Nebula Spectrograph (25 out of 33 galaxies, see Sect. 2.3.1), but it also includes observations from the literature and two new counter-dispersed imaging observations from FORS2@VLT (hence the attribute "extended" in the name of the survey). Some of the ePN.S galaxies have been the subject of previous studies (e.g., Douglas et al. 2007; Coccato et al. 2009; de Lorenzi et al. 2009; Napolitano et al. 2009, 2011; McNeil-Moylan et al. 2012; Cortesi et al. 2013a), which established many of the techniques for the analysis of the PN data used in this thesis.

2.3.1 The Planetary Nebula Spectrograph

The Planetary Nebula Spectrograph (PN.S) is a custom built instrument for simultaneous counter-dispersed imaging commissioned at the 4.2 m William Herschel Telescope in La Palma (Douglas et al. 2002). It uses a matched pair of gratings and cameras that create the effect of two identical spectrographs back to back. The incoming light from the telescope hits the two gratings butted together and is split in two identical beams, dispersed in opposite directions.

An example of the pair of images collected by the two arms of the spectrograph is shown in Fig. 2.2. Each PN is slightly displaced from its true position on the sky by an amount Δx determined by its exact emission wavelength, and hence by its velocity. Thus by matching the PNe in pairs in the final images, one directly obtains relative velocities and positions.

The clear advantage in observing PNe with the PN.S is that it uses the same observing time of an on-off band detection, but it delivers both positions and line-of-sight velocities. In addition, a PN detection in a PN.S observation comes from a pair of matching events in two images, hence there is more signal redundancy than a single peak of the same significance in a on-off band image.

To translate the difference in PN positions Δx in velocities, an arc line calibration is needed to correct for internal distortions and differences between the optics of the cameras. This is done by shining Cu-Ne-Ar lamps against a calibration mask placed in the focal plane of the instrument to create a map of the all the distortion terms. This procedure allows to measure line-of-sight velocities with an accuracy of $\sim$ 28 km s^{-1}. The final step of the calibration is to obtain accurate astrometry for the newly found PNe, by considering the intensity-weighted average positions of a few foreground stars in the two counter-dispersed images: (x_L, y) and (x_R, y): the mean $[(x_L + x_R)/2, y]$ can be considered as "true" stellar positions to compare with astrometric catalogs and obtain a plate solution.

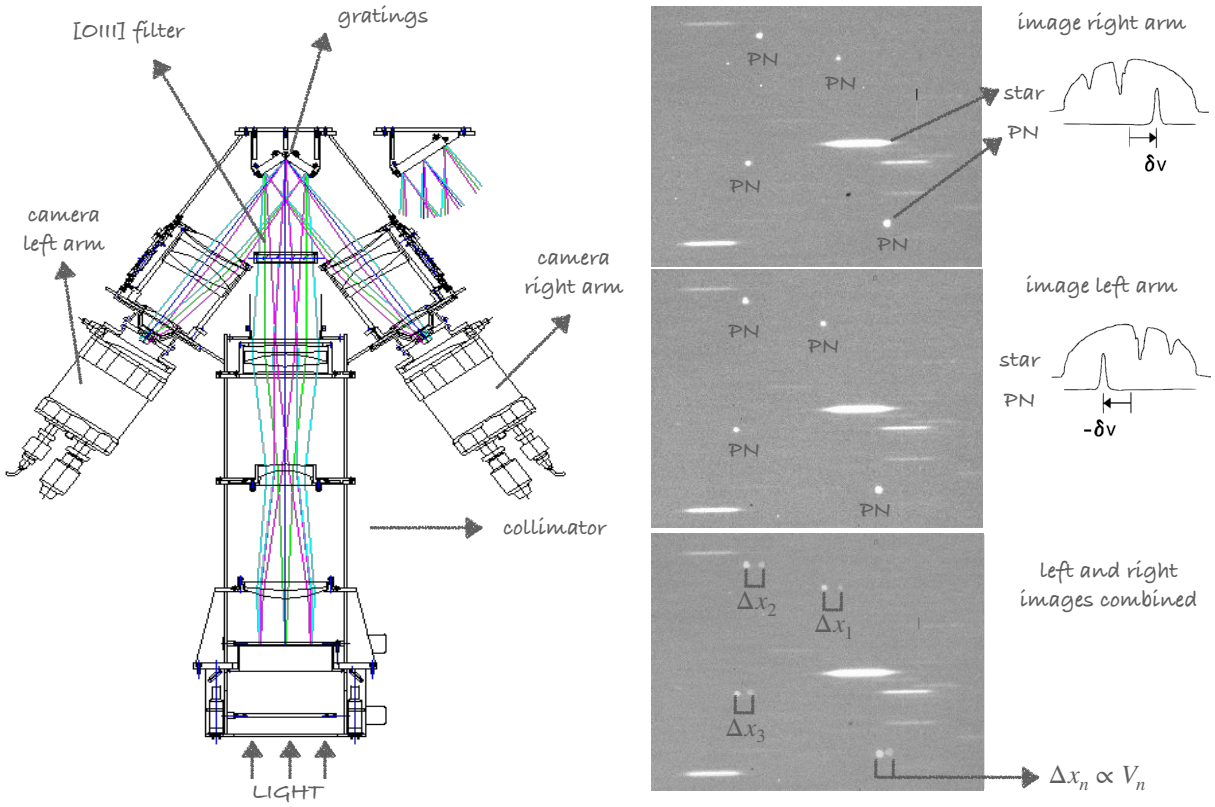

Figure 2.2: **Left**: Schematic representation of the PN.S, with the different components highlighted by the labels (adapted from Douglas et al. 2002). **Middle:** The dispersed images from the left and right arms. On the bottom is the combined image showing the difference in position of the PN images used to derive their true position and line-of-sight velocities. **Right**: Schematic image of a star and a PN dispersed by each arm of the PN.S (adapted from Douglas et al. 2002).

2.3.2 The sample of ETGs and validation of the PN catalogs

The ePN.S sample has been chosen to cover a wide range of structural parameters such as luminosity, central velocity dispersion, ellipticity, and isophotes shapes, in order to obtain a representative group of nearby ETGs. This includes lenticular galaxies, disky ellipticals, as well as massive fast and slow rotators, and three recent merger remnants (see Table 4.1 in Chapter 4).

All catalogs were uniformly validated for completeness and removal of spurious detections and kinematic outliers (Arnaboldi et al. in prep.). The contribution from any nearby satellites is identified using the probability membership method from McNeil-Moylan et al. (2012), which assigns to each PN the probability of belonging to the host or to the satellite based on both kinematic and photometric information. Each Bona Fide PN catalog produced contains positions, line-of-sight velocities, and magnitudes for 20 to more than 1000 PNe, depending on the mass of the galaxy, its distance, and the radial coverage of the data.

With a total of 8636 tracers, the ePN.S is the largest catalog to-date of extra-galactic PNe and, for the first time in such a large sample of ETGs, it extends the investigation of the stellar kinematics out to 6 Re on average.

Chapter 3

Cosmological hydrodynamical simulations

Cosmological simulations are an essential tool to understand galaxy evolution which allow to explore a large variety of astrophysical questions (see Somerville & Davé 2015 and Naab & Ostriker 2017 for a review). They model galaxy formation *ab initio*, starting from a nearly homogeneous initial density field of dark matter and gas at high redshift that simulates the primordial power spectrum of density fluctuations. Its evolution over cosmic time is derived by simultaneously solving equations for gravity, hydrodynamics, and thermodynamics for the particles or grid cells representing dark matter, stars, and gas.

Gravity drives the collapse of the dark matter halos, their growth through merging and accretion, and their clustering. The hydrodynamics and thermodynamics, together with gravity, and coupled with models for galaxy formation, model the gas physics, simulate flows and shocks, and determine the efficiency of gas cooling and dissipation of thermal energy in radiative processes. When the inter-stellar medium (ISM) becomes cold and dense, and exceeds some density or pressure threshold, it can start forming stars according to the adopted star formation model.

Despite differences in modeling, current cosmological hydrodynamical simulations agree in including a core set of physical processes that are considered fundamental in determining the formation and evolution of galaxies, their stellar and gas content, their structure, and their relation with the environment. Star formation is regulated at low and high galaxy masses, by including, respectively, stellar and AGN *feedback mechanisms*. These processes are commonly invoked to counter-act the gas cooling by transferring thermal and mechanical energy to this component. Simulations also model black hole formation and growth and follow the chemical evolution of the gas, which gets enriched with heavy elements from stellar ejecta and supernova (SN) explosions.

The complexity and challenge of cosmological hydrodynamical simulations lies in the numerous physical processes that interact with each other and influence a wide range of spatial scales, from sub-pc scales of individual stars to Mpc scales of clusters. Modern large-volume simulations can simulate cosmological boxes of tens to hundreds of comoving Mpc with spatial resolution of the order of $\lesssim$ 1 kpc, as in Illustris (Genel et al. 2014; Vogelsberger et al. 2014), IllustrisTNG (see Sect. 3.2), EAGLE (Schaye et al. 2015), Horizon-AGN (Dubois et al. 2015), Romulus (Tremmel et al. 2017), Simba (Davé et al. 2019), Magneticum (Teklu et al. 2015).

The extreme span of physical scales of the processes involved in galaxy formation, combined with the uncertainties on the physics at small scales, makes necessary the use of sub-grid mod-

els to reduce the dynamical range of the processes that are explicitly simulated and make the computational cost feasible. These sub-grid recipes describe the effects of physical process that happen on scales below the resolution level with simple analytical models integrated with the resolved hydrodynamical and gravitational scales. The free parameters of these models are then calibrated to match the observations.

A technique to increase the resolution of a simulated single galaxy or halo and its environs is *zoom simulations*. They start from a coarse-grain simulation of a cosmological volume to $z = 0$ and trace back in time all the mass within the region of interest to the starting z. This mass is re-evolved sampled at much higher resolution, while maintaining the surroundings coarser to provide the tidal field from the large scale structure. Typically the hydrodynamics is turned on only in the zoom region. Zoom simulations can reach spatial resolutions of a few tens of pc and allow the study of small-scale phenomena and the structural properties of the stellar and gaseous components, such as, for example, the internal structure of disks and their ISM. On the other hand they are limited to the study of a few selected objects and can not make statistical inferences on populations (e.g., Hopkins et al. 2014; Wang et al. 2015; Sawala et al. 2016; Grand et al. 2017; Bahé et al. 2017; Tremmel et al. 2019).

3.1 Reproducing galaxy properties

Simulations rely on a key set of observations that provide crucial constraints on the models. These include statistical distributions of global galaxy properties at different cosmic times (i.e., for example, the stellar mass function) and global scaling relations such as those between stellar mass and the star formation rate, the mean gas fraction, and the metallicity of stars and ISM. Models are proving successful in reproducing most of these quantities by tuning not only the free parameters of the sub-grid models but also the implementations of these models. However, some difficulties in reproducing observables at particular epochs or mass regimes are revealing some issues in our understanding of the actual physical processes (see Somerville & Davé 2015, for a review).

A fundamental observable that simulations need to reproduce is the luminosity function or the stellar mass function of galaxies (Blanton & Moustakas 2009), which is not naturally predicted by the ΛCDM paradigm (e.g., White & Frenk 1991). This issue can also be visualised in terms or the relation between stellar and dark matter halo mass as a function of halo mass (Behroozi et al. 2013), as shown in Fig. 3.1, which is a strongly peaked function at halo masses $\sim 10^{12} M_{\odot}$. This can be understood as strong decrease in the conversion efficiency of baryons into stars at low and high halo masses. In order to reduce this efficiency, models controlling star formation are invoked. It is now common wisdom that star formation feedback plays a crucial role in shaping the stellar-halo mass relation for halos with masses below $10^{12} M_{\odot}$, while at high masses AGN feedback dominates. The presence of AGN feedback is also required to maintain the gas in massive halos hot at X-ray temperatures (the "cooling flow problem", see McNamara & Nulsen 2007) and to keep massive galaxies quiescent. Even if signatures of BH-activity are commonly observed in the form of jets, the details of how these jets couple with the surrounding gas, how effective they are in exchanging energy with it and actually quench star formation are still unclear.

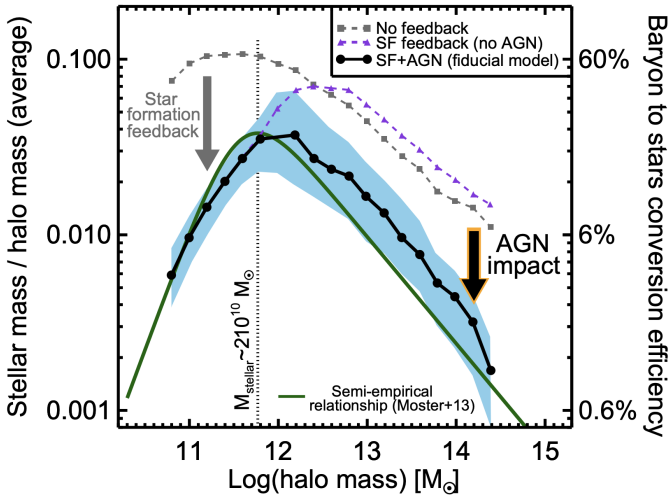

Figure 3.1: The ratio between the stellar mass and the halo mass as a function of halo mass. The semi-empirical relationship (Moster et al. 2013) is compared with three runs of a simulation from Somerville et al. (2008) with no feedback, including stellar feedback, and including stellar and AGN feedback (for this latter the quartiles of the distribution are also shown as shaded regions). The right y-axis shows the conversion efficiency of the available baryons into stars, determined as $M_*/[f_b \times M_{halo}]$, where the factor $fb = 0.17$ is the cosmological baryon fraction (figure from Harrison 2017).

This is reflected, for example, by the difficulty of models in quantitatively reproducing the red sequence in the color-mass distribution of galaxies (e.g., Gabor & Davé 2012; Vogelsberger et al. 2014), and by the on-going theoretical effort in updating the BH-feedback models as in the IllustrisTNG simulations (Weinberger et al. 2017).

Stellar feedback, on the other hand, has been proved fundamental to reproduce realistic disk galaxies. Early simulations produced compact disks with large spheroids and low angular momentum (the so-called "angular momentum catastrophe"). This was due to an over-cooling of the gas and, consequently, to an over-efficient star formation at early time in low mass galaxies. These then assembled in present-day galaxies in dry-mergers which dissipated angular momentum and produced spheroids (Maller & Dekel 2002). Increasing the resolution of the simulations and including efficient star formation feedback that counter-act the excessive gas cooling have proved to solve the problem (e.g., Okamoto et al. 2005). Stellar winds, preferentially expelling low angular momentum gas from the center of the galaxy into the halo, created a gas reservoir which can then be re-accreted at later times with angular momentum enhanced by non-linear gravitational torques or by mixing with the rotating halo gas (Marinacci et al. 2011; Brook et al. 2011; Übler et al. 2014). This gas reservoir plays a major role in the regrowth of the discs and in sustaining star formation even after merger events (e.g., Governato et al. 2009), while the decreased baryonic mass of small satellites reduces the growth of the spheroidal component at early times.

The new generation cosmological simulations are able to produce a rich variety of galaxy morphologies and to resolve the dynamical and stellar population properties of galaxies. The

observed trends between stellar populations, internal galaxy properties, and environment are qualitatively predicted, although some of the structural scaling relations such as, for example, the Faber-Jackson relation, are still reproduced with some offset with respect to the observations (e.g., van de Sande et al. 2019).

3.2 The IllustrisTNG simulations

In this section I focus on the IllustrisTNG simulations, which are used in Chapters 5 and 6 of this thesis. The IllustrisTNG simulations is a suite of cosmological magneto-hydrodynamical simulations for the formation and evolution of galaxies within the ΛCDM paradigm, starting from $z = 127$ to present day $z = 0$ (Springel et al. 2018; Pillepich et al. 2018a; Naiman et al. 2018; Marinacci et al. 2018; Nelson et al. 2018). IllustrisTNG builds and improves upon the Illustris simulation (Genel et al. 2014; Vogelsberger et al. 2014), using a refined galaxy formation model that includes improvements in the models for chemical enrichment, stellar and black hole feedback, and introduce new physics such as the growth and amplification of seed magnetic fields.

The project includes three cosmological volumes of roughly 50, 100, and 300 Mpc side length, with decreasing in steps of eight in mass resolution (two in spatial resolution) across levels. These are referred to as TNG50, TNG100, and TNG300, respectively. TNG300 provides the largest statistical sample of galaxies and enables the study of rare and massive objects such as galaxy clusters. TNG50 reaches resolutions typical of zoom-in simulations and allows the investigation of structural properties of galaxies and small-scale gas phenomena (Pillepich et al. 2019; Nelson et al. 2019a). TNG100 provides the ideal balance between a statistically significant number of simulated objects and satisfactory resolution of their inner structure (Fig. 3.2, Nelson et al. 2019b).

3.2.1 The TNG model

The TNG simulations use the moving mesh code AREPO (Springel 2010) to solve the coupled equations of magneto-hydrodynamics and self-gravity. Gravitational forces are calculated with a Tree-Particle-Mesh scheme (as in GADGET-4 Springel et al. 2020), while the solutions to the magneto-hydrodynamical equations are obtained in a quasi-Lagrangian fashion.

The IllustrisTNG simulations include the following key astrophysical processes implemented in a sub-grid manner (see Vogelsberger et al. 2013, Pillepich et al. 2018b, and Weinberger et al. 2017 for more details):

- **Star formation and evolution** - Star formation is implemented following the model from Springel & Hernquist (2003): when the gas exceeds the density of 0.1 atoms per cm^{-3} it is converted in stars following the Kennicutt-Schmidt law[1] and assuming a Chabrier (2003) initial mass function. To counter-act a too quick condensation of the gas and produce realistic disk galaxies, a pressure term from unresolved SNe is added in the equation of

[1]The star formation rate per unit area is proportional to the gas surface density to the power of 1.4 ± 0.15.

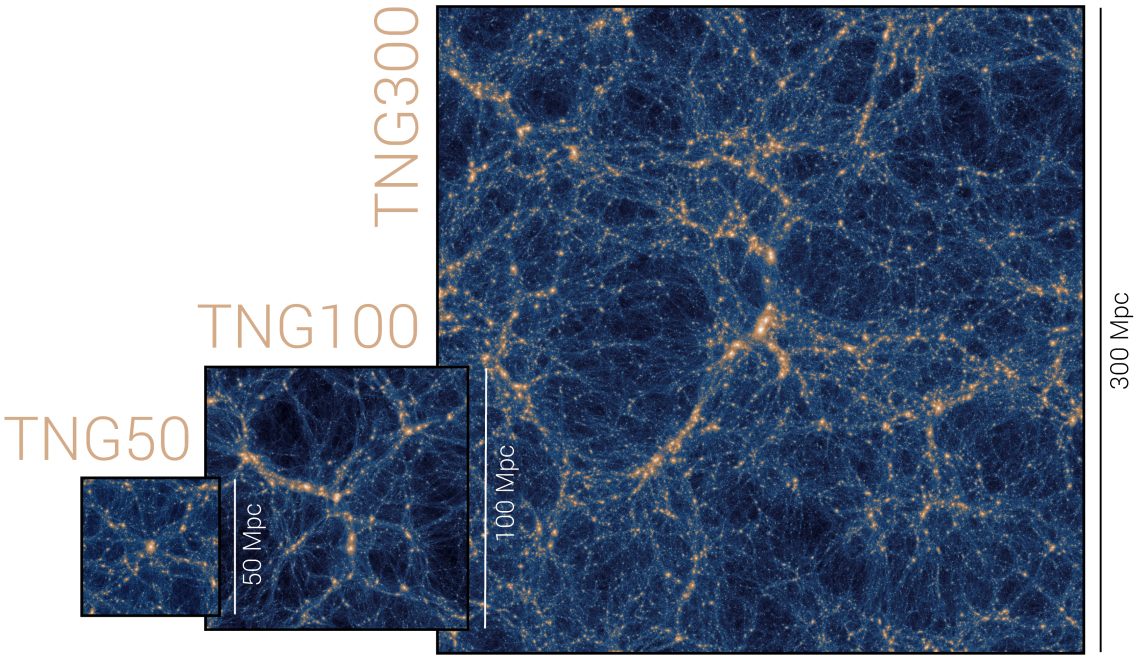

Figure 3.2: The three IllustrisTNG cosmological volumes: TNG50, TNG100, and TNG300. For each simulation the projected dark matter density is shown (credits: TNG Collaboration).

state of the star-forming gas. Each stellar particle produced is assumed to represent a single-age stellar population which is allowed to evolve and age.

- **Chemical enrichment of the ISM** - Stars evolve and return mass and metals to the ISM via SN explosions (of type I and II), and asymptotic giant branch winds. The chemical enrichment scheme follows the production and evolution of nine elements (H, He, C, N, O, Ne, Mg, Si, and Fe).

- **Primordial and metal-line gas cooling** - Metal-enriched gas looses energy through radiative processes. These are modelled including a redshift dependent, uniform, UV background radiation field simulating the energy input from quasars and high-z star-forming galaxies (Faucher-Giguère et al. 2009). The presence of metals influences the cooling rates by increasing the number of possible transitions. Their contribution is included using tabulated values as a function of density, temperature, metallicity, and z (Smith et al. 2008; Wiersma et al. 2009). The effect of the AGN emission onto the cooling rate of the gas is accounted by adding its radiation field to the background radiation.

- **Stellar feedback** - Although the ISM model implicitly invokes thermal SN feedback, this is not sufficient to avoid the over-cooling problem. Therefore additional stellar feedback is modeled in the form of winds, which are capable of efficiently removing baryonic material from the star-forming phase. These winds are launched isotropically directly from the star-forming gas in the form of wind particles, which inherit the properties of the gas in

proportion to the fraction of mass converted into wind, and naturally propagate to form large-scale galactic fountains. The energy release rate available to drive the winds depends on the local instantaneous star formation rate and is tied to the energy released by the SN. Part of this energy is carried by the wind particles in the form of thermal energy, which is radiated away as they travel. The wind injection velocity is redshift dependent as inspired by the results of semi-analytical models (Henriques et al. 2013). Given the initial wind speed, the mass load of the wind particles depends on metallicity so that winds are weaker in higher metallicity environments. After a travel distance of at most a few kpc, when the density falls below a certain threshold, the wind particle is re-coupled to the gas, donated to the gas cell where it is located.

- **Black hole formation, growth, and feedback** - Black holes (BHs) are represented by massive sink particles that are created at early times, and subsequently grow in mass by gas accretion or BH mergers. Seed BH particles of mass $8 \times 10^5 h^{-1} M_\odot$ are placed by hand in the potential minimum of halos that overcome a mass $5 \times 10^{10} h^{-1} M_\odot$ and that do not yet contain a BH. BHs merge when they are found within each other's the accretion region and continuously accrete mass at a pure Bondi accretion rate (Bondi 1952), limited by the Eddington accretion rate. Part of the accreted mass is liberated as feedback energy. In the low-accretion state, that is when the accretion rate is lower than a fraction χ of the Eddington rate (with χ in the range $0.001 - 0.1$, depending on the BH mass), the TNG model employs BH-driven kinetic winds that inject pure kinetic energy, by imparting an impulse in a random direction to a prescribed number of neighbouring gas cells. In the high-accretion state, a thermal feedback that heats the surrounding gas is invoked.

- **Amplification and evolution of seed magnetic fields** - The TNG model includes the treatment of primordial magnetic fields that are amplified by the collapse of structures in the early universe. An initial small magnetic field (10^{-10} physical Gauss at $z = 127$, in agreement with observational constraints on primordial magnetic fields Planck Collaboration et al. 2016), spatially homogeneous, and with a uniform field strength in an arbitrary orientation, is seeded at the beginning of the simulation. Results at $z = 0$ have been found to be invariant to the strength and direction of the seed (e.g., Pakmor et al. 2014).

3.2.2 Calibration

The TNG model is calibrated at the resolution of TNG100, but using a smaller cosmological box (~ 25 Mpc side), to reproduce the star formation rate density as a function of z, the galaxy stellar mass function at $z = 0$, and the stellar-to-halo mass relation at $z = 0$. This is done by running the same cosmological box with a series of perturbation of the TNG model and with the fiducial original Illustris model for comparison, starting from identical initial conditions at $z = 127$ to present-day. The fiducial TNG model is implemented by choosing the set of parameters that provide good overall agreement with benchmark observables and that, at the same time, alleviate some of the discrepancies of the original Illustris with observations. Therefore additional observables were considered to discriminate among different TNG models that performed similarly

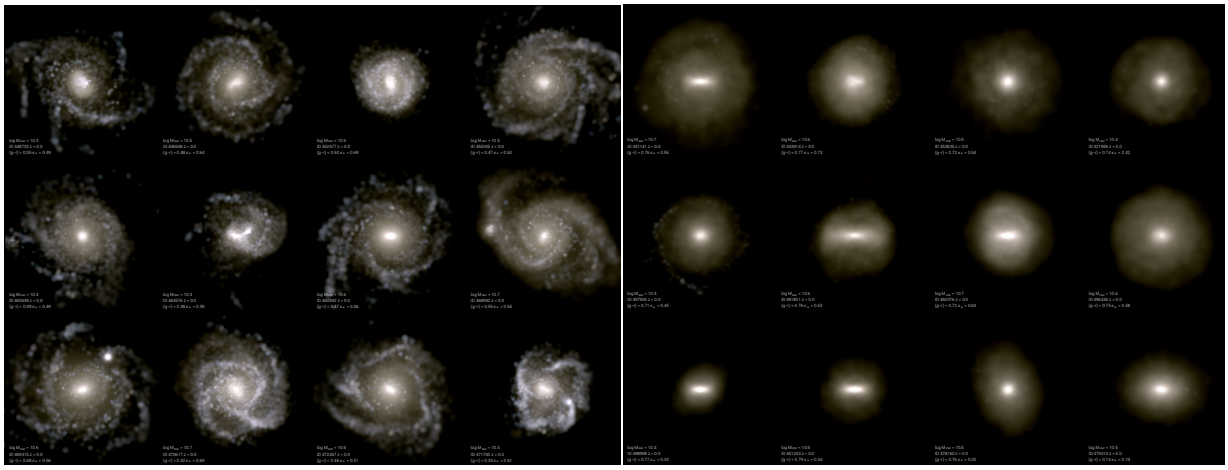

Figure 3.3: Synthetic images of simulated galaxies from the TNG100 simulation at $z = 0$ with halo mass in the range $10^{12} - 10^{12.2} M_{\odot}$. Galaxies in the **left** panel have blue colors ($g - r < 0.6$ mag) while galaxies in the **right** panel are extracted from the red sequence ($g - r > 0.6$ mag). The figure (adapted from Nelson et al. 2018) highlights the relation between morphology and colour in the TNG100 galaxies.

at reproducing the calibration observables. The BH mass versus stellar or halo mass relation, the halo gas fraction, and the galaxy half-mass radii were considered to guide the choice of the model parameters. These parameters are then kept fixed for different TNG resolution runs (e.g., TNG50 and TNG300) and are not adjusted to the different particle mass and spatial resolution ("strong resolution convergence", according to Schaye et al. 2015). This choice results in some of the properties of the simulated galaxies being resolution dependent (see Pillepich et al. 2018a).

3.2.3 Results

The IllustrisTNG models was found to satisfactorily agree with many observational constraints (e.g., Genel et al. 2018; Nelson et al. 2018) and to return a reasonable mix of morphological galaxy types (Rodriguez-Gomez et al. 2019). In particular it was demonstrated to improve the old Illustris model in reproducing observations such as, for example, the stellar sizes of galaxies and the strong galaxy color bimodality at intermediate to high galaxy masses (Nelson et al. 2015).

The new AGN feedback model is responsible for the quenching of galaxies in halos above $10^{12} M_{\odot}$, with resulting halo gas fractions in agreement with the observations (Weinberger et al. 2017). The faster and more effective stellar winds in TNG reduce the star formation efficiency at all masses and all times, resulting in a suppressed $z = 0$ galaxy stellar mass function for $M_* \lesssim 10^{10} M_{\odot}$, and smaller galaxy sizes (Pillepich et al. 2018b).

The IllustrisTNG model reproduces the observed present-day bimodality of galaxy colors in excellent agreement with observations. A key result that is exploited later in this thesis (Sect. 5.5.1) is that, at fixed stellar mass, redder galaxies have lower star formation rates, gas fractions, gas metallicities, and older stellar populations; redder simulated galaxies also correspond

to earlier morphological types (Nelson et al. 2018). The relation between color and morphology at fixed halo mass in the TNG100 galaxies is highlighted in Fig. 3.3. This allows to select a sample of (predominantly) early types by choosing red sequence galaxies in the color-mass diagram.

Chapter 4

The extended PN.S ETG survey – velocity fields at large radii

This chapter is published as the paper Pulsoni et al. (2018).

4.1 Introduction

Observations (e.g., Trujillo et al. 2006; van Dokkum et al. 2010) as well as simulations (e.g., Oser et al. 2010; Rodriguez-Gomez et al. 2016; Qu et al. 2017) suggest a two phase scenario for the formation of early type galaxies (ETGs). An initial fast assembly stage, in which the ETGs grow through rapid star formation fueled by the infall of cold gas ($z \gtrsim 1.5$) or through major merger events (Wuyts et al. 2010; Sommer-Larsen & Toft 2010; Bournaud et al. 2011; Wellons et al. 2016), is followed by a series of merger episodes which enrich the galaxy halos of stars and make them grow efficiently in size (Oser et al. 2010; Gabor & Davé 2012; Lackner et al. 2012; Buitrago et al. 2017). The hierarchical accretion scenario finds its best evidence in the observations of a rapid growth of stellar halos at redshift $z \lesssim 2$ with little or no star formation (e.g., Daddi et al. 2005; Trujillo et al. 2007; van Dokkum et al. 2010; Damjanov et al. 2011). In this context ETGs are layered structures in which the central regions are the remnant of the primordial stars formed in-situ, while the external halos are principally made of accreted material. The consequence is that the halos are expected to show significant variation with radius of properties such as light profiles (Huang et al. 2013a; D'Souza et al. 2014; Iodice et al. 2016; Spavone et al. 2017), and kinematics (Coccato et al. 2009; Romanowsky & Fall 2012; Arnold et al. 2014; Foster et al. 2016).

Long slit spectroscopic observations of ETGs (e.g., Davies et al. 1983; Franx et al. 1989; Bender et al. 1994) revealed that this apparently homogeneous class of objects actually displays a kinematic diversity which also correlates with the isophote shape (Bender 1988b; Kormendy & Bender 1996). Disky ellipticals generally rotate fast, while slowly rotating ellipticals have a rather boxy shape. A remarkable step forward in the comprehension of the nature of ETGs was attained by the Atlas3D project (Cappellari et al. 2011), which for the first time applied integral-field spectroscopy (IFS) over a statistically-significant sample, mapping kinematics, dynamics,

and stellar population properties within one effective radius (R_e). A new paradigm for ETGs was proposed, which distinguishes between fast (FRs) and slow rotators (SRs) according to the central projected specific angular momentum, λ_R (Emsellem et al. 2007). FRs include also S0 galaxies and represent the great majority (86%) of ETGs. These are apparently oblate systems with regular disk-like kinematics along the photometric major axis. SRs, on the other hand, often display kinematic features such as counter-rotating cores or twist of the kinematic position angle. They are relatively rounder systems, mildly triaxial, and tend to be massive (Cappellari et al. 2013a).

The two classes have been interpreted as the result of the variety of processes shaping galaxies, leading to a sequence of baryonic angular momentum (Emsellem et al. 2011; Naab et al. 2014; Wu et al. 2014). On-going surveys like MANGA (Bundy et al. 2015), CALIFA (Sánchez et al. 2012), SAMI (Croom et al. 2012; Bryant et al. 2015), and MASSIVE (Ma et al. 2014) are currently working on increasing the size of the sample of IFS mapped objects, and extending the study to a wider range of environment and mass.

However, a classification scheme based on the characteristics of the galaxies in the central regions (inside $\sim 1R_e$) may not be fully representative of the nature of these objects (e.g., Bellstedt et al. 2017b), raising the question of how complete our understanding is without a full knowledge of their properties on larger scales. The outer regions beyond R_e in fact contain half of the galaxies' stars and most of their dynamical mass. Dark matter is known to dominate there (e.g Mandelbaum et al. 2006; Humphrey et al. 2006; Koopmans et al. 2009; Churazov et al. 2010) and dynamical modeling of the outskirts is essential to constrain its distribution at intermediate radii (e.g., Gerhard et al. 2001; Romanowsky et al. 2003; Thomas et al. 2009a; Napolitano et al. 2011; Morganti et al. 2013). Stellar halos are predicted to host mostly accreted star material as shown by particle tagging simulations (Cooper et al. 2013) and hydro-dynamical simulations (Rodriguez-Gomez et al. 2016). In addition, these regions provide insight into the most recent dynamical phase of the galaxy. In the halos the settling times are of order 1 Gyr and so signatures of the most recent assembly events may still be apparent, providing a mine of information about their formation and evolution mechanisms (e.g., Bullock & Johnston 2005; Tal et al. 2009; Romanowsky et al. 2012; Coccato et al. 2013; Duc et al. 2015; Longobardi et al. 2015b). Thus extending investigations to the outer halos is crucial for having a complete picture of ETGs.

However kinematic measurements are not easily obtained for ETG halos, which generally lack cold gas (and so the 21 cm HI emission) used to probe the outer parts of spiral galaxies. Since the continuum light from the stars quickly drops with radius, absorption line spectroscopy is challenging beyond $1-2\,R_e$. This limits the assessment of the complicated dynamics of ETGs which, because dominated by dispersion, necessitates a good knowledge of the higher moments of the line of sight velocity distribution (LOSVD) in order to alleviate the anisotropy-potential-degeneracy (e.g., Gerhard 1993; Rix et al. 1997; Thomas et al. 2009a; de Lorenzi et al. 2009; Napolitano et al. 2009).

Kinematic studies of ETGs from integrated-light spectra out to large radii have been performed by Kelson et al. (2002); Weijmans et al. (2009); Coccato et al. (2010a); Murphy et al. (2011); Barbosa et al. (2018) using long slit spectroscopy or IFS on individual objects. More recently the SLUGGS survey (Arnold et al. 2014; Foster et al. 2016; Bellstedt et al. 2017a), the MASSIVE survey (Raskutti et al. 2014; Veale et al. 2017b), and Boardman et al. (2017) gen-

erated kinematic data from integral field spectrographs (IFSs) for larger samples of ETGs, but never reaching beyond $3-4R_e$[1].

The only possibility to probe the kinematics of a large sample of galaxies out to the very outskirts is through kinematic tracers that overcome the limit of the decreasing surface brightness, like globular clusters (e.g., Schuberth et al. 2010; Strader et al. 2011) or planetary nebulae.

Planetary nebulae (PNe) are established probes of the stellar population in ETG halos (e.g., Longobardi et al. 2013; Hartke et al. 2017). Their bright [OIII] line stands out against the faint galaxy background, making them relatively easy to detect. Since they are drawn from the main stellar population, their kinematics traces the bulk of the host-galaxy stars, and are directly comparable to integrated light measurements (Hui et al. 1995; Arnaboldi et al. 1996; Méndez et al. 2001; Coccato et al. 2009; Cortesi et al. 2013a). This makes PNe the ideal kinematic probes for the halos of ETGs. Globular clusters do not generally follow the surface brightness distribution of the stars and do not trace the stellar kinematics (e.g., Brodie & Strader 2006; Coccato et al. 2013; Veljanoski et al. 2014), and their color bimodality, suggesting two distinct formation mechanisms (Renaud et al. 2017, and references therein), complicates the interpretation of their use as kinematic tracers. The pioneering work of Coccato et al. (2009) studied the kinematics of 16 ETGs traced with PNe out to $8R_e$, finding evidence for kinematic transitions at large radii from the trends observed in the central regions (see also Arnold et al. 2014).

The extended Planetary Nebula Spectrograph (ePN.S) survey in based on observation mostly done with the Planetary Nebula Spectrograph (PN.S), and consists of catalogs of PNe for 33 ETGs. This dataset is the largest survey to-date of extragalactic PNe identified in the halos of ETGs, complementing the absorption line kinematics of the central regions available in the literature. The rationale of the survey, the sample definition, and the construction of the catalogs are described in detail in Arnaboldi et al. (in preparation). Sect. 4.2 is a brief description of the ePN.S sample. Section 4.3 describes the general procedure adopted for extracting the mean velocity fields from the measured radial velocities of PNe, and reviews the adaptive kernel smoothing technique introduced by Coccato et al. (2009). In Sect. 4.4 we evaluate the systemic velocity of the galaxies. The point-symmetry of the smoothed velocity fields is studied in Sect. 4.5, while the trends of the kinematic parameters, such as rotational velocity, kinematic position angle, and velocity dispersion, are derived in Sect. 4.6. The results are described in Sect. 4.7 with a detailed analysis of SRs and FRs. A discussion of the results is presented in Sect. 4.8. In Sect. 4.9 we give a summary of the work and draw our conclusions.

4.2 Description of the sample, observations, and data reduction

This work is based mostly on data collected with the Planetary Nebula Spectrograph (PN.S) at the William Herschel Telescope in La Palma. The PN.S is a custom-built instrument designed for counter-dispersed imaging (Douglas et al. 2002). Arnaboldi et al. (in prep.) collected catalogs

[1]The values of R_e used by most kinematic studies are measured in the bright central regions of galaxies, and may underestimate the half light radii (see discussion in Sect. 4.8.6).

of PNe for 25 galaxies from PN.S, 11 of which new, to which they added six further catalogs from the literature and two additional new catalogs, for a total of 33 ETGs. This ePN.S sample is magnitude limited and covers a wide range of internal parameters, such as luminosity, central velocity dispersion, ellipticity, boxy and diskyness (Table 4.1 summarizes the properties of the sample and the origin of the catalogs). Our catalogs contain a total of 8636 PNe, with data covering 4, 6, and 8 effective radii (R_e) for, respectively, 85%, 41%, and 17% of the sample, with median extension of 5.6 R_e (see R_{max} values of the last radial bins in Table 4.1). This makes the ePN.S the largest kinematic survey to-date of extragalactic PNe in the outer halos of ETGs.

Arnaboldi et al. (in prep.) give a full discussion of the extraction and validation of the catalogs; here we provide a brief description of the adopted procedures. All the datasets (the new catalogs, as well as the PN catalogs from the literature) are uniformly (re)analyzed, in order to obtain a homogeneous sample of ETG kinematics whose properties can be consistently compared. The new PN.S observations, the two additional new catalogs, and the reanalyzed catalogs will be described in Arnaboldi et al. (in prep.).

For each galaxy, after the raw catalog has been obtained, it is uniformly cleaned from possible spurious sources and from so-called velocity outliers. The first step for the removal of outliers among the PN candidates is the exclusion of all the detections with signal-to-noise ratio below a given threshold. We adopted $S/N \geq 2.5$ as good compromise value between a reasonable signal-to-noise and the number of detections that satisfy this requirement.

Next we separate PNe belonging to any satellites from those in the hosts. For this we use the probability membership method from McNeil-Moylan et al. (2012), which uses both kinematic and photometric information to assign to each star a probability of belonging to the satellite or host. Membership to the host galaxy is assigned only if the probability is greater than 90%.

The last step is the removal of outliers in the remaining host PN velocity distribution. Such outliers could, for example, arise because of contamination from other narrow emission-line sources (i.e., background star-forming galaxies) that are not resolved and appear point-like in the counter-dispersed images, similar to the monochromatic [OIII] 5007Å emission from a PN. We identify outliers using a robust sigma clipping procedure. The algorithm derives a robust mean velocity (v_{mean}) and velocity dispersion σ, using a running average in a 2D phase space (coordinate, v) with a window of N data points ($15 \lesssim N \lesssim 30$, according to the number of tracers in each galaxy) and a three data points step. An iterative procedure clips the PN candidates whose $|v - v_{mean}| > 2\sigma$, and evaluates v_{mean} and σ until the number of clipped objects stabilizes. In each iteration σ is corrected by a factor 1.14 to account for the 2σ cut of the LOSVD tails. Finally, to the 95% of a galaxy's PNe thus validated, the remaining 5% of the PNe are added back to the sample, using those clipped objects which are closest in v to the 2σ contours, so that the final PN sample also includes the objects expected in the approximately Gaussian tails of the LOSVD.

In the case of disk galaxies, dominated by rotation, a decomposition into disk and spheroid was performed following Cortesi et al. (2011): using both photometric data and kinematic information we assigned to each PN the probability of being associated with each photometric component. The tagging of the outliers from the disk and the spheroid separately allows us to account for their different kinematics when using the robust sigma clipping procedure. The disk is processed first, and its flagged PNe are added to the PNe of the bulge. Eventually the flagged bulge PNe are considered as outliers of the entire galaxy.

Finally, we estimated the number of background emitting galaxies, whose emission line might fall in the range of velocities determined in the procedure above. We employed the approach adopted in Longobardi et al. (2013), which uses the Lyman alpha (Lyα) luminosity function by Gronwall et al. (2007), and adapted it to the ePN.S survey. Given the limiting magnitude, the area coverage, and the filter band-passes of the PN.S, the number of expected background galaxies is 2. This is an upper limit, as the Gronwall et al. (2007) sample also includes [OII] emitters at $z \simeq 0.34$. These [OII] emitters are characterized by the oxygen doublet at 3726 – 3729Å that is resolved in wavelength at the resolution of the PN.S, so the [OII] emitters have already been removed from the PN candidate sample because they are not monochromatic emission. We discuss the effect of the Lyα background contaminants on the kinematics in Sect. 4.3.2. The datasets processed in this way are the Bona Fide PNe catalogs used in the following analysis.

4.3 Kernel smoothing method

The measured line-of-sight (LOS) velocities of the PNe are random samplings of the galaxy LOSVD function at the position of the source. Therefore each velocity measurement randomly deviates from the local mean velocity by an amount that depends on the local LOS velocity dispersion.

In order to extract the mean LOS velocity and the LOS velocity dispersion fields from this discrete velocity field, we use an adaptive kernel smoothing technique, as described in Coccato et al. (2009), that performs a local average of the measured discrete LOS velocities. In the following section we briefly review the smoothing technique, while we refer to Coccato et al. (2009) for a more detailed discussion. In appendix 4.A we validated the adopted procedure on simulated data, in order to test the effects of different statistical realizations of a given sample of tracers, the dependency on the number of tracers, and different V/σ ratios on the estimated kinematic parameters.

4.3.1 Averaging the discrete velocity field with the adaptive kernel smoothing technique

The smoothing of the discrete velocity field is carried out by computing the velocity at each position (x, y) in the sky as a weighted mean $\tilde{\mathrm{v}}(x, y)$ of all the PN LOS velocities v

$$\tilde{\mathrm{v}}(x, y) = \frac{\sum_i \mathrm{v}_i w_{i,p}}{\sum_i w_{i,p}}, \tag{4.1}$$

while the velocity dispersion $\tilde{\sigma}(x, y)$ is given by the square root of the variance of v with respect to $\tilde{\mathrm{v}}$

$$\begin{aligned} \tilde{\sigma}(x, y) &= (\langle \mathrm{v}^2 \rangle - \langle \mathrm{v} \rangle^2 - \delta \mathrm{v}^2)^{1/2} \\ &= \left[\frac{\sum_i \mathrm{v}_i^2 w_{i,p}}{\sum_i w_{i,p}} - \tilde{\mathrm{v}}(x, y)^2 - \delta \mathrm{v}^2 \right]^{1/2}. \end{aligned} \tag{4.2}$$

The weight $w_{i,p}$ of each PN is defined using a Gaussian Kernel that depends on the distance of the PN from the position (x, y), normalized by a kernel width K

$$w_{i,p} = \exp \frac{-D_i^2}{2K(x,y)^2} \qquad ; \qquad K(x,y) = A\sqrt{\frac{M}{\pi\rho}} + B. \tag{4.3}$$

The latter controls the spatial scale of the region over which the smoothing is performed, and hence the spatial resolution of the kinematic study. Large values of K, in fact, lead to smoother profiles in the mean LOS velocity fields, highlighting the general trends, but also suppressing the small scale structures, while smaller values of K allow a better spatial resolution but may amplify any noise pattern. Hence the optimal K should be a compromise between spatial resolution and statistical noise smoothing.

The width K is therefore defined to be linearly dependent on the distance between the position (x, y) and the M^{th} closest PN, so that K is a function of the local density of tracers $\rho(x, y)$. This allows K to be smaller in the innermost, dense regions of galaxies, and larger in the outskirts, where their density is usually lower. The optimal kernel parameters A and B are derived as described in Sect. 4.3.1. We chose $M = 20$, but Coccato et al. (2009) tested the procedure with $10 < M < 60$ finding no significant differences in the results.

Table 4.1: Properties of the ePN.S sample of ETG and list of references

Galaxy NGC	M_K[a] [mag]	D[b] [Mpc]	class F/S[c]	R_e[d] [arcsec]	R_{max}[e] [R_e]	PA_{phot}[f] [deg]	ϵ[g]	N_{PNe}[h]	Ref. PN data[i]	Ref. abs. line data[l]
0584	−24.23	20.2	F	33 (1)	7.4	63	0.339	25	(7)	(21)
0821	−23.99	23.4	F	40 (2)	4.8	31.2	0.35	122	(8)	(18;40;41)
1023	−23.89	10.5	F	48 (2)	6.8	83.3	0.63	181	(8);(9)	(18;30)
1316	−26.02	21.0	F	109 (3)	4.7	50	0.29*	737	(10)	(22)
1344	−24.21	20.9	F	30 (4)	7.8	167	0.333	192	(12)	(23)
1399	−25.29	20.9	S	127 (3)	4.	110	0.1*	145	(11)	(24)
2768	−24.77	22.4	F	63 (2)	6.2	91.6	0.57	312	(9)	(18;31)
2974	−23.76	22.3	F	38 (2)	5.8	44.2	0.37	22	(7)	(18)
3115	−24.02	9.5	F	93 (6)	4.7	43.5	0.607	183	(9)	(18;25)
3377	−22.78	11.0	F	35.5 (2)	7.7	46.3	0.33	136	(8)	(18;33)
3379	−23.80	10.3	F	40 (2)	5.3	68.2	0.13*	189	(8)	(19;32;40)
3384	−23.51	11.3	F	32.5 (2)	6.8	50	0.5	85	(9)	(19)
3489	−23.04	12.0	F	22.5 (2)	4.8	70.5	0.45	57	(9)	(19)
3608	−23.69	22.8	S	29.5 (2)	8.2	82	0.2*	92	(8)	(18)
3923	−25.33	23.1	S	86.4 (1)	4.9	48	0.271	99	(15)	(26)
4278	−23.80	15.6	F	31.5 (2)	7.6	39.5	0.09*	69	(7)	(18)
4339	−22.62	17.0	F	30 (2)	3.	15.7	0.07*	44	(7)	(20;38)
4365	−25.19	23.1	S	52.5 (2)	5.6	40.9	0.24*	227	(7)	(18)
4374	−25.12	18.5	S	52.5 (2)	5.9	128.8	0.05*	445	(8)	(18)
4472	−25.73	16.7	S	95.5 (2)	8.4	154.7	0.19*	431	(7)	(20;37)

Continued on next page

Continued from previous page

Galaxy NGC	M_K[a] [mag]	D[b] [Mpc]	class F/S[c]	R_e[d] [arcsec]	R_{max}[e] [R_e]	PA_{phot}[f] [deg]	ϵ[g]	N_{PNe}[h]	Ref. PN data[i]	Ref. abs. line data[l]
4473	−23.76	15.2	F	27. (2)	5.6	92.2	0.43	153	(7)	(18)
4494	−24.17	17.1	F	49 (2)	4.8	176.3	0.14*	255	(8)	(18;36)
4552	−24.32	16.0	S	34. (2)	9.2	132	0.11*	227	(7)	(19;38)
4564	−23.10	15.9	F	20.5 (2)	6.5	47	0.53	47	(8)	(18)
4594	−24.93	9.5	F	102 (5)	4.	88	0.521	258	(16)	(27)
4636	−24.35	14.3	S	89. (2)	3.	144.2	0.23*	189	(7)	(20;39)
4649	−25.35	16.5	F	66 (2)	4.5	91.3	0.16*	281	(13)	(18;34)
4697	−24.14	12.5	F	61.5 (1)	4.5	67.2	0.32	525	(14)	(18;35)
4742	−22.60	15.8	F	14.4 (4)	13.1	80	0.351	64	(7)	(28)
5128	−24.16	4.1	F	162.6 (1)	11.9	30	0.069*	1222	(17)	(29)
5846	−25.04	24.6	S	59 (2)	4.3	53.3	0.08*	118	(8)	(18)
5866	−23.99	14.8	F	36 (2)	9.4	125	0.58	150	(7)	(18)
7457	−22.38	12.9	F	36 (2)	3.2	124.8	0.47	108	(9)	(18)

[a] M_K is the total absolute luminosity in the K band. These values are obtained from the total apparent total magnitudes K_T of the 2MASS atlas (Skrutskie et al. 2006) using the distance D, and correcting for foreground galactic extinction A_B (Schlegel et al. 1998): $M_K = K_T - 5\log_{10} D - 25 - A_B/11.8$. We assume $A_B/A_K = 11.8$, consistently with Cappellari et al. (2011). The K_T magnitudes are from integrating the surface brightness profiles ($\propto \exp(-r/r_\alpha)^{(1/\beta)}$), extrapolated from the 20 mag/arcsec^2 isophote to $\sim 5r_\alpha$ (Jarrett et al. 2003).

[b] Distances of galaxies derived from the surface brightness fluctuation method. Whenever possible we adopt the distance moduli measured by Blakeslee et al. (2009, B09), otherwise we used the values from Jensen et al. (2003, J03) or from Tonry et al. (2001, T01). The distance moduli from J03 were rescaled to the zero-point calibration of B09 by applying a shift of +0.1 mag, while the distance moduli from T01 were zero-point- and bias-corrected using the formula from Blakeslee et al. (2010) and the data quality factor Q given by T01.

[c] The sample is divided into SRs (S) and FRs (F), according to the definition of Emsellem et al. (2011), from the kinematics within $1R_e$.

[d] Adopted effective radius. The index in parenthesis corresponds to the reference: (1)Ho et al. (2012), (2)Cappellari et al. (2011), (3)Caon et al. (1994), (4)Blakeslee et al. (2001), (5)Kormendy & Westpfahl (1989), (6)Capaccioli et al. (1987).

[e] Mean radius of the last radial bin in units of effective radii.

[f] Average value of the photometric position angle and

[g] ellipticity (ϵ), from Krajnović et al. (2011) (within $2.5 - 3R_e$) and Ho et al. (2011) (in the outer regions, where they converge to a constant value) For NGC 3384 and NGC 4564 we used the PA_{phot} from Meusinger & Ismail (2007) and Goudfrooij et al. (1994), respectively. (*) Objects for which we used circular radial bins ($\epsilon = 0$), see Sect. 4.3.2.

[h] Number of detected PNe.

[i] References for the PNe datasets: (7) are new PN.S catalogs presented in Arnaboldi et al. (in prep.), (8)Coccato et al. (2009), (9)Cortesi et al. (2013a), (10)McNeil-Moylan et al. (2012), (11)McNeil et al. (2010), (12)Teodorescu et al. (2005), (13)Teodorescu et al. (2011), (14)Méndez et al. (2009), (15) unpublished data from counter dispersed imaging (Arnaboldi et al. in prep.), (16) unpublished data from narrow band imaging and spectroscopic follow up (Arnaboldi et al. in prep.), (17)Peng et al. (2004) and Walsh et al. (2015).

[l] References for absorption line data: kinemetry from (18)Foster et al. (2016) on SLUGGS+Atlas3D data, from (19)Krajnović et al. (2008) and from (20)Krajnović et al. (2011), major axis long slit spectroscopy from (21)Davies & Illingworth (1983), (22)Bedregal et al. (2006), (23)Teodorescu et al. (2005), (24)Saglia et al. (2000) and Scott et al. (2014), (25)Norris et al. (2006), (26)Carter et al. (1998), (27)Kormendy & Illingworth (1982), (28)Davies et al. (1983), (29)Marcelin (1983)), (30)Simien & Prugniel (1997c), (31)Simien & Prugniel (1997a), (32)Statler & Smecker-Hane (1999), (33)Coccato et al. (2009), (34)De Bruyne et al. (2001), (35)de Lorenzi et al. (2008), (36)Napolitano et al. (2009), (37)Veale et al. (2017b), (38)Simien & Prugniel (1997b), (39)Pu & Han (2011), (40)Weijmans et al. (2009), (41)Forestell & Gebhardt (2010).

Deriving the optimal A and B kernel parameters

The parameters A and B in Eq. (4.3) are chosen so that the best compromise between spatial resolution and noise smoothing is achieved. We developed an iterative procedure in order to derive the optimal kernel parameters that realize this condition.

We first estimated the velocity gradient to be resolved by the smoothing procedure by performing a preliminary averaging with a fully adaptive kernel ($A = 1$ and $B = 0$). The derived mean velocity field, $\tilde{\mathrm{v}}_{A=1,B=0}$, is fitted with a cosine function, which, in general, approximately describes the velocity profiles of early type galaxies (see Cohen & Ryzhov 1997):

$$\tilde{\mathrm{v}}_{A=1,B=1}(\phi) = V_{\max} \cos(\phi - PA_{\mathrm{kin}}) + \mathrm{const.} \tag{4.4}$$

This interpolation function provides a measure of the position angle of the kinematic major axis (PA_{kin}), along which the steepest velocity gradient $d\tilde{\mathrm{v}}$ is expected to lie. The gradient $d\tilde{\mathrm{v}}$ is obtained by fitting a straight line to the velocities $\tilde{\mathrm{v}}$ of the PNe lying in a section along the PA_{kin} direction, as a function of the radius.

The best kernel parameters that allow to resolve spatial substructures with typical velocity gradient $d\tilde{\mathrm{v}}$ are derived by building simulated sets of PNe (see Coccato et al. 2009). The stars are spatially distributed according to a given density $\overline{\rho}$, while their velocities are assigned using the derived velocity gradient and adding a dispersion equal to the standard deviation of the observed radial velocities. The artificial sets are processed using different values of the kernel K until the simulated input velocity field is recovered: this provides the best K for this $\overline{\rho}$. The procedure is repeated for different values of $\overline{\rho}$, and the optimal A and B are the best fit values of Eq. (4.3) based on on the derived best K as a function of $\overline{\rho}$.

Errors in the derived velocity fields

Errors on $\tilde{\mathrm{v}}(x, y)$ and $\tilde{\sigma}(x, y)$ are obtained using Monte Carlo simulations, as also discussed in Coccato et al. (2009). For each galaxy, 100 PN datasets are built with simulated radial velocities at the same positions as the observed PNe. The radial velocity for each simulated object is obtained from the two-dimensional smoothed velocity field, adding a random value from a Gaussian distribution centered at 0 and with dispersion $\sigma = \sqrt{\tilde{\sigma}^2 + \delta\mathrm{v}^2}$ where δv is the velocity error. These simulated datasets are smoothed with the same kernel K as the real sample, and the standard deviations of the simulated velocity and velocity dispersion fields give the errors on $\tilde{\mathrm{v}}$ and $\tilde{\sigma}$. This procedure is validated in appendix 4.A.2 with PN velocity distributions generated from a simulated merger remnant galaxy, which are analyzed in an identical manner as the real galaxy PN samples. As an additional test, we have also extracted and analyzed kinematic information from 1000 subsamples of the original PN sample for all our galaxies and found kinematic parameters consistent with our full-sample results, as described in Sect. 4.3.2.

4.3.2 Fitting a rotation model

The mean velocity fields, derived from smoothing the discrete velocities, are divided into radial bins with equal numbers of PNe such that they contain at least 30 stars. If a galaxy contains less

than 60 tracers, we divide the sample in two bins in order to study possible radial trends.

The bins are circular for galaxies either with small flattening, that is $10 \times \epsilon < 3$, or whose PN spatial distribution has a rather square shape. For all the other galaxies we use elliptical bins oriented along the photometric major axis, with a flattening equal to a characteristic ellipticity of the isophotes of the galaxy (the adopted ellipticity, ϵ, and photometric position angle $PA_{\rm phot}$ are given in Table 4.1). We found that the results of our analysis do not depend on the chosen flattening but, since the spatial distribution of the PNe follows the light, and so it may be rather flattened, elliptical bins help to sample the field homogeneously in an azimuthally-unbiased way.

In each radial bin, we fitted the PN velocities $\tilde{v_i}$ of position $(R_i,\ \phi_i)$ with a rotation model $\tilde{v}(\phi, R)$ (see Sect. 4.3.2). Here ϕ_i is the eccentric anomaly of the PN in the bin of coordinates (x_i, y_i), $\phi_i(x_i, y_i) = \arctan[y_i/((1-\epsilon)x_i)]$, and ϵ is the ellipticity. R_i is the major axis distance of each PN and R is the mean R_i of the PNe in each bin.

Point-symmetric rotation model

A velocity map $\tilde{\rm v}(R, \phi)$ is a periodic function in ϕ, so it can be expanded in a Fourier series and approximated by a finite number of harmonics:

$$\tilde{\rm v}(R,\phi) = a_0(R) + \sum_{n=1}^{N} a_n(R)\cos(n\phi) + \sum_{n=1}^{N} b_n(R)\sin(n\phi). \tag{4.5}$$

Elliptical galaxies in dynamical equilibrium are triaxial systems (e.g., Statler 1994, and references therein), so the projection on the sky of the mean velocity field should be point-symmetric with respect to the systemic velocity a_0 (see Krajnović et al. 2006; Coccato et al. 2013), that is symmetric positions have equal velocities with opposite sign ($\tilde{\rm v}(\phi) = -\tilde{\rm v}(\phi + \pi)$). Deviations from this behavior arise from perturbations from equilibrium that may be due to interaction or merger episodes. If one of these processes, which plays a role in the formation and evolution of early type galaxies, occurred relatively recently (a few Gyrs ago), it is likely that some signatures in the kinematics and orbital structure of the galaxy are still observable, especially in the halo where the dynamic time-scales are longer.

The requirement of point-symmetry on $\tilde{\rm v}(R, \phi)$, namely $\tilde{\rm v}(R,\phi) - a_0 = -[\tilde{\rm v}(R, \phi + \pi) - a_0]$, allows only odd values for n in Eq. (4.5). The expansion in Eq. (4.5) can be rewritten in a more direct way, as a rotation around the kinematic axis plus higher order modes. This is achieved through a rotation such that

$$\begin{aligned}\tilde{\rm v}(R,\phi) = a_0(R) + \sum_{n=1,3,\ldots} c_n(R)\cos(n\phi - n\alpha) + \\ + \sum_{n=1,3,\ldots} s_n(R)\sin(n\phi - n\alpha),\end{aligned} \tag{4.6}$$

with

$$\begin{cases} a_n = c_n\cos(n\alpha) - s_n\sin(n\alpha) \\ b_n = c_n\sin(n\alpha) + s_n\cos(n\alpha). \end{cases} \tag{4.7}$$

The phase α can be chosen so that the amplitude of the first order sine term is 0: $s_1 = 0$ if $\alpha = \arctan(b_1/a_1)$. This implies that

$$\begin{aligned} c_1 &= \sqrt{a_1^2 + b_1^2} \\ c_n &= \frac{b_n}{\sin(n\alpha)} - \frac{s_n}{\tan(n\alpha)} \\ s_n &= \left(\frac{b_n/a_n - \tan(n\alpha)}{1 + \tan(n\alpha) b_n/a_n} \right) c_n, \end{aligned} \tag{4.8}$$

and

$$\begin{aligned} \tilde{\mathrm{v}}(R,\phi) &= a_0(R) + c_1(R)\cos(\phi - \alpha(R)) + \\ &+ \sum_{n=3,5,\ldots} c_n(R)\cos(n\phi - n\alpha(R)) + \sum_{n=3,5,\ldots} s_n(R)\sin(n\phi - n\alpha(R)). \end{aligned} \tag{4.9}$$

In this notation α coincides with the position angle of the kinematic major axis, $PA_{\rm kin}$, a_0 is the mean velocity of the PNe in the bin, and c_1 is the amplitude of the projected rotation, $V_{\rm rot}$. The amplitudes of the higher order harmonics, c_k and s_k, are corrections that account for deviations of the galaxy motion from the simple cosine rotation.

In practice the series in Eq. (4.9) can be truncated to the third order as the higher order harmonics are generally zero within the errors. The resulting function is fitted to the mean velocity estimates at all PN positions in each radial bin, with the position angle $PA_{\rm kin}$, the constant a_0, and the amplitudes $V_{\rm rot}$, s_3, and c_3, as free parameters. The fit of the parameter a_0 gives an estimate of the systemic velocity $V_{\rm sys}$ in the halo (see Sect. 4.4). Once $V_{\rm sys}$ is subtracted from the velocity fields, their point-symmetry can be studied (Sect. 4.5) and used to produce the final mean velocity fields for the point symmetric galaxies (see Sect. 4.6.1). The final mean velocity fields, after subtracting $V_{\rm sys}$, are eventually fitted with the function

$$\begin{aligned} \tilde{V}(R,\phi) = V_{\rm rot}(R)\cos(\phi - PA_{\rm kin}(R)) + s_3(R)\sin(3\phi - 3PA_{\rm kin}(R)) \\ + c_3(R)\cos(3\phi - 3PA_{\rm kin}(R)). \end{aligned} \tag{4.10}$$

where the only free parameters are $PA_{\rm kin}$, $V_{\rm rot}$, s_3, and c_3 (see Sect. 4.6.2).

The kinematic quantities $PA_{\rm kin}$ and $V_{\rm rot}$ obtained fitting the model in Eq. (4.10) on the smoothed velocity fields are comparable to the results from a kinemetry fit to IFS data (Krajnović et al. 2006, 2011; Foster et al. 2016). However, we do not apply kinemetry, because this would mean fitting ellipses to the PN smoothed velocity fields. Since these have been derived from small samples of discrete tracers which, by nature, have lower spatial resolution and signal-to-noise ratio, a more straightforward approach, with fewer free parameters, is preferable.

Errors on the fitted parameters

The errors on the fitted parameters, $a_0(R)$, $PA_{\rm kin}(R)$, $V_{\rm rot}(R)$, $c_3(R)$, and $s_3(R)$, are evaluated via Monte Carlo simulations: the 100 simulated datasets produced for deriving the errors on $\tilde{\mathrm{v}}$ and

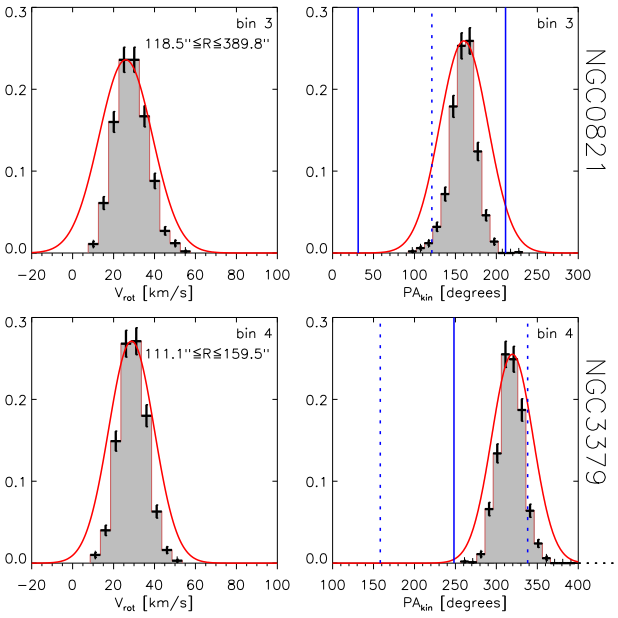

Figure 4.1: Distribution of the fitted $V_{\rm rot}$ and $PA_{\rm kin}$ in one radial bin obtained from 1000 PN subsamples extracted for NGC 0821 and NGC 3379 (gray histograms). The red curves are Gaussians centered on the $V_{\rm rot}$ and $PA_{\rm kin}$ fitted on the full dataset, and with dispersion given by the Monte Carlo simulations of the galaxy under study. The vertical solid lines show the position angle of the photometric major axis for the two galaxies; the dotted lines show the photometric minor axis. The values for $PA_{\rm phot}$ are listed in Table 4.1.

$\tilde{\sigma}$ (see Sect. 4.3.1) are divided into radial bins and modeled with Eq. (4.9). The errors are the standard deviations on the fitted parameters.

We tested whether the mean velocity field extracted through the smoothing procedure is sensitive to the relatively large velocities of objects belonging to the tails of the LOSVD. For this we selected subsamples of the observed dataset, re-extracted the kinematics, and studied the distribution of the fitted kinematic parameters. For each galaxy we used 1000 subsamples built with 80% of the observed PNe each. (We do not use bootstrap with replacement as it would not be consistent with the constraint for the PNe to follow light.) Figure 4.1 shows the distributions of the fitted $V_{\rm rot}$ and $PA_{\rm kin}$ in one radial bin for the PN subsamples extracted for NGC 0821 and NGC 3379. For all the ePN.S galaxies these distributions fall well within the statistical uncertainties of the fitted parameters from the full datasets. This shows that the values of $V_{\rm rot}$ and $PA_{\rm kin}$ measured are not driven by a few high velocity objects, but are properties of the whole PN sample.

In addition, we simulated the effect of the contamination by background Lyα emitters by adding two random velocity measurements (see Sect. 4.2), uniformly drawn in velocity from the filter band-pass used for each individual galaxy in our sample. We then re-extracted all the kinematic observables, and found that they are well within the 1 sigma errors of the measurements without contaminants.

Table 4.2: Measured parameters and typical errors for the smoothed velocity and velocity dispersion fields

Galaxy NGC	A[a] [arcsec^{-1}]	B[a]	δv[b] [km/s]	$\langle\Delta\tilde{V}\rangle$[c] [km/s]	$\langle\Delta\tilde{\sigma}\rangle$[d] [km/s]	$V_{\rm sys}$[e] [km/s]	$R_{\rm half}$[f] [arcsec]	$\log_{10}\left(\frac{M*1}{M_\odot}\right)$[g]	$\log_{10}\left(\frac{M_{*2}}{M_\odot}\right)$[h]	Ref. phot.[i]
0584	0.37	63.2	21.	21.	15.	1901.±27.	30	11.07	11.04	(4)
0821	0.50	9.7	21.	22.	16.	1697.±16.	38	10.97	10.87	(1;2)
1023	0.26	15.3	14.	19.	13.	618.± 9.	39	10.93	11.06	(6)
1316	0.46	21.3	30.	24.	21.	1749.±30.	115	11.84	11.64	(4)
1344	0.40	10.8	10.	21.	13.	1190.±13.	44	11.06	11.01	(7)
1399	0.84	5.2	37.	27.	18.	1401.±19.	122	11.53	11.51	(4)
2768	0.33	17.5	20.	26.	22.	1378.±14.	70	11.30	10.90	(15;19)
2974	0.57	33.6	21.	25.	21.	1803.±42.	43	10.87	11.06	(4)
3115	0.28	19.6	20.	30.	21.	624.±16.	73	10.98	10.96	(4)
3377	0.32	19.0	20.	12.	8.	708.± 9.	51	10.45	10.37	(1;2;3;19)
3379	0.34	16.2	20.	21.	14.	934.±17.	58	10.89	10.89	(8;9)
3384	0.25	18.9	20.	14.	10.	722.± 9.	42	10.77	10.88	(16;20)
3489	0.32	14.7	20.	14.	11.	707.±12.	22	10.56	10.61	(16)
3608	0.37	24.6	21.	15.	11.	1235.±16.	108	10.84	11.18	(2;3)
3923	0.60	24.3	30.	36.	26.	1677.±26.	164	11.54	11.66	(4)
4278	0.88	2.4	18.	18.	14.	605.±17.	59	10.89	10.87	(12;19)
4339	0.43	20.3	21.	8.	6.	1300.± 7.	27	10.38	10.18	(13;19)
4365	0.91	0.2	21.	20.	14.	1273.±11.	111	11.48	11.51	(14)
4374	0.86	1.6	23.	27.	19.	1050.±18.	122	11.45	11.56	(14)
4472	0.74	11.3	20.	38.	33.	959.±22.	193	11.71	11.76	(14)
4473	0.91	0.2	21.	18.	12.	2236.±13.	38	10.87	10.78	(17)
4494	0.41	12.8	21.	17.	12.	1348.±10.	49	11.05	10.87	(10)
4552	0.90	0.6	21.	23.	16.	361.±15.	101	11.11	11.18	(14)
4564	0.24	16.5	21.	19.	12.	1169.±17.	24	10.59	10.94	(1)
4594	0.54	19.3	30.	32.	28.	1060.±16.	102	11.37	11.10	(4;21)
4636	0.68	9.5	21.	24.	16.	903.±19.	172	11.12	11.27	(14)
4649	0.86	1.5	20.	25.	18.	1059.±18.	132	11.55	11.55	(14)
4697	0.45	6.0	35.	23.	16.	1274.±11.	123	11.03	11.05	(2;11)
4742	0.20	16.9	21.	13.	10.	1305.± 9.	13	10.38	10.37	(4;22)
5128	0.29	25.6	4.	25.	21.	536.±17.	414	11.04	11.20	(4)
5846	0.90	0.1	21.	25.	17.	1716.±19.	193	11.42	11.49	(5;18)
5866	0.34	18.7	21.	15.	10.	782.±10.	48	10.97	11.01	(16;19)
7457	0.28	10.5	20.	7.	6.	843.± 5.	62	10.28	10.63	(16;19)

Continued on next page

Continued from previous page

Galaxy	A[a]	B[a]	δv[b]	$\langle\Delta\tilde{V}\rangle$[c]	$\langle\Delta\tilde{\sigma}\rangle$[d]	$V_{\rm sys}$[e]	$R_{\rm half}$[f]	$\log_{10}\left(\frac{M*1}{M_\odot}\right)$[g]	$\log_{10}\left(\frac{M_{*2}}{M_\odot}\right)$[h]	Ref.
NGC	[arcsec^{-1}]		[km/s]	[km/s]	[km/s]	[km/s]	[arcsec]			phot.[i]

[a] Kernel parameters, A and B, used in the smoothing procedure, see Sect. 4.3.
[b] Mean error on the measured radial velocities.
[c] Mean error on the smoothed velocity field.
[d] Mean error on the velocity dispersion field.
[e] Subtracted systemic velocity.
[f] Half-light radius, see text.
[g] Logarithm of the stellar mass M_{*1} in solar units. M_{*1} are derived from the K-band luminosities M_K listed in Table 4.1, corrected for missing flux as in Scott et al. (2013): $M_{\rm Kcorr} = 1.07 \times M_K + 1.53$, and applying a mass-to-light ratio of 1 (appropriate for old stellar population with a Kroupa IMF, Forbes et al. 2016).
[h] Logarithm of the stellar mass M_{*2} in solar units. M_{*2} are derived using total luminosities obtained by fitting the surface brightness profiles with a Sérsic law and integrating till very large radii. The apparent magnitudes obtained are converted to absolute magnitudes using the distances listed in Table 4.1, corrected for foreground galactic extinction, and homogenized to B magnitude using color indexes from the HyperLeda[2] database and from Sandage & Visvanathan (1978). We then applied a stellar mass to light ratio given by the relation from Bell et al. (2003): $\log_{10}\frac{M}{L_B} = -9.42 + 1.737 \times (B-V)$, where the $(B-V)$ color index is from HyperLeda.
[i] References for the photometry: (1) Goudfrooij et al. (1994), (2) Lauer et al. (2005), (3) Jedrzejewski (1987), (4)Li et al. (2011), (5) Kronawitter et al. (2000), (6) Noordermeer et al. (2008), (7) Sikkema et al. (2007), (8) Capaccioli et al. (1990), (9) Gebhardt et al. (2000), (10) Napolitano et al. (2009), (11) de Lorenzi et al. (2008), (12) Peletier et al. (1990), (13) Caon et al. (1994), (14) Kormendy et al. (2009), (15) Hopkins et al. (2009b), (16) Krajnović et al. (2013a), (17) Caon et al. (1990), (18) Spavone et al. (2017), (19) Michard & Marchal (1993), (20) Meusinger & Ismail (2007), (21) Gadotti & Sánchez-Janssen (2012), (22) Lauer et al. (1995).

4.4 Systemic velocity subtraction

A measure of the systemic velocity of the galaxies is provided by the fit of the PN smoothed velocity field in radial bins with the harmonic expansion in Eq. (4.9). The bins are built as described in Sect. 4.3.2 and the adopted geometry for each galaxy (i.e. ellipticity, ϵ, and photometric position angle, $PA_{\rm phot}$) is listed in Table 4.1. The $a_0(R)$ parameter, in fact, represents the mean velocity of the tracers in the radial bin with radius R. When the galaxy does not display kinematic substructures (bulk motions), this mean velocity is an estimate of the systemic velocity of the galaxy which is constant with radius for a gravitationally bound system.

Since the PNe are not distributed uniformly on the sky, $a_0(R)$ gives actually a more precise evaluation of the systemic velocity than a straight average of the measured LOS velocities. The fit of Eq. (4.9) removes any contribution to the mean from rotation and is not sensitive to azimuthal completeness. Hence we can perform the fit leaving the parameter $a_0(R)$ free to vary in each bin. We find that $a_0(R)$ is generally constant with radius within the errors. Therefore we adopt, for each galaxy, a mean systemic velocity, $V_{\rm sys}$, defined as a mean of the $a_0(R)$ values, weighted with the errors on the fit:

$$V_{\rm sys} = \frac{\sum_{\rm bins} a_0(R_{\rm bin})/\Delta a_0^2(R_{\rm bin})}{\sum_{\rm bins} 1/\Delta a_0^2(R_{\rm bin})}. \tag{4.11}$$

We conservatively consider as error on $V_{\rm sys}$, $\Delta V_{\rm sys}$, the mean of the errors $\Delta a_0(R)$, since the single measures of $a_0(R)$, coming from a smoothed velocity field, are not independent quantities.

We find that $a_0(R)$ does sometimes display a trend with radius within the errors. This is due to the interplay between spatial inhomogeneities and smoothing, which may result in a slight asymmetry of one side of the galaxy with respect to the other. This effect naturally disappears as soon as the catalogs are folded by point-symmetry transformation (see Sect. 4.5), but we keep track of it in the uncertainties, by adding in quadrature the scatter of the $a_0(R)$ values to the error $\Delta V_{\rm sys}$.

NGC 1316 and NGC 5128 are treated separately with respect to the other galaxies. Their fitted $a_0(R)$ are constant in most radial bins, but they deviate in localized bins from this constant by more than twice the errors. At these radii the galaxies display important features in their velocity fields which cause an offset of the average velocity from the systemic value. We masked the most irregulars bins and use the fitted $a_0(R)$ on the others to compute the mean $V_{\rm sys}$.

The measured values of $V_{\rm sys}$ for all the galaxies are reported in Table 4.2. We do not observe any systematic bias in the measured values, and they all agree within twice the error on $V_{\rm sys}$ with the literature. Hereafter we will refer to the barycentric velocities using V, and to the smoothed barycentric velocities using $\tilde{\rm V}$.

4.5 Point symmetry analysis of the sample

In this section we investigate whether the galaxies in the ePN.S sample show any deviation from point-symmetry. We studied the point-symmetry of the velocity fields of the galaxies by comparing the velocities $\tilde{V}(R, \phi)$ with $0 \leq \phi < \pi$ with those with $\pi \leq \phi < 2\pi$, changed in sign, in each radial bin. Asymmetries in the velocity fields are visible where these quantities significantly differ from each other. Figure 4.2 shows a few examples of this analysis. NGC 4649 is point-symmetric, while the others show significant deviations. In the sample of 33 galaxies, five are found to be non-point-symmetric: NGC 1316, NGC 2768, NGC 4472, NGC 4594 and NGC 5128. The galaxies for which we find evidence for asymmetries are those with the richest PN catalogs. For these objects the kinematic details are best recovered.

The others galaxies are consistent with point-symmetry, so for these systems we used the folded catalogs to reconstruct the final velocity and velocity dispersion fields, as described in Sect. 4.6.1. Since the mean velocity fields are the result of a smoothing procedure, their point symmetry does not rule out kinematic asymmetries on smaller scales.

As first step, the PN smoothed velocities $\tilde{V}_i$ are modeled with the harmonic expansion in Eq. (4.9), which also provides a good description of the galaxy velocity field where the spatial distribution of the tracers is not azimuthally complete. We consider as possible deviations from point-symmetry any groups of at least three tracers whose velocity $\tilde{V}_i$ deviates more than twice the errors from the fitted point symmetric model.

We evaluate the significance of the observed deviations from point symmetry by using 100 models of the galaxies, constructed as described in appendix 4.A.3. These are built using the positions (x_i, y_i) of the PNe from the real dataset, and, by construction, have a point symmetric mean velocity field. If similar local deviations from point symmetry that we observe in the velocity field of the galaxy appear also in the smoothed velocity fields of the models, then we know that they are artifacts of the smoothing over that particular spatial distribution, and not properties

of the intrinsic galaxy velocity field. Hence, for each feature in the galaxy, we select in the models the groups of PNe having the same coordinates as the feature, and compute the distribution of deviations of their velocities from the harmonic expansion fitted to each model. This distribution will give the probability of occurrence of the feature due to statistical fluctuations.

We found that the features in NGC 2768 and NGC 4594 have a probability $< 1\%$ to happen in the symmetric models so they are likely real. Those in NGC 2768 might be related to asymmetries in light distribution clearly visible in deep optical images (e.g. the g and r maps of Duc et al. 2015)[3]. The features in NGC 4594 are more likely due to extinction effects from its dusty disk, which hampers the detection of a complete sample of PNe in that area. In both cases the deviations of the velocity fields from point symmetry are localized and do not influence the kinematic analysis.

For NGC 1316, NGC 4472, and NGC 5128 the velocity offsets and the phase-angle shifts of the $\tilde{V}(R, \phi)$ in ($0 \leq \phi < \pi$, red in Fig. 4.2) with respect to ($\pi \leq \phi < 2\pi$, blue in Fig. 4.2) cannot be reproduced by the point symmetric models. These galaxies are well known recent mergers. Their halos are dominated by the recently accreted component which is not yet in a phase-mixed equilibrium with the surroundings and hence it still maintains peculiar kinematics (see also appendix 4.D).

One may be tempted to identify the groups of PNe whose velocity significantly deviate from the model as those associated to the structure, but we need to keep in mind that their velocities are the result of an averaging procedure, and that the different kinematic components can only be separated by analyzing the full phase space (see e.g. the GMM modeling of Longobardi et al. 2015b); such a study is beyond the scope of this paper.

[3] http://www-astro.physics.ox.ac.uk/atlas3d/

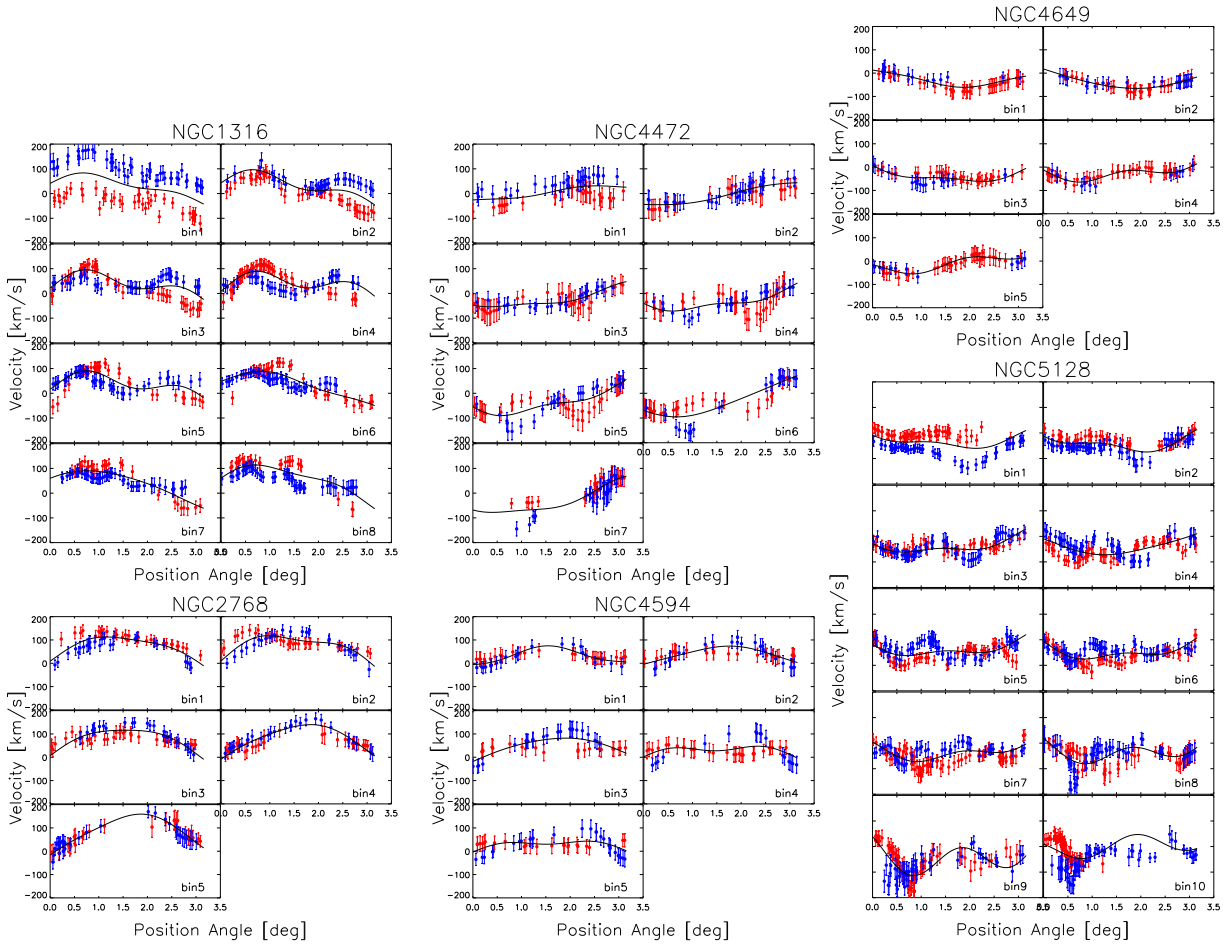

Figure 4.2: Galaxies with deviations from point symmetry. Mean velocity $\tilde{V}(R,\phi)$ as a function of the PN eccentric anomaly ϕ, folded around $\phi = \pi$, for each radial bin of NGC 1316, NGC 2768, NGC 4472, NGC 4594, NGC 4649, and NGC 5128. The black solid line is the fitted point-symmetric rotation model. The red points are the PN positions with $0 \leq \phi_i < \pi$; the blue points are those located at $\pi \leq \phi_i < 2\pi$, with their velocity changed in sign and coordinate ϕ shifted by π, i.e. $V(\phi)$ are compared with $-V(\phi+\pi)$. The overlap of PNe of opposite sides shows possible asymmetries in the velocity fields. NGC 2768 and NGC 4594 show localized small scale deviations from point symmetry, that do not influence the kinematic analysis. NGC 1316, NGC 4472, and NGC 5128 have non-point-symmetric velocity fields. By comparison NGC 4649 is point-symmetric.

4.6 The halo kinematics of ETGs

4.6.1 Velocity fields

A point symmetric system is, by definition, such that each point of the phase space (x, y, V) has a point-reflected counterpart $(-x, -y, -\mathrm{V})$. For the galaxies that do not show any significant deviation from point symmetry (Sect. 4.5), we assume that point symmetry holds. In these cases we can double the number of data-points by adding to the observed dataset its mirror dataset, and creating in this way a folded catalog (e.g Arnaboldi et al. 1998; Napolitano et al. 2001; Peng et al. 2004; Coccato et al. 2009). This helps in reducing the fluctuations in the recovered velocity fields. The results obtained using the folded catalogs are consistent with those from the unfolded datasets within the errors. Therefore for the galaxies consistent with point symmetry we will use the folded catalogs to produce the final mean velocity fields; for the others (i.e. NGC 1316, NGC 2768, NGC 4472, NGC 4594 and NGC 5128) the original catalogs are used.

Figure 4.3 shows the result for two galaxies with a similar number of tracers, NGC 4494 and NGC 4552. Both are point symmetric, so the velocity fields in Fig. 4.3 are built using the folded catalogs. NGC 4494 is a FR showing some rotation also in the halo. Its velocity dispersion field reveals that σ decreases with radius. The SR NGC 4552, by contrast, displays increasing rotation velocity about two perpendicular axes, and increasing velocity dispersion with radius.

The smoothed velocity fields for all the galaxies of the ePN.S sample are shown in appendix 4.E. For a more immediate visualization we present interpolations of the velocity fields, based on computing $\tilde{V}$ and $\tilde{\sigma}$ on a regular grid. The kinematics typically extends a median of 5.6 R_e, covering a minimum of $3R_\mathrm{e}$ to a maximum of 13 R_e. The adopted R_e values are listed in Table 4.1. Table 4.1 also shows the mean radius of the last radial bins, in which we can statistically determine $\tilde{\mathrm{V}}$ and $\tilde{\sigma}$.

The typical errors on the mean velocities and on the velocity dispersions, evaluated with Monte Carlo simulations, range from 10 to 40 km s^{-1}, being smaller for galaxies with a larger number of tracers and higher $\tilde{V}/\tilde{\sigma}$. These errors on the mean velocity fields, the mean errors on the radial velocity measurement, the kernel parameters A and B used in the smoothing procedure, and the systemic velocities subtracted are reported in Table 4.2.

A visual comparison with the kinematic maps published by the Atlas3D (Krajnović et al. 2011) and SLUGGS (Arnold et al. 2014; Foster et al. 2016) surveys shows a general good agreement for all the galaxies in the regions of overlap. By consistency or good agreement we mean that the values and trends in V_rot, σ from either kinemetry (by Krajnović et al. 2008; Foster et al. 2016) or slit absorption line kinematics agree within the errors with the kinematics from the PNe in the regions of overlap, or the latter extend such radial trends to the outer regions. See the appendix 4.D for a detailed description of the individual objects.

4.6.2 Kinematic parameters

We quantify the properties of the reconstructed mean velocity fields by evaluating the amplitude of rotation V_rot, the variation of the PA_kin with radius, and the possible misalignments with PA_phot. Therefore we model the velocities in each elliptical bin as a function of the angle ϕ (positive

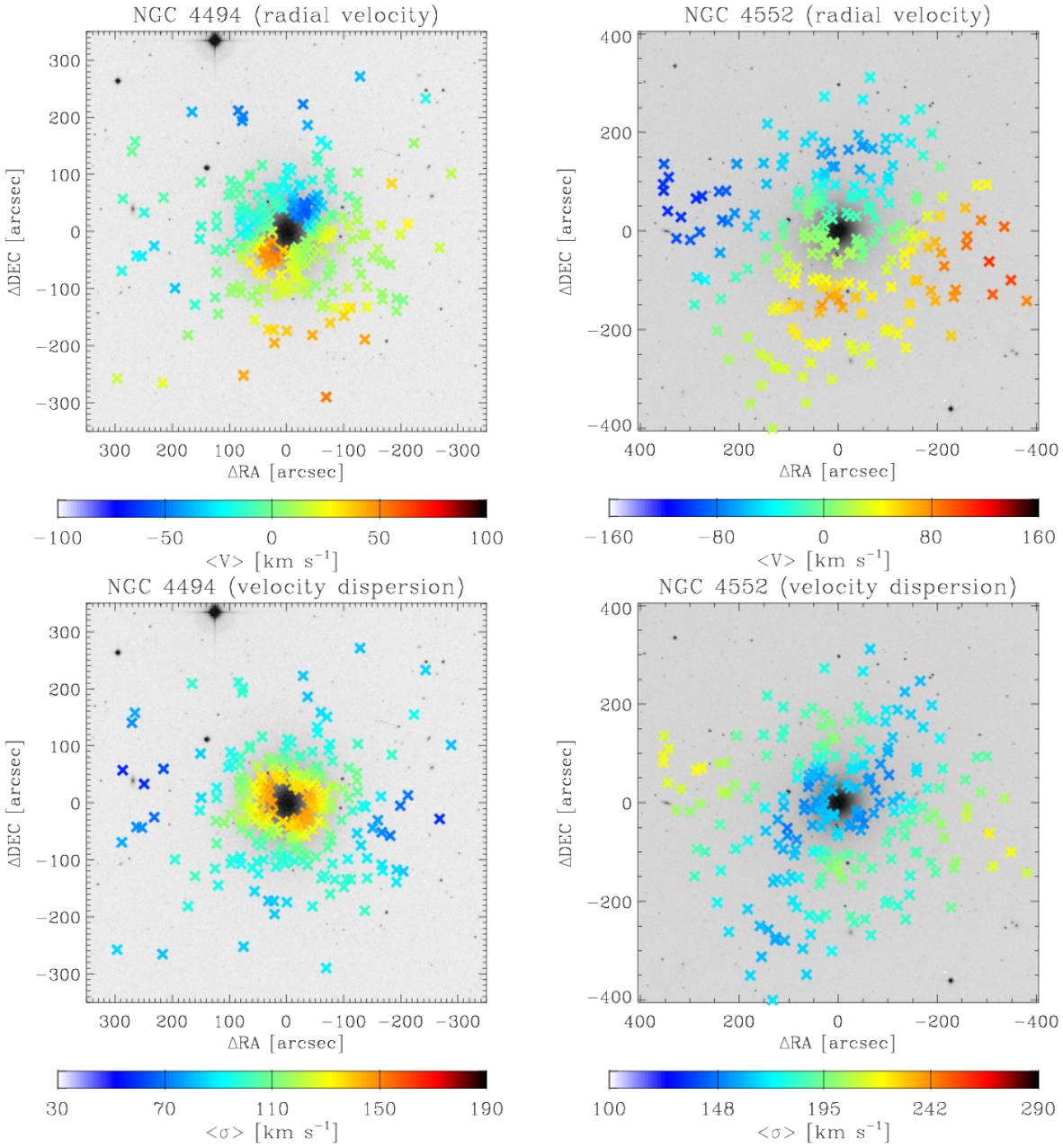

Figure 4.3: Top row: Smoothed velocity fields of NGC 4494 and NGC 4552; bottom row: velocity dispersion fields. The fields are built using the folded catalogs, but only the positions of the actual PN data points are shown. The images in the background are from the Digitized Sky Survey (DSS); north is up, east is left.

angles are from north to east, with the zero at north) with the rotation model in Eq. (4.10), as described in Sect. 4.3.2.

Figure 4.4 shows the smoothed velocity field $\tilde{V}(R, \phi)$ in each elliptical radial bin for a subsample of galaxies: a SR, NGC 4552, and four FRs, NGC 4473, NGC 4494, NGC 5866, and NGC 7457. The solid lines are the rotation models that give the best fit to the data, and from which we derive the kinematic parameters. The errors on the fitted parameters are derived from Monte Carlo simulations as described in Sect. 4.3.2, and depend on the number of tracers and the ratio $\tilde{V}/\tilde{\sigma}$. In the case of the galaxies show in Fig. 4.4, they are largest for NGC 4473, which has very low rotation in the halo, and smallest for the lenticular galaxy NGC 7457, which is dominated by rotation up to large radii.

We divided the sample of ETGs into FRs and SRs according to the definition of Emsellem et al. (2011), see Table 4.1. In Fig. 4.5 we show separately for both families the fitted parameters $V_{\rm rot}$, s_3 and c_3, as functions of the major axis distance R in units of $R_{\rm e}$. This is a reasonable choice in case of flattened systems rotating along the photometric major axis. In case of misalignment or twist of the $PA_{\rm kin}$, R does not correspond to the position of the peak in $\tilde{V}$ but to the major axis of the elliptical bin in which the amplitude $\tilde{V}$ is calculated. Figure 4.6 shows the misalignment Ψ of $PA_{\rm kin}$ with respect to $PA_{\rm phot}$, $\Psi = PA_{\rm kin}(R) - PA_{\rm phot}$. If the difference $PA_{\rm kin}({\rm bin1}) - PA_{\rm phot}$ (where $PA_{\rm kin}({\rm bin1})$ is the value measured in the first radial bin), is greater than 90 degrees, we define Ψ as $PA_{\rm kin}(R) - PA_{\rm phot} - \pi$. Since $PA_{\rm phot}$ is a constant value for each galaxy, a variation of $PA_{\rm kin}$ with radius corresponds to a variation of Ψ. We do not use the definition of Franx et al. (1991), $\sin\Psi = \sin\Big(PA_{\rm kin}(R) - PA_{\rm phot}\Big)$, as it does not allow the description of large position angle twists. The values and the references for the $PA_{\rm phot}$ used are in Table 4.1.

Both $V_{\rm rot}$ and Ψ are compared with literature values in Figs. 4.5 and 4.6. When available, we show the profiles from the kinemetric analysis of Foster et al. (2016) on the SLUGGS+Atlas3D data, or the kinemetric profiles from Krajnović et al. (2008). In these cases we rescale the radii of the profiles to major axis distances using the flattening $q_{\rm kin} = q_{\rm phot}$ given by Foster et al. (2016), or $\langle q_{\rm kin} \rangle$ given by Krajnović et al. (2008). For the other galaxies we plot the corresponding quantities from the kinemetry of Krajnović et al. (2011, namely $k_1^{\rm max}$ and $PA_{\rm kin}$ from their Table D1), or the kinematic profiles from long slit spectroscopy similarly rescaled (references in Table 4.1). While comparing with the literature, it is important to note the following effect. A kinematic measurement from a slit along the major axis of an edge-on fast rotating galaxy will give high velocities and low dispersions. On the other hand, the PN velocity fields are the results of a smoothing procedure, which averages together PNe belonging to the very flat disk with PN belonging to the spheroid. This might result in a systematically lower rotation and higher velocity dispersion (see Eq. 4.2) in the PN velocity fields. A decomposition of the PNe into disk and spheroid components has already been performed by Cortesi et al. (2013b) for some ePN.S galaxies, and it is beyond the scope of this paper to extend this to the whole sample of fast rotators. In addition, if the number of tracers or the ratio V/σ is low, our kinematic analysis provides a lower limit for the rotation velocity and an upper limit for the velocity dispersion. This issue is addressed in appendix 4.A. In such cases, the kinematics traced by the PNe may show systematic differences from that in the integrated light as consequence of the discrete spatial sampling of the velocity field by the adopted tracers.

The higher order harmonics amplitudes s_3 and c_3 differ from zero whenever the smoothed

velocity field deviates from simple disk-like rotation. This happens for example when the velocity field is cylindrical (see the case of NGC 3115), or in correspondence to components rotating at different position angles (e.g. NGC 4649).

Misalignments and twists of the $PA_{\rm kin}$ are typically displayed by triaxial galaxies, see Sect. 4.6.4. Figure 4.6 shows that both FRs and SRs can have radial variations of the $PA_{\rm kin}$ or a constant non-negligible Ψ. These galaxies may have a triaxial halo. A few galaxies instead have kinematically decoupled halos with respect to the regions $\lesssim 2R_{\rm e}$. Section 4.6.4 validates these results for each galaxy using models.

The asymmetric galaxies (i.e. NGC 1316, NGC 2768, NGC 4472, NGC 4594, and NGC 5128) are, by construction, not well represented by the point symmetric model and increasing the number of harmonics does not improve the quality of the fit. We can however still use the fitted parameters to obtain an approximate description of the shape of their velocity field.

4.6.3 Velocity dispersion profiles

Figure 4.7 shows the velocity dispersion profiles, azimuthally averaged in radial bins. These have been calculated using two different methods. In the first we used the interpolated velocity dispersion field $\tilde{\sigma}(x, y)$ in elliptical annuli of growing radius, with position angle and ellipticity as in Table 4.1. The values shown in the plots (solid lines) are averages over each elliptical annulus, and the errors (dotted lines) are taken conservatively as the means of the Monte Carlo simulated errors in the elliptical annulus (Sect. 4.3.2). The second method is binning the measured radial velocities v_i of the PNe in the radial bins built as described in Sect. 4.3.2. The PN catalogs are folded by point symmetry and the dispersion $\sigma_{\rm bin}$ with respect to the weighted mean velocity is computed in each bin. The weights are computed from the measurement errors. The errors on the dispersion are given by the expression: $\Delta\sigma_{\rm bin} = \sigma_{\rm bin}/\sqrt{2(N_{\rm bin}-1)}$, where $N_{\rm bin}$ is the number of PNe in each bin. The values and the trends given by the two methods are generally in good agreement.

The profiles obtained are compared with dispersion profiles from integrated light (red stars). For the galaxies in common with the SLUGGS survey, we show the profiles from the kinemetric analysis of Foster et al. (2016) on the SLUGGS+Atlas3D data in elliptical radial bins. For NGC 3384, NGC 3489, NGC 4339, NGC 4552, and NGC 4636, we extracted the azimuthally averaged profiles from the Atlas3D data (Cappellari et al. 2011; Emsellem et al. 2011) in elliptical bins (geometry in Table 4.1). For the other galaxies we show the velocity dispersion along the $PA_{\rm phot}$ from long slit spectroscopy (references in Table 4.1). Our dispersion profiles generally compare well with the literature in the regions of overlap (typically $R \lesssim 2R_{\rm e}$). The results are described in Sect. 4.7, separately for FRs and SRs.

We tested whether it is possible that the large scale trends in the velocity dispersion profiles are the result of statistical and smoothing effects, by using 100 models of the galaxies, built as described in appendix 4.A.3, created with a constant dispersion profile with radius. The velocity dispersion profiles are recovered with the same procedure as for the measured PN sample. We find that although artificial local structures may sometimes appear in the velocity dispersion maps, they are not such as to influence the trends with radius of the large scale velocity dispersion fields, and typically the error bars from Monte Carlo simulations give a good estimate of the

uncertainties.

4.6.4 Triaxiality

Significant twists of the $PA_{\rm kin}$, as well as its departures from $PA_{\rm phot}$ imply an intrinsic triaxial shape for the system. In an axisymmetric object both the projected photometric minor axis and the intrinsic angular momentum are aligned with the symmetry axis of the system, while in a triaxial galaxy the rotation axis can be in any direction in the plane containing both the short and long axis. This is because in a triaxial potential the main families of stable circulating orbits are tube orbits which loop around the minor (z-tube orbits) or the major axis (x-tube orbits) (see e.g., de Zeeuw 1985; Statler 1987; Schwarzschild 1993). The relative number of z- and x-tube orbits determines the direction of the intrinsic angular momentum. Thus, depending on the variation of this ratio with radius we can have that

- the measured $PA_{\rm kin}$ shows a smooth radial twist (e.g. NGC 4552 in Fig. 4.6, see Sect. 4.6.4);
- $PA_{\rm kin}$ has a sudden change in direction (i.e. the galaxy has a kinematically decoupled halo, like NGC 1399, see Sect. 4.6.4);
- $PA_{\rm kin}$ has a constant misalignment with respect to the $PA_{\rm phot}$ (e.g. NGC 3923, see Sect. 4.6.4).

Therefore we consider as triaxial galaxies the objects displaying at least one of these features in their velocity fields with statistical significance. We do not consider in this analysis galaxies that show significant variation of the kinematic position angle in the last radial bin only, as the geometrical shape of the survey area might prevent an azimuthally complete detection of PNe in the outermost bin. The statistical significance is determined by our MC modeling as described in appendix 4.A.3, which gives us the probability that a measured property of the smoothed velocity field is obtained in sequences of galaxy-specific simulated PN data sets without this feature. Table 4.3 provides a summary of the results, which are discussed in the following sections.

Galaxies with radial variation in the kinematic position angle

Figure 4.6 shows that the fitted $PA_{\rm kin}$ may show a smooth variation with radius. This happens in NGC 3377, NGC 3379, NGC 4494, NGC 4697, NGC 4649, NGC 5128, and NGC 5866, among the FRs, and in NGC 3608, NGC 4472, and NGC 4552 among the SRs.

We tested whether the variation with radius of the $PA_{\rm kin}$ for a galaxy is an artifact of the combination of a small number of tracers and the smoothing procedure. We looked at the fitted $PA_{\rm kin}$ in 100 models of each galaxy, built as described in appendix 4.A.3, which have by construction the $PA_{\rm kin}$ of the mean velocity field aligned with $PA_{\rm phot}$. For each radial bin we computed the probability of obtaining the observed misalignment Ψ from the distribution of the misalignments in the models. We found that the probability of observing a twist of 48 ± 24 degrees in models of NGC 3377 is $\sim 4\%$; it is $\sim 3\%$ for the twist of 71 ± 25 degrees in NGC 3379, $\sim 2\%$ for the twist

of 20 ± 12 degrees in NGC 3608, and ∼ 4% for the twist 32 ± 19 degrees in NGC 4494. For the other galaxies, none of the 100 models produces the observed trends of $PA_{\rm kin}$.

For NGC 4472 the determination of $PA_{\rm kin}$ is influenced by the kinematics of the in-falling satellite UGC 7636. An inspection of its smoothed velocity field suggests that the main body of the galaxy has approximately major axis rotation, once the PNe of the satellite are excluded. Nevertheless we include this galaxy in the sample of potentially triaxial galaxies, and we refer to Hartke et al. (2018) for a more detailed study.

NGC 5128 shows non point-symmetric kinematics, and rotation along both the photometric major and minor axes. The high number of tracers available for this galaxy (1222 PNe) makes this kinematic signature unambiguous.

NGC 1316 shows a small but significant jump of the $PA_{\rm kin}$ at $\sim 200 - 250$ arcsec, that is related to the perturbed kinematics of this galaxy.

NGC 4697 has a constant $PA_{\rm kin}$ profile consistent with the $PA_{\rm phot}$, with a sudden localized variation at $\sim 3R_{\rm e}$. The study of Sambhus et al. (2006) on the same PN dataset showed evidence for a secondary PN population in this galaxy that is not in dynamical equilibrium with the main population, and which has not been excluded in this analysis. The presence of this population does not determine any significant deviation from point symmetry of its smoothed velocity field. However we refrain to include this galaxy in the sample of galaxies with triaxial halo.

Therefore, excluding NGC 1316 and NGC 4697 that have local and irregular variations of $PA_{\rm kin}$, there are nine galaxies in the sample showing significant kinematic twist, of which six are FRs and 3 SRs.

Galaxies with kinematically decoupled halos

Galaxies with kinematically decoupled halos are galaxies whose outskirts rotate about a different direction than their inner regions, hence $PA_{\rm kin}$ shows a step function with radius. NGC 1399 and NGC 4365 both show this feature beyond $2R_{\rm e}$.

NGC 1399 is found to be slowly rotating around its $PA_{\rm phot}$ (i.e. $\Psi \sim 90$ degrees) at ~ 30 km s^{-1}inside $1R_{\rm e}$, in very good agreement with the integral field spectroscopic data of Scott et al. (2014). The halo $PA_{\rm kin}$, by contrast, is almost aligned with the $PA_{\rm phot}$ (i.e. $\Psi = 0$) degrees. We studied whether such a misalignment is an artifact of our procedure, using models that mimic the inner kinematics, that is with $PA_{\rm kin}$ aligned with the photometric minor axis . The probability of measuring a misalignment of the halo similar to the observed one is 2%.

The $PA_{\rm kin}$ of NGC 4365 is ill-constrained in the innermost regions where the kinematics is compatible with no rotation. At the center we do not recover the rolling about the minor axis visible in velocity fields from absorption line data (Emsellem et al. 2011; Arnold et al. 2014), because of smoothing over the inner velocity gradients. In these regions the bright background of the galaxy hampers the detection of PNe, and the resulting low number of tracers combined with the low V/σ leads to heavily smoothed velocities. We do detect a significant outer ($R \gtrsim 3R_{\rm e}$) rotation of $\sim$ 50 km s^{-1}along $PA_{\rm phot}$ ($\Psi \sim 0$ degrees), misaligned with respect to the inner kinematics reported in the literature. So we built mock models as described in appendix 4.A.3 but with $PA_{\rm kin}$ given by IFS data up to 1 $R_{\rm e}$(references are given in Table 4.1). We found that none of the models displays the observed step function in the $PA_{\rm kin}$ values.

We therefore conclude that the signature of a kinematically decoupled halo has a high probability to be real in both galaxies.

Galaxies with constant offset between photometric and kinematic major axis

The galaxies showing an approximately constant misalignment of the $PA_{\rm kin}$ with respect to the $PA_{\rm phot}$ are NGC 0821, NGC 1344, NGC 3115, NGC 4473, and NGC 4742 among the FRs, and NGC 3923, NGC 4374, NGC 4636, and NGC 5846 among the SRs (see Fig. 4.6). In these cases we can define the $PA_{\rm kin}$ using all the PNe, without radial binning. The derived quantities can be compared to the $PA_{\rm kin}$ measured in mock models built as described in appendix 4.A.3.

For most of the listed galaxies none of the models reproduces the observed misalignments. NGC 0821 has a misalignment of 50 degrees with $\sim 4\%$ probability in the Monte Carlo models, while the misalignment of 22 degrees of NGC 4742 has 1% probability. Because of the small number of tracers and the low V/σ ratio this probability is higher for NGC 5846 (9%). To these objects we add NGC 4473 whose $PA_{\rm kin}$ is not well determined from the PN kinematics because of the very low V/σ ratio in its halo, but Foster et al. (2013) already detected a significant rotation along the minor axis using absorption line data, showing this object to be triaxial.

The PN velocity field of NGC 3115 shows a constant misalignment of $\sim$ 10 degrees with respect to $PA_{\rm phot}$. This misalignment is probably related to perturbations at the interface between the disk and the spheroid, visible as deviations from axisymmetry in the photometry of the disk component (Capaccioli et al. 1987, see also discussion in appendix 4.D). NGC 3115 is a complicated case, and is not included in the sample of galaxies with triaxial halo.

Therefore in the ePN.S sample a total of eight galaxies, four FRs and four SRs, show a significant constant misalignment of $PA_{\rm kin}$ with $PA_{\rm phot}$.

Summary

We conclude that a total of 19 galaxies ($\sim$ 60%) of the ePN.S sample show smoothed velocity fields that reveal their non-axisymmetric nature. Nine objects (6 FRs and three SRs) have significant kinematic twists, and eight (four FRs and four SRs) show a significant constant misalignment of $PA_{\rm kin}$ with $PA_{\rm phot}$. In addition two SRs have a kinematically decoupled halo. The observed features are more than 2 sigma significant for most of the cases (1.7 sigma for NGC 5846), and they are not effects of the folding operation on the catalogs nor of the smoothing procedure.

All in all, we found that all the SRs and ten out of 24 FRs show indications of intrinsic triaxial morphology in the PN kinematics. We will discuss the signature of triaxiality in the photometry in Sect. 4.8.4.

Table 4.3: Results of the kinematic analysis

Galaxy NGC	point symm.[a]	features in $PA_{\rm kin}$(R)[b]	multiple comp.[c]	triaxial[d]	R_T[e] [arcsec]	NOTES[f]
0584	y	n	n	n	———	small number of tracers
0821	y	y	n	y	60 ± 30	(A,C)
1023	y	n	n	n	160 ± 20	(A)
1316	n	y	y	n	75 ± 25	(A) - merger remnant
1344	y	y	n	y	30 ± 15	(C) - prolate rotation
1399	y	y	y	y	30 ± 15	(B) - kinematically decoupled halo
2768	n	n	n	n	145 ± 45	(A) - fast rotating halo
2974	y	n	n	n	———	small number of tracers
3115	y	y	n	n	135 ± 45	(A) - photometry reveals a perturbed disk at the interface with the spheroid component
3377	y	y	y	y	55 ± 15	(A)
3379	y	y	y	y	60 ± 20	(A,C) - hints for growing rotation in the outskirts
3384	y	n	n	n	———	extended disk
3489	y	n	n	n	———	small number of tracers
3608	y	y	n	y	55 ± 35	(B)
3923	y	y	n	y	70 ± 30	(B)
4278	y	n	n	n	25 ± 15	(A)
4339	y	n	n	n	———	small number of tracers
4365	y	y	y	y	125 ± 25	(C) - kinematically decoupled halo
4374	y	y	n	y	83 ± 33	(B)
4472	n	y	y	y	25 ± 10	(B) - recent merger; kinematics dominated by infalling satellite
4473	y	y	n	y	25 ± 13	(A) - minor axis rotation observed by Foster et al. (2013)
4494	y	y	y	y	93 ± 43	(A)
4552	y	y	y	y	73 ± 58	(B,C)
4564	y	n	n	n	85 ± 45	(A) - fast rotating halo
4594	y	n	n	n	180 ± 90	(A) - no detections in the plane of the disk (dust absorption)
4636	y	y	y	y	140 ± 40	(C)
4649	y	y	y	y	115 ± 15	(A) - no detections on the west side of the galaxy
4697	y	y	n	n	85 ± 65	(A) - hints for growing rotation in the outskirts; this PN sample contains a secondary PN population out of dynamical equilibrium (Sambhus et al. 2006)
4742	y	y	n	y	43 ± 32	(C)
5128	n	y	y	y	95 ± 55	(C) - recent merger
5846	y	y	n	y	100 ± 50	(B)
5866	y	y	n	y	75 ± 25	(A) - fast rotating halo
7457	y	n	n	n	———	extended disk

Continued on next page

Continued from previous page

Galaxy NGC	point symm.[a]	features in $PA_{\rm kin}$(R)[b]	multiple comp.[c]	triaxial[d]	R_T[e] [arcsec]	NOTES[f]

[a] Point symmetry properties of the PN smoothed velocity fields: "y" marks point symmetric galaxies while "n" marks galaxies showing asymmetries, see Sect. 4.5.

[b] Significant kinematic twist or misalignment of $PA_{\rm kin}$ with respect to $PA_{\rm phot}$: "y" marks galaxies showing at least one of these, see Sect. 4.6.4.

[c] For the galaxies marked with "y", the PN smoothed velocity fields reveal rotation along two perpendicular axes or a halo which is kinematically decoupled with respect to the innermost regions, see Sects. 4.7 and 4.6.4.

[d] Galaxies marked with "y" have been classified as triaxial in Sect. 4.6.4.

[e] $R_T \pm \Delta R_T$ is the radial range of the kinematic transition.

[f] Criteria (A, B, C) used to define the radial range $R_T \pm \Delta R_T$ as described in the text (Sect. 4.8), and notes on individual galaxies (see also the dedicated appendix 4.D)

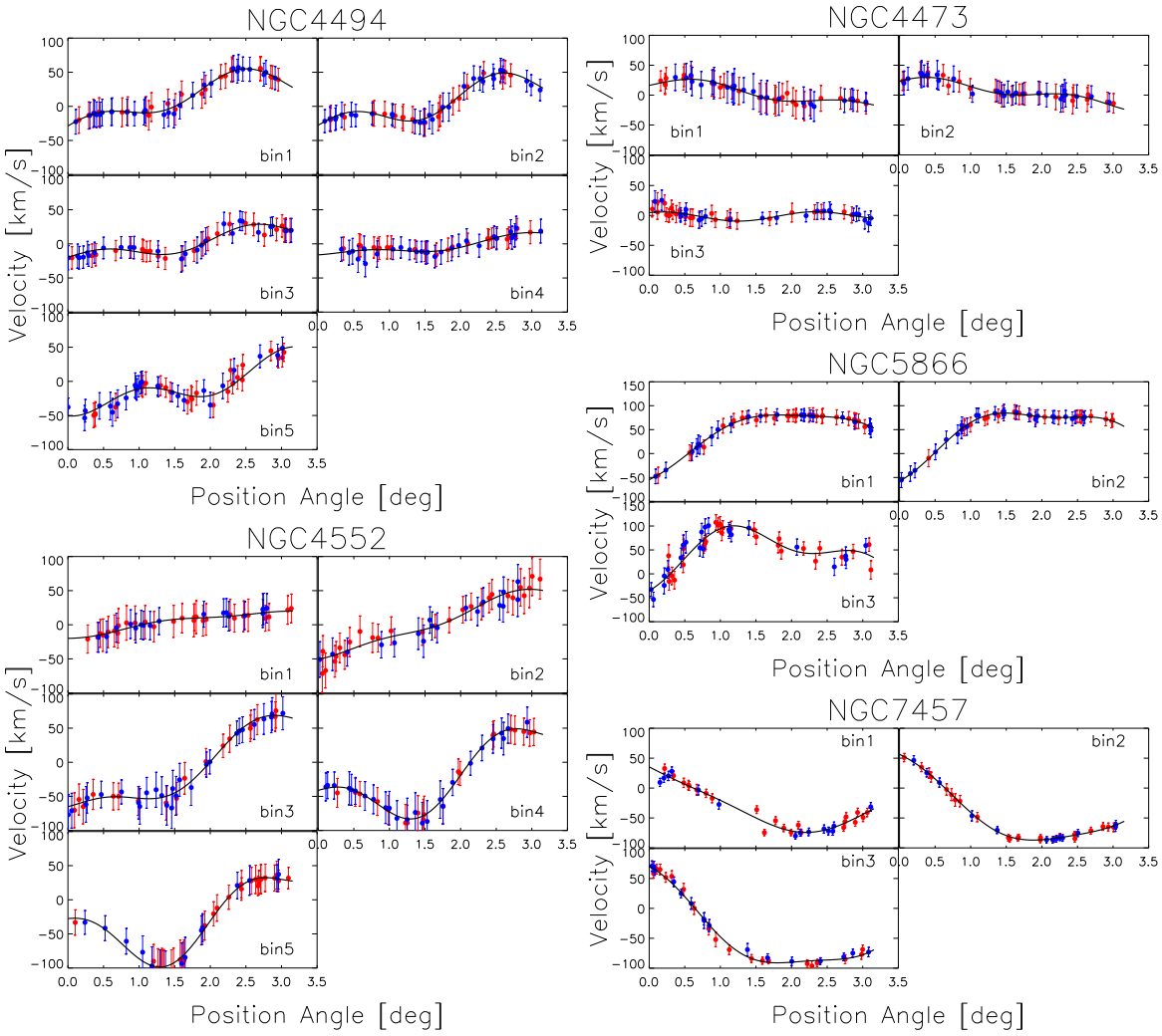

Figure 4.4: Point symmetric galaxies. Mean velocity field $\tilde{V}(R,\phi)$ in elliptical annuli as a function of the PN eccentric anomaly ϕ, folded around $\phi = \pi$ for the FRs NGC 4473, NGC 4494, NGC 5866 and NGC 7457, and the SR NGC 4552 (colors as in Fig. 4.2). $\tilde{V}(R,\phi)$ is reconstructed using the folded catalogs, and shown at the position (R_i,ϕ_i) of the actually observed PNe. The solid lines are the best rotation model (see Eq. 4.10) fit to the velocity field.

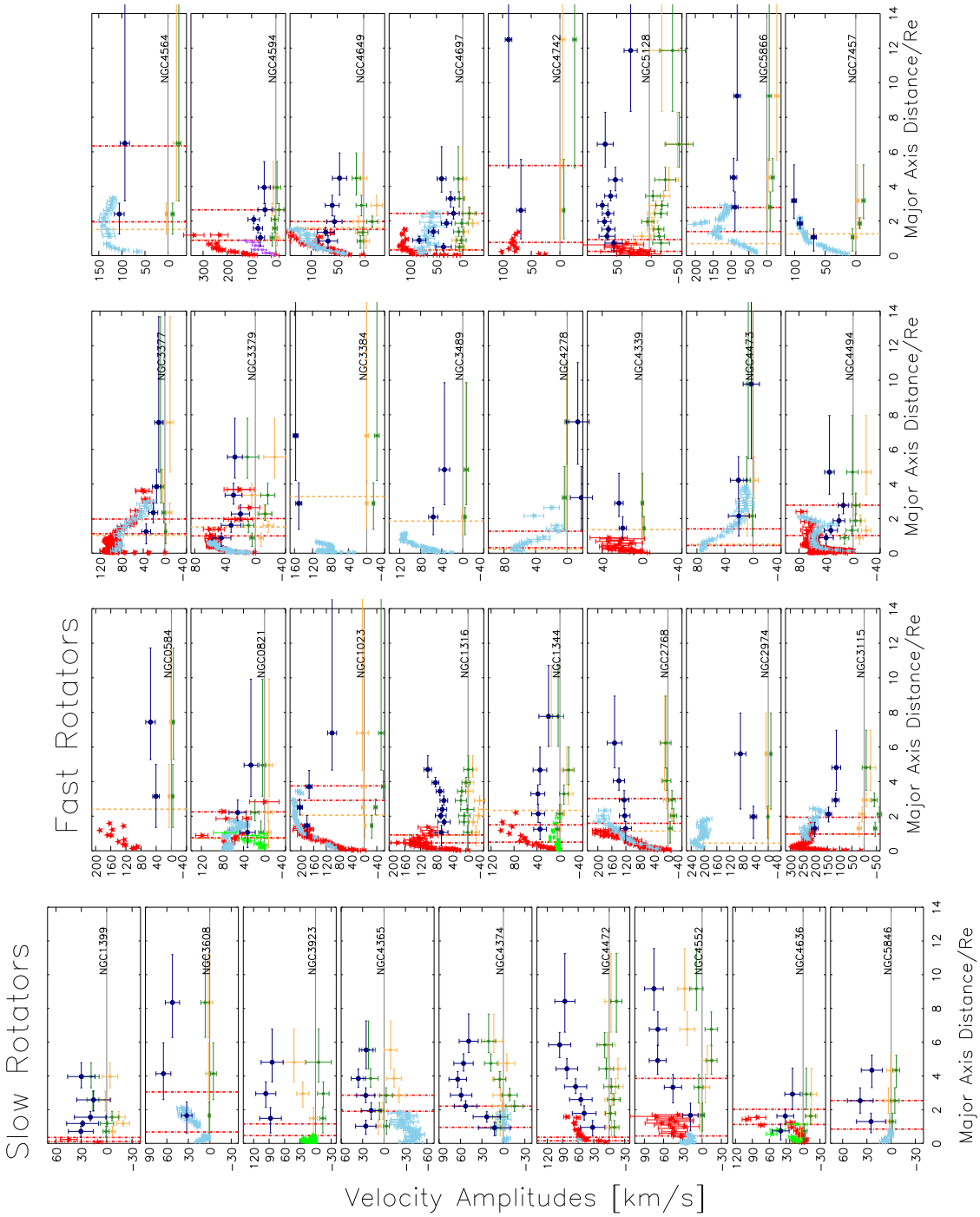

Figure 4.5: Fitted rotation velocities $V_{\rm rot}(R)$ (full circles) and third order harmonics amplitudes, $c_3(R)$ in green and $s_3(R)$ in orange, as functions of the major axis distance for SRs and FRs. The comparison values for $V_{\rm rot}$ from absorption line data from the literature are shown with colored stars. Whenever available we show kinemetric profiles (light blue stars); for the other galaxies we show velocities from long slit spectroscopy along the photometric major axis (red stars) or minor axis (green stars). The references are in Table 4.1. For NGC 4594 we show in addition the stellar kinematics from a slit along $PA_{\rm phot}$, offset by 30 arcsec (purple stars). The dashed vertical lines for the FRs show the disk half light radius $R_{1/2}$, see Sect. 4.7.3. The red dot-dashed vertical lines report the radial transition range $R_T \pm \Delta R_T$, see Sect. 4.8.6.

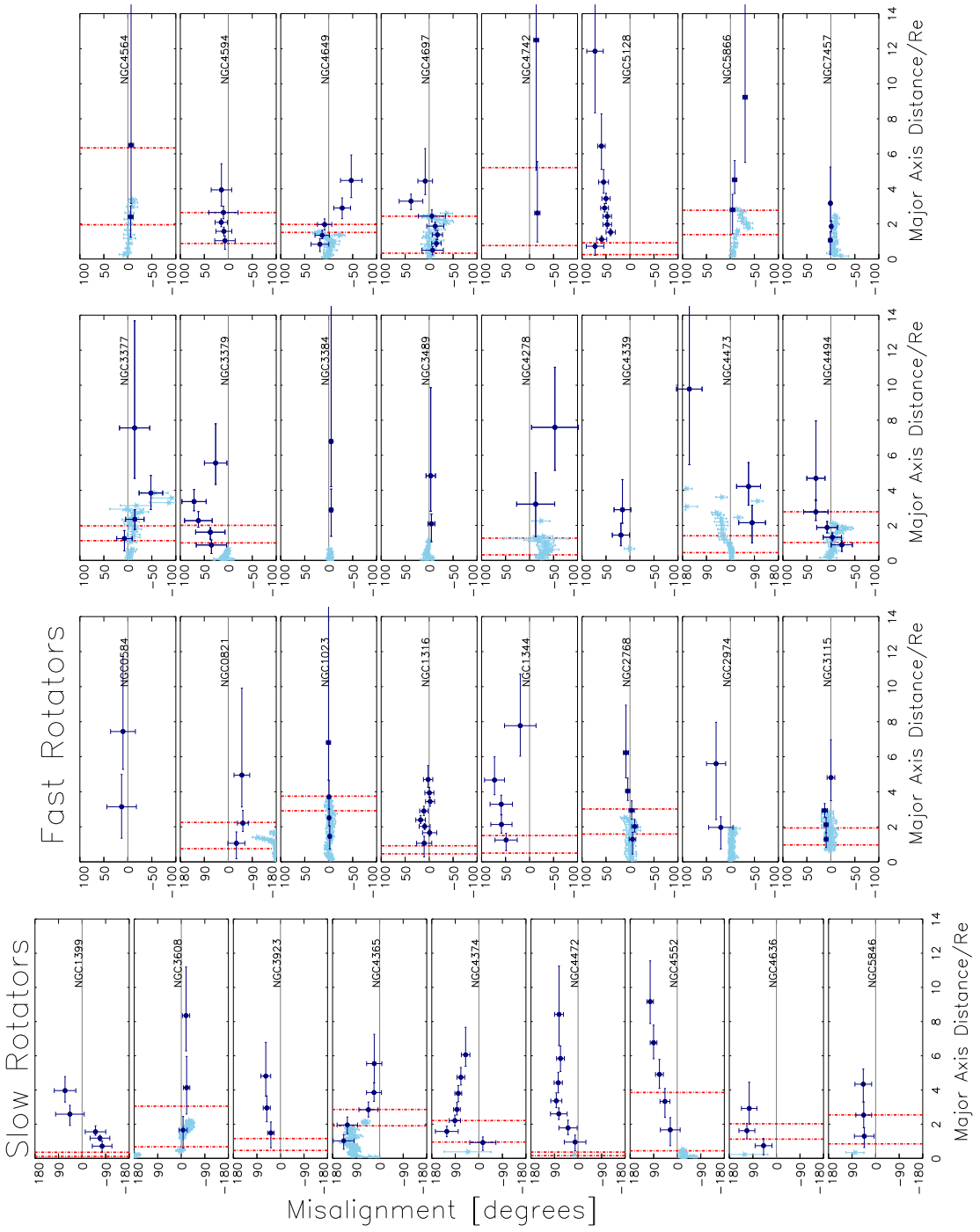

Figure 4.6: Misalignments $\Psi(R)$ (full circles) as function of the major axis distance for FRs and SRs. The horizontal solid line shows the $\Psi = 0$ axis. The light blue stars are the Ψ values calculated on $PA_{\rm kin}$ from the kinemetry of Foster et al. (2016), Krajnović et al. (2008), and Krajnović et al. (2011); for the other galaxies the $PA_{\rm kin}$ is not previously available in the literature. The red dot-dashed vertical lines report the radial transition range $R_T \pm \Delta R_T$, see Sect. 4.8.6. Signatures of triaxial halos are seen in NGC 0821, NGC 1344, NGC 1399, NGC 3377, NGC 3379, NGC 3608, NGC 3923, NGC 4365, NGC 4374, NGC 4472, NGC 4473, NGC 4494, NGC 4552, NGC 4636, NGC 4649, NGC 4742, NGC 5128, NGC 5846, and NGC 5866.

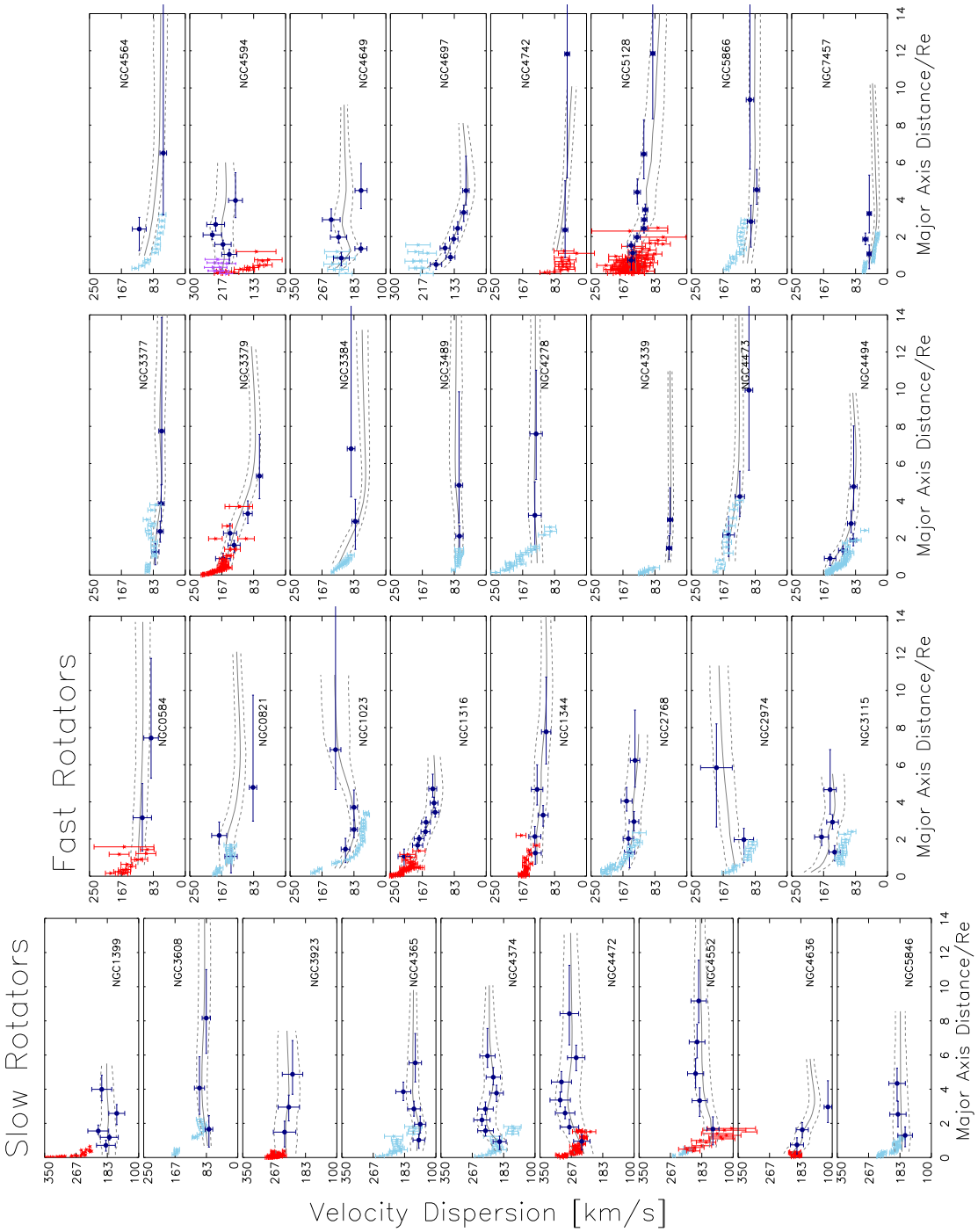

Figure 4.7: Azimuthally averaged velocity dispersion profiles as functions of the major axis distance in units of R_e for SRs and FRs (full circles). The gray solid lines represent the profiles from the interpolated velocity fields with their errors (dashed lines, see text). The stars show dispersion from integrated light: when available we plot the kinemetric analysis of Foster et al. (2016) on the SLUGGS+Atlas3D data in elliptical bins (light blue stars); for NGC 3384, NGC 3489, NGC 4339, NGC 4472, NGC 4552, and NGC 4636, we show azimuthally averaged profiles from Atlas3D data (Cappellari et al. 2011; Emsellem et al. 2011); for the other galaxies we show data from long slit spectroscopy along PA_{phot} (red stars, references in Table 4.1). For NGC 4594 we also plot the stellar velocity dispersion profile in a slit parallel to the major axis but 30 arcsec offset from the center (purple stars).

4.7 Results per family

4.7.1 Slow rotators

In the sample of 33 galaxies nine are SRs. Figure 4.5 shows that they typically display some more pronounced rotation at large radii when compared to rotation in their central regions as measured from absorption line spectroscopy. The PN velocity fields show gently increasing profiles for the $V_{\rm rot}$ amplitude which, eventually, flatten around ~ 50 km s^{-1}. Twists or misalignments of the $PA_{\rm kin}$ are commonly observed, so that all the SRs show signatures of a triaxial halo (see Fig. 4.6). In particular, we found that the halos of NGC 1399 and NGC 4365 are kinematically decoupled with respect to the innermost regions as mapped by Scott et al. (2014) and Arnold et al. (2014). NGC 4472 has a non point-symmetric velocity field, as a result of a recent accretion event. The complicated kinematics of the SRs is also reflected in the amplitudes of the third order harmonics, which describe the presence of additional kinematic components, and twists of the $PA_{\rm kin}$.

The velocity dispersion profiles, shown in Fig. 4.7, are generally flat in the halo. Some galaxies (e.g. NGC 1399, NGC 3608) reach such a constant value around $\sim 1-2R_{\rm e}$. Others (e.g. NGC 4374, NGC 4552) flatten only beyond $\sim 4-5R_{\rm e}$, after a small increase. NGC 4636 is the only SR showing a falling profile.

4.7.2 Fast rotators

In the ePN.S sample 24 galaxies are classified as FRs (Table 4.3). Figures 4.5 and 4.6 show that the majority of the objects have regular rotation along the photometric major axis. The comparison between inner and outer parts reveals that the rotation amplitudes $V_{\rm rot}$ show declining trends with more or less steep gradients for 14 out of 24 FRs: some galaxies show very small or no rotation in the outskirts (e.g. NGC 4278 and NGC 4473), while others reach a minimum, after which their rotation increases (e.g. NGC 4494 or NGC 4697). Among the remaining galaxies, three have fairly constant profiles (NGC 2768, NGC 4564, and NGC 5866), and 3 show increasing rotation (NGC 3384, NGC 4742, and NGC 7457). For NGC 0584, NGC 2974, NGC 3489 and NGC 4339, the limited number of tracers leads to heavy smoothing, allowing only an estimate of a lower limit for the rotation in the halo.

The $PA_{\rm kin}$ is well aligned with the photometric major axis in the majority of cases, but ten out of 24 galaxies display a kinematic twist (NGC 3377, NGC 3379, NGC 4494, NGC 4649, NGC 5128, and NGC 5866) or a constant misalignment with $PA_{\rm phot}$ (i.e. NGC 0821, NGC 1344, NGC 4473, and NGC 4742). The smoothed velocity fields of four galaxies (NGC 3379, NGC 4649, NGC 5128, and NGC 4494, see figures in appendix 4.E) show indications of additional components rotating along the minor axis of the system, while NGC 1344 has prolate rotation. All these features are generally interpreted as evidences of triaxiality of the systems (see Sect. 4.6.4) and 40% of the fast rotating galaxies of the sample display them in the halo.

The azimuthally averaged velocity dispersion profiles (Fig. 4.7) are found to be either constant (e.g. NGC 3377), or decreasing with radius. Some profiles decline gently (e.g. NGC 1344), while others decrease steeply in the halo (e.g. NGC 3379). This diversity between flat and falling profiles is also reflected in the variety of the $V_{\rm rms}$ profiles, as already observed by

Coccato et al. (2009), and is the result of differences in the mass distributions (Gerhard et al. 2001; Romanowsky et al. 2003; Deason et al. 2012; Morganti et al. 2013; Cappellari et al. 2015; Alabi et al. 2016; Veale et al. 2018) or the presence of radial anisotropy in the orbits (Gerhard et al. 1998; de Lorenzi et al. 2009; Napolitano et al. 2009), which may contribute to a lower projected velocity dispersion. For some lenticular galaxies (e.g. NGC 1023 or NGC 3115), the two-dimensional velocity dispersion maps (see figures in appendix 4.E) reveal the presence of the colder disk along its major axis, while the dispersion is higher along the minor axes. For NGC 1023 the presence of the disk is evident also in the azimuthally averaged velocity dispersion profile, which increases with radius as the contribution of the disk to the light decreases.

Among the fast rotating galaxies there are two mergers, NGC 1316 and NGC 5128. Their velocity fields are highly disturbed by the recent accretion events and are not very well described by point-symmetric rotation models, see appendix 4.D for more details.

The comparison of the PN kinematics with integrated light data shows a general good agreement in the overlapping regions, confirming once again that the PNe are reliable tracers of the kinematics of the parent stellar population. The tension with the stellar kinematics in cases of high rotation and low dispersion (see e.g. NGC 1023, NGC 2768, NGC 4594) is primarily related to the presence of a known near edge-on very flat disk that dominates the major axis stellar kinematics but not that of the PNe. Because our velocity fields are the results of an averaging operation that does not distinguish the PNe from the disk from those belonging to the spheroid, the velocity gradients are underestimated. Likewise the discrepancy between the integrated light data of NGC 4494 and its PNe could be explained by a face on disk fading into the spheroid at radii beyond the coverage of the stellar kinematics, combined with the lower spatial resolution of the PN smoothed velocity field.

In addition, if the disk is obscured by dust, the fraction of observed disk PNe is reduced, causing a drop in the measured rotation and a higher dispersion. An example is the case of NGC 4594. This galaxy has a dusty disk which affects the detections of PNe in that region, leading to heavily absorbed light in this component and hence inhibit the PNe detections in that region where the rotation is highest. The rotational velocity and the dispersion profiles from PNe agree well with slit data along a direction slightly offset (30 arcsec) from the disk plane (purple stars in Figs. 4.5, 4.7 and 4.8), but are offset with respect to the major axis profiles. With this in mind, we shall consider the smoothed velocity fields as giving a global description of the halo kinematics, but not of their small-scale spatial structures, unless the number of tracers is very large (as, for example, in the case of NGC 1316).

4.7.3 Embedded disks in fast rotators

The observed negative gradients of $V_{\rm rot}(R)$ observed for many FRs at large radii has been interpreted as signatures of a rotating disk component embedded in a dispersion dominated spheroid (Coccato et al. 2009; Arnold et al. 2014). Using a photometric disk-spheroid decomposition and maximum-likelihood fit, Cortesi et al. (2013b) reconstructed the kinematics of the disk and the spheroid separately in six of the ePN.S lenticular galaxies (NGC 1023, NGC 2768, NGC 3115, NGC 3384, NGC 3489 and NGC 7457). Arnold et al. (2014) reproduced the rotation profile of the E5-6 galaxy NGC 3377 also performing a disk-bulge decomposition. These works showed

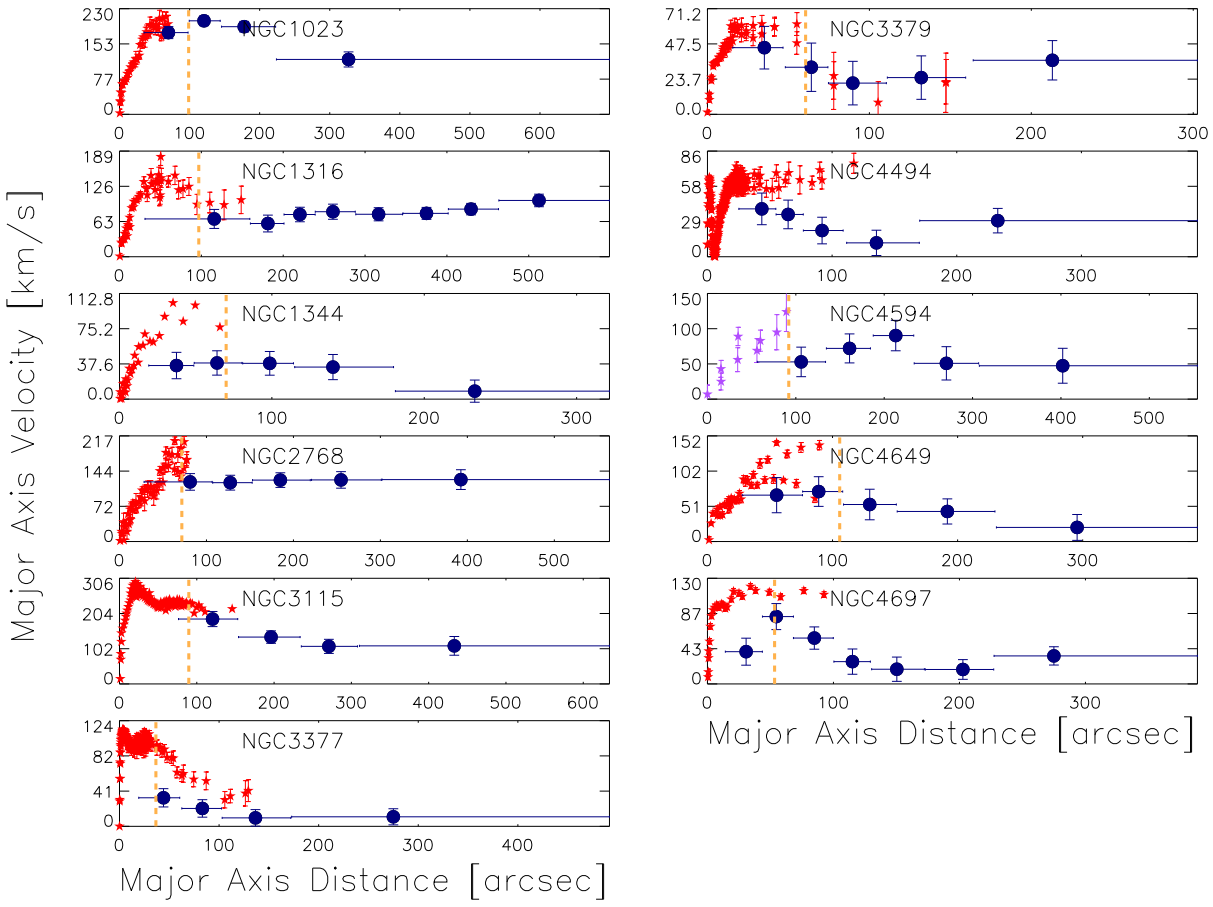

Figure 4.8: Rotation velocity profiles for the FRs with highest number of tracers along the major axis. The full circles show the fitted amplitude $V_{\mathrm{maj.ax.}}$ on the PN velocity fields (see Eq. 4.12). The red stars are stellar kinematics along the photometric major axis from the literature (references in Table 4.1). The PN kinematics of NGC 4594 is compared with the stellar kinematics from a slit parallel to the major axis, offset by 30 arcsec (purple stars). The orange vertical lines mark the sizes of the photometric disks (see text). NGC 4494 shows a decrease in $V_{\mathrm{maj.ax.}}$ but there is no photometric evidence for a stellar disk. When the disk fades in the slowly rotating spheroid, the rotation velocity decreases. In addition, the PN rotation velocity may be lower than the values from absorption line spectroscopy at the same radii because of the smoothing that averages disk and spheroid PNe for near edge-on disks.

that the variation in rotation reflects the transition between disk and bulge dominance in light, and their different spatial contribution in each galaxy explains the variety in the observed λ_R profiles (the detailed study of the λ_R profiles for the ePN.S sample is the subject of a separate paper, Coccato et al. in prep.). In the following we use the term "disk component" for a highly flattened, but definitely three-dimensional, oblate rotating structure (see also Sect. 4.8.4).

Here we can verify the interpretation for the negative gradients of $V_{\rm rot}(R)$ by estimating and comparing the "size" of the disk components given by the photometry, and the radius at which we observe the decrease in rotation. Figure 4.8 shows a subsample of the galaxies with the highest number of tracers, in order to have the best possible statistics. Most of them show a decreasing rotation amplitude. We fitted their radially binned smoothed velocity fields with a cosine, whose position angle is aligned with the photometric major axis,

$$\tilde{V}(R,\phi) = V_{\rm maj.ax.}(R)\cos\Big(\phi - PA_{\rm phot}\Big), \tag{4.12}$$

in order to extract the velocity profiles along the major axis. The fitted amplitudes are shown in Fig. 4.8. Overlaid in red is the stellar kinematics along the photometric major axis from literature slit data (references in Table 4.1). The orange vertical lines indicate the characteristic scale of the disks. For all the galaxies shown, the quantity plotted is the disk half light radius: $R_{1/2} \simeq 1.67R_h$. R_h is the disk scale length from an exponential fit of the disk component (R_h from Burkhead 1986; Scorza et al. 1998; Pignatelli 1999; Laurikainen et al. 2010; Beletsky et al. 2011; Krajnović et al. 2013a; Cortesi et al. 2013b, for Figs. 4.5 and 4.8).

We can see that the radial distance at which the decrease in the rotation occurs is consistent with the size of the disk. Therefore we interpret this behavior as the transition between a flat component that rotates fast and a dispersion dominated rounder spheroid. For NGC 4494 there is no photometric evidence for a disk component. In this case the stellar disk component might be absent or very faint if the galaxy is seen nearly face on ($\epsilon \sim 0.14$ for NGC 4494). In the other FRs that are not shown in Fig. 4.8, but displaying a drop in the amplitude of rotation, the comparison between slow rotating PN system and rapid rotation in the absorption line kinematics, suggests similar transition at smaller radii.

Figure 4.5 shows that the three galaxies with approximately constant $V_{\rm rot}$ profiles (NGC 2768, NGC 4564, and NGC 5866) do actually show a small decrease in rotation in correspondence to $R_{1/2}$, when compared with the values from absorption line spectroscopy. At larger radii their fast-rotating spheroidal halo (NGC 2768, Cortesi et al. 2013b), or alternatively an unidentified outer disk component, dominates the kinematics. Among the remaining three galaxies in Fig. 4.5 with increasing $V_{\rm rot}$ profiles, two of them (NGC 3384 and NGC 7457) have an extended disk component, to which most of the PNe belong (Cortesi et al. 2013b). NGC 4742, by contrast, does not have any photometric evidence for a disk component, hence the high rotation at large radii is likely associated with the spheroid.

4.7.4 Summary

Our results show that the kinematics of ETGs at large radii can be substantially different from that in the inner regions. For the SRs we observe a growth in the amplitude of rotation. For the

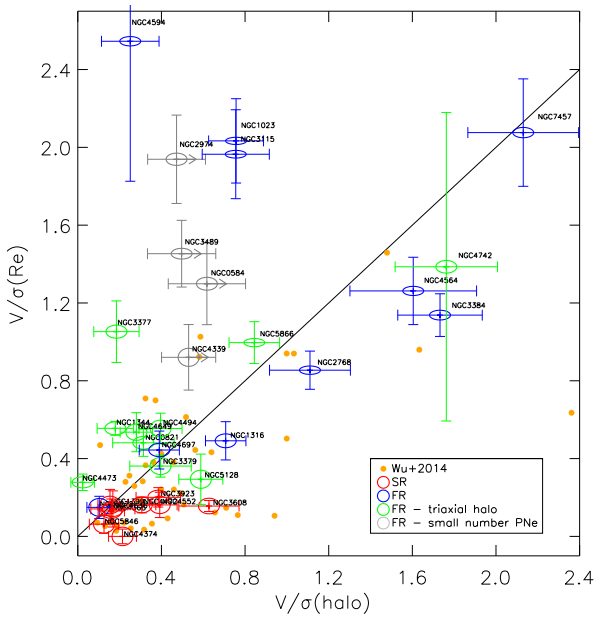

Figure 4.9: $V/\sigma(R_e)$ from absorption line data compared with V/σ(halo) from PN data. References for the absorption line data are in Table 4.1; for NGC 1399 and NGC 3923 data are available up to $R_e/2$ and $R_e/4$, respectively. The flattening of the ellipses used to plot the galaxies correspond to the ϵ values of Table 4.1. FRs and SRs are shown with different colors, as are the FR with triaxial halos. The gray open ellipses represent the galaxies (all FRs) with fewer tracers, for which our analysis provides a lower limit for V/σ(halo). The solid line traces equal values of $V/\sigma(R_e)$ and V/σ(halo). The orange circles shows the V/σ of simulated galaxies from Wu et al. (2014), divided by a factor 0.57 to rescale their two dimensional flux-weighted measurement to one-dimensional quantities (Cappellari et al. 2007). While the SRs show increased rotation in their halos, the majority of the FRs show a drop in rotation at large radii.

FRs, this variation in the kinematics manifests as a decrease in the amplitude of rotation or a twist in the $PA_{\rm kin}$. We interpreted this behavior as the transition from the inner disk component into the spheroidal halo, which is dispersion dominated and might deviate from axisymmetry.

Figure 4.9 illustrates this conclusion by comparing the V/σ ratio in the halo and in the inner regions (at $1R_{\rm e}$). The $V/\sigma(R_e)$ values are derived by interpolating the $V_{\rm rot}$ and σ profiles from integrated light (shown in Figs. 4.5 and 4.7, see references in Table 4.1) at $R = R_{\rm e}$, while V/σ(halo) is the ratio of $V_{\rm rot}$ and σ estimated in the outermost radial bin of the PN velocity fields (see Table 4.1 for the outermost mean radius).

All the SRs fall below the 1:1 line, showing higher rotational support at large radii. The spread of the FRs in the diagram reflects their different intrinsic structure and kinematics. The halos of most FRs have V/σ ratio similar to the V/σ(halo) of SRs. Among these the scatter in $V/\sigma(R_{\rm e})$ is probably driven by the presence of a more or less prominent disk component seen at different inclinations, and embedded into the dispersion-dominated spheroid. The flattening of the ellipses in Fig. 4.9, in fact, shows that galaxies with higher ϵ also display higher $V/\sigma(R_{\rm e})$.

A second group of FRs with high rotational support in the halo populate the diagram on the right of the 1:1 line. These galaxies are either dominated by disk rotation at all radii (NGC 3384 and NGC 7457), or have a rapidly rotating spheroid (NGC 2768, Cortesi et al. 2013b), or either of these (NGC 4564, NGC 4742).

The FRs with triaxial halos typically show equal values of $V/\sigma(R_{\rm e})$ and V/σ(halo), spanning all values in V/σ(halo). It is possible that the group of galaxies near the 1:1 line but without signature of triaxiality in the current data could show such signatures with higher resolution in the kinematics. Therefore we cannot presently determine whether these last two subset of FRs are different or not.

The orange full circles in the V/σ plot show the inner-halo kinematics from Wu et al. (2014), who studied the kinematics of ETGs in cosmological zoom simulations (Oser et al. 2010; Naab et al. 2014) out to $5R_{\rm e}$. Their $V/\sigma(R_{\rm e})$ and $V/\sigma(5R_{\rm e})$ were divided by a factor 0.57 to rescale their two dimensional flux-weighted measurements to one-dimensional quantities (Cappellari et al. 2007). The comparison with the observations shows that these simulations do not adequately reproduce the observed properties of fast rotating galaxies, which span a much wider spectrum of kinematic properties at large radii.

4.8 Discussion

4.8.1 Halo rotation versus central rotation

The PN velocity fields show that ETGs may have very different kinematics at large radii compared to their inner regions. We found that SRs typically increase their rotation in the halo, while most of the FRs display a decrease of $V_{\rm rot}$ toward large radii.

The observed variety of radial trends for the rotation amplitudes is consistent with the different shapes of the λ_R parameter profiles observed in the smaller sample of Coccato et al. (2009), and confirmed by Arnold et al. (2014) and Foster et al. (2016). The study of the λ_R profiles for the current sample of galaxies is the subject of a future paper (Coccato et al. in prep.).

The existence of these radial trends was recently questioned by Raskutti et al. (2014) and Boardman et al. (2017), who found no evidence for a change in their stellar kinematics beyond R_e. The divergence from our results may arise from the different radial coverage; their kinematics does not reach to the distances where the drop in rotation typically occurs, beyond $\sim 1R_e$. An example is the lenticular galaxy NGC 1023, in common between the two samples. For this galaxy Boardman et al. (2017) report a rising λ_R profile to almost $2R_e$, in agreement with our observation of a decrease in rotation only beyond $\sim 3R_e$.

The onset of rotation of the SRs at larger radii, often along directions that do not coincide with the major axis of the galaxy, may trace the accreted stellar component, which maintains a memory of the orbital angular momentum of the accreted progenitors. The decreased rotational support of the FRs is discussed in the next section.

4.8.2 Fast rotators with disks embedded in slowly rotating halos

The sharp drop in angular momentum in some FRs has been interpreted as the fading of an embedded disk structure of in-situ stars in a dispersion dominated spheroidal halo (Coccato et al. 2009; Arnold et al. 2014). We qualitatively verified this scenario in Sect. 4.7.3, where we observed that the radius at which the rotation along the major axis drops is consistent with the half light radius of the inner disk component.

Our results suggest that FRs contain a more or less extended rotating disk component, embedded in a more or less prominent halo with its own kinematic signature. This is reflected in the distribution of these objects in the V/σ plane (Fig. 4.9). We found that while a smaller group of FRs shows high rotation also in the halo, the halos of most FRs have rotational support comparable to that of the halos of SRs. This result is corroborated by the observation that the ePN.S FRs tend to become rounder at large radii (see Fig. 4.10).

This variety of kinematic properties is consistent with the variety of physical processes that may drive the evolution of these objects (minor mergers, major mergers that lead to a spin-up of the remnant, gas accretion, interactions with the environment, secular evolution; Duc et al. 2011; Naab et al. 2014; Penoyre et al. 2017; Smethurst et al. 2018) while preserving a rotating disk structure at the center. The comparison of our observations with simulated data from Wu et al. (2014) in Fig. 4.9 indicates, however, that those simulations do not yet reproduce the full diversity in the variety of these processes.

4.8.3 Signatures of triaxial halos in the kinematics

In Sect. 4.6.4 we studied the velocity fields and their kinematic position angle profiles $PA_{\rm kin}(R)$, and linked the observed misalignments and twists with the triaxiality of the halos. SRs are known to be mildly triaxial in their central regions, while the FRs are predominantly oblate (Weijmans et al. 2014; Foster et al. 2017). Kinematic twists and misalignments for the FRs are rare and small in the central regions. By sampling the kinematics at more than twice the distances probed by previous studies, the PNe line-of-sight velocities show that these features become more frequent and pronounced in the outskirts. Based on these signatures, we classified the halos of 40% of the

FR galaxies as triaxial, while the remaining ones are still consistent with being axisymmetric at the resolution of the ePN.S survey. For these objects the triaxiality of the halos is not ruled out.

On the other hand, it is in principle possible that axisymmetric galaxies with a recent merger might display kinematic twists and misalignments because of the contribution of the unrelaxed accreted component to the PN velocity field. However, if the size of the accreted satellite is such as to significantly contribute to the PN population of the the host halo, and so as to produce features in the PN velocity field, then the effect is short lived. This makes the probability of occurrence of such circumstance low. Deviations from a point-symmetric velocity field were found for 5/33 cases in Sect. 4.5, probably due to recent accretion or mergers in four cases and due to dust in one case. These galaxies are not included in the triaxial classification.

An examination of the smoothed velocity fields in appendix 4.E shows that for some galaxies the trends in $PA_{\rm kin}$ with radius reflect a two-component velocity field in which rotation along one axis dominates at intermediate radii and rotation along the other axis dominates further out. This is the case for NGC 3379 and NGC 4649 among the FRs, and for NGC 4552 and NGC 4636 among the SRs. The velocity field of NGC 1344, instead, shows that this galaxy is a prolate rotator. Up to now there are not many observations of this phenomenon (Tsatsi et al. 2017, and references therein), which is probably related to a recent merger (Ebrová & Łokas 2017), as the shells of this galaxy attest. Our sample contains two other galaxies (NGC 3923 and NGC 4365) known to have prolate rotation at their centers, but their halos are decoupled with respect to the inner kinematics.

A previous study of the intrinsic shapes of ETG halos was performed by Foster et al. (2016) who, using the observed distribution of ellipticities and misalignments for the SLUGGS galaxies out to $\sim 2.5R_{\rm e}$ were unable to rule out triaxiality in the outskirts of FRs. The same authors had previously found strong evidence for minor axis rotation, hence a triaxial halo, in NGC 4473 (Foster et al. 2013). Viaene et al. (2018) recently observed a strong kinematic twist beyond 1.5 $R_{\rm e}$for the massive FR NGC 5626. The extended PN kinematics allow us to generalize this result to a significant fraction of the FRs.

4.8.4 Signatures of triaxial halos in extended photometry

If the kinematic twists seen in the PN velocity fields for a significant fraction of ETGs indeed indicate triaxial halos in these systems, one expects additional evidence for triaxiality to come from observations of isophotal twists (Carter 1978; Leach 1981). Hence in this section we compare with photometric data from the literature, We do not expect to see a one-to-one correspondence between variations of $PA_{\rm kin}$ and variations of $PA_{\rm phot}$ (see also Foster et al. 2016), as the former are driven by the total potential of the galaxy, including dark matter, while the latter trace variations of the distribution of the light alone.

The isophotes of ETGs are well-described by ellipses, with deviations from perfect elliptical shape typically at the $\sim 0.5\%$ level (e.g., Bender et al. 1988). Hence the constant luminosity surfaces of ETGs can be approximated by ellipsoids (for a review see Merritt 1992). The projection on the sky of a coaxial triaxial ellipsoidal distribution of stars can result in twisting isophotes only if their axial ratios varies with radius (Stark 1977; Benacchio & Galletta 1980). The effects of triaxiality on the $PA_{\rm phot}$ profiles are model dependent (e.g., Benacchio & Galletta 1980; Franx

1988; Madejsky & Moellenhoff 1990). In general considerable twists (> 10 degrees) can be produced by moderately triaxial models, but their relative frequency is low, $\lesssim 10\%$, as the effects on the $PA_{\rm phot}$ are small whenever the systems are viewed close enough to one of their principal planes, and the magnitude of the twists depends on how much the axial ratios change.

Figure 4.B.1 in appendix 4.B shows extended ellipticity and $PA_{\rm phot}$ profiles from the literature for both FRs and SRs, for three quarters of the ePN.S sample. We chose to consider only galaxies with photometric data reaching at least 4 $R_{\rm e}$. Twists of $PA_{\rm phot}$ are observed for almost all the galaxies classified as triaxial in Sect. 4.6.4, and for several other FRs with no evidence for triaxiality at the spatial sampling of the PN kinematics. It is evident, however, that the variation of $PA_{\rm phot}$ measured for the FRs is modest (< 10 degrees) in $12/19 = 63\%$ of the cases. Thus we verify whether the occurrence of small photometric twists is consistent with the presence of a triaxial halo. We do this by constructing illustrative, observationally motivated photometric models for triaxial FR galaxies, and comparing the statistical distribution of photometric twists in these models with that observed for the ePN.S sample of FR galaxies.

The models are built on the kinematic evidence found in the previous sections suggesting that centrally flat FRs are embedded in dispersion dominated spheroids, which can be triaxial. The intrinsic shape of the central regions of FRs were investigated by Weijmans et al. (2014, Atlas3D survey) and Foster et al. (2017, SAMI survey), who found that these galaxies are close to oblate ($p = 1$)[4] with mean flattening $q \sim 0.3$. SRs are, instead, less flattened ($q \sim 0.6$), and mildly triaxial but, because of the small number of these galaxies in the Atlas3D and SAMI samples, their intrinsic shape distribution is not well constrained.

In our models, the central regions of the FRs have intrinsic shape in agreement with the previous results. In their halos, a significant fraction of the FRs has kinematics similar to the SRs (see Fig. 4.9). This is consistent with the expectation that the satellites accreted into the halo should be largely uncorrelated with the dynamics of the central galaxy. Thus for our first two halo models we assume outer halo axis ratios like those for the SRs, in which the accreted stars are expected to reach down to small radii (Cooper et al. 2013; Rodriguez-Gomez et al. 2016). This choice is supported by the evidence that the ellipticity profiles of FRs generally show decreasing trends at large radii (see Figs. 4.10 and 4.B.1 in appendix). However, some FRs in Fig. 4.9 rotate rapidly also in their halos; thus we also investigate triaxial halos with flatter isophotes. We parametrize the transition between inner and outer regions in different ways. The models are described in detail in appendix 4.B.2. In summary we use:

- Model 1: a single component with a Sérsic $n = 4$ density distribution and variable flattening: $q = 0.3$ and $p = 1$ at the center, $q = 0.6$ and $p = 0.9$ in the outskirts. The transition between these regions happens at $R =< R_T >= 1.8R_{\rm e}$, where R_T is the kinematic transition radius defined in Sect. 4.8.6.

- Model 2: a two-component model including a cored Sérsic $n = 4$ halo with intrinsic constant flattening $q = 0.6$ and $p = 0.9$ plus an embedded spheroidal-exponential disk with flattening $q = 0.3$ and $p = 1$. The scale length of the disk is taken to be such that

[4]Here p and q are the intrinsic axis ratios, such that $1 \geq p \geq q \geq 0$.

$1.67h =< R_T >$, as qualitatively observed in Sect. 4.7.3. Within $r = R_T$ the total luminosity of the disk in this model is ~ 3.5 times that of the halo.

- Model 3: as Model 2, but with a maximally triaxial halo with $q = 0.6$, $p = 0.8$.

- Model 4: as Model 2, but with strongly flattened, slightly prolate-triaxial halo with $q = 0.4$, $p = 0.8$.

Figure 4.10 shows the maximum photometric twist and the mean projected ellipticity measured for the subsample of the ePN.S FRs with extended photometry (references in Table 4.2; the profiles are shown in appendix 4.B.1). The distribution of the galaxies in this diagram is compared with the same quantities from the four triaxial models, each observed at 100 random viewing angles. We find that:

1) the fraction of twists larger than 10 degrees is of order 30% (45% for Model 3). Large twists occur for viewing angles $\theta \lesssim 50$ degrees for Models 1 and 2, and for $\theta \lesssim 65$ degrees for Models 3 and 4 ($\theta = 0$ for face-on view).

2) The comparison of the model prediction of twist angles with the data points for the ePN.S FRs in Fig. 4.10 shows that most of the model projections have low twists of the same magnitude as the majority (63%) of the galaxies. Within the statistical uncertainties, the models represent well the locations of the galaxies in Fig. 4.10: an average $\sim 35\%$ of the models are above the 10 degrees threshold. From the models distribution $\sim 1-2$ galaxies with photometric twists larger than 30 degrees and mean ellipticity ~ 0.1 would be expected but are not observed. The missing ePN.S FRs in that region of the diagram could be a result of small number statistics, observational bias for near face-on systems, or model details.

3) Since the photometric twists are thus expected to be small in most galaxies, the most obvious signature of a change in the intrinsic shape is the variation of the projected ellipticity with radius, as shown in Fig. 4.B.2 in the appendix. The change in ellipticity observed in the majority of the FRs in Fig. 4.B.1 (see also appendix 4.B.1) independently suggests the fading of the central disk component in a more spheroidal halo, as we previously inferred from rotation profiles.

This analysis based on illustrative oblate-triaxial photometric models shows that the presence of small photometric twists, as observed for the majority of the ePN.S FRs, is consistent with the presence of a triaxial halo. This means that it is likely that individual oblate-triaxial models for these galaxies can be constructed that are consistent with the measured photometric twist angles.

We infer that many of the ePN.S FRs show small photometric twists because of the highly flattened, oblate shape of their central regions and the gradual transition to a triaxial halo. The consequence is a near-alignment within ~ 10 degrees between the inner kinematics and outer photometry of most these galaxies, as analogously observed for most of the FRs (Krajnović et al. 2011; Fogarty et al. 2015, however, this numerical value also depends on sample selection effects, see the following section). Hence extended kinematic studies that sample the outer regions

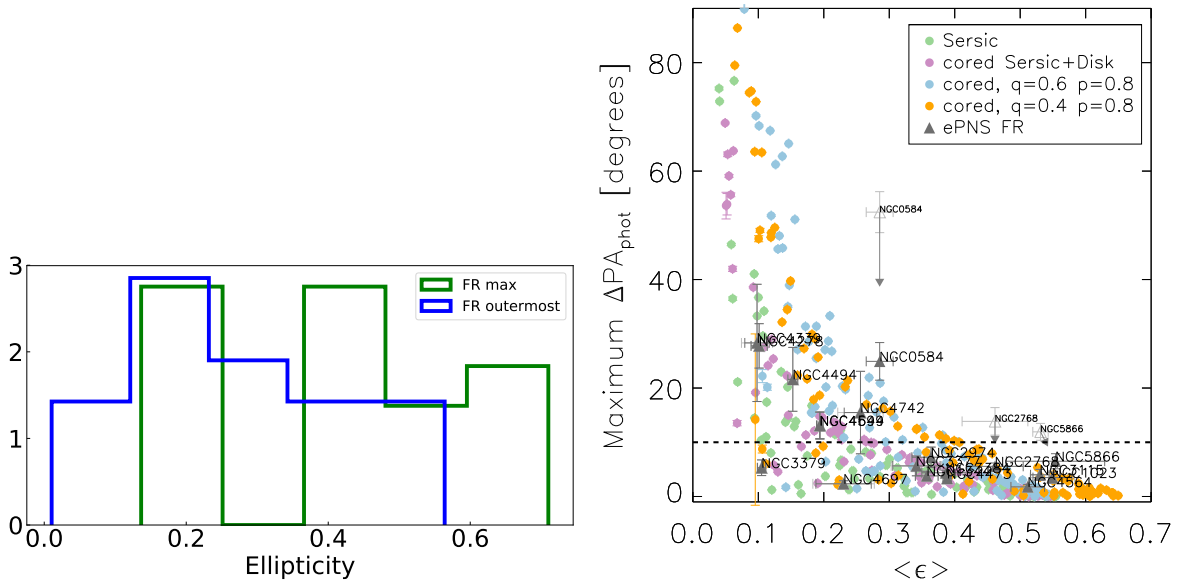

Figure 4.10: Left panel: Ellipticity distribution for the FRs. The histogram of the maximum measured ellipticity at $R > 0.5R_e$ is in green; the histogram of the outermost measured values is in blue. The distributions show that the FRs tend to have halos rounder than their central regions. Right panel: Maximum photometric twist versus mean projected ellipticity for a subsample of the ePN.S FRs with extended photometric data (gray triangles; see text and appendix 4.B.1, references in Table 4.2). The errors reflect the scatter between contiguous data points in the photometric profiles. For the galaxies with indications for ongoing interactions in the outermost photometry (see appendix 4.B.1 and 4.D) we estimated the mean ellipticity and maximum position angle twist both from the complete profiles (open symbols) and considering only the regions with regular photometry (filled symbols). For NGC 1023 and NGC 3384 we show quantities derived excluding the regions where the bar dominates. The horizontal dashed line marks $\Delta PA_{\rm phot} = 10$ degrees. The statistical distribution of points is consistent with simple photometric triaxial models, shown each with 100 random projections (solid circles as described in the legend; see text and appendix 4.B.2).

of these FRs are important to unveil the kinematic transition and thus the change of the intrinsic shape.

Both PN kinematics and photometry are therefore consistent with a picture in which FRs have a central disk component embedded in a spheroidal dispersion dominated component. We found this component to be triaxial for at least 40% of the FRs in the ePN.S sample. The presence of photometric twists also for other FRs without evidence for a kinematic twist in the PN data, suggests that the fraction of galaxies with a triaxial halo might be higher. In the following sections we will see that the spheroidal component is most prominent in the most massive objects, and that the comparison with cosmological simulations suggests an ex-situ origin for it.

4.8.5 Comparison with the results of the Atlas3D survey

The results discussed in the previous sections challenge a simple interpretation of the Atlas3D survey results in terms of a dichotomy between disk FRs and triaxial SRs (see Cappellari 2016, for a review on the subject).

The Atlas3D (A3D) survey carried out IFS and photometric observations of the central regions of a complete sample of 260 ETGs, morphologically selected from a volume-limited sample of galaxies brighter than $M_K < -21.5$ (Cappellari et al. 2011). Their sample of ETGs spans luminosities $-21.57 \geq M_K \geq -25.78$ and mostly contains lenticular galaxies, which means galaxies with T type $T > -3.5$: only 24% of their ETGs are ellipticals ($T \leq -3.5$, Cappellari et al. 2011). The ePN.S sample is, on average, 1 mag more luminous in the K band ($-22.38 \geq M_K \geq -26.02$), and the majority of the galaxies (73%) are ellipticals, according to their T type from HyperLeda (see Arnaboldi et al. in prep. for more details on the sample selection). The A3D IFS kinematics covers typically radii up to $\sim 1R_e$ (Emsellem et al. 2011). The fraction of R_e covered is actually a decreasing function of galaxy luminosity, as R_e depends on M_K (Cappellari et al. 2011), hence, for the ePN.S galaxies in common with the A3D sample, the mean radial coverage is $0.49R_e$. Finally if one considers that the values adopted for R_e may underestimate the half light radii for the brightest objects (see discussion in Sect. 4.8.6), this fraction is actually smaller: $0.35R_{\rm halflight}$, where $R_{\rm halflight}$ is defined in Sect. 4.8.6.

Figure 4.11 shows the stellar mass versus ellipticity plane for both samples. The ePN.S galaxies are on average more massive and less flattened than the A3D ETGs. In particular, the ePN.S FRs with triaxial halos are among the most massive A3D FRs. For these galaxies the PNe kinematics generally show fairly large twists of the $PA_{\rm kin}$, as the limited spatial resolution of the survey prevents the measurement of small differences in angle. In the ePN.S sample 40% of the FRs show signatures of a triaxial halo. The comparison with the photometry in Sect. 4.8.4 and in appendix 4.B.1 suggests that the number of FRs with triaxial halos in the ePN.S sample might actually be higher.

Where the data overlap, the PN kinematics agrees well with the IFS observations of the central regions, where the rotating disk component dominates the kinematics of the FRs. At larger radii both kinematics and photometry suggest that these galaxies show a transition to a spheroidal component. If we interpret this component with different kinematics and flattening as mainly formed by accreted, ex-situ, stars, we find that for the most massive galaxies it dominates at smaller fractions of R_e, in agreement with simulations (Rodriguez-Gomez et al. 2016, see

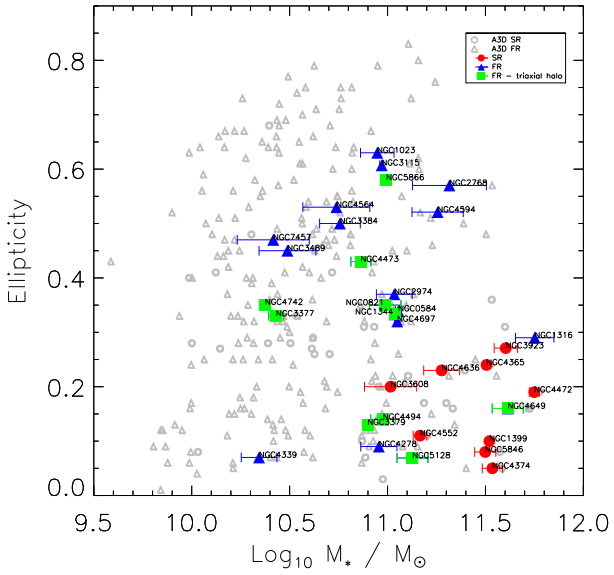

Figure 4.11: EPN.S and Atlas3D samples compared in the stellar mass versus ellipticity plane. The Atlas3D sample of ETGs is displayed with gray open symbols (triangles for the FRs, circles for the SRs). For these galaxies we show the ellipticity values from Krajnović et al. (2011) and $M_* = M_{JAM} = (\mathrm{M/L})_{\mathrm{JAM}} \times L_{\mathrm{tot,r}}$ from Cappellari et al. (2013b) as in their Eq. (28). The ePN.S galaxies are shown with full symbols: red circles for the SRs, blue triangles for the FRs, and green squares for the FRs with triaxial halos. For the ePN.S ETGs M_* is the mean between $\mathrm{M_{JAM}}$ (Cappellari et al. 2013b, when available), and the masses M_{*1} and M_{*2} reported in Table 4.2. The error bars on the mass show the rms scatter between these different mass determinations. The values for the ellipticity are listed in Table 4.1.

Sect. 4.8.6). This dependence on mass, combined with the smaller radial coverage of the A3D kinematics, explains the different conclusions drawn by the two surveys: low mass FRs are dominated by the disk rotation up to large radii; the spheroid is more prominent in the most massive FRs, where the accreted envelope reaches smaller fractions of R_e. Even so the radial coverage of the A3D kinematics does not reach the transition radius (see Sect. 4.8.6), since the fraction of R_e observed also depends on mass, as discussed above.

The present work shows that the wider spatial coverage of the kinematics by the ePN.S survey delivers new informations about ETGs that extend the results of previous surveys. FRs do contain inner disk components, but many of them are not simply highly flattened oblate objects. The results presented in this paper point to a more complex scenario for ETGs than the simple fast and slow rotator dichotomy. As predicted by simulations (Naab et al. 2014; Rodriguez-Gomez et al. 2016), FR galaxies appear to be more diverse objects than previously thought.

4.8.6 Kinematic transition radius

We found that most of the galaxies in the sample show a transition in their kinematics, marked by a change in the rotation velocity $V_{\rm rot}$ or in the kinematic position angle $PA_{\rm kin}$. In the framework of the two-phase formation scenario, we can interpret such kinematic differences as tracing stellar components with different origins, such as the in- and the ex-situ components. From simulations (Rodriguez-Gomez et al. 2016, and references therein) it is predicted that the in-situ stars are concentrated in the central regions of galaxies, while the accreted stars dominate the halos, and that their relative contribution is related primarily to the total mass. Within this framework we can define a transition radius R_T as the distance at which we observe the described transition in the kinematics, and compare it with the total stellar mass.

The radial range $R_T \pm \Delta R_T$ is here quantified using
(A) in case of a declining $V_{\rm rot}$ profile, the interval between the radius at which $V_{\rm rot}$ is maximum and the radius at which it decreases by ~ 50 km s^{-1}
(B) in case of an increasing $V_{\rm rot}$ profile, the radial range in which $V_{\rm rot}$ increases from ~ 0 to ~ 50 km s^{-1}
(C) in case of a kinematic twist, the radial range in which $PA_{\rm kin}$ changes significantly.
Table 4.3 lists the $R_T \pm \Delta R_T$ values measured, and specifies the criteria (A,B,C) used for deriving it. $R_T \pm \Delta R_T$ is also plotted in Figs. 4.5 and 4.6 with vertical lines.
For each galaxy we estimate the stellar mass using two different approaches, designated by M_{*1} and M_{*2}, to have also an estimate of the systematic uncertainties. The values for the masses are listed in Table 4.2, along with the description of the procedure used for calculating them.

Figure 4.12 shows the stellar mass of the galaxies versus R_T/R_e. The full circles show the same quantities in three bins of R_T/R_e; the error bars represent the standard deviation of the mass and of the R_T/R_e ratio in the bin. A clear correlation exists between total stellar mass and R_T/R_e, in the sense that the more massive galaxies tend to have transition radii at smaller fractions of R_e. The shaded region in Figure 4.12 shows the corresponding quantities from the N-body simulations of Cooper et al. (2013). Using their stellar mass surface density profiles in bins of dark halo virial mass ($M_{200}/M_\odot$; their Figure 6), we estimated the transition radius in units of half mass radii as the distance at which the accreted component overcomes the in-situ

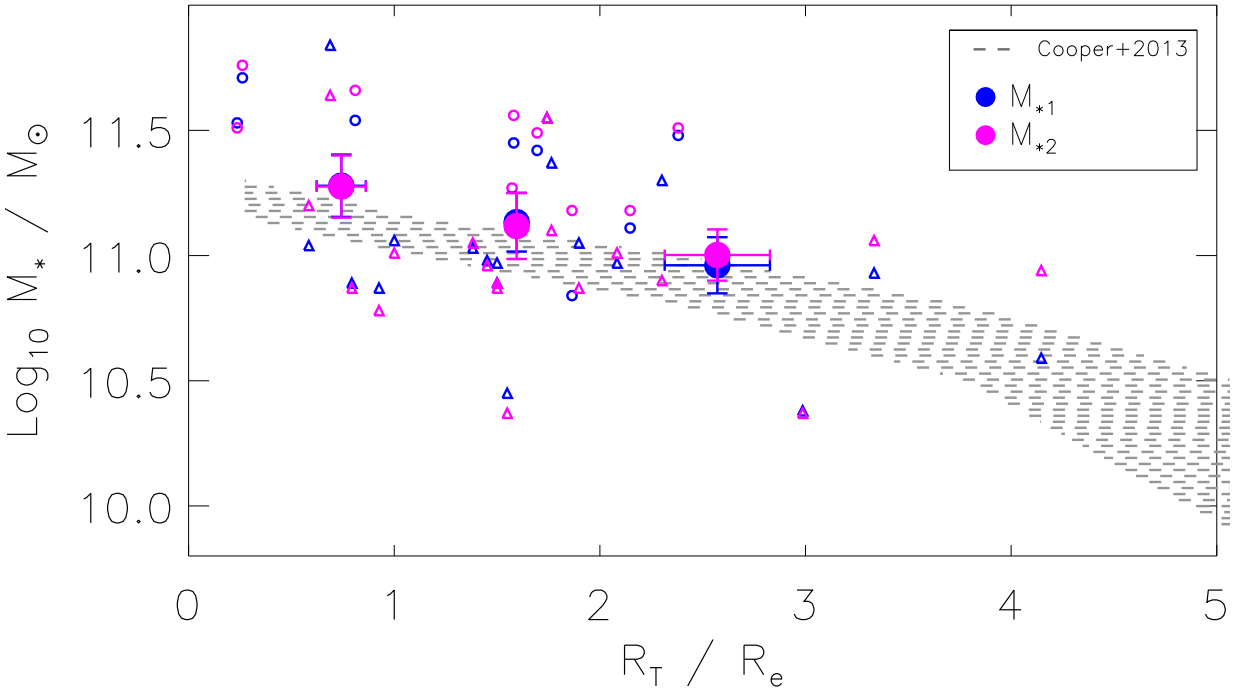

Figure 4.12: Transition radius in units of R_e versus total stellar mass (open symbols: circles for SRs, triangles for FRs). The full symbols show the same quantities in bins of R_T/R_e. Different colors show the results of two different procedures for calculating the total stellar mass, see Table 4.2 for details. The shaded region shows the corresponding quantities from the simulations of Cooper et al. (2013), see text.

component. The total masses M_{200} are converted to stellar masses via abundance matching, using the prescription given by Behroozi et al. (2010). Both data and simulation follow the same trend.

We also observe a higher scatter in R_T/R_e for the lower mass galaxies, in agreement with the results of Rodriguez-Gomez et al. (2016) from the Illustris simulations. They defined a three-dimensional transition radius r_T as the distance at which the accreted stellar mass fraction overcomes the in-situ, and normalized it by the stellar half mass radius $r_{\mathrm{half},*}$. Their study shows an additional dependence of $r_T/r_{\mathrm{half},*}$ on morphology, halo formation time, and recent merger history, and that $r_T/r_{\mathrm{half},*}$ tightly correlates with the ex-situ stellar mass fraction.

We tested the dependence of the correlation found on the choice of the value of R_e. The used values (listed in Table 4.1) derive mostly from a calibrated average between 2MASS and RC3 determinations (Cappellari et al. 2011). Deeper photometric data would deliver larger values for R_e for the brightest galaxies (Kormendy et al. 2009). For this reason we carried out a simple photometric analysis, to be completed in a future study, with the goal of having a homogeneous determination of R_e for all the sample galaxies which takes the shallower surface brightness profile of the brightest galaxies into account. Using the surface brightness profiles available in the literature (references in Table 4.2), we fitted a Sérsic law in the outermost regions of the galaxies and extrapolated the profiles up to very large radii to include all the stellar light. We then

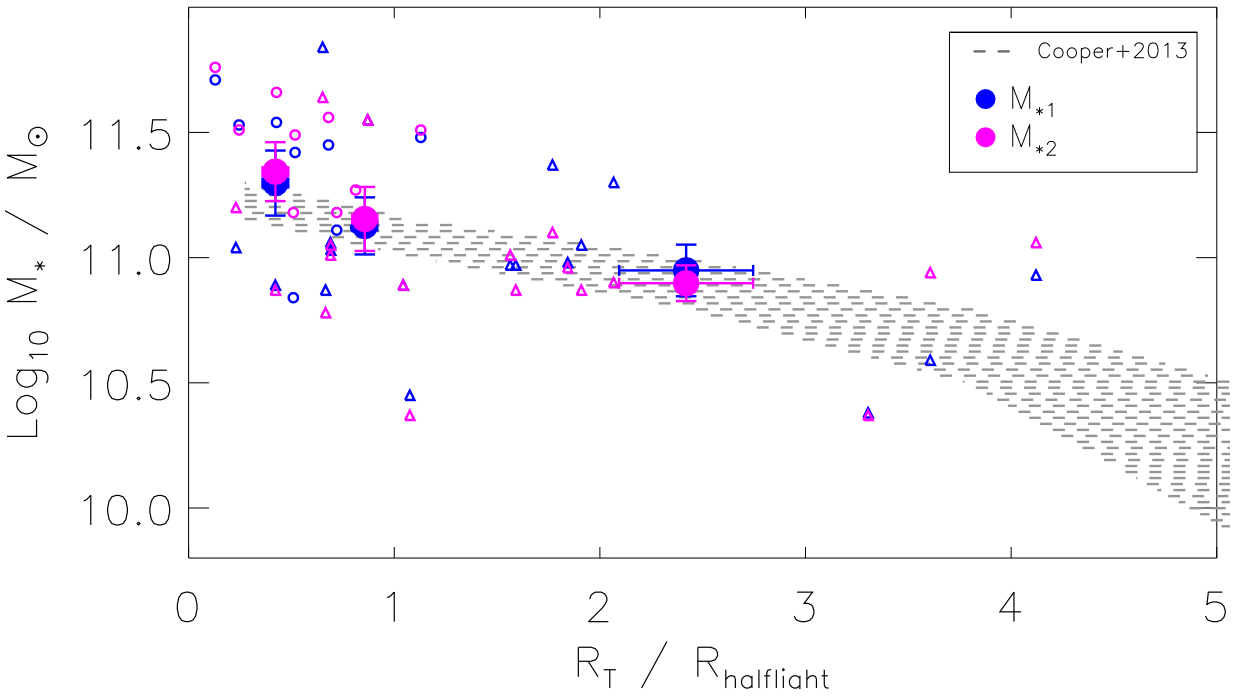

Figure 4.13: Transition radius in units of $R_{\rm halflight}$ versus total stellar mass (open symbols: circles for SRs, triangles for FRs). The full symbols show the same quantities in bins of $R_T/R_{\rm halflight}$. Different colors show the results of two different procedures for calculating the total stellar mass, see Table 4.2 for details.

evaluated the half-light radius $R_{\rm halflight}$ from the growth curves (see Table 4.2). Figure 4.13 shows that with these half-light radii, the relation between $R_T/R_{\rm halflight}$ and total stellar mass becomes steeper and agrees even better with the predicted trend from the simulations.

Spavone et al. (2017) quantified transition radii for a subsample of the ePN.S SRs using a parametrization of the light profiles with a multicomponents Sérsic fit. Their three-components model describes the superposition of an in-situ component dominating the central regions, a relaxed, phase-mixed accreted component, to which is associated the transition radius R_{tr1}, and an outer diffuse component of unrelaxed accreted material with transition radius R_{tr2}. The transition radius is defined there as the radius at which one component overcomes the other. The R_T derived from the kinematics generally compares with R_{tr1} for the same galaxies.

D'Souza et al. (2014), using image stacking of a large sample of galaxies, defined $R_{\rm acc}$ as the radius at which the outer component of a double Sérsic model begins to dominate the integrated stellar light. They found a dependence of $R_{\rm acc}$ on the stellar mass, and, at comparable masses, their photometric values $R_{\rm acc}$ [kpc] are in the same range as our kinematic R_T [kpc]. This is interesting considering the different approaches used to derive these quantities.

4.8.7 The diverse halo formation histories

Cosmological simulations (Naab et al. 2014; Penoyre et al. 2017) show that FRs, as well as SRs, are the result of different formation pathways, characterized by factors like the number of mergers, the merger mass ratio, the timing of mergers, and the gas fraction. We note, however, that the adopted star formation and AGN feedback models influence the resulting morphologies and kinematic properties, so that definitive statements about the origin of FRs and SRs cannot yet be made (see Naab & Ostriker 2017, for a recent review). In the two-phase scenario, if the formation history is dominated by dissipation, then it is likely that the system becomes a fast rotator. Dissipation is particularly important in the early stages of galaxy formation, when the in-situ component generally settles down in a flattened rotating disk component (Rodriguez-Gomez et al. 2016; Qu et al. 2017), so that before redshift ~ 1 the progenitors of the FRs and SRs are nearly indistinguishable (Penoyre et al. 2017). Later on, the evolution of galaxies is determined by the stochasticity of merging events, which at low redshift are mostly gas-poor (e.g., Lee & Yi 2013). Major mergers contribute to the loss of spin of the remnant, while minor mergers are responsible for the growth in size and mass. The accretion of stars happens preferentially on radial orbits, and frequent mergers efficiently mix the in-situ and the accreted stellar populations while changing the intrinsic shape toward a more spheroidal form (e.g Jesseit et al. 2005; Hilz et al. 2012, 2013; Röttgers et al. 2014). Fast rotating galaxies experience a lower number of mergers when compared to the more massive slowly rotating systems, so their in-situ component is preserved in the central regions, in an axisymmetric, rotationally supported disk (e.g., Naab et al. 2014; Penoyre et al. 2017). Their halos, which host most of the accreted component, are not necessarily axisymmetric.

4.9 Summary and conclusions

In this paper we reconstructed and analyzed the velocity fields of 33 ETGs into their outer halos using planetary nebulae (PNe) as tracers. For the total ePN.S sample, we combined 25 galaxies from the PN.S ETG survey with eight objects observed with counter-dispersed imaging or multi-object spectroscopy from other sources (Arnaboldi et al. in prep.). In the extended PN.S (ePN.S) sample, 24 galaxies are classified as FRs (following the definition by Emsellem et al. 2011), and nine are SRs. The kinematic information typically extends to 6 effective radii (R_e), from a minimum of $3R_e$ to a maximum of $13R_e$.

We derived kinematic quantities such as the amplitude of rotation, the kinematic position angle (PA_{kin}), and the velocity dispersion, using an adaptive kernel smoothing technique validated with simulated velocity fields. In this process, we checked whether the galaxy velocity fields were point-symmetric as expected for triaxial galaxies in dynamical equilibrium, and whether the systemic velocity is unchanged in the outer halo.

We supplemented the PN kinematics with absorption line kinematic data from the literature (typically limited to the regions inside $\sim 1-2R_e$), in order to have a complete picture of the nature of the objects, and compared the results from different datasets in the regions of overlap. Highlights of the results are:

(1) Most FRs (70%) have decreasing rotation amplitudes with radius, while a minority shows constant (15%) or increasing (15%) trends. 60% have PA_{kin} in their halos aligned with the photometric major axis at the spatial sampling of the ePN.S survey. The SRs display modest but significant rotation in their outskirts. Among the FRs, 10% have very weak or no rotation in their outskirts.

(2) SRs have approximately constant velocity dispersion profiles with radius, except for NGC 4636 which shows a steep drop in dispersion beyond 200 arcsec. The FRs display a variety of velocity dispersion profile shapes: some are approximately constant, others decrease steeply with radius (Fig. 4.7).

(3) From their velocity fields, all of the SRs and 40% of the FRs show signatures of a triaxial halo (Fig. 4.6). For these galaxies we observe either a twist in the PA_{kin} or a constant misalignment with the photometric major axis. In addition, two SRs have halos that are decoupled in their PA_{kin}.

(4) Five galaxies show deviations from point symmetry. For NGC 2768 and NGC 4594 these effects are small (probably related asymmetries in the light distribution, in the former, and to extinction effects in the latter) and do not influence our kinematic analysis. NGC 1316, NGC 4472, and NGC 5128 instead display strong features, that indicate halos not in dynamical equilibrium. NGC 5128 is a merger remnant with clear minor axis rotation, and hence it is a triaxial system. For NGC 4472 the determination of the PA_{kin} is influenced by the presence of an in-falling satellite. While we included this SR among the triaxial objects, we note that the galaxy would have approximately major axis rotation once the PNe of the satellite are removed, and we refer to Hartke et al. (2018) for a more detailed study. NGC 1316 is a merger remnant with pronounced major axis rotation in the halo.

(5) In a $V/\sigma(R_e)$ versus V/σ(halo) diagram (Fig. 4.9), the previous results imply different locations for the slow and the FRs. The latter separate further between FRs with slowly rotating

outer spheroid and FRs that rotate rapidly at large radii also. The high values of V/σ(halo) are either due to a dominating disk component (e.g. NGC 7457) or to a rapidly rotating outer spheroid (NGC 2768). The FRs with triaxial halos show approximately equal values of $V/\sigma(R_e)$ and V/σ(halo), and span all values of V/σ(halo).

(6) In the 11 FR galaxies with the largest number of PN tracers, we see a decrease in the rotation velocity profile. In 10 cases this occurs approximately at a transition radius R_T similar to the scale radius of the known stellar disk component[5], suggesting that the transition from rapid to slow rotation is due to the radial fading of the stellar disk in a slowly rotating outer spheroid. For NGC 4494 there is no photometric evidence for a disk. In the other FRs with fewer tracers that also show a decrease in rotation, the comparison between the slow rotation of the PN system and the rapid rotation in the absorption line kinematics, which is related to an inner disk, suggests a similar transition at smaller radii.

(7) In extended photometry, the ePN.S FRs with triaxial halos show small but significant isophote twists, typically of $\sim 5-15$ degrees, lower than for the rounder SRs. The comparison with illustrative, observationally motivated, oblate-triaxial models shows that the distribution of observed photometric twists for the ePN.S FRs is consistent with the presence of a triaxial halo.

(8) For SRs, we estimate a kinematic transition radius R_T from a variation in the rotation or in the $PA_{\rm kin}$ profile. Combining with the transition radii of FRs, we find a relation between the ratio R_T/R_e and stellar mass, such that the most massive galaxies have the lowest R_T/R_e (Fig. 4.12). In the framework of the two-phase formation scenario we can interpret R_T as marking the transition between the inner regions, dominated by the in-situ stellar component, and the halo, which is mostly accreted. The comparison with photometric studies (D'Souza et al. 2014) and cosmological simulations (Cooper et al. 2013; Rodriguez-Gomez et al. 2016) shows good agreement, in particular the prediction from simulations is quantitatively confirmed.

(9) In the mass-ellipticity plane (Fig. 4.11), the ePN.S FRs with triaxial halos are amongst the most massive of the FRs in the Atlas3D survey. If we interpret the triaxial envelopes of these galaxies as mainly formed by accreted, ex-situ, stars, the observed mass dependence is in agreement with simulations (Rodriguez-Gomez et al. 2016) which predict that the accreted component dominates down to smaller fractions of R_e for more massive galaxies (Fig. 4.13). The dependence on mass, combined with the fainter survey limit and smaller radial coverage of the Atlas3D kinematics, explains the different conclusions drawn by the two surveys: low mass FRs are dominated by the disk rotation up to large radii; however, in the more massive FRs the spheroid is more prominent, where the accreted envelope reaches smaller fractions of R_e. In the massive FRs, the inner disks frequently fade in slowly rotating outer spheroids which are often triaxial.

In the data presented here, we see

- SRs
- FRs without apparent disks (NGC 4494 and NGC 4742)
- FRs with only inner disks and slowly rotating spheroids (e.g. NGC 3377)

[5] Throughout this paper we indicate with "disk component" a highly flattened, but definitely three-dimensional, oblate, rotating component.

- FRs with dominant disks all the way to their outermost regions (e.g. NGC 7457)
- FRs with inner disks and rapidly rotating spheroids (e.g. NGC 2768)
- FRs with triaxial halos that are dominated by dispersion (e.g. NGC 4649) or that rotate rapidly (NGC 4742 and NGC 5866)

Thus we conclude that ETGs show considerably more diversity in their halos than is apparent from their central bright regions. We also see clear signatures of the two-phase formation scenario: three galaxies show out of equilibrium kinematics in their halos, and more generally the inner and outer regions of ETGs often have different kinematic properties, where the transition radius depends on the stellar mass as predicted by cosmological simulations.

Appendix

4.A Testing the adaptive kernel smoothing procedure on simulated data

Our procedure for the measurement of the mean velocity and velocity dispersion fields from the observed LOS velocities of the PNe is based on performing a weighted local average, where the weights depend on the local density of tracers. The derived quantities depend on how well the detected PNe statistically sample the parent galaxy in the phase space. In particular the spatial distribution of the PNe plays an important role, as the smoothing averages over objects that are close together on the sky. Appendix 4.A.1 describes what determines the observed PN spatial distribution and how this, combined with a smoothing procedure, may affect the results. Appendices 4.A.2 and 4.A.3 study and quantify these effects on a simulated galaxy (with variable number of tracers and V/σ ratio) and on simulated velocity fields, with the same spatial distribution as the observed galaxies. We found that the smoothing procedure does not create artifacts in the velocity fields above the 1σ level; any features above this threshold are probably real.

4.A.1 PN spatial distribution and completeness

The observed PN spatial distribution depends on several factors. The most evident one is the incompleteness in the central high surface brightness regions because of the difficulty in detecting faint point sources against a bright background (Arnaboldi et al. in prep., Coccato et al. 2009). This is a strong function of the radius and it is quantified by the *completeness function*, the fraction of detected objects in different radial ranges.

In addition, the PN number density is proportional to the local surface brightness of the galaxy. This means that the number of tracers decreases with radius following the steep decrease of the surface brightness, and features in the surface brightness distribution may generate under- or over-densities of PNe. Of course at our typical number of tracers ($\sim$ 200) these features in density are barely distinguishable from statistical effects.

The adopted smoothing procedure takes the natural non-uniformity of the PNe distribution into account through the use of an adaptive kernel technique, which optimizes the size of the kernel to the local density of tracers. Nevertheless a local average of the velocities over a non-uniform spatial distribution, combined with the statistics in the LOSVD sampling, may in principle generate features in the kinematic maps or biases in the estimate of the kinematic parameters.

On the other hand, averaging over voids or over sparsely distributed tracers unavoidably leads to over-smoothed velocity amplitudes and to under-resolved velocity gradients. The residual velocities from the unresolved gradients may artificially boost the dispersion , creating local maxima in the velocity dispersion maps. In appendices 4.A.2 and 4.A.3 we assess the impact of such biases using simulated data.

4.A.2 Tests with data from a simulated galaxy

We used a simulated major merger remnant, sampled by 10000 particles. We reproduced a realistic observed dataset by locating the simulated galaxy at a distance of 20 Mpc, and applying to it a completeness function similar to those observed (see Arnaboldi et al. in prep.). We observed the galaxy in a field of view similar to that of the ePN.S, 800×800 arcsec^2 wide centered on to the galaxy. At this point, the simulated galaxy can be used as a test case for the procedure: we can explore how the results change by varying the number of tracers at our disposal, by selecting randomly typical numbers of observed PNe; different random extractions of tracers give us different statistical realizations of the system, and different projections of the galaxy on the sky plane give us different V/σ ratios.

Figure 4.A.1 shows an example of such an experiment. The smoothed velocity and velocity dispersion fields are plotted for the 10000 particle simulation, together with the maps for 400 stars and 200 stars. For the 200 particles case we show two typical statistical realizations (A and B) in order to illustrate the effects of limited statistics on the kinematic quantities. The panels at the bottom right show the fitted kinematic position angles, the amplitudes of the rotational velocity, and the azimuthally averaged velocity dispersion profiles in circular bins. The kinematic quantities are in general well recovered within the errors. The simulation is point symmetric in the region selected, and so are the limited statistical realizations. The statistical fluctuations that appear in the smoothed fields usually do not cause a deviation from point symmetry nor a variation of the kinematic position angle larger than the error bars. The velocity dispersion may be marginally boosted at the center of the galaxy, associated with the lack of detections, (see the case of 200 stars in Fig. 4.A.1), but the dispersion profile is recovered within the errors. So we conclude that the procedure to calibrate the smoothing parameters through Monte Carlo simulations (Sect. 4.3.1) works very well in reconstructing the mean properties of the velocity and velocity dispersion fields. Even though the smoothing procedure may create artificial peaks or deeps in the velocity maps, all these features are generally within the 1σ level. Any radial trends can therefore be considered significant only if it is outside the statistical uncertainties.

However, we can notice that as the number of tracers drops or the ratio V/σ decreases, the amplitude of rotation is systematically underestimated, while the velocity dispersion is systematically higher (see also Napolitano et al. 2001). This happens because lower numbers of stars or higher statistical noise require larger smoothing scales, which eventually become larger than the actual spatial scales of the velocity gradients. Oversmoothed velocity amplitudes (i.e. lower $\langle v \rangle$), imply higher $\tilde{\sigma}$ in Eq. (4.2). There is no way to estimate this offsets unless the mean velocity and velocity dispersion fields of the galaxy are known from independent data, since the effects of the smoothing jointly depend on the local density of tracers, on the V/σ ratio, and on the particular statistical realization (e.g. A and B in Fig. 4.A.1), hence they vary from case to case. It is how-

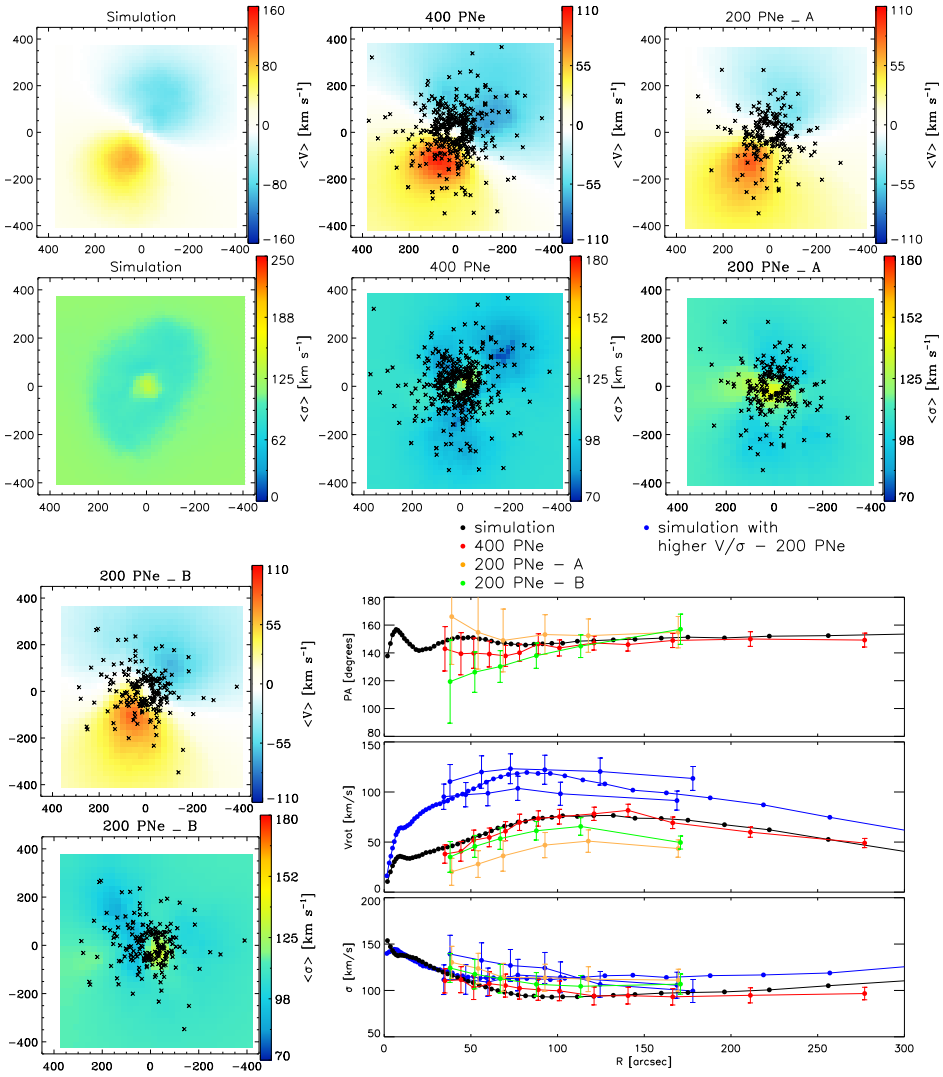

Figure 4.A.1: Smoothed velocity and velocity dispersion fields in the ePN.S field of view for a simulated ETG, traced by 10000 particles, 400, and 200 stars after the convolution with a completeness function. For the 200 particle case, we show two typical statistical realizations (A and B) of the extracted sample, to illustrate the effects of the limited statistics on the smoothed quantities. The global features of the simulation are preserved in the different fields but, as expected, the spatial and velocity resolution of the local gradients is downgraded when the number of tracers decreases. The lower right panels display the fitted kinematic position angle PA, the rotation velocity $V_{\rm rot}$, and the azimuthally averaged velocity dispersion σ in circular radial bins as function of radius. It is evident that the radial gradients are less resolved with fewer tracers, and that the amplitude of rotation for the case with 200 stars is oversmoothed. This happens because the kernel width is larger than the real spatial scale of the velocity gradients due to the sparse distribution of the tracers. The blue full circles show a simulation with higher V/σ ratio and two of its typical statistical realizations sampled by 200 objects to illustrate how of the accuracy of the reconstructed velocity amplitudes depends on the statistical noise. Errors for the kinematic profiles are determined from Monte Carlo simulations using the smoothed velocity and velocity dispersion fields as described in Sect. 4.3.2.

ever safe to say that for the galaxies with limited statistics the recovered kinematics provides a lower limit to the amplitude of rotation and an upper limit for the velocity dispersion in the halos.

4.A.3 Statistical tests with simulated velocity fields on real galaxies

Simulated velocity fields were used to verify the results obtained for the ePN.S sample of galaxies, such as assessing the significance of deviations from point symmetry or the radial trends of the kinematic parameters. These simulated velocity fields are featureless and trend-less (fixed kinematic position angle and constant velocity dispersion) and are built for each galaxy using the positions of the observed PNe. This means that the incompleteness function is already built into the simulated catalogs and is identical to that for the real galaxy under study. In this way we can check how the smoothing procedure correlates spatially close PNe, as the degree of spatial correlation in the models will be identical to that of the real datasets.

The simulated velocity field at the positions (x_i, y_i) of the ith PNe, from the real datasets, is interpolated with the simple function

$$V(\phi_i, R_i) = V_{\rm rot} \cos\Big(\phi_i - PA_{\rm phot}\Big) \arctanh(R_i/h), \tag{4.13}$$

where ϕ_i is the position angle of the ith PN with coordinates (x_i, y_i), R_i its distance from the center, and h is a scale-length that defines the steepness of the central velocity radial gradient. $V_{\rm rot}$ is chosen to be equal to the maximum fitted rotational amplitude for the galaxy in consideration, while h has the dimension of the central void of the detections ($\sim$ 50 arcsec). We choose to align the rotation of the simulated velocity field with the real photometric position angle of the galaxy, in order to simulate the velocity field of a regular, point-symmetric disk. The model velocity field $V(x_i, y_i)$ is sampled with a constant dispersion σ, which is equal to the mean velocity dispersion of the galaxy under study. This is done by extracting random values from a Gaussian distribution centered at 0 and with dispersion σ, and adding them to $V(x_i, y_i)$. The assumption of constant dispersion is certainly unrealistic for the central regions of the galaxies, but it is reasonable at large radii. We produced 100 statistical realizations for each galaxy, and each of those is treated as a real dataset for obtaining a total of 100 smoothed velocity fields.

The smoothed velocity fields obtained in this way were used to assess whether an observed feature in the galaxy velocity or velocity dispersion field is real, by studying whether it can be produced by statistical effects in a featureless velocity field, and how typically this happens (see Sects. 4.5 and 4.6.3). Also, the 100 models can provide a statistic for the fitted kinematic parameters (Eq. 4.9) to check the probability that statistical noise combined with the smoothing procedure artificially produce effects like twists of the kinematic position angle or misalignments with the photometric axes (Sect. 4.6.4).

4.B Photometric profiles and models

In this appendix we report extended photometric data from the literature for three quarters of the ePN.S galaxies to compare with the PN kinematic analysis of this paper, as discussed in Sect.

4.8.4. Furthermore we present illustrative photometric models which reproduce the main trends seen in the photometric profiles of the galaxies.

4.B.1 Photometric profiles from the literature

Figure 4.B.1 shows ellipticity and $PA_{\rm phot}$ profiles from the literature for the subsample of the ePN.S galaxies (references in Table 4.2) with photometric data reaching at least 4 $R_{\rm e}$, excluding the merger remnants NGC 1316, NGC 4472, and NGC 5128. For three galaxies, NGC 0584, NGC 2768, and NGC 5866, we marked the outermost photometric measurements that may be affected by perturbations from ongoing interactions (see appendix 4.D). For NGC 1023 and NGC 3384 the presence of multiple components, like for example the bar, affect the $PA_{\rm phot}$ and ellipticity profiles. Therefore for these galaxies we flagged the corresponding regions, as described in appendix 4.D. These regions are highlighted with open symbols and black vertical lines in Fig. 4.B.1.

The $PA_{\rm phot}$ profiles in Fig. 4.B.1 show more or less pronounced variations with radius for most of the galaxies. All SRs have isophote twists, typically $\sim 10-40$ degrees with a very large twist in NGC 4374. For the fast rotating galaxies classified as triaxial in Sect. 4.6.4 photometric twists range from $\sim 3-20$ degrees with the largest twist in NGC 4494 (~ 22 degrees). For the other FRs the photometric twists range from $\sim 0-28$ degrees, with two galaxies NGC 4278 and NGC 0584 having twists of ~ 28 degrees. The latter objects are consistent with axisymmetry at the resolution of the kinematic survey, but the photometry suggests that some of them might be triaxial as well.

The ellipticity profiles show that while most of the SRs become flatter in the outskirts, the opposite is true for the FRs. Most of the FRs shown in Fig. 4.B.1 have decreasing ellipticity profiles at large radii, approximately at the distance where $V_{\rm rot}$ is observed to drop. The vertical lines indicate the radial range of the kinematic transition discussed in Sect. 4.8.6. This is also evident from the distribution of the maximum ellipticity and of the outermost measured values in Fig. 4.10, and it is consistent with a picture where the FRs are dominated by a disk component in the central regions, embedded in a rounder, dispersion dominated outer component which is triaxial for a fraction of the sample. The exceptions to the decreasing trend in ellipticity at large radii are NGC 1344, a prolate rotator in the halo, NGC 3379 and NGC 4494 which are both very round at all radii, and NGC 2974, NGC 3384 and NGC 4339 for which the small number of tracers does not allow us to resolve any kinematic transition.

4.B.2 Photometric models of a FR with triaxial halo

Here we describe triaxial photometric models for FR galaxies which explain the magnitude of the photometric twists seen in Fig. 4.10, and which are used in the discussion in Sect. 4.8.4. These simple models are not meant to provide an exact description of the intrinsic shape of a galaxy. Their purpose is to obtain a reasonable representation of the structure of FRs with triaxial halos, to derive what is the maximum isophotal twist expected, and compare it with the observations.

To build these models we use the results of previous studies on the intrinsic shapes of FRs that constrain their central regions. Weijmans et al. (2014) and Foster et al. (2017) found that FRs are

close to oblate ($p \sim 1$), and rather flat ($q \sim 0.3$). Guided by the PN kinematic results, we assume that the intrinsic shape of the FR model changes from flat and oblate in the innermost regions, to rounder and mildly triaxial beyond the transition radius in the outer regions, as discussed in Sect. 4.8.4. Weijmans et al. (2014) and Foster et al. (2017) found that SRs have $q \sim 0.6$, but the p value is not well constrained (their analysis failed to converge). The main reason for this is the rather small number of SRs in the ATLAS^{3D} and in the SAMI samples. In addition, as argued by Foster et al. (2017), the family of SRs comprises both truly spheroidal pressure dominated systems and flattened non-regular rotators, which might prevent the analysis to converge.

We present here four different photometric models, that have similar axis ratios in the central regions but different halos intrinsic shapes, as well as different realizations in how the transition between central-oblate regions and triaxial halos occurs:

- the *Sérsic model* (Model 1) is a one component model built using the three-dimensional Sérsic deprojection proposed by Lima Neto et al. (1999) with Sérsic index $n = 4$ and variable flattening. The effective radius of the two-dimensional profile is set equal to the average of the observed $R_e = 50$ arcsec. The transition radius is also the average of the measured values for the FRs: $R_T = 1.8R_e$. We used (q = 0.3, p = 1) for the inner axis ratios, as measured by Weijmans et al. (2014) and Foster et al. (2017). For the outer regions we choose (q = 0.6, p = 0.9), close to values found by Weijmans et al. (2014) for the SRs. The variation between inner and outer values of flattening is modeled by an arctangent function; the width of the radial transition is chosen to be 50 arcsec (mean ΔR_T, Sect. 4.8.6) .

- the *cored Sérsic halo plus disk model* (Model 2) is a two component model built from the sum of deprojections of an $n = 4$ spheroid and $n = 1$ spheroidal-exponential disk as in Lima Neto et al. (1999), but we added a core with radius $R_{\rm core} = R_T = 1.8 \times 50$ arcsec to the deprojected $n = 4$ profile. Both the spheroid and the disk have constant flattening: (q = 0.6, p = 0.9) for the former, (q = 0.3, p = 1) for the latter. The horizontal scale-height of the disk is such that $1.67h = R_T$, which means that the transition radius is equal to the half-light radius of the disk, as qualitatively observed in Sect. 4.7.3. The effective radius of the two-dimensional profile of the spheroid is $R_e = 150$ arcsec. The luminosity density of the disk is scaled so that it equals the luminosity density of the spheroid at $r = R_T$, hence in this model the disk component dominates the luminosity density from the center out to R_T. This choice makes the total integrated light of the disk inside $r = R_T$ circa 3.5 times the total luminosity of the spheroidal component inside R_T. The intrinsic axis ratios of the spheroid are (q = 0.6, p = 0.9), those of the disk are (q = 0.3, p = 1).

- the *maximally triaxial cored Sérsic halo plus disk model* (Model 3) is built as Model 2 but with axis ratios (q = 0.6, p = 0.8) for the halo.

- Model 4 has a *strongly flattened triaxial halo* plus disk. The model is built as Model 2 with a cored Sérsic halo, but the axis ratios are (q = 0.4, p = 0.8).

Each model is observed at 100 random viewing angles. We chose a coordinate system with axes (x, y, z) aligned, respectively, with the major, the intermediate, and the minor axis of model ellipsoids, and called ϕ and θ the azimuthal and polar angles that define the direction of the line-of-sight (LOS). We choose the LOS by random samplings of the solid angle centered on the center of the ellipsoids $d\Omega = \sin\theta d\theta d\phi$. This makes the probability of observing the galaxy face-on (i.e. $\theta = 0$) lower with respect to edge-on ($\theta = 90$). The models, projected on a plane

orthogonal to the LOS, are fitted with ellipses using the IRAF task ELLIPSE (Tody 1993), to derive surface brightness, ellipticity and position angle profiles.

Figure 4.B.2 shows the result of this analysis on three models for six different values of θ in bins of 15 degrees. The shapes of the model ellipticity and position angle profiles are qualitatively similar to the observed profiles in Fig. 4.B.1. Large photometric twists ($>$ 10 degrees) are observed for viewing angles $\theta \lesssim 50$ degrees for Models 1 and 2, and for $\theta \lesssim 65$ degrees for Models 3 and 4. The rate of occurrence of large twists is of order $\sim$ 30% for our models (45% for Model 3), as shown also in Fig. 4.10 in Sect. 4.8.4 where we report the maximum twist versus the mean ellipticity. The distribution of the models in this diagram represent well the location of the ePN.S FRs, for which we observe a fraction 37% having photometric twists larger than 10 degrees. This analysis based on simple triaxial photometric models shows that the presence of small photometric twists, as typically observed for most of the FRs, is consistent with the presence of a triaxial halo. This means that it is likely that detailed individual models of these galaxies can be constructed that are consistent with the measured kinematic and photometric twist angles.

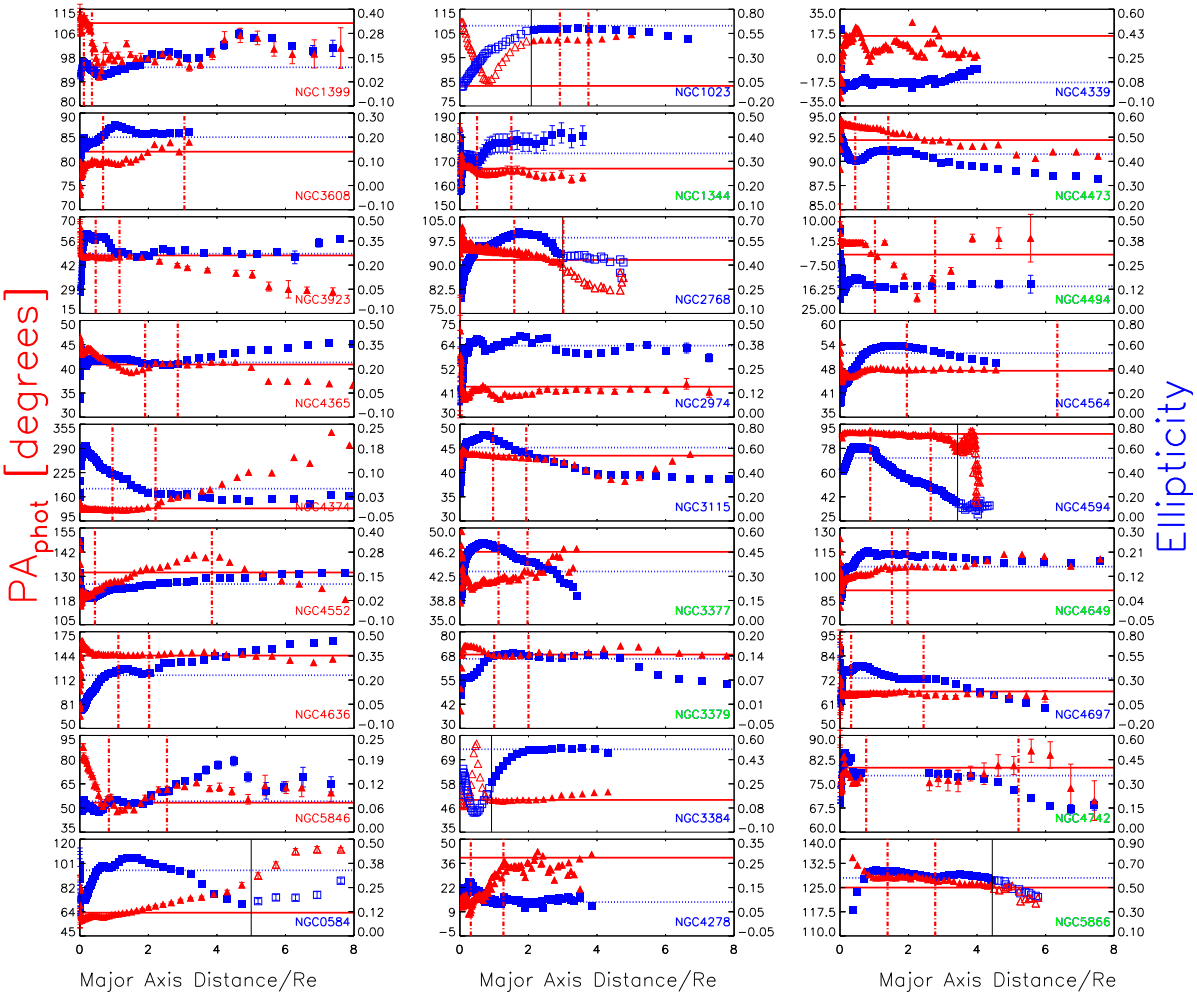

Figure 4.B.1: Position angle (red triangles, y axis on the left) and ellipticity profiles (dark blue squares, y axis on the right) for the subsample of the ePN.S galaxies with literature photometry reaching at least $4R_e$ (references in Table 4.2). The NGC numbers of the galaxies are shown in red for the SRs, in blue for the FRs, and in green for the FRs with triaxial halos. The open symbols and the black vertical line for NGC 0584, 2768, 5866 mark regions that are probably affected by ongoing interactions, and for NGC 1023 and NGC 3384 the regions affected by the presence of other photometric components, e.g. the bar (see appendix 4.D). For NGC 4594 we excluded the data beyond 350" where the small ellipticity corresponds to large uncertainties in the $PA_{\rm phot}$ measurements. The horizontal lines report the $PA_{\rm phot}$ (solid line) and ϵ (dotted line) with values listed in Table 4.1. The red dot-dashed vertical lines show the kinematic transition range $R_T \pm \Delta R_T$ from Sect. 4.8.6.

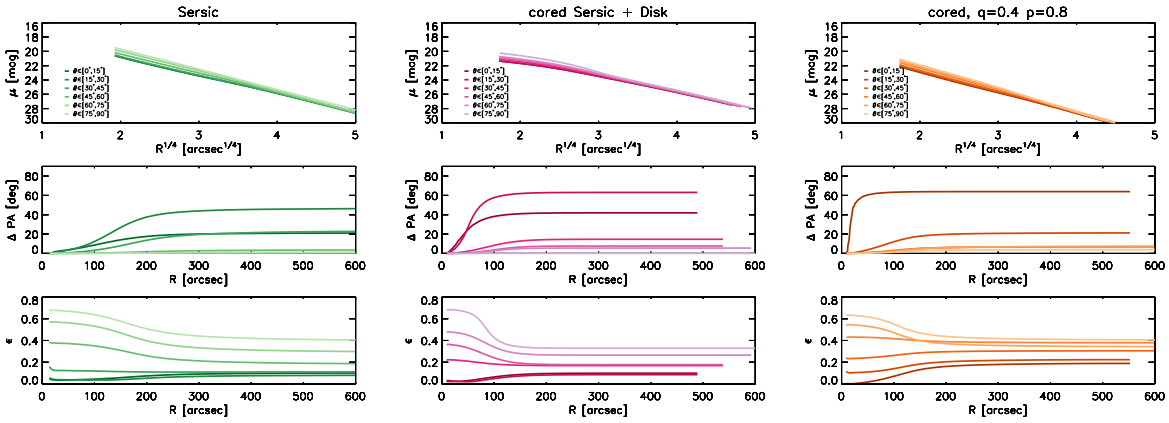

Figure 4.B.2: Surface brightness, position angle, and ellipticity profiles for three photometric models described in this appendix 4.B.2, at different inclinations θ ($\theta = 0$ for face-on, $\theta = 90$ edge-on). For each photometric model, we show one random projection in each of six intervals $\Delta\theta = 15$ degrees, starting from near face-on ($\Delta\theta = 0 - 15$ degrees, darkest color profile), through $\Delta\theta = 15 - 30$ degrees, etc., to near edge-on ($\Delta\theta = 75 - 90$ degrees, lightest profile). These $\Delta\theta$ intervals represent 3%, 10%, 20%, 19%, 21%, 27% of 100 random directions, from face-on (darkest) to edge-on (lightest profiles).

4.C Algorithm for building the photometric model

By approximating the iso-density surfaces of a model galaxy as a family of concentric ellipsoids, we derive its projection on the plane of the sky w. This is the plane orthogonal to the line-of-sight defined by the two viewing angles (θ, ϕ).

We consider a coordinate system centered at the center of an ellipsoid, with the axes x, y, z aligned with the long, intermediate, and short axis of the ellipsoid, respectively:

$$\frac{x^2}{r^2} + \frac{y^2}{(rq_y)^2} + \frac{z^2}{(rq_z)^2} = 1 \tag{4.14}$$

with $1 \geq q_y \geq q_z$. We indicate with θ and ϕ the polar and the azimuthal angles, so that a line-of-sight direction vector $\hat{n}$ has components

$$\begin{cases} a &= \cos\phi\sin\theta \\ b &= \sin\phi\sin\theta \\ c &= \cos\theta, \end{cases} \tag{4.15}$$

such that the norm $|\hat{n}| = \sqrt{a^2 + b^2 + c^2} = 1$. We now write the equation of a plane w orthogonal to $\hat{n}$:

$$a\,x + b\,y + c\,z - 1 = 0. \tag{4.16}$$

All the points (x, y, z) that satisfy this equation belong to a plane w orthogonal to the vector **P** along the line-of-sight. For simplicity, we derive the projection of the model galaxy on the plane w_0 intersecting the center of the ellipsoid.

We define a second coordinate system (x_0, y_0, z_0) with the origin at the center of the ellipsoid, the axes x_0 and y_0 in the plane w_0, and the axis z_0 orthogonal to w_0 (hence z_0 is aligned with the line-of-sight: $\hat{z_0} = \hat{n}$). We choose x_0 aligned with the intersection of the plane w_0 with the plane $z = 0$:

$$\begin{cases} z = 0 \rightarrow xa + yb = 1 \\ \text{if } x = 0, y = \frac{1}{b} \\ \text{if } x = 1, y = \frac{1-a}{b} \end{cases} \tag{4.17}$$

The vector **s**, defined as

$$\left(1 - 0,\ \frac{1-a}{b} - \frac{1}{b} = -\frac{a}{b},\ 0\right), \tag{4.18}$$

is parallel to $\hat{x_0}$. Hence

$$\hat{x_0} = -(\frac{\mathbf{s}}{|\ \mathbf{s}\ |}) = \left(\frac{-b}{\sqrt{b^2 + a^2}}, \frac{+a}{\sqrt{(b^2 + a^2)}}, 0\right) \tag{4.19}$$

The axes $(\hat{x_0}, \hat{y_0}, \hat{z_0})$ have therefore coordinates

$$\begin{cases} \hat{x_0} = (-\sin\phi, \cos\phi, 0) \\ \hat{y_0} = \hat{z_0} \times \hat{x_0} = (-\cos\theta\cos\phi, -\cos\theta\sin\phi, \sin\theta) \\ \hat{z_0} = \hat{n} = (\cos\phi\sin\theta, \sin\phi\sin\theta, \cos\theta) \end{cases} \tag{4.20}$$

A point P_0 in the plane w_0 has coordinates $P_0 = (X_0, Y_0, 0)$, and can be written as

$$\begin{aligned} P_0 &= X_0\hat{x_0} + Y_0\hat{y_0} + 0\hat{z_0} \\ &= -X_0\sin\phi\hat{x} + X_0\cos\phi\hat{y} + -Y_0\cos\theta\cos\phi\hat{x} - Y_0\cos\theta\sin\phi\hat{y} + Y_0\sin\theta\hat{z}, \end{aligned} \tag{4.21}$$

therefore P_0 as coordinates

$$\begin{cases} P_x &= -X_0\sin\phi - Y_0\cos\theta\cos\phi \\ P_y &= X_0\cos\phi - Y_0\cos\theta\sin\phi \\ P_z &= Y_0\sin\theta \end{cases} \tag{4.22}$$

A line through each point $P(X_0, Y_0, 0)$ and orthogonal to the plane w_0 (line-of-sight) can be parametrized as

$$\begin{cases} x_0 = X_0 \\ y_0 = Y_0 \\ z_0 = t \end{cases} \tag{4.23}$$

which in the frame (x, y, z) translates in

$$\begin{cases} x &= -X_0 \sin\phi - Y_0 \cos\theta \cos\phi + \sin\theta \cos\phi t \equiv d + at \\ y &= X_0 \cos\phi - Y_0 \cos\theta \sin\phi + \sin\theta \sin\phi t \equiv e + bt \\ z &= Y_0 \sin\theta + \cos\theta t \equiv k + ct \end{cases} \tag{4.24}$$

The intersections of the line-of-sight with the ellipsoid can be derived by solving this system

$$\begin{cases} x = d + at \\ y = e + bt \\ z = k + ct \\ \frac{x^2}{r^2} + \frac{y^2}{(rq_y)^2} + \frac{z^2}{(rq_z)^2} = 1, \end{cases} \tag{4.25}$$

which translated into a quadratic equation in t:

$$\left(\frac{a^2}{r^2} + \frac{b^2}{(rq_y)^2} + \frac{c^2}{(rq_z)^2}\right)t^2 + 2\left(\frac{ad}{r^2} + \frac{eb}{(rq_y)^2} + \frac{kc}{(rq_z)^2}\right)t + \left(\frac{d^2}{r^2} + \frac{e^2}{(rq_y)^2} + \frac{k^2}{(rq_z)^2} - 1\right) = 0. \tag{4.26}$$

The equation $Dt^2 + Et + F = 0$ admits solutions if $\Delta = E^2 - 4DF \geq 0$. If $\Delta > 0$ there are two intersection points of the line-of-sight with the ellipsoid $t_{1,2} = \frac{-E \pm \sqrt{E^2-4DF}}{2D}$; if $\Delta = 0$ the line of sight is tangent to the ellipsoid in the point $t1 = \frac{-E}{2D}$. If $\Delta = 0$ the line of sight is external to the ellipsoid.

Given a family of ellipsoids describing the density distribution of the model galaxy and a line-of-sight specified by (θ, ϕ), we integrate the density along the line-of-sight by summing the density of the ellipsoids intersected. The projection of the model on the sky plane is then derived by integrating along all the lines-of-sight through each point of the plane.

Algorithm for building a photometric model of an ellipsoidal FR galaxy:

1. For each radius r, we build a family of concentric ellipsoids with semi-major axis r and density $\rho(r)$;
2. we build the plane of the sky w_0: this is a grid with coordinates (X_0, Y_0)
3. we choose a value for the viewing angles (θ, ϕ) that defines the line-of-sight. These are extracted randomly as follows:

```
import numpy as np

phi = np.random.random(N)*np.pi/2
costheta = np.random.random(N)
theta = np.arccos(costheta)

# here we are extracting N random lines-of-sight for N projections
```

```

for tt, theta_i in enumerate(theta):

# for each line-of-sight, the sky plane is defined by Eq.~\eqref{eq:
    equation_plane}, we derive $a$, $b$, and $c$

    phi_i = phi[tt]
    a   = np.cos(phi_i) * np.sin(theta_i)
    b   = np.sin(phi_i) * np.sin(theta_i)
    c   = np.cos(theta_i)
```

4. for each point in the plane of the sky (X_0, Y_0), build the equation of the line of sight as in (4.24) by calculating d, e, k

```
    for i in x0:
        for j in y0:
            d = - i * np.sin(phi_i) - j * np.cos(theta_i) * np.cos(phi_i)
            e = + i * np.cos(phi_i) - j * np.cos(theta_i) * np.sin(phi_i)
            k = j * np.sin(theta_i)
```

5. We solve equation (4.26) to determine the intersections of the line-of-sight with the family of ellipsoids

```
            AA = qz**2 * qy**2 * a**2 + qz**2 * b**2 + qy**2 * c**2
            BB = 2 * (qz**2 * qy**2 * a * d + qz**2 * e * b + qy**2 * k * c)
            CC = qz**2 * qy**2 * d**2 + qz**2 * e**2 + qy**2 * k**2 - a**2 *
    qy**2 * qz**2
            DELTA = BB**2 - 4 * AA * CC

            rho_a = []
            a_inters = []
            t = []
            sol = np.where(DELTA > 0)
            if np.array(sol).size > 0:

            # sol gives which ellipsods are crossed in 2 points
                a_inters = a[sol]
                rho_a = np.append(lumDensity[sol],rho_a)
                rho_a = np.append(lumDensity[sol],rho_a)
                BBp = BB[sol]
                DELTAp = DELTA[sol]
                AAp = AA[sol]
                t = np.append( (-BBp + np.sqrt(DELTAp) ) / (2 * AAp), t)
                t = np.append( (-BBp - np.sqrt(DELTAp) ) / (2 * AAp), t)
            counts = np.count_nonzero(DELTA == 0)
            if counts > 0:
                sol0 = np.where(DELTA == 0)
                # sol0 gives which ellipsods are crossed in 1 point =
    tangent line
```

```
                a_inters = np.append(a[sol0], a_inters)
                rho_a = np.append(lumDensity[sol0],rho_a)
                BB0 = BB[sol0]
                DELTA0 = DELTA[sol0]
                AA0 = AA[sol0]
                t = np.append( -BB0  / (2 * AA0), t)
```

6. Each solution t corresponds to an intersection with an ellipsoid with major axis r and density $\rho(r)$. The surface brightness projected on the point of coordinates (X_0, Y_0) in the sky plane is given by the sum of all the contributions of the ellipsoids intercepted by the line-of-sight through (X_0, Y_0). Hence, for each t all the values $\rho(t)$ are interpolated along t and integrated.

7. The projection of the model galaxy is stored in the matrix image[x_0, y_0]

```
            if np.array(t).size > 0 :
                s = np.argsort(t)
                t = t[s]
                rho_a = rho_a[s]
                tinterp = np.linspace(min(t),max(t),201)
                rhointerp = np.interp(tinterp, t, rho_a)
                int_light = np.trapz(rhointerp,tinterp)
            if  np.array(sol).size == 0 and counts == 0 :
                int_light = 0.0
            x_coords = (i+max(x0)).astype(int)
            y_coords = (j+max(y0)).astype(int)
            image[x_coords,y_coords] = int_light
```

4.D Notes on single galaxies and comparison with the literature

4.D.1 Fast rotators

- **NGC 0584**. This is the brightest member of a small cluster containing mostly E galaxies (van den Bergh 1961). It is classified as a E4 in the NED catalog, but seems to contain a disk structure (Michard & Marchal 1994). Our PN kinematic data show that the galaxy halo rotates with at least $\sim$ 50 km s^{-1}along the photometric major axis, and has a velocity dispersion of $\sim$ 100 km s^{-1}. The galaxy has central ellipticity $\epsilon \sim 0.4$ which falls to ~ 0.1 at $150'' \sim 5R_e$ from whereon ϵ increases again. The photometry shows pronounced isophote twist starting at $\sim 1R_e$, which steepens beyond $5R_e$. Both the outer increase in ellipticity and the rapid outer isophote twist may be related to the nearby companion galaxy, NGC 0586; therefore we consider only the region where the ellipticity decreases as intrinsic to the galaxy.

- **NGC 0821**. This is a field E6 galaxy. The ATLAS^{3D} velocity field (Emsellem et al. 2004) maps the inner regions of the galaxy where it behaves like a regular rotator along the photometric major axis. The PNe sample, instead, probes the kinematics from 1 to $5R_e$ and show a sustained rotation along the photometric minor axis with a maximum amplitude of 51 ± 16 km s^{-1}, suggesting the triaxiality of the object. No rotation is detected along the major axis. The long-slit data from Proctor et al. (2009) and the integral field map of Arnold et al. (2014) agree in detecting rotation along the photometric major axis, with decreasing amplitude (80 km s^{-1}at $0.3R_e$ to very slow rotation at $R < 2R_e$). They do not detect any rotation along the minor axis, but their data do not extend far beyond $1.5R_e$ along that axis. The kinemetry of Foster et al. (2016), based on the same data used by Arnold et al. (2014) but with a more careful treatment of outliers, shows a radial twist of the PA_{kin} between 40 to 60 arcsec toward the same position angle measured from the PNe. Long slit data from Weijmans et al. (2009) and Forestell & Gebhardt (2010) also show some minor axis rotation at large radii. PN data are consistent with the kinematics of the blue GCs (see Pota et al. 2013), which are found to rotate at ∼ 85 km s^{-1}along a direction consistent with the photometric minor axis. The red GCs instead appear to faintly counter-rotate with respect to the host galaxy stars. The outer gradient of the velocity dispersion radial profile has been debated in the literature, with implications on the inferred dark matter content of the galaxy. The PN data combined with the long slit stellar kinematics show a decrease of the velocity dispersion as a function of radius, consistently as both red and blue GCs show, while Proctor et al. (2009) and Forestell & Gebhardt (2010) found a flat profile within 100 arcsec.

- **NGC 1023**. This is a barred lenticular galaxy (SB0), brightest member of a group of 13 galaxies (Tonry et al. 2001). It has a small companion NGC 1023A, which is probably interacting with the main galaxy (Sancisi et al. 1984), but it is likely too small to cause significant disruptions in the dynamical state of the main galaxy (Noordermeer et al. 2008). The ATLAS^{3D} velocity map (Emsellem et al. 2004) covers the innermost regions of the galaxy, up to half effective radii, and displays rotation with maximum amplitude of ∼ 120 km s^{-1}and strong twist of the zero-velocity line. The stellar kinematics along the major axis of Debattista et al. (2002) and Boardman et al. (2017) show that the rotation continues to increase mildly in the outer regions exceeding 200 km s^{-1}beyond $2R_e$. Both the PN and SLUGGS (Arnold et al. 2014) velocity maps show decreasing rotation beyond $3R_e$, (see also Noordermeer et al. 2008; Coccato et al. 2009; Cortesi et al. 2013b). The galaxy does not show any twist of the kinematic position angle or any misalignment with the photometric axis. The non zero third order harmonics amplitudes describe a rather cylindrical velocity field. The velocity dispersion map shows minimum values ($\sigma \sim 40$ km s^{-1}) at the location of the disk, while the outermost (bulge) PNe are hotter ($\sigma \sim 120$ km s^{-1}). The photometric position angle profile is influenced by the presence of the bar at $R < 100$" (Barbon & Capaccioli 1975), therefore we excluded these regions from our discussion of the photometric twists.

- **NGC 1316**. This is a giant elliptical (also classified as a peculiar S0), member of the

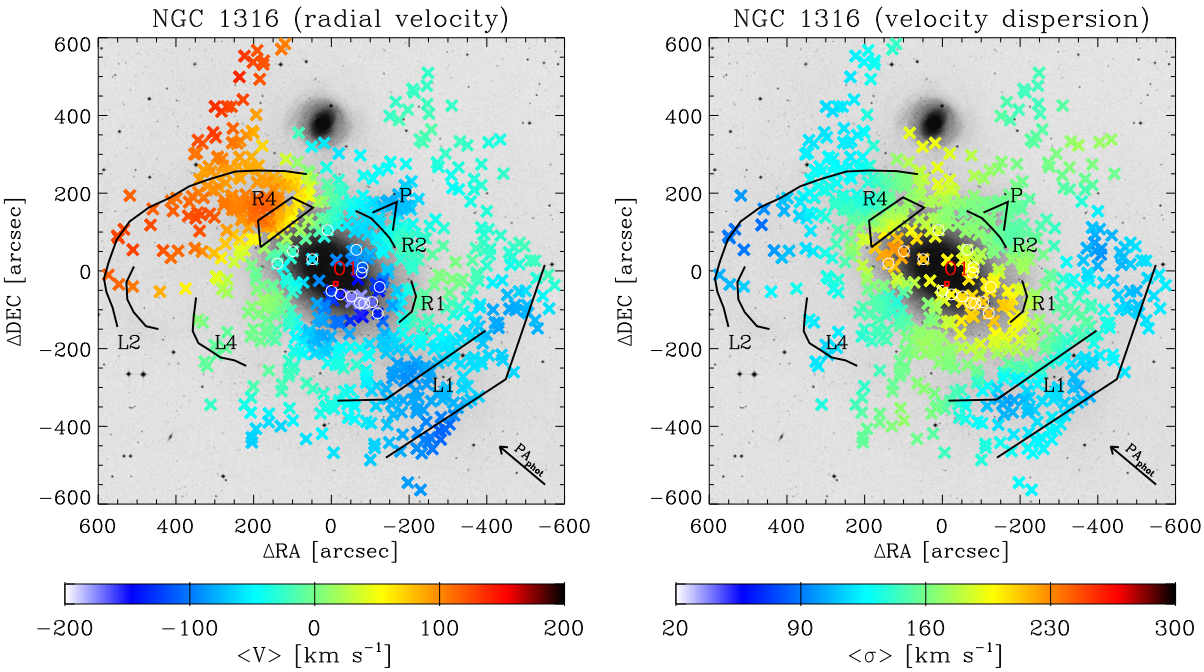

Figure 4.D.1: Smoothed velocity field and velocity dispersion field of NGC 1316 shown on the DSS image; north is up, east is left. The circles highlight the PNe belonging to a structure in the phase space, discussed in the text. The black contours trace features in the surface brightness distribution (designations from Schweizer 1980). In red is marked the position of the feature O1 observed by Richtler et al. (2014). The arrow at the bottom right shows the direction of the $PA_{\rm phot}$.

Fornax cluster (Fornax A). NGC 1316 is a known merger remnant. Its photometric substructures were mapped for the first time by Schweizer (1980), and were recently studied by Iodice et al. (2017). The PN velocity field is highly asymmetric, showing that the galaxy is in a non-equilibrium phase. The modeling with a point-symmetric rotation model gives an approximate description of the properties of the galaxy. The fit of the $a_0(R)$ parameter of the rotation model (see Eq. 4.10) in radial bins shows the presence of peculiar bulk motions in groups of PNe. There is no kinematics from integral field spectroscopy in literature, and the comparison with the long-slit observations from Bedregal et al. (2006) shows general good agreement with our data in the regions of overlap. The PNe in the halo of NGC 1316 (Fig. 4.D.1) reveal that the galaxy rotates along the major axis with an amplitude of ~ 65 km s^{-1}, as already observed by Arnaboldi et al. (1998); McNeil-Moylan et al. (2012). The structures in the velocity field can be spatially associated with corresponding surface brightness features in the same location. There is an overdensity of PNe on the north-eastern part, co-located spatially with the ripple R4 (the designations of the photometric features are from Schweizer 1980, and their positions are indicated in black in Fig. 4.D.1), with velocities that do not have a point symmetric counterpart. Other groups of PNe that result in non-point-symmetric velocities are those possibly related with the loop L1, on the

south-west side, and to the plume P in the north-west. Figure 4.2 shows that the PNe of NGC 1316 in the innermost radial bin ($\sim$ 100 arcsec) have a velocity offset of $\gtrsim$ 150 km s^{-1}with respect to the systemic velocity. This is produced by a group of relatively slower PNe with mean velocity $\sim$ 1325 km s^{-1}and dispersion $\sim$ 60 km s^{-1}(highlighted in Fig. 4.D.1 with white circles, along with the photometric feature O1 found by Richtler et al. 2014, in red). These PNe are not associated with any substructures in the light, and the fact that they are very localized in the phase space challenges (but does not rule out) the possibility that they could be contaminants. More likely this kinematic feature is the result of a combination of spatial incompleteness and differential absorption from localized dust in the galaxy, producing local lacks of detections in the phase space and so more negative smoothed velocities $\tilde{V}$. A more detailed study is beyond the scope of this paper.

- **NGC 1344**. This galaxy, also known as NGC 1340, is an E5 elliptical belonging to the Fornax cluster. It is characterized by the presence of internal and external concentric shells (Malin & Carter 1980), as consequences of a recent merger activity. The smoothed velocity field does not deviate from point symmetry, however it shows that the galaxy in the outskirts rolls around the photometric major axis. The velocity dispersion field shows a gently decreasing profile. Unfortunately there is no integral field stellar kinematics available for a comparison with the PNe kinematics. The long slit stellar kinematics (Teodorescu et al. 2005) show sustained rotation along the photometric major axis that reaches $\sim$ 100 km s^{-1}at 1.3R_e and a decreasing velocity dispersion. The σ values from the spectroscopy are in agreement with those found with the PN data. We do not detect such an strong rotation, probably because of the different radial coverage of the PN data.

- **NGC 2768**. This S0 is a field galaxy (Madore et al. 2004) or member of a poor group (Fouque et al. 1992). NGC 2768 has a cylindrical velocity field (Emsellem et al. 2004) whose amplitude remains constant at around $\sim$ 130 km s^{-1}from the innermost regions (Emsellem et al. 2004) to the outskirts (see Proctor et al. 2009; Pota et al. 2013). Our velocity map is in good agreement with that presented by Arnold et al. (2014) and extends it beyond 6R_e. There is some discrepancy between the PN V_{rot} and the kinemetry fit from Foster et al. (2016) in the innermost radial bins where the disk strongly dominates. This is due to the fact that the smoothed PN velocity field in these bins is an average over the fast rotating PNe in the disk and the more slowly rotating PNe from the spheroid. A kinematic study of the different components of this galaxy was published by Cortesi et al. (2013b). At larger radii ($r \gtrsim 3R_e$) the contribution of the disk weakens and the PN kinematics trace the spheroid. In this region we find a constant sustained ($V \sim$ 130 km s^{-1}) rotation along the photometric major axis. The velocity dispersion profile is flat at $\sim$ 140 km s^{-1}. The PN smoothed velocity field of NGC 2768 shows localized, small scale deviations from point symmetry. These asymmetries do not influence the kinematic analysis, but we used the unfolded catalog to build the velocity fields. The light distribution shows asymmetries beyond $\sim$ 20 kpc radius (Duc et al. 2015) which cause an increased isophote twist beyond $3R_e = 186'' \sim 20$ kpc. The PN velocity field is aligned with the major axis except in the last bin which could be related to these asymmetries. Therefore the galaxy is classified

as consistent with axisymmetry. The PN kinematics agrees with that of GCs. Pota et al. (2013) found significant rotation only for the red GCs along the photometric major axis and with constant amplitude. Their velocity dispersion decreases with radius.

- **NGC 2974**. This is an elliptical (E4) field galaxy. Its kinematics was mapped by the SAURON survey (Emsellem et al. 2004), showing that the galaxy is rotating at $\sim$ 120 km s^{-1}along the photometric major axis, while the velocity dispersion has a steep decreasing profile. PN kinematic data show that the galaxy halo rotates at least at $\sim$ 70 km s^{-1}along the photometric major axis, and has a velocity dispersion of 150 km s^{-1}.

- **NGC 3115**. This is an S0 associated with a loose group of galaxies (Fouque et al. 1992). It has a nearly edge-on disk (i = 86 degrees) which flares outward (Capaccioli et al. 1987). The long slit spectroscopy from Norris et al. (2006) and the IFS observations of Guérou et al. (2016) show that the rotation velocity increases steeply from the innermost regions to $\sim$ 230 km s^{-1}around $\sim 1R_e = 93''$. The major axis profile from Guérou et al. (2016) offset by 20 arcsec along the minor axis show that also the spheroidal component has pronounced rotation. The velocity dispersion field is colder ($\sigma \sim$ 120 km s^{-1}) in the region dominated by the disk, and hotter along the minor axis ($\sigma \sim$ 220km s^{-1}). The kinemetry of Foster et al. (2016) on SLUGGS data show that the amplitude of rotation decreases from $\sim$ 1 Re outward. The PN data show a cylindrical velocity field with gently decreasing rotation amplitude reaching $\sim$ 120 km s^{-1}at $\sim 3R_e$, where the spheroid dominates. The PA_{kin} has a constant misalignment of $\sim$ 10 $\pm$ 5 degrees with respect to PA_{phot}. By comparison the kinemetry from Foster et al. (2016) in Fig. 4.6 has $\sim$ 5 $\pm$ 10 degrees misalignment at 200" major axis radius, slightly offset from the PA_{phot} in the same direction as the PNe, showing that both datasets agree within the errors. This misalignment is probably related to perturbations at the interface between the disk and the spheroid, visible as deviations from axisymmetry in the photometry of the disk component. Capaccioli et al. (1987) found that the spheroidal component of this galaxy shows a photometric twist of $\sim$ 4 degrees, from $\sim$ 45 degrees at 10 arcsec to $\sim$ 41 degrees at 350 arcsec. The disk instead flares (Fig. 23 from Capaccioli et al. 1987) and has a warp of few degrees (their Fig. 24) in the same direction of the PN velocity field. The same features are visible in the photometry of Guérou et al. (2016) (their Fig. 11) and in new observations with the VST telescope (VEGAS survey, Iodice private communication). This shows that NGC 3115 is indeed a complicated case, and we therefore do not include it in the sample of galaxies with triaxial halo.

- **NGC 3377**. It is an E6 galaxy in the Leo I group. The absorption line kinematics (Coccato et al. 2009; Emsellem et al. 2004; Foster et al. 2016) shows that the galaxy displays a disk-like rotation in the inner regions, which starts to decrease at $\sim 1.5R_e$. Our analysis of the PN kinematics shows that the decreasing trend continues out to large radii, where it becomes 16 $\pm$ 8 km s^{-1}at $\sim 4R_e$ and 11 $\pm$ 7 km s^{-1}beyond $\sim 7R_e$. The kinematic major axis position angle twists with radius in the outskirts in agreement with Foster et al. (2016). The velocity dispersion at large radii decreases very gently with radius, from $\sim$ 80 km s^{-1}at 1 R_e and to $\lesssim$ 60 km s^{-1}at 8 R_e. This is consistent with the GC study of Pota et al. (2013),

whose kinematics reaches $\sim 8R_e$. While the red GCs show a constant rotation of ~ 50 km s^{-1}, the blue ones do not rotate significantly in agreement with the PNe. The velocity dispersion of the whole GC sample is consistent with that from PNe.

- **NGC 3379**. This is the largest galaxy in the Leo I group, classified as an E1. The PN system of this galaxy is has been widely studied in literature (Ciardullo et al. 1993; Romanowsky et al. 2003; Sluis & Williams 2006). The velocity maps from Emsellem et al. (2004) reveal that the galaxy rotates regularly along its photometric major axis ($V_{\rm rot}^{MAX} \sim 63$ km s^{-1}), while the velocity dispersion has a central peak of ~ 220 km s^{-1}and it decreases to 180 km s^{-1}around $0.25R_e$. Then, the long slit data of Statler & Smecker-Hane (1999) and Weijmans et al. (2009) show that the profile gently declines to ~ 120 km s^{-1}at $\sim 2R_e$. The PN smoothed velocity field is in good agreement with the inner kinematics and extends it to $6R_e$. We find that the galaxy has a rotation along an axis that twists from the photometric major axis position angle ($\sim 70°$ at ~ 15 arcsec) toward higher values at large radii. We observe the onset of a rotation along the minor axis at $\sim 2.5R_e$. This is reflected in the trend of the fitted kinematic position angle and in the amplitudes of the third order harmonics. The amplitude of this additional rotation is ~ 30 km s^{-1}. At the moment there are no integral field kinematic data covering these large distances from the center of the galaxy. The velocity dispersion map shows that the decline continues up to $6R_e$ where it reaches values around 70 km s^{-1}.

- **NGC 3384**. This lenticular galaxy is a member of the Leo I group (Fouque et al. 1992). We find a rotation velocity of 160 ± 7 km s^{-1}at $\sim 7R_e$, consistent with the rotation amplitude published by Krajnović et al. (2011). We do not observe any twist of the kinematic position angle or any misalignment with the photometric one, and the motion is that of a regular rotator. The velocity dispersion map in Emsellem et al. (2004) shows that the σ has a double peak at the center ($\sigma \sim 155$ km s^{-1}), and a declining profile that reaches ~ 80 km s^{-1}at $\sim 0.5R_e$. The PN data show a velocity dispersion of ~ 80 km s^{-1}. Cortesi et al. (2013b) performed a kinematic analysis of the disk and spheroid component separately. The photometric study of Meusinger & Ismail (2007) showed the presence of an "inner component" and and "elongated" component, visible in the $PA_{\rm phot}$ profiles as a local minimum at $R = 3$" and a local maximum at $R = 15$". Therefore we considered only the regions at $R > 30$" in our discussion in Sect. 4.8.4.

- **NGC 3489**. This S0 galaxy belongs to the Leo I group. The ATLAS^{3D} kinematic map (Krajnović et al. 2011) shows a fast rotation along the photometric major axis, whose amplitude reaches ~ 115 km s^{-1}at $\sim 1R_e$. PN data show that the halo of this galaxy is also rotating at > 40 km s^{-1}. The dispersion is around 80 km s^{-1}, consistent with Cappellari et al. (2011). We refer to Cortesi et al. (2013b) for a kinematic analysis of the the disk and spheroid component separately.

- **NGC 4278**. This a rather round elliptical galaxy (E1-2), member of the Coma I group. The ATLAS^{3D} kinematic map Krajnović et al. (2011) shows that stars are regularly rotating only within $0.5R_e$ along a direction slightly offset from the photometric major axis, while

there is very weak or no rotation farther out. The kinemetry of Foster et al. (2016) shows that the galaxy does not significantly rotate beyond $1R_e$. The PN velocity field does not show any significant rotation, hence also the kinematic position angle is not very well defined. Pota et al. (2013) do not find any evidence of rotation for the metal rich GCs, while the blue metal poor GCs display a weak rotation in the outer regions, along a direction between the major and the minor axes. The velocity dispersion falls rapidly with radius from a central value of ~ 270 km s^{-1}to ~ 120 km s^{-1}at $\sim 2R_e$ (Bender et al. 1994; Emsellem et al. 2004; Foster et al. 2016). Our map shows values of σ almost constant at 130 km s^{-1}, in good agreement with the literature.

- **NGC 4339**. This is a member of the Virgo cluster, classified as intermediate type between E0 and S0. It is regular FR, showing no misalignment between the photometric and kinematic major axis (Cappellari et al. 2011). The PN motion agrees with the stellar kinematics showing a rotation of > 20 km s^{-1}and a dispersion of 30 km s^{-1}.

- **NGC 4473**. This Virgo galaxy is an E5 disky elliptical. It is well known for its multi-component central kinematics (Emsellem et al. 2004): it is a fast but non-regular rotator ($V_{\rm rot}^{MAX} = 63$ km s^{-1}, along the photometric major axis) and the velocity dispersion map displays a double peak, which have been interpreted as the presence of a counter-rotating disk (Cappellari et al. 2007), maybe formed in binary disk major mergers (Bois et al. 2011). We detect a low amplitude rotation of ~ 30 km s^{-1}along a direction tilted with respect to the photometric major axis. The kinematics from integrated light of Foster et al. (2013) already proved this object to be triaxial. Our velocity dispersion map does show the double peaked structure along the major axis, where $\sigma \sim 160$ km s^{-1}. The velocity dispersion decreases to ~ 100 km s^{-1}at $10R_e$.

- **NGC 4494**. This is an E1 galaxy in the NGC 4565 group. The velocity map from Krajnović et al. (2011) shows a kinematically distinct core. The galaxy rotates almost constantly at ~ 60 km s^{-1}up to $2R_e$ (Napolitano et al. 2009; Foster et al. 2016). In the halo we find that this amplitude decreases with radius. There is evidence for an additional component rotating along the photometric minor axis at ~ 25 km s^{-1}, as also shown by the twist of the $PA_{\rm kin}$. The velocity dispersion field shows a peak at the center ($\sigma \sim 150$ km s^{-1}), and then decreases to ~ 80 km s^{-1}at $R \gtrsim 5R_e$, in very good agreement with the stellar kinematics. The four-fold structure that appears in the σ map is a result from smoothing procedure, and reflects some unresolved gradient in the velocity field. The trend of the rotation amplitude from PN kinematics seems to be confirmed by the kinematic map from Arnold et al. (2014), but their data do not extend out in radii enough to show any rotation along the minor axis. The kinematics of GCs is studied by Foster et al. (2011) out to $\sim 3.5R_e$. They found that the metal poor GCs rotate with similar amplitude as the galaxy stars, while the metal-rich GCs show marginal rotation. The velocity dispersion profile of the global GC sample is consistent with that of the stars.

- **NGC 4564**. NGC 4564 is an E4 galaxy in the Virgo cluster. It shows a prominent stellar disk along the apparent major axis, so that it has also been referred as an S0 (Michard

& Marchal 1994). We agree with the stellar kinematic from Foster et al. (2016) and we extend it beyond $6R_e$, where the galaxy is still clearly rotating along its photometric major axis ($V_{rot} \sim 95$ km s^{-1}). The velocity dispersion profile is decreasing, from the central peak of 180 km s^{-1}(Emsellem et al. 2004) to $\sim$ 70 km s^{-1}at $6R_e$.

- **NGC 4594**. NGC 4594, also known as "the Sombrero" (M 104), is an SAa galaxy in the Virgo cluster. It has an extremely bright bulge, while its disk contributes only 10% of the light (Burkhead 1986) and has pronounced dust lanes. Kinematics from line-profile measurements show that the galaxy rotates along its major axis reaching $\sim$ 250 km s^{-1}at $\sim 1R_e$, where the rotation curve flattens to a constant amplitude (Kormendy & Illingworth 1982; van der Marel et al. 1994). The velocity dispersion declines from the central value of $\sim$ 280 km s^{-1}to values close to 100 km s^{-1}where the disk component dominates. The bulge, instead, has a dispersion remarkably constant at 210 km s^{-1}. Our PN data extend beyond $4R_e$, but there is a void in the detections along the major axis because of the dust lane. For this reason the PNe do not trace the fast rotating disk, and their kinematics is in very good agreement with the integrated light kinematics of Kormendy & Westpfahl (1989) from a slit parallel to the major axis, offset by 30 arcsec. Extinction effects are probably also responsible for the slight asymmetry of the smoothed velocity field, so the kinematic analysis is performed on the unfolded catalog. These asymmetries are localized and do not significantly influence the kinematic results. The only studies of the kinematics of this galaxy at large radii is from Bridges et al. (2007) and Dowell et al. (2014) using GCs. The latter sample distances out to 24' with 360 tracers, finding little or no evidence of rotation in the GC system as a whole, and within the red and blue subpopulations. The photometry shows ellipticity less than 0.1 and a correspondingly uncertain large isophote twist beyond 350" which we do not include in the photometric analysis.

- **NGC 4649**. Also known as M 60, it is an E2 galaxy in the Virgo cluster. It forms a close optical pair with NGC 4647, but the lack of evidence of strong tidal interaction features (e.g., Young et al. 2006) suggests that the galaxies are at different distances. The ATLAS^{3D} velocity map shows a regular, cylindrical rotation of $\sim$ 95 km s^{-1}(Krajnović et al. 2011), while the dispersion has a central peak of $\sim$ 370 km s^{-1}and it decreases to $\sim$ 260 km s^{-1}at $0.5R_e$. The kinematic maps from Arnold et al. (2014) shows that the cylindrical rotation extends up to $2R_e$, while there the dispersion is $\sim$ 120 km s^{-1}. The PN data extend out to 5 R_e. The smoothed PN velocity field shows that the amplitude of the rotation along the photometric major axis decreases with radius, and no rotation along the major axis is detected beyond $2R_e$. In the outer regions, instead, the system rotates along a nearly orthogonal direction, suggesting a triaxial halo. The velocity dispersion is roughly constant at $\sim$ 200 km s^{-1}from 1 to 5 R_e. We see a slight bump in the dispersion profile at 3 R_e, but it may be associated to an unresolved velocity gradient. There are several studies of the GC kinematics in NGC 4649. The most recent, with the largest sample is from Pota et al. (2015). The red GCs display a nearly constant rotation with radius along the photometric major axis. Interestingly they observe a dip in rotation velocity between 100 and 200 arcsec, where we observe the inner rotation decreasing also. The blue GCs also

show hints of rotation at all radii, with lower amplitude, and generally along the major axis of the galaxy. Blue GCs also appear to have a minor axis rotating component at 300 arcsec, coinciding with the one found with the PNe. The velocity dispersion of GCs is constant at $\sigma = 240 \pm 30$ km s^{-1}.

- **NGC 4697**. This is an E6 galaxy in the Virgo southern extension, belonging to a group of 18 galaxies (Garcia 1993). This galaxy has 535 PN detections by Méndez et al. (2001). In this dataset Sambhus et al. (2006) found evidence for two separate PN populations, with different luminosity functions, spatial distributions, and radial velocities. In particular the secondary population of PNe is found to be azimuthally unmixed and not in dynamical equilibrium. The velocity field shows a rotation along the photometric major axis with amplitude decreasing with radius from the maximum $\sim$ 90 km s^{-1}at $1R_e$ to $\sim$ 15 km s^{-1}at 2.5. There is a hint for an increase in the amplitude of rotation at larger distances ($\sim$ 40 km s^{-1}at $4.5R_e$). The kinematic position angle is constant, aligned with the photometric major axis. There is a variation of the PA_{kin} profile at $\sim 3R_e$, but we did not interpreted it as signature of a triaxial halo, as the present dataset still includes the secondary not-in-equilibrium population of PNe. The velocity dispersion steady declines with radius, from $\sim$ 180 km s^{-1}at $0.5R_e$ to $\sim$ 100 km s^{-1}at $4.5R_e$. The kinematic maps from Krajnović et al. (2011) and Spiniello et al. (2015) show a regular disk-like rotation with a maximum amplitude of 111 km s^{-1}, confirming the trend for the rotation amplitudes that we find. Arnold et al. (2014) also observes a clear decline of the rotation and of the velocity dispersion, in agreement with PN data.

- **NGC 4742**. This is a field E4 galaxy. It is a faint object, so the number of PN detections is relatively low. We detect a rotation of at least $\sim$ 74 km s^{-1}, in agreement with the stellar kinematics of Davies et al. (1983). The direction of rotation is along a direction misaligned with respect to the photometric position angle. The dispersion decreases from 100 km s^{-1}at 1.5 arcsec (Davies et al. 1983) to below 50 km s^{-1}in the outskirts. The photometric PA profile from Li et al. (2011) shows a jump inside $\sim 40''$ which is in disagreement with Lauer et al. (1995) based on HST data. Because the PA from Lauer et al. (1995) agrees with the outer profile from Li et al. (2011) we therefore use combined ellipticity and PA profiles from both sources.

- **NGC 5128**. Also known as Centaurus A, it is a giant elliptical (often classified as a peculiar lenticular) in the Centaurus group. It shows clear signs of its accretion history in tidal streams and shells (Malin et al. 1983; Peng et al. 2002; Crnojević et al. 2016), evidences of major nuclear activity (see e.g. Neumayer 2010), and jet-induced star forming regions (e.g., Rejkuba et al. 2002). Its kinematics probed by PNe reflects the presence of regions which are not in equilibrium, showing a highly asymmetric and rich in subcomponents velocity field. The fit of the $a_0(R)$ parameter of the rotation model (4.10) in radial bins shows the presence of peculiar bulk motions in groups of PNe. The galaxy shows a rotation along the photometric major axis (NE direction) with increasing amplitude, from $\sim$ 50 km s^{-1}at $\sim$ 200 arcsec ($\sim 1.5R_e$) till at least $\sim$ 150 km s^{-1}at 800 arcsec ($\sim 5R_e$). The system also displays strong rotation ($\sim$ 100 km s^{-1}) along the minor axis, revealing its triaxiality (see

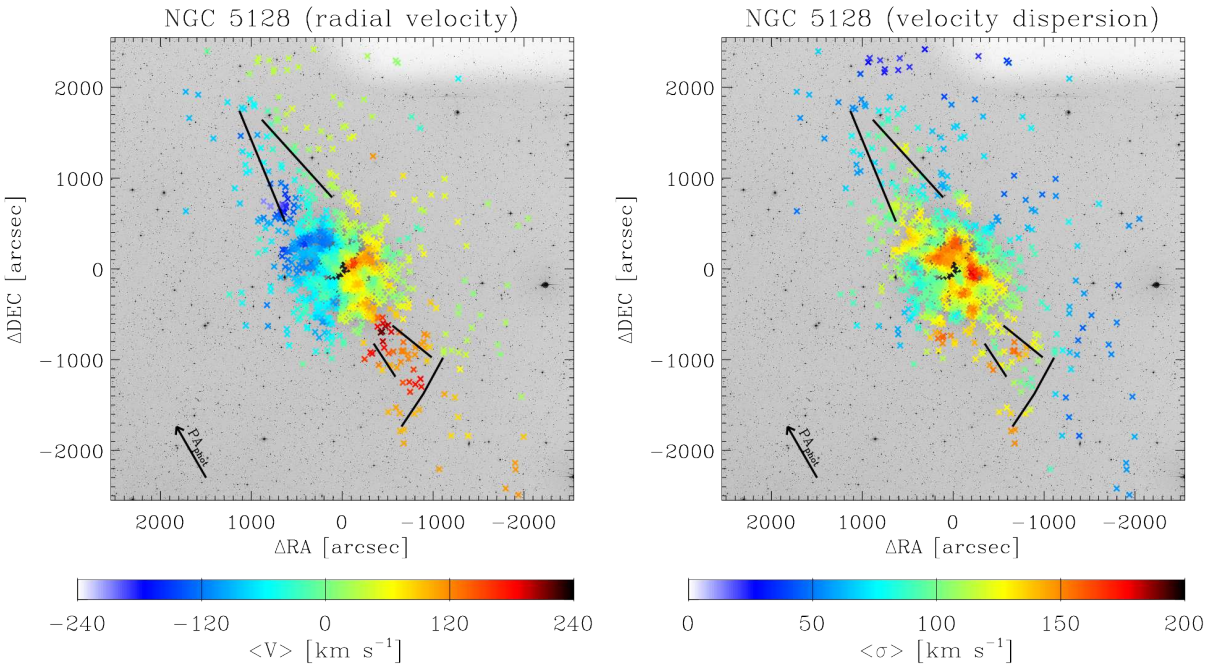

Figure 4.D.2: Smoothed velocity field and velocity dispersion field of NGC 5128 shown on the DSS image; north is up, east is left. Features in the surface brightness distribution spatially consistent with features in the PN kinematics are contoured in black. The arrow at the bottom left shows the direction of the $PA_{\rm phot}$.

also Peng et al. 2004). The deviation from point-symmetry of the kinematics in almost all the radial bins is accompanied by several features in the light. In particular the outermost regions, from 700 arcsec outward, show the most important kinematic features (Coccato et al. 2013), in correspondence to the elongated structure (sketched with black contours in Fig. 4.D.2) in light extending roughly along the radio jets (Haynes et al. 1983).

- **NGC 5866**. NGC 5866 is an SA0 galaxy belonging to a loose group (Sengupta & Balasubramanyam 2006). It has a narrow, clear-cut dark lane, running along the disk at an angle with respect to the photometric major axis. It is a regular, disk-like rotator (Krajnović et al. 2011) with a maximum amplitude of $\sim 150 - 180$ km s^{-1}Foster et al. (2016) at $\sim 2R_{\rm e}$, beyond which the rotation decreases to 110 km s^{-1}at $\sim 3\ R_{\rm e}$. Our velocity map shows that the galaxy keeps rotating at approximately constant speed (~ 85 km s^{-1}) at large radii (up to 9 $R_{\rm e}$), with a progressive twist of the kinematic position angle. The PN velocity dispersion map and velocity dispersion profile have values around 90 km s^{-1}that are constant within the errors from 2 up to 9 $R_{\rm e}$. We refer to Cortesi et al. (in prep.) for a kinematic study of the disk and spheroid components. The photometric position angle is constant from 30"-80", then decreasing by ~ 2 degrees until 160" = 4.5 $R_{\rm e}$ (Michard & Marchal 1993). Beyond 160" the profile becomes more irregular which coincides with a flare or X-like structure on the deep image by Duc et al. (2015) that could be due to tidal debris along a radial orbit

nearly aligned with the disk.

- **NGC 7457** This is a field S0. The velocity maps from Emsellem et al. (2004) and Arnold et al. (2014) show that this galaxy is a regular rotator along the major axis. Our PN velocity map shows that the rotation velocity is growing with radius, reaching 100 km s^{-1}at $\sim 3.5R_e$. No twisting of the kinematic major axis is observed. The velocity dispersion is relatively low, around $\sim$ 60 km s^{-1}at $1R_e$, $\sim$ 40 km s^{-1}at $\sim 3R_e$. There is good agreement between the PN kinematics and the kinemetry from Foster et al. (2016).

4.D.2 Slow rotators

- **NGC 1399**. It is a CD galaxy in the Fornax I cluster. We observe a very low amplitude (30±15 km s^{-1}) rotation inside $1R_e$ along the photometric minor axis, and a slow rotation also in the halo ($R \sim 4R_e$), which almost counter-rotates with respect to the inner regions. The rotation velocity is also very low in the innermost regions as reported by integral light kinematics studies (e.g., Graham et al. 1998; Saglia et al. 2000; Loubser et al. 2008; Scott et al. 2014), which are in good agreement with the PN data. In particular the integral field map from Scott et al. (2014) shows that NGC 1399 does not display important ordered motions in the central regions, while at a radius of $\sim$ 30 arcsec it rotates along the minor axis ($\sim$ 45 km s^{-1}). The velocity dispersion, instead, is relatively high: it rises steeply in the inner 10 arcsec, reaching $\sim$ 370 km s^{-1}at the center (e.g., Saglia et al. 2000), while at large radii (from $\sim 1R_e$) the PN σ flattens at $\lesssim$ 200 km s^{-1}. McNeil et al. (2010) showed that kinematics of the red GCs of NGC 1399 is in excellent agreement with the PNe.

- **NGC 3608**. This is an E2 galaxy in the Leo II group. It is known to have a counter-rotating core (Jedrzejewski & Schechter 1988) in the central $0.27R_e$, aligned with the photometric major axis and rotating at $\sim$ 20 km s^{-1}(Halliday et al. 2001; Emsellem et al. 2004). From $\sim 1R_e$ galaxy starts to rotate at approximately along the photometric major axis (Foster et al. 2016). The PN kinematics shows that the growing trend continues at larger radii, where the amplitude of rotation reaches $\sim$ 65 km s^{-1}. The twist of the PA_{kin} reveals that the system is triaxial. The velocity dispersion decreases from the central value of $\sim$ 220 km s^{-1}to 100 km s^{-1}at $\sim 1R_e$ (Halliday et al. 2001). We find a constant velocity dispersion profile in the halo ($\sim$ 90 km s^{-1}).

- **NGC 3923**. This an E4-5 galaxy in a group of eight galaxies (Brough et al. 2006). We detect a cylindrical velocity field along an intermediate direction between the minor and the major axes, which rotate at $\sim$ 75 km s^{-1}. The velocity dispersion is constant around 235 km s^{-1}. Long-slit kinematics from Carter et al. (1998) inside $\sim 1R_e$ shows that NGC 3923 does not rotate significantly along the photometric major axis for $R \lesssim 0.5R_e$, but it displays a weak rotation ($\sim$ 20 km s^{-1}) along the photometric minor axis. They also found a falling dispersion profile, from the central value of $\sim$ 285 km s^{-1}to $\sim$ 240 km s^{-1}at $0.7R_e$. Norris et al. (2012) studied the kinematics of 79 GC/UCD extended to more than $6R_e$. They do not show appreciable rotation, and their velocity dispersion seem constant with radius.

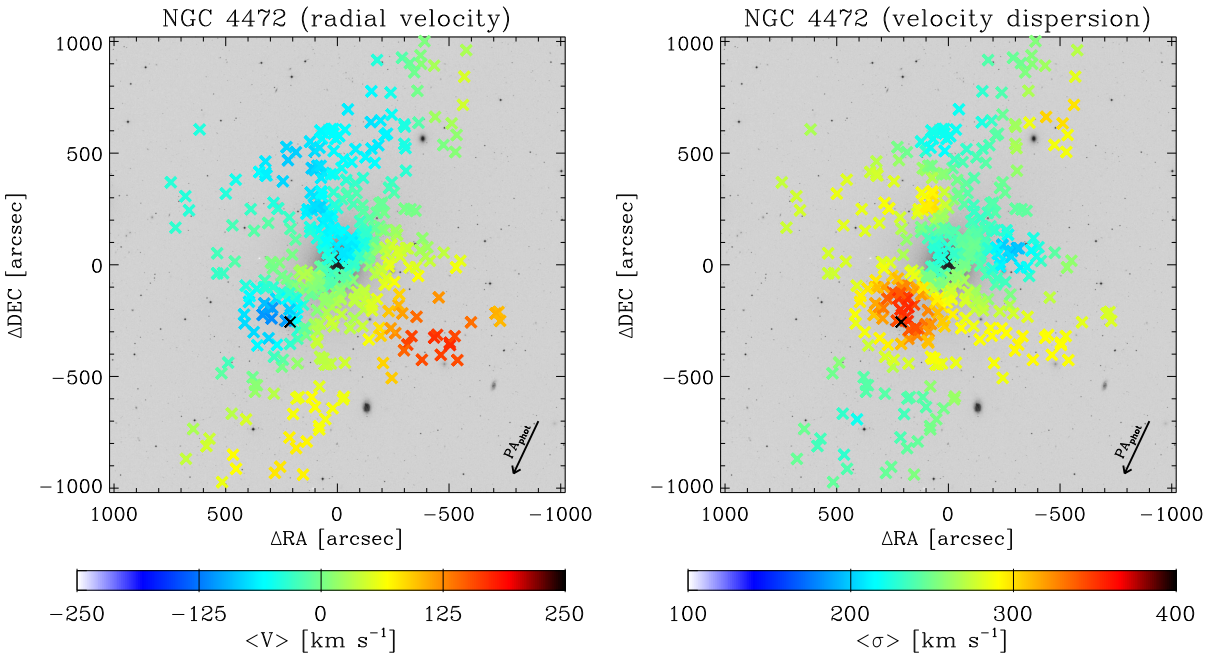

Figure 4.D.3: Smoothed velocity field and velocity dispersion field of NGC 4472 shown on the DSS image; north is up, east is left. The black cross marks the position of the in-falling dwarf UGC 7636. The arrow at the bottom right shows the direction of the $PA_{\rm phot}$.

- **NGC 4365**. It is an E3 galaxy, one of the brightest member of the Virgo cluster. It has a complex kinematic structure with a counter-rotating core (Bender 1988a), aligned with the photometric major axis, and a prolate rotation of $\sim$ 61 km s^{-1}(Davies et al. 2001), which indicates a triaxial potential. Our PN velocity field extends to $6R_{\rm e}$. The inner kinematics ($R \lesssim 2R_{\rm e}$) is compatible with no rotation. We do not detect the rolling about the minor axis that Arnold et al. (2014) report, probably because of the smoothing over the inner velocity gradients. We do measure a significant outer ($R \gtrsim 3R_{\rm e}$) rotation of $\sim$ 50 km s^{-1}along the major axis, counter-rotating with respect to the kinematically decoupled core. The velocity dispersion map has almost constant values, around $\sim$ 150 km s^{-1}, with slightly lower values in the region along the major axis ($\sim$ 140 km s^{-1}). The velocity dispersion measured by Davies et al. (2001) shows a inner value of $>$ 250 km s^{-1}which decreases to $\sim$ 185 km s^{-1}at $0.5R_{\rm e}$. Arnold et al. (2014) measure a $\sigma \sim$ 150 km s^{-1}at $2R_{\rm e}$, consistent with the values found with PNe. Blom et al. (2012), studying the GC kinematics, found that the intermediate metallicity subpopulation (green) rotates along the photometric minor axis, as the stellar population at intermediate radii, while the red GCs rotate only at large radii along the photometric major axis in the opposite direction of the core of the galaxy, in agreement with the PN kinematics at large radii.

- **NGC 4374**. Also known as M84, it is a bright E1 galaxy in the Virgo cluster. The galaxy does not show significant rotation in the innermost $\sim$ $0.4R_{\rm e}$, as reported by Emsellem

et al. (2004) and Foster et al. (2016), while the velocity dispersion steeply decreases from 310 km s^{-1}at the center to $\sim$ 200 km s^{-1}at $\sim 1R_e$. The PN velocity field shows evidence for rotation only at large radii ($R \gtrsim 2R_e$), with constant amplitude $\sim$ 60 km $s^{-1}$and along a direction compatible with the minor axis. The velocity dispersion is rather constant around $\sim$ 220 km s^{-1}up to $6R_e$. Our kinematics is in agreement with that from the SLUGGS velocity maps (Arnold et al. 2014; Foster et al. 2016), but their data extend only to $\sim 2R_e$. The long slit kinematics of Coccato et al. (2009) reaches almost $3R_e$ and agrees in showing no signs of rotation along the major axis, the onset of rotation along the minor, and constant velocity dispersion in the outer regions around $\sim$ 230 km s^{-1}.

- **NGC 4472**. NGC 4472 (M 49) is an E2 galaxy, the brightest object in the Virgo cluster. It is surrounded by a complex system of diffuse shells and other features in light which are evidences of its recent and still ongoing accretion activity (see Janowiecki et al. 2010; Arrigoni Battaia et al. 2012; Hartke et al. 2018). It is classified as a non regular rotator by Krajnović et al. (2011), who also found evidence for a counter-rotating core. From $R \sim 0.2R_e$ the galaxy rotates at $\sim$ 60 km s^{-1}(Cappellari et al. 2011; Veale et al. 2017b). Beyond $\sim 3R_e$ the PN data show a complicated and out of equilibrium kinematics. The halo rotates along a direction compatible with the galaxy minor axis. This motion is neither point- nor axi-symmetric, and is dominated by the kinematics of the in-falling satellite, the dwarf UGC 7636. A visual inspection of the smoothed velocity field reveals that the main body of the galaxy would show major axis rotation once the PNe belonging to the satellite are excluded (see Hartke et al. 2018, for a detailed study). While the velocity dispersion profile is flat over $4R_e$ at $\sim$ 250 km s^{-1}, we notice a high dispersion feature with $\sigma \sim$ 350 km s^{-1}in a position corresponding to the coordinates of UGC 7636.

- **NGC 4552**. NGC 4552 (M 89) is an E0-1 galaxy in Virgo. It known to possess a kinematically distinct core, with the innermost region rotating at $\sim$ 30 km s^{-1}, and the region outside $0.3R_e$ having very weak rotation (Simien & Prugniel 1997b; Emsellem et al. 2004). Our PN smoothed velocity field shows that the galaxy start rotating beyond $3R_e$. The smoothed velocity field reveal that the rotation is about two perpendicular directions. This is reflected in the twist of the kinematic position angle with radius. The velocity dispersion map from the data is consistent with the one from the integrated light (Emsellem et al. 2004), and it shows constant values with radius, around 180 km s^{-1}.

- **NGC 4636**. This is an E0-1 galaxy in the Virgo cluster. The velocity map from Krajnović et al. (2011) does not show significant rotation in the innermost region ($R < 0.25R_e$). The velocity dispersion, instead, has a central value of $\sim$ 240 km $s^{-1}$and it decreases to 190 km s^{-1}at $0.25R_e$. The long slit kinematics from Pu & Han (2011) show that the galaxy starts rotating along the minor axis at $\sim$ 40 arcsec (0.2 R_e), and along the major axis at $\sim$ 85 arcsec ($\sim 1R_e$). The σ profile is gently decreasing along the minor axis, reaching $\sim$ 100 km s^{-1}at 0.5 R_e, while it is rather flat along the major, around 190 km s^{-1}, then it decreases to $\sim$ 150 km $s^{-1}$where the rotation starts. We detect a weak rotation (40 ± 15 km s^{-1}) along a direction compatible with the minor axis. In addition, in the smoothed velocity map there is evidence for a rotation of comparable magnitude at larger radii ($R \sim 1R_e$)

around the major axis, in very good agreement with Pu & Han (2011). The PN velocity dispersion profile decreases abruptly from $\sim$ 180 km s^{-1}at $R < 2R_e$ to $\sim$ 110 km s^{-1}at $3R_e$. Schuberth et al. (2012) find a strong rotation signature for the blue GCs ($V \sim 88$ km s^{-1}along the major axis, but in opposite direction with respect to the outermost PNe). The red GCs have a weaker rotation ($V \sim 30$ km s^{-1}) along an axis that changes with being aligned with the minor axis to the photometric major axis, in agreement with the PN kinematics. For radii beyond $1.5R_e$ the axis of rotation remains constant along the direction of the major axis. The dispersion profile of the blue GC declines with radius, while the red GCs show values of $\sigma \sim 135$ km s^{-1}.

- **NGC 5846**. This is an E0 galaxy, the brightest member in a group of ten. Emsellem et al. (2004) detect a low rotation of $\lesssim 30$ km s^{-1}and a high central dispersion of 255 km s^{-1}. PN smoothed velocity field is consistent with low amplitude rotation. We find constant values for the velocity dispersion around 180 km s^{-1}. The SLUGGS kinematic maps Arnold et al. (2014); Foster et al. (2016) are consistent with PN data. Pota et al. (2013) showed that neither the GC subpopulations show significant rotation. The velocity dispersion of the red GCs has a flat profile, around values comparable with those found for the PNe. The blue GCs have systematically higher $\sigma \sim 260$ km s^{-1}.

4.E Velocity and Velocity Dispersion Fields

Smoothed velocity and velocity dispersion fields. The maps are interpolated on a regular grid of coordinates, as described in Sect. 4.6.1. The fields are rotated such that the photometric major axis is horizontal ($PA_{\rm phot}$ values are listed in Table 4.1); the orientation is specified by the direction of the arrows indicating north and east. The X and Y axes units are arc seconds. The elliptical contours displayed on the velocity fields are ellipses of constant ellipticity ϵ as given in Table 4.1, and of major axes radii equal to even multiples of R_e (Table 4.1).

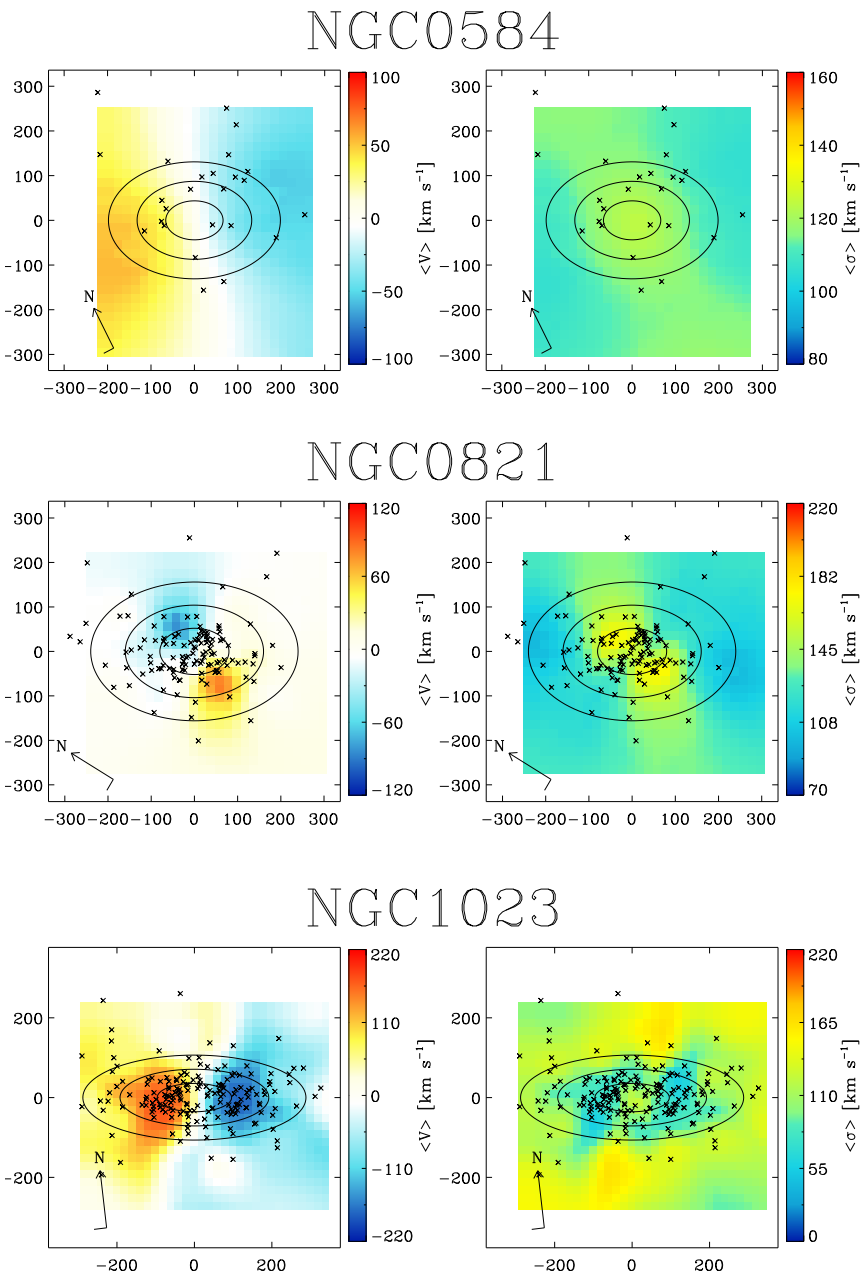

Figure 4.E.1: Smoothed velocity and velocity dispersion fields, interpolated on a grid of coordinates as described in the text.

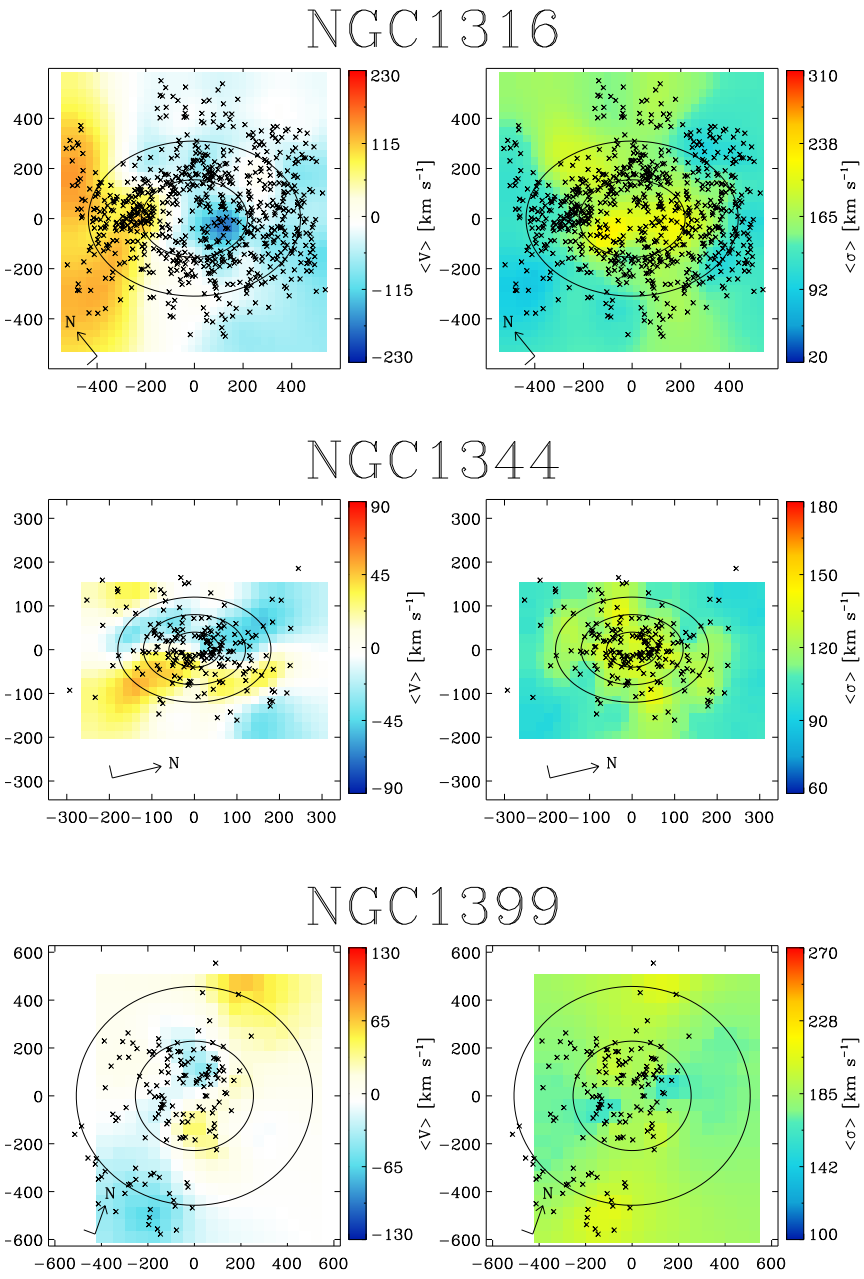

Figure 4.E.1: Continued.

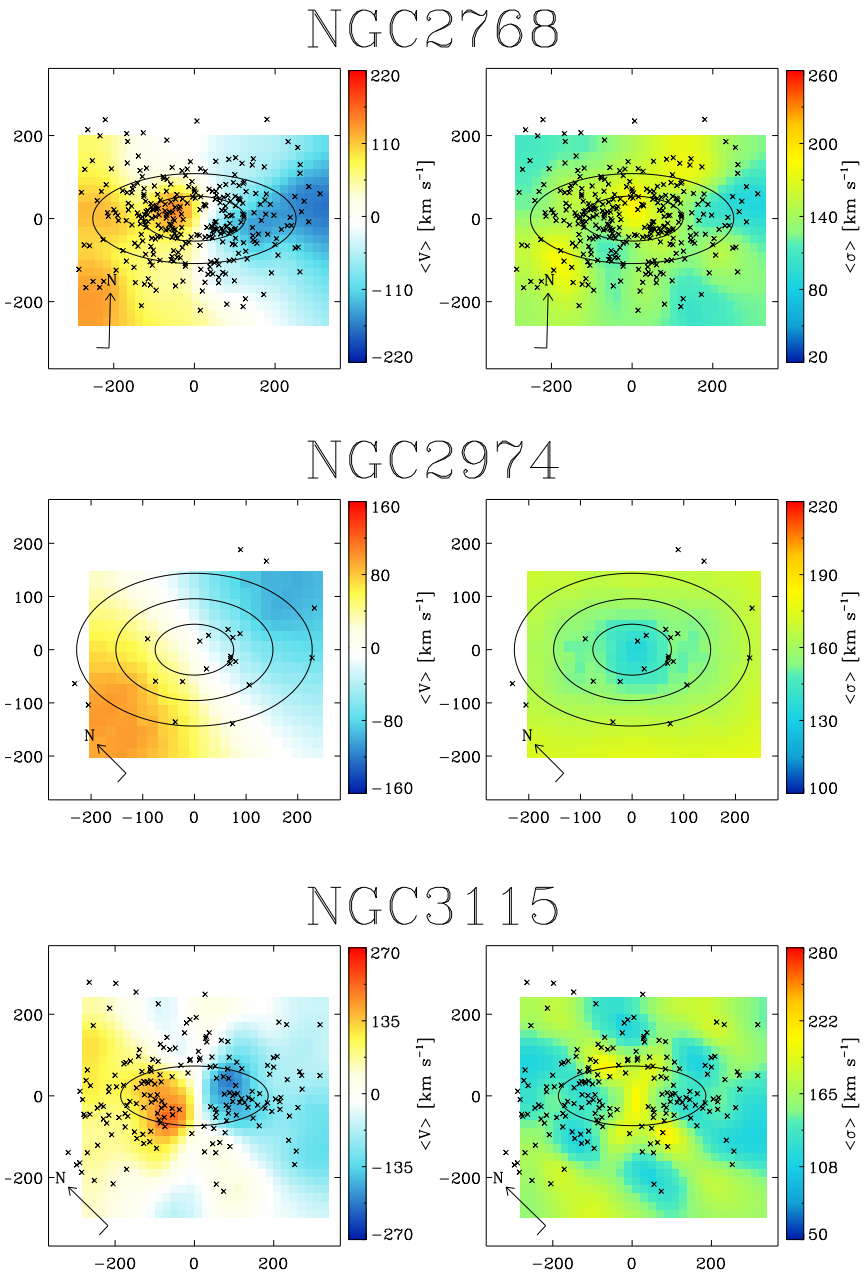

Figure 4.E.1: Continued.

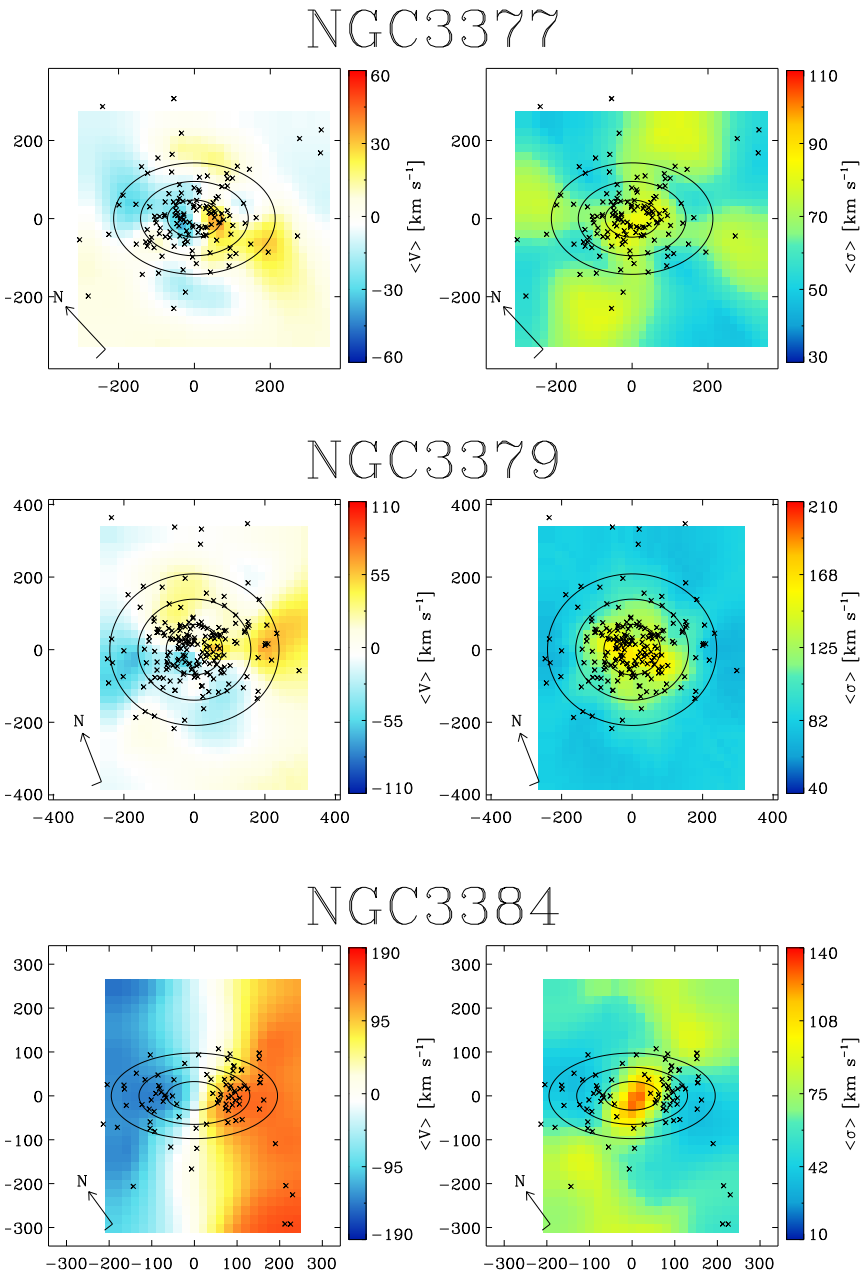

Figure 4.E.1: Continued.

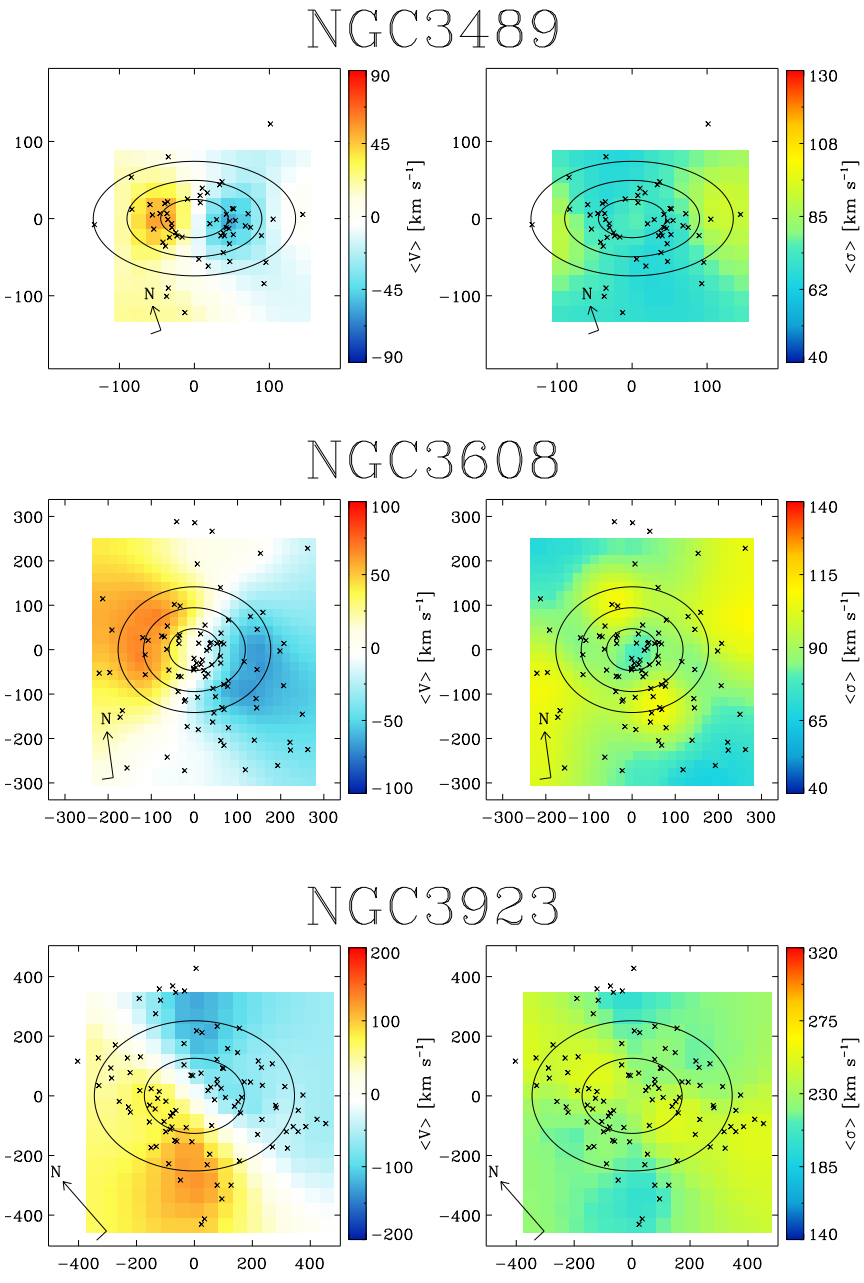

Figure 4.E.1: Continued.

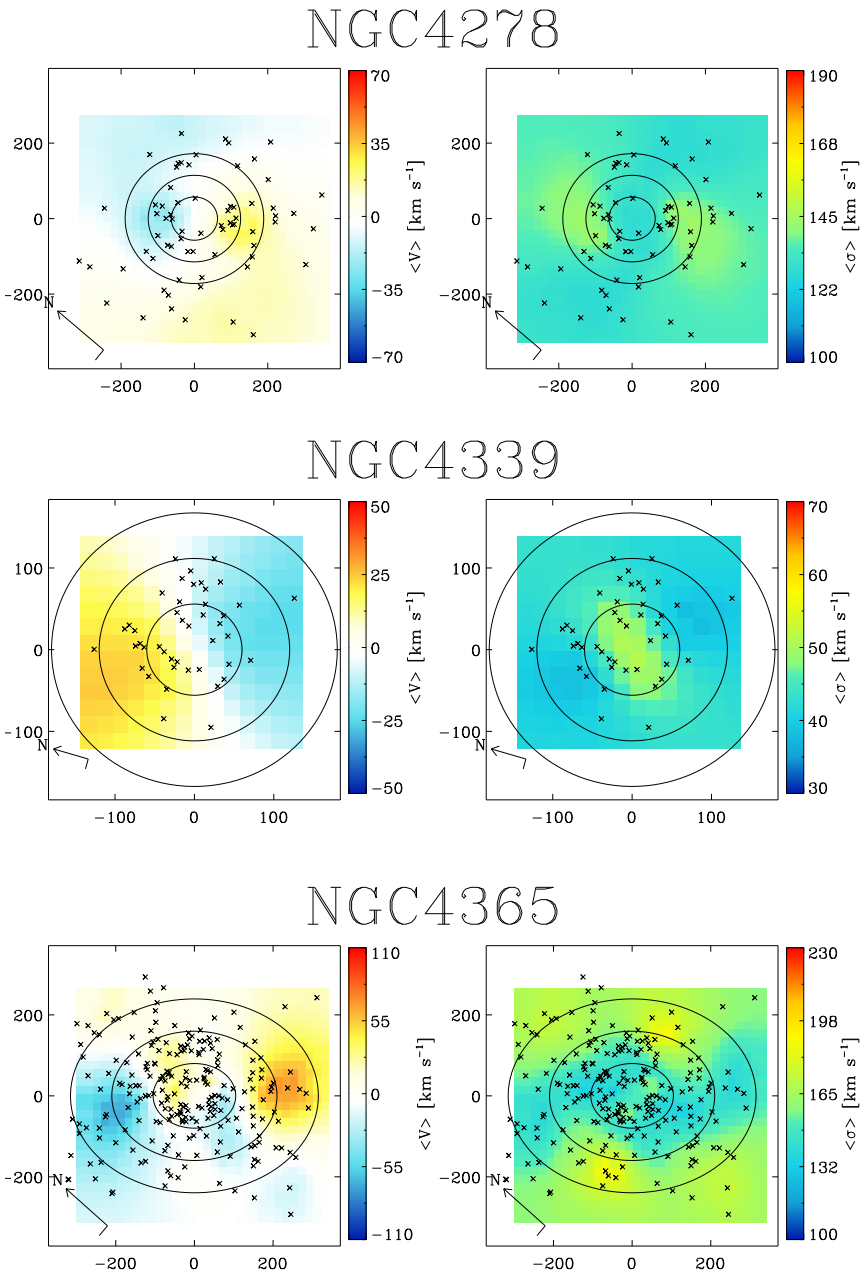

Figure 4.E.1: Continued.

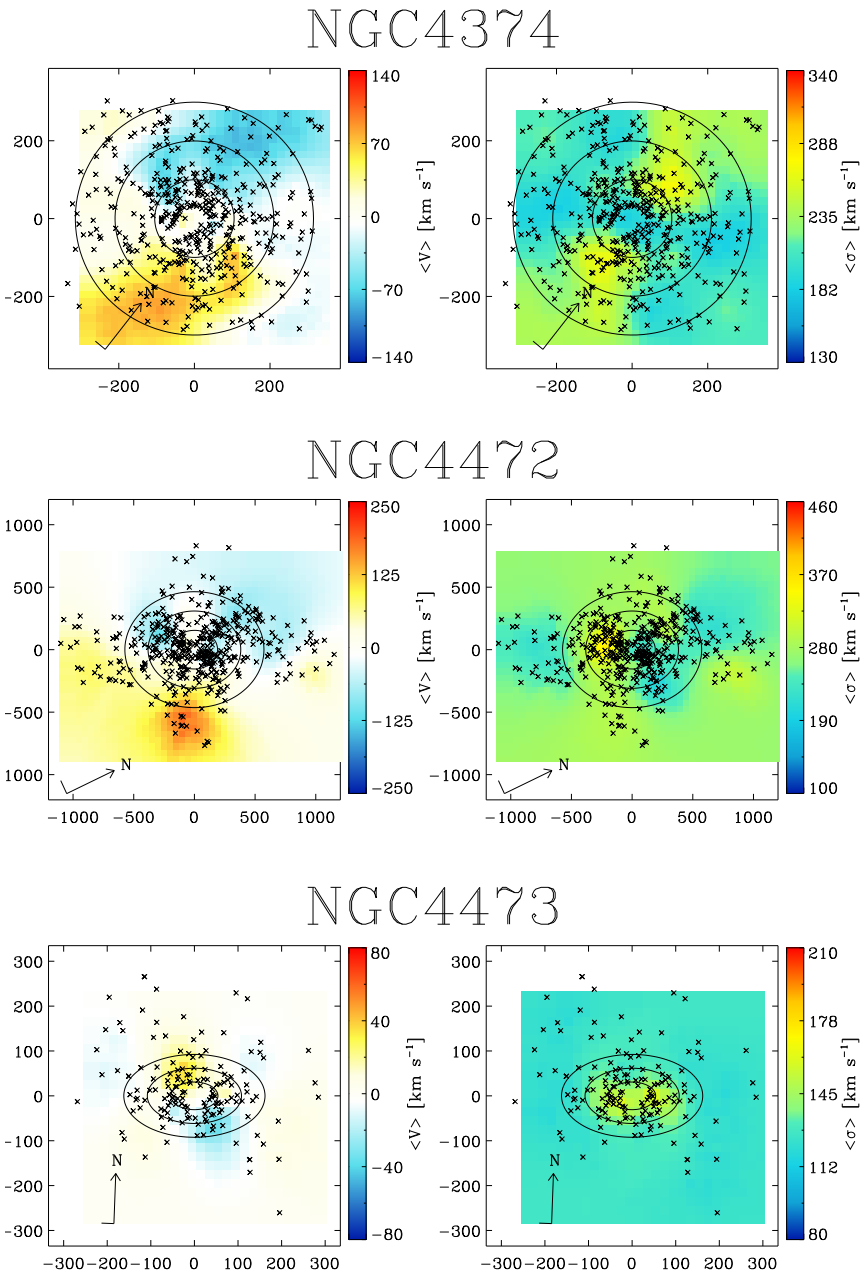

Figure 4.E.1: Continued.

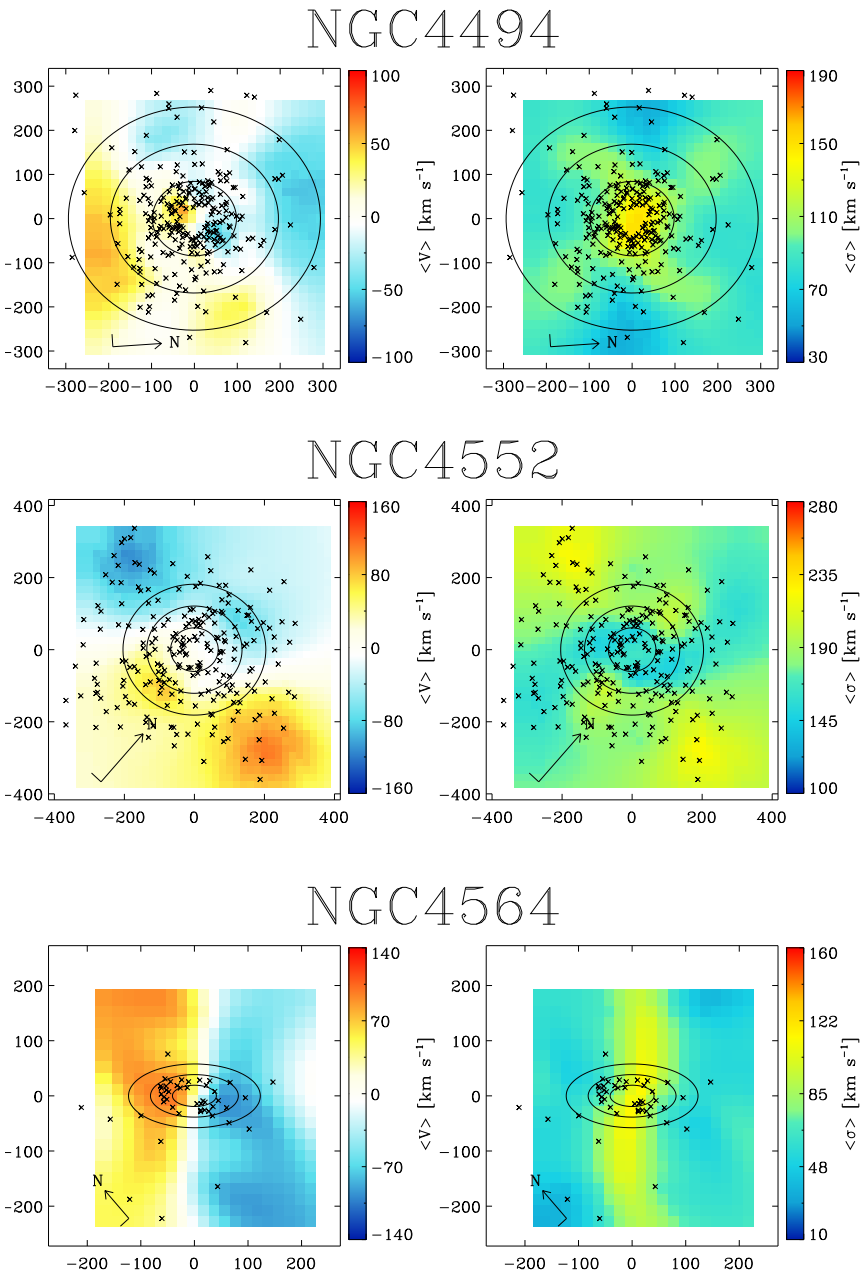

Figure 4.E.1: Continued.

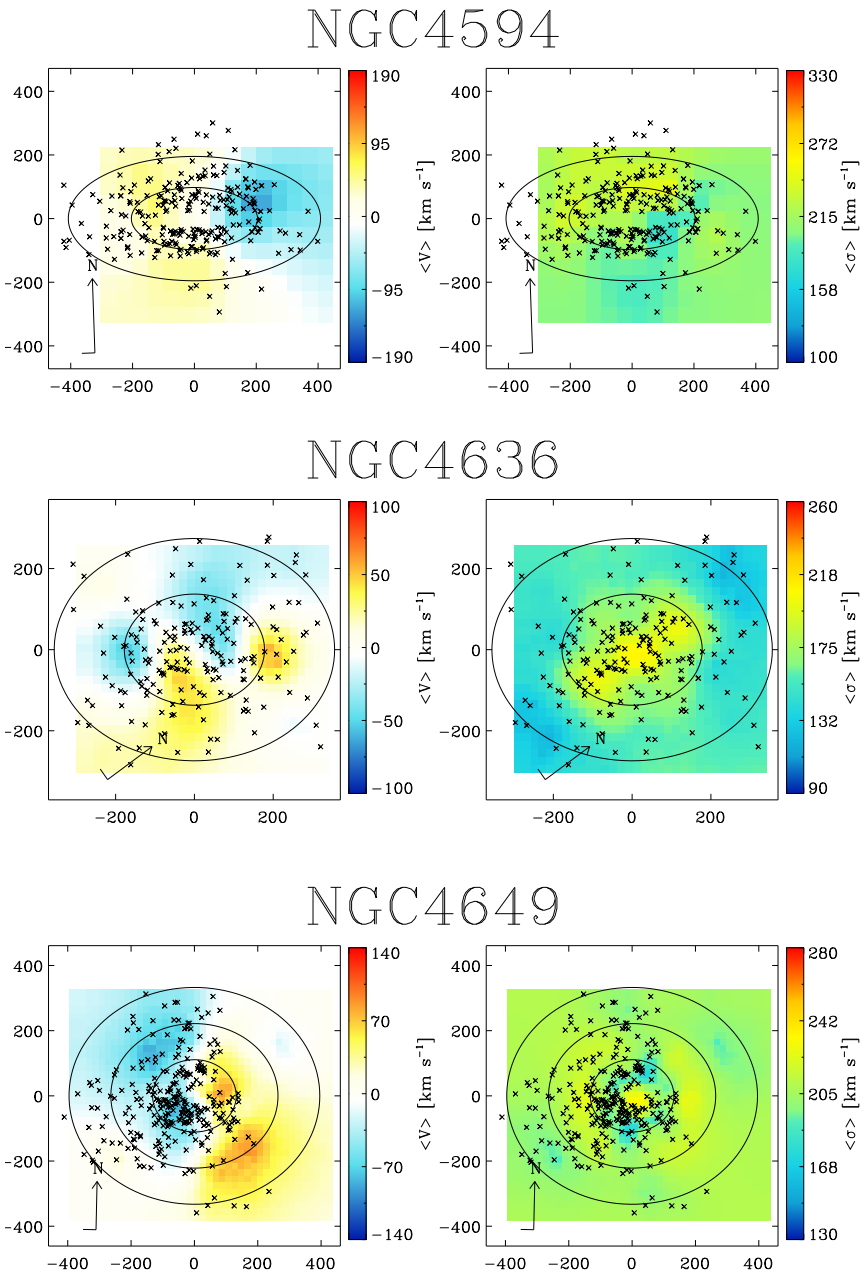

Figure 4.E.1: Continued.

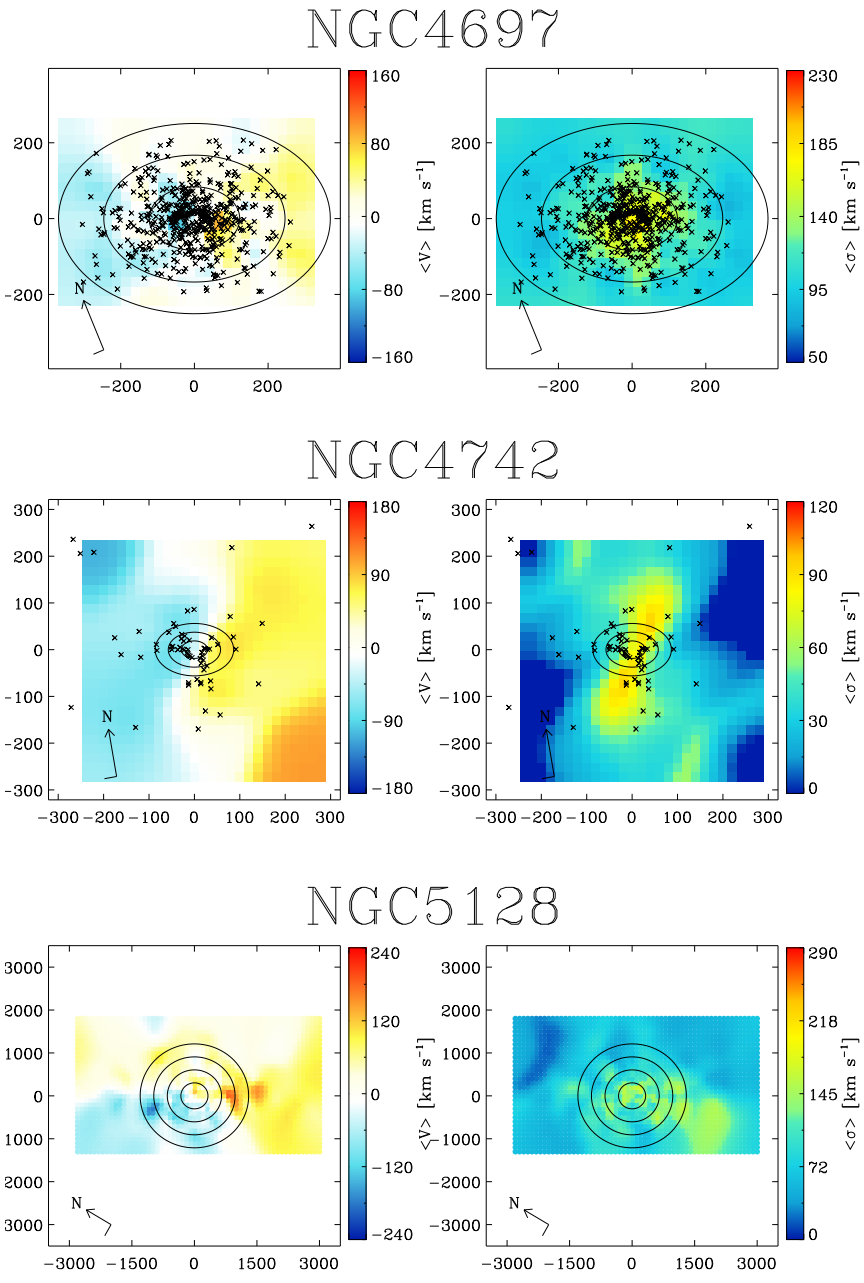

Figure 4.E.1: Continued.

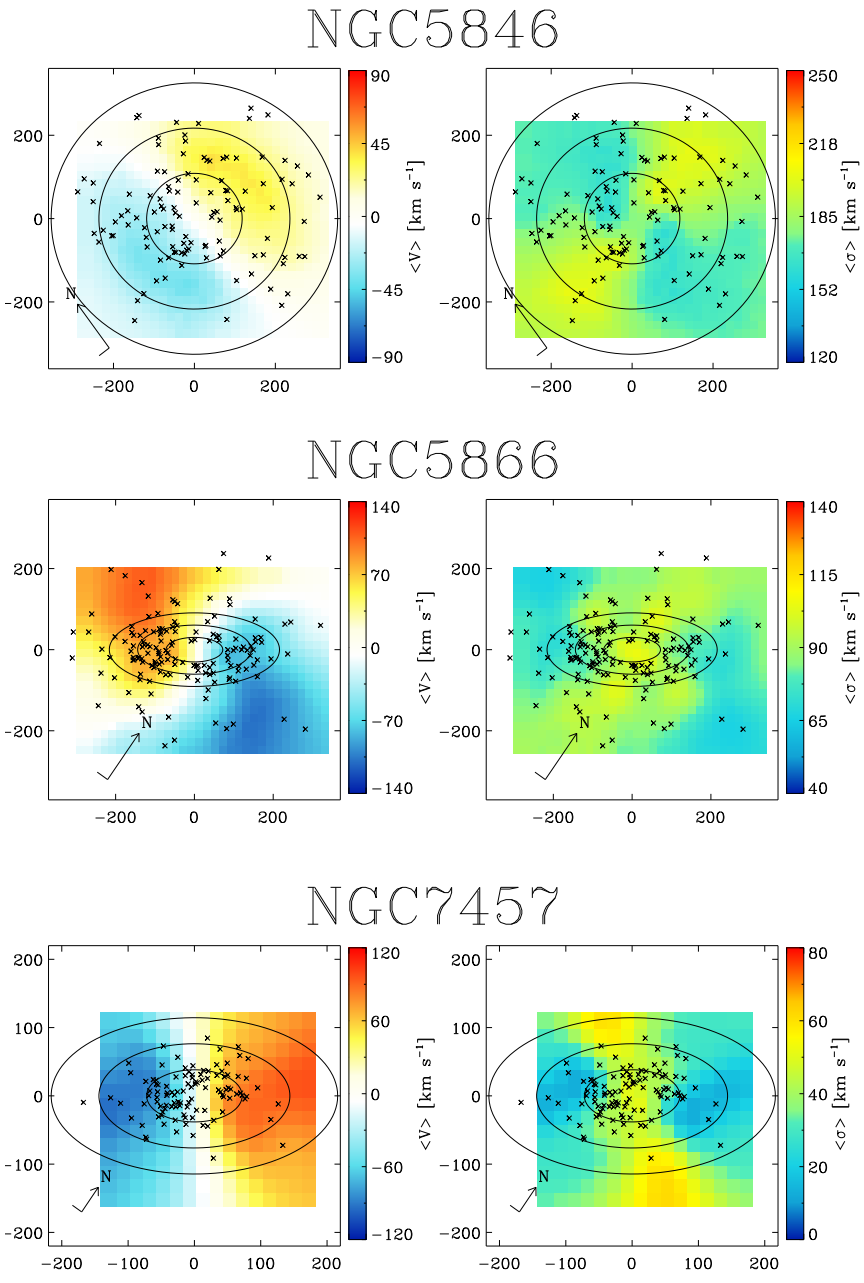

Figure 4.E.1: Continued.

Chapter 5

The stellar halos of ETGs in the IllustrisTNG simulations: The photometric and kinematic diversity of galaxies at large radii

This chapter is published as the paper Pulsoni et al. (2020).

5.1 Introduction

The family of early type galaxies (ETGs) encompasses galaxies that have typically ceased their star formation at early times, with red colors and small amounts of cold gas and dust today, and that mainly consist of elliptical and lenticular galaxies (Roberts & Haynes 1994; Kauffmann et al. 2003; Blanton & Moustakas 2009). Ellipticals are essentially divided into two classes with distinct physical properties (e.g., Kormendy et al. 2009, and references therein): those with low to intermediate masses and coreless luminosity profiles that rotate rapidly are relatively isotropic and oblate-spheroidal, and have high ellipticities and disky-distorted isophotes; and those which are frequently among the most massive galaxies, with cored profiles, mostly non-rotating, anisotropic and triaxial, relatively rounder than than coreless systems, and with boxy-distorted isophotes. Thus, the dichotomy in the light distributions of the ellipticals roughly corresponds to different kinematic properties, with coreless disky objects being rotationally supported, and cored boxy galaxies having low rotation (Bender 1987). With the advent of integral field spectroscopy (IFS), the classification of elliptical galaxies has shifted to a kinematics-based division between fast rotators (FR) and slow rotators (SR) (Emsellem et al. 2011; Graham et al. 2018). In particular, low-mass, coreless, FR ellipticals share similar properties with lenticular galaxies, which are are also included in the FR family, while massive cored ellipticals are typically SRs.

The formation of massive ETGs is believed to have occurred in two phases (e.g. Oser et al. 2010). In an initial assembly stage, gas collapses in dark matter halos and forms stars in a

brief intense burst which is quickly quenched (e.g., Thomas et al. 2005a; Conroy et al. 2014; Peng et al. 2010). Present-day simulations agree in that the progenitors of FR and SR at these high redshifts are indistinguishable (Penoyre et al. 2017; Lagos et al. 2017; Schulze et al. 2018, with Illustris, Eagle, and Magneticum, respectively). At $z \lesssim 1$ the accretion-dominated phase overtakes, whereby ETGs grow efficiently in size through a series of merger episodes, mainly dry minor mergers (Naab et al. 2009; Johansson et al. 2012), which enrich the galaxies with accreted (ex-situ) stars. The ΛCDM cosmology predicts that structures form hierarchically, in which more massive systems form through the accretion of less massive objects. This means that more massive galaxies can have accreted fractions larger than 80%, while lower mass galaxies are mostly made of in-situ stars, and the accreted components are mainly deposited in the outskirts (Rodriguez-Gomez et al. 2016; Pillepich et al. 2018a). The slow and fast rotator (i.e., the core and coreless) classes result from different formation pathways characterized by different numbers of mergers, merger mass ratio, timing, and gas fractions (Naab et al. 2014; Penoyre et al. 2017, see also the discussion in Kormendy et al. 2009), although the details still depend on the star formation and AGN feedback models adopted by the numerical models (Naab & Ostriker 2017). In general, the result of a formation history dominated by gas dissipation is most likely a coreless FR, while dry major mergers often result in SRs.

The two-phase formation scenario is supported both by observations of compact red nuggets at $z \sim 2$, a factor of 2-4 smaller than present day ellipticals (Daddi et al. 2005; Trujillo et al. 2007; van Dokkum et al. 2008), and by evidence for a subsequent rapid size growth with little or no star formation (e.g. van Dokkum et al. 2010; Damjanov et al. 2011; van der Wel et al. 2014; Buitrago et al. 2017). The merger-driven size growth is supported by the observed rate of mergers from pair counts and identified interacting galaxies (Hopkins et al. 2008; Robaina et al. 2010), as well as the observed tidal debris from recent accretion events in the halos of many galaxies (e.g. Malin & Carter 1983; Janowiecki et al. 2010; Longobardi et al. 2015b; Iodice et al. 2017; Mancillas et al. 2019).

A consequence of the two-phase formation is that ETGs are layered structures in which the central regions are the remnants of the stars formed in-situ, while the external stellar halos are principally made of accreted material (Bullock & Johnston 2005; Cooper et al. 2010), even though the details strongly depend on stellar mass (Pillepich et al. 2018a). Because of the different nature of the stellar halos, galaxies are expected to show significant variation of physical properties from central regions to large radii, such as shapes of the light profiles (Huang et al. 2013a; D'Souza et al. 2014; Spavone et al. 2017), stellar populations (Pastorello et al. 2014; Zibetti et al. 2020), and kinematics (Coccato et al. 2009; Romanowsky & Fall 2012; Arnold et al. 2014; Foster et al. 2016).

Kinematic measurements in the outer halos of ETGs require alternative kinematic tracers to overcome the limitations from the faint surface brightness in these regions, such as planetary nebulae (PNe) (e.g., the ePN.S survey, Arnaboldi et al. 2017, see Sect. 5.3), or globular clusters (e.g., the SLUGGS survey, Brodie et al. 2014). Recently, Pulsoni et al. (2018) found evidence from the ePN.S survey for a kinematic transition between the central regions and the outskirts of ETGs. Despite the FR/SR dichotomy of their central regions, these ETG halos display a variety of kinematic behaviors. A considerable fraction of the ePN.S FRs show reduced rotational support at large radii, which has been interpreted as the fading of a rotating, disk-like component

into a more dispersion dominated spheroid; almost half of the FR sample shows kinematic twists or misalignments at large radii, indicating a variation of their intrinsic shapes, from oblate at the center to triaxial in the halo. SRs, instead, have increased rotational support at large radii. While a smaller group of FRs stands out for having particularly high V/σ ratio in the halo, most of the ePN.S FRs and SRs have similar V/σ ratio in the halo regions. These results suggest the idea that at large radii the dynamical structure of these galaxies could be much more similar than in their high-density centers: if halos are mainly formed from accreted material, their common origin would explain their similarities. The radii of the observed kinematic transitions to the halo and their dependence on the galaxies' stellar mass seem to support such an interpretation.

To date, only a few studies of the kinematic properties of stellar halos in simulations are available in the literature. Wu et al. (2014) analysed the kinematics of 42 cosmological zoom simulations of galaxies and found a variety of V/σ profile shapes (rising, flat, or with a maximum), in agreement with observations. However, these early simulations did not reproduce the whole spectrum of properties of observed FRs, especially the fast rotating and extended disks (Emsellem et al. 2011; Pulsoni et al. 2018). Recently, Schulze et al. (2020) using the Magneticum Pathfinder simulations showed that these simulations reproduce the observed kinematic properties of galaxies more closely, and that extended kinematics is a valuable tool for gaining insight into galaxy accretion histories. They also found that the kinematic transition radius is a good estimator of radius of the transition between in-situ and ex-situ dominated regions for a subset of galaxies with decreasing V/σ profiles, especially those that did not undergo major mergers in their evolution.

The goal of this paper is to better understand the structural changes between the centers and stellar halos of ETGs with a large and well-resolved sample of simulated galaxies. We study the stellar halo structure, that is, the rotational support and intrinsic shapes of the simulated galaxies, we compare the results with observations, and we investigate how the radial variations in rotational support relate to changes in the halo shapes. We use the IllustrisTNG simulations (Springel et al. 2018; Pillepich et al. 2018a; Naiman et al. 2018; Marinacci et al. 2018; Nelson et al. 2018, 2019b), a suite of magnetohydrodynamical simulations that models the formation and evolution of galaxies within the ΛCDM paradigm. It builds and improves upon the Illustris simulation (Genel et al. 2014; Vogelsberger et al. 2014), using a refined galaxy formation model. For this work we consider two cosmological volumes with side lengths $\sim$ 100 Mpc and $\sim$ 50 Mpc, which are referred to as TNG100 and TNG50. TNG50 is the highest resolution realization of the IllustrisTNG project (Pillepich et al. 2019; Nelson et al. 2019a) with particle resolution more than 15 times better than TNG100.

The paper is organized as follows. For the comparison of the TNG galaxies properties with observations, we first summarize in Section 5.3 how different ETG surveys select their samples and how physical quantities are measured. Section 5.4 then describes and illustrates our methods to derive photometric and kinematic measurements for the simulated galaxies. After selecting the sample of ETGs from the TNG100 and TNG50 simulations (Section 5.5), we proceed to show the photometric results in Section 5.6 and the kinematic results in Section 5.7. Section 5.8 relates the variation in the kinematic properties from central regions to halos to the parallel changes in the intrinsic structure of galaxies. In a companion paper we will explore the dependence of these properties on the accretion history of galaxies. Finally, Section 5.9 summarizes our conclusions.

Table 5.1: Table of physical and numerical parameters for TNG50 and TNG100. These are the volume of the box, the initial number of particles (gas cells and dark matter particles), the target baryon mass, the dark matter particle mass, and the $z = 0$ Plummer equivalent gravitational softening length for the collisionless component.

Run name	Volume [Mpc^3]	N_{part}	$m_{baryons}$ [$10^5 M_\odot$]	m_{DM} [$10^5 M_\odot$]	r_{soft} [pc]
TNG50	51.7^3	2×2160^3	0.85	4.5	288
TNG100	110.7^3	2×1820^3	14	75	738

5.2 The IllustrisTNG simulations

The IllustrisTNG simulations are a new generation of cosmological magnetohydrodynamical simulations using the moving mesh code AREPO (Springel 2010). Compared to the previous Illustris simulations, they include improvements in the models for chemical enrichment, stellar and black hole feedback, and introduce new physics such as the growth and amplification of seed magnetic fields.

The baryonic physics model contains a new implementation of black hole feedback (Weinberger et al. 2017), as well as updates to the galactic wind feedback, stellar evolution and gas chemical enrichment models (Pillepich et al. 2018b). These modifications, in particular those for the two feedback mechanisms, were required to alleviate some of the tensions between Illustris and observations, such as the large galaxy stellar masses below the knee of the galaxy stellar mass function and the gas fractions within group-mass halos. They in turn also improve on the too large stellar sizes of galaxies and the lack of a strong galaxy color bimodality at intermediate and high galaxy masses in Illustris (Nelson et al. 2015).

The IllustrisTNG fiducial model was chosen by assessing the outcome of many different models against the original Illustris by using additional observables, specifically the halo gas mass fraction and the galaxy half-mass radii, with respect to those used to calibrate the Illustris model against observational findings, such as, the star formation rate density as a function of z, the galaxy stellar mass function at $z = 0$, the $z = 0$ black hole mass versus halo mass relation, and the $z = 0$ stellar-to-halo mass relation.

The new AGN feedback model is responsible for the quenching of galaxies in massive halos and for the production of red and passive galaxies at late times, alleviating the discrepancies with observational data at the massive end of the halo mass function (Weinberger et al. 2017; Nelson et al. 2018; Donnari et al. 2019). The faster and more effective winds in TNG reduce the star formation at all masses and all times, resulting in a suppressed $z = 0$ galaxy stellar mass function for $M_* \lesssim 10^{10} M_\odot$, and smaller galaxy sizes (Pillepich et al. 2018b). Overall the TNG model has been demonstrated to agree satisfactorily with many observational constraints (e.g., Genel et al. 2018; Nelson et al. 2018) and to return a reasonable mix of morphological galaxy types (Rodriguez-Gomez et al. 2019).

In this study we consider two simulation runs, TNG100 and TNG50, which are the two highest resolution realizations of the IllustrisTNG intermediate and small cosmological volumes.

TNG100 has a volume and resolution comparable with Illustris, while TNG50 reaches resolutions typical of zoom-in simulations. Table 5.1 summarizes and compares the characteristic parameters of the two simulations.

The TNG model is calibrated at the resolution of TNG100 and all the TNG runs adopt identical galaxy formation models with parameters that are independent of particle mass and spatial resolution ("strong resolution convergence", according to Schaye et al. 2015). This imposition results in some of the properties of the simulated galaxies being resolution dependent. As discussed by Pillepich et al. (2018b), this can be primarily explained by the fact that better resolution allows the sampling of higher gas densities, hence more gas mass is eligible for star formation and the star formation rate accelerates. This means that, for example, at progressively better resolution, galaxies tend to have increased stellar masses at fixed halo mass and smaller sizes at fixed stellar mass (see also Pillepich et al. 2019 for a quantification of these effects).

5.3 Observed parameters of ETGs

In this paper we compare the kinematic results for the central regions of the simulated TNG galaxies with IFS measurements from the surveys Atlas3D (Cappellari et al. 2011), MANGA (Bundy et al. 2015), SAMI (Croom et al. 2012), and MASSIVE (Ma et al. 2014).

Kinematics measurement at large radii are notably difficult to obtain for ETGs, and therefore discrete kinematic tracers such as planetary nebulae (PNe) and globular clusters (GCs) are typically used to overcome the limitations of absorption line spectroscopy, which is restricted to the central 1-2 R_e. PNe are established probes of the stellar kinematics in ETG halos (Hui et al. 1995; Arnaboldi et al. 1996; Méndez et al. 2001; Coccato et al. 2009; Cortesi et al. 2013a), out to very large radii (Longobardi et al. 2015a; Hartke et al. 2018). Since they are drawn from the main stellar population, their kinematics traces the bulk of the host-galaxy stars, and are directly comparable to integrated light measurements. The relation between GCs and the underlying galaxy stellar population is less straightforward (Forbes & Remus 2018). In general GCs do not necessarily follow the surface brightness distribution and kinematics of the stars (e.g., Brodie & Strader 2006; Coccato et al. 2013; Veljanoski et al. 2014), although there is growing evidence for red, metal-rich GCs to be tracers of the host galaxy properties (Fahrion et al. 2020; Dolfi et al. 2020). Therefore we here compare the kinematics of the simulated galaxies and their stellar halos at large radii with PN kinematic results from the ePN.S early-type galaxy survey (Arnaboldi et al. 2017, Arnaboldi et. al., in prep.).

Below we describe the sample properties for the different surveys and we give details and sources of the measured quantities used though out this paper.

Sample properties - The Atlas3D survey selected ETGs from a volume-limited sampe of galaxies, with distance within 42 Mpc, and sky declination δ such that $|\delta - 29°| < 35°$), brighter than $M_K < -21.5$ mag. From this parent sample ETGs were morphologically selected as all the galaxies without visible spiral structure. This morphological selection is broadly similar to a selection of the red sequence (Cappellari et al. 2011). The Atlas3D ETG sample contains 68 Es and 192 S0s. The SAMI survey (Croom et al. 2012) selected a volume and magnitude limited sample of galaxies in the redshift range $0.004 < z < 0.095$, covering a broad range in galaxy

stellar mass ($M_* = 10^8 - 10^{12} M_\odot$) and environment (field, group, and clusters). This sample is not morphologically selected, but we use the data from van de Sande et al. (2017) where the quality cuts and the imposed threshold on the velocity dispersion $\sigma > 70$ km/s bias the sample towards the ETGs (82%). The galaxies of the MANGA survey (Bundy et al. 2015) are selected from the NASA-Sloan Atlas[1] (NSA) catalog (which is based on the Sloan Digital Sky Survey (SDSS) Data Release 8, Aihara et al. 2011) at low redshift ($0.01 < z < 0.15$), to follow a flat distribution in stellar mass in the range $M_* = 10^9 - 10^{12}$; in this paper we will compare only with MANGA's galaxies classified as ellipticals or lenticulars as in Graham et al. (2018). The MASSIVE survey (Ma et al. 2014) targets all the most massive ETGs ($M_* \gtrsim 10^{11.5} M_\odot$) within a distance of 108 Mpc. Finally, the ePN.S sample of ETGs is magnitude limited $M_K \lesssim -23$, and includes objects with different structural parameters. This ensures the sample to be a representative group of nearby ETGs. The ePN.S kinematic results (Pulsoni et al. 2018) combine PN kinematics in the halos with literature absorption line data for the central regions.

Colors - The MANGA galaxies, and most of the Atlas3D and MASSIVE objects, have measured $g - r$ colors in the NSA catalog. For the SAMI galaxies van de Sande et al. (2017) report $g - i$ colors, which we convert to $g - r$ using the transformation equation derived in App. 5.A. For all of the ePN.S sample, and some of the Atlas3D and MASSIVE galaxies that are not in the NSA catalog, we use $B - V$ colors corrected for galactic extinction from the Hyperleda[2] catalog (Makarov et al. 2014), and convert to $g - r$ colors using the relations in App. 5.A.

Sizes - For the Atlas3D sample we use the effective radii (R_e) values in Table 3 of (Cappellari et al. 2011). Those for the MASSIVE galaxies are from Ma et al. (2014, Table 3), where we adopt the NSA measurements, where available, or the 2MASS values corrected using their Equation 4. The data for MANGA are from Graham et al. (2018). For SAMI we use the data presented in van de Sande et al. (2017), and we circularize the effective semi-major axis by using the reported value for the ellipticity. The half light radii for the ePN.S galaxies are in Table 2 of Pulsoni et al. (2018). These are effective semi-major axis distances measured from the most extended photometric profiles available from the literature, extrapolated to very large radii with a Sérsic fit. The ellipticity assumed is in their table 1. Section 5.6.1 discusses the systematic effects in comparing observed effective radii and half-mass radii in simulated galaxies.

Stellar masses - The IllustrisTNG model assumes a Chabrier (2003) initial mass function (IMF). The stellar masses for the SAMI survey in van de Sande et al. (2017) are derived using a color–mass relation, and a Chabrier IMF. For Atlas3D, MASSIVE, and MANGA we use the total absolute K-band luminosity M_K from the same tables referenced above, which are derived from the 2MASS extended source catalog (Jarrett et al. 2003), and already corrected for galactic extinction. The luminosities M_K are then corrected for missing flux as in Scott et al. (2013), $M_{K_{corr}} = 1.07 M_K + 1.53$, and converted to stellar masses with the formula from van de Sande et al. (2019):

$$\log_{10} M_* = 10.39 - 0.46(M_{K_{corr}} + 23), \tag{5.1}$$

which uses the stellar population model-based mass-to-light ratio from Cappellari et al. (2013a), their $[\log(M/L)_{\rm Salp}]$, converted to a Chabrier IMF. The missing flux correction takes into account

[1] http://www.nsatlas.org

[2] http://www.leda.univ-lyon1.fr

the over-subtraction of the sky background by the 2MASS data reduction pipeline (Schombert & Smith 2012) and the limited $4R_e$ aperture of the 2MASS measurement.

For the ePN.S sample we derive stellar masses using integrated luminosities from the most extended photometric profiles available in the literature, extrapolated to infinity with a Sérsic fit (references in Pulsoni et al. 2018). We convert the integrated values to stellar masses by using the non-dereddened relations between colors and mass-to-light ratios for ellipticals and S0 galaxies from García-Benito et al. (2019), which assume a Chabrier IMF.

There are several sources of errors in the stellar mass estimates of observed galaxies. The uncertainty in the magnitudes derived from the 2MASS photometry are typically ~ 0.25 mag (Scott et al. 2013). The uncertainty in the distances typically translate into an error of 0.1 mag on the absolute magnitudes but can reach up to 0.5 mag (van de Sande et al. 2017). These uncertainties correspond to an error on the stellar mass of typically ~ 0.1 dex and up to ~ 0.2 dex. In addition the total luminosity, and hence the total stellar mass, can be underestimated if the photometry is not deep enough to measure the faint surface brightness of the stellar halos, especially in massive galaxies with large Sérsic indices or described by multiple Sérsic components. Since the stellar masses of the simulated galaxies are evaluated using the total bound stellar mass (Section 5.5.1), this may cause a systematic difference between observed and simulated stellar masses at the high mass end; see also Section 5.6.1.

Ellipticities - For the Atlas3D galaxies we use the ellipticity ε measurements within 1 $R_e$reported in Table B1 of Emsellem et al. (2011). 17 out of 260 Atlas3D objects have obvious bar components: for these cases the ellipticity is measured at larger radii (typically 2.5 - $3R_e$). Ellipticities for the SAMI galaxies are from van de Sande et al. (2017), and are average ellipticities of the galaxies within 1 R_e. MANGA's ellipticities from Graham et al. (2018) are also measurements within the 1 $R_e$isophote, while for the MASSIVE sample Veale et al. (2017a) uses ellipticities from NSA where available, and from 2MASS otherwise, which are globally fitted values. The ellipticity profiles for the ePN.S galaxies are referenced in Pulsoni et al. (2018). The measurement errors on the ellipticities are per se very small ($O(10^{-3})$, Kormendy et al. 2009), but the characteristic ellipticities used by different surveys for the same galaxies can differ within a root-mean-square scatter of ~ 0.05 (see e.g., Veale et al. 2017a and Figure 2 from Graham et al. 2018).

Angular momentum parameters λ_e - The parameter λ_e is derived in the different surveys using different integration areas. While Emsellem et al. (2011, Atlas3D) and Veale et al. (2017a, MASSIVE) use circular apertures of radius R_e, van de Sande et al. (2017, SAMI) prefer elliptical apertures with semi-major axis R_e, and Graham et al. (2018, MANGA) integrate over the half-light ellipse (an ellipse covering the same area as a circle with radius R_e, that is, with semi-major axis $R_e\sqrt{1-\varepsilon}$, where ε is the ellipticity).

The uncertainties on the measured λ_e for the Atlas3D galaxies are generally small, $\Delta\lambda_e \simeq 0.01$ (Emsellem et al. 2011). Similar errors apply for the MASSIVE sample, $\Delta\lambda_e \lesssim 0.01$ (Veale et al. 2017a). SAMI and MANGA instead target objects at larger distances with lower apparent sizes and spatial resolution. For these galaxies the measurement uncertainties are combined with seeing effects, which generally tend to systematically decrease λ_e. In the SAMI galaxies, for a typical seeing of 2 arcsec, van de Sande et al. (2017) find that measurement errors ($\Delta\lambda_e \sim 0.01$) and seeing effects cancel out for galaxies with $\lambda_e < 0.2$, while for $\lambda_e > 0.2$ seeing is the dominant

effect and causes a median decrease in λ_e of 0.05. For the MANGA regular rotators in the cleaned sample, Graham et al. (2018) estimate mean $\Delta\lambda_e = [0.005, -0.041]$ and median errors $\Delta\lambda_e = [0.004, -0.027]$.

V/σ profiles - The V/σ profiles for the Atlas3D and the ePN.S galaxies are derived from the ratio of the rotation velocity $V_{\rm rot}$ and the azimuthally averaged velocity dispersion in elliptical radial bins. For the Atlas3D galaxies we apply the procedure described in Sect. 5.4.4 directly to the velocity fields from Emsellem et al. (2004) and Cappellari et al. (2011), giving a median error on V/σ of the order of 0.03.

For the ePN.S galaxies the procedure is applied to the PN velocity fields, whereas for the central regions we use the $V_{\rm rot}$ and σ from kinemetry analysis on IFS data from Krajnović et al. (2008, 2011); Foster et al. (2016), when available. In the other cases we use $V_{\rm rot}$ and σ from major axis slits (see references in the ePN.S paper). For the ePN.S galaxies the measurement uncertainties on the V/σ profiles are dominated by the statistical error on the PN velocity fields. The median $\Delta(V/\sigma) = 0.08$.

5.4 Methods: IllustrisTNG photometry and kinematics

In this section we describe the method for measuring photometry and kinematics in the IllustrisTNG galaxies. For each simulated galaxy we define a coordinate system (x, y, z) aligned with the axes of the simulation box, and centered at the position of the most bound particle in the galaxy. Galaxies are observed both edge-on and along a random fixed line-of-sight (LOS) direction. The edge-on projection is obtained by rotating the particles according to the principal axes of the moment of the inertia tensor I_{ij}:

$$I_{ij} = \frac{\sum_n M_n x_{n,i} x_{n,j}}{\sum_n M_n}, \tag{5.2}$$

where the sum is performed over the 50% most bound stellar particles; $x_{n,i}$ is their coordinates, M_n their mass. The random LOS direction is arbitrarily chosen to be the z axis of the simulation box. In this work we will indicate with the lowercase letters x_i, v_i, and r_i the 3D coordinates, velocities, and radii, and we reserve capital letters for the corresponding 2D quantities projected on the sky. The coordinate r indicates the intrinsic semi-major axis distance, while R indicates the projected semi-major axis distance.

For any projection, we rotate the galaxies so that the X axis corresponds to the projected major axis, and the Y axis to the projected minor axis. This is done by evaluating the inertia tensor in Eq.5.2 using the 2D projected coordinates, and summing over the 50% most bound particles. We choose to weight quantities by the mass and not by luminosity, as the former are not affected by uncertainties from stellar population modeling and attenuation effects, for example, from dust. The difference between mass weighted and luminosity weighted quantities, such as in the K band, is generally small for old stellar populations (e.g., Forbes et al. 2008). Radial profiles are shown in units of effective radii $R_{\rm e}$, which are evaluated as described in Sect. 5.6.1.

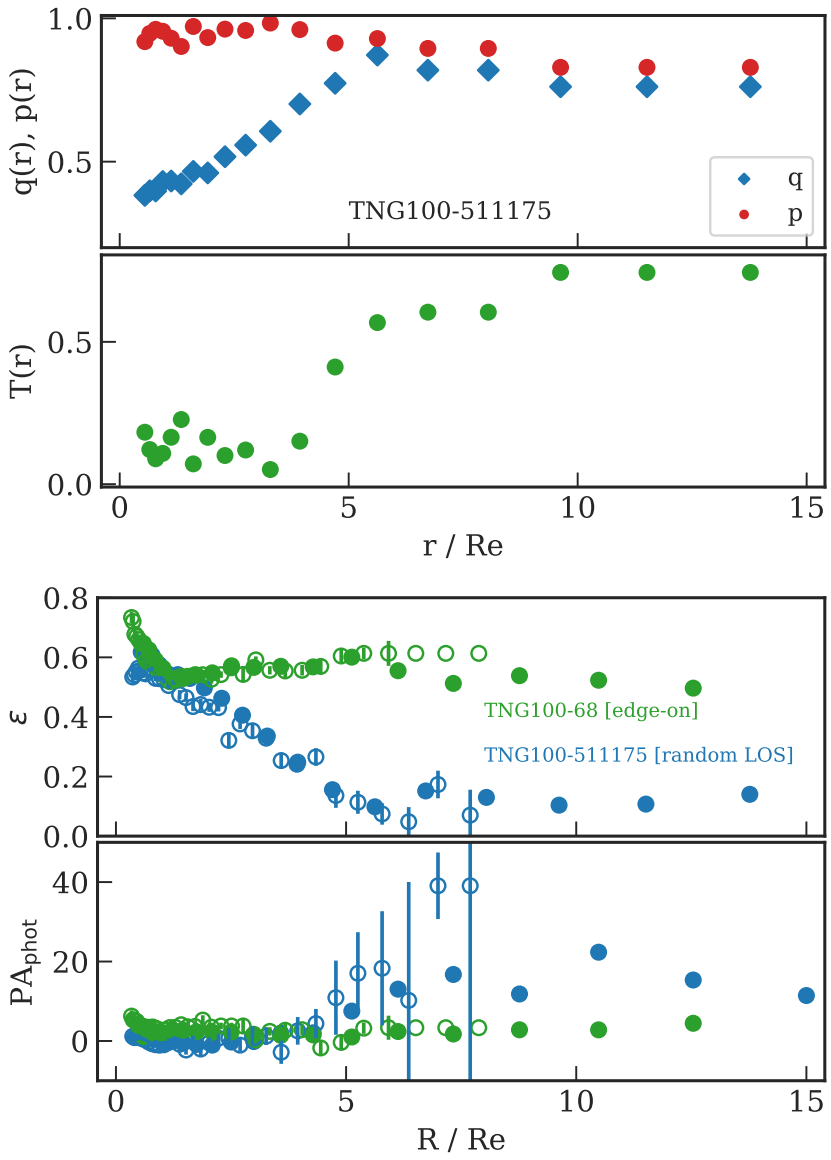

Figure 5.1: Photometric measurements. **Top:** Intrinsic shape of an example galaxy from TNG100 as a function of the intrinsic major axis distance r/R_e; axis ratios and triaxiality parameter are shown in separate panels. This simulated galaxy is oblate with $q \sim 0.4$ and $p \sim 0.95$ in the central $3R_e$, and becomes near-prolate ($T > 0.7$) in the outer halo. In this galaxy $9r_{soft}$ correspond to $0.48R_e$. **Bottom:** Ellipticity and photometric position angle profiles for two example galaxies from TNG100 as a function of the projected major axis distance R/R_e. The quantities derived from the inertia tensor are shown with solid symbols, those from the mock images with open symbols.

5.4.1 Intrinsic shapes

The three-dimensional intrinsic shapes of the galaxies are evaluated by diagonalizing the inertia tensor I_{ij} in Eq. (5.2), summed over stellar particles enclosed in elliptical shells. This definition of $I_{i,j}$ without any weight factors is shown by Zemp et al. (2011) to be the least biased method for measuring the local intrinsic shape of a distribution of particles, and we refer to their work for a detailed description of the procedure.

In brief, the galaxies are divided in spherical shells of radii r and $r + \Delta r$. In each shell we calculate the tensor $I_{i,j}$: the square root of the ratio of its eigenvalues give the axis ratios p and q (with $p \geq q$) of the principal axes, the eigenvectors their directions. The spherical shell is subsequently deformed to a homeoid of semi-axes $a = r$, $b = pa$ and $c = qa$. We repeat the procedure iteratively until the homeoid is adjusted to the iso-density surface, and the fractional difference between two iteration steps in both axis ratios is smaller than 1%. The values of p and q as functions of the principal major axis length r give the intrinsic shape profiles of the galaxies. We require a minimum number of 1000 particles in each shell as suggested by Zemp et al. (2011), which assures small errors from particle statistics, and, at the same time, the possibility of measuring intrinsic shape profiles out to at least $8R_{\rm e}$for $\sim 96\%$ of the selected TNG galaxies. The directions of the principal axes of the galaxies as functions of the galactocentric distance r are given by the eigenvectors $\hat{e}_j$ (with $j = a, b, c$) of the inertia tensor.

We also use the triaxiality parameter,

$$T(r) = \frac{1 - p(r)^2}{1 - q(r)^2}, \tag{5.3}$$

to quantify the intrinsic shape.

In App. 5.B we find that shape measurements at $1R_{\rm e}$ are affected by the resolution of gravitational forces only for the lowest mass galaxies, for which the absolute error on p and q is ~ 0.1 at the resolution on TNG100. At $r \sim 9r_{\rm soft}$, which is $r \sim 3.5R_{\rm e}$ for the lowest mass galaxies, and $r \sim 1.1R_{\rm e}$ for $M* = 10^{11} M_{\odot}$, these resolution effects are negligible, and the error on the shape measurements is then due to particle noise and is ~ 0.02 in TNG100. This uncertainty translates into an error of $\Delta T = 0.2$ on the T parameter for typical values of the axis ratios in fast rotator ETGs (i.e., $p = 0.9$ and $q = 0.5$). As discussed in App.5.B, we consider the triaxiality profiles reliable starting from $r = 9r_{\rm soft}$; at smaller radii, where ΔT is larger, we quantify shapes using p and q which are better defined. These results for TNG100 are summarized in Table 5.2. For the TNG50 galaxies, we expect similar or lower uncertainties.

In the paper, we consider halos as near-oblate when $T \leq 0.3$, and near-prolate when $T > 0.7$. Halos with intermediate values of T parameter are designated as triaxial. Figure 5.1 (top panel) shows the principal axis ratios $q(r)$ and $p(r)$ as a function of the major axis distance r for one example TNG galaxy, normalized by the $R_{\rm e}$of the edge-on projection. The galaxy shown in the example is close to oblate in the central regions, with $q(1R_{\rm e}) = 0.43$ and $p(1R_{\rm e}) = 0.95$ ($T < 0.3$). At large radii the galaxy becomes close to prolate with $q(10R_{\rm e}) = 0.76$, $p(10R_{\rm e}) = 0.83$, and triaxiality parameter $T > 0.7$. For the galaxy shown, $9r_{\rm soft} = 0.48R_{\rm e}$.

Table 5.2: Absolute uncertainties on the shape measurements in TNG100 galaxies: Δp, Δ_q, and ΔT at $2r_{\rm soft}$ and $9r_{\rm soft}$ (first two rows), which correspond to different multiples of $R_{\rm e}$ for galaxies of different mass as shown in the last three rows. Triaxiality measurements are considered unreliable for $r < 9r_{\rm soft}$. The radius $r_{\rm out}$ indicates the mean radius of the outermost shell that contains at least 1000 particles for at least 95% of the galaxies within the indicated stellar mass bins.

	$r \sim 2r_{\rm soft}$	$r \geq 9r_{\rm soft}$	
Δp, Δq	$\lesssim 0.1$	~ 0.02	
ΔT	–	~ 0.2	
	$2r_{\rm soft}$	$9r_{\rm soft}$	$r_{\rm out}$
$\log_{10}M_*/M_\odot : 10.3 - 10.4$	$0.76R_{\rm e}$	$3.5R_{\rm e}$	$\sim 8R_{\rm e}$
$\log_{10}M_*/M_\odot : 10.6 - 10.7$	$0.47R_{\rm e}$	$2R_{\rm e}$	$\sim 8R_{\rm e}$
$\log_{10}M_*/M_\odot > 11$	$< 0.25R_{\rm e}$	$\lesssim 1R_{\rm e}$	$\sim 11R_{\rm e}$

5.4.2 Ellipticity and photometric position angle profiles

Mass weighted photometry is derived by diagonalizing the 2D inertia tensor (Eq. (5.2)) using the projected coordinates for a given LOS. We use an iterative procedure similar to the one described in Sect. 5.4.1 for the 3D intrinsic shape. The square root of the ratio of the two eigenvalues of I_{ij} gives the projected flattening, hence the projected ellipticity $\varepsilon(R)$; the components of the eigenvectors define the photometric position angle $PA_{\rm phot}(R)$. The zero point of the $PA_{\rm phot}(R)$ is chosen to be the X axis of the galaxies.

As an independent check on the results, we derived $\varepsilon(R)$ and $PA_{\rm phot}(R)$ also from fitting ellipses to mock images of the galaxies, and obtained very similar results. The bottom panels of Fig. 5.1 shows the $\varepsilon(R)$ and $PA_{\rm phot}(R)$ profiles obtained from the inertia tensor (solid symbols) and from the images (open symbols) for two example galaxies. The galaxy TNG100-511175, shown with blue symbols, is the same as the one shown in the top panels of Fig. 5.1: the increased axis ratio $q(r)$ at $r \geq 3R_{\rm e}$ is reflected in a decreased projected ellipticity. The example also shows that at low ellipticities the uncertainty on the measured $PA_{\rm phot}(R)$ becomes larger, as is well known. We quantified that our method allows us to measure reliably position angles down to ellipticities $\varepsilon = 0.1$, where the error $\Delta PA_{\rm phot}(R)$ from particle noise is $\sim 6^\circ$. Below 0.1 $\Delta PA_{\rm phot}(R)$ increases exponentially when ε decreases towards 0.

5.4.3 Central kinematics

For each TNG galaxy we build projected mean velocity and dispersion fields for two projections (edge-on and random LOS). We use a resolution of 0.2 kpc, which corresponds to 2 arcsecs for a galaxy observed at 20 Mpc, comparable to present day IFS surveys (e.g., Law et al. 2016, for MANGA). The stellar particles are binned on a regular spatial grid centered on the galaxy and $8R_{\rm e}$ wide.

The binned data are then combined into Voronoi bins as described in Cappellari & Copin (2003), so that each bin contains at least 100 stellar particles. In each i-th bin we calculate the projected mean velocity and the mean velocity dispersion as the weighted averages:

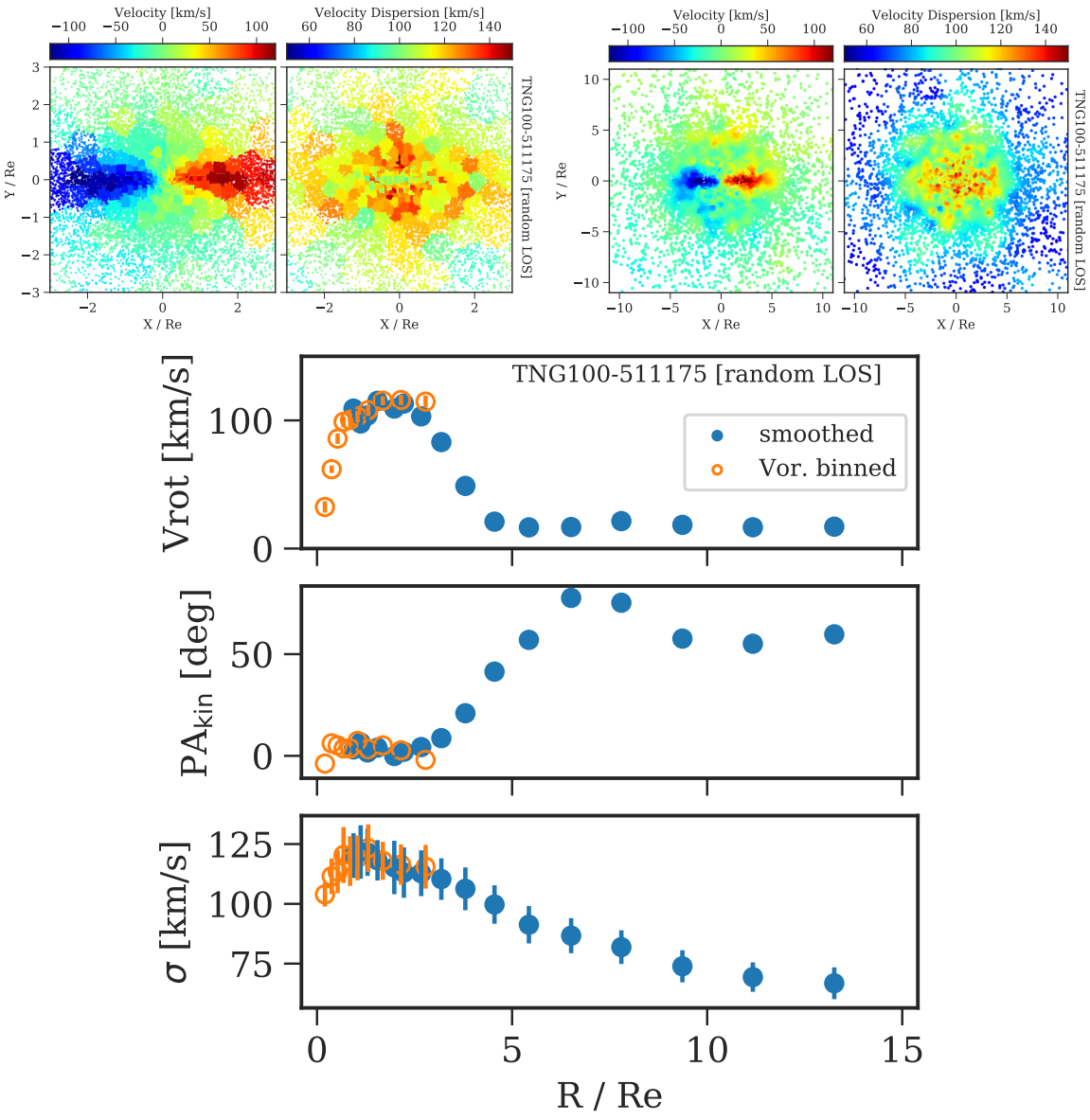

Figure 5.2: Stellar kinematic measurements. **Top left**: Voronoi binned mean velocity fields for an example TNG100 galaxy, with a central bulge and a relatively massive disk. For this galaxy the random LOS projection almost coincides with the edge-on projection. The projected major axis is aligned with the X axis. The data points show the projected (X, Y) positions of the stellar particles, and are colored according to the mean velocity and velocity dispersion of the corresponding Voronoi bin as shown by the colorbars. **Top right**: Smoothed velocity and velocity dispersion fields for the same example galaxy above. The central disk structure is embedded in a spheroidal stellar halo. **Bottom**: Kinematic parameters of the galaxy shown above, derived from the Voronoi binned velocity fields (orange open circles) and from the smoothed velocity fields (blue points).

$$V_i = \frac{\sum_n M_{n,i} V_{n,i}}{\sum_n M_{n,i}} \quad ; \quad \sigma_i = \sqrt{\frac{\sum_n M_{n,i} \left(V_{n,i} - V_i\right)^2}{\frac{N_i}{N_i - 1} \sum_j M_{n,i}}}, \tag{5.4}$$

where the index n runs over the particles in the bin, and N_i is the number of particles in the i-th bin. The top panel of Fig. 5.2 shows the result for one example galaxy; the middle and bottom panels show the halo kinematics and the derived kinematic parameters as described in the next section. The example illustrates that in the central regions, where the density of particles is highest, the velocity field is sampled at the highest resolution. At larger radii, the Voronoi bins combine the data in progressively larger bins in order to reach the required minimum number of particles.

The systemic velocity of the galaxy is derived by fitting a harmonic expansion as in Pulsoni et al. (2018, their section 4) to the central regions (i.e., at $R \leq 2R_e$) of the projected velocity field. The fitted constant term is then subtracted from the velocity fields V_i.

From the velocity fields we calculate the angular momentum parameter λ_e following the definition of Emsellem et al. (2011)

$$\lambda_e = \frac{\sum_i M_i R_{\mathrm{circ},i} |V_i|}{\sum_i M_i R_{\mathrm{circ},i} \sqrt{V_i^2 + \sigma_i^2}}, \tag{5.5}$$

where the weighting with the flux is substituted here with a weighting with the mass M_i of each Voronoi bin of index i, $M_i = \sum_n M_{n,i}$, and $R_{\mathrm{circ},i}$ is the circular radius of the i-th bin. The cumulative λ_e is derived by summing over all the Voronoi bins contained inside an elliptical aperture of semi-major axis R_e and flattening given by the ellipticity $\varepsilon(1R_e)$. By comparison, the differential $\lambda(R)$ is summed in elliptical shells. As discussed in App. 5.B the angular momentum parameter is not affected by resolution at $R \gtrsim 1R_e$ for the selected sample of galaxies.

5.4.4 Halo kinematics

The mean velocity and velocity dispersion fields at large radii are derived using the adaptive smoothing kernel technique (Coccato et al. 2009), used by Pulsoni et al. (2018) to derive halo velocity fields from the discrete velocities of planetary nebulae in the ePN.S survey. For the simulated galaxies, the discrete velocities of the particles at $R > 2R_e$ are smoothed with a fully adaptive kernel ($A = 1$, $B = 0$), and their stellar masses are included in the weighting.

We verified that the kinematic measurements from the adaptively smoothed and the Voronoi binned velocity fields return consistent values in the regions of spatial overlap. The bottom panel of Fig. 5.2 shows the rotation velocity V_{rot}, kinematic position angle PA_{kin}, and velocity dispersion σ profiles derived from the Voronoi binned velocity fields (in orange), and from the smoothed velocity fields (in blue). V_{rot} and PA_{kin} are derived from fitting a harmonic expansion as in Pulsoni et al. (2018), and σ is azimuthally averaged in elliptical annuli whose flattening follows the ellipticity profile of the galaxies. The zero point of PA_{kin} is defined to be the X axis of the galaxies, consistently with the zero point of PA_{phot}. Error bars on the $\sigma(R)$ profiles are derived from the standard deviation of the σ values inside each annulus. The values obtained

Table 5.3: Absolute uncertainties on the kinematic parameters $\lambda(R)$ and $V/\sigma(R)$ for different particle number at the resolution of TNG100.

$\log_{10}\frac{M_*}{M_\odot}$:	10.3 − 10.5	10.5 − 11	11 − 12
$\Delta\lambda(2R_e)$	~ 0.006	~ 0.004	$\lesssim 0.002$
$\Delta(V/\sigma)(2R_e)$	~ 0.01	~ 0.007	~ 0.003
$\Delta\lambda(8R_e)$	~ 0.02	~ 0.013	$\lesssim 0.007$
$\Delta(V/\sigma)(8R_e)$	~ 0.03	~ 0.02	~ 0.01

with the smoothed velocity fields are very well consistent with those from the Voronoi binned velocity fields.

We also evaluated differential λ profiles using Eq. (5.5), where the summation is performed over the Voronoi bins and the particles, each weighted by their mass, in elliptical annuli. We estimated uncertainties on the differential $\lambda(R)$ and on $V/\sigma(R)$ in TNG100 by considering a few kinematically representative galaxies in three stellar mass bins and studied the kinematic parameter distributions derived from 1000 simulations respectively, with particle numbers decreased to the typical numbers at different multiples of R_e. Table 5.3 lists the standard deviation of the distributions for typical numbers of particles at $2R_e$ and $8R_e$.

The example galaxy shown in Fig. 5.2 has a massive disk ($q \lesssim 0.4$, see Fig. 5.1, top panels) embedded in a spheroidal halo with high T ($T \gtrsim 0.7$). The variation in intrinsic shape from near-oblate in the center to strongly triaxial at large radii is accompanied by a modest photometric twist (Fig. 5.1, bottom panels), and a much larger kinematic twist (Fig. 5.2) which follows the rotation along the projected minor axis visible in the top panel. At the same radii the rotation velocity V_{rot} is observed to drop, together with the local λ parameter.

5.5 Selection of the sample of ETGs in the IllustrisTNG simulations

5.5.1 Selection in color and mass

The purpose of this paper is to study the stellar halos of a volume- and stellar mass-limited sample of simulated ETGs, and compare with observations. Nelson et al. (2018) verified that TNG100 reproduces well the $(g - r)$ color of $10^{10} < M_*/M_\odot < 10^{12.5}$ galaxies at $z = 0$, by comparing with the observed distribution from SDSS (Strateva et al. 2001). They also showed that redder galaxies have lower star formation rates, gas fractions, gas metallicities, and older stellar populations, and that they correspond to earlier morphological types (their Figure 13).

Thus we extract our sample of ETGs from the TNG50 and TNG100 snapshots at $z = 0$ in the color-stellar mass diagram, isolating galaxies in the red sequence. To obtain a sample of galaxies in the same area occupied by the Atlas3D and the ePN.S samples (see Sect. 5.3), we chose

$$(g - r) \geq 0.05 \log_{10}(M_*/M_\odot) + 0.1\text{mag}. \quad (5.6)$$

For M_* we use the total bound stellar mass of the galaxies. We do not include any dust extinction model in the calculation of the simulated colors in order to avoid the contamination from dust-reddened late type galaxies. Even in this case, this sample of simulated galaxies unavoidably contains some red disks, while in Atlas3D some of the disks have been removed (see Sect. 5.3).

We limited the sample stellar mass range to $10^{10.3} \leq M_* \leq 10^{12} M_\odot$. This choice assures that the TNG100 galaxies are resolved by at least 2×10^4 stellar particles. By comparison, the minimum number of stellar particles in the selected TNG50 galaxies is 36×10^4.

In addition, we impose that the galaxies' effective radius (see Sect. 5.6.1) $R_\mathrm{e} \geq 2r_\mathrm{soft}$, to guarantee that the region at $r = R_\mathrm{e}$ is well resolved for all simulated galaxies. For TNG100 $r_\mathrm{soft} = 0.74$ kpc at $z = 0$, which excludes 38 galaxies at the low mass end (see Fig. 5.7). In TNG50 all the galaxies have $R_\mathrm{e} > 2 \times r_\mathrm{soft}$, where $r_\mathrm{soft} = 0.288$ kpc. These criteria select a sample of 2250 galaxies in TNG100 and 168 galaxies in TNG50.

Figure 5.3 shows the color-stellar mass diagram for the simulated galaxies from TNG100 and TNG50, and for observed galaxies from several IFS surveys. Our selection criteria are highlighted with dashed lines. Most of the observed ETGs, including the SAMI galaxies and the MANGA ellipticals and lenticulars are in the selected region of the diagram.

The histograms in the top panel of Fig. 5.4 show the stellar mass functions for the color-mass-selected samples. The bottom panel instead shows the stellar mass functions of the final samples as defined by adding constraints from the lambda-ellipticity diagram in Sect. 5.5.2. The red and hatched histograms show the Atlas3D and ePN.S samples, respectively. Here we consider the Atlas3D sample properties to validate our selection criteria, as this survey is especially targeted to study a volume-limited sample of ETGs. The ePN.S sample, which will be used to compare with properties at large radii, is also shown, and it contains on average higher mass galaxies. Both TNG50 and TNG100 are in reasonable agreement with Atlas3D. We remark that a more generous color selection, including bluer galaxies, would produce a too large number of high ellipticity galaxies, especially in TNG50.

In the following, whenever we compare simulated and observed galaxy samples, we apply to the observed galaxies the same color and stellar mass selection criteria that we used for the TNG sample.

5.5.2 Selection of ETGs in the lambda-ellipticity diagram: fast and slow rotators

Figure 5.5 shows the λ_e-$\varepsilon(1R_\mathrm{e})$ diagram for the simulated ETGs in three stellar mass bins, and compares with observed ETG samples. The top row features the diagram for the TNG50 (crosses) and TNG100 (circles) galaxies selected as described in Sect. 5.5.1, and projected along a random LOS. The middle row shows again the TNG50 and TNG100 galaxies after the additional selection discussed in this section. The bottom row shows the similar diagram for the observed ETG samples (selected in various ways as described in Sect. 5.3), in the same color and stellar mass region as defined in Sect. 5.5.1. Here we also include for comparison the spiral and irregular galaxies from the MANGA sample (marked as LTGs).

We observe that a significant fraction of the TNG galaxies shown in the top row populate a

region to the right of the λ_e-$\varepsilon(1R_e)$ diagram where there are no observed counterparts, i.e. below the magenta line and with $\varepsilon(1R_e) > 0.5$. By color coding the galaxies according to their intrinsic axis ratios at $r \sim 1R_e$, we find that these galaxies have elongated, triaxial shapes. These systems occur at all values of λ_e, that is, some rotate as rapidly as the MANGA disk galaxies, but others do not show any rotation (Fig. 5.C.1).

It is possible that some of the rapidly rotating elongated systems are barred galaxies. Rosas-Guevara et al. (2020) showed that within a dynamically selected sample of disk galaxies the TNG100 simulation produces barred systems in fractions consistent with observational results. The majority of these systems, all characterized (per definition) by high rotation, are quenched and hence will overlap with the colour range of our sample of red galaxies. Some barred galaxies are also expected to be present among the observed ETG samples. For example, in the Atlas3D sample 7% of the galaxies show a clear bar component. For these objects the ε-values shown in Fig. 5.5 were measured at larger radii, to avoid the influence of the bar on the estimate of ε (Emsellem et al. 2011). However, if their actual $\varepsilon(1R_e)$ values were used and placed these objects in the region of the λ_e-$\varepsilon(1R_e)$ populated by the centrally elongated (at $r \sim 1R_e$) TNG galaxies, their fraction would not be large enough to explain the abundance of simulated galaxies in the same region, and none of these have $\lambda_e < 0.2$. Therefore the presence of a large fraction of centrally elongated galaxies with high ellipticity and intermediate to low λ_e in the TNG sample cannot be explained as a simple sample selection bias (note also that resolution effects on the intrinsic shapes at $1R_e$ are at most of the order of 0.1, for the low mass galaxies, see App.5.B).

In App. 5.C we discuss the properties of these galaxies further, and suggest that they are likely a class of galaxies that are produced by the simulation but are not present in nature. These galaxies occupy a particular mass range that depends on resolution and they are the reddest systems for their mass. We found no similar concentration of elongated systems among the red galaxies in the Illustris simulation, and the $\lambda - \varepsilon$ diagrams for simulated galaxies in Magneticum (Schulze et al. 2018) and EAGLE (Walo-Martín et al. 2020) do not contain many objects with large ellipticities and intermediate to low λ_e. This indicates that the new galaxy formation model in TNG is involved in the occurrence of these centrally elongated galaxies. The elongated components typically extend up to 3 R_e and are embedded in near-oblate spheroids with a wide range of flattening q, with lower median value in TNG50 ($q \sim 0.3$) than in TNG100 ($q \sim 0.45$), indicating a relation to disk building and bar instability. However, some of these do not contain a disk component (Fig.5.C.1), and they populate a wide range of rotation (λ_e) approximately uniformly all the way from edge-on $\lambda_e = 0.7$ to no rotation (Fig.5.C.2). Therefore we suggest that the centrally elongated galaxies in TNG may be systems that were in the process of forming a disk, whose evolution has been interrupted or derailed by rapid dynamical instability, star formation, and feedback in the simulations, in the particular mass range in which they occur.

For these reasons we exclude the centrally elongated objects from our sample of galaxies. We do this by performing a selection in intrinsic shape, and reject all galaxies with intermediate to major axis ratio $p < 0.6$ at $r \sim 1R_e$. This choice is motivated by the fact that the intrinsic shape distribution of real galaxies is known (Weijmans et al. 2014; Foster et al. 2017; Li et al. 2018; Ene et al. 2018) although with large uncertainties (Bassett & Foster 2019), and galaxies with $p < 0.6$ are rare, even among the the slow rotators. By applying this selection criterion we obtain our final sample of simulated ETG galaxies, 1114 objects in TNG100 and 80 in TNG50.

The middle row of Fig. 5.5 shows that the final selected sample of ETGs lies in the region of the diagram populated by the observed galaxies. The fraction of simulated galaxies in the region of avoidance (i.e., above the black and below the magenta lines) is in agreement with the $\lambda_e - \varepsilon$ observations. The location of the simulated galaxies in the plane follows closely the Atlas3D, SAMI, and MASSIVE galaxies. In the MANGA sample there is a large fraction S0 galaxies with $\lambda_e > 0.7$ that are not present in the other surveys, and are likely due to differences in the data analysis, possibly to the beam corrections applied by Graham et al. (2018) on the MANGA data (see discussion in Falcón-Barroso et al. 2019).

Figure 5.6 demonstrates that the distribution of stellar halo properties which we are interested in, that is, λ and triaxiality parameter, are not affected by the sample selection based on $p(1R_e)$. The distributions do not systematically depend on the intrinsic shape of the central regions of the galaxies. As discussed in a companion paper, the properties of the galaxies at large radii are mainly set by their accretion history and not by the details of the star formation in the central regions of galaxies.

The bottom panel of Fig. 5.4 shows the stellar mass function for the final sample of ETGs, compared with observations. The stellar mass function of the TNG100 ETGs is still similar to Atlas3D. For TNG50 the additional selection has excluded a large fraction of red galaxies in the stellar mass range $\sim 10^{10.3} - 10^{11} M_\odot$. This results in a stellar mass function skewed towards high masses (and so more similar to ePN.S).

Henceforth we classify galaxies as slow rotators (SRs) and fast rotators (FRs), using the dividing line introduced by Emsellem et al. (2011),

$$\lambda_e = 0.31 \sqrt{\varepsilon_e}, \tag{5.7}$$

shown in Fig. 5.5 with the black line: galaxies above this threshold are FRs, and galaxies below are SRs. To reduce the effects of inclination, we choose to classify the simulated galaxies using the values of λ_e and ellipticity for their edge-on projection (shown in Fig. 5.C.2).

5.5.3 Summary of the sample selection criteria

The sample of ETG galaxies used in the remainder of this paper is extracted from the TNG50 and TNG100 simulations by

- selecting galaxies in the stellar mass range $10^{10.3} \leq M_* \leq 10^{12} M_\odot$ and with red $(g-r)$ color as in Eq. (5.6) (see Fig. 5.3);
- excluding a small number of objects with $R_e < 2r_{soft}$, to assure sufficient resolution at $1R_e$;
- finally, removing a class of centrally elongated, triaxial galaxies with $p(1R_e) < 0.6$, which are systems not present in the observed ETG samples that probably became bar-unstable and quenched during the process of (central) disk formation.

The selected sample has a distribution of $\lambda_e - \varepsilon(1R_e)$ that is similar to observed ETGs (Fig. 5.5) and halo properties that are unbiased by the selection in intrinsic shape (Fig. 5.6). The mass functions of the selected TNG50 and TNG100 ETG samples are given in Fig. 5.4 and the mass-size relations are shown in Fig. 5.7.

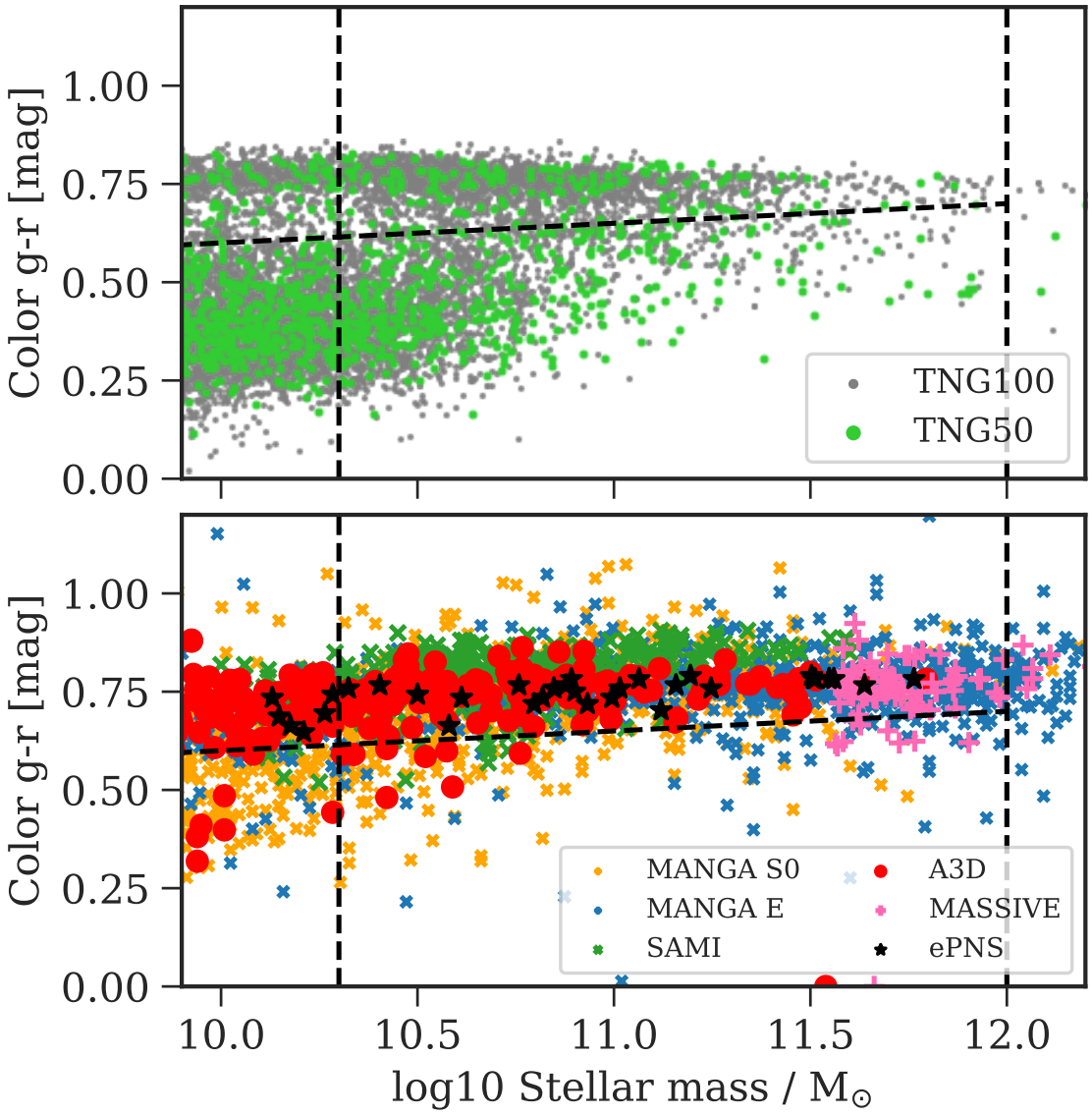

Figure 5.3: Selection of galaxies in color and stellar mass. **Top:** The $g - r$ color - stellar mass diagram of the simulated galaxies in TNG50 and TNG100. Red sequence galaxies are selected above the tilted dashed line, in the mass range $10^{10.3} < M_*/M_\odot < 10^{12}$. **Bottom:** ETGs from recent IFS surveys as indicated. Most of the observed ETGs in this mass range fall in the same red sequence region.

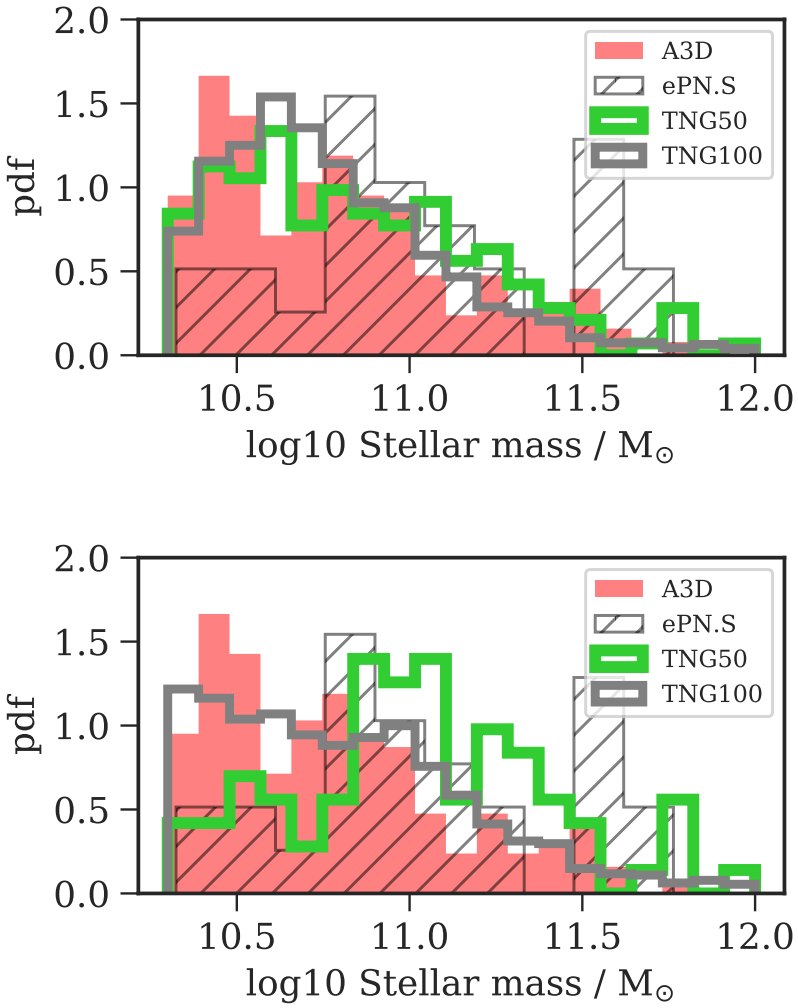

Figure 5.4: Stellar mass function of the TNG galaxies compared with those of the Atlas3D and ePN.S surveys. **Top**: Stellar mass function of the TNG galaxies selected in color and stellar mass, and whose effective radii are well-resolved, as described in Sect. 5.5.1. The stellar mass functions of both TNG50 and TNG100 agree well with Atlas3D. **Bottom**: Stellar mass function of the final sample of ETGs, selected in color, stellar mass, and intrinsic shape as described in Sect. 5.5.1 and Sect. 5.5.2. The removal of centrally elongated objects mostly changes the low-mass part of the TNG50 mass function, while that of TNG100 is still in good agreement with Atlas3D.

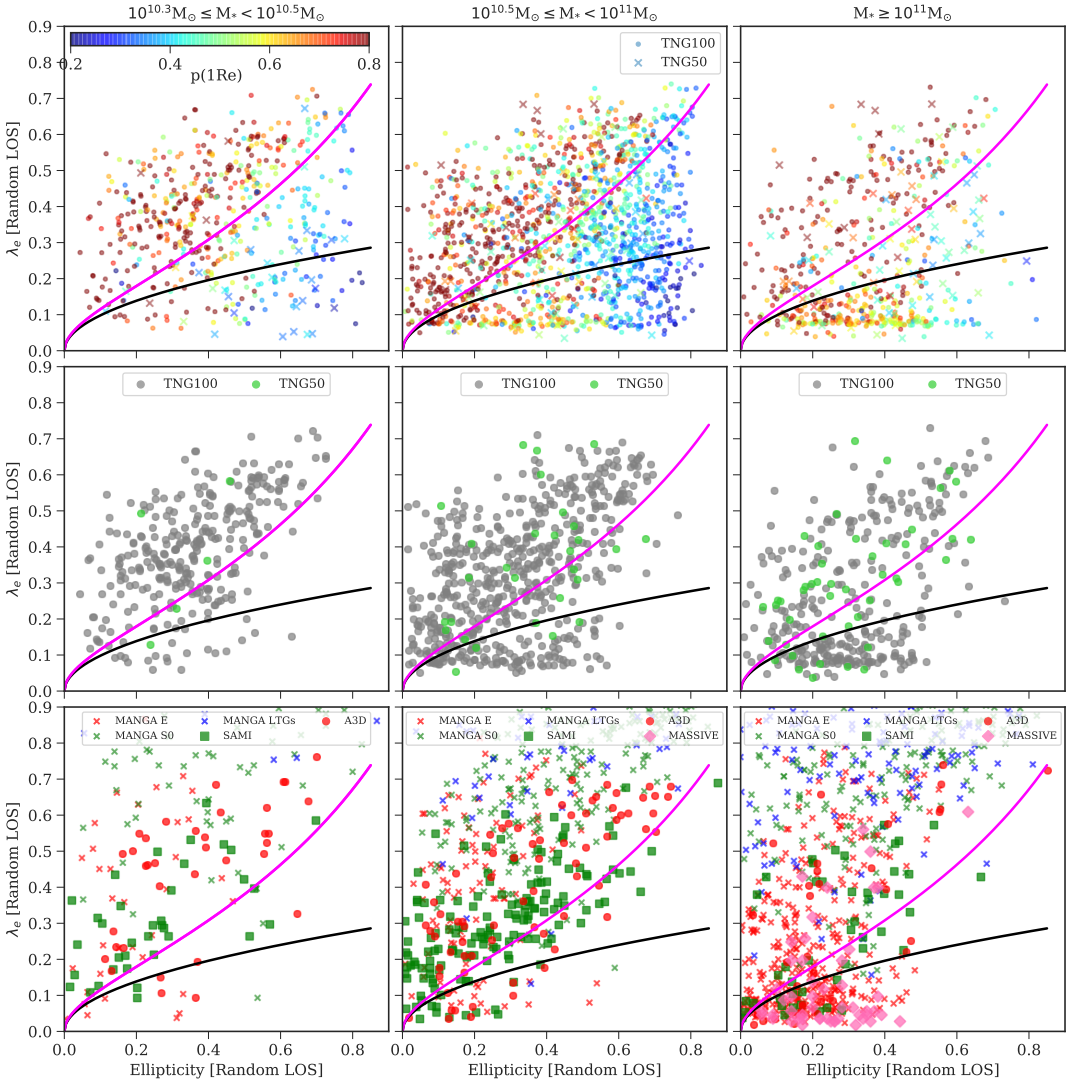

Figure 5.5: $\lambda_e - \varepsilon(1R_e)$ diagrams for TNG and observed galaxy samples, in stellar mass bins. **Top row**: λ−ellipticity diagram for the sample of TNG50 and TNG100 ETGs selected by color and mass as in Fig. 5.3, observed along a random LOS. The galaxies are color coded according to their intermediate to major axis ratios p at 1Re. **Middle row**: λ-ellipticity diagram for the TNG galaxies after the additional selection $p(1R_e) \geq 0.6$. **Bottom row**: λ-ellipticity plots for observed ETG samples as shown in the legend, including also late-type galaxies from the MANGA survey for comparison. Their λ_e and $\varepsilon(1R_e)$ are as described in Sect. 5.3. The solid black line is the threshold separating fast and slow rotators as defined in Emsellem et al. (2011): $\lambda_e = 0.31\sqrt{\varepsilon}$. The magenta line shows the semi-empirical prediction for edge-on axisymmetric rotators with anisotropy parameter $\delta = 0.70\varepsilon_{\rm intr}$ from Cappellari et al. (2007). After the additional removal of centrally elongated systems, the colour and mass selected TNG ETG samples give a good representation of the observed ETG samples in the $\lambda_e - \varepsilon(1R_e)$-plane, with the exception of the high-λ_e (> 0.7) S0 disks specific to the MANGA survey.

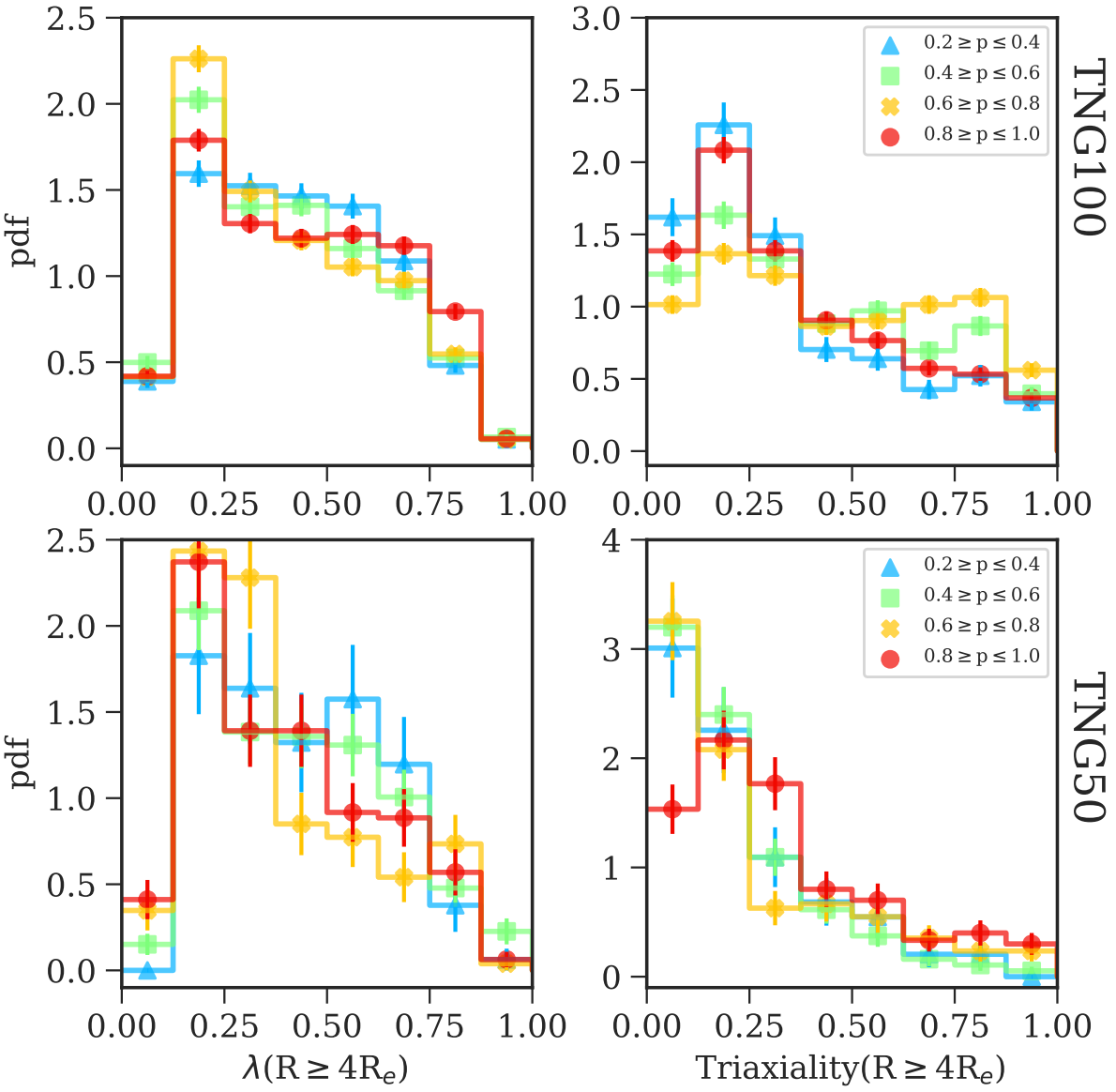

Figure 5.6: Distribution of λ parameter and triaxiality in the stellar halos (i.e. at $R \geq 4R_e$) for different intrinsic shapes in the central regions, parametrized by the intermediate to major axis ratio $p(1R_e)$. TNG100 and TNG50 galaxies are shown separately, in the top and bottom panels respectively. These distributions are not systematically dependent on $p(1R_e)$, and thus the stellar halo spin and triaxiality remain unbiased after implementing a sample selection based on $p(1R_e)$.

5.6 Photometric properties of the TNG ETG samples

In this section, we study the photometric properties of the selected sample of TNG galaxies and how they vary with radius. Section 5.6.1 discusses the measured galaxy sizes and how our definition of effective radii compares with effective radii inferred from ETG photometry. Section 5.6.2 compares the distribution of projected ellipticities at $1R_e$ with that from ETG surveys and validates our sample selection. Section 5.6.3 studies the TNG ellipticity profiles out to the stellar halo, Sect. 5.6.4 explores the intrinsic shape distribution of stellar halos and its dependence on stellar mass, and Sect. 5.6.5 investigates the dependence of galaxy triaxiality on radius and stellar mass in the simulated samples. Finally, Sect. 5.6.6 tests the ability of photometric twist measurements to establish the underlying triaxiality in the TNG galaxies.

5.6.1 Sizes of the TNG galaxies

We first discuss the adopted measurement of the effective radius for the simulated galaxies, which we will use in the paper as galactocentric distance unit.

The effective radius $R_e$is derived for each projection (edge-on or random LOS) of the galaxies by using cumulative mass profiles in elliptical apertures: $R_e$is the major axis radius of the aperture that contains half of the total bound stellar mass.

Figure 5.7 shows the circularized $R_e$as a function of M_* for the final samples of ETGs, and compares it to the distribution of observed effective radii from the different surveys. The $R_e$in TNG100 are larger than most of the observed R_e at $M_* \gtrsim 10^{10.75}$, but they are in reasonable agreement with the ePN.S measurements. TNG50 produces smaller galaxies compared to TNG100 and to observations at intermediate stellar masses (Pillepich et al. 2019). This is purely a resolution effect, as discussed in Sect. 5.2. On the other hand, comparisons to observed $R_e$strongly depend on the operational definitions of galaxy sizes, as discussed by Genel et al. (2018).

Observers measure $R_e$by integrating light profiles fitted to the bright central regions to large radii. This definition of $R_e$tends to underestimate the size (and at the same time the total stellar mass) of the galaxies if the photometric data are not deep enough to sample the light distribution in the halos, especially in massive galaxies with high Sérsic indices. Pulsoni et al. (2018) determined $R_e$of the ePN.S galaxies from the most extended photometric profiles available in the literature, using a Sérsic fit of the outermost regions to integrate to large radii. This approach leads to an average increase of the $R_e$by a factor of ~ 2 for the most massive objects with $M_* > 10^{11} M_\odot$. However it does not take into account the possibility of an extra halo component/intra-group or intra-cluster light (ICL) at large radii. For the simulated galaxies, defining the stellar content of the galaxies as all the bound stellar particles identified by the SUBFIND algorithm, automatically includes also ICL stars in the most massive halos, thus overestimating both $R_e$and M_*.

To quantify these effects requires separating a galaxy from the surrounding ICL. A kinematic separation of the ICL similar to Longobardi et al. (2015a) is beyond the scope of this paper. However, Kluge et al. (2020) recently found that if the ICL component in bright cluster galaxies is identified as the outer component of a double Sérsic fit, the radius at which it starts dominating is ~ 100 kpc with a very large scatter (5 to 400 kpc in their figure 16). We evaluated the differences in $R_e$and M_* that we would obtain if instead of using the whole bound stellar mass we limit

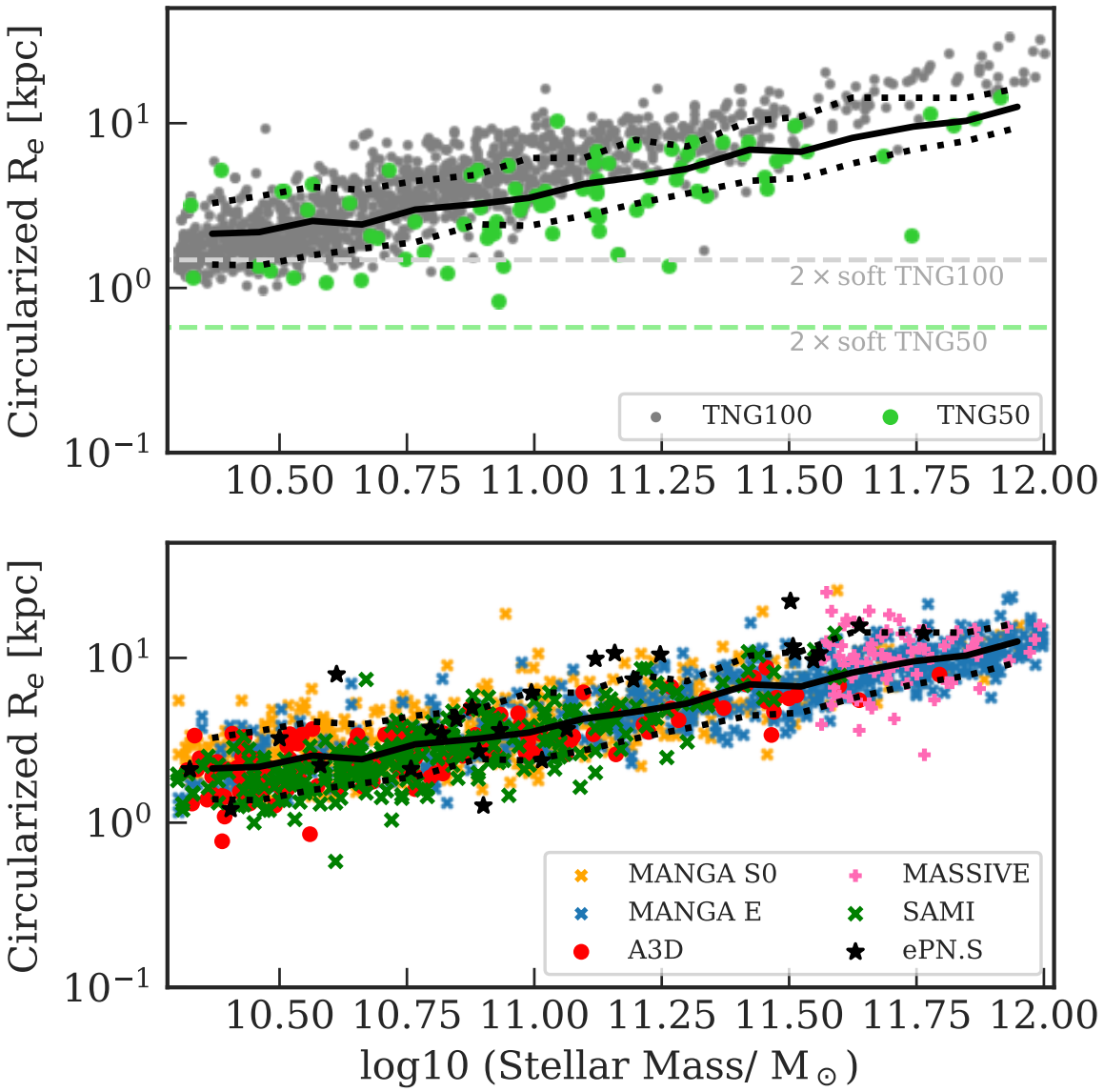

Figure 5.7: Circularized effective radii, i.e. $R_e\sqrt{1-\varepsilon}$, of the selected ETG samples in the TNG100 and TNG50 simulations as a function of stellar mass, and comparison with observations (bottom panel). The black curves show the median profile of the distribution of galaxy R_e from all surveys and the 10th and 90th percentiles, in both panels. The dashed lines in the top panel indicate the resolution of the two simulations.

the galaxy to the mass within 100 kpc. We find that in TNG100 galaxies with $M_* < 10^{10.5}$ the effects are negligible; in $10^{10.5} M_\odot < M_* < 10^{11} M_\odot$ objects the differences in the derived $R_e$and stellar masses are within 10% and 5% respectively, while between $10^{11} M_\odot < M_* < 10^{11.5} M_\odot$ they are within 30% and 15%. At higher masses the differences in $R_e$can be larger than 50% and those in M_* larger than 25%, with a very large scatter. These effects are half as pronounced in TNG50. A size-stellar mass diagram analogous to Fig. 5.7 using the 100 kpc aperture instead of the total bound mass shows an improved agreement with the observed R_e, but TNG100 galaxies with $M_* > 10^{10.75}$ are still larger on average. This may indicate that TNG100 predicts too large sizes for high mass galaxies (see also Genel et al. 2018).

Because of the somewhat arbitrary choice of the 100 kpc limit, on the one hand, and the uncertainties in the observed R_e distribution on the other (from differences in sample selection, quality of the photometric data, definition of total stellar light, the mass-to-light ratio to obtain total stellar masses), here we define $R_e$for the simulated galaxies as the half mass radius of the total bound stellar mass and consider the above uncertainties in the discussion of the results where relevant.

5.6.2 Ellipticity distribution in the central regions

Figure 5.8a shows the distributions of the ellipticities measured at 1 $R_e$for the final sample of selected ETGs, compared with Atlas3D and ePN.S. In the top panels are the SRs and in the bottom the FRs.

The TNG50 and TNG100 simulations predict a significant fraction of SR galaxies with $\varepsilon(1R_e) > 0.4$, while the observed SRs are relatively rounder. This is a common feature of current simulations (Naab et al. 2014; Schulze et al. 2018) and its origin is yet to be understood. In the case of the FR class, the ellipticity distributions are rather flat-topped, and in good agreement with Atlas3D. By comparison the ePN.S sample contains on average rounder (and also more massive, see the bottom panel of Fig. 5.4) galaxies and, hence, a lower number of disk galaxies: none of the ePN.S FRs have ellipticity higher than 0.7.

Overall, Fig. 5.8a shows that the selected sample of ETGs contains a mixture of galaxy types consistent with observations, with a similar balance between disks and spheroids.

5.6.3 Ellipticity profiles

The ellipticity profiles of the TNG galaxies are compared over an extended radial range with those of the ePN.S galaxies in Fig. 5.8b. There we show profiles for randomly selected subsamples of the simulated galaxies. Figure 5.8c instead shows the distribution of ellipticities at different radii for the fast and the slow rotators separately.

The observed profiles for the ePN.S SRs generally mildly increase with radius, reaching $\varepsilon \sim 0.3$ at $4R_e$. By comparison, the simulated SRs have more nearly constant ellipticity profiles. This can also be seen in the histograms of Fig. 5.8c where the ε distribution is almost unvaried between different radii.

Most of the simulated FRs have decreasing ellipticity profiles with radius, while a fraction have high ellipticity also at large radii, as also shown by the ePN.S galaxies. Thus, Fig. 5.8c

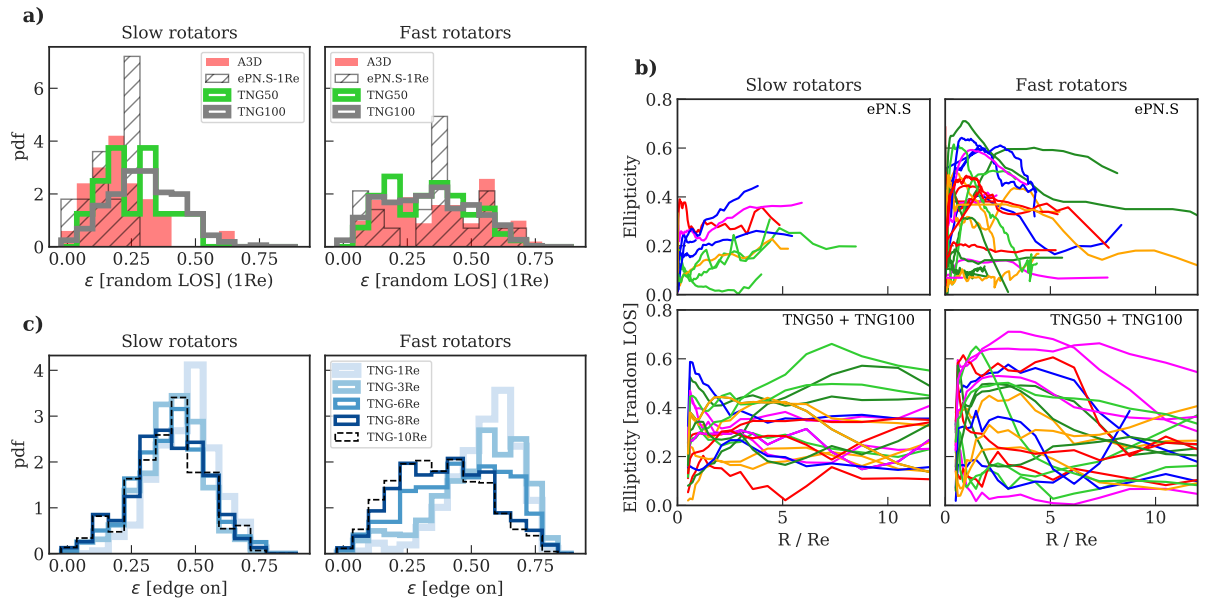

Figure 5.8: Ellipticity distribution and profiles of the selected TNG ETGs. **a)** Distribution of the random LOS $\varepsilon(1R_e)$ compared with Atlas3D and ePN.S as indicated in the legend. Despite some differences between the Atlas3D and the TNG SRs, the good agreement of FR distributions shows that the selected sample of TNG galaxies contains a mixture of disk and spheroidal galaxies consistent with Atlas3D. **b)** Ellipticity profiles for the ePN.S galaxies (top) and 10 randomly selected example galaxies from TNG100 and 10 from TNG50, projected along a random LOS (bottom). The comparison between TNG and ePN.S galaxies highlights the variety of projected ellipticity profiles in both samples. **c)** Distribution of the edge-on projected ellipticity values at different radii predicted by TNG. SRs have a rather constant ellipticity distribution with radius. The FRs have a large variety of shapes at large radii as shown by the broadening of the distribution, while the shift of the peak to lower ellipticities shows the tendency of most galaxies to become rounder in their halos.

shows that at larger radii the FR ellipticity distribution peaks at smaller ε and, at the same time, it broadens.

The decrease in ellipticity of the majority of the FRs supports the idea of a change in structure of these galaxies at large radii. The large range of flattening in the stellar halos indicates a variety in the stellar halo properties. By comparison, the SRs show only small structural variations.

5.6.4 Intrinsic shape distribution of the stellar halos

In this section, we quantify the distribution of the galaxy intrinsic shapes at large radii. Here we refer to stellar halo as the outer regions of the galaxies, where the physical properties are markedly different from those of the central regions. While this region may begin at different radii in each ETG, we will see in the next section that the median triaxiality profiles for our sample reach constant values beyond $\sim 5R_e$. Hence we measure the stellar halo intrinsic shape

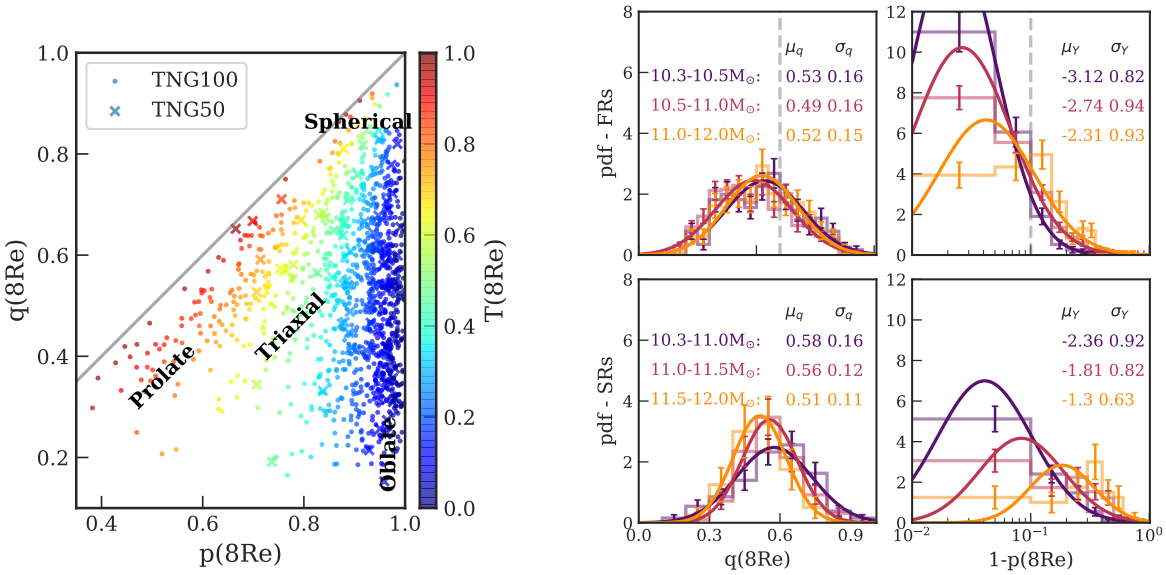

Figure 5.9: Intrinsic shape distribution of ETG stellar halos in TNG. **Left**: Minor to major axis ratio q versus intermediate to major axis ratio p coloured by triaxiality as measured at $8R_e$. TNG50 and TNG100 galaxies are shown with different symbols as in the legend. **Right**: Intrinsic shape distribution for the halos ($r \sim 8R_e$) of the FRs (top panels) and SRs (bottom panels) in mass intervals, shown with different colors as indicated in the figure. The fitted functions are shown with solid lines, and the fitted parameters are reported in the legend. The vertical dashed lines show the comparison with the photometric model used in Pulsoni et al. (2018) to reproduce the observed photometric twists and average ellipticities for the ePN.S survey. Most low-mass TNG galaxies have near-oblate stellar halos (top), changing towards more triaxial shapes with increasing stellar mass (bottom panels).

distributions by deriving the intrinsic axes ratios in a shell around 8 R_e, 1.5$R_e$thick, which is the maximal radius at which also the lowest mass systems contain enough particles to reliably measure intrinsic shapes, see Sect.5.4.1. Different choices of the shell thickness, or slightly different choices of the radius (for example 7 instead of 8R_e) at which we measure p and q deliver similar results.

The top panel of Fig. 5.9 shows the minor to major axis ratio q as a function of the intermediate to major axis ratio p: we find a large variety of possible shapes, from very flat near-oblate with $q \sim 0.3$, to prolate with $q \sim p \sim 0.5$. The majority of (low-mass) galaxies appear to have near-oblate stellar halos, with a large scatter in minor to major axis ratio q. The bottom panels of Fig. 5.9 show the intrinsic shape distributions for the fast and slow rotators separately. The distributions of the minor to major axis ratio q resemble Gaussians and fitted as such, the FRs have mean $\mu_q \sim 0.5$ and dispersion $\sigma_q \sim 0.16$ in all stellar mass bins. The SRs have $\mu_q \sim 0.6$ and $\sigma_q \sim 0.15$, with a tendency for the highest mass galaxies to be flatter.

The distribution of the intermediate to major axis ratio p can be approximated by a log-normal distribution in $Y = \ln(1 - p)$. The shape of this distribution shows a dependence on stellar mass: at higher stellar masses μ_Y increases, together with the width of the distribution. This means that at higher stellar masses, in both the FR and SR classes, the fraction of near-oblate galaxies with $p \sim 1$ decreases.

The vertical dashed lines in Fig. 5.9 shows the comparison with the photometric model used by Pulsoni et al. (2018) to reproduce the distribution of maximum photometric twists versus mean ellipticity of the observed FRs. Their model parameters, $\mu_q = 0.6$ and $\mu_p = 0.9$, are within 1σ of the mean values obtained from the distribution of simulated FRs.

5.6.5 Triaxiality profiles

We can study how the intrinsic shapes of galaxies vary as a function of radius by looking at their triaxiality profiles. We recall from Sect. 5.4.1 that because of the error due to resolution effects in the central regions, T profiles are considered well-defined only beyond $r = 9r_{\rm soft}$, where their error $\Delta T \sim 0.2$ for typical FR axis ratios (App.5.B). Thus we show profiles only for $r > 3.5R_e$ for the lowest mass objects, and for $r > 1.16R_e$ for galaxies with $M* \sim 10^{11} M_\odot$.

The left panels of Fig. 5.10 show the median triaxiality profiles for FRs and SRs. These median profiles were built by binning the galaxies according to their values of the triaxiality parameter T at 8R_e, and are plotted against the intrinsic major axis distance r. The scale radius R_e that normalizes the three dimensional radius is the 2D projected effective radius for the edge-on projection of each galaxy. The right panels show the median of the distribution of the triaxiality parameter measured at 8$R_e$as a function of the stellar mass.

FRs are characterized by increasing T profiles, which tend to plateau at $r > 5R_e$ where the TNG galaxies show a broad range of intrinsic shapes despite all having near-oblate centers. SRs tend to have flatter profiles.

We find that the stellar halo intrinsic shape distribution is a function of stellar mass. This is visible in the right hand side of Fig. 5.10, for FRs and SRs separately. At lower masses the TNG galaxies have preferentially near-oblate shapes, with $T \lesssim 0.2$, but at larger masses the median triaxiality parameter increases, so that at $M_* > 10^{11} M_\odot$ there is a non-negligible fraction

of galaxies with prolate-triaxial halos, even among the FRs. We note a systematic difference between TNG50 and TNG100 in the triaxiality of the SR stellar halos. In TNG50, the SRs tend to be much more oblate, indicating some higher degree of dissipation involved in their evolution compared to the SRs in TNG100. The statistical significance of this difference is marginal since TNG50 contains only 14 SRs.

5.6.6 Photometric twists and triaxiality in TNG ETGs

Isophotal twists in photometry are generally considered to be signatures of triaxiality. This is because the projection on the sky of coaxial triaxial ellipsoids with varying axis ratios approximating the constant luminosity/mass surfaces of ETGs can result in twisting isophotes (e.g., Benacchio & Galletta 1980). However, the effects of triaxiality on the $PA_{\rm phot}$ profiles are model dependent, that is they depend on axis ratio, on how much the axis ratios changes with radius, as well as on the viewing angles.

Figure 5.11 shows the distribution of maximum photometric twist, that is, the maximum variation of $PA_{\rm phot}(R)$, measured between 1 and 8 $R_{\rm e}$, as a function of the halo triaxiality at 8 $R_{\rm e}$, where the triaxiality profiles have reached a constant value. Each symbol in the diagram is color coded by the median projected ellipticity between 1 and 8 $R_{\rm e}$. Galaxies with ellipticity lower than 0.1 have the photometric position angle poorly determined, and are shown with smaller symbols.

We observe that the amplitude of the photometric twists is only weakly dependent on the triaxiality. Near-oblate and near-prolate galaxies are slightly less likely to have constant $PA_{\rm phot}$ than triaxial galaxies, but the majority of the galaxies have small twists irrespective of $T(8R_{\rm e})$. This is explained by the fact that large twists can be measured for viewing angles close enough to face-on (Pulsoni et al. 2018, that is lower ellipticities in Fig. 5.11), at which even small values of T can produce large twists. From Fig. 5.11, we conclude that the amplitude of the photometric twists is a poor indicator for galaxy triaxiality and that very small photometric twists are intrinsically compatible with triaxial shapes.

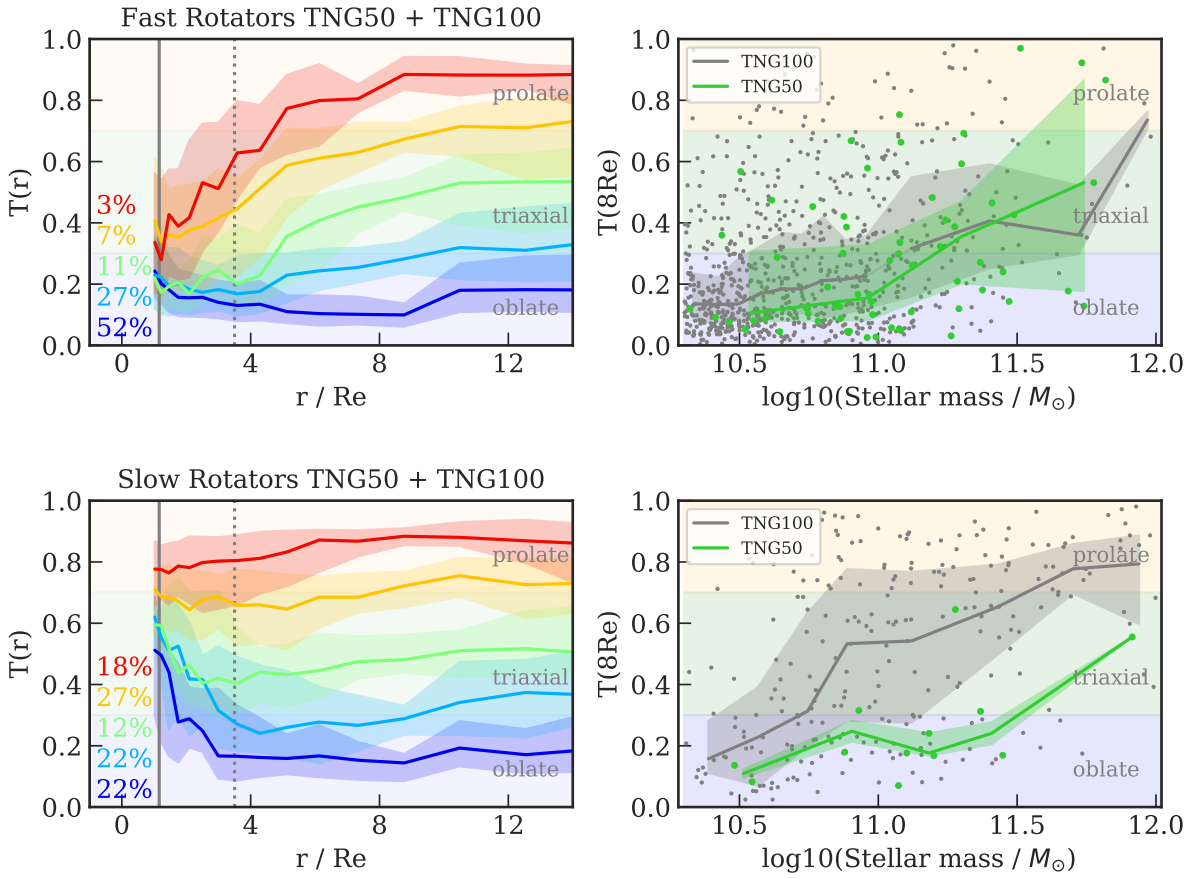

Figure 5.10: **Left panels**: Median triaxiality profiles for the fast rotators (top) and the slow rotators (bottom). The numbers on the left indicate the percentage of FRs or SRs populating each profile. The vertical dotted lines show $r = 9r_{\rm soft}$ for TNG100 galaxies with $M_* \sim 10^{10.3} M_\odot$, the solid lines show $r = 9r_{\rm soft}$ for TNG100 galaxies with $M_* \sim 10^{11} M_\odot$. At radii larger than these the profiles are not affected by resolution issues. **Right panels**: Median of the stellar halo triaxiality distribution measured at $8R_{\rm e}$as a function of stellar mass. The shaded areas are contoured by the 25th and 75th percentiles of the distribution. TNG100 and TNG50 are shown separately, FRs are on top, SRs on the bottom. On average the triaxiality parameter increases with radius and with stellar mass. The FRs have increasing $T(r)$ profiles, while SRs have either constant or decreasing profiles.

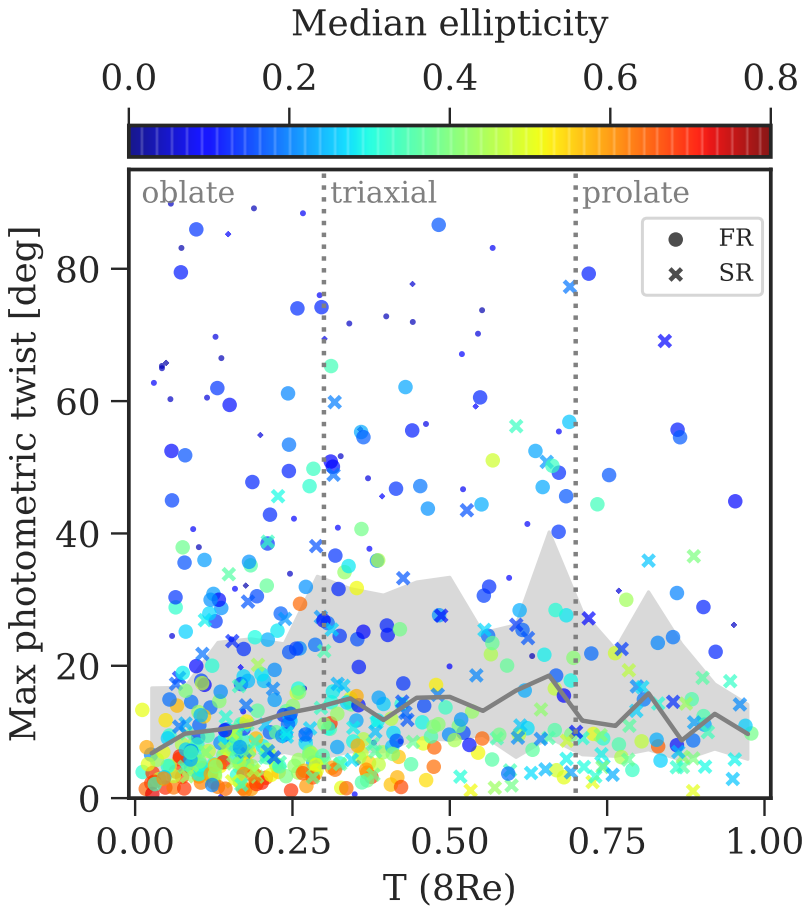

Figure 5.11: Maximum measured photometric twist between 1 and 8 $R_e$as a function of the halo triaxiality $T(8R_e)$ for the TNG50 and TNG100 galaxies projected along a random LOS. FRs and SRs are shown with different symbols as in the legend. Smaller symbols are used to represent galaxies with ellipticity < 0.1, for which the errors on PA_{phot} are large. The color-bar indicates the median ellipticity measured between 1 and $8R_e$. The gray solid line shows the median of the photometric twist distribution as a function of $T(8R_e)$; the shaded area encloses the 25th and 75th percentiles. The amplitude of the photometric twists in TNG galaxies is only weakly dependent on the triaxiality parameter.

5.7 The kinematics properties

In this section, we study how the kinematic properties of the TNG galaxies vary with radius. In Sect. 5.7.1, we derive median differential $\lambda(R)$ profiles to quantify the variety of kinematic behaviors in the outskirts of FRs and SRs. Sections 5.7.2 and 5.7.3 compare the shapes of the $V_{\rm rot}/\sigma$ profiles of the simulated ETGs with the observed galaxies in the Atlas3D and ePN.S surveys. Finally, Sect. 5.7.4 uses the simulated galaxies to assess kinematic misalignments and twists as signatures of triaxial shapes in galaxies.

5.7.1 Lambda profiles

The top panels of Fig. 5.12 show the median differential λ profiles for FRs and SRs in their edge-on projection. Galaxies are binned together according to the shape of their profiles. We achieve this by binning the FRs according to their values of λ at $R = 4R_{\rm e}$ and at $R = 8R_{\rm e}$. For the SRs the shape of the $\lambda(R)$ profiles is generally a monotonic function of R: in this case we binned the profiles according to their $\lambda(7R_{\rm e})$.

Most of the FRs reach their maximum $\lambda(R)$ around $3R_{\rm e}$; only 7% of the galaxies increase $\lambda(R)$ between 3 and 10 $R_{\rm e}$. FRs divide almost evenly among a third (34%) that have flat λ profiles with $\lambda(8R_{\rm e}) > 0.6$, a third (40%) with gently decreasing profiles and $0.3 > \lambda(10R_{\rm e}) \geq 0.6$, and another third (26%) with very low rotation in the halo ($\lambda(10R_{\rm e}) \leq 0.3$).

The SRs essentially divide between a half (53%) with non-rotating halos ($\lambda(7R_{\rm e}) < 0.2$) and a half with increased rotational support at large radii compared to the central regions. We observe that a small fraction of the SRs (5% of the TNG100 SRs and 15% of the TNG50 SRs) reach very high values of λ at large radii ($\lambda(7R_{\rm e}) > 0.6$). The majority of these galaxies are genuine slow rotators with strongly rotating halos similar in terms of velocity fields and λ profiles to observed SRs like NGC 3608 (Pulsoni et al. 2018). The others are galaxies with a clear extended disk structure characterized by rapid rotation and low velocity dispersion, but whose central kinematics is dominated by a non-rotating bulge. There are no observed counterparts for the latter in both the ePN.S (33 galaxies) and the SLUGGS surveys (Foster et al. 2016, 25 galaxies, of which 18 are in common with ePN.S). A larger sample of galaxies with extended kinematic data would be needed to confirm or rule out these objects.

For the SRs we note a mismatch in the amount of halo rotational support between TNG50 and TNG100, analogous to the difference observed for the halo triaxiality (Sect. 5.6.5): on average TNG50 SR halos rotate faster and have more oblate shapes. These differences in halo properties might be due to the dependence of the galaxy formation model on the resolution of the simulations, although the number of SRs in TNG50 (only 14 galaxies) is too small to draw strong conclusions.

For both FRs and SRs, and in both TNG50 and TNG100, the stellar halo rotational support depends weakly on stellar mass up to $M_* \sim 10^{11.3} M_\odot$ (Fig. 5.12). However, at high stellar masses the fraction of galaxies with significant rotation in the halo decreases, so that at $M_* > 10^{11.5} M_\odot$ most of the galaxies have non rotating halos. The broad range of possible $\lambda(R)$ profile shapes in Fig. 5.12 shows that the IllustrisTNG simulations encompass, if not exceed, the observed variety

of halo rotational support found in the ePN.S survey, of which one of the key results was the large kinematic diversity of stellar halos.

5.7.2 Simulated versus observed rotation profiles - central regions

Figure 5.13 shows the median $V_{\rm rot}/\sigma$ profiles of the TNG100 and TNG50 galaxies compared with median profiles from Atlas3D and individual galaxy profiles from the ePN.S sample for $0 \leq R \leq 4R_{\rm e}$. Here we normalize the radii by the circularized $R_{\rm e}$, i.e. $R_{\rm e}\sqrt{1-\epsilon(1R_{\rm e})}$, for an appropriate comparison with the Atlas3D $R_{\rm e}$.

The profiles of the simulated SRs are similar to the observed profiles. The FRs instead show a difference in how quickly $V_{\rm rot}/\sigma$ rises with radius: observed FR galaxies have on average more steeply rising $V_{\rm rot}/\sigma$ profiles than the simulated ETGs. Very few TNG FRs reach $V_{\rm rot}/\sigma \geq 1$ within $1R_{\rm e}$ compared to the Atlas3D galaxies, and almost none exceeds $V_{\rm rot}\sigma(1R_{\rm e}) = 1.5$ in either TNG100 or TNG50.

The different shapes of the $V_{\rm rot}/\sigma$ profiles in observations and simulations cannot be explained with resolution effects, as in both TNG50 and TNG100 the $V_{\rm rot}/\sigma$ profiles tend to peak at a median radius of $R \sim 3R_{\rm e}$. By comparison, the ePN.S FRs tend to peak at smaller fractions of $R_{\rm e}$, at a median $1.3R_{\rm e}$.

This difference between the observed and simulated FRs is not a consequence of the selection functions of the samples. The TNG galaxies are selected according to color, mass and intermediate to major axis ratio p. The selection in p removes centrally elongated galaxies, most of which have intermediate to low $\lambda(1R_{\rm e})$ (Fig. 5.5). The Atlas3D sample, selected as described in Sect. 5.3, has some of the disk galaxies removed which as in MANGA (Fig. 5.5) will be mostly located at high $\lambda(1R_{\rm e})$. We recall that in the comparison we consistently matched the color selection and mass range of the Atlas3D sample to the selection criteria adopted for the TNG galaxies. Thus the TNG sample should in principle contain a larger number of late type galaxies with strong disks, i.e. high $V_{\rm rot}/\sigma$, by comparison with Atlas3D. Figure 5.13 shows instead that the TNG100 and TNG50 ETG samples lack galaxies with high rotational support at $1R_{\rm e}$.

In Sect. 5.6.1 we discussed that the effective radii used to normalize the radial scales in TNG would be expected to be systematically slightly overestimated compared to the observed $R_{\rm e}$since they are defined using the total bound stellar mass which is often inaccessible in observations. If taken into account, this effect would increase the gap between simulated and observed samples. On the other hand, since the mass-size relation is roughly reproduced in the simulations (Fig. 5.7), the different steepness of the $V_{\rm rot}/\sigma$ profiles in observations and simulations implies a different distribution of the angular momentum as a function of radius in the simulated galaxies. This could be due to a too efficient condensation of the gas into stars that does not allow the gas to dissipate and collapse to small enough radii.

5.7.3 Simulated versus observed profiles - outskirts

Figure 5.14 compares the relation between $V_{\rm rot}/\sigma$ in the central regions and $V_{\rm rot}/\sigma$ in the stellar halos for the simulated and observed galaxies. The observed galaxies are from the ePN.S survey (Pulsoni et al. 2018, their figure 9) and are reported in the top left panel. Their measurements

use absorption line data at $1R_e$ and PN data for the halos, which on average cover $6R_e$ with a large scatter (minimum $3R_e$, maximum $13R_e$). The central and right top panels show $V_{rot}/\sigma(6R_e)$ versus $V_{rot}/\sigma(1R_e)$ for TNG100 and TNG50 ETGs, respectively. Galaxies close to the dashed 1:1 lines show similar rotational support in the central regions and in the outskirts; galaxies below the lines have increased rotational support in their stellar halos; galaxies above the lines instead have reduced rotation at large radii.

The position of the observed SRs below the one-to-one line is reproduced by the simulations. As already discussed in Sect. 5.7.1, there are a few outliers among the simulated SRs with $V_{rot}/\sigma(6R_e) \gtrsim 1$, some of which are actually extended disks with prominent bulges at the center. These represent a small fraction of the SR family and do not have observed counterparts in the ePN.S and SLUGGS surveys.

For the TNG FRs, we find a different distribution when comparing rotational support at the same radii: most of these galaxies fill the bottom half of the diagram, with very few reaching $V_{rot}/\sigma(1R_e) > 1.5$, and a large fraction having significant V_{rot}/σ at $6R_e$. This difference is explained by the shallower $V_{rot}/\sigma(R)$ profiles of the simulated galaxies compared to the observed FRs, as discussed in Sect. 5.7.2. Since the simulated galaxies tend to peak at larger radii than the observed ETGs, there are almost no objects that reach $V_{rot}/\sigma > 1.5$ already at $1R_e$.

In the bottom panels of Fig. 5.14 we show the comparison at adjusted radii: $V_{rot}/\sigma(3R_e)$ (i.e. at the median radius where the TNG V_{rot}/σ profiles tend to reach the maximum) versus $V_{rot}/\sigma(8R_e)$ (i.e. where the decreasing rotation profiles finally reach their minimum, see also Fig. 5.12), and find better agreement. Now the FRs spread in the region of the diagram above the one-to-one line as they do for the ePN.S observations in the top left panel of Fig. 5.14, with a sub-population of objects showing $V/_{rot}\sigma(8R_e) > V/\sigma(3R_e)$. We note that FRs with near-prolate stellar halos occupy mostly the lower left corner with low $V_{rot}/\sigma(3R_e)$ and low $V_{rot}/\sigma(8R_e)$. Galaxies with triaxial halos tend to distribute on the left side of the diagram, galaxies with oblate halos tend to have higher $V_{rot}/\sigma(8R_e)$. It is interesting that, aside for the differences in the central regions at $R \lesssim 3R_e$, the observed galaxies with and without signatures for triaxial stellar halos distribute similarly as the simulated triaxial and near-oblate stellar halos, respectively, with the triaxial halos having on average lower $V_{rot}/\sigma(8R_e)$.

From Fig. 5.14, we conclude that even though the quantitative details between simulated and observed ETGs galaxies do not agree, the simulations do reproduce the observed kinematic transitions between central regions and outskirts, as well as the variety of halo kinematic classes.

5.7.4 Relation of kinematic misalignments and twists with triaxiality in TNG ETGs

Kinematic signatures of galaxy triaxiality can be found from observations of minor axis rotation, kinematic twists, and misalignment of the kinematic position angle PA_{kin} with the photometric PA_{phot} (see e.g. Binney 1985; Franx et al. 1991).

Figure 5.15 shows the distribution of misalignments $\Psi = PA_{kin}(1R_e) - PA_{phot}(1R_e)$ as a function of the ellipticity for the random LOS projected TNG galaxies. The solid lines show the unweighted root-mean-square deviation from zero of the data points as a function of the elliptic-

ity for the FR and the SR classes separately, computed by mirroring the data points around zero (i.e. using $[\Psi, -\Psi]$). The dashed lines show the same quantities for observed galaxies in Atlas3D and MANGA (Krajnović et al. 2011; Graham et al. 2018). Simulated and observed galaxies show very similar trends with ellipticity, with very flat galaxies being strongly aligned, and kinematic misalignment increasing with rounder shapes. Simulated FRs are found to be much more aligned than SRs, in agreement with observations.

Data points in Fig. 5.15 are color-coded according to the intermediate to major axis ratio p at $1R_e$. At these radii the errors on the axis ratios are at most 0.1 for the low mass systems (see App.5.B), so $p(1R_e)$ measurements are generally well defined. We find that many TNG galaxies, both SRs and FRs show a high degree of alignment ($|\Psi| < 10°$) even though they are far from being oblate (i.e. with $p < 0.9$). This result agrees with the analysis of Bassett & Foster (2019) of Illustris galaxies, among which they found many triaxial and prolate objects with small Ψ. Although we can not draw conclusions on the shape distribution of the real galaxies, Fig. 5.15 implies that near-alignment of the kinematic and photometric position angles does not exclude triaxiality for the IllustrisTNG FR galaxies even at $1R_e$.

Simulated FRs and SRs do show kinematic position angle variations as a function of radius. An example is the object shown in Figs. 5.1 and 5.2, a galaxy with central disk embedded in a triaxial stellar halo, which shows a variation in the direction of rotation corresponding to the sudden change in the triaxiality profile around $r \sim 5R_e$.

The top panel of Fig. 5.16 shows the distribution of the maximum kinematic twists, that is, the maximum variation of PA_{kin}, measured between 1 and 8 $R_e$for all the TNG galaxies, as a function of the stellar halo triaxiality measured at $8R_e$, i.e. where the median T profiles are constant with radius (see Fig. 5.10). We find that the large majority of TNG galaxies have small kinematic twists compared to typical measurement errors of PA_{kin} from discrete tracers (the median error for the ePN.S galaxies is $\sim 35°$). Aside for a small group of near-oblate galaxies with counter-rotating disks (twist $\sim 180°$), the main dependence of the amplitude of the twist with the triaxiality parameter is such that galaxies with high T are more likely to have large kinematic twists, as shown by the solid gray line in Fig. 5.10 representing the median twist as a function of T. This highlights the importance of kinematics as a fundamental tool to investigate the intrinsic structure of galaxies besides photometry alone (see Sect. 5.6.6). On the other hand Fig. 5.10 points out that not all the triaxial and prolate galaxies in IllustrisTNG display kinematic twists. This suggests that also in observations a galaxy's triaxiality may not be easily revealed by kinematic misalignments.

IFS kinematics show that the central regions of FR have PA_{kin} and PA_{phot} aligned within ~ 10 degrees, while SRs are generally misaligned (Krajnović et al. 2011; Fogarty et al. 2015; Ene et al. 2018; Graham et al. 2018). This difference in the misalignment distribution was interpreted as signature of a different intrinsic shape distribution for the two classes, with the FRs being consistent with having oblate shapes, and the SRs being moderately triaxial. This interpretation is not supported by the results in Fig. 5.15.

Even though the central regions of FRs have been found to have PA_{kin} well aligned with PA_{phot}, kinematic twists are observed in the halos. By extending the kinematic study at larger radii using planetary nebulae, Pulsoni et al. (2018) found that kinematic twists are relatively frequent in the ePN.S sample of FRs ($\sim 40\%$). They concluded that if the central regions of FRs

are oblate, kinematic twists would indicate a transition to halos with triaxial shapes.

In the bottom panel of Fig. 5.16, we compare the distribution of kinematic twists in the IllustrisTNG galaxies with the observed distribution in the ePN.S sample. To do that we match the TNG mass function to that of the ePN.S sample by randomly selecting the appropriate fraction of TNG galaxies in mass bins. The filled green histogram in Fig. 5.16 shows the distribution of kinematic twists for 100 random realizations of PNS-like samples extracted from the TNG galaxies. We then convolved the resulting distribution with a Gaussian error of 35 degrees, which is the median error of the ePN.S measurements (gray histogram). We find that the simulated galaxies show a similar distribution as the ePN.S galaxies, although there is an indication for a lower fraction of galaxies with large kinematic twists in IllustrisTNG. This might be due to a different sample selection between simulations and ePN.S, with the former potentially containing a larger fraction of disk galaxies even after the matching of the mass functions. Figures 5.4 and 5.8a in fact show that the ePN.S sample is on average more massive and contains rounder galaxies than TNG100.

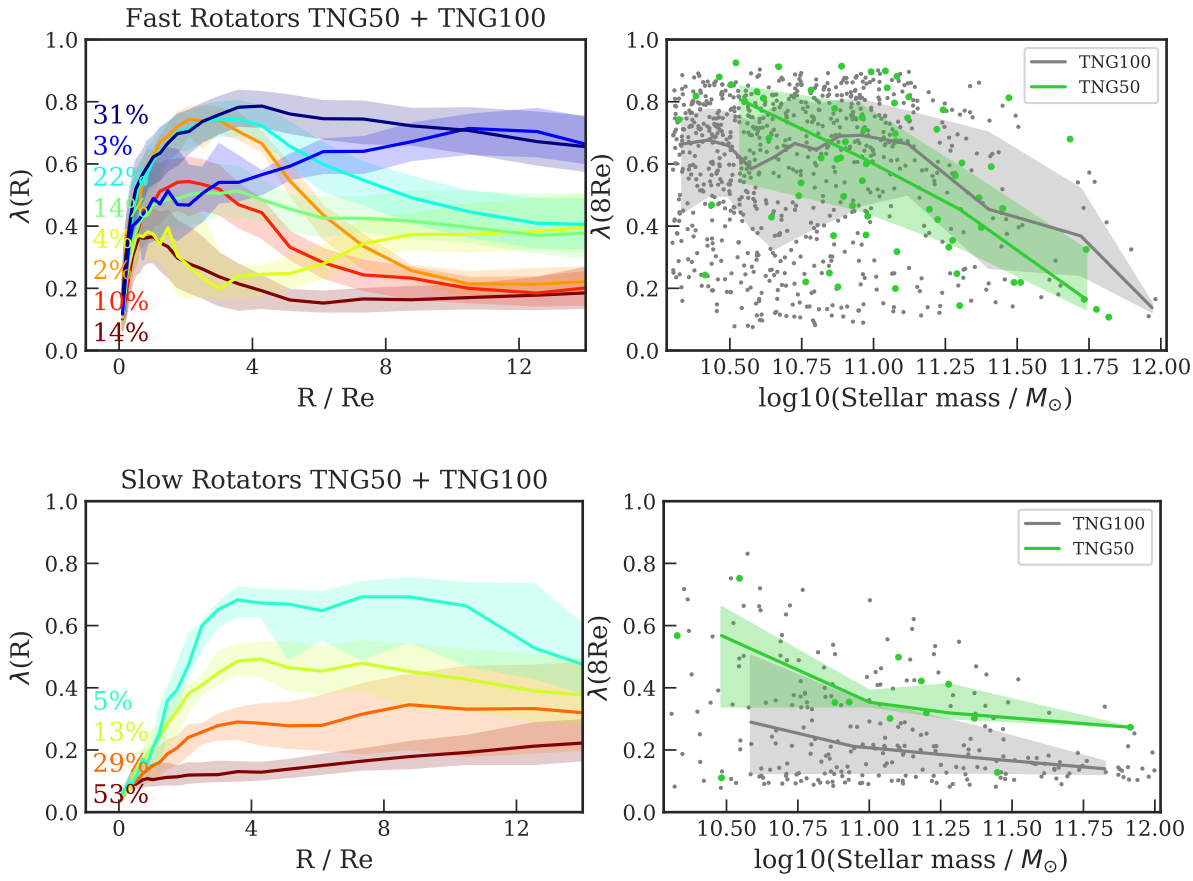

Figure 5.12: **Left**: Median λ profiles for fast rotators (upper left) and slow rotators (lower left panel) in their edge on projection. The median profiles are built by binning the galaxies according to the shape of their λ profiles; see text. The shaded areas are bounded by the 25th and 75th percentiles of the distributions. The numbers on the left indicate the percentage of FRs or SRs populating each profile. **Right**: Distribution of $\lambda(8R_e)$ for the full sample, as a function of stellar mass. FRs and SRs are shown separately, as well as TNG50 and TNG100. FR galaxies show a large variety of λ profiles, whereas SRs have either constant or increased λ in the stellar halo. Overall the halo rotational support decreases at high stellar masses.

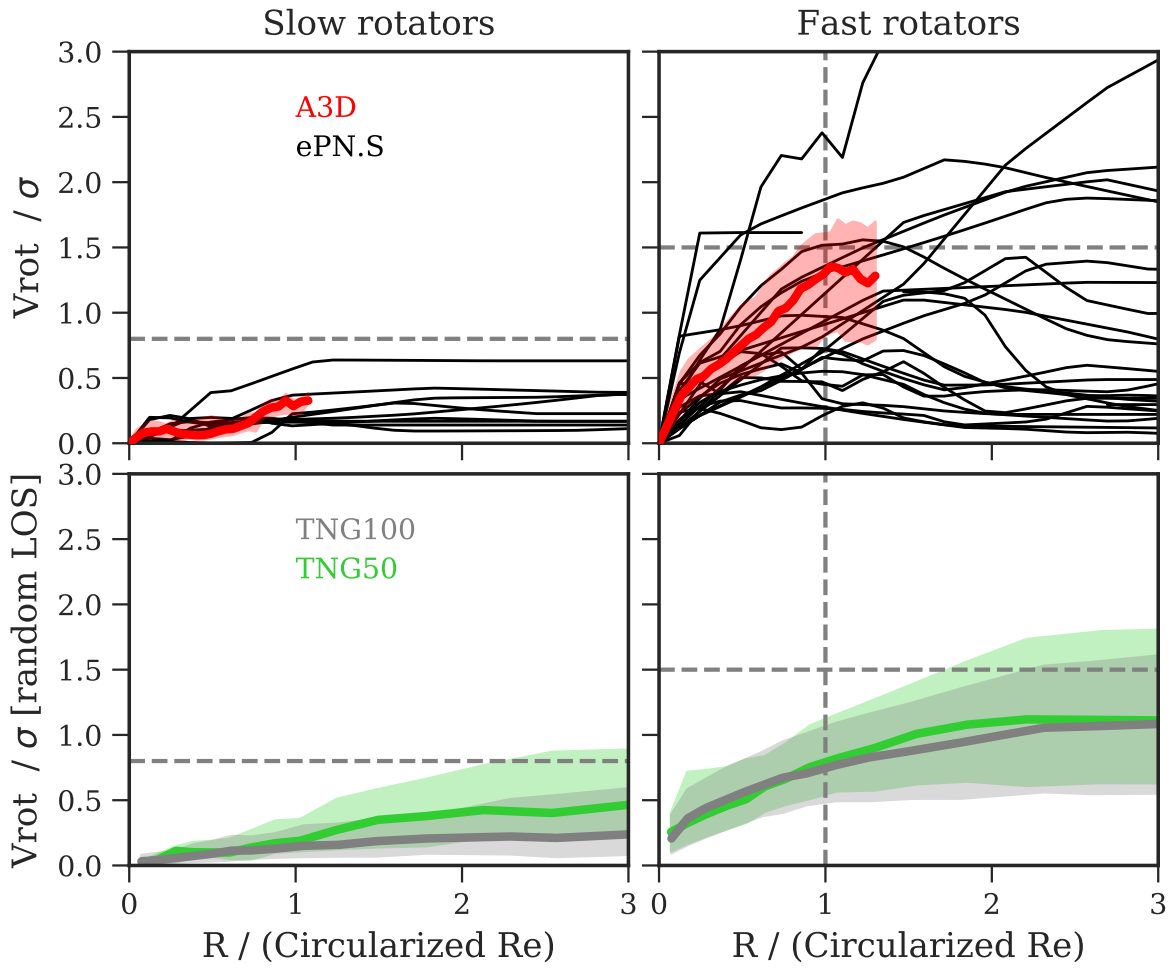

Figure 5.13: Median $V_{\rm rot}/\sigma$ profiles for slow rotators (left) and fast rotators (right panels). **Top**: Observations from Atlas3D and ePN.S. For the former we show median profiles and shaded areas bounded by the 20th and the 80th percentiles of the distribution. For the ePN.S galaxies we show individual profiles. **Bottom**: Median profiles and 20%-80% distributions for the TNG50 and TNG100 ETGs, projected along a random LOS. Vertical and horizontal dashed lines are for guiding the eyes in comparing top with bottom panels. This shows that the average $V_{\rm rot}/\sigma$ profiles of the simulated ETGs are shallower than the observed profiles.

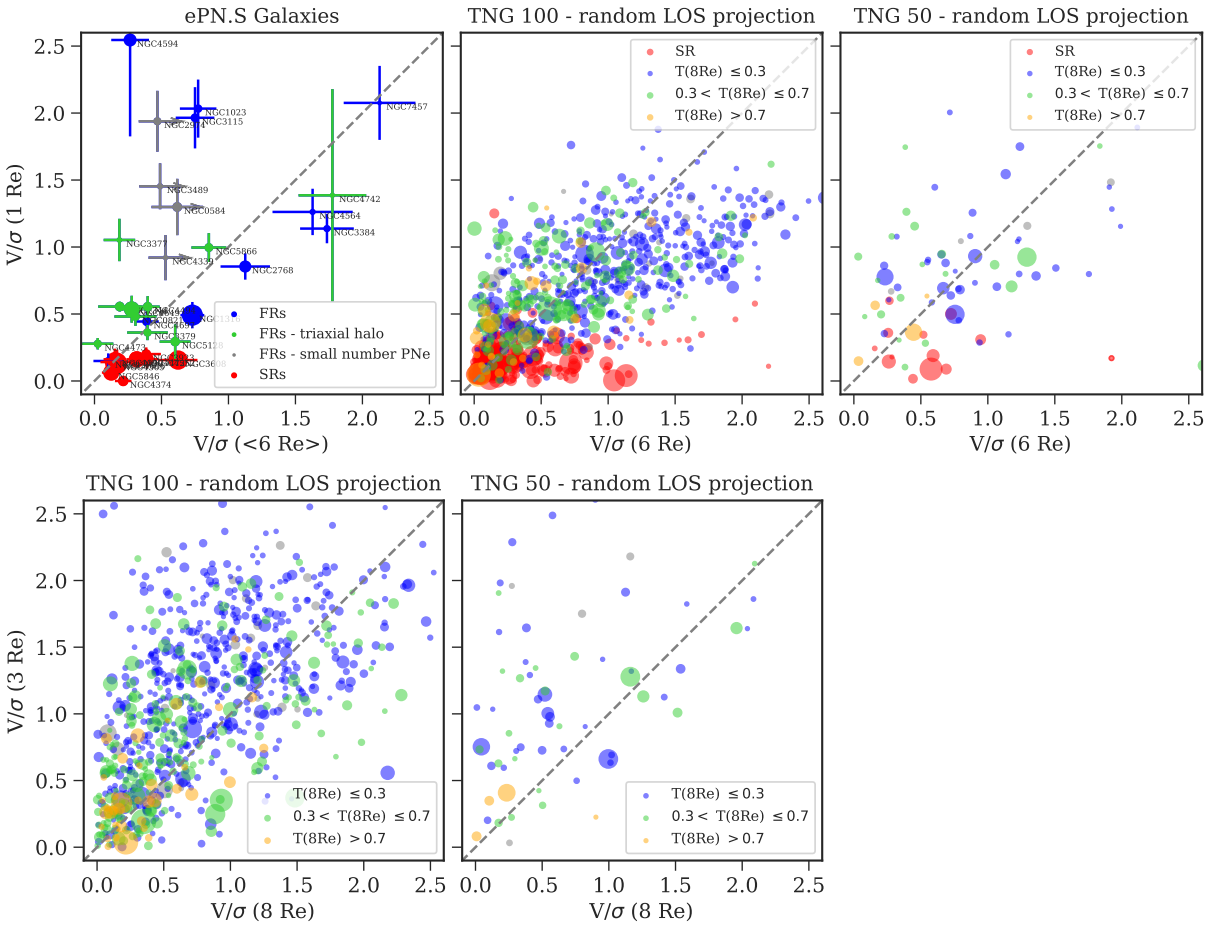

Figure 5.14: V/σ ratio in the central regions compared with the V/σ at large radii. **Top**: $V/\sigma(1R_e)$ versus $V/\sigma(6R_e)$ for the ePN.S galaxies (left), TNG100 (middle), and TNG50 (right). **Bottom**: $V/\sigma(3R_e)$ versus $V/\sigma(8R_e)$ for TNG100 (left) and TNG50 (right). Different colors in the ePN.S sample mark the SRs (in red), the FRs with kinematic signatures for triaxial halos (i.e. with kinematic twists or misaligments, in green), and FRs with PA_{kin} aligned with PA_{phot} (in blue). The gray points stand for ePN.S FRs for which the measured $V_{rot}/\sigma(< 6R_e >)$ is a lower limit. For the simulated galaxies the different colors mark SRs, and FRs with different halo $T(8R_e)$: FRs that have near-oblate halos (in blue); FRs with triaxial halos (in green); near-prolate FRs (in orange). The gray symbols show simulated galaxies with too few particles at $8R_e$ for measuring T. The size of the data points is proportional to the stellar mass. The gray dashed lines show the 1:1 relation. The TNG simulations reproduce the diversity of observed ETG halo kinematics and they echo the observed kinematic transitions between the central regions and outskirts of the FR galaxies, albeit at larger radii.

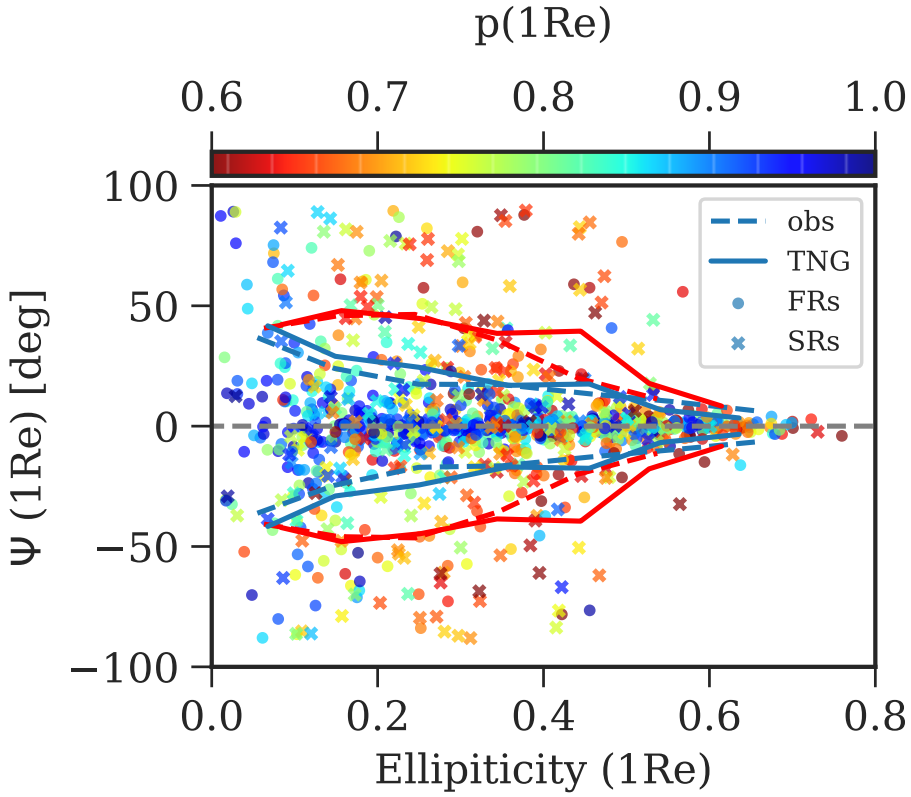

Figure 5.15: Distribution of the misalignments $\Psi = PA_{\rm kin} - PA_{\rm phot}$ at $1R_{\rm e}$ as a function of the ellipticity for both TNG100 and TNG50 galaxies. Data points are color coded according to their intermediate to major axis ratio $p(1R_{\rm e})$; open symbols are SRs, filled symbols are FRs. The solid lines show the scatter of the misalignments as a function of the ellipticity for the TNG galaxies, calculated on the mirrored $(\Psi, -\Psi)$ data. The dashed lines show the scatter for the MANGA and Atlas3D galaxies. Red lines are for the SRs, blue lines for the FRs. The triaxiality of the IllustrisTNG FRs is consistent with the near-alignment of their kinematic and photometric position angles.

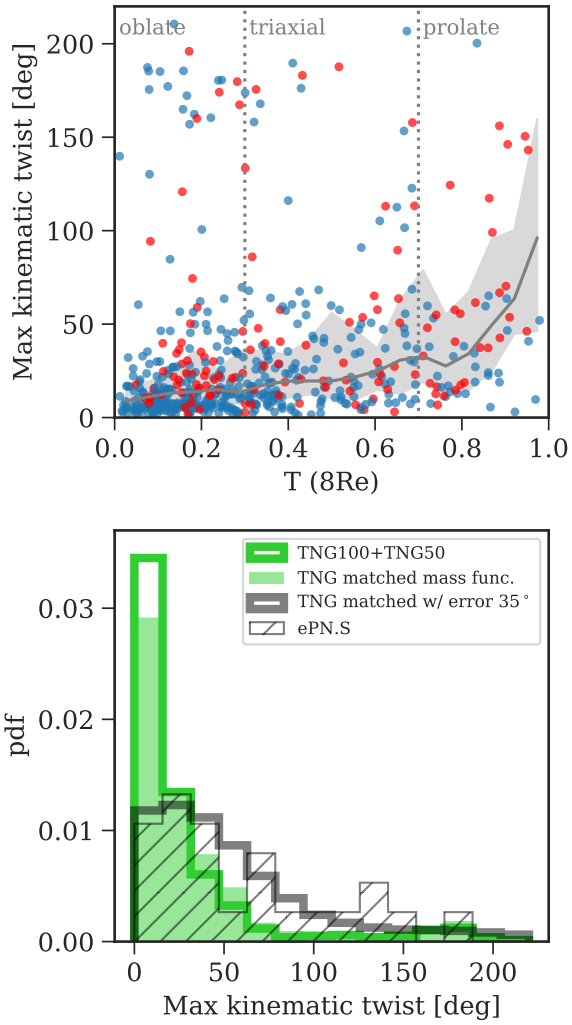

Figure 5.16: **Top**: Maximum kinematic twist measured between 1 and 8 $R_e$as a function of the stellar halo triaxiality $T(8R_e)$. FRs are shown in blue, SRs in red; both TNG50 and TNG100 samples are shown. The gray line and shaded band show the median of the twist distribution as a function of $T(8R_e)$ and the 25th and 75th percentiles. Even though the majority of the TNG galaxies have small kinematic twists, high T galaxies are more like to display a kinematic twist. **Bottom**: Distribution of the maximum kinematic twist for the TNG50 and TNG100 samples (green step histogram) compared with the ePN.S sample (hatched histogram). The filled green histogram shows the distribution of the TNG galaxies after their mass function is matched to that of the ePN.S sample; the gray histogram is the mass-matched TNG distribution convolved with a measurement error and is consistent with the data.

5.8 Stellar halo angular momentum and shape

In Sect. 5.7.3, we observed that the rotational support in the stellar halo correlates with the intrinsic shape: stellar halos with high $V_{\rm rot}/\sigma$ are likely near-oblate, while halos with lower $V_{\rm rot}/\sigma$ can have larger triaxiality. In this section we connect the variation of rotational support in the stellar halos to variations of their intrinsic shape.

The top panel of Fig. 5.17 shows the differential $\lambda(R)$ (measured for the edge on projection), the axis ratio $q(r)$, and the triaxiality parameter profile $T(r)$ for an example galaxy. It has a decreasing $\lambda(R)$ profile in the halo, while $q(r)$ and $T(r)$ increase: for this object the decreased rotational support marks a variation in the intrinsic shape of the galaxy from relatively flat and near-oblate at $R \sim 2R_{\rm e}$, where the rotation is highest, to triaxial spheroidal in the outskirts. In observations the drop in rotation of the ePN.S FRs is often related to a decrease in ellipticity. This led to the idea that central fast rotating regions of FRs are embedded in a more dispersion dominated spheroidal stellar halo.

We verify this conclusion in Fig. 5.17. Here the outskirts of galaxies are divided into 6 ellipsoidal shells of major axis r between 3.5 to $8R_{\rm e}$. This radial range is motivated by the requirement that r is large enough so that the errors on the T parameter are small for galaxies of all masses, but also such that most of the galaxies (96%) have enough particles at large radii ($8R_{\rm e}$) in order to measure their intrinsic shapes. In each ellipsoidal shell of major axis r and width Δr we measure the axis ratio q and the triaxiality parameter. Then we measure the edge on projected $\lambda(R)$ in an elliptical shell of major axis $R = r$ and width $\Delta R = \Delta r$. Figure 5.17 shows the halo edge-on projected $\lambda(R)$ for all shells and all TNG galaxies in four galaxy stellar mass bins, as a function of the minor to major axis ratio $q(r)$ and of the triaxiality parameter $T(r)$.

We find indeed a relation between λ and shape. High rotational support is related to flattened (i.e. low q) near-oblate (i.e. low T) shapes. Where λ decreases q grows towards more spheroidal shapes, although the scatter in possible stellar halo shapes is large ($\sigma_q \sim 0.15$). Stellar halos of both FRs and SRs with high triaxiality generally have low λ, but lower T is compatible with all values of λ. This means that the decrease in the rotational support of the TNG FRs follows a change in the structure of the galaxies, which become more spheroidal in the outskirts. These outer spheroidal components can span all values of triaxiality. By comparison to the FRs, the SRs show smaller variations in both intrinsic shapes (Fig. 5.10) and λ.

Figure 5.17 confirms the dependence of the stellar halo intrinsic shape and rotational support on stellar mass already described in Sects. 5.6.4, 5.6.5, and 5.7.1. Lower mass galaxies host more rotationally supported stellar halos with near-oblate shapes. At progressively higher masses the fraction of dispersion dominated stellar halos increases as well as the fraction of halos with high triaxiality.

It is interesting to note that there is no clear separation in Figure 5.17 between the stellar halo properties of the FRs and SRs, but rather a continuity of properties among the two classes, with the low T-high λ extreme dominated by the FRs, the high T-low λ limit by the SRs, and the relative importance of the two populations gradually changing with stellar mass. This result implies that there is no qualitative difference between the structure of the galaxies at large radii despite the bimodality of the FR/SR classification of the centers. The IllustrisTNG galaxies agree with the ePN.S observations in that FRs and SRs tend be more similar at large radii, especially

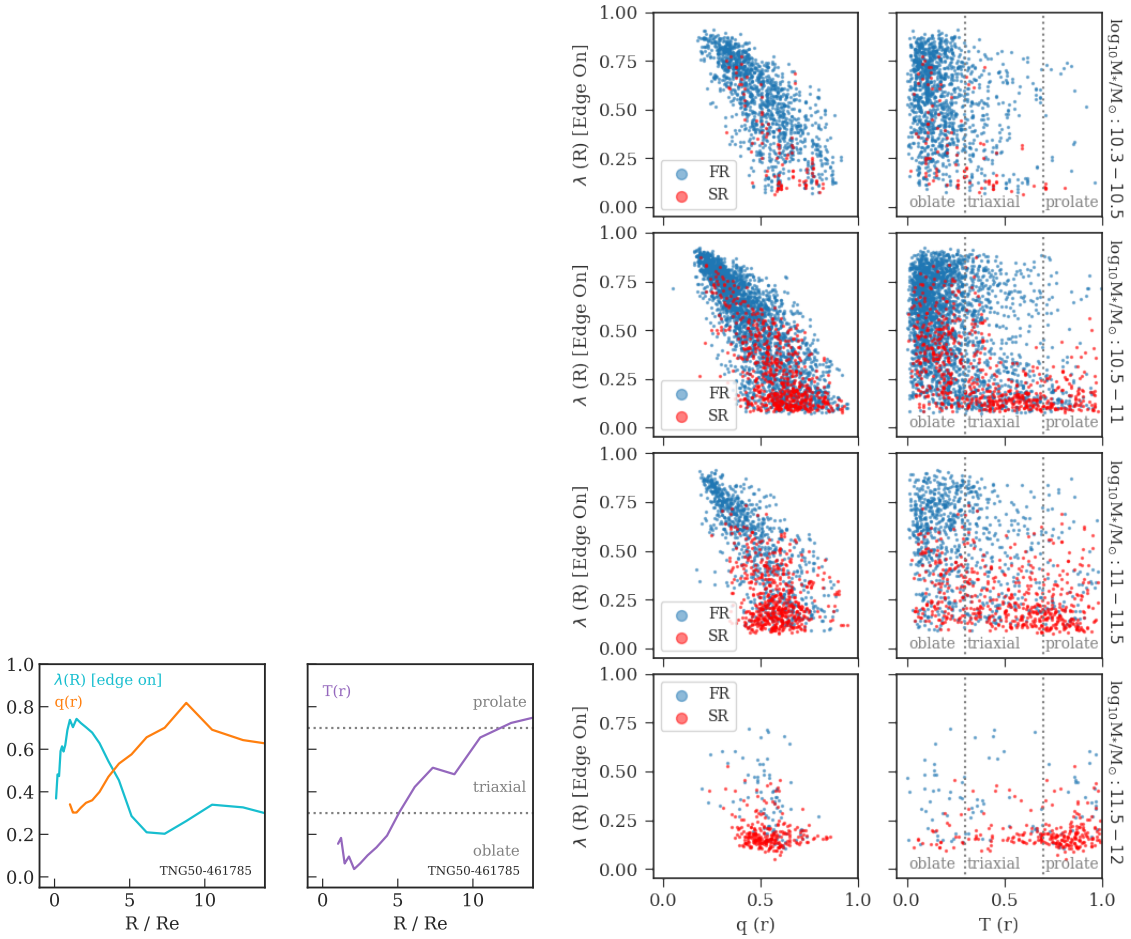

Figure 5.17: **Left**: $\lambda(R)$, axis ratio $q(r)$ and triaxiality $T(r)$ profiles for an example galaxy. **Right**: λ for the edge-on projection versus minor to major axis (left panels) and triaxiality parameter (right panels) in stellar mass bins. Each data point is a local measurement within a shell of major axis $R = r$: each TNG galaxy is represented by ~ 6 data points measured between $3.5 - 8R_e$. FRs and SRs are shown with different colors as in the legend. The mass bins are labelled on the right margins. Lower rotational support λ in the stellar halos is related to rounder shapes, with a wide range of triaxiality which depends on stellar mass. FRs and SRs exhibit a continuity in stellar halo properties rather than a bimodality.

at intermediate to high masses. The similarity of the overall shapes of the $\lambda(R)$ (or $V_{\rm rot}/\sigma(R)$) profiles and of the $\varepsilon(R)$ profiles between ePN.S and TNG galaxies described in in Sects. 5.6.3 and 5.7.3 suggests that intrinsic shape variations similar to those found in the TNG galaxies also exist in real galaxies.

5.9 Summary and conclusions

In this paper, we have analysed the kinematic and photometric properties of $\sim$ 1200 early type galaxies (ETGs) from the IllustrisTNG cosmological simulations TNG100 and TNG50, with a focus on their stellar halos. The sample of simulated ETGs was selected in stellar mass and in color (Fig. 5.3) and in the $\lambda_e - \varepsilon$ diagram (Fig. 5.5). There we excluded simulated objects that do not match the observed properties in the central regions of fast rotators (FRs) and slow rotators (SRs), and that appear as highly centrally elongated red galaxies. We verified that this does not affect our results on the stellar halo properties of the simulated galaxies. The resulting ETG sample has mass-, size-, and central kinematics distributions consistent with observations.

For the selected sample we determined mean velocity fields, kinematic, and photometric profiles, and studied the intrinsic shapes of the simulated galaxies from the central regions into their outskirts, up to $15R_{\rm e}$. The purpose of the paper is to study the kinematic properties of stellar halos and connect them to variations in the structural properties of their galaxies from the central regions to the halos. Our conclusions are as follows:

1) The differential λ profiles and the triaxiality profiles (Figs. 5.10 and 5.12) successfully reproduce the diversity of kinematic and photometric properties of stellar halos observed in the ePN.S survey.

- We find that simulated FRs divide almost evenly among a third with flat λ profiles, a third with gently decreasing profiles, and another third with very low rotation in the halo. Half of the SRs do not show any rotation in the halo, while the other half has increased rotational support at large radii.

- FRs generally tend to show increased triaxiality with radius, although the majority (partially driven by the numerous low mass fast rotators) have stellar halos consistent with oblate shapes.

- Both halo triaxiality and rotational support are found to depend on stellar mass, with higher mass galaxies being more triaxial and more dispersion dominated at large radii.

2) Halo intrinsic shape and rotational support are strongly related (Fig. 5.17):

- High λ is related to flattened oblate shapes.

- Where λ decreases with radius, galaxies tend to become rounder, but with a wide range of triaxiality.

3) The FR class in TNG shows the largest variety in stellar halo properties and the largest variations with radius in both intrinsic shapes and rotational support. Among these galaxies we can find rotationally supported stellar halos with flattened oblate shapes, as well as FRs that have central rotating disk-like structures embedded in more spheroidal components. For a subset of these the stellar halos can reach high triaxiality values. SRs, by comparison, display milder changes in structure with radius.

4) The TNG FRs exhibit shallower $V_{\rm rot}/\sigma(R)$ profiles than the Atlas3D and ePN.S galaxies (Fig. 5.13). Both TNG50 and TNG100 FRs tend to reach a peak in rotation at a median radius of $\sim 3R_{\rm e}$, compared to $\sim 1-1.3R_{\rm e}$ for the Atlas3D and ePN.S galaxies. This result implies a more extended distribution of the angular momentum with radius in the TNG galaxies than observed.

5) However, even though the $V_{\rm rot}/\sigma(R)$ profiles do not agree quantitatively between simulated and observed ETGs galaxies, the simulations do reproduce the observed kinematic transitions between central regions and outskirts. The similarity between the scaled shapes of the $V_{\rm rot}/\sigma(R)$, and the $\varepsilon(R)$ profiles between ePN.S and TNG galaxies (Figs. 5.8b and 5.14) suggests that also the observed variations in the kinematics between central regions and halos trace changes in the intrinsic structure of the galaxies.

6) We find that most of the triaxial TNG galaxies display modest photometric twists that only weakly depend on triaxiality (Fig. 5.11). For these galaxies, kinematic twists are larger (Fig. 5.16), but in many cases they are not large enough to be measured by currently available data.

7) By comparing the distributions of the minor-to-major axis ratios q, triaxiality parameters T, and angular momentum parameters λ (Fig. 5.17), we find that lower rotational support in the stellar halos is related to rounder shapes, with a wide range of triaxiality which depends on stellar mass. In this there is no qualitative difference between the FRs and SRs. Rather, despite the bimodality of the central regions, the two classes show a continuity of halo properties with the FRs dominating the low T-high λ end of the distribution and the SRs dominating in the high T-low λ extreme. The relative weight of the different sides of the distribution gradually changes with stellar mass. This is in agreement with ePN.S observations of ETG halos. In a companion paper we will investigate the dependence of the stellar halo parameters on the accretion history of galaxies and explore the relation between stellar and dark matter halo properties.

Appendix

5.A Color transformation equations

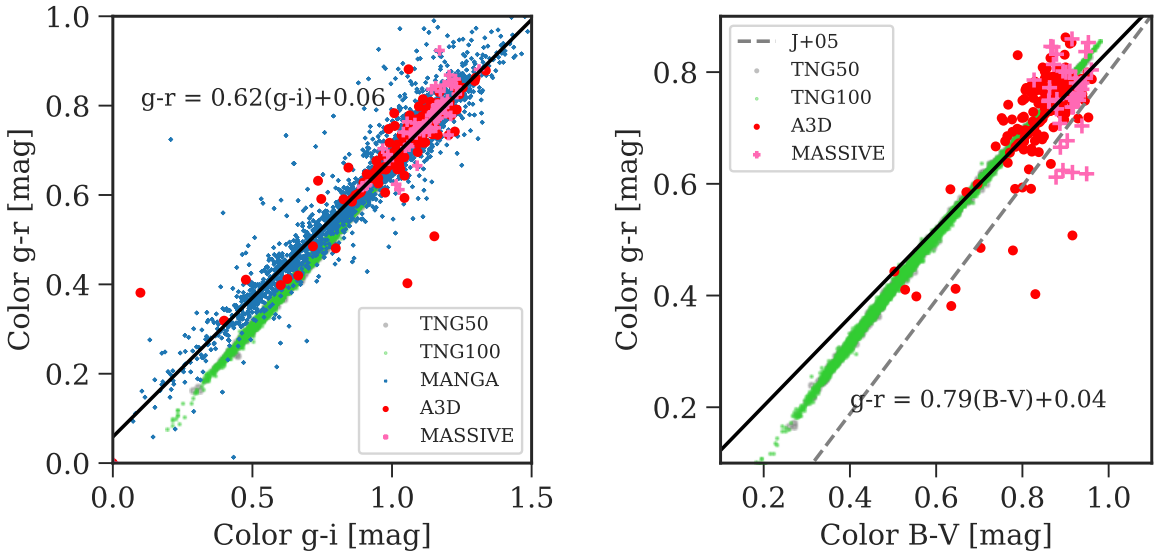

Figure 5.A.1: Relation between colors for the observed galaxies, as shown in the legend. The simulated galaxies with $M_* \geq 10^{10} M_\odot$ are also shown but without any modeling for dust attenuation, which probably explains why they tend to follow a different color relation than the observations. The solid lines show the linear fit to the observations, while the dashed line shows the color transformation equation from Jester et al. (2005).

In Sect. 5.5.1 we selected a sample of ETGs from TNG50 and TNG100 by using a cut in $g - r$ color and stellar mass, and compare with observations. Most of the observed galaxies have $g - r$ colors in the NSA catalog. For a small fraction of the observations, only $B - V$ or $g - i$ colors are available. Jester et al. (2005) published transformation equations between the SDSS and UBVRcIc magnitudes valid for stars and quasars, which provide reasonable results for galaxies. We note, however, that these transformation equations do not readily apply to the observed galaxies. In Fig. 5.A.1 we show the relation between colors in galaxies that have measured both $g - r$ and $B - V$, and $g - r$ and $g - i$. $g - r$ and $g - i$ colors are from the NSA

catalog, $B-V$ colors are from Hyperleda. We find that the observed ETGs follow the relations:

$$\begin{aligned} g-r &= 0.79(g-i)-0.04 \\ g-r &= 0.62(B-V)-0.06. \end{aligned} \tag{5.8}$$

Hence we use these derived transformation equations to transform the measured $B-V$ or $g-i$ colors in $g-r$.

5.B Accuracy on the measured intrinsic shapes and angular momentum parameter

Physical properties measured in simulated galaxies are affected by resolution effects coming from the discrete particle nature of these systems. In a collisionless dark matter-only (DMO) simulation the resolution of the gravitational potential depends on the softening length and the particle mass resolution (i.e., the number of particles), which particularly affect measurements in the central regions of the simulated systems (e.g. Power et al. 2003). In a full physics simulation instead, like TNG100 and TNG50, the resolution has additional effects on the baryon physics, which require the models to be calibrated on observations (Schaye et al. 2015; Pillepich et al. 2018b). In this section we are not concerned with the latter effects, which also have an impact on the galaxy properties. Here we aim at quantifying the effects from the resolution of the gravitational potential on shape and spin measurements at $1R_{\rm e}$ and beyond.

Chua et al. (2019) analyzed the convergence of intrinsic shape profiles in the Illustris-DMO simulation, with the procedure recommended by Zemp et al. (2011), also used in this paper and outlined in Sect. 5.4.1. From their Fig. 1, we find that the shape profiles are converged within 0.1 in both p and q already at $r \sim 2r_{\rm soft}$. Since TNG100 has similar particle resolution as Illustris-DMO (and smaller $r_{\rm soft}$), we can apply a similar convergence criterion in TNG100. We verified that the two simulations have comparable particle numbers at $r \sim 9r_{\rm soft}$, that is, where full convergence is achieved according to the prescription of Chua et al. (2019). At smaller radii, the full physics TNG100 simulation has more particles than the DMO simulation since the baryons are subjected to dissipation; hence we expect similar, if not better, convergence in TNG100.

Twice the softening radius in both TNG50 and TNG100 corresponds to a radius $\lesssim R_{\rm e}$ for all the selected galaxies (see Fig. 5.7, and note that in TNG100 we excluded the galaxies with $R_{\rm e} < 2r_{\rm soft}$ from the sample). Since $R_{\rm e}$ increases with stellar mass, the more massive systems are better resolved. For example, in TNG100 the median effective radius at $M* = 10^{11}M_{\odot}$ is $1R_{\rm e} \sim 7.8r_{\rm soft}$, where the resolution effects on both p and q are $\lesssim 0.02$. Thus the absolute error on the axes ratios p and q measured at $r = 1R_{\rm e}$ is mass dependent, and it is at most 0.1 for the low mass systems. At $r \gtrsim 9r_{\rm soft}$, which corresponds to $r \gtrsim 3.5R_{\rm e}$ at the low mass end, and to $1.16R_{\rm e}$ for $M_* = 10^{11}M_{\odot}$, the softening effects are negligible compared to the errors coming from particle statistics. For a minimum required number of 1000 particles per ellipsoidal shell we found that these errors are generally $\lesssim 0.02$ on both p and q. Hence at $r \gtrsim 9r_{\rm soft}$ the uncertainty on the axes ratios is of the order of 0.02.

Throughout the paper, we quantify the intrinsic shapes of galaxies also with the triaxiality parameter. Because of its definition (Eq. (5.3)), the error ΔT is shape dependent, as well as mass

dependent as discussed above. In this work we consider reliable T measurements performed at $r \geq 9r_{\rm soft}$, where the uncertainties on the axes ratios are ~ 0.02, corresponding to $\Delta T \sim 0.2$ for typical FRs axis ratios (i.e. $p = 0.9$ and $q = 0.5$). At smaller radii, where ΔT grows large for the low mass galaxies, we quantify the intrinsic shapes using only the better determined p and q (e.g., in Fig. 5.15).

The angular momentum parameter λ_e is evaluated by integrating over all the particles within $R \leq 1R_{\rm e}$, hence, by definition, it is derived more reliably than the flattening. This is apparent in the convergence study of Lagos et al. (2017) on the EAGLE simulations, which have particle mass resolution and gravitational softening length very similar to TNG100. The study shows that the angular momentum within $1R_{\rm e}$ is well converged already at stellar masses above $M_* = 10^{9.5} M_\odot$, i.e. within galaxies resolved by about 2000 particles. The selected galaxies in the TNG100 sample are resolved with more than 2×10^4 particles, hence the measured λ_e is independent of the softening and particle mass resolution. In conclusion, we find that both angular momentum and shapes are not (or only marginally in case of the shape) affected by the resolution of the gravitational potential and by the particle number at $r \gtrsim 1R_{\rm e}$, and they are well-determined at larger radii.

5.C Elongated galaxies in IllustrisTNG

In Sect. 5.5.2, we further restrict the sample selection by excluding an excess of centrally elongated galaxies not present in the observed samples. The inconsistency is revealed in the $\lambda_e - \varepsilon(1R_{\rm e})$ diagram of Fig. 5.5, in which the centrally elongated galaxies distribute in a region at high ellipticity where there are few observed counterparts. In App.5.B we showed that the resolution effects at $1R_{\rm e}$ on the intrinsic shapes are at most of the order of 0.1: these are not enough to explain the differences with observations in the λ_e-ellipticity diagram, nor the extreme values measured for the flattening $p(1R_{\rm e})$.

Figure 5.C.1 shows example velocity fields for two of these centrally elongated objects (i.e. with $p(1R_{\rm e}) < 0.6$) projected edge-on. The colors show the line-of-sight mean velocity divided by the velocity dispersion at the position of each particle. The two galaxies shown have similar flattening in the central regions $p(1R_{\rm e}) \sim 0.4$ and $q(1R_{\rm e} \sim 0.3)$, but in one case (top panel) the galaxy contains an extended disk, in the other the galaxy is spheroidal in the outskirts (bottom panel). Most of the selected systems with $p(1R_{\rm e}) < 0.6$ have velocity fields with rotation around the intrinsic minor axis (as the example in Fig.5.C.1). However, Fig.5.C.2 shows that these galaxies (in blue to yellow colors) can exhibit different degrees of edge-on rotation at 1 $R_{\rm e}$ and some of them do not rotate at all (see also bottom panel of Fig. 5.C.1), which is at odds with what is typically seen in barred galaxies (e.g. Falcón-Barroso et al. 2019).

The top panels of Fig. 5.C.3 show the median $p(r)$ profiles for the centrally elongated galaxies. The profiles are built by binning together the galaxies according to the values of $p(1R_{\rm e})$ and $p(6R_{\rm e})$. The percentages next to each profiles gives the fraction of centrally elongated TNG100 or TNG50 galaxies that populate the median profile. The elongated regions can extend up to a few Re, typically $\sim 3R_{\rm e}$. Outside these radii, galaxies are near-oblate, with median $p(5R_{\rm e}) \sim 0.9$, and a large scatter on the flattening $q(5R_{\rm e})$ (bottom panels in Fig. 5.C.3). The TNG100 galaxies

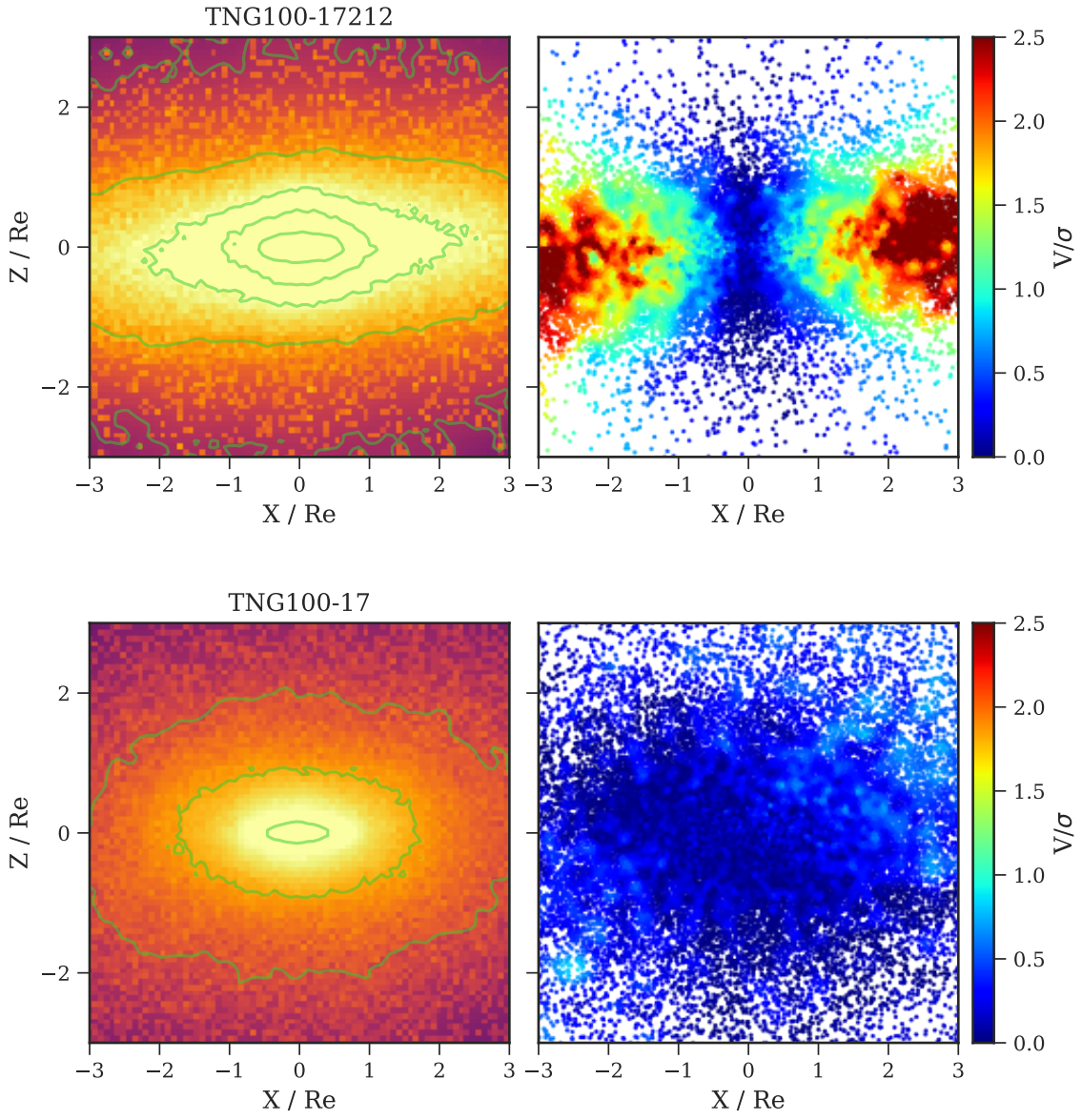

Figure 5.C.1: Stellar mass distribution (**left**) and V/σ fields (**right**) of the central 3 Re for two examples of the centrally elongated galaxies projected edge-on. In the top panel the elongated central component ($p(1R_e) = 0.42$, $q(1R_e) = 0.33$, and $\lambda_e = 0.54$) is embedded in a disk structure ($q(5R_e) = 0.33$). In the bottom panel the bar-like structure ($p(1R_e) = 0.39$, $q(1R_e) = 0.30$, and $\lambda_e = 0.10$) is embedded in a spheroid ($q(5R_e) = 0.61$).

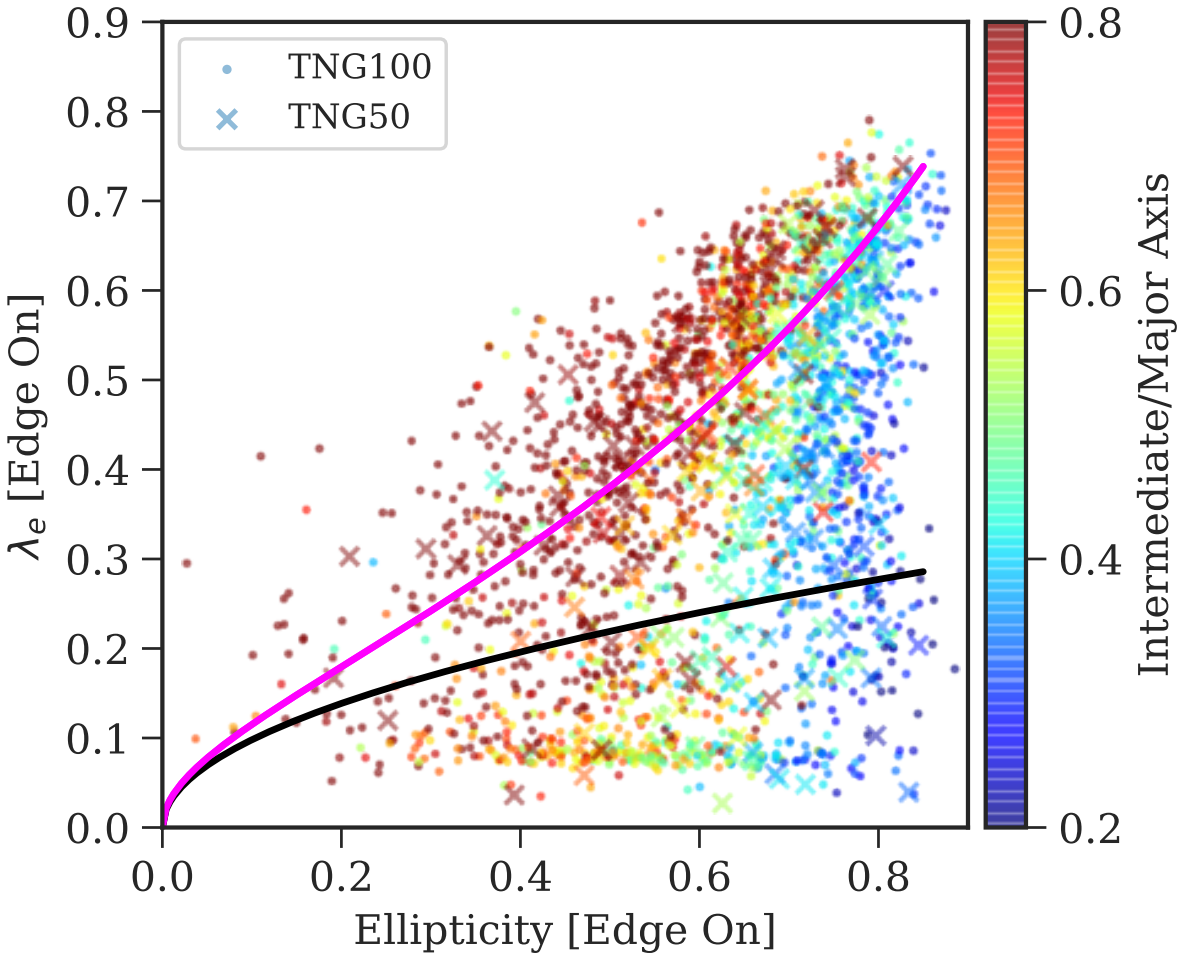

Figure 5.C.2: λ_e-ellipticity ($1R_e$) diagram for the TNG galaxies selected in color and stellar mass as in Sect. 5.5.1, and - differently from Fig. 5.5 - projected edge-on. The symbols are colored according to the intermediate to major axis ratio measured at $1R_e$. The black and magenta lines are as in Fig. 5.5.

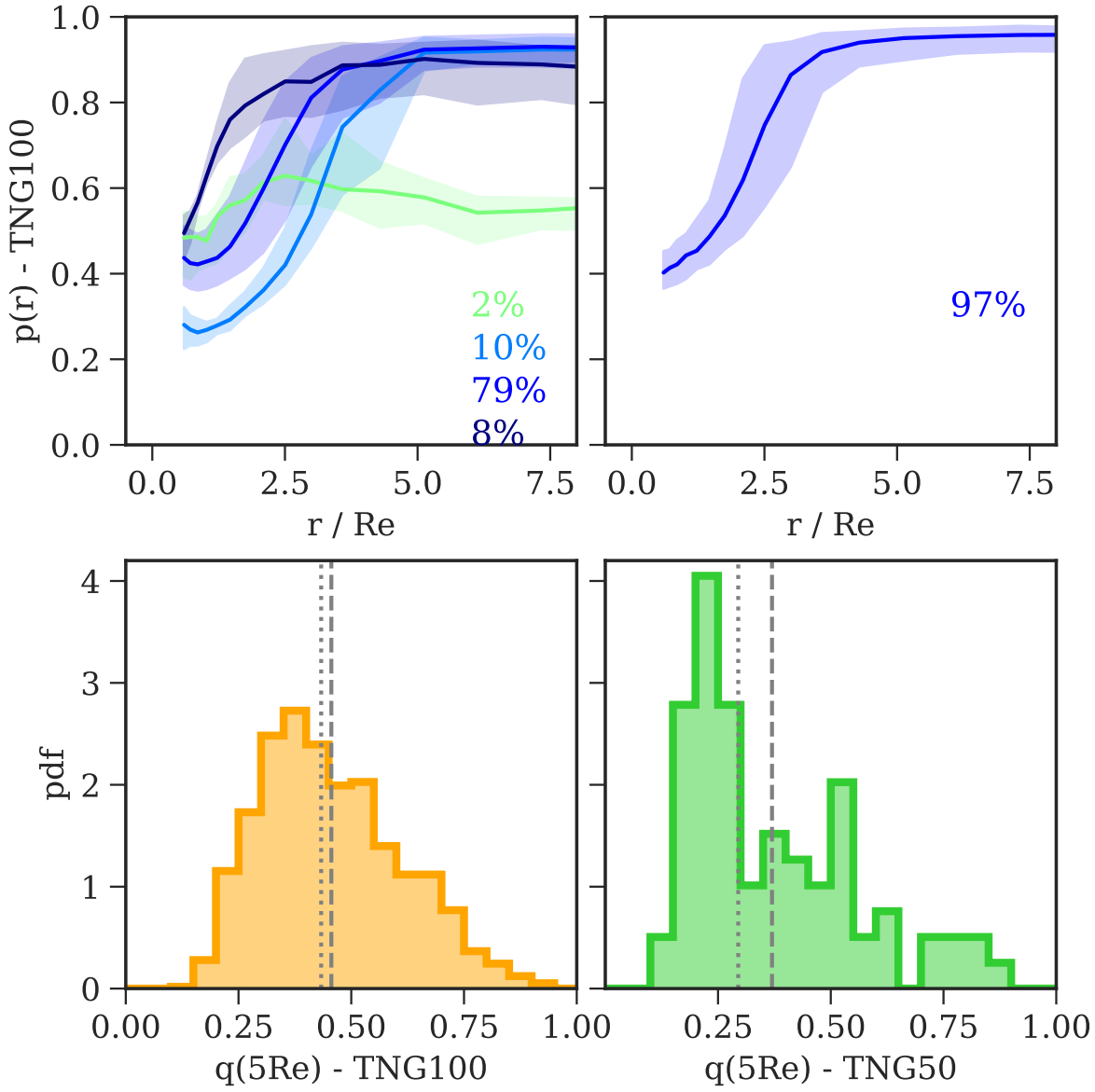

Figure 5.C.3: **Top**: Median $p(r)$ profiles for the galaxies with $p(1Re) < 0.6$ in TNG100 (**left**) and TNG50 (**right**). Only bins with more than 10 galaxies are shown. The percentages indicate the fraction of centrally elongated galaxies that populate each median profile. **Bottom**: Distribution of the axis ratio $q(5R_e)$ in the centrally elongated galaxies of TNG100 (**left**) and TNG50 (**right**). Dashed and dotted vertical lines show the mean and the median of the distributions, respectively. The galaxies with $p(1Re) < 0.6$ have elongated shapes up to $\sim 3-4$ Re; outside this regions ($r \sim 5R_e$) they are mostly near-oblate ($p \sim 0.9$) with median flattening $q \sim 0.3-0.4$, depending on the simulation.

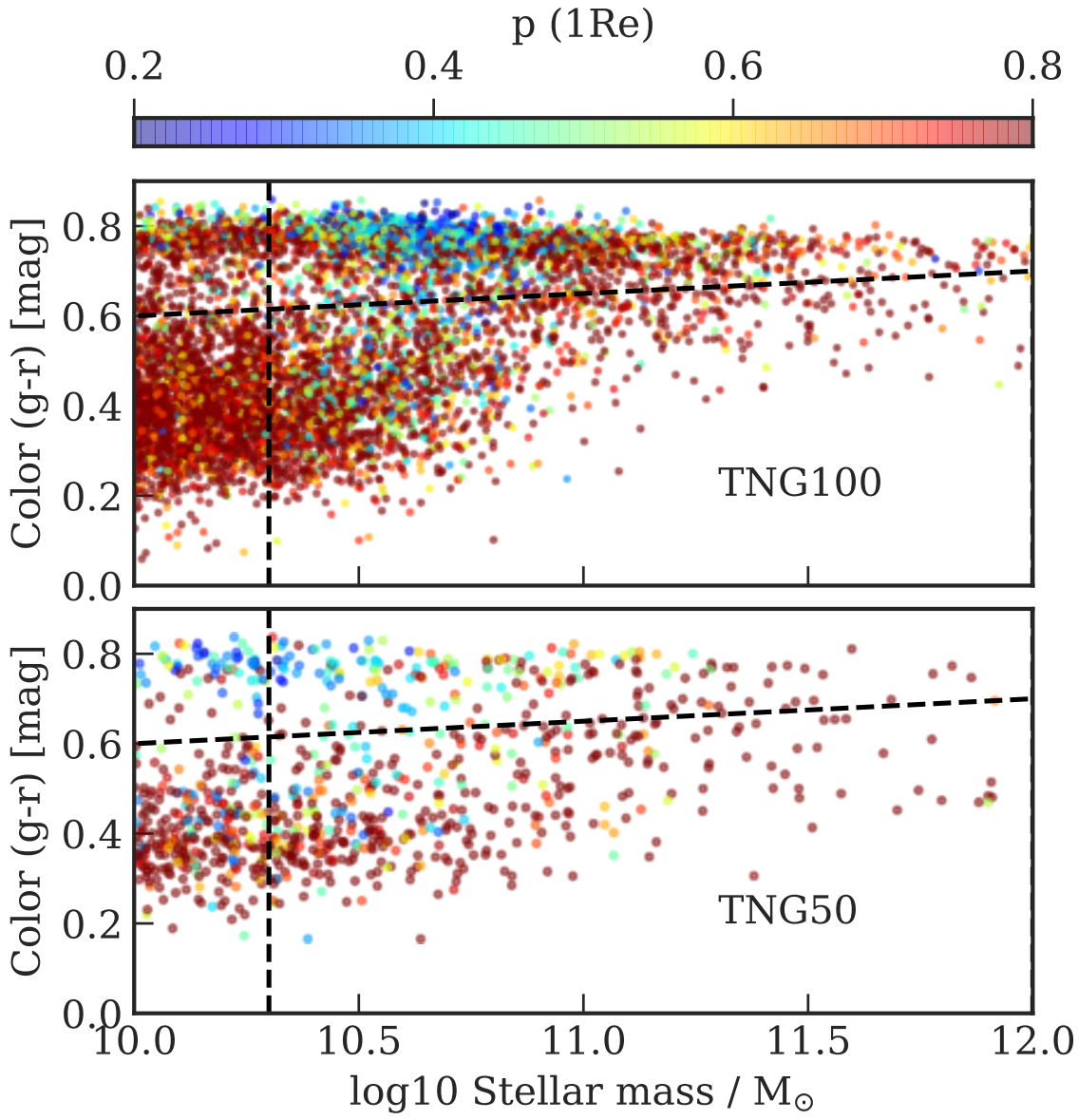

Figure 5.C.4: Color (g-r) as a function of the stellar mass. The **top** panel shows TNG100, the **bottom** panel TNG50. The dashed lines illustrate the selection of the sample of ETGs with masses $10^{10.3} \leq M_*/M_\odot \leq 10^{12}$, and red color (Sect. 5.5.1). The colors indicate the axis ratios $p(1R_e)$.

have rather spheroidal shapes with $q(5R_e) \sim 0.45$; the TNG50 galaxies tend to be flatter with $q(5R_e) \sim 0.3$, and a peak in the distribution at ~ 0.2.

Finally Fig. 5.C.4 shows the color-stellar mass diagram for the galaxies in TNG100 and TNG50 separately. The axis ratio $p(1R_e)$ is shown by the color of the data points. The centrally elongated systems occur prominently among the redder simulated galaxies, and in specific stellar mass ranges. In TNG100 they are numerous in the interval $10^{10.4} M_\odot \lesssim M_* \lesssim 10^{10.9} M_\odot$, while in TNG50 they have $10^{10.0} M_\odot \lesssim M_* \lesssim 10^{10.5} M_\odot$.

The fact that these centrally elongated galaxies are preferentially produced in a particular mass range and that most of them are old, red systems, points towards these objects being a class of galaxies that are produced by the simulation but are not present in nature, probably related to the way the simulated galaxies accrete gas, form stars, and quench during a rapid dynamical evolution in this specific mass range. The difference between TNG100 and TNG50 in the stellar mass range where the centrally elongated systems are produced could be explained by the higher star formation efficiency in the higher resolution simulation (Pillepich et al. 2018b). This hypothesis is strengthened by the absence of a similar concentration of centrally elongated systems among the red galaxies of intermediate masses in the Illustris simulation: hence the presence of this population of galaxies is due to the galaxy formation model. We note that in TNG100 this mass range approximately coincides with the knee in the stellar mass-halo mass relation (e.g., Behroozi et al. 2013, and reference therein), where accretion could be particularly efficient.

As Fig. 5.C.3 shows, these centrally elongated systems are embedded in an near-oblate component with various flattening q, and q tends to be smaller in TNG50. This difference in flattening is likely due to the better resolution of TNG50, which allows to resolve thinner disks (Pillepich et al. 2019, their appendix B and C). From App. 5.B above the error on q due to the spatial resolution is of the order of 0.1 at $\sim 1R_e$ for the lowest mass systems, so that the measured thickness of a thin disk with radius $\sim 5R_e$ and $q \sim 0.2$ may be subject to a similar uncertainty. If the centrally elongated galaxy components in TNG100 and TNG50 actually form within disks, then they could be the result of a bar instability, such that at the particular stellar mass range where the bars are produced, too much cold gas forms stars too quickly, while building massive bar-unstable disks. Then the feedback from the intense star formation would sweep away the remaining gas, quench the star formation, and lead to the formation of preferentially red bar-like inner components. For some of these objects the time-scale for dynamical friction against the surrounding stars and dark matter might be short enough to slow down their rotation, generating the wide range of λ_e values seen in Fig. 5.C.2.

This suggests that these centrally elongated galaxies may be systems that were in the process of forming a disk, whose evolution was interrupted or derailed by rapid dynamical instability, star formation, and feedback in the simulations, in the particular mass range in which they occur. Fig. 5.6 in the main text demonstrates that the distributions of angular momentum and triaxiality in the surrounding stellar halos are not affected by the central elongation $p(1R_e)$ of the simulated galaxies. Thus these over-elongated systems can simply be excluded from the sample selected for our main analysis.

Chapter 6

The stellar halos of ETGs in the IllustrisTNG simulations: II. Accretion, merger history, and dark halo connection

This chapter is published as the paper Pulsoni et al. (2021).

6.1 Introduction

The ΛCDM cosmology predicts that structures form hierarchically, meaning that more massive systems form through the accretion of less massive objects (White & Rees 1978; Peebles 1980). In this model, the formation of massive early-type galaxies (ETGs) is believed to have occurred in two phases (e.g., Oser et al. 2010). After an initial assembly stage, where ETGs form stars in a brief, intense burst which is quickly quenched (e.g., Thomas et al. 2005a; Conroy et al. 2014; Peng et al. 2010), at $z \lesssim 1$ galaxies grow efficiently in size through a series of merger episodes, mainly dry minor mergers (e.g., Naab et al. 2009), which enrich the galaxies with accreted (ex-situ) stars. More massive galaxies can have accreted fractions larger than 80%, while lower mass systems are mostly made of in-situ stars and their accreted component is mainly deposited in the outskirts (e.g., Cooper et al. 2013; Rodriguez-Gomez et al. 2016; Pillepich et al. 2018a; Tacchella et al. 2019; Davison et al. 2020).

Elliptical galaxies can be divided into two classes with distinct physical properties (e.g., Kormendy et al. 2009; Cappellari 2016): those with low to intermediate masses and coreless luminosity profiles, and those that are frequently among the most massive galaxies, with cored profiles. This dichotomy in light distribution roughly corresponds to different kinematic properties, with coreless disky objects being rotationally supported, and cored boxy galaxies having low rotation (Bender 1987). In the last decade, the advent of integral field kinematics has lead to a kinematics-based division between fast rotators (FRs) and slow rotators (SRs, Emsellem et al. 2011; van de Sande et al. 2017; Veale et al. 2017a; Graham et al. 2018): low mass, coreless, FR ellipticals share similar properties with lenticular galaxies, which are also included in the FR family, while massive cored ellipticals are typically SRs.

State-of-the-art cosmological simulations find that the progenitors of FR and SR at high redshifts ($z \sim 1$) are indistinguishable (Penoyre et al. 2017; Lagos et al. 2017; Schulze et al. 2018, with Illustris, Eagle, and Magneticum, respectively). Present-day SR and FR (i.e., the core and coreless) classes result from different formation pathways characterized by different numbers of mergers, merger mass ratio, timing, and gas fractions (Naab et al. 2014; Penoyre et al. 2017, see also the discussion in Kormendy et al. 2009), although the details still depend on the star formation and AGN feedback models adopted by the numerical models (Naab & Ostriker 2017). In general, the result of a formation history dominated by gas dissipation is most likely a coreless FR, while dry major mergers often result in SRs.

A consequence of the two-phase formation is that ETG central regions are the remnants of the stars formed in-situ while the external stellar halos are principally made of accreted material (Bullock & Johnston 2005; Cooper et al. 2010), even though the details strongly depend on stellar mass (Pillepich et al. 2018a). Because of the different origin of central regions and stellar halos, galaxies are expected to show significant variation in their physical properties with radius, such as the shapes of their light profiles (Huang et al. 2013a; D'Souza et al. 2014; Spavone et al. 2017; Buitrago et al. 2017), their stellar populations (Coccato et al. 2010b; Pastorello et al. 2014; Zibetti et al. 2020), and their kinematics (Coccato et al. 2009; Romanowsky & Fall 2012; Arnold et al. 2014; Foster et al. 2016).

Pulsoni et al. (2018) found evidence for a kinematic transition between the central regions and the outskirts in the majority of the ETGs from the ePN.S survey (Arnaboldi et al. 2017), consisting in variations of the rotational support or changes in the direction of rotation at large radii (see also Coccato et al. 2009; Foster et al. 2016). As a result, ePN.S ETG halos display a variety of kinematic behaviors despite the FR–SR dichotomy of their central regions, with most of the stellar halos displaying similar rotational support V/σ across classes (where V is the rotation velocity and σ the velocity dispersion). These findings suggest that at large radii the dynamical structure of FRs and SRs could be much more similar than in their centers: if halos are mainly formed from accreted material, their common origin would explain their similarities. The measured kinematic transition radii and their dependence on galaxy stellar mass seem to support such an interpretation. Recently, Schulze et al. (2020), using the Magneticum Pathfinder simulations, found that the kinematic transition radius, estimated as the position of the peak in rotation for a subset of FRs with decreasing V/σ profiles, is a good estimator of radius of the transition between in-situ- and ex-situ-dominated regions, especially in galaxies that did not undergo major mergers in their evolution.

In Pulsoni et al. (2020, hereafter Paper I) we investigated the kinematic and photometric properties of simulated ETGs from the IllustrisTNG simulations, TNG50 and TNG100, finding that simulations reproduce the diversity of kinematic properties observed in ETG halos: FRs divide approximately into one-third with flat rotation profiles and high halo rotational support, one-third with gently decreasing profiles, and another third with low halo rotation; while SRs tend to increase rotational support in the outskirts and half of them exceed angular momentum parameter $\lambda = 0.2$. Simulated stellar halos are also characterized by a large variety of intrinsic shapes which are strongly related to their rotational support: high rotation is associated with flattened near-oblate shapes; decreasing rotational support with radius is accompanied by a change towards more spheroidal intrinsic shape, with a wide range of triaxiality. These variations in the

intrinsic structure of ETGs results in a blurring of the FR–SR bimodality at large radii, with the two families showing a gradual transition in stellar halo properties.

The present study builds upon the results of Paper I. The goal is to relate the kinematic and photometric properties of stellar halos to the galaxy accretion history, parametrized by the total fraction of accreted stellar mass, the mass fraction contributed by different mass ratio mergers, and the fraction of recently accreted cold gas. We then extend the investigation to the properties of the dark matter halos and their relation with the stellar component depending on accretion.

Dark matter halo and galaxy properties are known to be related. Primordially, large-scale tidal fields generate tidal stretching (Catelan et al. 2001) and tidal torquing (Schäfer 2009, for a review) on both baryons and dark matter, inducing shape and spin alignments. In the subsequent evolution, baryonic physics modifies the shapes of inner dark matter halos from triaxial towards rounder and more oblate shapes (e.g., Kazantzidis et al. 2004; Bryan et al. 2013; Chua et al. 2019), while galaxy central regions and outer dark matter halos are more uncorrelated (e.g., Bailin et al. 2005; Deason et al. 2011; Tenneti et al. 2015). This is due to the fact that both centers and outskirts evolve away from the initial shape and angular momentum correlations predicted from the tidal torque theory. On one hand, the outer dark matter halos continue to accumulate accreted material, while on the other, the central regions gain angular momentum through nonlinear tidal torques and dissipation exerted by the gas flows entering the dark matter halos, and are affected by disk instabilities and feedback processes that make the galaxy spins (and shapes) deviate from the halo spins (Zjupa & Springel 2017; Ganeshaiah Veena et al. 2019). Since mergers deposit stars and dark matter alike in the galaxy outskirts, which both follow a collisionless dynamics, then we would expect the (accreted) stellar and dark matter halos to have a similar structure at large radii. This is investigated in the last section of this paper.

The paper is organized as follows. Section 6.2 summarizes the main characteristics of the IllustrisTNG simulations and describes the selection of the analyzed ETG sample. Section 6.3 details how physical quantities are measured from the simulated galaxies. Section 6.4 gives an overview of the accretion parameters used in the main analysis to parametrize galaxy accretion history and their dependence on stellar mass, and studies the different radial distribution of accreted stars in TNG ETGs. Sections 6.5 and 6.6 present our analysis of the dependence of the rotational support $V/\sigma(R)$, the axis ratio $q(r)$, and the triaxiality $T(r)$ profile shapes on the fraction of in-situ stars. We study how mergers shape the galaxy structure and setup local correlations between physical parameters and accreted fraction. Section 6.7 investigates the connection between stellar and dark matter halos. Section 6.8 considers the fraction of TNG ETGs with cores made of stars from early compact progenitors, comparing their evolution with respect to ETGs of similar masses. Section 6.9 discusses some of the main results of the paper. Section 6.10 summarizes the work and Sect. 6.11 lists our conclusions.

6.2 Selection of the sample of ETGs in the IllustrisTNG simulations

The IllustrisTNG simulations are a new generation of cosmological magnetohydrodynamical simulations that model the formation and evolution of galaxies within the ΛCDM paradigm (Springel et al. 2018; Nelson et al. 2018; Pillepich et al. 2018a; Naiman et al. 2018; Marinacci et al. 2018). The model for galaxy formation described in Weinberger et al. (2017) and Pillepich et al. (2018b) includes prescriptions for star formation and evolution, chemical enrichment of the interstellar medium, gas cooling and heating, and black hole and supernova feedback. It builds and improves upon the Illustris simulation (Genel et al. 2014; Vogelsberger et al. 2014) including improvements in the models for chemical enrichment and feedback, and introduces new physics such as the growth and amplification of seed magnetic fields. Overall, the TNG model has been demonstrated to agree satisfactorily with many observational constraints (e.g., Genel et al. 2018; Nelson et al. 2018) and to return a reasonable mix of morphological galaxy types (Rodriguez-Gomez et al. 2019).

In this study we consider the highest resolution realization of the intermediate 110.7^3 Mpc^3 cosmological volume, TNG100 (which is now publicly available; Nelson et al. 2019b), in order to exploit the statistically significant number of simulated objects and at the same time satisfactorily resolve their inner structure. The simulation follows the evolution of 2×1820^3 initial resolution elements. The mean mass of the stellar particles is $1.4 \times 10^6 M_\odot$, while the dark matter component is sampled by $7.5 \times 10^6 M_\odot$ mass particles. The Plummer equivalent gravitational softening length for the collisionless component at redshift $z = 0$ is $r_{\rm soft} = 0.74$ kpc.

The purpose of this paper is to study the properties of ETG halos and their relation to the accretion history. Here we refer to stellar halos as the outer regions of the galaxies beyond a few effective radii (R_e), where the physical properties are often markedly different from those of the central regions within $\sim 1R_e$.

We consider a volume- and stellar mass-limited sample of simulated ETGs that were selected as in Paper I. There we used a selection in color and intrinsic shape to extract a sample of ETGs with properties consistent with observations. In particular, we considered the Atlas3D sample properties to validate our selection criteria, as this survey was especially targeted to study a volume-limited sample of ETGs (Cappellari et al. 2011).

Briefly, from the $(g - r)$ color–stellar mass diagram we isolated galaxies in the red sequence by imposing

$$(g - r) \geq 0.05 \log_{10}(M_*/M_\odot) + 0.1\text{mag}. \tag{6.1}$$

We restricted the stellar mass range to $10^{10.3} \leq M_* \leq 10^{12} M_\odot$. This limit in stellar mass assures that the galaxies are resolved by at least 2×10^4 stellar particles. In addition, we selected galaxies with effective radius $R_{\rm e} \geq 2r_{\rm soft}$ to guarantee that the regions at $r = R_{\rm e}$ of all simulated galaxies are well resolved. This excludes 42 galaxies at the low-mass end.

The final sample was obtained by further selecting galaxies in the $\lambda_e - \varepsilon$ diagram, where ε is the ellipticity. There we excluded a fraction of bar-like objects, whose $\lambda_e - \varepsilon$ properties are not consistent with those of observed ETGs. In Paper I we found that this latter selection does not affect our results on the halo properties of the simulated galaxies. This final criterion

restricts the sample to 1114 ETGs, including both centrals (61% of the sample) and satellites, of which 855 are FRs and 259 are SRs. The classification in FRs and SRs uses the threshold $\lambda_e = 0.31\sqrt{\varepsilon}$ defined by Emsellem et al. (2011), applied to the edge-on projected galaxies to minimize inclination effects. In Paper I we showed that the mass function of the selected sample is in good agreement with the Atlas3D ETGs. In addition, the comparison of the ellipticity distribution at $1R_e$ of the simulated galaxies with the Atlas3D sample showed that overall the selected sample of ETGs contains a balance between disk-dominated and spheroid-dominated galaxies consistent with the observations of a volume- and magnitude-limited sample of ETGs.

6.3 Methods and definitions

In this section we describe how physical quantities are evaluated from the simulated galaxies. We define the total stellar mass M_* as the total bound stellar mass of the galaxy, $M_* = \sum_n m_n$, where the index n runs over the stellar particles of mass m_n. The effective radius, R_e, used throughout the paper to normalize radial distances is the edge-on projected half-mass radius. This is the semi-major axis of the elliptical aperture that contains half of the total bound stellar mass. The ellipticity of the aperture is given by the projected flattening of the galaxy at $1R_e$, measured using the 2D inertia tensor as in Paper I.

6.3.1 Characterizing the galaxy merger and accretion histories

Stellar particles in the simulated galaxies are tagged as accreted (or ex-situ) or as in-situ following the definition in Rodriguez-Gomez et al. (2016). In-situ stars form within the "main progenitor branch" of the galaxy merger tree, independently of the origin of the star-forming gas. Ex-situ stars form outside the main progenitor branch and are subsequently accreted onto the host galaxy through mergers or stripping events (the fraction of smoothly accreted stars that were not bound to other subhalos at formation is negligible; Rodriguez-Gomez et al. 2016). As mergers can contribute to a significant fraction of gas in the host, which can lead to in-situ star formation, the total ex-situ stellar mass fraction does not directly quantify the merger history but measures the relative importance of dry merging with respect to dissipative processes that increase the fraction of in-situ stars (e.g., Oser et al. 2010).

By definition, the total bound stellar mass of a galaxy is given by the sum of the mass in the in-situ and the ex-situ components $M_* = M_{\rm insitu} + M_{\rm exsitu}$. The total in-situ or ex-situ mass fraction is then M_i/M_*, with $i \in \{\rm insitu, exsitu\}$. Throughout the paper we consider also the local in-situ and ex-situ mass fractions, which are the stellar mass fractions measured within a given radial bin. These are indicated by $f_{\rm insitu}$ and $f_{\rm exsitu}$, respectively.

The ex-situ stars can be distinguished according to whether they were stripped from a surviving galaxy, for example in a flyby or in a merger that is still ongoing at $z = 0$, or whether they originated from completed mergers. In the case of completed mergers, we classify the stars according to the merger stellar mass ratio. We distinguish between major mergers (i.e., with stellar mass ratio $\mu > 1/4$), minor mergers ($1/10 < \mu \leq 1/4$), and mini mergers ($\mu \leq 1/10$).

To describe the galaxy accretion histories, we consider the following parameters:

- the total in-situ mass fraction;
- the mean accreted "cold" (star forming) gas fraction of the accreted galaxies at all epochs, weighted by their stellar mass. The gas fraction and stellar mass of the accreted galaxy are measured at the time when its stellar mass is maximum (Rodriguez-Gomez et al. 2017);
- the redshift of its last major merger z_{last};
- the fraction of in-situ stars that are produced after a certain redshift $\bar{z}$, $\Delta_{\mathrm{insitu},z\leq\bar{z}}$:

$$\Delta_{\mathrm{insitu},z\leq\bar{z}} = [M_{\mathrm{insitu}}(z=0) - M_{\mathrm{insitu}}(\bar{z})]/M_*(z=0). \tag{6.2}$$

6.3.2 Intrinsic shapes

The intrinsic shapes of the galaxies are evaluated using the moment of inertia tensor. For each galaxy we define a coordinate system (x, y, z) centered on the position of the most bound particle, and aligned with the principal axes of the stellar component, such that x is along the intrinsic major axis of the galaxy and z is along the intrinsic minor axis. As the direction of the principal axes of a galaxy might change with the distance from the center, we choose (x, y, z) to be the directions of the principal axes derived for the 50% most bound particles using the inertia tensor I_{ij},

$$I_{ij} = \frac{\sum_n m_n x_{n,i} x_{n,j}}{\sum_n m_n}, \tag{6.3}$$

where the sum is performed over the particles concerned, and $x_{n,i}$ are their coordinates in a system of reference centered on the galaxy and with axes oriented along the sides of the simulation box. Then the edge-on projection of each galaxy is obtained by choosing the y-axis as the line of sight. In this work we indicate with the lower-case letters (x, y, z), (v_x, v_y, v_z), and r the 3D coordinates, velocities, and radii. We reserve capital letters for the edge-on projected quantities. The coordinate r indicates the three-dimensional radius, in the case of quantities calculated in spherical bins, or the intrinsic semi-major axis distance, in the case of quantities calculated in ellipsoidal bins. The coordinate R indicates the edge-on projected semi-major axis distance.

The intrinsic shapes of the galaxies are evaluated by diagonalizing the inertia tensor I_{ij} in Eq. (6.3) summed over particles in ellipsoidal shells. We follow the same iterative procedure outlined in Paper I for the stellar and dark matter components separately. Each component is divided into spherical shells between galactocentric distances r and $r + \Delta r$. In each shell the tensor $I_{i,j}$ is derived: the square root of the ratio of its eigenvalues gives the axis ratios $p = b/a$ and $q = c/a$ of the principal axes of the ellipsoid (with $a \geq b \geq c$), and the eigenvectors $\hat{e}_j$ (with $j = a, b, c$) their directions. The spherical shell is then iteratively rotated and deformed to a homeoid of semi-axes $a = r$, $b = pa$, and $c = qa$ until convergence in the values p and q is reached, that is, the fractional difference between two iteration steps in both axis ratios is smaller than 1%.

The triaxiality parameter is defined as

$$T(r) = \frac{1 - p(r)^2}{1 - q(r)^2}, \tag{6.4}$$

where r is the intrinsic semi-major axis distance. We consider shapes with $T \leq 0.3$ as near-oblate and shapes with $T > 0.7$ as near-prolate. Intermediate values of the triaxiality parameter define triaxial shapes.

In Paper I we verified that the intrinsic shape measurements are affected by the resolution of the gravitational potential and by the number of particles only for the lowest mass systems, for which we estimated an absolute error of 0.1 on both p and q measured at $1R_e$. More massive galaxies $M_* > 10^{11} M_\odot$ are much better resolved at $r \sim 1R_e$. At $r \geq 9r_{soft}$, where r_{soft} is the softening length of the simulation (i.e., at $\gtrsim 3.5R_e$ for $M_* \sim 10^{10.3} M_\odot$ and at $\gtrsim 1R_e$ for $M_* \sim 10^{11} M_\odot$), the resolution effects are negligible compared to the errors from limited particle numbers, which we quantified as being of the order of 0.02. This implies an uncertainty on the triaxiality parameter of $\Delta T \sim 0.2$ for typical FR axis ratios (i.e., $q \sim 0.5$ and $p = 0.9$). At $r < 9r_{soft}$, ΔT increases and then intrinsic shapes are better quantified by p and q. The error on the direction of the principal axes is generally very small, but it increases with the axis ratios. For axis ratio p or $q/p = 0.5$ it is of the order of 1°, and reaches $\sim 6°$ for axis ratio of 0.9. At higher values of p and of q/p the uncertainties on the direction of the major axis and minor axis, respectively, grow exponentially. These considerations hold for both stars and dark matter, because the gravitational softening length is identical for both components; the above limitations are derived from the results of Chua et al. (2019) for the Illustris dark matter only simulation. Because the full physics simulation TNG100 has very similar resolution and a larger number of particles in the central regions compared to this dark-matter-only simulation, it is reasonable to expect similar or better convergence in TNG100.

In the paper, we consider shape measurements from shells with at least 1000 particles as reliable (Zemp et al. 2011). This means that we are able to measure intrinsic shapes for the stellar component out to $8R_e$ for 96% of the selected galaxies. Beyond that limit the lower mass objects begin to lack sufficient numbers of stellar particles (see Paper I).

6.3.3 Rotational support

Ordered rotation in a galaxy is quantified by the ratio V/σ, where V is the mean velocity and σ the velocity dispersion. Summing the components of the angular momentum vectors of all particles in a shell S, weighted by one over the product of the particle mass m_n times radius $r_n = |\overrightarrow{r_n}|$, we define a mean rotation velocity vector in the shell,

$$u_i(r) \equiv \left[\frac{\left(\sum_n m_n \overrightarrow{r_n} \times \overrightarrow{v_n} \right)_i}{\sum_n |\overrightarrow{r_n}| m_n} \right]_{n|\overrightarrow{r_n} \in S\,[r, r+dr]}, \tag{6.5}$$

from which, together with twice the kinetic energy per unit mass k in the shell,

$$k(r) = \left[\frac{\sum_n m_n (v_{x,n}^2 + v_{y,n}^2 + v_{z,n}^2)}{\sum_n m_n} \right]_{n|\overrightarrow{r_n} \in S\,[r, r+dr]}, \tag{6.6}$$

we define a mean 3D velocity

$$V(r) = \sqrt{u_x^2(r) + u_y^2(r) + u_z^2(r)}, \tag{6.7}$$

and velocity dispersion

$$\sigma(r) = \sqrt{k(r) - V(r)^2}. \tag{6.8}$$

The index n runs over the particles within the chosen ellipsoidal or spherical shell $S[r, r+dr]$. In Sect. 6.7, where we compare the rotational support of the stellar component to that of the dark matter, we derive V/σ for the two components separately, summing over stellar or dark matter particles within spherical shells of radii r and $r + dr$.

In Sect. 6.5 we study the rotational support of galaxies using their edge-on projections in order to minimize inclination effects but at the same time use quantities that are as close as possible to observables. In this case, we calculate quantities within elliptical radial bins of semi-major axis R and $R + dR$ and consider only the particle velocities along the line-of-sight y, $V_{Y,n} = v_{y,n}$, so that

$$V(R) = \sqrt{U_X^2(R) + U_Z^2(R)}, \tag{6.9}$$

and

$$\sigma(R) = \sqrt{k(R) - V(R)^2}. \tag{6.10}$$

In Eq. (6.9), R is the semi-major axis of the elliptical annulus and U_X and U_Z are defined analogously to Eq. (6.5), where the particles are weighted by one over their masses multiplied by projected circular radius. The ratio between Eqs. (6.9) and (6.10) gives the edge-on projected rotational support which, for the stellar component, is denoted by $V_*/\sigma_*(R)$.

The $V_*/\sigma_*(R)$ ratio defined in this way differs from the quantities presented in Paper I where, instead of the mean velocity, we used the rotational velocity derived from 2D mean velocity fields which maximizes the V/σ ratio. The $V_*/\sigma_*(R)$ measured here directly from the star particles is roughly equal to the ratio of the mass-weighted average velocity and the mass-weighted average velocity dispersion obtained from the 2D mean velocity fields as built in Paper I:

$$V_*/\sigma_*(R) \sim \left[\frac{\sum_n m_n \langle V_n \rangle}{\sum_n m_n \langle \sigma_n \rangle}\right]_{n|\overrightarrow{R_n} \in S[R,R+dR]}. \tag{6.11}$$

Here, the n index runs over the Voronoi bins of total mass m_n, mean velocity $< V_n >$, and mean velocity dispersion $< \sigma_n >$ in the regions where the velocity fields are Voronoi binned (Cappellari & Copin 2003), and it runs over the stellar particles of mass m_n, mean velocity $< V_n >$, and mean velocity dispersion $< \sigma_n >$ in the regions where the velocity fields are smoothed with the adaptive kernel technique (Coccato et al. 2009). Figure 6.1 shows the similarity between the $V_*/\sigma_*(R)$ profile (dashed green line) with the rotational support derived from the smoothed velocity fields (Eq. 6.11, open circles) for one example galaxy.

6.3.4 Rotational support of the in-situ and ex-situ components

We derive the rotational support for the in-situ ($V_{\rm insitu}(R)$) and the ex-situ stars ($V_{\rm exsitu}(R)$) using Eq. (6.9) for the two components separately. We then normalize the mean velocities by the velocity dispersion of the total stellar component $\sigma_*(R)$, although we note that the results of Sect. 6.5 are unchanged if we normalize by the respective $\sigma_{\rm insitu}(R)$ and $\sigma_{\rm exsitu}(R)$. For all three components, we use elliptical radial bins with identical edges in each galaxy.

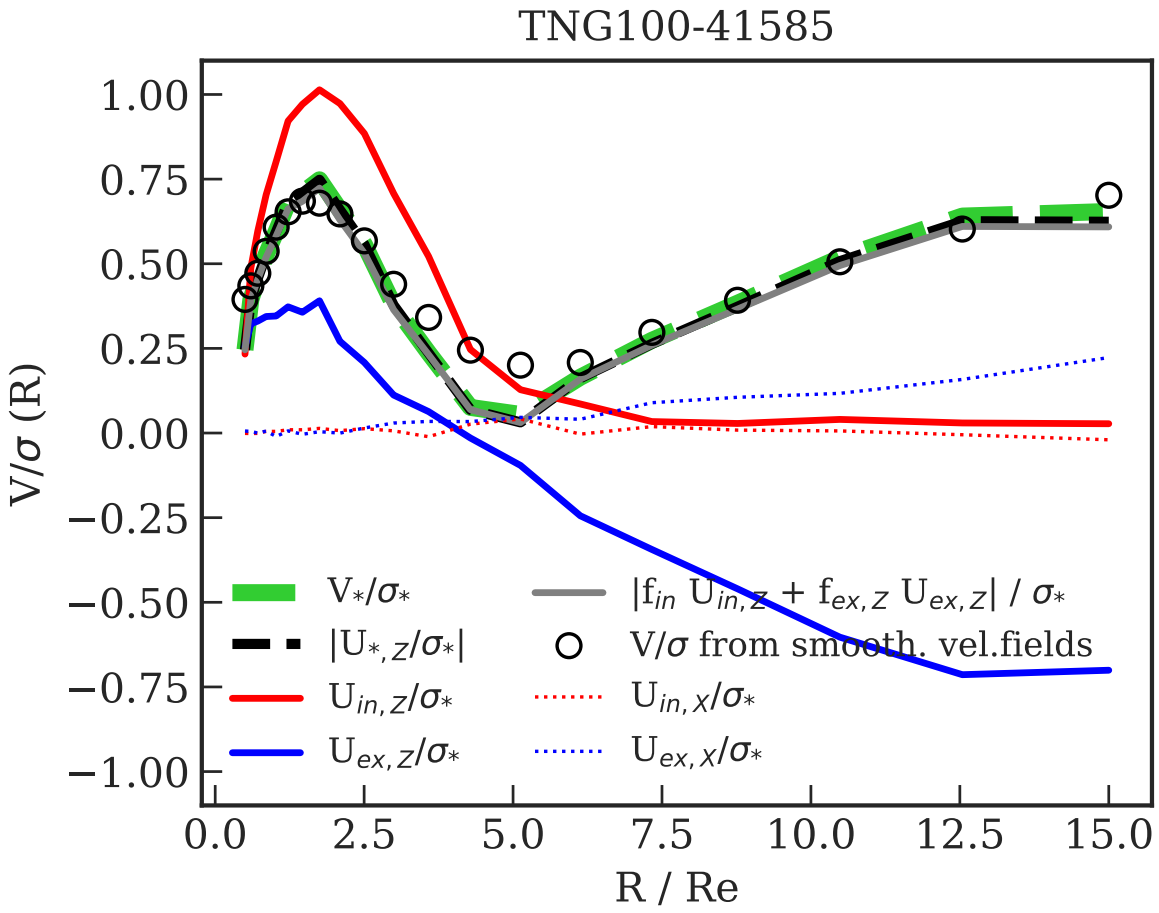

Figure 6.1: V/σ profiles for an example FR galaxy with $M_* = 10^{11.4} M_\odot$ and counter-rotating ex-situ component in the halo. The $V_*/\sigma_*(R)$ profile for the stars (Eqs. 6.9 and 6.10, green dashed line) is compared with the $V/\sigma(R)$ profile derivable from the smoothed velocity fields as in Eq. 6.11 (open circles), with the $|U_{*,Z}(R)|/[\sigma_*(R)]$ profile (dashed black line), and with the weighted sum of the in-situ and ex-situ contributions (as in Eq. 6.12, dashed gray curve). The individual un-weighted profiles of the in-situ and ex-situ stars are shown with red and blue curves: the solid lines show the contribution to the mean velocity from the major axis rotation $U_{\rm i,Z}(R)/[\sigma_*(R)]$, the dotted lines show the contribution from minor axis rotation $U_{\rm i,X}(R)/[\sigma_*(R)]$.

In the same radial bins, we derive the surface mass density of all the stellar particles $\Sigma_*(R)$, of the in-situ stars $\Sigma_{\rm insitu}(R)$, and of the ex-situ stars $\Sigma_{\rm exsitu}(R)$. From these, we define the local in-situ and ex-situ fractions as $f_i(R) = \Sigma_i(R)/\Sigma_*(R)$ with $i \in \{\rm insitu, exsitu\}$. As each star is either classified as in-situ or ex-situ, $M_* = M_{\rm insitu} + M_{\rm exsitu}$ and $f_{\rm insitu}(R) + f_{\rm exsitu}(R) = 1$.

By approximating $V_*/\sigma_*(R) \sim \left|U_{*,Z}(R)/\sigma_*(R)\right|$, we find that the $V/\sigma(R)$ profiles of the galaxies are almost exactly approximated by the sum of the rotational support of the in-situ and ex-situ components, weighted by the their local mass fraction $f_i(R)$ profiles,

$$\begin{aligned} V_*/\sigma_*(R) &\sim \left|U_{*,Z}(R)\right|/[\sigma_*(R)] \sim \\ &\sim \left|\,[f_{\rm insitu}(R)\,U_{\rm insitu,Z}(R) + f_{\rm exsitu}(R)\,U_{\rm exsitu,Z}(R)]\,\right|/\sigma_*(R). \end{aligned} \tag{6.12}$$

The $U_{i,Z}$ components need to be summed with their sign, as it is not uncommon for the in-situ and the ex-situ stars to counter-rotate ($\sim 20\%$ of the cases for our sample). We assume a positive sign for the component rotating with the same sign as the total $U_{*,Z}$ at its maximum rotation.

The approximation $V_* \sim \left|U_{*,Z}\right|$ holds for the majority of the selected TNG galaxies, for which the median$(\left|U_{*,X}/U_{*,Z}\right|) = 0.04$. For the in-situ and ex-situ components separately, the $U_{i,X}$ component is also negligible in most cases median$(\left(\left|U_{\rm insitu,X}/U_{\rm insitu,Z}\right|\right) = 0.04$ and median $\left(\left|U_{\rm exsitu,X}/U_{\rm exsitu,Z}\right|\right) = 0.14$) but not at large radii or for high-mass systems (e.g., at $R = 8R_{\rm e}$ for $M_* > 10^{11.5} M_\odot$, median $\left(\left|U_{*,X}/U_{*,Z}\right|\right) = 0.45$).

Figure 6.1 shows as an example a massive FR galaxy with $M_* = 10^{11.4} M_\odot$. Its $V_*/\sigma_*(R)$ profile, derived from the ratio of Eqs. 6.9 and 6.10 and shown with a green dashed curve, has a peak at $R \sim 2R_{\rm e}$, decreases to 0 at $\sim 5R_{\rm e}$, and increases again at larger radii. The dashed black curve shows that, for this galaxy, the approximation of the mean velocity $V_*(R)$ with the mean major axis rotation $|U_{*,Z}(R)|$ holds at all radii. The gray curve shows the weighted sum of the major axis mean rotation of the in-situ and ex-situ stars divided by the total velocity dispersion, as in Eq. (6.12): solid green, dashed black, and solid gray curves agree almost perfectly along the whole radial range considered. The rotational support of the in-situ and ex-situ stars is shown by separating the major ($U_{i,Z}(R)$) and minor axis ($U_{i,Y}(R)$) rotation contributions. For this galaxy the contribution from minor axis rotation is negligible at all radii for the in-situ component and out to $\sim 8R_{\rm e}$ for the ex-situ component. The in-situ stars have a "peaked and outwardly decreasing" rotation profile (solid red curve), while the ex-situ stars have a co-rotating central component and a counter-rotating component at large radii contributing to almost all the galaxy rotational support at $R > 5R_{\rm e}$.

6.4 Accretion histories of ETGs in TNG100

We begin by studying the dependence of the main accretion parameters on stellar mass for the selected sample of ETGs. For each galaxy, we consider the total fraction of in-situ stars, the mean accreted "cold" (star forming) gas fraction weighted by the mass of the merged galaxies at all epochs, the fraction of in-situ stars produced since $z = 1$, and the redshift of its last major merger (i.e., with mass ratio $\mu > 1/4$); see Sect. 6.3.1.

Figure 6.2 shows the distribution of these parameters for all the sample galaxies and for the FRs and SRs separately. We find a strong dependence with stellar mass in that more massive galaxies have lower in-situ fractions, had recent major mergers, and on average the accreted satellites were poorer in gas (dry mergers). The total ex-situ mass fractions for the IllustrisTNG have already been presented by Pillepich et al. (2018a). Their strong variation with stellar mass was observed there and in different sets of simulations (e.g., Rodriguez-Gomez et al. 2016 in the original Illustris, Davison et al. 2020 in EAGLE), although with some differences due to the different galaxy formation models.

In Fig. 2, FRs and SRs follow similar trends of the accretion parameters versus stellar mass M_*, but at fixed M_*, the SRs have lower in-situ fractions and had more recent and drier mergers. This is consistent with the findings of previous studies on the relation between galaxy angular momentum, gas accretion, and morphology (e.g., Naab et al. 2014; Rodriguez-Gomez et al. 2017; Lagos et al. 2018b; Tacchella et al. 2019).

Each relation comes with a significant amount of scatter, because at each stellar mass, galaxies are characterized by an individual history parametrized by a combination of parameters including the fraction of accreted stellar mass, the time during which this mass was accreted, and how much gas was involved in the accretion. This is shown by the comparison of the relations between the total in-situ mass fraction and the fraction of new in-situ stars since $z = 1$ ($\Delta_{\mathrm{insitu},z\leq1}$) with total stellar mass. Similar to the total in-situ fraction, $\Delta_{\mathrm{insitu},z\leq1}$ is a steep function of stellar mass. The most massive galaxies have little in-situ star formation overall and also at $z \leq 1$, while galaxies at the low-mass end with total in-situ fractions larger than 90% and $\Delta_{\mathrm{insitu},z\leq1} \sim 0.6$ exhibit a large variety of recent in-situ star formation histories (the scatter in $\Delta_{\mathrm{insitu},z\leq1}$ is 0.2 while the scatter in in-situ mass fraction is 0.07), which are also influenced by the different timing of their gas accretion and star formation. In addition to the considered accretion parameters, the orbital parameters of the mergers also play a role in determining the properties of the remnant (Lagos et al. 2018b). This additional investigation is outside of the scope of this study.

6.4.1 Accretion classes

For each simulated galaxy we derive edge-on projected stellar-mass-density profiles in elliptical radial bins with flattening given by the ellipticity profile of the galaxy. In each bin we obtain the stellar mass density of all the stars $\Sigma_*(R)$ and of the in-situ and ex-situ stars ($\Sigma_{\mathrm{insitu}}(R)$ and $\Sigma_{\mathrm{exsitu}}(R)$). Within the selected TNG galaxies we can identify four groups, or accretion classes, according to their relative radial distribution of ex-situ stars with respect to the in-situ component. The assignment of each galaxy to an accretion class is done by analyzing the sign of the function $\Sigma_{\mathrm{insitu}}(R) - \Sigma_{\mathrm{exsitu}}(R)$ and the positions of its zeros. The top panel of Fig. 6.3 displays the median stellar-mass-density profiles of all the galaxies in each accretion class. The median cumulative stellar-mass-fraction profiles are also shown in the bottom panels. The median stellar-mass-density and cumulative stellar-mass-fraction profiles are available in tabulated form in Appendix 6.A. Figure 6.4 shows that each of the defined accretion classes dominates in a different interval of stellar mass and is characterized by different accreted fractions.

Class 1 - Galaxies in class1 are in-situ-dominated at all radii, and represent 20% of the selected galaxies. More than 53% of the low-mass galaxies ($M \leq 10^{10.5} M_\odot$) belong to this

group.

Class 2 - Galaxies in this class are dominated by the in-situ stars in the central regions, and by the ex-situ stars in the outskirts. For these galaxies, it is possible to define a transition radius $R_{\rm exsitu}$ as the galactocentric distance at which the ex-situ stars dominate over the in-situ ones (Cooper et al. 2013; Rodriguez-Gomez et al. 2016). These galaxies represent 57% of the selected TNG100 galaxies, most of them with intermediate stellar masses.

Class 3 - Class 3 contains all the galaxies where the in-situ and ex-situ stars interchange dominance at different radii ($\sim$ 14% of the total sample), and galaxies with ex-situ core and in-situ outskirts ($\sim$ 1% of the total sample).

Class 4 - Galaxies in this group are dominated by ex-situ stars at all radii. This group constitutes about 8% of the sample, although at stellar masses $M_* \geq 10^{11.5} M_\odot$ nearly 64% of the galaxies are in class 4.

As different accretion classes dominate at different stellar masses and the in-situ mass fraction tightly correlates with the stellar mass (Fig. 6.4), measuring the stellar mass of an ETG gives a good first prediction for its accretion properties. We note that in the original Illustris simulation the great majority (85%) of the galaxies with $M_* \geq 10^{10.3} M_\odot$ belong to class 2, that is, they have segregated in-situ-dominated central regions and ex-situ-dominated outskirts (see also Rodriguez-Gomez et al. 2016). In TNG100, 60% (57%) of all (ETG) galaxies with $M_* \geq 10^{10.3} M_\odot$ are in class 2. These differences between the distributions of in-situ and ex-situ stars in galaxies from the two simulations are likely due to the changes implemented in the feedback model for TNG100, as discussed by Tacchella et al. (2019).

6.4.2 Local in-situ and ex-situ density fractions and the contributions from different mass-ratio mergers

From the surface density profiles of the in-situ and ex-situ stellar components we can define the local in-situ and ex-situ fractions $f_i = \Sigma_i(R)/\Sigma_*(R)$ with $i \in \{\text{insitu, exsitu}\}$. We tagged the ex-situ stars according to their origin (i.e., whether they were stripped or accreted through mergers of different μ; see Sect. 6.3.1) and derived the local fractions of the ex-situ stars accreted from the different merger classes from the corresponding edge-on projected density profiles $f_j(R) = \Sigma_j(R)/\Sigma_*(R)$ with $j \in \{\text{major, minor, mini, stripped}\}$, such that $\sum_j f_j = f_{\rm exsitu}$. Figure 6.5 shows radial profiles of the median local fraction of in-situ stars $f_{\rm insitu}(R)$, ex-situ stars $f_{\rm exsitu}(R)$, and of the accreted stars contributed by different mass ratio mergers. Galaxies are divided according to their accretion class (left column) and in stellar mass bins that best "isolate" the accretion classes (as shown in Fig. 6.4 with vertical dashed lines).

Figure 6.5 shows how the spatial distributions of these stellar components differ between the accretion classes and stellar mass bins. For lower mass galaxies, the accreted stars represent less than 10% of the total M_*. These come mainly from mini mergers and are distributed at large radii, determining growing $f_{\rm exsitu}(R)$ profiles. At progressively higher stellar masses, the accreted mass fraction increases. The local fraction from major mergers $f_{\rm major}(R)$ is overall higher at all radii and dominates in the central regions over the other components. The $f_{\rm mini}(R)$ profiles instead tend to become flatter at increasing M_*. The median $f_{\rm minor}(R)$ profiles show that, on average,

the fraction of stellar mass contributed by minor mergers is much lower than that from mini and major mergers. This is driven by the fact that in each mass bin there is a significant fraction of galaxies in which the accreted satellites with mass ratio $1/10 < \mu < 1/4$ contribute less than 10% of the total accreted mass. This can also be seen in the right panels of Fig. 6.6 where we show the median mass fraction from different components as a function of the total stellar mass.

In the left column of Fig. 6.5 we can see again —but in a different form from that of Fig. 6.3— how the different accretion classes are defined in terms of their $f_{\rm insitu}(R)$ and $f_{\rm exsitu}(R)$ profiles. The median $f_j(R)$ (with $j \in$ {major, minor, mini, stripped}) profiles follow roughly the same behavior as the corresponding stellar mass bin, considering that class 2 galaxies span a wide range of stellar masses (from $10^{10.4} M_\odot$ to above $10^{11.2} M_\odot$). We observe that most of the galaxies in class 3 have centrally peaked $f_{\rm mini}(R)$ profiles. These could be explained by the accretion of small compact satellites that are able to reach the central regions of the galaxies before disrupting (e.g., Amorisco 2017).

The overall trends of the median $f_{\rm insitu}(R)$ and $f_{\rm exsitu}(R)$ profiles with stellar mass are consistent with the results of Rodriguez-Gomez et al. (2016) for the original Illustris galaxies, although with some quantitative differences as already noted. The median accreted mass fraction from all mergers is larger in IllustrisTNG than in Illustris for all galaxies with $M_* \geq 10^{10.3} M_\odot$ (Fig. 10 in Tacchella et al. 2019). However, in both simulations the median fraction of stellar mass contributed by minor mergers ($\Delta M_{*,\rm minor}/M_*$) is consistently lower than those from major ($\Delta M_{*,\rm major}/M_*$) or mini mergers ($\Delta M_{*,\rm mini}/M_*$); see Fig. 6.6 above and Fig. 4 in Rodriguez-Gomez et al. (2016).

6.4.3 Accretion classes and merger histories

In Sect. 6.4.2 we observed that galaxies of different stellar mass, or, almost equivalently, different accretion classes, distribute their in-situ and accreted stars differently. In this section, we show that this is the result of different merger histories.

The left column of Fig. 6.6 shows the different accretion history parameters —defined in Sect. 6.3.1 and specified in the headings of the plot— as a function of stellar mass. In the right column we show the stellar mass fraction of the stars accreted from different mass ratio mergers and from stripping events as a function of total stellar mass.

Galaxies of **class 1** had few major mergers at early times (high z_{last}). These contributed to few ex-situ stars compared to the total stellar mass at $z = 0$, but brought in a large fraction of gas which contributed to the in-situ star formation. Their recent history (after $z \sim 2$) is quieter than in galaxies of class 2 with similar M_*: they accreted very little and most of their ex-situ stars come from mini mergers which are deposited in the outskirts (Fig. 6.5).

Class 2 contain a large variety of objects. The least massive are similar to class 1 galaxies, with early gas-rich major mergers and outskirts enriched with ex-situ stars from low-mass (i.e., minor and mini) mergers, although by comparison their last major mergers happened more recently ($z_{\rm last} \sim 2$ versus $z_{\rm last} \sim 4$) and with less gas (45% versus 55%). This implies a larger fraction of ex-situ stars from major mergers, as shown in the top right panel of Fig. 6.6. The more massive galaxies of class 2 have larger ex-situ fractions: these are contributed by both major and low-mass mergers in similar amounts at $10^{10.5} < M_*/M_\odot < 10^{11}$ ($\sim$ 15% and $\sim$ 15%), but at

higher stellar masses the contribution from major mergers dominates. Some of the most massive systems ($M_* \gtrsim 10^{11.2} M_\odot$) had multiple recent ($z < 1$) major mergers.

The ex-situ-dominated **class 4** contains massive galaxies whose evolution is dominated by dry mergers (lowest mean gas fraction). Almost all class 4 galaxies recently ($z \leq 1$) went through a dry major merger, half of them more than once. Compared to the most massive systems of class 2, the class 4 galaxies had a more gas-poor history, and on average more recent and more numerous major mergers.

Class 3 collects objects with accreted fractions of ~ 0.5, but with stellar masses ranging from $10^{10.5}$ to $10^{11.5} M_\odot$, and very different accretion histories. The galaxies with ($M_* \lesssim 10^{11.2} M_\odot$) are recent (at $z < 1$) major mergers. These accretion events are more gas-poor compared to galaxies of class 2 with similar masses. The high-mass end of class 3 are galaxies that have not undergone recent major mergers. They had on average a larger mean accreted gas fraction and higher fractions of newly formed in-situ stars compared to class 2 and 4 galaxies of similar stellar masses. We also note that, overall, class 3 galaxies have the highest fraction of stars accreted by mini mergers, and that 81% of class 3 galaxies are fast rotators.

As shown in Fig. 6.7, FRs and SRs populate all four accretion classes but with very different relative fractions: only 3% of all the FRs populate class 4 and only 5% of the SRs are in class 1. Of the FRs with high $M_* > 10^{11.2}$, 33% belong to class 2, 41% to class 3, and 25% to class 4. Massive SRs belong almost exclusively to class 4 (57%) and class 2 (37%). This underlines both the importance of (dry) mergers in the formation of SRs and that different formation pathways can lead to the formation of a fast or a slow rotating galaxy, in agreement with previous studies (e.g., Naab et al. 2014; Penoyre et al. 2017).

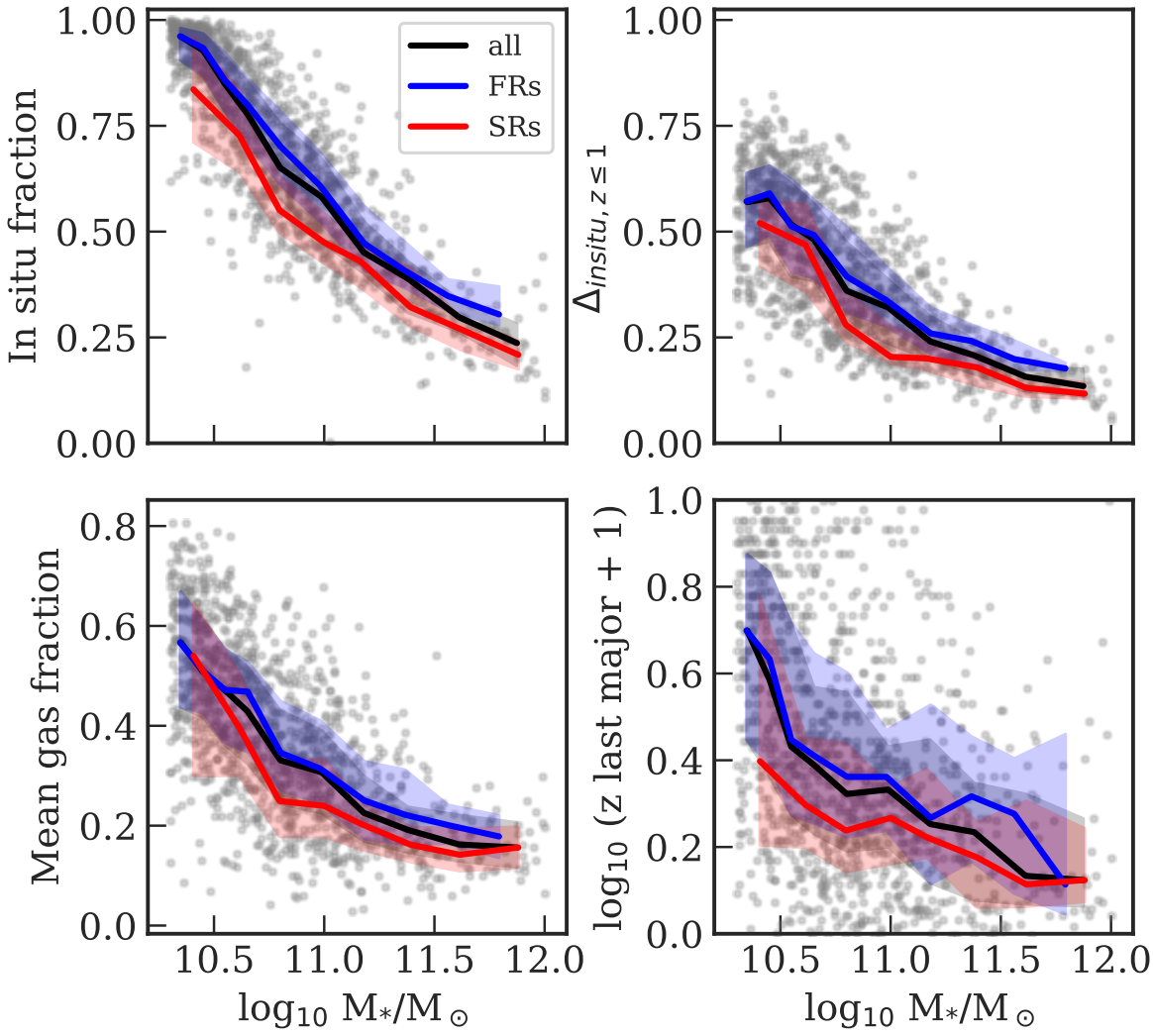

Figure 6.2: Accretion parameters as a function of stellar mass for ETGs in TNG100, and separately for FRs and SRs: total in-situ mass fraction (**top left**), fraction of new in-situ stars since $z = 1$ (**top right**), mean accreted gas fraction (**bottom left**), and redshift of the last major merger (**bottom right**). The solid lines show the median profiles for the whole sample (black) and for FRs (blue) and SRs (red). The shaded regions show the quartiles of the distributions. FRs and SRs follow similar trends with M_* , but at fixed M_*, SRs have on average more accreted stars, they accreted less gas, and they had more recent major mergers.

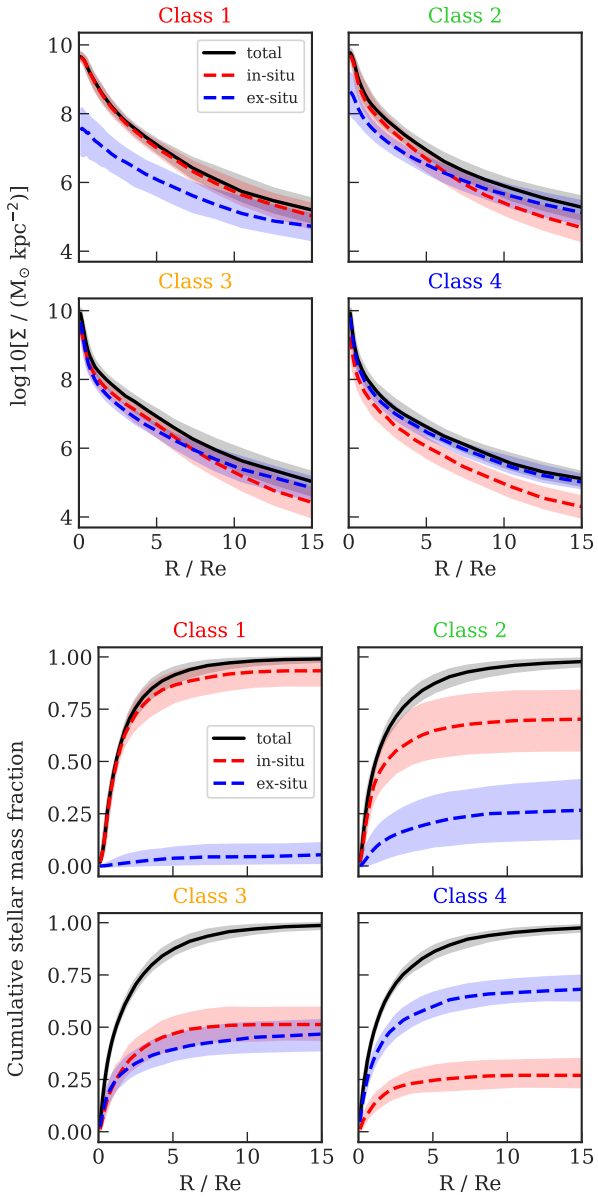

Figure 6.3: Accretion classes for the simulated sample of ETGs. **Top**: Median stellar-mass-density profiles for each of the four classes defined in Sect. 6.4.1. The black lines show the median total density profiles, and the red and blue lines show the median density profiles of the in-situ and the ex-situ stars respectively. The shaded regions show the quartiles of the distributions. **Bottom**: Median cumulative stellar-mass-fraction profiles for the in-situ and ex-situ components in the four accretion classes. The shaded regions show the quartiles of the distributions.

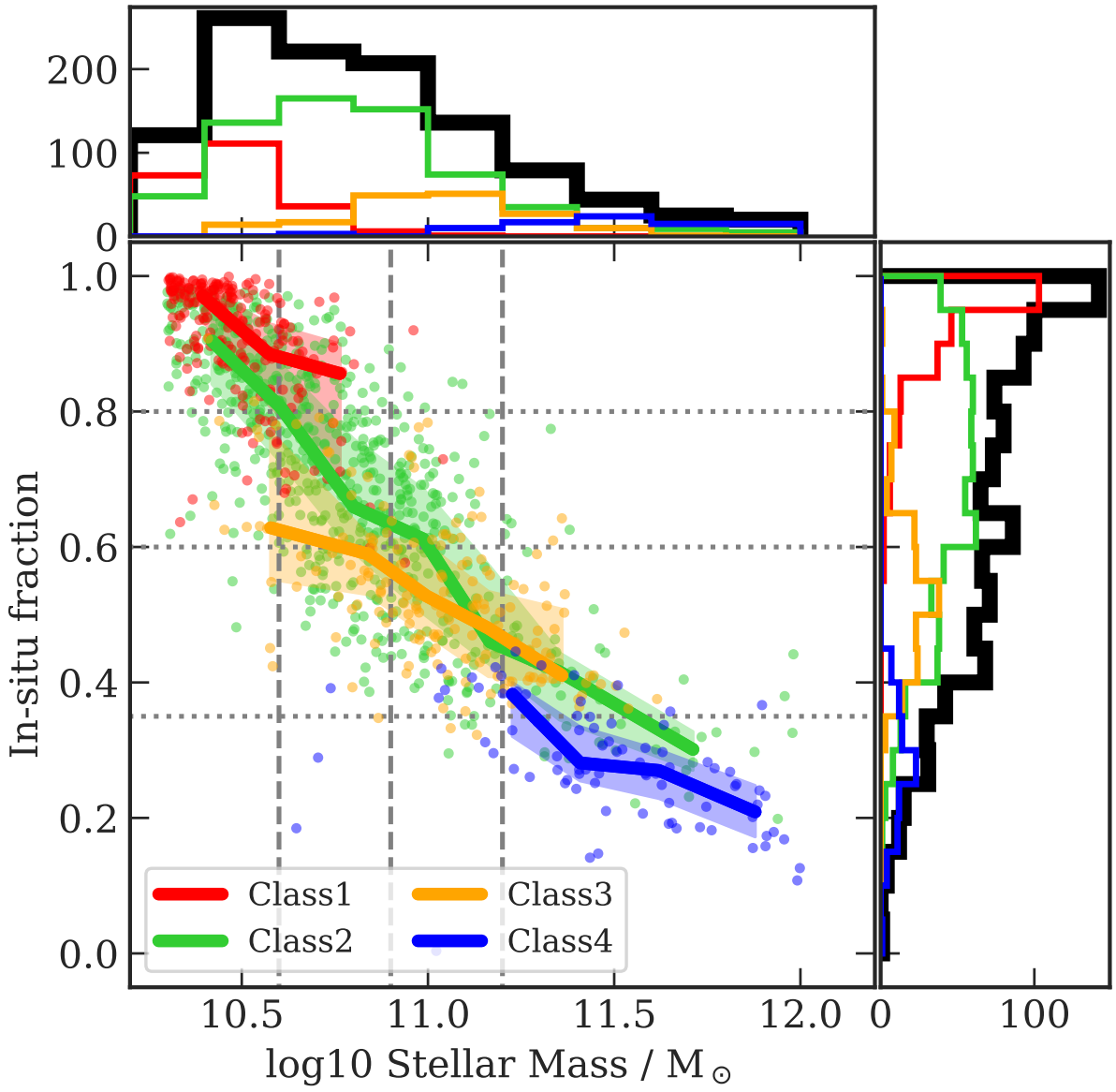

Figure 6.4: Total in-situ mass fraction as a function of the stellar mass for the four accretion classes. Solid lines show the median profiles for each class and the shaded regions the 25th to 75th percentiles. Dashed vertical lines show the stellar mass bins considered in the text. The dotted horizontal lines show the bins in in-situ mass fraction. Each accretion class dominates at a different stellar mass and is characterized by a different total in-situ mass fraction.

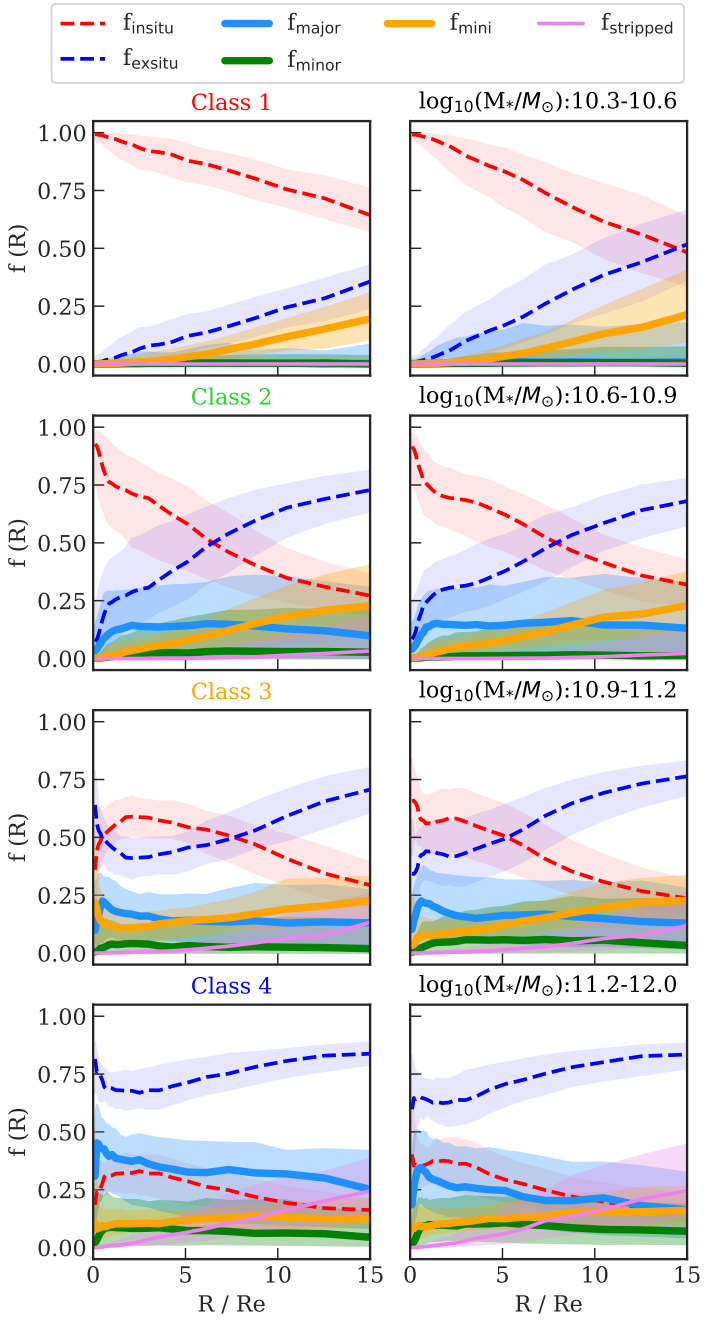

Figure 6.5: Local median mass fraction $f(R)$ of the in-situ and ex-situ stars (dashed lines). The ex-situ component is then split according to its origin from major, minor, mini mergers, or from stripped galaxies (solid lines, see legend). Galaxies are shown divided into accretion classes (left column) and into stellar mass bins (right column). The spatial distributions of the in-situ and ex-situ components, as well as of the accreted stars contributed by different kinds of mergers, vary for different accretion classes and stellar mass bins.

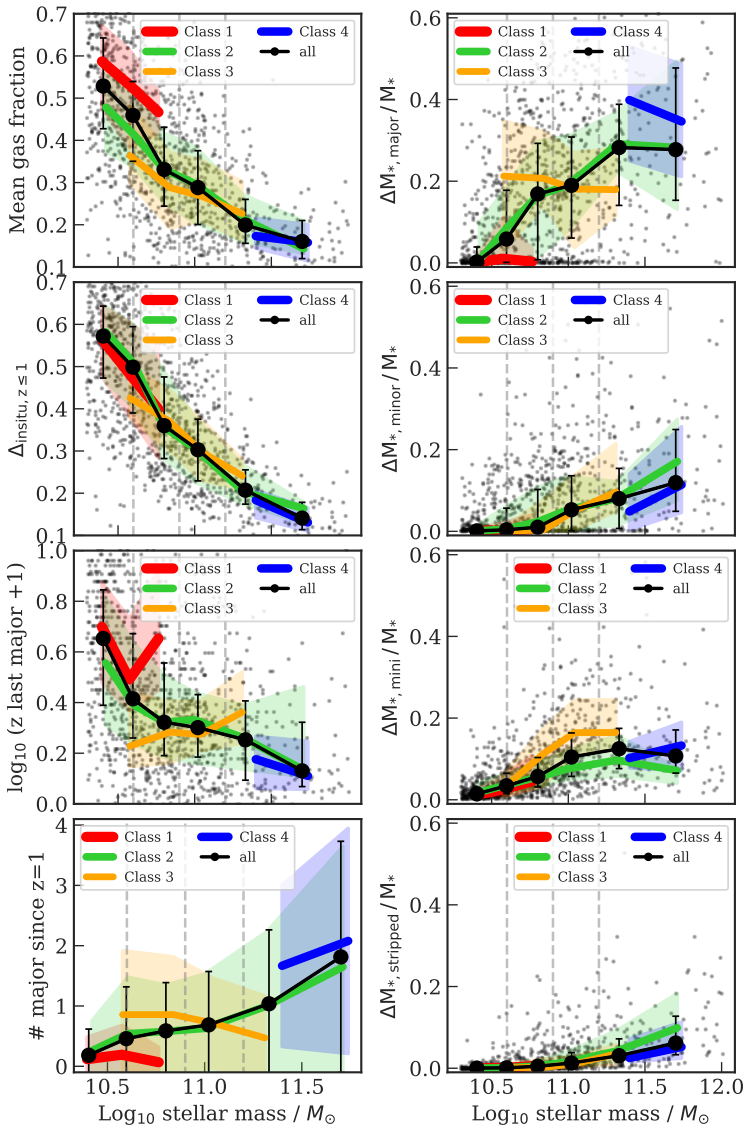

Figure 6.6: Merger history in different accretion classes. **Left:** Median accretion history parameters as a function of the stellar mass. **Right:** Median mass fractions from different mass ratio mergers and from stripped galaxies as a function of the stellar mass. Shaded regions or error bars show the 25th to 75th percentiles of the distributions. In the bottom left panel (number of major mergers since $z = 1$) we show mean profiles and standard deviations around the mean. Galaxies are divided into the accretion classes as shown in the legend. The accretion classes defined in Sect. 6.4.1 are the results of different merger histories.

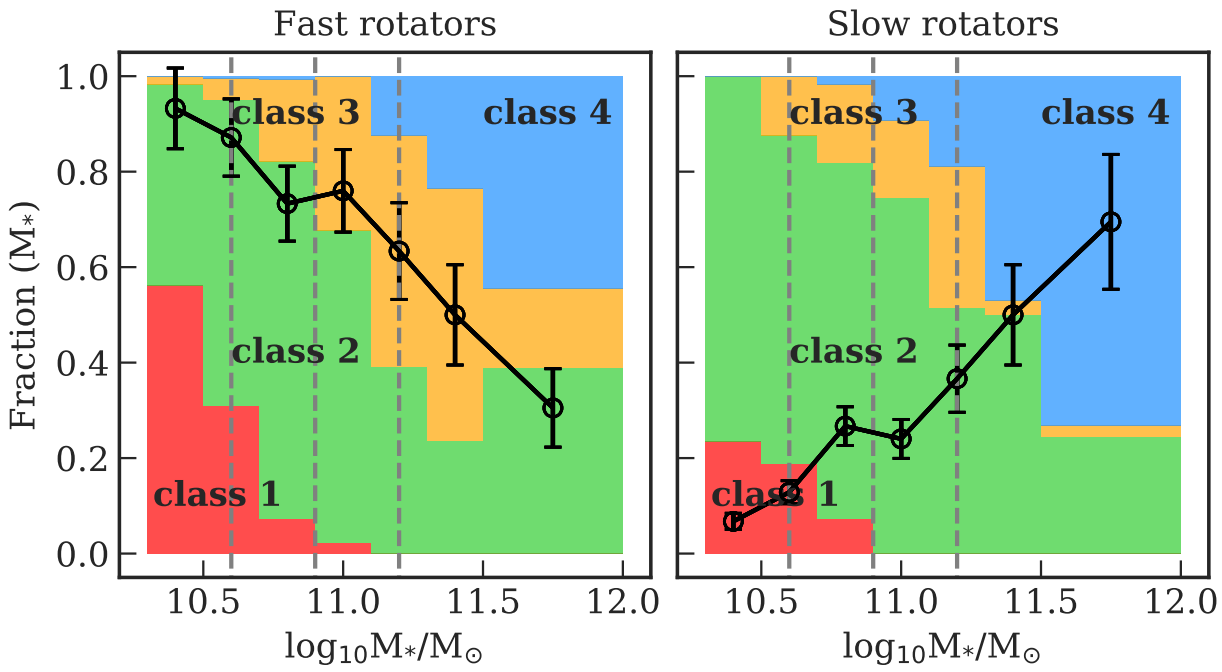

Figure 6.7: Fraction of FRs (**left**) and SRs (**right**) that populate each accretion class as a function of stellar mass, represented with a cumulative bar plot. The open circles show the fraction of fast or slow rotators in each mass bin. The vertical dashed lines represent the stellar mass bins adopted in the paper. FRs and SRs populate the four accretion classes differently, highlighting the different accretion histories of the two classes, but also that several formation pathways can lead to the formation of a FR or a SR.

6.5 V/$\sigma(R)$ profiles and accretion history

In this section we study how galaxy rotational support depends on accretion history. We do not distinguish galaxies using the accretion classes themselves as defined in the previous section, which cannot be readily derived from observations, but we rather divide them into stellar mass bins that best match the different classes.

6.5.1 V/$\sigma(R)$ profiles and in-situ fractions

We start by quantifying the galaxy rotational support using the edge-on projected $V_*/\sigma_*(R)$ profiles of the all the stars derived as in Sect. 6.3.3. Figure 6.8 shows median $V/\sigma_*(R)$ profiles in stellar mass bins for FRs and SRs in two separate arrays of figures. The top panels of Fig. 6.8 show the median $V_*/\sigma_*(R)$ for the total stellar component. For the FRs, the median profiles typically have a peaked and outwardly decreasing shape while the SRs show on average a mild increase of rotational support at large radii. However, in each mass bin, galaxies come with a variety of profile shapes, from approximately constant with radius to steeply declining for the FRs, and more or less increasing with radius for the SRs. This is reflected in the large scatter around the median. As for the $\lambda(R)$ profiles (Pulsoni et al. 2020), the shapes of the median $V_*/\sigma_*(R)$ profiles weakly depend on stellar mass. For the most massive galaxies, the peak in the $V_*/\sigma_*(R)$ profiles of the FRs is nearly absent, and the median halo rotation ($R \sim 8R_e$) is also suppressed compared to lower mass galaxies (see Paper I).

In Sect. 6.3.4 we showed that the total $V_*/\sigma_*(R)$ profiles can be well approximated by the weighted sum of the rotational support of the in-situ and ex-situ stars (Eq. (6.12)). This is done by neglecting the contribution to the angular momentum from minor axis rotation, which is small in most cases. As already observed in Paper I, only a small fraction of the selected TNG ETGs display significant kinematic twist. The red and blue curves in the top panels of the two arrays of Fig. 6.8 show the median in-situ and ex-situ contribution $f_i(R)U_{i,Z}(R)/\sigma_*(R)$, with $i \in \{\mathrm{insitu}, \mathrm{exsitu}\}$. The median in each radial bin takes into account the few systems with counter-rotating in-situ and ex-situ components, namely with $U_{i,Z}(R)$ having opposite sign (Sect 6.3.4). The sum of these median profiles approximates the total median $V_*/\sigma_*(R)$ profile in each mass bin very well, within an absolute median difference of 0.02 (the absolute maximum difference is 0.12).

The contribution from the in-situ stars to $V_*/\sigma_*(R)$ is on average a peaked profile, even in the case of the low-mass SRs. By comparison, the ex-situ stars have flat $f_{\mathrm{exsitu}}(R)U_{\mathrm{exsitu},Z}(R)/\sigma_*(R)$ profiles with radius and contribute little to the total rotation, except for the high-mass ($M_* > 10^{11.2}M_\odot$) FRs and for the intermediate-to-high-mass ($M_* > 10^{10.9}M_\odot$) SRs, meaning that in most of the sample galaxy rotation is driven by the in-situ stars.

We see a clear dependence on stellar mass of the contribution of the in-situ and ex-situ components to the total profiles, which is due to the strong mass dependence of the weights $f_i(R)$ (Fig. 6.5) more than to a variation with mass of the rotational support of the individual components (see below). At progressively higher masses, the contribution from the in-situ stars to the total rotational support decreases, while that from the accreted component mildly increases, resulting in a median total $V_*/\sigma_*(R)$ that is almost independent of stellar mass for FRs with

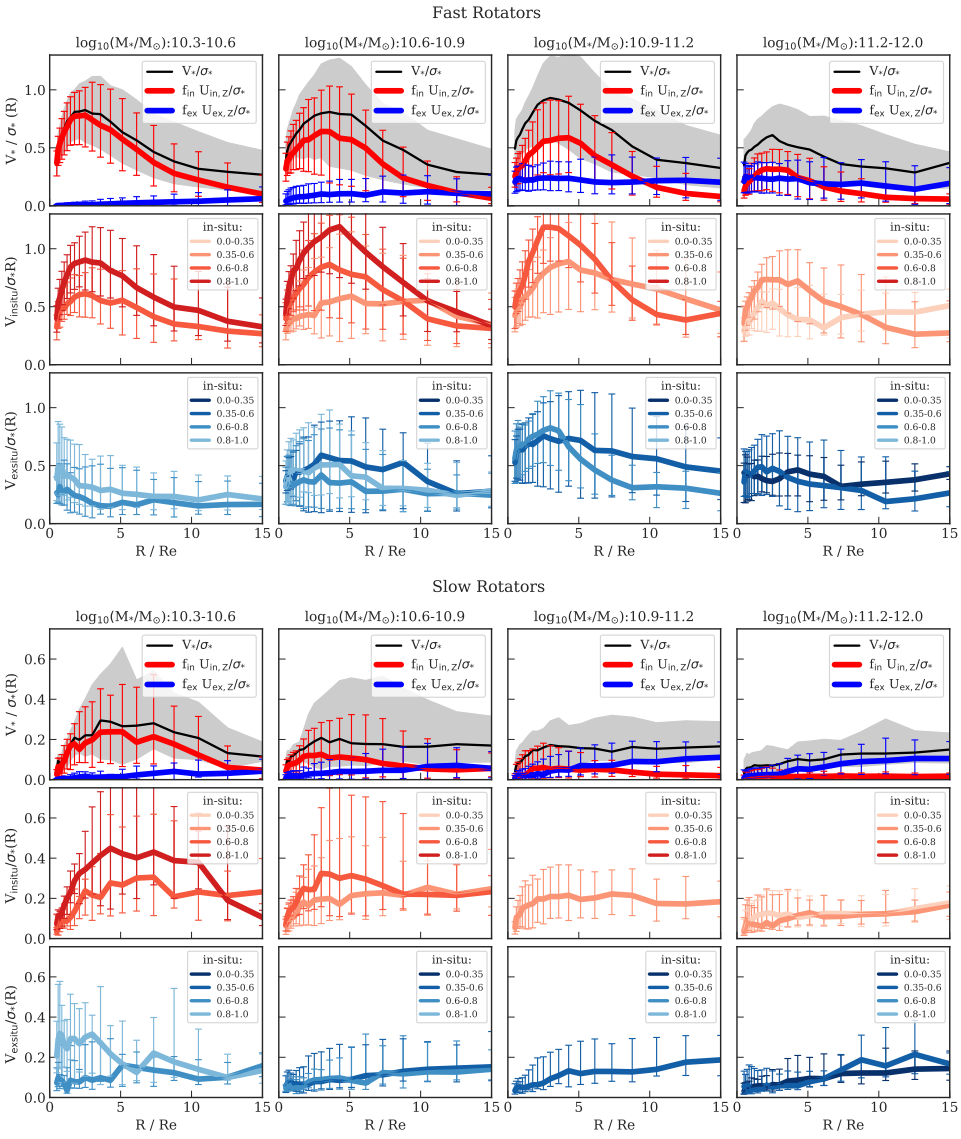

Figure 6.8: $V/\sigma(R)$ profiles for the TNG FRs (**top panels**) and SRs (**bottom panels**) divided into mass bins. In the two sets of panels, the **first rows** show the median V_*/σ_* profiles of all the stars in black. The red and blue curves are the median $f_i(R)U_{i,Z}(R)/\sigma_*(R)$ profiles for the in-situ and ex-situ stars, respectively. The sum of these median profiles approximates the median $V_*/\sigma_*(R)$ profiles up to a median absolute difference of 0.02. The **middle** and **bottom** rows show the median $V_i/\sigma_*(R) = \left|\sqrt{U^2_{i,X}(R) + U^2_{i,Z}(R)}\right|/\sigma_*(R)$ profiles of the in-situ and ex-situ components, respectively. Here the galaxies have been divided according to their total in-situ fraction, as shown in the legend. Error-bars and shaded regions trace the quartiles of the distributions. The in-situ stars are characterized by a peaked and outwardly decreasing $V_{\rm insitu}/\sigma_*(R)$ profile, while the ex-situ stars typically add a constant level of (subdominant) rotational support.

$M_* \lesssim 10^{11.2} M_\odot$ and for SRs with $M_* \lesssim 10^{10.9} M_\odot$. At larger stellar masses, the rotation of the in-situ stars is almost erased and the in-situ contribution $f_{\rm insitu}(R) U_{{\rm insitu},Z}/\sigma_*(R)$ becomes comparable to that of the ex-situ component.

The middle and bottom rows of both arrays in Fig. 6.8 show the median $V_{\rm insitu}/\sigma_*(R)$ and $V_{\rm exsitu}/\sigma_*(R)$ profiles, now defined as the ratio of Eqs. (6.9) and (6.10), meaning that $V_i/\sigma_*(R)$ is always a positive quantity. In each mass bin we divide galaxies according to their total in-situ mass fraction (bins as in Fig. 6.4). Galaxies with similar stellar mass have, on average, more peaked $V_{\rm insitu}/\sigma_*(R)$ profiles if their in-situ fraction is higher, meaning that the peak value of the $V_{\rm insitu}/\sigma_*(R)$ profiles is approximately proportional to the in-situ mass fraction. The maximum rotational support of the in-situ stars themselves only weakly depends on stellar mass, (again) except for high-mass FRs and intermediate-to-high mass SRs.

The median $V_{\rm exsitu}/\sigma_*(R)$ are generally quite flat and independent of the in-situ (or, equivalently, of the ex-situ) mass fraction. While for the SRs the $V_{\rm exsitu}/\sigma_*(R)$ profiles seem also insensitive to stellar mass, in the FRs we find an overall increase in the mean rotation of the ex-situ stars with stellar mass. On the other hand, the scatter on the $V_{\rm exsitu}/\sigma_*(R)$ profiles is much larger than the median variations among stellar mass bins, reflecting the variety of merger histories of the FRs at all stellar masses (see also Fig. 6.7 and Sect. 6.4.3). We verified that the scatter around the median in-situ and ex-situ profiles does not reduce for different binning choices of the in-situ mass fraction.

In the FRs, the typical peaked and outwardly decreasing shape of the total $V_*/\sigma_*(R)$ profiles is due to the in-situ stars, while the ex-situ component sets a constant level of rotational support at large radii. Galaxies with negligible accreted mass also display peaked and outwardly decreasing $V_*/\sigma_*(R)$ profiles (see also Fig. 6.9B). We verified that this is true for both central and satellite galaxies (figure omitted for brevity). An increasing fraction of ex-situ stars (or a decreasing in-situ fraction) is accompanied with progressive weakening of the peak and a flattening of the $V_{\rm insitu}/\sigma_*(R)$ profiles at large radii. At the same time the rotational support of the ex-situ stars, $V_{\rm exsitu}/\sigma_*(R)$, is insensitive to variations in the ex-situ fraction. These results imply that in the TNG FRs the decrease of rotational support in the stellar halo is not simply explainable as the weighted sum of a rotating disk-like in-situ component and a dispersion-dominated spheroidal ex-situ component. The kinematic transition into the spheroidal dispersion-dominated halo in the TNG FRs is driven mainly by the in-situ stars. In addition, Fig. 6.8 indirectly shows that (major) mergers dynamically suppress rotation also in the in-situ component thereby determining the flattening of the $V_{\rm insitu}/\sigma_*(R)$ profiles and an overall decreased rotation from the centers $1-2R_{\rm e}$ to the outskirts ($\gtrsim 8R_{\rm e}$).

This conclusion is also supported by the comparison of the $\mathrm{V}_{\rm insitu}/\sigma_{\rm tot}(R)$ profiles between FRs and SRs in Fig. 6.8. At fixed stellar mass, the SRs have on average larger fractions of major mergers and a more recent, more gas-poor accretion history (Sect. 6.4). Therefore, at fixed stellar mass and in-situ fraction, SR galaxies have distinctly flatter rotation profiles.

6.5.2 $\mathrm{V}/\sigma(R)$ profiles and merger mass ratio

In this section we study how mergers affect the shapes of the ETG $V_*/\sigma_*(R)$ profiles. We start with the effect of major mergers. In Fig. 6.6 we show that the fraction of accreted mass from

major mergers $\Delta M_{*,\rm major}/M_*$ depends on mass, with the lowest mass galaxies having negligible $\Delta M_{*,\rm major}/M_*$ while for higher mass galaxies ($M_* > 10^{10.75} M_\odot$) the ex-situ fraction from major mergers spans a wide range, from 0 to 60% and up to 80% for a few objects above $10^{11.5} M_\odot$. Figure 6.9A shows the effect of major mergers on the galaxy rotational support. The left panels of Fig. 6.9A show how the $V_*/\sigma_*(R)$ profiles vary in bins of $\Delta M_{*,\rm major}/M_*$ in FRs (top panels) and SRs (bottom panels). Increasing $\Delta M_{*,\rm major}/M_*$ clearly erases the peak in rotation and flattens the profiles. In extreme cases, where the FRs have $\Delta M_{*,\rm major}/M_* \gtrsim 0.4$, the $\rm V_{tot}/\sigma_{tot}$(R) profiles are flat from the central regions to the halos. In SRs, major mergers prove to be much more effective in flattening the profiles, as for these galaxies mergers are more gas poor and more recent (see Sect. 6.4.3).

The left panels of Fig. 6.9A show together FRs and SRs of stellar masses from $10^{10.3}$ to $10^{12} M_\odot$, which assemble at different epochs and with different gas fractions. Each of these variables plays a role in determining the final shape of the $V_*/\sigma_*(R)$ profiles. The right panels of Fig. 6.9A show, for example, the role of recent cold gas accretion (parametrized here by $\Delta_{\rm insitu,z\leq1}$) for galaxies with a similar fraction of stellar mass accreted from major mergers (here we show $0.1 \leq \Delta M_{*,\rm major}/M_* \leq 0.3$). The presence of gas (in situ or accreted in the mergers) is essential to preserve/build up the central rotating disk-like structure. The comparison between the median profiles of FRs and SRs with similar $\Delta M_{*,\rm major}/M_*$ and $\Delta_{\rm insitu,z\leq1}$ suggests that other variables may determine the shape of the profiles, such as for example the timing of the merger. A galaxy may or may not have its rotating component destroyed if its accreted mass comes from a more recent merger and it has not had time to rebuild the disk.

To isolate the effect of mini mergers, we select galaxies that accreted a negligible fraction of mass from major mergers, minor mergers, or stripped from surviving galaxies (less than 1% of M_* from each). Most of these galaxies have low stellar masses, $M_* < 10^{10.5} M_\odot$, but some reach $M_* < 10^{10.9} M_\odot$. The selected galaxies are mostly FRs ($\sim 97\%$) and have accreted mass fractions from mini mergers $\Delta M_{*,\rm mini}/M_*$ ranging from 0 to 30%. The median number of mini mergers per galaxy is 30. Figure 6.5 shows that the accreted star from mini mergers for galaxies with $M_* < 10^{10.9} M_\odot$ are mainly deposited in the outskirts.

Figure 6.9B shows the median $V_*/\sigma_*(R)$ profiles for this group of galaxies for different $\Delta M_{*,\rm mini}/M_*$ fractions. We distinguished between galaxies with a low fraction of recently formed in-situ stars $\Delta_{\rm insitu,z\leq1}$ (left panel) and galaxies with high $\Delta_{\rm insitu,z\leq1}$ (right panel). In this way, we take into account variations in the $V_*/\sigma_*(R)$ profiles due to the recent accretion of gas. We find that, independently of $\Delta_{\rm insitu,z\leq1}$, galaxies with the lowest $\Delta M_{*,\rm mini}/M_*$ fractions have peaked and outwardly decreasing profiles. Higher $\Delta M_{*,\rm mini}/M_*$ fractions progressively increase the rotational support of the outermost regions while roughly conserving the height of the peak. These trends persist when considering only central galaxies (not shown here for brevity). The recent gas accretion parametrized by $\Delta_{\rm insitu,z\leq1}$ has the overall effect of increasing the peak of rotation from a median ~ 0.75 to a median ~ 1.

Finally, we studied (although do not show here for brevity) the effect of minor mergers. We selected a sample of galaxies within a narrow range of accreted stellar mass from major mergers ($\Delta M_{*,\rm major}/M_* \in [0.1, 0.2]$, giving the minor mergers) to include more massive systems and at the same time limit the impact of major mergers. Minor mergers have a somewhat similar effect to the major mergers. If their contribution is high enough, they can weaken the peak of rotation,

meaning that galaxies with $\Delta M_{*,\mathrm{minor}}/M_* \gtrsim 10\%$ have a significantly lower maximum in their $V_*/\sigma_*(R)$ profiles (peak value$\sim$ 0.5) with respect to galaxies with $\Delta M_{*,\mathrm{minor}}/M_* < 5\%$ (peak value $\sim$ 0.9). On the other hand, we find that the rotational support of the halo regions ($R \sim 8R_\mathrm{e}$) is independent of $\Delta M_{*,\mathrm{minor}}/M_*$.

6.5.3 Dependence of the $V/\sigma(R)$ profiles on other parameters

In Section 6.5.2 we demonstrate that the shape of the $V_*/\sigma_*(R)$ profiles is influenced by several physical processes that are at work in the galaxy assembly history. Accretion parameters correlate more or less tightly with stellar mass, and hence with each other (Figs. 6.2 and 6.6; see also Rodriguez-Gomez et al. 2017). For example, galaxies with the lowest stellar mass have on average the highest in-situ mass fraction and the highest mean accreted gas fraction. Assuming that the total stellar mass and the in-situ mass fraction (or, equivalently, the ex-situ mass fraction) are the two fundamental variables (Sec. 6.5.1), we studied whether there are additional residual correlations with other accretion history properties.

We inspected (albeit not shown for brevity) the $V_\mathrm{insitu}/\sigma_*(R)$ profiles in bins of stellar mass and in-situ fractions for variations of mean gas fraction, in-situ stellar mass formed after $z = 1$, stellar mass accreted via major mergers, redshift of the last major merger, and number of major mergers: we find no secondary dependencies. The lack of such correlations indicates that even though the shape of the $V_\mathrm{insitu}/\sigma_\mathrm{tot}(R)$ profiles is sensitive to different accretion parameters which describe the details of the galaxy formation histories, their effect is already taken into account by the total stellar mass and the total in-situ mass fraction. We repeated this study for the total $V_*/\sigma_*(R)$ profiles and found almost identical results.

6.5.4 Rotational support and the local accreted fraction

The $V_*/\sigma_*(R)$ profile shapes at different stellar masses are primarily regulated by the in-situ mass fraction (Sect. 6.5.1). The typical profile of a low-mass galaxy with negligible accreted fraction is a peaked profile that decreases at large radii. At higher stellar masses and ex-situ fractions, mergers modify the rotational support of the in-situ components and add the contribution of the ex-situ stars, meaning that the outskirts of galaxies ($R > 2-3R_\mathrm{e}$) show a large variety of stellar halo rotational support in qualitative agreement with extended kinematic studies of observed ETGs (Pulsoni et al. 2018, see also Paper I). However, Fig. 6.8 shows that, at fixed stellar mass and in-situ mass fraction, galaxies exhibit a large scatter around the median profiles. In Sect. 6.5.3 we show that this scatter is not due to the additional accretion parameters investigated.

A possible explanation for the large scatter in the profiles comes from Figs. 6.4 and 6.5: galaxies with similar masses and similar total in-situ fractions can have different spatial distribution of in-situ and accreted stars, for example if they belong to different accretion classes. This results in a scatter around the median $f_\mathrm{exsitu}(R)$ profiles. In this section we investigate whether the stellar halo rotational support has a clearer dependence on the local fraction of accreted stars (i.e., both measured at the same radius) rather than on the total accreted mass fraction.

We proceed as follows. The outer regions ($3-8R_\mathrm{e}$) of each TNG100 galaxy are divided into seven elliptical shells with semi-major axis R and flattening following the ellipticity profile of the

galaxy. In each shell, we measure the rotational support of the stellar particles $V_*/\sigma_*(R)$ and the local ex-situ mass fraction $f_{\rm exsitu}$. The minimum radius of $3R_{\rm e}$ is motivated by the requirement that R should be sufficiently large that the $V_*/\sigma_*(R)$ profiles of the TNG FRs reach their peak rotation, which occurs at a median radius of $\sim 2.7R_{\rm e}$.

Figure 6.10 shows the rotational support $V_*/\sigma_*(R)$ as a function of $f_{\rm exsitu}(R)$ measured in the same radial bins. Each data point in the diagram corresponds to a local measurement within one galaxy, meaning that each galaxy is represented by seven data points. Galaxies are divided into stellar mass bins, and FRs and SRs are shown with different colors.

Figure 6.10 reveals that there is a strong anti-correlation between these V_*/σ_* and $f_{\rm exsitu}$: wherever the local ex-situ contribution $f_{\rm exsitu}$ is high the rotational support is low. As $f_{\rm exsitu}$ decreases, V_*/σ_* tends to increase but at low $f_{\rm exsitu} \lesssim 0.2$, $V_*/\sigma_*(R)$ is independent of $f_{\rm exsitu}$. These cases correspond mainly to low-mass in-situ-dominated galaxies, in which the kinematic transition to the dispersion-dominated stellar halo is caused by the in-situ stars alone.

The strong dependence of V/σ on the local $f_{\rm exsitu}$, together with the variations of $f_{\rm exsitu}$ among different galaxies at the same radius, partially explains the large scatter in $V/\sigma(R)$ profiles. The scatter on the median $\rm V_{tot}/\sigma_{tot}(f_{exsitu})$ profiles is reduced by a factor of ~ 1.4 compared to the scatter on the median $V_*/\sigma_*(R)$.

Slow rotators sit on the the same anti-correlation traced by the FRs and populate the tail of the FR stellar halo parameter distributions at high $f_{\rm exsitu}$. This continuity of local properties between the two classes can be reconciled with the systematic differences in median $V_*/\sigma_*(R)$ profiles of FRs and SRs with similar mass and in-situ fraction seen in Fig. 6.8 by considering their different radial distribution of in-situ versus ex-situ stars as implied in Figs. 6.5 and 6.7. Finally, we note that we observe that if we assume that a similar $V_*/\sigma_* - f_{\rm exsitu}$ correlation holds in real galaxies, then one could in principle use the observationally accessible $\rm V/\sigma(R)$ profiles in the stellar halos and stellar masses to estimate the local ex-situ contribution $f_{\rm exsitu}(R)$ in observed galaxies within approximately ± 0.16. This range is derived from the average width of the $f_{\rm exsitu}$ distribution at the 10-90 percentiles for different V_*/σ_* and stellar mass bins. The median and quartiles of the local V_*/σ_* distribution as a function of the local $f_{\rm exsitu}$ for ETGs with $M_* > 10^{10.6} M_\odot$ is reported in Table 6.A.5.

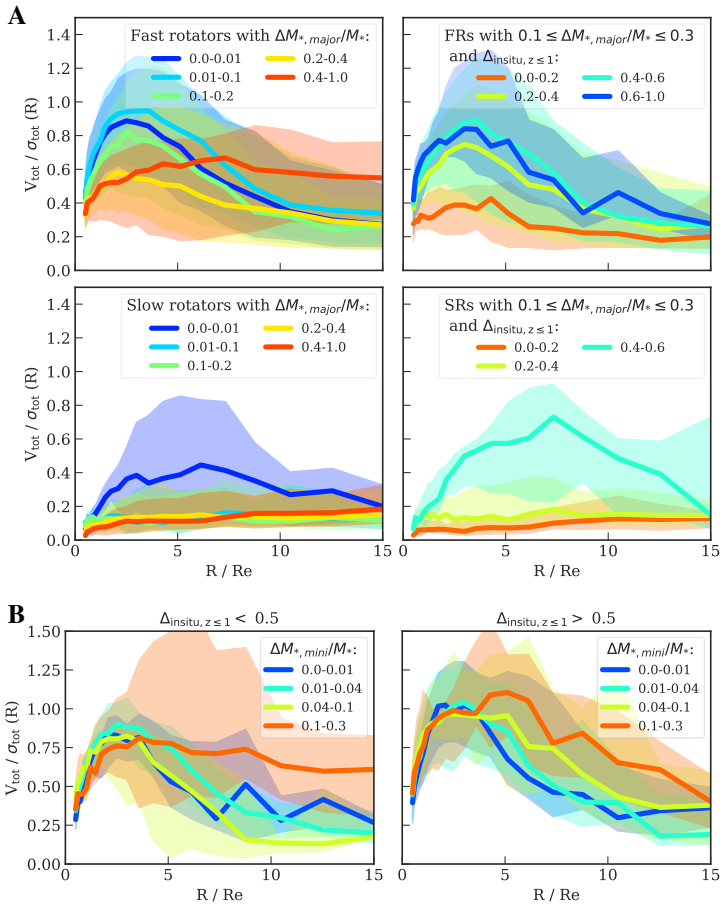

Figure 6.9: Effect of mergers on the $V_*/\sigma_*(R)$ profiles. **A**: Major mergers. Median profiles for the FRs (**top left**) and the SRs (**bottom left**) in bins of accreted mass fraction from major mergers $\Delta M_{*,\mathrm{major}}/M_*$. The **right panels** show the median $V_*/\sigma_*(R)$ for different $\Delta_{\mathrm{insitu,z\leq 1}}$ fractions and within a narrow range of $\Delta M_{*,\mathrm{major}}/M_*$ fractions. Major mergers erase the peak in rotation and flatten the profiles. The presence of cold gas preserves or builds up the centrally rotating component. **B**: Mini mergers. Median profiles for ETGs with negligible fraction of accreted mass from major, minor mergers, or stripped from surviving galaxies in bins of accreted mass fraction from mini mergers $\Delta M_{*,\mathrm{mini}}/M_*$. The **left panel** shows galaxies with $\Delta_{\mathrm{insitu,z\leq 1}}$ lower than the median $\Delta_{\mathrm{insitu,z=0}} = 0.61$ for class 1 galaxies (i.e., with lower recent star formation), while the **right panel** shows those with $\Delta_{\mathrm{insitu,z\leq 1}}$ higher than the median. Mini mergers are not massive enough to modify the peak in rotation, but on average, and for low-mass systems, tend to increase the rotational support at large radii.

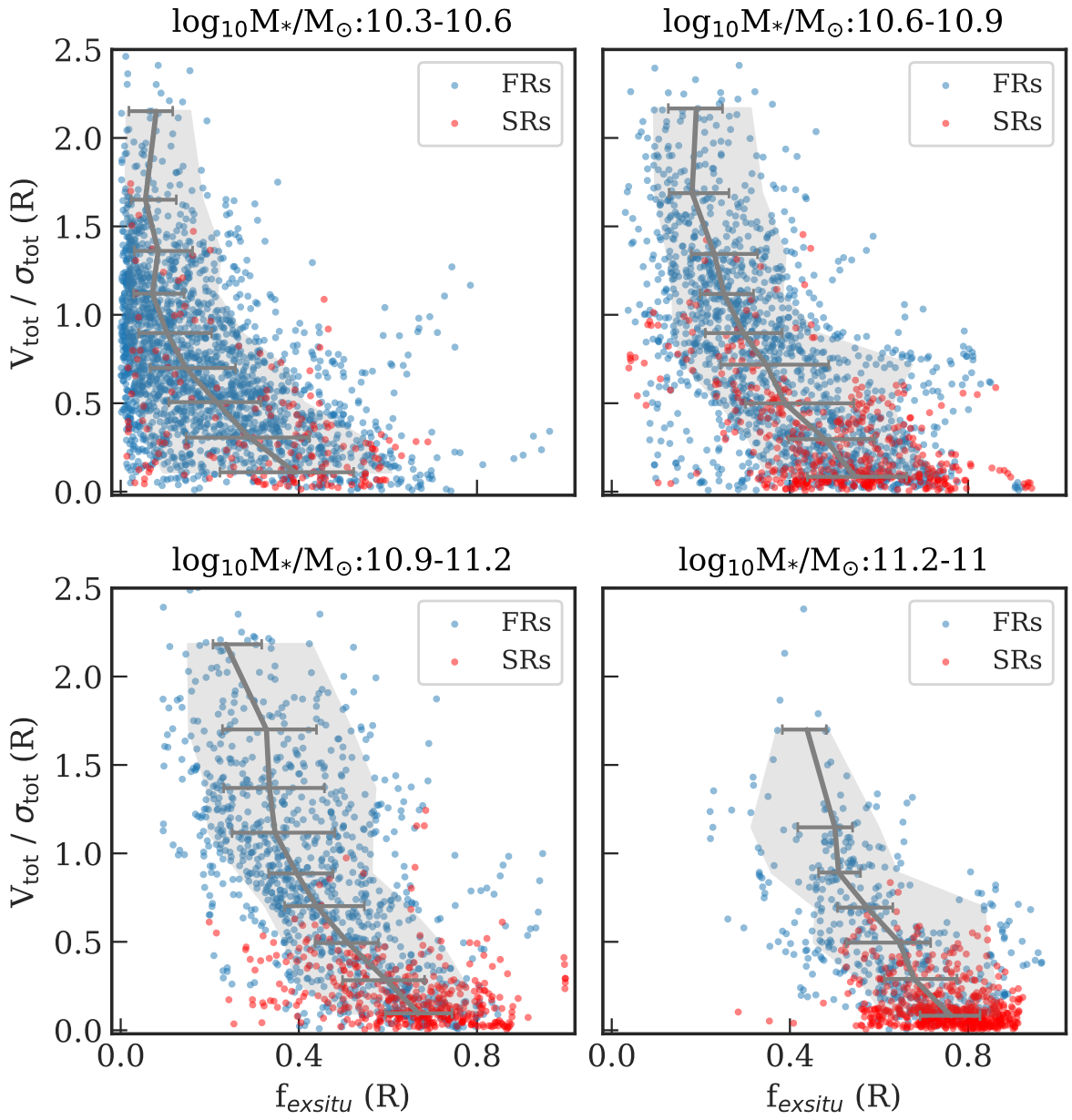

Figure 6.10: Local correlation between rotational support and accreted fraction in the stellar halos. Each data point corresponds to a local measurement at a radius $R \in [3-8R_e]$ within each galaxy. Blue circles show measurements within FRs, red circles within SRs. The solid lines show the median, the error-bars the quartiles, and the shaded regions the 10-90 percentiles of the $V_*/\sigma_*(f_{\rm exsitu})$ distributions. Galaxies are divided into stellar mass bins as labeled. At high local ex-situ mass fractions the stellar halo rotational support V_*/σ_* decreases.

6.6 Intrinsic shapes and accretion history

In Paper I we determined the intrinsic shapes of our sample of simulated ETGs and found that kinematics and intrinsic shapes are closely related, such that the kinematic transitions into the stellar halos are accompanied by changes in the galaxy intrinsic shapes. The FRs that decrease in rotational support at large radii tend also to become more spherical in the outskirts, while a fraction with high stellar halo rotation show constant axis ratio $q(r)$ profiles out to large radii. The majority of low-mass FRs have stellar halos consistent with oblate shapes, but at higher stellar masses the fraction of FRs with triaxial stellar halos increases. By comparison, the SRs display milder structural changes with radius, exhibiting rather constant $q(r)$ and triaxiality $T(r)$ profiles. In this section we study the dependence of galaxy intrinsic shapes on accretion.

6.6.1 Intrinsic shape profiles and in-situ fractions

Figure 6.11 shows median $q(r)$ and $T(r)$ profiles for FRs and SRs divided into bins of stellar mass and in-situ fraction. The median profiles are built using the profiles of the single galaxies at the radii where resolution effects are small ($r \geq 2r_{\rm soft}$ for $q(r)$ and $r \geq 9r_{\rm soft}$ for $T(r)$; see Sect. 6.3.2).

In Paper I we found that triaxiality increases with radius in FRs and that in both FRs and SRs the stellar halo triaxiality ($T(8R_{\rm e})$) increases with stellar mass. These trends are visible also in Fig. 6.11. As M_* tightly correlates with the total fraction of in-situ stars (Fig. 6.2), similar behaviors are found as a function of this variable.

Fast-rotating galaxies with higher M_* and in-situ fractions reach the largest values of T in the stellar halo. In the SRs the dependence of $T(r)$ on these parameters is much more striking, such that at similar stellar mass and total in-situ mass fraction, triaxiality is overall systematically higher than in FRs.

From the median $q(r)$ profiles, we see that FRs tend to become slightly rounder at increasing M_* and decreasing total in-situ fraction. FRs with higher M_*/lower in-situ fraction have rather constant median $q(r)$ profiles while those with lower M_*/higher in-situ fractions show more pronounced dips in q at radii corresponding to the positions of the peaks in the median $V_*/\sigma_*(R)$ profiles of Fig. 6.8. The $q(r)$ profiles in SRs are almost independent of these parameters, although SRs with $M_* > 10^{11.2} M_\odot$ or with in-situ fractions < 0.35 have significantly flatter intrinsic shapes at large radii (see also Sect. 6.6.3), similarly to the few SRs with in-situ fractions > 0.8.

Overall galaxy intrinsic shapes depend on both stellar mass and in-situ fraction but we find (although we do not show here) that at fixed stellar mass the galaxies with highest triaxiality and lowest flattening are those with low in-situ mass fraction (see the scatter in in-situ fraction values in Fig. 6.2). The results of Fig. 6.11 indicate that the stellar component that is born in-situ tends to preserve the near-oblate flattened disk-like structure of the star forming gas, at least in the central regions. Therefore, FRs with higher in-situ fractions and lower stellar masses show larger variations of the median $q(r)$ profiles with radius, with the outskirts being rounder than the centers. Instead, galaxies with higher accreted fractions and stellar masses have milder variations of flattening with radius but have overall increased triaxiality at large (FRs) or all (SRs) radii. The collisionless dynamics of gas-poor mergers, which enrich the galaxies with ex-situ stars, is the

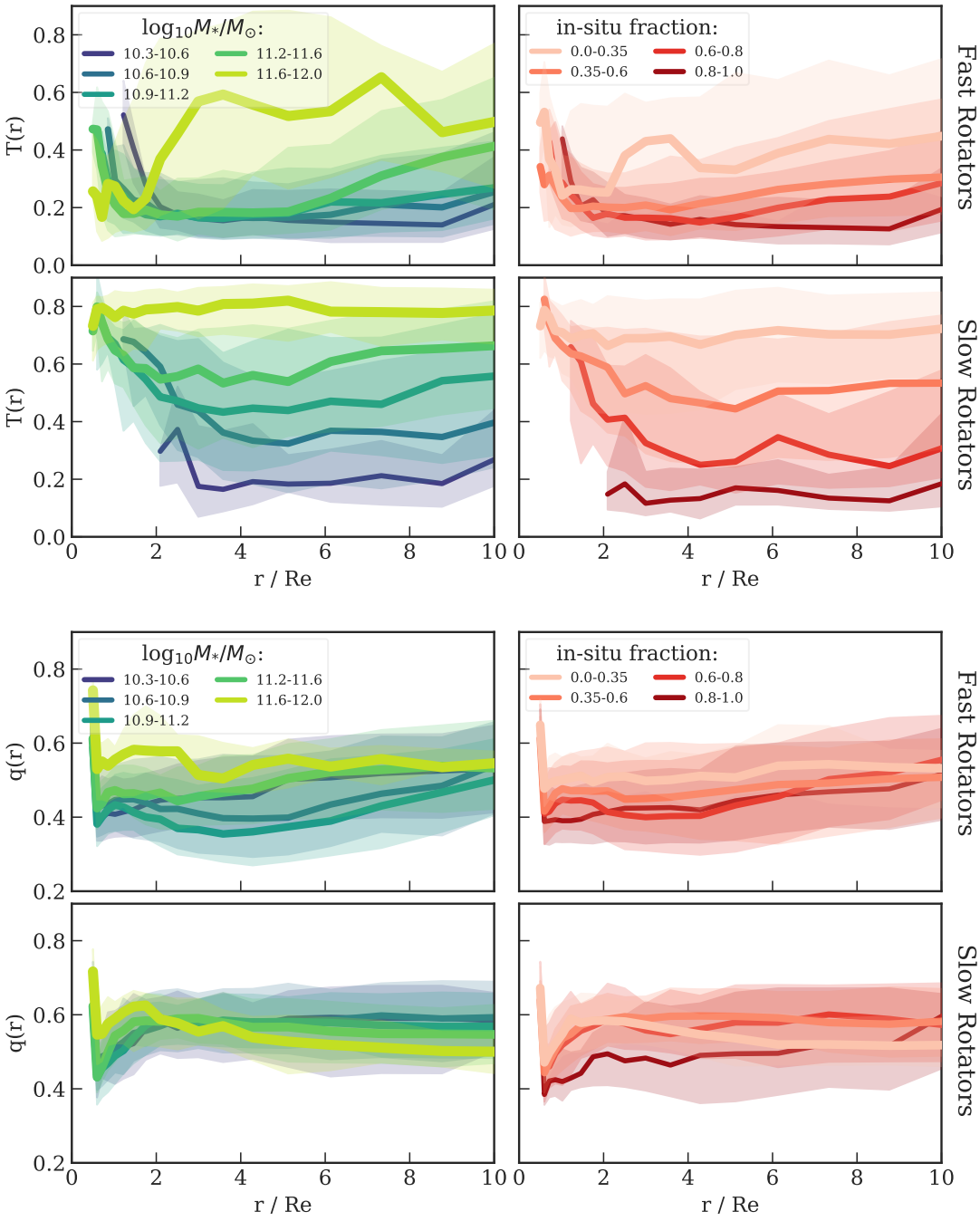

Figure 6.11: Median stellar intrinsic shape profiles for FRs and SRs as labeled on the right margins. The **top** panels show the triaxiality $T(r)$, the **bottom** panels show the axis ratio $q(r)$. Galaxies on the **left** are divided into stellar mass bins, and galaxies on the **right** are divided in bins of total in-situ mass fraction. The solid lines show the median profiles, and the shaded regions trace the quartiles of the distributions. Higher stellar masses and accreted fractions correspond to higher triaxiality and less flattened shapes.

primary mechanism responsible for changing the intrinsic shapes from near-oblate to spheroidal triaxial, as we demonstrate in Sect. 6.6.2.

6.6.2 Intrinsic shape profiles and mergers

In this section we analyze how mergers affect the intrinsic shapes of galaxies. The effects of major mergers on the triaxiality profiles is shown in Fig. 6.12A. The left panels show median profiles in bins of $\Delta M_{*,\rm major}/M_*$ for our sample of ETGs divided in FRs and SRs. While for the SRs the effect of $\Delta M_{*,\rm major}/M_*$ in increasing the median $T(r)$ is rather clear, for the FRs the picture is complicated by the higher fractions of accreted gas (Fig. 6.2), which on the other hand tend to decrease $T(r)$. The right panels of Fig. 6.12A show that, at fixed fraction of accreted mass from major mergers $\Delta M_{*,\rm major}/M_*$, the galaxies with lowest recent in-situ star formation $\Delta_{\rm insitu,z\leq1}$ (i.e., those that did not recently accrete gas) whose recent mergers were then gas-poor are the FRs with increasing $T(r)$ profiles and the SRs with the highest median $T(r)$. Major mergers also affect the $q(r)$ profiles (not shown here) in that galaxies with higher $\Delta M_{*,\rm major}/M_*$ and lower $\Delta_{\rm insitu,z\leq1}$ tend to be on average more spherical, although the effect is not as pronounced as on the $T(r)$ profiles (see Sect. 6.6.3).

Figure 6.12B shows the effect of mini mergers on the intrinsic shape profiles. Analogously to Sect. 6.5.2 we isolate the effect of mini mergers by considering galaxies with negligible accreted mass from other accretion channels (i.e., with $\Delta M_{*,\rm major}/M_*$, $\Delta M_{*,\rm minor}/M_*$, and $\Delta M_{*,\rm stripped}/M_*$ less than 1% each). The selected galaxies, mostly FRs with $M_* < 10^{10.5} M_\odot$, have their accreted mass accumulated mainly at large radii (Fig. 6.5). We group the galaxies into bins of accreted mass fraction from mini mergers ($\Delta M_{*,\rm mini}$) and use $\Delta_{insitu,z\leq1} = 0.5$ to distinguish between galaxies with recent gas accretion and in-situ star formation (right panels in Fig. 6.12B) and those with more quiescent recent star formation history (left panels).

We see that mini mergers do not clearly affect the triaxiality profiles; the majority of the selected galaxies are consistent with being near-oblate ($T \leq 0.3$) at all radii. On the other hand, we find that, independently of $\Delta_{insitu,z\leq1}$, galaxies with negligible $\Delta M_{*,\rm mini}/M_*$ have low $q \sim 0.4$ at $r \sim 1R_{\rm e}$ which increases to $q \sim 0.6$ at $r > 4R_{\rm e}$. Increasing contributions of mini mergers tend to flatten the stellar halos along with increasing their rotational support (Fig. 6.9B). Finally, galaxies with higher recent star formation (i.e., recent cold gas accretion) tend to have on average more flattened shapes, both at the centers and at large radii. Figure 6.12B shows results consistent those in Fig. 6.9B. Galaxies dominated by in-situ stars at all radii with negligible accreted mass ($\Delta M_{*,\rm mini}/M_* < 0.02$ in Fig. 6.12B) display characteristic peaked and outwardly decreasing $V_*/\sigma_*(R)$ profile shapes and growing $q(r)$ profiles in the stellar halo. The kinematic transition is accompanied by a change in the dynamical structure of these galaxies, both completely driven by the in-situ stars. We verified, although we do not show for brevity, that these results also hold if we consider central galaxies alone.

Figure 6.12B indirectly shows that high-mass-ratio mergers are essential for galaxies to reach high values of triaxiality. We found (but do not show here for brevity) that minor mergers, studied in a sample of galaxies selected within a narrow range of accreted mass fractions from major mergers $\Delta M_{*,\rm major}/M_* \in [0.1, 0.2]$ (see also Sect. 6.5.2), can have the effect of increasing the galaxy triaxiality at large radii if their contribution is large enough (> 10% of the total stellar

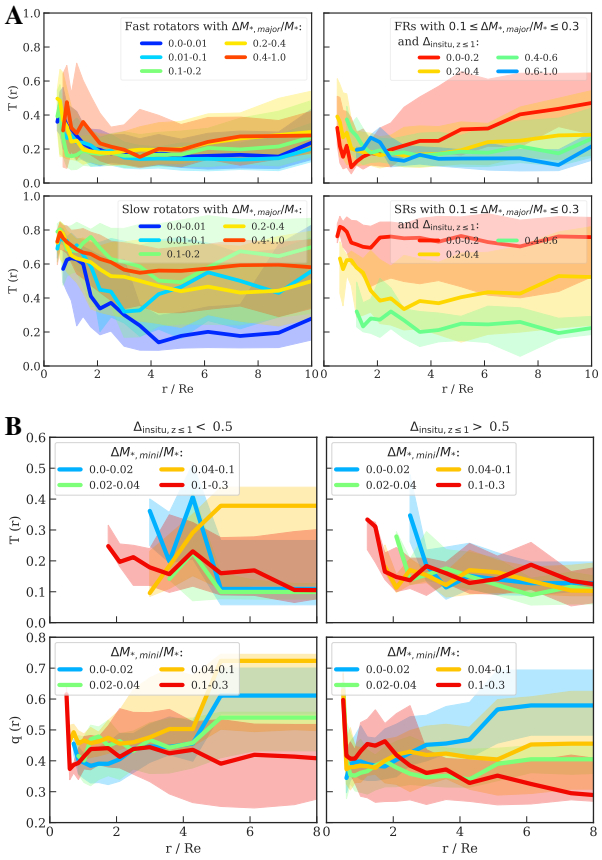

Figure 6.12: Effect of mergers on the intrinsic shape profiles. **A**: Major mergers in FRs (**top**) and SRs (**bottom**). The solid lines show the median triaxiality profiles in bins of accreted mass fraction from major mergers $\Delta M_{*,\mathrm{major}}/M_*$ (**left panel**) and in bins of $\Delta_{\mathrm{insitu,z\leq 1}}$ for $0.1 \leq \Delta M_{*,\mathrm{major}}/M_* \leq 0.3$ (**right panel**). The shaded regions show the quartiles of the distributions. Major mergers increase the triaxiality at large radii, especially when the fraction of recently accreted gas is low. **B**: Effect of mini mergers on the intrinsic shape profiles $T(r)$ (**top**) and $q(r)$ (**bottom**) for ETGs with negligible accreted mass from major mergers, minor mergers, and stripped from surviving galaxies. The solid lines show median profiles in bins of accreted mass fraction from mini mergers $\Delta M_{*,\mathrm{mini}}/M_*$; the shaded regions show the quartiles of the distributions. The **left panel** shows galaxies with $\Delta_{\mathrm{insitu,z\leq 1}} < 0.5$ (i.e., with lower recent star formation), the **right panel** those with $\Delta_{\mathrm{insitu,z\leq 1}} > 0.5$. Mini mergers do not significantly influence the galaxy triaxiality but tend to increase the stellar halo flattening.

mass). Contrary to mini mergers, higher fractions of $\Delta M_{*,\mathrm{minor}}/M_*$ lead to less flattened shapes ($q \gtrsim 0.5$).

The results described in this section demonstrate that the galaxy accretion history models the intrinsic shapes of galaxies in different ways according to the contribution of the various accretion channels. On the other hand, the fact that the gas fraction, the recent formation of in-situ stars, and the fraction of accreted mass from major mergers are all tightly correlated with stellar mass (Fig. 6.6), reduces the degree of freedom of these parameters. We conducted a study on the intrinsic shape profiles similar to that for the $V_*/\sigma_*(R)$ profiles in Sect. 6.5.3 to test their dependence on accretion parameters other than the total in-situ mass fraction. As for the $V_*/\sigma_*(R)$ profiles, we find no additional dependence once the total stellar mass and the total in-situ mass fraction have been taken into account.

6.6.3 Intrinsic shapes and the local accreted fractions

Here we explore the relation between local galaxy intrinsic shapes and accreted stellar mass fraction. This is done by measuring the mass fraction of accreted stars within three-dimensional ellipsoidal shells that approximate the isodensity surfaces. The outskirts of galaxies between $3.5 \leq r/R_\mathrm{e} \leq 8$ are divided into six spherical radial bins. Each of these spherical bins is deformed into a homeoid with fixed semi-major axis length following the iterative procedure described in Sect. 6.3.2. The ratios of the homeoid semi-axes give the local intrinsic shapes; within each homeoid we derive the total three-dimensional stellar mass density $\rho_*(r)$, and three-dimensional density of the ex-situ component $\rho_\mathrm{exsitu}(r)$. From the ratio $f_\mathrm{exsitu}(r) = \rho_\mathrm{exsitu}(r)/\rho_\mathrm{tot}(r)$ we obtain the local three-dimensional ex-situ fraction.

Figure 6.13 shows the intrinsic shape parameters $q(r)$ and $T(r)$ as functions of the local ex-situ fraction $f_\mathrm{exsitu}(r)$. Galaxies are plotted in stellar mass bins, and SRs and FRs are shown with different colors. We find that the halo intrinsic shapes and f_exsitu are correlated. Their relation is more complicated than the simple linear correlation between rotational support and $f_\mathrm{exsitu}(R)$ observed in Fig. 6.10. We find that stellar halos are near-oblate where $f_\mathrm{exsitu} < 0.4$ but at larger local ex-situ fractions they show increasingly larger triaxiality. The axis ratio $q(r)$ strongly correlates with $f_\mathrm{exsitu}(r)$ up to a break at $f_\mathrm{exsitu} \sim 0.7$, beyond which the $q(f_\mathrm{exsitu})$ is an anti-correlation. The break of the $q(f_\mathrm{exsitu})$ relation explains the modest effects of the total in-situ fraction on the median $q(r)$ profiles for galaxies with large total ex-situ fractions, such as the massive FRs and the intermediate- to high-mass SRs, as well as the change in trend seen in the median profiles of the SRs with $M_* > 10^{11.2} M_\odot$ in Fig. 6.11. We note that class 1 galaxies, mainly present in the lowest stellar mass bin at low f_exsitu, do not follow the $q(f_\mathrm{exsitu})$ correlation, as changes in flattening are driven by the in-situ stars only (see Sect. 6.6.2). For $M_* \geq 10^{10.6} M_\odot$ galaxies, the $q(f_\mathrm{exsitu})$ and $T(f_\mathrm{exsitu})$ relations are clear. The median and quartiles of the distributions of q and T as a function of the local f_exsitu for ETGs with $M_* > 10^{10.6} M_\odot$ are reported in Table 6.A.5.

The $q(f_\mathrm{exsitu})$ and $T(f_\mathrm{exsitu})$ relations are followed by both FRs and SRs in each stellar mass bin, but with relative fractions varying with stellar mass. FRs and SRs again show a continuity of stellar halo properties across the two classes, with the SRs significantly overlapping with the FRs but crowding at the high f_exsitu extreme. The systematic differences between median shape profiles of FRs and SRs with similar stellar mass and in-situ fractions observed in Fig. 6.11 are

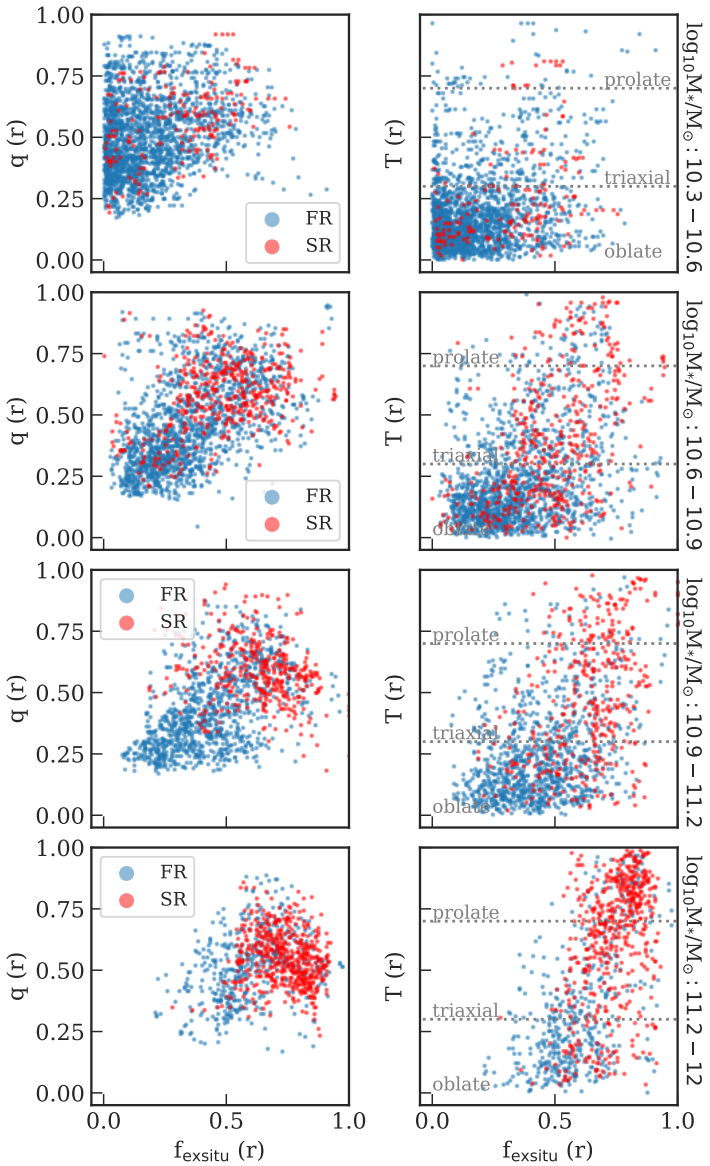

Figure 6.13: Local correlation between stellar halo intrinsic shape and fraction of accreted stars in stellar mass bins. Each galaxy is represented by about six data points, measured in ellipsoidal shell with semi-major axis $r \in [3.5 - 8R_e]$. The correlations are clear for galaxies more massive than $M_* > 10^{10.6} M_\odot$. Low $f_{\rm exsitu}$ is consistent with near-oblate shapes with low axis ratio q. At higher $f_{\rm exsitu}$ the stellar halo triaxiality parameter increases while the $q(f_{\rm exsitu})$ correlation reaches a maximum of $q \sim 0.6$ for $f_{\rm exsitu} \sim 0.7$, beyond which the q decreases.

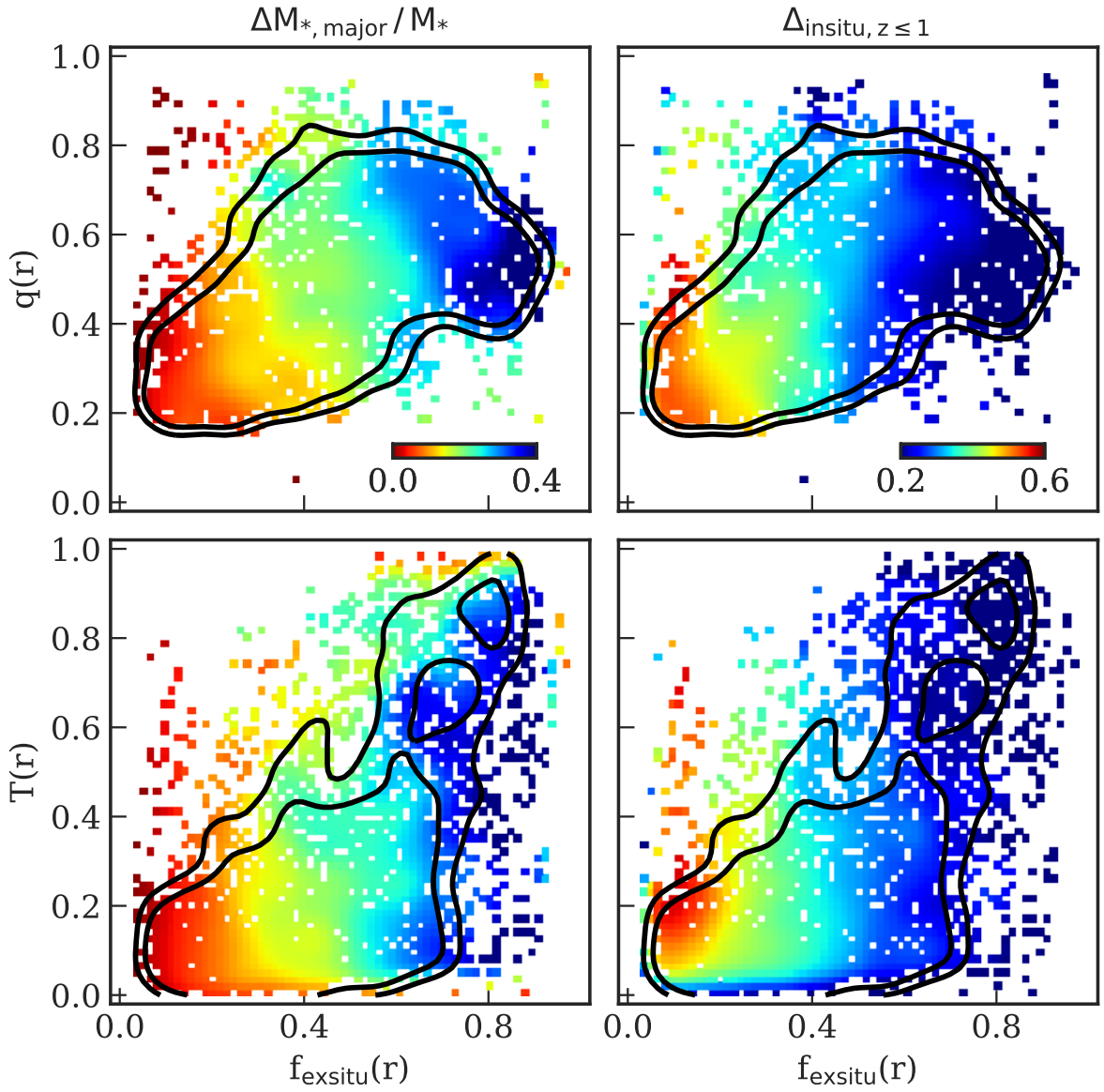

Figure 6.14: Local relation between galaxy intrinsic shapes and the local fraction of accreted stars for galaxies with $M_* \geq 10^{10.6} M_\odot$. The **top** panels show $q(f_{\rm exsitu})$, the **bottom** panels $T(f_{\rm exsitu})$. In the **left** panels, galaxies are color-coded according to the fraction of accreted mass from major mergers $\Delta M_{*,\rm major}/M_*$, in the **right** panels colors indicate the fraction of in-situ stars produced since $z = 1$, $\Delta_{\rm in-situ,z\leq 1}$. The local ex-situ fraction parametrizes the different galaxy accretion histories: the break in $q(f_{\rm exsitu})$ is driven by recent dry major mergers in massive systems; the most triaxial galaxies are systems with the lowest fractions of recently accreted cold gas, while low T stellar halos are formed in more gas-rich systems.

therefore due to the different radial distribution of in-situ versus ex-situ stars in the two families, which is probably at the root of the FR–SR bimodality. At large radii, where the local $f_{\rm exsitu}$ fractions are higher, stellar halos display a more continuous sequence of properties.

Figure 6.14 shows the local $q(f_{\rm exsitu})$ and $T(f_{\rm exsitu})$ correlations for all the galaxies with $M_* \geq 10^{10.6} M_\odot$, colored according to the total accreted mass fraction from major mergers and the fraction of in-situ stars produced since $z = 1$. As both $\Delta M_{*,\rm major}/M_*$ and $\Delta_{\rm insitu,z\leq1}$ correlate with stellar mass (Fig. 6.6), as well as with the total ex-situ fraction (Fig. 6.4), this results in gradients of these global properties with the local $f_{\rm exsitu}$ fraction. These gradients indicate that galaxies reaching high $f_{\rm exsitu}$ have accreted larger fractions of their mass from major mergers and have not recently produced many in-situ stars, implying that their recent merger history is gas-poor. Figure 6.14 shows that the most triaxial galaxies (i.e., those with $T > 0.4 - 0.5$) have a wide range of $\Delta M_{*,\rm major}/M_*$ fractions, but they all had a recent dry merger history ($\Delta_{\rm insitu,z\leq1} \lesssim 0.3$). On the other hand, galaxies with high $f_{\rm exsitu} > 0.4$ that have near-oblate intrinsic shapes accreted less mass from major mergers and have accreted only slightly more gas than their near-prolate counterparts. Finally, Fig. 6.14 reveals that the knee in the $q(f_{\rm exsitu})$ relation at $f_{\rm exsitu} \sim 0.7$ is driven by galaxies with the highest accreted mass fractions from major mergers with the lowest $\Delta_{\rm insitu,z\leq1}$.

6.7 Stars and dark matter halo relation

In this part of the paper we investigate the relation between the rotation and structural properties of the stellar and the dark matter halos. Because the local rotational support and the intrinsic shape of the stellar halos are linked to the accretion history (parametrized in Figs. 6.10 and 6.13 by $f_{\rm exsitu}$) and because stars and dark matter are accreted jointly, we expect that accretion has a similar influence on the dark matter component.

6.7.1 Relation between dark matter and stellar halo parameters and local ex-situ fraction

The intrinsic shape of the dark matter halo is derived following the same iterative procedure used in Sect. 6.3.2 for the stellar particles. For both components we use shells with the same fixed semi-major axes lengths r and $r + \Delta r$, but we allow the direction of the principal axes to vary, as well as the axis ratios p and q. The rotational support of the stellar and the dark matter components is derived in spherical shells of radii r and $r + \Delta r$. In each radial bin, we use the stellar and the dark matter particles separately to calculate the $V/\sigma(r)$ of the two components. In the same spherical shell we derive the local fraction of ex-situ stars $f_{\rm exsitu}(r)$ from the ratio of the stellar mass densities within the shell $\rho_{\rm exsitu}(r)/\rho_{\rm stars}(r)$.

Figure 6.15 shows the relation between rotational support V/σ and axis ratios q and p of the stellar and the dark matter components. Each galaxy is divided into 12 radial bins (ellipsoidal or spherical, as described above) in the range $r \in [1R_{\rm e}, 8R_{\rm e}]$, and therefore each galaxy is

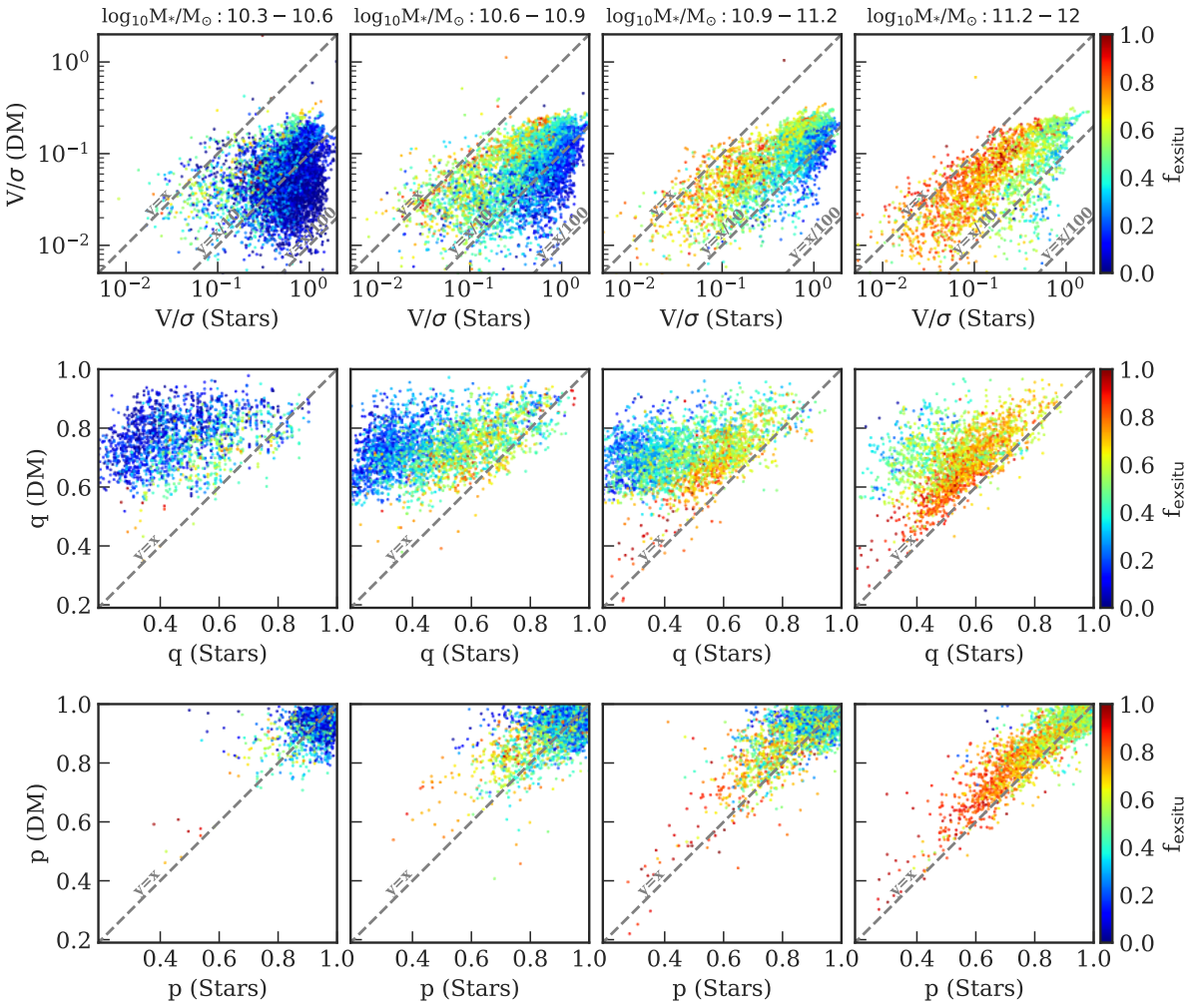

Figure 6.15: Local stellar vs. dark matter rotational support (V/σ, **top panels**) and intrinsic shape (axis ratios q and p, respectively in the **middle** and **bottom panels**) for all galaxies in 12 radial shells with $r \in [1R_e - 8R_e]$. Local measurements are color coded according to the local ex-situ fraction f_{exsitu}. Galaxies are divided into stellar mass bins as labeled at the top of the respective columns. The dashed diagonal lines show the relations $y = x$, $y = x/10$, and $y = x/100$. Rotation and shapes of stars and dark matter halo become similar with increasing f_{exsitu}.

represented by approximately 12 data points[1] in Fig. 6.15.

We see that in general the stellar component rotates faster than the dark matter and is more flattened (i.e., q(stars) < q(DM)). In particular, while the stars have an axis ratio q(stars) that can vary from 0.2 to 0.8, the dark matter flattening is contained in a much narrower range of values ($0.6 \lesssim q(\mathrm{DM}) \lesssim 0.9$, stretching to lower values only in very few cases). In high-mass galaxies ($M_* > 10^{10.9} M_\odot$), the dark matter is more elongated than the stars (p(stars) > p(DM)) but at lower masses and at low f_{exsitu} it is as oblate as the stellar component (p(DM) ~ p(stars) > 0.8). The stars show progressively lower rotational support with increasing stellar mass and move from the lower right corner of the diagrams, around the $y = x/10$ line, towards the 1:1 line. Their intrinsic shapes show a similar behavior, becoming rounder (i.e., with higher q), while both stars and dark matter become more triaxial (i.e., with lower p).

Each data point in Fig. 6.15 is color coded by the local ex-situ fraction f_{exsitu} derived at the same radius r at which the rotational support and the intrinsic shapes are measured. The colors show that the stellar and the dark matter components tend to have a similar amount of rotational support and similar intrinsic shapes where the fraction of the ex-situ stars is high ($f_{\mathrm{exsitu}} \gtrsim 0.5$).

6.7.2 Principal axes and direction of rotation of dark matter and stellar components

The similarity between stellar and dark matter components at growing f_{exsitu} also extends to their directions of rotation and directions of the principal axes. Misalignments between the major axes and between the minor axes $\Delta\vartheta_j$ of the stellar and dark matter components are derived from the dot product of the eigenvectors $\hat{e}_j$ of their inertia tensor at each radius r:

$$\Delta\theta_j = \cos^{-1}(\hat{e}_{\mathrm{stars},j} \cdot \hat{e}_{\mathrm{DM},j}), \tag{6.13}$$

where $j \in [\mathrm{major\,axis}, \mathrm{minor\,axis}]$.

The misalignment angle between the direction of rotation of the stars and of the dark matter, $\Delta\theta_{\mathrm{rot}}(r)$, is measured in each spherical shell of radius r from the direction of the velocity vectors including their sign, meaning that $\Delta\theta_{\mathrm{rot}} \in [0, 180]$ degrees. For each galaxy, we derive $\Delta\theta_j(r)$, $\Delta\theta_{\mathrm{rot}}(r)$, and $f_{\mathrm{exsitu}}(r)$ in radial bins of radius r. Figure 6.16 shows the distributions of $\Delta\theta_j(r)$ and $\Delta\theta_{\mathrm{rot}}$ in bins of f_{exsitu}: the left panels show the distributions from shells with radii $1R_{\mathrm{e}} \leq r \leq 2R_{\mathrm{e}}$, while the right panels those from shells with radii $4R_{\mathrm{e}} \leq r \leq 8R_{\mathrm{e}}$. [2]

[1] As already discussed in Sect. 6.3.2, we can reliably measure intrinsic shapes out to $8R_{\mathrm{e}}$ for 96% of the selected ETGs.

[2] In the distributions of the principal axes misalignments, we excluded $\Delta\theta_{\mathrm{major}}(r)$ and $\Delta\theta_{\mathrm{minor}}(r)$ measurements from ellipsoids with intrinsic shapes respectively close to oblate (p(stars) > 0.9 or p(dm) > 0.9, 77% of the ellipsoids) and to prolate (q/p(stars) > 0.9 or q/p(dm) > 0.9, 19% of the ellipsoids), for which the direction of the principal axes is more uncertain (see Sect. 6.3.2). Thus the distribution of $\Delta\theta_{\mathrm{major}}(r)$ applies for the remaining triaxial to prolate shapes, while the $\Delta\theta_{\mathrm{minor}}(r)$ for the triaxial to oblate shapes. The consequence is that, for example, the distribution of $\Delta\theta_{\mathrm{major}}(r)$ for galaxies with low f_{exsitu} is not well sampled, as most galaxies are near-oblate (see Fig. 6.13). Therefore we should assess misalignments by considering together the $\Delta\theta_{\mathrm{major}}(r)$ and $\Delta\theta_{\mathrm{minor}}(r)$ distributions.

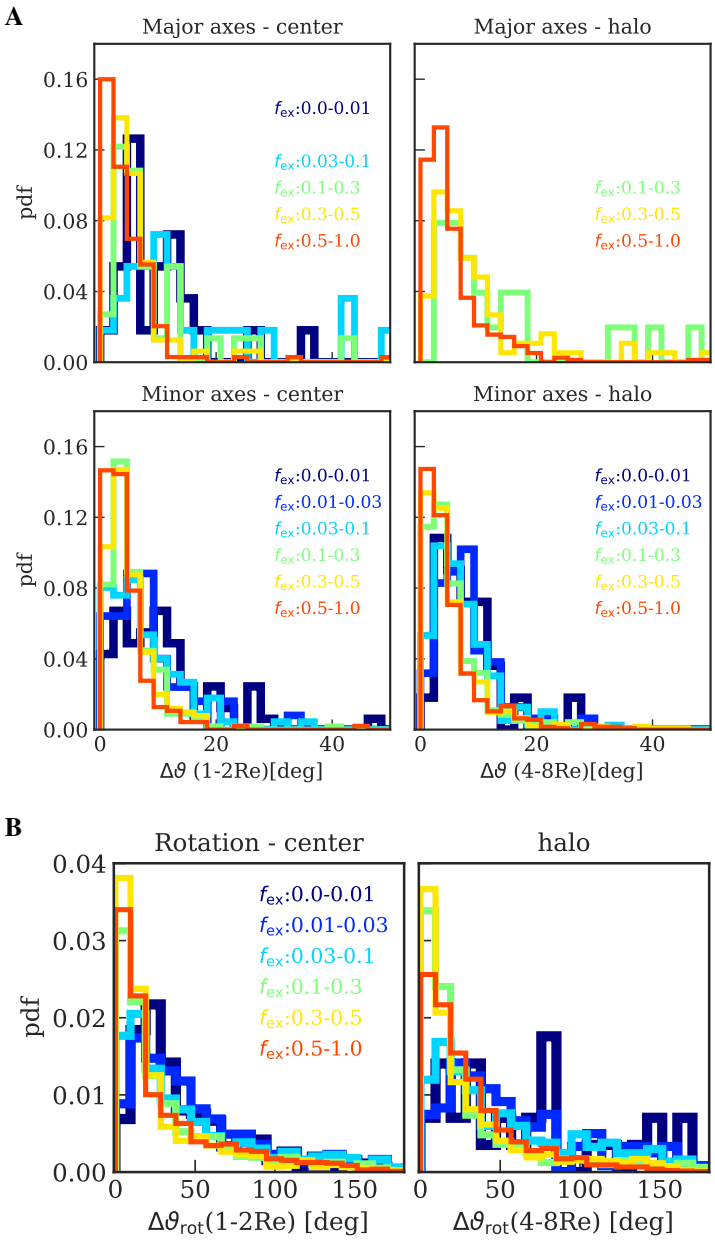

Figure 6.16: **A:** Distribution of misalignments of the principal axes of the stellar and dark matter components for different local ex-situ fractions $f_{\rm exsitu}$ as shown in the legend. **Top panels**: Misalignments of major axes for the nonoblate systems. **Bottom panels**: Misalignments of minor axes for the nonprolate systems. **B:** Distribution of misalignments in the direction of rotation of the stellar and dark matter components for different local ex-situ fractions $f_{\rm exsitu}$. In each panel, we distinguish between central regions (1-2$R_{\rm e}$) and outskirts (4-8$R_{\rm e}$) and we show only distributions containing at least 20 galaxies. Stellar and dark matter components are increasingly aligned with increasing $f_{\rm exsitu}$.

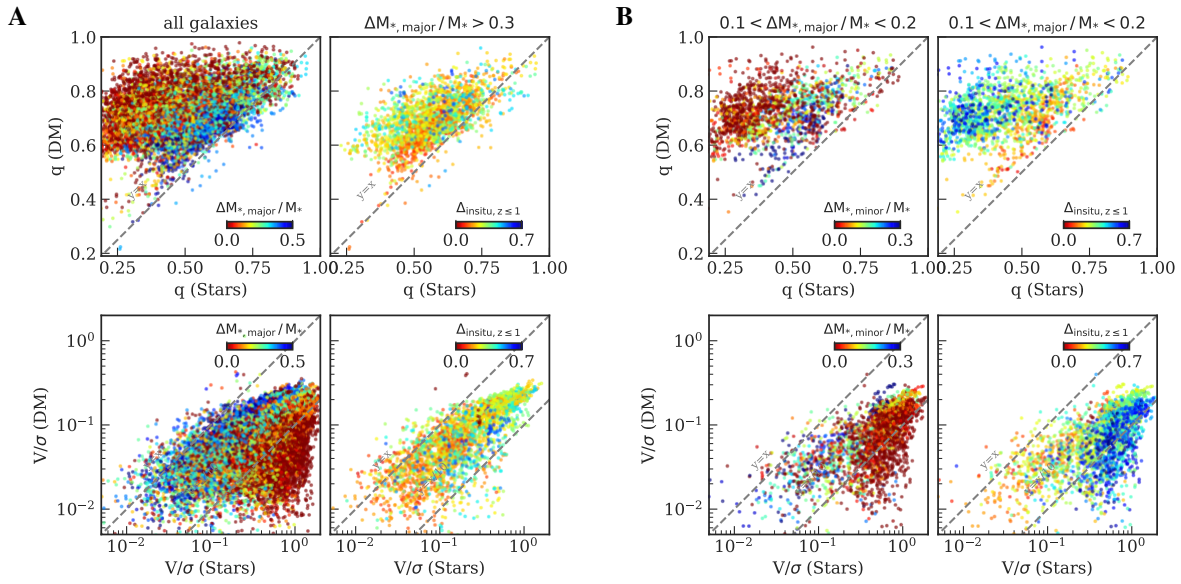

Figure 6.17: Coupling between stellar and dark matter components from major and minor mergers. **A:** Major mergers. The **left** panels show all the TNG ETGs, color coded by their fraction of stellar mass accreted by major mergers. On the **right** we consider only galaxies with at least 30% of their stellar mass accreted from major mergers and color code them according to the fraction of recently produced in-situ stars $\Delta_{\mathrm{insitu,z\leq 1}}$. Major mergers cause the coupling between stellar and dark matter components, especially in galaxies that have not recently accreted cold gas. **B**: Minor mergers. Here we consider galaxies with stellar mass fraction accreted from major mergers in the narrow range $0.1 < \Delta M_{*,\mathrm{major}}/M_* < 0.2$. In the **left** panels, galaxies are color coded by the fraction of stellar mass accreted from minor mergers $\Delta M_{*,\mathrm{minor}}/M_*$ and on the **right** by the fraction of recently produced in-situ stars $\Delta_{\mathrm{insitu,z\leq 1}}$. Dry minor mergers also help to set up the similarity between stellar and dark matter halo structure.

Stellar and dark matter halo components generally have well-aligned principal axes, within ~ 20 deg, both in the centers and in the outskirts. Their alignment improves with higher ex-situ stellar contribution in both regions. Together, Figs. 6.15 and 6.16 reveal that wherever the local fraction of ex-situ stars is large enough ($f_{\mathrm{exsitu}} \gtrsim 50\%$), stellar and dark matter components tend to have similar intrinsic shapes and better aligned principal axes. The right panels in Fig. 6.16 show that also the directions of rotation of the stellar and dark matter components tend to better align for high f_{exsitu}. Therefore, with growing f_{exsitu}, the stellar and dark matter halo acquire a similar degree of rotational support (Fig. 6.15).

6.7.3 Mergers and coupling between stellar and dark matter components

We now explore the dependence of the coupling between the stellar and dark matter components on the merger history. We look first to the major mergers. Major mergers are known to efficiently mix together stellar and dark matter particles through violent relaxation (e.g., Hilz et al. 2012).

Figure 6.17A shows again the local relation between intrinsic shapes and rotational support of the dark matter and stellar components. All galaxies, each represented by approximately 12 data points as in Fig. 6.15, are now color-coded according to the total fraction of stellar mass from major mergers $\Delta M_{*,\mathrm{major}}/M_*$. From Fig. 6.17A, it is clear that in galaxies with higher $\Delta M_{*,\mathrm{major}}/M_*$ stars and dark matter have more similar structure. In particular, if we isolate the galaxies with the highest $\Delta M_{*,\mathrm{major}}/M_*$ fractions, we see that those with the lowest fraction of new in-situ stars $\Delta_{\mathrm{insitu,z\leq1}}$ are closest to the 1:1 line. As $\Delta_{\mathrm{insitu,z\leq1}}$, $\Delta M_{*,\mathrm{major}}/M_*$, and z_{last} tightly depend on stellar mass (Fig. 6.6), the galaxies with high $\Delta M_{*,\mathrm{major}}/M_*$ and low $\Delta_{\mathrm{insitu,z\leq1}}$ are massive recent dry major merger remnants. The stars of low-mass galaxies with low ex-situ fractions (see the leftmost panels in Fig. 6.15) are not coupled with the dark matter component. Most of these systems are in-situ dominated and their accreted mass is contributed mainly by mini mergers (Fig. 6.5), which are not massive enough to influence the dark matter halo. However, minor mergers can play a role in producing the stars/dark matter coupling. Figure 6.17B isolates galaxies within a narrow range of $\Delta M_{*,\mathrm{major}}/M_* \in [0.1, 0.2]$. This selection includes higher mass systems but, at the same time, limits the contribution from major mergers. Figure 6.17B shows a correlation with the fraction of mass from minor mergers $\Delta M_{*,\mathrm{minor}}/M_*$. The most coupled galaxies are, on average, those with the largest $\Delta M_{*,\mathrm{minor}}/M_*$ fractions and those with lowest recent in-situ star formation. On the other hand, we find that the position of this sample of galaxies relative to the 1:1 line does not correlate with the fraction of mass accreted from mini mergers $\Delta M_{*,\mathrm{mini}}/M_*$, or with that from major mergers within the interval $0.1 \leq \Delta M_{*,\mathrm{major}}/M_* \leq 0.2$. A coupling between star and dark matter from minor mergers might originate from the simultaneous stripping of stellar and dark matter particles, which are added coherently to the host.

6.8 Early-type galaxies with cores made of stars from a high-redshift compact progenitor

Massive ETGs are thought to form early, at $z > 2$, beginning with intense bursts of star formation producing compact, massive ($M_* \gtrsim 10^{11} M_\odot$), disk-like galaxies, which quickly evolve into passive red galaxies (Daddi et al. 2005; Buitrago et al. 2008; van Dokkum et al. 2008; Damjanov et al. 2009, as also found in cosmological simulations, e.g., Wellons et al. 2015 using Illustris). The evolution of these objects into present-day ETGs is dominated by a strong growth in size driven by mergers and renewed star formation (e.g., Hernquist et al. 1993; Trujillo et al. 2006; Naab et al. 2009; van Dokkum et al. 2010; van der Wel et al. 2014; Furlong et al. 2017).

A fraction of these compact red early galaxies formed at high z may survive intact to present times as relic galaxies (Buitrago et al. 2018; Scognamiglio et al. 2020), but these are extremely rare objects and, to date, only a handful have been spectroscopically confirmed (Trujillo et al. 2014; Ferré-Mateu et al. 2017; Spiniello et al. 2020). However, the compact red progenitor galaxies are also expected to be found in the cores of present-day massive ETGs (e.g., Hopkins et al. 2009a; Bezanson et al. 2009). The study of such systems at $z = 0$ is crucial for understanding the properties of the primordial in-situ component of ETGs, giving insights into the conditions

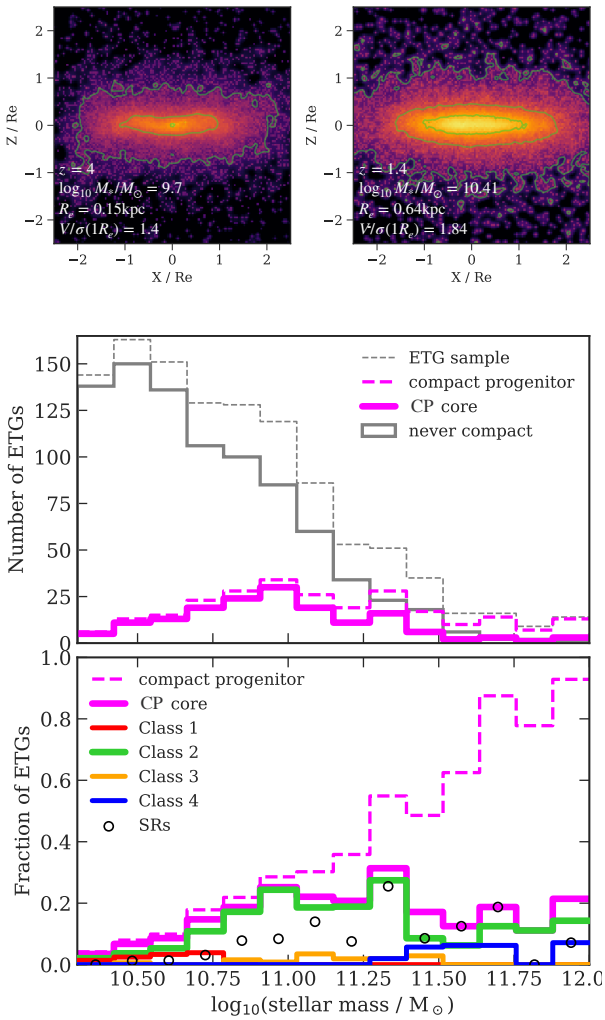

Figure 6.18: **Top**: Two examples of high-redshift CPs. in TNG100, progenitors of a FR (left) and of a SR (right). Both CPs are shown edge-on and have rather disky shapes. Physical parameters are reported in the figure. **Center**: Mass functions of the entire sample of TNG ETGs (gray dashed), of the ETGs descending from a compact progenitor (magenta dashed), and of the ETGs with "surviving compact progenitor cores" (CP-cores, magenta solid line). The distribution of galaxies whose main progenitors were never compact is also shown (gray solid line). **Bottom**: Fraction of galaxies, in mass bins, with compact progenitors, with surviving CP-cores, and with surviving CP-cores for SRs only and split by accretion class. The fraction of galaxies with CPs is a strong function of stellar mass but the fraction of objects with surviving CP-cores is nearly constant at $\sim 20\%$ at $M_* \gtrsim 10^{10.7} M_\odot$, and decreases at lower masses.

for the formation of these objects and the mechanisms that regulated star formation at high z.

Simulations such as IllustrisTNG can provide information about which present-day ETGs are likely to contain cores dominated by stars from a compact progenitor (CP) galaxy and how these could be disentangled from the accreted component. In Sect. 6.4.1, we show that ex-situ stars can be distributed very differently in ETGs according to their merger history and that the most massive galaxies in our sample are dominated by ex-situ stars up to their very central regions (Fig. 6.3). In this section, we identify simulated ETGs that still contain a core made of CP stars and characterize their structural and accretion properties.

We first identified the galaxies whose progenitors are compact galaxies by studying the compactness of each galaxy as a function of time. The compactness can be quantified through the observationally motivated parameter (e.g., Barro et al. 2013),

$$\Sigma_{1.5} = M_*/r_e^{1.5}, \tag{6.14}$$

where r_e is the spherical stellar half-mass radius. For each galaxy, we tracked $\Sigma_{1.5}$ back in redshift along the main progenitor branch of its merger tree. Following Wellons et al. (2016), we consider any galaxy exceeding the threshold

$$\log_{10} \Sigma_{1.5} \mathrm{kpc}^{1.5}/\mathrm{M}_\odot = M_*/r_e^{1.5} > 10.5 \tag{6.15}$$

as compact.

As shown by the mass functions in the central panel of Fig. 6.18, not all ETGs in our TNG sample descend from a CP; that is, only a fraction of the galaxies overcome the threshold in Eq. (6.15) at some point in their history. The fraction of ETGs with a CP is a strong function of stellar mass: in the range $10^{10.5} M_\odot \leq M_* \leq 10^{11} M_\odot$ only 18% of the ETGs were compact in the past, while at $M_* > 10^{11.5} M_\odot$ this fraction rises to 80%. We find that the compact phase of a galaxy can occur at different epochs, in the range $1 \lesssim z \lesssim 4$. Wellons et al. (2016) found very similar results using the original Illustris simulation. In particular, they observed a trend between compactness of the progenitor, present-day stellar mass, and galaxy formation time. This correlation is still present for the TNG100 ETGs and can to some extent explain the strong mass dependence of the fraction of ETGs with CPs: low-mass galaxies tend to form later, when the universe is less dense and less gas-rich, and the conditions are less favorable to the formation of compact objects.

Once the sample of ETGs with a CP is identified, we use the unique indices for each stellar particle to determine the mass fraction of compact progenitor stars in present-day ETGs, within a radius of 2 kpc from the center. We refer to galaxies with central CP mass fraction higher than 50% as ETGs with "surviving compact progenitor core" or CP-core ETGs. Figure 6.18 shows the stellar mass distribution of these objects. We find that the fraction of CP-core ETGs grows with stellar mass in the range $10.3 \leq \log_{10} M_*/M_\odot \lesssim 10.7$, together with the fraction of ETGs with CPs. At higher masses, while the latter continues to grow, the fraction of surviving CP-cores remains constant at $\sim 20\%$ almost independent of stellar mass. This indicates that at low masses, whenever a galaxy descends from a CP, the primordial in-situ population typically survives in its central regions. At stellar masses above $10^{10.7} M_\odot$, even though the fraction of CPs increases with mass, the chances of CP-core survival decrease, as the CP-cores are more likely destroyed

by major merger events (see Fig. 6.6). This is also shown by the distribution of CP-cores divided by accretion class in Fig. 6.18: CP-core ETGs belong almost exclusively to class 2 and include both FRs and SRs.[3]

Figure 6.19 compares the properties of the CP-core ETGs to those of the whole sample of TNG100 ETGs. While the total in-situ mass fractions and the mean accreted gas fractions (not shown here for brevity) are similar among galaxies of similar mass, the fraction of recently formed in-situ stars is systematically lower in CP-core ETGs, especially at $M_* < 10^{11} M_\odot$. In other words, the recent accretion of gas and subsequent formation of new in-situ stars contributes to reducing the central mass fraction of primordial CP stars. Similarly mild differences are also found in the recent accretion history of CP-cores: even though their accreted stellar mass fractions from major mergers are comparable to ETGs with similar mass (not shown here), these accretion events happened at earlier times (Fig. 6.19). Therefore, CP-core ETGs formed their in-situ population earlier than normal ETGs and their subsequent evolution is relatively quieter in terms of recent gas accretion, star formation, and accretion from late mergers. The lower rate of recent gas accretion in CP-core galaxies is related to lower rotational support in their central regions as well as somewhat more spherical shapes (bottom panels of Fig. 6.19).

We note that many of the early progenitors of the CP-core ETGs have rather disky shapes and are dominated by rotational support; the two examples shown in the top panels of Fig. 6.18 have $V/\sigma(1R_e) > 1$. On the other hand, in Fig. 6.19 almost none of the CP-core ETGs overcomes $V/\sigma(1R_e) > 1$. This is in agreement with kinematic results from relic galaxies (e.g., Ferré-Mateu et al. 2017), which are all characterized by high rotation velocity ($\sim 200 - 300$ km/s), while the CP-core galaxy NGC3311 has negligible rotation (Barbosa et al. 2018, 2020). The investigation of the merger histories of these systems and of how mergers modify the dynamical properties of the CP-cores will be the subject of a future study.

Based on the results from the TNG100 simulation, selecting slowly rotating, rounder galaxies in observational studies can increase the probability of finding a CP-core. For example, a limit on $V/\sigma(1R_e) < 0.1$ or, alternatively, a limit on $q(1R_e) > 0.6$, doubles the fraction of CP-cores in a sample with $M_* > 10^{10.7} M_\odot$.

[3]We note the presence of a few class 4 galaxies among CP-core ETGs. For these galaxies, the central CP mass fraction is not larger than 65%, and already their CPs contain a large population of ex-situ stars, up to 73%.

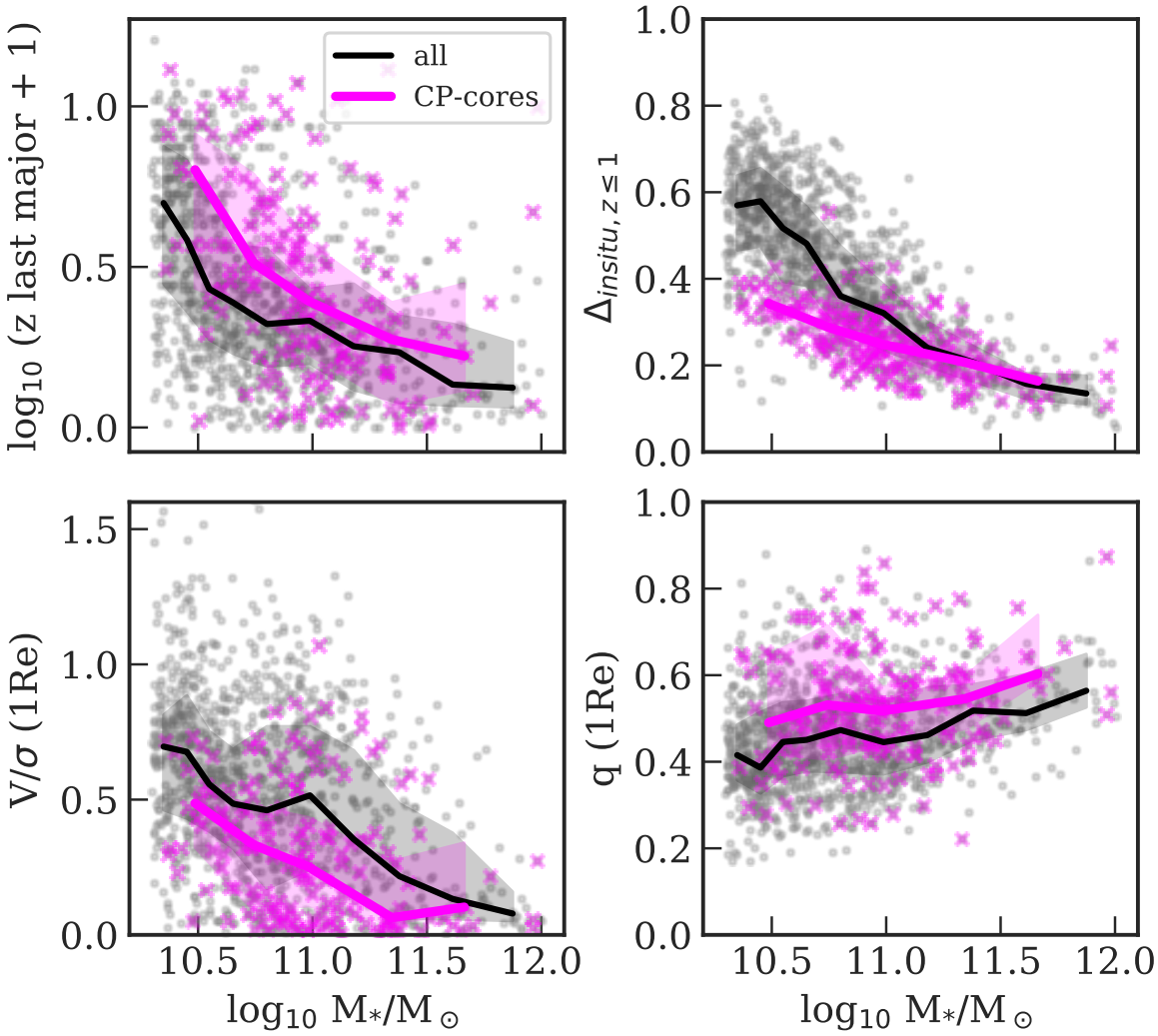

Figure 6.19: Sample of galaxies with surviving CP cores (magenta) compared to the whole sample of ETGs (gray). Panels show redshift of the last major merger, fraction of recently formed in-situ stars $\Delta_{\mathrm{insitu},z\leq1}$, rotational support V/σ, and minor-to-major axis ratio q at 1 R_{e} as functions of stellar mass. Solid lines show the median profiles and shaded regions enclose the quartiles of the distributions. Galaxies with CP-cores had fewer recent major mergers, formed fewer in-situ stars after redshift $z = 1$, and are characterized by lower rotational support and rounder shapes than all ETGs of similar mass.

6.9 Discussion

6.9.1 Rotational support and intrinsic shape versus accretion history

Sections 6.5 and 6.6 show how the rotational support and intrinsic shape profiles of the ETGs in TNG100 depend on their accretion history. In the selected sample of ETGs, we find that low-mass in-situ-dominated galaxies with negligible accreted fractions are characterized by peaked and outwardly decreasing $V_*/\sigma_*(R)$ profiles (Fig. 6.8), near-oblate stellar shapes, and increasing axis ratio $q(r)$ profiles at large radii that follow the decrease in rotation (e.g., Fig. 6.12B). In galaxies with larger masses, the in-situ components have similarly shaped rotation profiles, but the galaxy structure is altered by the accreted stars and gas from merger events in a way that is strongly dependent on stellar mass. In this work we mostly focus on the effect of different mass-ratio mergers and the influence of the recently accreted cold gas (parametrized by $\Delta_{\mathrm{insitu},z\leq1}$). We find that the merger history of TNG100 ETGs is dominated by major and mini mergers (see Sect. 6.4.2). Major mergers, especially the gas-poor ones, are effective in erasing the peak of rotation and flattening the $V_*/\sigma_*(R)$ profiles (Fig. 6.9A), while at the same time they lead to more spherical shapes and increased triaxiality (Fig. 6.12A). Minor mergers are less effective than major mergers but they can also contribute to more spherical-triaxial stellar halo shapes and suppressed rotation. In low-mass galaxies without major and minor mergers, mini mergers have the somewhat unexpected effect of increasing the median galaxy rotational support at large radii (Fig. 6.9B) and at the same time decreasing their median axis ratio q while keeping the shapes near-oblate (Fig. 6.12B), as if they contributed to a size increase of the host disk. This effect would only be possible if the accretion of these low-mass satellites occurred in the plane of the in-situ rotating disk-like component on rather circular orbits (Amorisco 2017). Karademir et al. (2019) found that mini mergers can indeed increase the size of the galaxy disk provided that the impact occurs in the disk plane. Whether or not mini mergers are generally accreted from preferential directions is an interesting subject for a future study.

The dependence of galaxy structure and rotational support on the merger history of galaxies generates a correlation between the $V_*/\sigma_*(R)$, $q(r)$, and $T(r)$ profile shapes and the total stellar mass, and therefore fraction of in-situ (or accreted) stars (Figs. 6.8 and 6.11), and between the local rotational support and intrinsic shapes and the local ex-situ mass fraction f_{exsitu} (Figs. 6.10 and 6.13). With increasing contribution of ex-situ stars, the stellar halo V_*/σ_* decreases and shapes become rounder and more triaxial. Low-mass, in-situ-dominated galaxies show poor correlations between rotational support and shapes and the local f_{exsitu}, as they are completely determined by the in-situ star.

6.9.2 Kinematic transition radius

Previous studies proposed kinematic transitions as signatures of the two-phase formation scenario, with the drop in rotational support marking the transition from in-situ- to ex-situ-dominated regions (e.g., Foster et al. 2016; Pulsoni et al. 2018). In Sect. 6.5.1 we demonstrate that, for the TNG ETGs, the decrease in rotation is mainly driven by the in-situ stars. In particular, we observe that kinematic transitions typically occur in the in-situ-dominated parts of galaxies, where

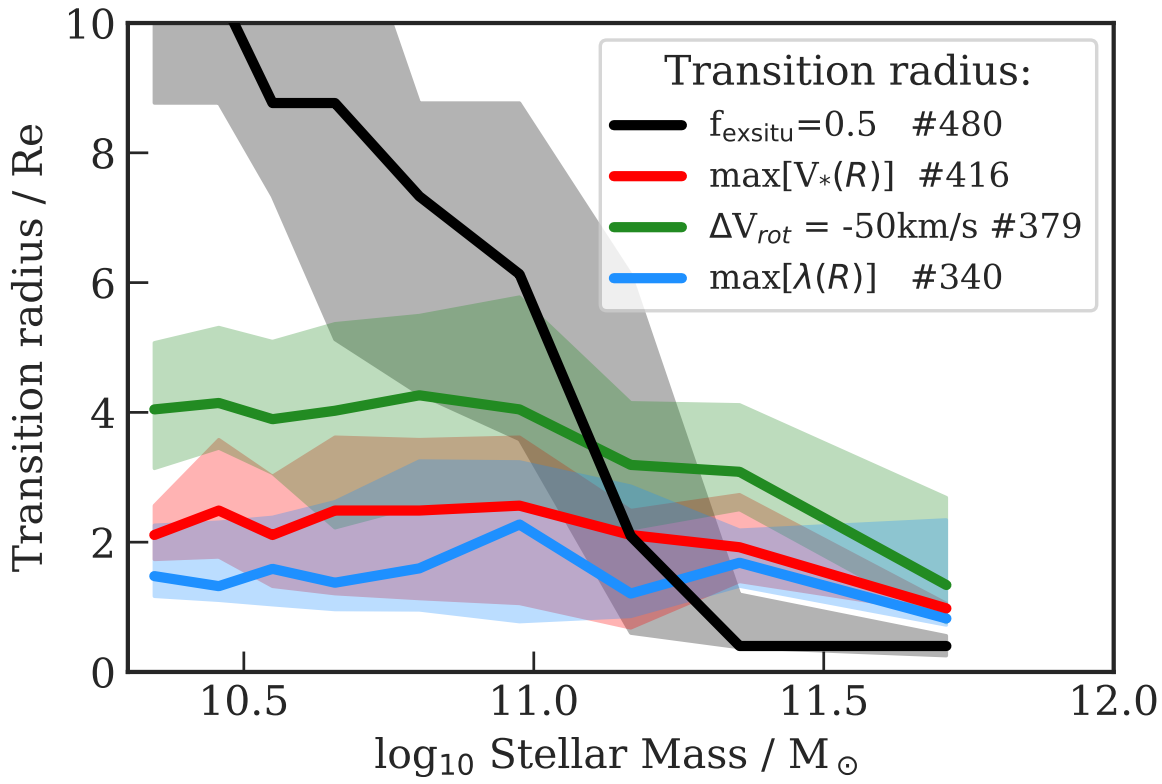

Figure 6.20: Median TNG100 kinematic transition radii (red, green, and blue solid curves) as a function of galaxy stellar mass, compared with the median transition radius $R_{\rm T,exsitu}$ between in-situ- and ex-situ-dominated regions (black line). All the curves are obtained from FR galaxies of class 2 (see Fig. 6.3) with well-defined $R_{\rm exsitu}$ between in-situ-dominated centers and ex-situ-dominated outskirts. The number of galaxies used to produce each curve is reported in the legend.

the fraction of accreted stars is irrelevant everywhere ($f_{\rm exsitu}(R) < 0.1$). This why a kinematic transition radius $R_{\rm T,kin}$ defined by either the drop in rotation (Pulsoni et al. 2018) or the location of the peak in λ parameter (Schulze et al. 2020) does not generally trace a particular value of $f_{\rm exsitu}$ in the TNG galaxies. This means that the kinematic transition radius in TNG galaxies does not generally correspond to the transition radius $R_{\rm T,exsitu}$ between the in-situ- and the ex-situ-dominated regions where $f_{\rm exsitu} = 0.5$.

This is shown in Fig. 6.20. We considered FRs in accretion class 2 for which we can define a transition radius $R_{\rm T,exsitu}$ from in-situ-dominated centers to ex-situ-dominated outskirts. This is similar, although not identical, to the definition of $R_{\rm T,exsitu}$ in Rodriguez-Gomez et al. (2016) for the original Illustris simulation. The median $R_{\rm T,exsitu}$ as a function of stellar mass is shown in Fig. 6.20 with a black curve (see also Table 6.A.6). The other curves represent the median kinematic transition radii $R_{\rm T,kin}$ for the same group of galaxies derived using different definitions:

- by taking the position of the maximum of $V_*(R)$ as defined in Eq. 6.9 (red curve);
- by considering the mean radius between the position of the peak in the rotational velocity profile $V_{\rm rot}(R)$ and the radius at which $V_{\rm rot}(R)$ decreases by 50 km/s (as in Pulsoni et al. 2018, $V_{\rm rot}(R)$ derived as in Paper I, green curve); and
- by taking the peak in the differential $\lambda(R)$ profile (as in Schulze et al. 2020, $\lambda(R)$ derived as in Paper I, blue curve).

Figure 6.20 shows that the kinematic transition radius in TNG is not related to the transition radius between in-situ- and ex-situ-dominated regions. While the median $R_{\rm T,exsitu}(M_*)$ decreases quickly with increasing stellar mass, the median $R_{\rm T,kin}$ shows a weaker dependence on M_*. Lower mass systems have kinematic transition radii that are systematically smaller than $R_{\rm T,exsitu}$. For these galaxies the kinematic transition occurs in in-situ-dominated regions (at $f_{\rm exsitu} < 0.2$ for $M_* < 10^{10.7} M_\odot$), while the ex-situ transition radius occurs at much larger radii. As $f_{\rm exsitu}(R)$ depends on stellar mass (Fig. 6.5), in more massive systems the contribution of ex-situ stars to the rotational support is larger and sufficient to determine the anti-correlation $V_*/\sigma_*(f_{\rm exsitu})$. In these cases the kinematic transition accidentally occurs at radii closer to $R_{\rm T,exsitu}$, because also for these galaxies the peaked and outwardly decreasing rotation profile shape is mainly determined by the rotation profile of in-situ stars (Fig. 6.8). This is demonstrated by the galaxies at the high-mass end of Fig. 6.20 whose kinematic transition radius is much larger than $R_{\rm T,exsitu}$, showing again that the kinematic transition radius does not trace $R_{\rm T,exsitu}$ in the IllustrisTNG ETGs.

Schulze et al. (2020) recently showed similar kinematic results using the Magneticum Pathfinder simulations but drew different conclusions. In their work, they selected 492 galaxies with stellar masses larger than $10^{10.3} M_\odot$, although their cuts on the number of particles at $R > 3R_{\rm e}$ excluded the majority of the galaxies with $M_* < 10^{10.6} M_\odot$. A subset of this sample (19%) have peaked and outwardly decreasing differential $\lambda(R)$ profiles: this is made of galaxies that, on average, had the smallest fraction of accreted stars and did not undergo major mergers. Schulze et al. (2020) argue that for these galaxies the accretion histories, dominated by mini and minor mergers, lead to the characteristic profile shape. This is motivated by the fact that the disruption of low-mass satellites merging from random directions would enhance the dispersion in the halo without affecting the central embedded disk and create the decreasing $\lambda(R)$ profiles. On the other hand,

their Fig. 11 reveals that the fraction of galaxies with this characteristic $\lambda(R)$ profile shape was much higher at $z = 2$, when the galaxies are mostly made of in-situ stars. At lower redshifts, when galaxies progressively increase their stellar mass through both in-situ star formation and accretion, the fraction of peaked and outwardly decreasing $\lambda(R)$ profiles drops in favor of other profile shapes. This suggests that the peaked and outwardly decreasing $\lambda(R)$ profile is already set at high z by the in-situ stars and is not determined by the subsequent minor and mini mergers. The example galaxy shown in their Figs. 12 and 13 seems to confirm this conclusion.

Figure 15 in Schulze et al. (2020) shows the relation between $R_{\mathrm{T,kin}}$ and $R_{\mathrm{T,exsitu}}$ for a fraction of their sample of galaxies with such peaked and outwardly decreasing $\lambda(R)$ profiles. For these galaxies, the figure shows a trend for galaxies with higher $\Delta M_{*,\mathrm{major}}/M_*$ to have kinematic transition radii larger than $R_{\mathrm{T,exsitu}}$, and for galaxies with lower $\Delta M_{*,\mathrm{major}}/M_*$ to have $R_{\mathrm{T,kin}} \sim R_{\mathrm{T,exsitu}}$. Even though it is not straightforward without further data to estimate the stellar masses of the systems shown, if we assume that the Magneticum galaxies have a similar merger history to that of the TNG100 ETGs, the galaxies with higher $\Delta M_{*,\mathrm{major}}/M_*$ are also the more massive systems. Therefore, the apparent dependence on merger mass ratio in their Fig. 15 together with the selection against low-mass systems may actually be consistent with a stellar mass dependence similar to that observed for the TNG ETGs in Fig. 6.20, in which the kinematic transition radius traces $R_{\mathrm{T,exsitu}}$ only for a special mass range, but not generally.

6.9.3 Stars and dark matter halo relation

In Sect. 6.7 we investigate the relation between the stellar and the dark matter components and show that the two are coupled where the fraction of accreted stars is highest; at $f_{\mathrm{exsitu}} \gtrsim 0.5$ the stars have similar intrinsic shape and rotational support to the underlying dark matter component. Such high local ex-situ fractions occur in the most massive systems ($M_* > 10^{11.2} M_\odot$) but also at sufficiently large radii in intermediate-mass systems (Fig. 6.5) such as the class 2 galaxies which dominate at $M_* > 10^{10.6} M_\odot$ (Fig. 6.4).

The relation between the intrinsic shapes of the galaxies and their dark matter halos, as well as the alignment of their spins and of their principal axes, has been widely investigated in the literature with different sets of simulations. The co-evolution of galaxies and inner dark matter halos ($r \sim 0.1 r_{200}$) correlates their shapes and angular momenta in the central regions (e.g., Kazantzidis et al. 2004; Bryan et al. 2013; Chua et al. 2019), while centers and outer dark matter halos are found to be more misaligned (e.g., Bailin et al. 2005; Deason et al. 2011; Tenneti et al. 2015).

In this work we show that if we follow the variations of galaxy properties with radius and analyze the relation between stellar and dark matter components locally, we find that the two components are also correlated at large radii (see also Wu et al. 2014). We find that gas-poor accretion, quantified by f_{exsitu}, efficiently couples the stars to the dark matter component. This might be due to either the efficient mixing of stars and dark matter in major mergers or to the coherent accretion of baryonic and dark matter at large radii in the case of minor mergers. The accreted stellar and dark matter components therefore gather on roughly similar orbits, meaning that the rotational support and shapes of both components would be similar. Thus, where the accreted component dominates the mass, they would follow each other in the overall dynamics.

In-situ-dominated regions instead rotate faster than the dark matter halo, have more flattened shapes, and show larger misalignments with the dark matter component at the same radius.

Our results are in line with those of previous studies. For example, Tenneti et al. (2015), using the MassiveBlack-II cosmological hydrodynamic simulation, observed a tendency for galaxies with high triaxiality parameter (those with highest $f_{\rm exsitu}$ in TNG; see Fig. 6.13) to be more aligned with the dark matter halo, while oblate galaxies have higher misalignments. Zjupa & Springel (2017), using the original Illustris simulation, found that the stellar and dark matter total angular momenta are progressively better aligned at higher masses, where the mostly old stellar populations interact gravitationally with the dark matter and not hydrodynamically with the gas. In lower mass halos, galaxies are typically younger and their stellar angular momentum aligns well with the gas, which, as opposed to the dark matter, is strongly influenced by feedback processes. Ganeshaiah Veena et al. (2019) found that the galaxies in the EAGLE simulation with spin oriented perpendicularly relative to their filament, which are galaxies that are more massive and of earlier type, are the best aligned with their host halo, while galaxies with parallel spin show poor alignment. Lastly, for the most massive galaxies, which are those with the highest global ex-situ fractions, the slope of the spherically averaged radial mass profiles of the stellar halos has been found to tend towards that of the underlying dark matter (slope of about -3; Pillepich et al. 2014, 2018a).

The local coupling of stellar and dark matter halos at high local ex-situ fractions ($f_{\rm exsitu} > 0.5$) implies that in sufficiently massive galaxies, or at sufficiently large radii, we can approximate the intrinsic shapes and rotational support of the dark matter component with that measured from deep photometry of stellar halos and from kinematic tracers such as planetary nebulae or globular clusters.

6.10 Summary

This paper is a follow-up study of Pulsoni et al. (2020), where we characterized the stellar halo kinematic properties in a sample of early-type galaxies (ETGs) selected from the IllustrisTNG cosmological simulations and connected them to variations in their intrinsic shapes. In the present paper we present a study of the dependence of the kinematics and structure of the simulated galaxies on their accretion history, using the same sample of ETGs from TNG100. We also extended the investigation to the dark matter halos and studied how their rotation and shape properties are related with those of the stellar halos.

In Sect. 6.4 we characterize the accretion history of the selected sample of ETGs by considering the total fraction of the accreted mass, the mass fraction contributed by different mass ratio mergers, the fraction of accreted cold gas, and the recent in-situ star formation. The tight correlation between stellar mass and these accretion parameters implies that the stellar mass of a galaxy is a good indicator of its accretion history. The different merger histories of the TNG ETGs lead to different radial distribution of accreted stars within the galaxies so that galaxies can be divided into four accretion classes, each dominating in different intervals of stellar mass and total in-situ mass fraction (Fig. 6.4): low-mass ETGs (up to $M_* \sim 10^{10.6} M_\odot$) are in-situ dominated at all radii; intermediate ETGs have in-situ-dominated central regions and ex-situ-dominated outskirts, with

a smaller group in which in-situ and ex-situ components interchangeably dominate at small and intermediate radii; and high-mass galaxies ($M_* > 10^{11.2} M_\odot$) are mostly ex-situ dominated from the center to the halo. Fast and slow rotators follow similar trends with stellar mass but, at fixed mass, SRs on average contain more accreted stars, they have accreted less gas, and they have undergone more recent major mergers (Figs. 6.2 and 6.7).

In Sect. 6.5 we characterize the shape of the $V_*/\sigma_*(R)$ profiles as a function of stellar mass and total in-situ fraction (Fig. 6.8). For both FRs and SRs, the total median $V_*/\sigma_*(R)$ profiles in stellar mass bins can be approximated by the weighted sum of the rotational profiles of the in-situ and ex-situ components. We show that the $V_{\rm insitu}/\sigma_*(R)$ profiles of the in-situ stars typically have a peaked and outwardly decreasing" form, with peaks in rotation decreasing at higher stellar mass and accreted fraction because of the effects of mergers; the ex-situ stars have median $V_{\rm exsitu}/\sigma_*(R)$ profiles that are largely constant with radius and independent of stellar mass (Fig. 6.8); and the median shapes of the overall $V_*/\sigma_*(R)$ profiles are essentially determined by the stellar mass and total in-situ fraction (or equivalently, total accreted mass fraction), whereas we found no residual correlations with other accretion parameters.

Galaxy intrinsic shapes are also found to vary as a function of the in-situ fraction and stellar mass (Sect. 6.6), such that low-mass galaxies with negligible fractions of accreted stars are consistent with near-oblate shapes and increasing axial ratio $q(r)$ in the halo, while galaxies with higher stellar mass and accreted fractions are less flattened and more triaxial (Fig. 6.11).

In Sections 6.5.2 and 6.6.2 we show that mergers and recent gas accretion, whose importance strongly depends on stellar mass, change the galaxy structure by modifying both rotational support and intrinsic shape: major mergers tend to erase the peak in rotation and flatten the $V_*/\sigma_*(R)$ profiles (Fig. 6.9A) while at the same time they increase the triaxiality and make the halo rounder; and the recent accretion of cold gas acts in the opposite direction by preserving or building up the central rotation and making shapes closer to oblate (Fig. 6.12A). Minor mergers are less effective than major mergers but they can also contribute to more spherical-triaxial stellar halo shapes and suppressed rotation. We find that in low-mass galaxies with no major and minor mergers, mini mergers tend to increase the size of the host disks by building up an extended, flattened, rotating component (Figs. 6.9B and 6.12B).

Mergers and recent gas accretion also play an important role in the evolution of the stellar population mixture within galaxies. In Sect. 6.8 we show that in about 20% of high-mass ETGs the central regions are dominated by stars from a compact high-redshift progenitor galaxy. These systems had a quieter recent evolution with respect to galaxies of similar mass in terms of late mergers and recent star formation. In particular, the lower rate of recent cold gas accretion in these galaxies is related to a higher probability of observing them among ETGs with slow rotation and rounder shapes.

As the peaked and outwardly decreasing $V_*/\sigma_*(R)$ profiles in the IllustrisTNG galaxies are characteristic of the low-mass ($M_* < 10^{10.6} M_\odot$) class 1 galaxies with little ex-situ stars and, more generally, of the in-situ component, a kinematic transition radius defined either by the rotation peak or the drop in rotation does not trace a particular $f_{\rm exsitu}$ value (Fig. 6.20). Only in sufficiently massive systems does the kinematic transition radius become (accidentally) similar to the transition radius between in-situ-dominated and ex-situ-dominated regions ($R_{\rm exsitu}$). Therefore, our results cast some doubt on the use of the kinematic transition radius as a tracer of $R_{\rm exsitu}$.

However, if we exclude the low-mass galaxies with $M_* < 10^{10.6} M_\odot$) in which radial variations of rotation and flattening are driven by the in-situ stars alone, we find clear relations between the stellar halo structural parameters and the local fraction of ex-situ stars $f_{\rm exsitu}$. The median stellar halo rotational support decreases strongly with $f_{\rm exsitu}$, with an average scatter of 0.16 in $f_{\rm exsitu}$ at constant $V_*/\sigma_*(R)$ (Fig. 6.10). Low $f_{\rm exsitu}$ is consistent with near-oblate shapes with low q. At higher $f_{\rm exsitu}$ the stellar halo triaxiality increases, while the $q(f_{\rm exsitu})$ reaches a maximum of $q \sim 0.6$ at $f_{\rm exsitu} \sim 0.7$, beyond which it decreases again (Fig. 6.13). SRs populate the same correlations in the stellar halo parameter distribution as the FRs, but at the high $f_{\rm exsitu}$ end. At large radii, where the local ex-situ fractions are high the two classes show a continuous sequence of stellar halo properties with a significant overlap.

If these correlations between the stellar halo rotational support, intrinsic shapes, and local $f_{\rm exsitu}$ found here also hold for real massive galaxies (with $M_* > 10^{10.6}$), the measurement of these observationally accessible quantities could provide an estimate of the local ex-situ contribution. The sensitivity of these correlations to the adopted galaxy formation model in the simulations, which could for example influence the distribution of $f_{\rm exsitu}$ with radius (e.g., see Sect. 6.4.1), should be tested with different sets of cosmological simulations.

In Sect. 6.7 we show that stellar and dark matter components are dynamically coupled in regions of high ex-situ fraction: For local ex-situ fractions $f_{\rm exsitu} \gtrsim 0.5$, stellar and dark matter halos have similar intrinsic shapes and well-aligned principal axes, a similar amount of rotational support, and a similar direction of rotation (Figs. 6.15 and 6.16). Galaxies with higher accreted fractions from (dry) major mergers are the systems with the closest coupling between stellar and dark matter components (Fig. 6.17A), but we find that minor mergers can also contribute (Fig. 6.17B). The coupling of stars and dark matter may be due to the simultaneous mixing of stars and dark matter in major mergers (Fig. 6.17A), or also to the coherent accretion of stars and dark matter on similar orbits in mergers with smaller mass ratios (Fig. 6.17B).

6.11 Conclusions

Finally, we summarize our main conclusions from these results:

1) The stellar mass of an ETG in the TNG100 cosmological simulations is tightly correlated with its accretion history and with the distribution of the accreted stars. Low-mass galaxies are dominated by the in-situ component, intermediate-mass systems typically have in-situ-dominated cores and ex-situ-dominated halos, and the highest mass systems are everywhere dominated by accreted, ex-situ stars.

2) The in-situ stars dominating in low-mass ETGs typically have characteristic peaked and outwardly decreasing rotation profiles and near-oblate shapes with axial ratio q(r) increasing in the halo. At higher stellar masses and accreted mass fractions, the rotation peak decreases but is still dominated by the in-situ stars, and the galaxy halos become more triaxial. A kinematic transition radius defined by the position of either the peak or the drop in rotation therefore does not trace the transition between in-situ-dominated and ex-situ-dominated regions in a galaxy.

3) Major mergers (with mass ratio μ >1:4) dominate the accreted mass fraction in TNG100

ETGs over mini mergers (μ <1:10) and finally minor mergers (1:4> μ >1:10). Dry major mergers tend to decrease the peak in rotation and flatten the $V_*/\sigma_*(R)$ profiles, while at the same time they increase the triaxiality T and make the halo rounder. Therefore, an approximate estimate of the local ex-situ mass fraction $f_{\rm exsitu}(R)$ in massive ETGs can be obtained from the local rotational support $V_*/\sigma_*(R)$ and intrinsic shape parameters $q(r)$ and $T(r)$.

4) Fast rotators and slow rotators populate the same overall correlations between stellar halo rotational support, intrinsic shape, and local ex-situ fraction $f_{\rm exsitu}$, but SRs are concentrated at the high-$f_{\rm exsitu}$ end. Low-mass ETGs are mostly FRs with near-oblate shapes while only a few are SRs. At higher masses, FRs acquire accretion-dominated halos with slow rotation and triaxial shapes, while at the highest stellar masses most ETGs are SRs.

5) Early-type galaxies with a high-redshift compact progenitor galaxy surviving in their cores are systems which had a quieter recent evolution compared to other galaxies of similar mass in terms of mergers and recent star formation. This prevented the central regions from being diluted both by accreted and newly formed in-situ stars, leading to lower average rotation.

6) In regions where accreted stars dominate (i.e., where the local $f_{\rm exsitu} > 0.5$), stellar and dark matter halos have similar intrinsic shapes and rotational support, and similar principal and rotation axes. Therefore, in sufficiently massive ETGs or at sufficiently large radii the local intrinsic shape and rotational support of the dark matter halos can be approximated with those obtained from photometry and extended kinematics of their stellar halos.

These results show that the properties of ETG stellar halos are largely determined by the balance between the in-situ component and the stars accreted through mergers. This is driven strongly by stellar mass: in low-mass systems($M_* < 10^{10.6} M_\odot$), the in-situ stars dominate out to very large radii. In massive ETGs, mergers and accretion shape the structure of stellar halos and dynamically couples them to the dark matter component.

Appendix

6.A Tables

Here, we provide tables reporting relevant physical relations derived throughout this paper. Tables 6.A.1, 6.A.2, 6.A.3, and 6.A.4 contain the median stellar mass density and cumulative stellar mass fraction profiles for the in-situ and the ex-situ components in each of the four accretion classes, as shown in Fig. 6.3. Table 6.A.5 reports the median local relations between ex-situ mass fraction $f_{\rm exsitu}$, rotational support V_*/σ_*, and intrinsic shapes (quantified by the triaxiality parameter T and the minor-to-major axis ratio q), as in Figs. 6.10 and 6.13. These relations are derived using all the ETGs more massive than $10^{10.6} M_\odot$, without dividing into stellar mass bins. Table 6.A.6 contains the median transition radius $R_{\rm T,exsitu}$ between the in-situ- and ex-situ-dominated regions in class 2 ETGs (as in Fig. 6.20, black curve).

Table 6.A.1: Stellar-mass-density and cumulative stellar-mass-fraction profiles for the in-situ and ex-situ components of ETGs in accretion class 1. We report the median, first (Q1), and third quartiles (Q3) of the distribution.

Class 1	In-situ component						Ex-situ component					
R/R_e	$\log_{10}\Sigma/(M_\odot kpc^{-2})$			Cum. mass fract.			$\log_{10}\Sigma/(M_\odot kpc^{-2})$			Cum. mass fract.		
	Q1	median	Q3	Q1	median	Q3	Q1	median	Q3	Q1	median	Q3
0.1	9.55	9.64	9.75	0.01	0.020	0.02		7.52	8.17	0.00	0.00	0.00
0.2	9.52	9.61	9.71	0.03	0.040	0.06	6.79	7.57	8.14	0.00	0.00	0.00
0.3	9.45	9.56	9.68	0.05	0.080	0.1	6.78	7.53	8.06	0.00	0.00	0.00
0.4	9.37	9.48	9.63	0.09	0.130	0.16	6.85	7.5	8	0.00	0.00	0.00
0.5	9.26	9.39	9.55	0.14	0.180	0.22	6.81	7.44	7.95	0.00	0.00	0.01
0.6	9.13	9.28	9.43	0.22	0.250	0.28	6.81	7.45	7.94	0.00	0.00	0.01
0.7	9.02	9.19	9.36	0.26	0.300	0.32	6.73	7.38	7.87	0.00	0.00	0.01
0.8	8.93	9.11	9.27	0.31	0.340	0.37	6.69	7.33	7.84	0.00	0.00	0.02
0.9	8.84	9.02	9.17	0.36	0.380	0.41	6.67	7.28	7.8	0.00	0.01	0.02
1	8.74	8.93	9.09	0.4	0.420	0.44	6.65	7.23	7.76	0.00	0.01	0.03
2	8.07	8.24	8.40	0.61	0.660	0.7	6.38	6.87	7.32	0.00	0.02	0.05
3	7.60	7.73	7.86	0.69	0.770	0.83	6.1	6.59	6.97	0.01	0.02	0.07
4	7.21	7.37	7.50	0.74	0.830	0.89	5.85	6.33	6.7	0.01	0.03	0.07
6	6.52	6.73	6.93	0.81	0.880	0.94	5.43	5.89	6.26	0.01	0.04	0.09
8	5.95	6.19	6.48	0.84	0.910	0.96	5.09	5.51	5.89	0.01	0.04	0.10
10	5.50	5.77	6.10	0.86	0.930	0.97	4.81	5.19	5.62	0.01	0.04	0.10
12	5.14	5.44	5.76	0.86	0.930	0.97	4.6	4.95	5.39	0.02	0.05	0.10
14	4.85	5.19	5.50	0.87	0.930	0.97	4.43	4.79	5.18	0.02	0.05	0.10

Table 6.A.2: As in Table 6.A.1, but for ETGs in accretion class 2.

Class 2	In-situ component						Ex-situ component					
R/R_e	$\log_{10}\Sigma/(M_\odot kpc^{-2})$			Cum. mass fract.			$\log_{10}\Sigma/(M_\odot kpc^{-2})$			Cum. mass fract.		
	Q1	median	Q3	Q1	median	Q3	Q1	median	Q3	Q1	median	Q3
0.1	9.60	9.70	9.81	0.02	0.02	0.03	7.99	8.64	9.16	0.00	0.00	0.01
0.2	9.48	9.62	9.74	0.04	0.06	0.08	7.96	8.59	9.08	0.00	0.01	0.02
0.3	9.27	9.49	9.65	0.08	0.10	0.14	7.91	8.50	8.93	0.00	0.01	0.04
0.4	9.03	9.30	9.53	0.12	0.15	0.19	7.86	8.39	8.74	0.00	0.02	0.06
0.5	8.79	9.10	9.40	0.16	0.20	0.24	7.81	8.28	8.60	0.00	0.03	0.08
0.6	8.60	8.91	9.26	0.21	0.24	0.28	7.75	8.17	8.47	0.01	0.04	0.10
0.7	8.47	8.78	9.15	0.24	0.28	0.32	7.70	8.08	8.37	0.01	0.05	0.12
0.8	8.36	8.66	9.06	0.27	0.31	0.35	7.66	8.00	8.28	0.01	0.06	0.13
0.9	8.24	8.55	8.97	0.29	0.35	0.38	7.61	7.91	8.19	0.01	0.07	0.14
1	8.14	8.45	8.88	0.31	0.38	0.42	7.55	7.84	8.11	0.02	0.08	0.15
2	7.46	7.85	8.14	0.41	0.51	0.62	7.13	7.37	7.55	0.04	0.13	0.23
3	7.03	7.42	7.67	0.47	0.57	0.71	6.80	7.02	7.20	0.07	0.16	0.27
4	6.70	7.06	7.30	0.5	0.62	0.76	6.56	6.76	6.94	0.08	0.19	0.31
6	6.07	6.38	6.63	0.53	0.66	0.8	6.07	6.31	6.52	0.10	0.22	0.35
8	5.55	5.85	6.16	0.54	0.68	0.82	5.71	5.97	6.21	0.12	0.24	0.37
10	5.12	5.43	5.74	0.55	0.69	0.83	5.39	5.68	5.95	0.12	0.25	0.38
12	4.76	5.10	5.40	0.55	0.70	0.83	5.12	5.44	5.73	0.13	0.26	0.39
14	4.48	4.84	5.15	0.56	0.70	0.83	4.91	5.24	5.55	0.13	0.26	0.40

Table 6.A.3: As in Table 6.A.1, but for ETGs in accretion class 3.

Class 3	In-situ component						Ex-situ component					
R/R_e	$\log_{10}\Sigma/(M_\odot kpc^{-2})$			Cum. mass fract.			$\log_{10}\Sigma/(M_\odot kpc^{-2})$			Cum. mass fract.		
	Q1	median	Q3	Q1	median	Q3	Q1	median	Q3	Q1	median	Q3
0.1	9.27	9.46	9.62	0.010	0.01	0.020	9.43	9.67	9.9	0.01	0.02	0.04
0.2	9.15	9.31	9.47	0.030	0.04	0.060	9.21	9.4	9.6	0.04	0.06	0.08
0.3	8.91	9.12	9.3	0.050	0.07	0.090	8.93	9.13	9.28	0.07	0.09	0.12
0.4	8.68	8.90	9.11	0.070	0.1	0.130	8.65	8.86	9.07	0.09	0.13	0.15
0.5	8.49	8.70	8.91	0.090	0.13	0.160	8.46	8.66	8.84	0.11	0.15	0.18
0.6	8.33	8.53	8.75	0.120	0.16	0.190	8.29	8.46	8.65	0.13	0.18	0.21
0.7	8.23	8.41	8.61	0.140	0.18	0.210	8.17	8.34	8.54	0.15	0.19	0.23
0.8	8.14	8.32	8.51	0.150	0.19	0.240	8.06	8.23	8.41	0.16	0.2	0.25
0.9	8.05	8.23	8.42	0.170	0.21	0.260	7.96	8.12	8.29	0.18	0.22	0.26
1	7.97	8.15	8.35	0.180	0.22	0.280	7.88	8.02	8.21	0.19	0.23	0.28
2	7.45	7.65	7.86	0.280	0.34	0.400	7.32	7.46	7.63	0.26	0.3	0.36
3	7.05	7.29	7.51	0.340	0.4	0.460	6.94	7.08	7.23	0.3	0.35	0.41
4	6.69	7.01	7.2	0.370	0.44	0.510	6.64	6.79	6.95	0.32	0.37	0.44
6	6.04	6.39	6.61	0.410	0.49	0.560	6.08	6.28	6.43	0.36	0.41	0.48
8	5.45	5.83	6.16	0.440	0.5	0.590	5.59	5.85	6.09	0.38	0.43	0.5
10	4.96	5.34	5.72	0.440	0.51	0.590	5.17	5.49	5.81	0.38	0.45	0.52
12	4.53	4.92	5.34	0.440	0.51	0.590	4.89	5.22	5.54	0.39	0.46	0.52
14	4.20	4.60	5.03	0.440	0.51	0.590	4.64	4.99	5.29	0.39	0.46	0.53

Table 6.A.4: As in Table 6.A.1, but for ETGs in accretion class 4.

Class 4	In-situ component						Ex-situ component					
R/R_e	$\log_{10}\Sigma/(M_\odot kpc^{-2})$			Cum. mass fract.			$\log_{10}\Sigma/(M_\odot kpc^{-2})$			Cum. mass fract.		
	Q1	median	Q3	Q1	median	Q3	Q1	median	Q3	Q1	median	Q3
0.1	9.02	9.24	9.47	0.010	0.01	0.020	9.68	9.81	9.95	0.03	0.05	0.06
0.2	8.65	8.88	9.22	0.020	0.03	0.050	9.27	9.42	9.61	0.09	0.1	0.12
0.3	8.30	8.60	8.92	0.030	0.05	0.060	8.9	9.06	9.22	0.14	0.15	0.17
0.4	8.07	8.37	8.65	0.040	0.06	0.080	8.65	8.8	8.95	0.17	0.19	0.21
0.5	7.92	8.18	8.45	0.050	0.07	0.100	8.43	8.59	8.75	0.2	0.22	0.24
0.6	7.76	8.05	8.28	0.070	0.08	0.120	8.26	8.41	8.57	0.23	0.25	0.28
0.7	7.64	7.94	8.17	0.070	0.09	0.130	8.14	8.3	8.45	0.25	0.28	0.3
0.8	7.55	7.84	8.08	0.080	0.11	0.140	8.03	8.19	8.35	0.27	0.3	0.33
0.9	7.47	7.74	7.99	0.090	0.12	0.150	7.93	8.09	8.26	0.29	0.32	0.35
1	7.38	7.66	7.91	0.100	0.13	0.160	7.85	7.99	8.16	0.31	0.34	0.37
2	6.78	7.08	7.34	0.150	0.19	0.230	7.25	7.39	7.56	0.42	0.47	0.5
3	6.36	6.64	6.97	0.180	0.22	0.270	6.86	7	7.18	0.48	0.53	0.59
4	6.05	6.35	6.64	0.190	0.24	0.300	6.58	6.74	6.89	0.52	0.57	0.63
6	5.50	5.82	6.03	0.200	0.25	0.320	6.12	6.27	6.4	0.57	0.63	0.68
8	5.09	5.37	5.59	0.210	0.26	0.330	5.72	5.89	6.04	0.6	0.65	0.71
10	4.71	4.99	5.22	0.220	0.27	0.340	5.39	5.55	5.78	0.62	0.66	0.72
12	4.38	4.66	4.93	0.220	0.27	0.340	5.12	5.28	5.54	0.63	0.67	0.73
14	4.13	4.42	4.7	0.220	0.27	0.340	4.93	5.1	5.33	0.63	0.68	0.74

Table 6.A.5: Local relations between the stellar halo structural parameters (rotational support V_{tot}/σ_{tot}, minor-to-major axis ratio q, and triaxiality parameter T) and the fraction of ex-situ stars f_{exsitu}. For each value of f_{exsitu}, we provide the median, first (Q1), and third quartiles (Q3) of the distribution of the structural parameters in ETGs with $M_* > 10^{10.6} M_\odot$ (Figs. 6.10 and 6.13).

f_{exsitu}	V_{tot}/σ_{tot}			q			T		
	Q1	median	Q3	Q1	median	Q3	Q1	median	Q3
0.1	0.85	1.24	1.64	0.25	0.3	0.39	0.08	0.14	0.22
0.2	0.82	1.17	1.49	0.27	0.32	0.41	0.08	0.14	0.23
0.3	0.59	0.93	1.22	0.32	0.39	0.5	0.09	0.17	0.27
0.4	0.31	0.65	0.95	0.36	0.47	0.6	0.11	0.22	0.39
0.5	0.21	0.46	0.8	0.41	0.52	0.64	0.13	0.24	0.41
0.6	0.12	0.29	0.51	0.49	0.58	0.67	0.19	0.36	0.58
0.7	0.07	0.13	0.27	0.53	0.59	0.66	0.27	0.52	0.71
0.8	0.05	0.11	0.23	0.47	0.54	0.6	0.49	0.71	0.85
0.9	0.04	0.1	0.21	0.45	0.52	0.58	0.53	0.73	0.86

Table 6.A.6: Median transition radius $R_{\mathrm{T,exsitu}}$ between in-situ and ex-situ-dominated regions in class 2 ETGs as a function of stellar mass (Fig. 6.20). Q1 and Q3 are the first and third quartiles of the distribution of $R_{\mathrm{T,exsitu}}$.

$\log_{10} M_*/M_\odot$	$R_{\mathrm{T,exsitu}}$		
	Q1	median	Q3
10.35	8.77	10.49	14.9
10.4	8.77	10.49	13.8
10.5	8.1	9.68	12.54
10.6	6.29	8.77	12.54
10.8	4.3	7.36	8.84
11	3.2	5.61	8.43
11.2	0.56	1.8	5.27
11.4	0.36	0.4	1.12
11.7	0.25	0.4	0.58

Chapter 7

Summary and conclusions

This thesis is dedicated to the study of the kinematic and photometric structure of stellar halos in early type galaxies (ETGs) and to the investigation of the origin of their properties. Using the largest catalog to-date of extra-galactic planetary nebulae (PNe), I conducted a kinematic analysis on 33 nearby ETGs (ePN.S survey) pushing the investigation of the stellar kinematics at large radii out to 6 effective radii (Re) on average. This unprecedented radial coverage in such a large sample of galaxies allowed to characterize the kinematic behavior of ETGs at large radii and unveil changes in their structure with radius (Chapter 4). Using the new-generation cosmological magneto-hydrodynamical simulation IllustrisTNG, I selected a sample of simulated ETGs and modelled their kinematics and photometry to consistently compare with observations (Chapter 5). Then I investigated the origin of the radial trends found in the ePN.S survey, focusing on the impact of the galaxy accretion history on the intrinsic shapes and the rotational support of stellar halos (Chapter 6). This work addresses some of the outstanding questions about the nature of ETGs and contributes to a better understanding of their dynamical structure at large radii.

The bright central regions ($\sim 1R_e$) of ETGs have long been known to display a bimodal distribution of physical properties (e.g., see Kormendy et al. 2009 and Cappellari 2016 for a review). In the last decade, they have been thoroughly mapped by integral field spectroscopy surveys which introduced the kinematic-based classification of ETGs in fast (FRs) and slow rotators (SRs, Emsellem et al. 2011). A parallel effort from simulators has established that the FR/SR dichotomy is the result of formation histories dominated by either gas dissipation, in the case of FRs, or by dry major mergers, in the case of SRs (e.g., Naab et al. 2014; Penoyre et al. 2017; Choi & Yi 2017; Schulze et al. 2018; Walo-Martín et al. 2020).

However, when this picture is contextualized into the complex and highly stochastic process of structure formation in the Universe, in which higher mass systems hierarchically assemble from smaller ones (White & Rees 1978), it is immediately evident that there is a conceptual gap between galaxy bimodality and cosmological background. Where do ETGs show the effects of hierarchical accretion? Both observations and simulations demonstrated that more massive ETGs are born at higher redshift and built up most of their stellar mass in merger events, while lower mass systems are younger and formed most of their stars in-situ (e.g., Spavone et al. 2018; Pillepich et al. 2018a). The mass fraction of accreted stars in fact tightly correlates with the stellar mass of the host galaxy and the ex-situ component is mostly distributed in the external

regions of galaxies (e.g., Rodriguez-Gomez et al. 2016). This means that the accreted stellar halos are expected to display properties that are largely independent from the properties of the cores. Then, should we not expect that massive FRs exhibit different properties than low mass FRs, if not in the center, perhaps at large radii? Are the restricted radial scales a limitation for the FR/SR paradigm?

Part of the unknown, of course, comes from the fact that the kinematic and photometric properties of the ETG outer regions are poorly explored compared to their bright centers, both observationally and theoretically. From the observational side, the low surface brightness that characterizes the galaxy outskirts makes the stellar kinematic measurements challenging and confined to the central $2-3R_e$ (e.g., Kelson et al. 2002; Weijmans et al. 2009; Coccato et al. 2010a; Murphy et al. 2011; Boardman et al. 2017; Barbosa et al. 2018; Arnold et al. 2014; Foster et al. 2016; Veale et al. 2017b). The use of alternative kinematic tracers such as PNe can overcome this limitation and allow to explore the outermost reaches of stellar halos (Longobardi et al. 2013; Hartke et al. 2018, 2020). Before this work, PN-based kinematic studies of ETGs were limited to single galaxies (e.g., Douglas et al. 2007; de Lorenzi et al. 2009; Napolitano et al. 2009, 2011; McNeil-Moylan et al. 2012) or small samples (Coccato et al. 2009; Cortesi et al. 2013a), which were too limited to establish the presence of galaxy population trends.

With more than twice the sample size of Coccato et al. (2009), the ePN.S survey uses PNe to explore the kinematics of stellar halos at more than twice the distances probed by previous studies based on absorption line spectroscopy, typically 6 R_e, in a statistically significant number of ETGs. This analysis interestingly revealed that

- ETGs show a considerable kinematic diversity in their halos compared to their central regions (Fig. 4.9).
- Most of the ePN.S FRs display a change in their intrinsic structure in the outer regions.

This is shown by the presence of kinematic transitions to lower rotational support in the halo in the majority of the ePN.S FRs, often accompanied by decreasing ellipticity profiles, which indicate that the central rotating regions are embedded in a more dispersion dominated spheroidal components. In 40% of the ePN.S FRs, the presence of kinematic twists and misalignments indicates that this outer spheroidal component often has a triaxial shape.

- Structural variations are milder for the SRs, which display increased but still modest rotational support at large radii and triaxial shapes.
- The changes in the dynamical structures of FRs are more prominent in rounder and more massive galaxies (Figs. 4.11 and 4.13). These results suggest that the stellar halos of (massive) FRs might have more similar structure as those of the SRs compared to the cores.

The ePN.S kinematic results are described in Chapter 4 (Pulsoni et al. 2018). These were validated using simulations to assess the effects of statistical noise and spatial completeness of the PN tracers. The conclusions on the changes with radius of the intrinsic shapes in FRs were corroborated by the comparison of their photometric data with photometric models motivated by the kinematic results, i.e. with oblate central regions embedded in triaxial halos.

Analogous kinematic variations with radius were already observed in previous works based on PN measurements with smaller galaxy samples (Coccato et al. 2009), or using kinematics from integrated light but limited to smaller radial distances (2-3 R_e, Arnold et al. 2014; Foster et al. 2016), but the systematic presence of kinematic radial trends was not yet established. In particular, the transitions to lower rotational support in the halos of FRs were questioned by studies like Raskutti et al. (2014) and Boardman et al. (2017), also based on stellar kinematics and confined to the central 2-3 R_e. Similarly, the presence of kinematic signatures of triaxial halos in FRs was found before in studies featuring single galaxies (e.g., in NGC 4473, Foster et al. 2013, and in NGC 5626, Viaene et al. 2018) or, again, in previous investigations of halo kinematics with PNe (e.g., Peng et al. 2004; Coccato et al. 2009), while other works supported the idea that the outskirts of FRs are axisymmetric as their cores, based on the alignment between central kinematics at $1R_e$ and photometry at $3R_e$ (Cappellari 2016). The unprecedented sample size and radial coverage of the ePN.S survey has allowed to convincingly establish the presence of structural variations with radius for a significant fraction of the FRs.

From the theoretical side, cosmological simulations are becoming more and more accurate in returning galaxy populations with global properties that reproduce the observations. Therefore, most of kinematic and photometric studies of simulated galaxies up to now were focused on investigating the central regions and the fundamental galaxy relations. In this thesis, I used the state-of-the-art IllustrisTNG simulations to extend the analysis to the stellar halos. The large number of simulated ETGs ($> 10^3$ galaxies with stellar masses $M_* \geq 10^{10.3} M_\odot$) allowed to obtain a good representation of the frequency of halo properties in a galaxy population, a goal that is still difficult to achieve by the sample sizes of current observative surveys.

In Chapter 5 (Pulsoni et al. 2020) I selected a sample of simulated ETGs with properties consistent with those of a mass- and volume-limited sample of ETGs, and determined the mean velocity fields, kinematic and photometric profiles, and intrinsic shapes from the central regions out to $15R_e$. This was done using similar techniques as those used to measure physical quantities in real galaxies, to ensure a consistent comparison between simulated and observed galaxies. The simulated galaxies from IllustrisTNG successfully reproduce the diversity of kinematic properties measured in ETG halos (Fig. 5.14).

- The variations of kinematic properties with radius found in the ePN.S FRs are connected to changes in the intrinsic shapes: transitions to lower rotational support in the halos are related to changes from flattened and oblate to more spheroidal shapes, with a higher degree of triaxiality depending on stellar mass (Figs. 5.12 and 5.10).

- SRs are found to have more homogeneous structures with radius, with overall high triaxiality and modest rotational support (Figs. 5.12 and 5.10).

- There is no clear qualitative differences between stellar halos of FRs and SRs, despite the clear bimodality in the central regions (Fig. 5.17): the two classes show a continuity of halo properties with the low mass FRs dominating the low-triaxiality-high-rotational support trend of the distribution and the massive SRs dominating in the high-triaxiality-low-rotational support extreme.

The presence of radial trends in the kinematics and in the photometry of ETGs was interpreted as evidence of the two-phase formation scenario (Coccato et al. 2009; Arnold et al. 2014; Foster et al. 2016): since halo and central regions have different origins, it is only natural to expect them to have different dynamical properties. Cosmological simulations in fact predict that the central regions of galaxies are mostly made of in-situ born stars, while the outskirts are dominated by accreted stars (Cooper et al. 2013; Rodriguez-Gomez et al. 2016; Pillepich et al. 2018a). The transition radius R_T between these two regimes was found to depend on the stellar mass and on the ex-situ mass fraction (Rodriguez-Gomez et al. 2016). If the transitions from central disk-like regions to dispersion-dominated spheroidal halos are due to a change in dominance between the in-situ and ex-situ components, then the *kinematic transition radius* can in principle be promising for observationally constraining the transition radii from in-situ to ex-situ components (R_T, see Sect. 4.8.6 of this thesis). A parallel study from Schulze et al. (2020) using the Magneticum Pathfinder simulation confirmed the kinematic diversity of ETGs at large radii and found that (for intermediate mass galaxies, as discussed in Sect. 6.9.2) the kinematic transition radius can approximate R_T.

In Chapter 6 (Pulsoni et al. 2021), I used the IllustrisTNG simulations to study how the galaxy merger history shapes their kinematics and intrinsic shapes. The results of this analysis show that

- The most important parameter driving the radial structural variations observed in simulated ETGs, and presumably also in real ETGs, is the stellar mass, which scales with the median accretion parameters (Fig. 6.6) and the contribution of the accreted stars at each radius (Fig. 6.3).

In low mass systems ($M_* < 10^{10.6} M_\odot$), the in-situ stars dominate at all radii, and determine peaked rotation profiles and near-oblate shapes with flattening decreasing with radius. Hence, surprisingly,

- In simulated low mass galaxies, the kinematic transition is completely driven by the in-situ stars, arranged in a high-angular momentum disk-like component embedded in low-angular momentum spheroid.

This means that kinematic transitions do not necessarily trace the transitions between in-situ-dominated and ex-situ-dominated regions in galaxies: only in intermediate mass galaxies the kinematic transition radius occurs approximately at $\sim R_T$, but this is not a general result.

- In higher mass systems ($M_* > 10^{10.6} M_\odot$), instead, mergers modify both rotation and shape profiles, generating local correlations between rotational support, shapes, and ex-situ fractions.

Both FRs an SRs populate these relations: at large radii massive FRs acquire accretion-dominated halos with slow rotation and triaxial shapes, while at the largest fraction of accreted stars most ETGs are SRs. In addition,

- Mergers dynamically couple stars and dark matter: where the fraction of ex-situ stars dominates, both components tend to have similar intrinsic shapes and rotational support, and nearly aligned principal axes and spin directions.

These results are in line with previous and current findings using cosmological simulations demonstrating the strong dependence of galaxy accretion history on stellar mass (e.g., Rodriguez-Gomez et al. 2016, 2017 with Illustris, Pillepich et al. 2018a and Tacchella et al. 2019 with IllustrisTNG, Davison et al. 2020 with EAGLE, and Remus & Forbes 2021 with Magneticum) and the role of gas accretion and mergers in determining the angular momentum distribution in galaxies (e.g., Naab et al. 2014; Lagos et al. 2017, 2018b). The novelty of this work is the investigation of the structural variations of FR and SR galaxies with radius, the study of their dependence on the local contribution of ex-situ stars, and the finding of a local relation between stellar and dark matter components as a function of accretion.

The idea emerging from these results is that the large variety of kinematic properties and intrinsic shapes observed in the outer halos of ETGs, and their mass dependence, is the direct consequence of the evolution of ETGs in a cosmological context. At large radii the FR/SR dichotomy of the cores partially breaks and is substituted by a smooth continuity of halo properties, in which the local contribution of the ex-situ stars plays a major role: wherever the accreted stars dominate, galaxies have suppressed rotational support, triaxial spheroidal shapes, and have similar structure as their dark matter halos. In this sense, ETG stellar halos represent the transition between the galaxy cores, with their bimodal distribution of properties (gas poor versus gas rich evolution), and the accretion dominated regime linked to the large scale structure formation in the Universe.

Bibliography

Abadi, M. G., Navarro, J. F., & Steinmetz, M. 2006, MNRAS, 365, 747

Aihara, H., Allende Prieto, C., An, D., et al. 2011, ApJS, 193, 29

Alabi, A. B., Forbes, D. A., Romanowsky, A. J., et al. 2016, MNRAS, 460, 3838

Allgood, B., Flores, R. A., Primack, J. R., et al. 2006, MNRAS, 367, 1781

Amorisco, N. C. 2017, MNRAS, 464, 2882

Anderson, M. E., Bregman, J. N., & Dai, X. 2013, ApJ, 762, 106

Anderson, M. E., Gaspari, M., White, S. D. M., Wang, W., & Dai, X. 2015, MNRAS, 449, 3806

Arnaboldi, M., Freeman, K. C., Gerhard, O., et al. 1998, ApJ, 507, 759

Arnaboldi, M., Freeman, K. C., Mendez, R. H., et al. 1996, ApJ, 472, 145

Arnaboldi, M., Freeman, K. C., Okamura, S., et al. 2003, AJ, 125, 514

Arnaboldi, M., Freeman, K. C., Saha, P., et al. 1994, in American Astronomical Society Meeting Abstracts, Vol. 184, American Astronomical Society Meeting Abstracts #184, 49.03

Arnaboldi, M., Gerhard, O., Okamura, S., et al. 2007, PASJ, 59, 419

Arnaboldi, M., Pulsoni, C., Gerhard, O., & PN. S Consortium. 2017, in IAU Symposium, Vol. 323, Planetary Nebulae: Multi-Wavelength Probes of Stellar and Galactic Evolution, ed. X. Liu, L. Stanghellini, & A. Karakas, 279–283

Arnold, J. A., Romanowsky, A. J., Brodie, J. P., et al. 2014, ApJ, 791, 80

Arrigoni Battaia, F., Gavazzi, G., Fumagalli, M., et al. 2012, A&A, 543, A112

Bahé, Y. M., Barnes, D. J., Dalla Vecchia, C., et al. 2017, MNRAS, 470, 4186

Bailin, J., Kawata, D., Gibson, B. K., et al. 2005, ApJ, 627, L17

Barbon, R. & Capaccioli, M. 1975, A&A, 42, 103

Barbosa, C. E., Arnaboldi, M., Coccato, L., et al. 2018, A&A, 609, A78

Barbosa, C. E., Spiniello, C., Arnaboldi, M., et al. 2020, arXiv e-prints, arXiv:2012.11609

Barro, G., Faber, S. M., Pérez-González, P. G., et al. 2013, ApJ, 765, 104

Bassett, R. & Foster, C. 2019, MNRAS, 487, 2354

Bedregal, A. G., Aragón-Salamanca, A., Merrifield, M. R., & Milvang-Jensen, B. 2006, MNRAS, 371, 1912

Behroozi, P. S., Conroy, C., & Wechsler, R. H. 2010, ApJ, 717, 379

Behroozi, P. S., Wechsler, R. H., & Conroy, C. 2013, ApJ, 770, 57

Beletsky, Y., Gadotti, D. A., Moiseev, A., Alves, J., & Kniazev, A. 2011, MNRAS, 418, L6

Bell, E. F., McIntosh, D. H., Katz, N., & Weinberg, M. D. 2003, ApJS, 149, 289

Bell, E. F., Wolf, C., Meisenheimer, K., et al. 2004, ApJ, 608, 752

Bellstedt, S., Forbes, D. A., Foster, C., et al. 2017a, MNRAS, 467, 4540

Bellstedt, S., Graham, A. W., Forbes, D. A., et al. 2017b, MNRAS, 470, 1321

Benacchio, L. & Galletta, G. 1980, MNRAS, 193, 885

Bender, R. 1987, Mitteilungen der Astronomischen Gesellschaft Hamburg, 70, 226

Bender, R. 1988a, A&A, 202, L5

Bender, R. 1988b, A&A, 193, L7

Bender, R., Doebereiner, S., & Moellenhoff, C. 1988, A&AS, 74, 385

Bender, R. & Moellenhoff, C. 1987, A&A, 177, 71

Bender, R., Saglia, R. P., & Gerhard, O. E. 1994, MNRAS, 269, 785

Bender, R., Surma, P., Doebereiner, S., Moellenhoff, C., & Madejsky, R. 1989, A&A, 217, 35

Benson, A. J. 2005, MNRAS, 358, 551

Bernardi, M., Shankar, F., Hyde, J. B., et al. 2010, MNRAS, 404, 2087

Bezanson, R., van Dokkum, P. G., Tal, T., et al. 2009, ApJ, 697, 1290

Binggeli, B. 1980, A&A, 82, 289

Binggeli, B., Sandage, A., & Tammann, G. A. 1988, ARA&A, 26, 509

Binney, J. 1976, MNRAS, 177, 19

Binney, J. 1978, MNRAS, 183, 501

Binney, J. 1985, MNRAS, 212, 767

Binney, J. 2005, MNRAS, 363, 937

Binney, J. & Mamon, G. A. 1982, MNRAS, 200, 361

Binney, J. & Merrifield, M. 1998, Galactic Astronomy (Princeton University Press)

Binney, J. & Tremaine, S. 2008, Galactic Dynamics: Second Edition (Princeton University Press)

Blaña Díaz, M., Wegg, C., Gerhard, O., et al. 2017, MNRAS, 466, 4279

Blakeslee, J. P., Cantiello, M., Mei, S., et al. 2010, ApJ, 724, 657

Blakeslee, J. P., Jordán, A., Mei, S., et al. 2009, ApJ, 694, 556

Blakeslee, J. P., Lucey, J. R., Barris, B. J., Hudson, M. J., & Tonry, J. L. 2001, MNRAS, 327, 1004

Blanton, M. R. & Moustakas, J. 2009, ARA&A, 47, 159

Blom, C., Forbes, D. A., Brodie, J. P., et al. 2012, MNRAS, 426, 1959

Boardman, N. F., Weijmans, A.-M., van den Bosch, R., et al. 2017, MNRAS, 471, 4005

Bois, M., Emsellem, E., Bournaud, F., et al. 2011, MNRAS, 416, 1654

Bondi, H. 1952, MNRAS, 112, 195

Bosma, A. 1978, PhD thesis, -

Bournaud, F., Chapon, D., Teyssier, R., et al. 2011, ApJ, 730, 4

Bridges, T. J., Rhode, K. L., Zepf, S. E., & Freeman, K. C. 2007, ApJ, 658, 980

Brodie, J. P., Romanowsky, A. J., Strader, J., et al. 2014, ApJ, 796, 52

Brodie, J. P. & Strader, J. 2006, ARA&A, 44, 193

Brook, C. B., Governato, F., Roškar, R., et al. 2011, MNRAS, 415, 1051

Brough, S., Forbes, D. A., Kilborn, V. A., & Couch, W. 2006, MNRAS, 370, 1223

Brough, S., van de Sande, J., Owers, M. S., et al. 2017, ApJ, 844, 59

Bryan, S. E., Kay, S. T., Duffy, A. R., et al. 2013, MNRAS, 429, 3316

Bryant, J. J., Owers, M. S., Robotham, A. S. G., et al. 2015, MNRAS, 447, 2857

Buitrago, F., Ferreras, I., Kelvin, L. S., et al. 2018, A&A, 619, A137

Buitrago, F., Trujillo, I., Conselice, C. J., et al. 2008, ApJ, 687, L61

Buitrago, F., Trujillo, I., Curtis-Lake, E., et al. 2017, MNRAS, 466, 4888

Bullock, J. S. & Boylan-Kolchin, M. 2017, ARA&A, 55, 343

Bullock, J. S. & Johnston, K. V. 2005, ApJ, 635, 931

Bundy, K., Bershady, M. A., Law, D. R., et al. 2015, ApJ, 798, 7

Burkhead, M. S. 1986, AJ, 91, 777

Buta, R., Mitra, S., de Vaucouleurs, G., & Corwin, H. G., J. 1994, AJ, 107, 118

Buzzoni, A., Arnaboldi, M., & Corradi, R. L. M. 2006, MNRAS, 368, 877

Caon, N., Capaccioli, M., & D'Onofrio, M. 1993, MNRAS, 265, 1013

Caon, N., Capaccioli, M., & D'Onofrio, M. 1994, A&AS, 106, 199

Caon, N., Capaccioli, M., & Rampazzo, R. 1990, A&AS, 86, 429

Capaccioli, M., Held, E. V., Lorenz, H., & Vietri, M. . 1990, AJ, 99, 1813

Capaccioli, M., Held, E. V., & Nieto, J.-L. 1987, AJ, 94, 1519

Cappellari, M. 2008, MNRAS, 390, 71

Cappellari, M. 2016, ARA&A, 54, 597

Cappellari, M., Bacon, R., Bureau, M., et al. 2006, MNRAS, 366, 1126

Cappellari, M. & Copin, Y. 2003, MNRAS, 342, 345

Cappellari, M., Emsellem, E., Bacon, R., et al. 2007, MNRAS, 379, 418

Cappellari, M., Emsellem, E., Krajnović, D., et al. 2011, MNRAS, 413, 813

Cappellari, M., McDermid, R. M., Alatalo, K., et al. 2013a, MNRAS, 432, 1862

Cappellari, M., Romanowsky, A. J., Brodie, J. P., et al. 2015, ApJ, 804, L21

Cappellari, M., Scott, N., Alatalo, K., et al. 2013b, MNRAS, 432, 1709

Carter, D. 1978, MNRAS, 182, 797

Carter, D., Thomson, R. C., & Hau, G. K. T. 1998, MNRAS, 294, 182

Catelan, P., Kamionkowski, M., & Blandford, R. D. 2001, MNRAS, 320, L7

Chabrier, G. 2003, PASP, 115, 763

Choi, H. & Yi, S. K. 2017, ApJ, 837, 68

Chua, K. T. E., Pillepich, A., Vogelsberger, M., & Hernquist, L. 2019, MNRAS, 484, 476

Churazov, E., Tremaine, S., Forman, W., et al. 2010, MNRAS, 404, 1165

Ciardullo, R., Jacoby, G. H., & Dejonghe, H. B. 1993, ApJ, 414, 454

Cimatti, A., Daddi, E., & Renzini, A. 2006, A&A, 453, L29

Coccato, L., Arnaboldi, M., & Gerhard, O. 2013, MNRAS, 436, 1322

Coccato, L., Arnaboldi, M., Gerhard, O., et al. 2010a, A&A, 519, A95

Coccato, L., Gerhard, O., & Arnaboldi, M. 2010b, MNRAS, 407, L26

Coccato, L., Gerhard, O., Arnaboldi, M., et al. 2009, MNRAS, 394, 1249

Cohen, J. G. & Ryzhov, A. 1997, ApJ, 486, 230

Conroy, C., Graves, G. J., & van Dokkum, P. G. 2014, ApJ, 780, 33

Cooper, A. P., Cole, S., Frenk, C. S., et al. 2010, MNRAS, 406, 744

Cooper, A. P., D'Souza, R., Kauffmann, G., et al. 2013, MNRAS, 434, 3348–3367

Cortesi, A., Arnaboldi, M., Coccato, L., et al. 2013a, A&A, 549, A115

Cortesi, A., Merrifield, M. R., Arnaboldi, M., et al. 2011, MNRAS, 414, 642

Cortesi, A., Merrifield, M. R., Coccato, L., et al. 2013b, MNRAS, 432, 1010

Côté, P., Ferrarese, L., Jordán, A., et al. 2007, ApJ, 671, 1456

Courteau, S., Cappellari, M., de Jong, R. S., et al. 2014, Reviews of Modern Physics, 86, 47

Crnojević, D., Sand, D. J., Spekkens, K., et al. 2016, ApJ, 823, 19

Croom, S. M., Lawrence, J. S., Bland-Hawthorn, J., et al. 2012, MNRAS, 421, 872

Daddi, E., Renzini, A., Pirzkal, N., et al. 2005, ApJ, 626, 680

Damjanov, I., Abraham, R. G., Glazebrook, K., et al. 2011, ApJ, 739, L44

Damjanov, I., McCarthy, P. J., Abraham, R. G., et al. 2009, ApJ, 695, 101

Davé, R., Anglés-Alcázar, D., Narayanan, D., et al. 2019, MNRAS, 486, 2827

Davies, R. L., Efstathiou, G., Fall, S. M., Illingw orth, G., & Schechter, P. L. 1983, ApJ, 266, 41

Davies, R. L. & Illingworth, G. 1983, ApJ, 266, 516

Davies, R. L., Kuntschner, H., Emsellem, E., et al. 2001, ApJ, 548, L33

Davis, M., Efstathiou, G., Frenk, C. S., & White, S. D. M. 1985, ApJ, 292, 371

Davison, T. A., Norris, M. A., Pfeffer, J. L., Davies, J. J., & Crain, R. A. 2020, MNRAS, 497, 81

De Bruyne, V., Dejonghe, H., Pizzella, A., Bernardi , M., & Zeilinger, W. W. 2001, ApJ, 546, 903

de Lorenzi, F., Gerhard, O., Coccato, L., et al. 2009, MNRAS, 395, 76

de Lorenzi, F., Gerhard, O., Saglia, R. P., et al. 2008, MNRAS, 385, 1729

de Vaucouleurs, G. 1961, ApJS, 5, 233

de Zeeuw, T. 1985, MNRAS, 216, 273

Deason, A. J., Belokurov, V., Evans, N. W., & McCarth y, I. G. 2012, ApJ, 748, 2

Deason, A. J., McCarthy, I. G., Font, A. S., et al. 2011, MNRAS, 415, 2607

Debattista, V. P., Corsini, E. M., & Aguerri, J. A. L. 2002, MNRAS, 332, 65

Dehnen, W. & Gerhard, O. E. 1993, MNRAS, 261, 311

Dekel, A. & Birnboim, Y. 2006, MNRAS, 368, 2

Dolfi, A., Forbes, D. A., Couch, W. J., et al. 2020, MNRAS, 495, 1321

Donnari, M., Pillepich, A., Nelson, D., et al. 2019, MNRAS, 485, 4817

Dopita, M. A., Jacoby, G. H., & Vassiliadis, E. 1992, ApJ, 389, 27

Douglas, N. G., Arnaboldi, M., Freeman, K. C., et al. 2002, PASP, 114, 1234

Douglas, N. G., Napolitano, N. R., Romanowsky, A. J., et al. 2007, ApJ, 664, 257

Douglas, N. G. & Taylor, K. 1999, MNRAS, 307, 190

Dowell, J. L., Rhode, K. L., Bridges, T. J., et al. 2014, AJ, 147, 150

Dressler, A. 1980, ApJ, 236, 351

D'Souza, R., Kauffman, G., Wang, J., & Vegetti, S. 2014, MNRAS, 443, 1433

Dubinski, J. & Carlberg, R. G. 1991, ApJ, 378, 496

Dubois, Y., Volonteri, M., Silk, J., et al. 2015, MNRAS, 452, 1502

Duc, P.-A., Cuillandre, J.-C., Karabal, E., et al. 2015, MNRAS, 446, 120

Duc, P.-A., Cuillandre, J.-C., Serra, P., et al. 2011, MNRAS, 417, 863

Ebrová, I. & Łokas, E. L. 2017, ApJ, 850, 144

Eggen, O. J., Lynden-Bell, D., & Sandage, A. R. 1962, ApJ, 136, 748

Emsellem, E., Cappellari, M., Krajnović, D., et al. 2011, MNRAS, 414, 888

Emsellem, E., Cappellari, M., Krajnović, D., et al. 2007, MNRAS, 379, 401

Emsellem, E., Cappellari, M., Peletier, R. F., et al. 2004, MNRAS, 352, 721

Ene, I., Ma, C.-P., Veale, M., et al. 2018, MNRAS, 479, 2810

Faber, S. M., Tremaine, S., Ajhar, E. A., et al. 1997, AJ, 114, 1771

Faber, S. M., Willmer, C. N. A., Wolf, C., et al. 2007, ApJ, 665, 265

Fahrion, K., Lyubenova, M., Hilker, M., et al. 2020, A&A, 637, A26

Falcón-Barroso, J., van de Ven, G., Lyubenova, M., et al. 2019, A&A, 632, A59

Fall, S. M. 1979, Nature, 281, 200

Fall, S. M. & Efstathiou, G. 1980, MNRAS, 193, 189

Faucher-Giguère, C.-A., Lidz, A., Zaldarriaga, M., & Hernquist, L. 2009, ApJ, 703, 1416

Ferrarese, L., Côté, P., Jordán, A., et al. 2006, ApJS, 164, 334

Ferrarese, L., van den Bosch, F. C., Ford, H. C., Jaffe, W., & O'Connell, R. W. 1994, AJ, 108, 1598

Ferré-Mateu, A., Trujillo, I., Martín-Navarro, I., et al. 2017, MNRAS, 467, 1929

Fogarty, L. M. R., Scott, N., Owers, M. S., et al. 2015, MNRAS, 454, 2050

Forbes, D. A., Beasley, M. A., Bekki, K., Brodie, J. P., & Strader, J. 2003, Science, 301, 1217

Forbes, D. A., Lasky, P., Graham, A. W., & Spitler, L. 2008, MNRAS, 389, 1924

Forbes, D. A. & Remus, R.-S. 2018, MNRAS, 479, 4760

Forbes, D. A., Romanowsky, A. J., Pastorello, N., et al. 2016, MNRAS, 457, 1242

Forestell, A. D. & Gebhardt, K. 2010, ApJ, 716, 370

Förster Schreiber, N. M., Genzel, R., Lehnert, M. D., et al. 2006, ApJ, 645, 1062

Foster, C., Arnold, J. A., Forbes, D. A., et al. 2013, MNRAS, 435, 3587

Foster, C., Pastorello, N., Roediger, J., et al. 2016, MNRAS, 457, 147

Foster, C., Spitler, L. R., Romanowsky, A. J., et al. 2011, MNRAS, 415, 3393

Foster, C., van de Sande, J., D'Eugenio, F., et al. 2017, MNRAS, 472, 966

Fouque, P., Gourgoulhon, E., Chamaraux, P., & Paturel , G. 1992, A&AS, 93, 211

Franx, M. 1988, MNRAS, 231, 285

Franx, M., Illingworth, G., & de Zeeuw, T. 1991, ApJ, 383, 112

Franx, M., Illingworth, G., & Heckman, T. 1989, ApJ, 344, 613

Freeman, K. C. 1970, ApJ, 160, 811

Fukazawa, Y., Botoya-Nonesa, J. G., Pu, J., Ohto, A., & Kawano, N. 2006, ApJ, 636, 698

Furlong, M., Bower, R. G., Crain, R. A., et al. 2017, MNRAS, 465, 722

Gabor, J. M. & Davé, R. 2012, MNRAS, 427, 1816

Gadotti, D. A. & Sánchez-Janssen, R. 2012, MNRAS, 423, 877

Ganeshaiah Veena, P., Cautun, M., Tempel, E., van de Weygaert, R., & Frenk, C. S. 2019, MNRAS, 487, 1607

Garcia, A. M. 1993, A&AS, 100, 47

García-Benito, R., González Delgado, R. M., Pérez, E., et al. 2019, A&A, 621, A120

Gavazzi, G., Fumagalli, M., Cucciati, O., & Boselli, A. 2010, A&A, 517, A73

Gebhardt, K., Richstone, D., Kormendy, J., et al. 2000, AJ, 119, 1157

Genel, S., Nelson, D., Pillepich, A., et al. 2018, MNRAS, 474, 3976

Genel, S., Vogelsberger, M., Springel, V., et al. 2014, MNRAS, 445, 175

Genzel, R., Tacconi, L. J., Eisenhauer, F., et al. 2006, Nature, 442, 786

Gerhard, O. 2013, in The Intriguing Life of Massive Galaxies, ed. D. Thomas, A. Pasquali, & I. Ferreras, Vol. 295, 211–220

Gerhard, O., Arnaboldi, M., Freeman, K. C., et al. 2005, ApJ, 621, L93

Gerhard, O., Arnaboldi, M., Freeman, K. C., et al. 2007, A&A, 468, 815

Gerhard, O., Jeske, G., Saglia, R. P., & Bender, R. 1998, MNRAS, 295, 197

Gerhard, O., Kronawitter, A., Saglia, R. P., & Bender, R. 2001, AJ, 121, 1936

Gerhard, O. E. 1993, MNRAS, 265, 213

Gerhard, O. E. 1994, Elliptical galaxies, ed. G. Contopoulos, N. K. Spyrou, & L. Vlahos, Vol. 433 (Lecture Notes in Physics), 191–274

Gerhard, O. E. & Binney, J. J. 1996, MNRAS, 279, 993

Gnedin, O. Y., Kravtsov, A. V., Klypin, A. A., & Nagai, D. 2004, ApJ, 616, 16

Goudfrooij, P., Hansen, L., Jorgensen, H. E., et al. 1994, A&AS, 104, 179

Governato, F., Brook, C. B., Brooks, A. M., et al. 2009, MNRAS, 398, 312

Graham, A. W., Colless, M. M., Busarello, G., Zaggia, S., & Longo, G. 1998, A&AS, 133, 325

Graham, M. T., Cappellari, M., Li, H., et al. 2018, MNRAS, 477, 4711

Grand, R. J. J., Gómez, F. A., Marinacci, F., et al. 2017, MNRAS, 467, 179

Greene, J. E., Leauthaud, A., Emsellem, E., et al. 2017, ApJ, 851, L33

Gronwall, C., Ciardullo, R., Hickey, T., et al. 2007, ApJ, 667, 79

Guérou, A., Emsellem, E., Krajnović, D., et al. 2016, A&A, 591, A143

Gunn, J. E. & Gott, J. Richard, I. 1972, ApJ, 176, 1

Halliday, C., Davies, R. L., Kuntschner, H., et al. 2001, MNRAS, 326, 473

Harrison, C. M. 2017, Nature Astronomy, 1, 0165

Hartke, J., Arnaboldi, M., Gerhard, O., et al. 2018, A&A, 616, A123

Hartke, J., Arnaboldi, M., Gerhard, O., et al. 2020, A&A, 642, A46

Hartke, J., Arnaboldi, M., Longobardi, A., et al. 2017, A&A, 603, A104

Haynes, R. F., Cannon, R. D., & Ekers, R. D. 1983, Proceedings of the Astronomical Society of Australia, 5, 241

Henriques, B. M. B., White, S. D. M., Thomas, P. A., et al. 2013, MNRAS, 431, 3373

Hernquist, L. 1992, ApJ, 400, 460

Hernquist, L., Spergel, D. N., & Heyl, J. S. 1993, ApJ, 416, 415

Hilz, M., Naab, T., & Ostriker, J. P. 2013, MNRAS, 429, 2924

Hilz, M., Naab, T., Ostriker, J. P., Thomas, J. an d Burkert, A., & Jesseit, R. 2012, MNRAS, 425, 3119

Ho, L. C., Li, Z.-Y., Barth, A. J., Seigar, M. S., & Peng, C. Y. 2011, ApJS, 197, 21

Ho, L. C., Li, Z.-Y., Barth, A. J., Seigar, M. S., & Peng, C. Y. 2012, VizieR Online Data Catalog, 219

Hopkins, P. F., Bundy, K., Murray, N., et al. 2009a, MNRAS, 398, 898

Hopkins, P. F., Cox, T. J., Dutta, S. N., et al. 2009b, ApJS, 181, 135

Hopkins, P. F., Hernquist, L., Cox, T. J., & Kereš, D. 2008, ApJS, 175, 356

Hopkins, P. F., Kereš, D., Oñorbe, J., et al. 2014, MNRAS, 445, 581

Houghton, R. C. W., Magorrian, J., Sarzi, M., et al. 2006, MNRAS, 367, 2

Hoyle, F. 1951, in Problems of Cosmical Aerodynamics, 195

Huang, S., Ho, L. C., Peng, C. Y., Li, Z.-Y., & Barth, A. J. 2013a, ApJ, 768, L28

Huang, S., Ho, L. C., Peng, C. Y., Li, Z.-Y., & Barth, A. J. 2013b, ApJ, 766, 47

Hubble, E. P. 1936, Realm of the Nebulae (Yale University Press)

Hui, X., Ford, H. C., Ciardullo, R., & Jacoby, G. H. 1993, ApJ, 414, 463

Hui, X., Ford, H. C., Freeman, K. C., & Dopita, M. A. . 1995, ApJ, 449, 592

Humphrey, P. J., Buote, D. A., Gastaldello, F., et al. 2006, ApJ, 646, 899

Humphrey, P. J., Buote, D. A., O'Sullivan, E., & Ponman, T. J. 2012, ApJ, 755, 166

Illingworth, G. 1977, ApJ, 218, L43

Iodice, E., Capaccioli, M., Grado, A., et al. 2016, ApJ, 820, 42

Iodice, E., Spavone, M., Capaccioli, M., et al. 2017, ApJ, 839, 21

Jacoby, G. H., Ciardullo, R., & Ford, H. C. 1990, ApJ, 356, 332

Janowiecki, S., Mihos, J. C., Harding, P., et al. 2010, ApJ, 715, 972

Jarrett, T. H., Chester, T., Cutri, R., Schneider, S. E., & Huchra, J. P. 2003, AJ, 125, 525

Jeans, J. H. 1922, MNRAS, 82, 122

Jedrzejewski, R. & Schechter, P. L. 1988, ApJ, 330, L87

Jedrzejewski, R. I. 1987, MNRAS, 226, 747

Jensen, J. B., Tonry, J. L., Barris, B. J., et al. 2003, ApJ, 583, 712

Jesseit, R., Cappellari, M., Naab, T., Emsellem, E., & Burkert, A. 2009, MNRAS, 397, 1202

Jesseit, R., Naab, T., & Burkert, A. 2005, MNRAS, 360, 1185

Jester, S., Schneider, D. P., Richards, G. T., et al. 2005, AJ, 130, 873

Johansson, P. H., Naab, T., & Ostriker, J. P. 2012, ApJ, 754, 115

Johnston, E. J., Merrifield, M., & Aragón-Salamanca, A. 2018, MNRAS, 478, 4255

Karademir, G. S., Remus, R.-S., Burkert, A., et al. 2019, MNRAS, 487, 318

Kauffmann, G., Heckman, T. M., White, S. D. M., et al. 2003, MNRAS, 341, 54

Kazantzidis, S., Kravtsov, A. V., Zentner, A. R., et al. 2004, ApJ, 611, L73

Kelson, D. D., Zabludoff, A. I., Williams, K. A., et al. 2002, ApJ, 576, 720

Kereš, D., Katz, N., Weinberg, D. H., & Davé, R. 2005, MNRAS, 363, 2

Kluge, M., Bender, R., Riffeser, A., et al. 2021, ApJS, 252, 27

Kluge, M., Neureiter, B., Riffeser, A., et al. 2020, ApJS, 247, 43

Koopmans, L. V. E., Bolton, A., Treu, T., et al. 2009, ApJ, 703, L51

Kormendy, J. & Bender, R. 1996, ApJ, 464, L119

Kormendy, J., Fisher, D. B., Cornell, M. E., & Bender, R. 2009, ApJS, 182, 216

Kormendy, J. & Illingworth, G. 1982, ApJ, 256, 460

Kormendy, J. & Westpfahl, D. J. 1989, ApJ, 338, 752

Krajnović, D., Alatalo, K., Blitz, L., et al. 2013a, MNRAS, 432, 1768

Krajnović, D., Bacon, R., Cappellari, M., et al. 2008, MNRAS, 390, 93

Krajnović, D., Cappellari, M., de Zeeuw, P. T., & Copin, Y. 2006, MNRAS, 366, 787

Krajnović, D., Emsellem, E., Cappellari, M., et al. 2011, MNRAS, 414, 2923

Krajnović, D., Karick, A. M., Davies, R. L., et al. 2013b, MNRAS, 433, 2812

Kronawitter, A., Saglia, R. P., Gerhard, O., & Bender, R. 2000, A&AS, 144, 53

Kudritzki, R. P., Méndez, R. H., Feldmeier, J. J., et al. 2000, ApJ, 536, 19

Lackner, C. N., Cen, R., Ostriker, J. P., & Joung, M. . R. 2012, MNRAS, 425, 641

Lagos, C. d. P., Emsellem, E., van de Sande, J., et al. 2020, arXiv e-prints, arXiv:2012.08060

Lagos, C. d. P., Schaye, J., Bahé, Y., et al. 2018a, MNRAS, 476, 4327

Lagos, C. d. P., Stevens, A. R. H., Bower, R. G., et al. 2018b, MNRAS, 473, 4956

Lagos, C. d. P., Theuns, T., Stevens, A. R. H., et al. 2017, MNRAS, 464, 3850

Lambas, D. G., Maddox, S. J., & Loveday, J. 1992, MNRAS, 258, 404

Larson, R. B., Tinsley, B. M., & Caldwell, C. N. 1980, ApJ, 237, 692

Lauer, T. R., Ajhar, E. A., Byun, Y. I., et al. 1995, AJ, 110, 2622

Lauer, T. R., Faber, S. M., Gebhardt, K., et al. 2005, AJ, 129, 2138

Laurikainen, E., Salo, H., Buta, R., Knapen, J. H., & Comerón, S. 2010, MNRAS, 405, 1089

Law, D. R., Cherinka, B., Yan, R., et al. 2016, AJ, 152, 83

Leach, R. 1981, ApJ, 248, 485

Lee, J. & Yi, S. K. 2013, ApJ, 766, 38

Li, H., Mao, S., Cappellari, M., et al. 2018, ApJ, 863, L19

Li, Z.-Y., Ho, L. C., Barth, A. J., & Peng, C. Y. 2011, ApJS, 197, 22

Lima Neto, G. B., Gerbal, D., & Márquez, I. 1999, MNRAS, 309, 481

Longobardi, A., Arnaboldi, M., Gerhard, O., et al. 2013, A&A, 558, A42

Longobardi, A., Arnaboldi, M., Gerhard, O., & Hanuschik, R. 2015a, A&A, 579, A135

Longobardi, A., Arnaboldi, M., Gerhard, O., & Mihos, J. C. 2015b, A&A, 579, L3

Loubser, S. I., Sansom, A. E., Sánchez-Blázquez, P., Soechting, I. K., & Bromage, G. E. 2008, MNRAS, 391, 1009

Lynden-Bell, D. 1967, MNRAS, 136, 101

Ma, C.-P., Greene, J. E., McConnell, N., et al. 2014, ApJ, 795, 158

Macciò, A. V., Dutton, A. A., & van den Bosch, F. C. 2008, MNRAS, 391, 1940

Madejsky, R. & Moellenhoff, C. 1990, A&A, 234, 119

Madore, B. F., Freedman, W. L., & Bothun, G. D. 2004, ApJ, 607, 810

Magrini, L., Leisy, P., Corradi, R. L. M., et al. 2005, A&A, 443, 115

Makarov, D., Prugniel, P., Terekhova, N., Courtois, H., & Vauglin, I. 2014, A&A, 570, A13

Malin, D. F. & Carter, D. 1980, Nature, 285, 643

Malin, D. F. & Carter, D. 1983, ApJ, 274, 534

Malin, D. F., Quinn, P. J., & Graham, J. A. 1983, ApJ, 272, L5

Maller, A. H. & Dekel, A. 2002, MNRAS, 335, 487

Mancillas, B., Duc, P.-A., Combes, F., et al. 2019, A&A, 632, A122

Mandelbaum, R., Seljak, U., Kauffmann, G., Hirata, C. M., & Brinkmann, J. 2006, MNRAS, 368, 715

Marcelin, M. 1983, in IAU Symposium, Vol. 100, Internal Kinematics and Dynamics of Galaxies, ed. E. Athanassoula, 335

Marinacci, F., Fraternali, F., Nipoti, C., et al. 2011, MNRAS, 415, 1534

Marinacci, F., Vogelsberger, M., Pakmor, R., et al. 2018, MNRAS, 480, 5113

Martin, D. C., Wyder, T. K., Schiminovich, D., et al. 2007, ApJS, 173, 342

McNamara, B. R. & Nulsen, P. E. J. 2007, ARA&A, 45, 117

McNaught-Roberts, T., Norberg, P., Baugh, C., et al. 2014, MNRAS, 445, 2125

McNeil, E. K., Arnaboldi, M., Freeman, K. C., et al. 2010, A&A, 518, A44

McNeil-Moylan, E. K., Freeman, K. C., Arnaboldi, M., & Gerhard, O. E. 2012, A&A, 539, A11

Mehrgan, K., Thomas, J., Saglia, R., et al. 2019, ApJ, 887, 195

Méndez, R. H., Riffeser, A., Kudritzki, R.-P., et al. 2001, ApJ, 563, 135

Méndez, R. H., Teodorescu, A. M., Kudritzki, R.-P., & Burkert, A. 2009, ApJ, 691, 228

Merritt, D. 1992, in BAAS, Vol. 24, Bulletin of the American Astronomical Society, 522–524

Meusinger, H. & Ismail, H. A. 2007, Astronomische Nachrichten, 328, 562

Michard, R. & Marchal, J. 1993, A&AS, 98, 29

Michard, R. & Marchal, J. 1994, A&AS, 105, 481

Mihos, J. C. & Hernquist, L. 1994, ApJ, 437, L47

Moore, B., Katz, N., Lake, G., Dressler, A., & Oemler, A. 1996, Nature, 379, 613

Morganti, L., Gerhard, O., Coccato, L., Martinez-Va lpuesta, I., & Arnaboldi, M. 2013, MNRAS, 431, 3570

Moster, B. P., Naab, T., & White, S. D. M. 2013, MNRAS, 428, 3121

Murphy, J. D., Gebhardt, K., & Adams, J. J. 2011, ApJ, 729, 129

Naab, T., Johansson, P. H., & Ostriker, J. P. 2009, ApJ, 699, L178

Naab, T., Oser, L., Emsellem, E., et al. 2014, MNRAS, 444, 3357

Naab, T. & Ostriker, J. P. 2017, ARA&A, 55, 59

Naiman, J. P., Pillepich, A., Springel, V., et al. 2018, MNRAS, 477, 1206

Napolitano, N. R., Arnaboldi, M., Freeman, K. C., & Capaccioli, M. 2001, A&A, 377, 784

Napolitano, N. R., Capaccioli, M., Romanowsky, A. J., et al. 2005, MNRAS, 357, 691

Napolitano, N. R., Romanowsky, A. J., Capaccioli, M. an d Douglas, N. G., et al. 2011, MNRAS, 411, 2035

Napolitano, N. R., Romanowsky, A. J., Coccato, L., et al. 2009, MNRAS, 393, 329

Navarro, J. F., Frenk, C. S., & White, S. D. M. 1996, ApJ, 462, 563

Navarro, J. F., Frenk, C. S., & White, S. D. M. 1997, ApJ, 490, 493

Neistein, E., van den Bosch, F. C., & Dekel, A. 2006, MNRAS, 372, 933

Nelson, D., Pillepich, A., Genel, S., et al. 2015, Astronomy and Computing, 13, 12

Nelson, D., Pillepich, A., Springel, V., et al. 2019a, MNRAS, 490, 3234

Nelson, D., Pillepich, A., Springel, V., et al. 2018, MNRAS, 475, 624

Nelson, D., Springel, V., Pillepich, A., et al. 2019b, Computational Astrophysics and Cosmology, 6, 2

Neumayer, N. 2010, PASA, 27, 449

Nieto, J. L., Capaccioli, M., & Held, E. V. 1988, A&A, 195, L1

Nolthenius, R. & Ford, H. C. 1987, ApJ, 317, 62

Noordermeer, E., Merrifield, M. R., Coccato, L., et al. 2008, MNRAS, 384, 943

Norris, M. A., Gebhardt, K., Sharples, R. M., et al. 2012, MNRAS, 421, 1485

Norris, M. A., Sharples, R. M., & Kuntschner, H. 2006, MNRAS, 367, 815

Okamoto, T., Eke, V. R., Frenk, C. S., & Jenkins, A. 2005, MNRAS, 363, 1299

Oser, L., Ostriker, J. P., Naab, T., Johansson, P. H., & Burkert, A. 2010, ApJ, 725, 2312

Padilla, N. D. & Strauss, M. A. 2008, MNRAS, 388, 1321

Pakmor, R., Marinacci, F., & Springel, V. 2014, ApJ, 783, L20

Pastorello, N., Forbes, D. A., Foster, C., et al. 2014, MNRAS, 442, 1003

Peebles, P. 1980, The Large-scale Structure of the Universe, Princeton series in physics (Princeton University Press)

Peebles, P. J. E. 1969, ApJ, 155, 393

Peletier, R. F., Davies, R. L., Illingworth, G. D., Davis, L. E., & Cawson, M. 1990, AJ, 100, 1091

Pellegrini, S. 2005, MNRAS, 364, 169

Peng, E. W., Ford, H. C., & Freeman, K. C. 2004, ApJ, 602, 685

Peng, E. W., Ford, H. C., Freeman, K. C., & White, R. . L. 2002, AJ, 124, 3144

Peng, Y.-j., Lilly, S. J., Kovač, K., et al. 2010, ApJ, 721, 193

Penoyre, Z., Moster, B. P., Sijacki, D., & Genel, S. 2017, MNRAS, 468, 3883

Perlmutter, S., Aldering, G., Goldhaber, G., et al. 1999, ApJ, 517, 565

Pignatelli, E. 1999, ArXiv Astrophysics e-prints [astro-ph/9906378]

Pillepich, A., Nelson, D., Hernquist, L., et al. 2018a, MNRAS, 475, 648

Pillepich, A., Nelson, D., Springel, V., et al. 2019, MNRAS, 490, 3196

Pillepich, A., Springel, V., Nelson, D., et al. 2018b, MNRAS, 473, 4077

Pillepich, A., Vogelsberger, M., Deason, A., et al. 2014, MNRAS, 444, 237

Planck Collaboration, Ade, P. A. R., Aghanim, N., et al. 2016, A&A, 594, A19

Planck Collaboration, Aghanim, N., Akrami, Y., et al. 2018, arXiv e-prints, arXiv:1807.06209

Portail, M., Gerhard, O., Wegg, C., & Ness, M. 2017, MNRAS, 465, 1621

Postman, M. & Geller, M. J. 1984, ApJ, 281, 95

Pota, V., Brodie, J. P., Bridges, T., et al. 2015, MNRAS, 450, 1962

Pota, V., Forbes, D. A., Romanowsky, A. J., et al. 2013, MNRAS, 428, 389

Power, C., Navarro, J. F., Jenkins, A., et al. 2003, MNRAS, 338, 14

Proctor, R. N., Forbes, D. A., Romanowsky, A. J., et al. 2009, MNRAS, 398, 91

Pu, S.-B. & Han, Z.-W. 2011, Research in Astronomy and Astrophysics, 11, 909

Pulsoni, C., Gerhard, O., Arnaboldi, M., et al. 2018, A&A, 618, A94

Pulsoni, C., Gerhard, O., Arnaboldi, M., et al. 2020, A&A, 641, A60

Pulsoni, C., Gerhard, O., Arnaboldi, M., et al. 2021, A&A, 647, A95

Qu, Y., Di Matteo, P., Lehnert, M., van Driel, W., & Jog, C. J. 2010, A&A, 515, A11

Qu, Y., Helly, J. C., Bower, R. G., et al. 2017, MNRAS, 464, 1659

Raskutti, S., Greene, J. E., & Murphy, J. D. 2014, ApJ, 786, 23

Rejkuba, M., Minniti, D., Courbin, F., & Silva, D. R. . 2002, ApJ, 564, 688

Remus, R.-S. & Forbes, D. A. 2021, arXiv e-prints, arXiv:2101.12216

Renaud, F., Agertz, O., & Gieles, M. 2017, MNRAS, 465, 3622

Richtler, T., Hilker, M., Kumar, B., et al. 2014, A&A, 569, A41

Riess, A. G., Filippenko, A. V., Challis, P., et al. 1998, AJ, 116, 1009

Rix, H.-W., de Zeeuw, P. T., Cretton, N., van der M arel, R. P., & Carollo, C. M. 1997, ApJ, 488, 702

Robaina, A. R., Bell, E. F., van der Wel, A., et al. 2010, ApJ, 719, 844

Roberts, M. S. & Haynes, M. P. 1994, ARA&A, 32, 115

Roberts, M. S. & Whitehurst, R. N. 1975, ApJ, 201, 327

Roberts, P. H. 1962, ApJ, 136, 1108

Rodriguez-Gomez, V., Pillepich, A., Sales, L. V., et al. 2016, MNRAS, 458, 2371

Rodriguez-Gomez, V., Sales, L. V., Genel, S., et al. 2017, MNRAS, 467, 3083

Rodriguez-Gomez, V., Snyder, G. F., Lotz, J. M., et al. 2019, MNRAS, 483, 4140

Romanowsky, A. J., Douglas, N. G., Arnaboldi, M., et al. 2003, Science, 301, 1696

Romanowsky, A. J. & Fall, S. M. 2012, ApJS, 203, 17

Romanowsky, A. J., Strader, J., Brodie, J. P., et al. 2012, ApJ, 748, 29

Rosas-Guevara, Y., Bonoli, S., Dotti, M., et al. 2020, MNRAS, 491, 2547

Röttgers, B., Naab, T., & Oser, L. 2014, MNRAS, 445, 1065

Rubin, V. C., Burley, J., Kiasatpoor, A., et al. 1962, AJ, 67, 491

Rubin, V. C., Ford, W. K., J., & Thonnard, N. 1980, ApJ, 238, 471

Rubin, V. C. & Ford, W. Kent, J. 1970, ApJ, 159, 379

Rybicki, G. B. 1987, in Structure and Dynamics of Elliptical Galaxies, ed. P. T. de Zeeuw, Vol. 127, 397

Ryden, B. 1992, ApJ, 396, 445

Saglia, R. P., Kronawitter, A., Gerhard, O., & Bender, R. 2000, AJ, 119, 153

Sambhus, N., Gerhard, O., & Méndez, R. H. 2006, AJ, 131, 837

Sánchez, S. F., Kennicutt, R. C., Gil de Paz, A. an d van de Ven, G., et al. 2012, A&A, 538, A8

Sancisi, R., van Woerden, H., Davies, R. D., & Hart, L. 1984, MNRAS, 210, 497

Sandage, A., Freeman, K. C., & Stokes, N. R. 1970, ApJ, 160, 831

Sandage, A. & Visvanathan, N. 1978, ApJ, 223, 707

Sarzi, M., Mamon, G. A., Cappellari, M., et al. 2011, MNRAS, 415, 2832

Sawala, T., Frenk, C. S., Fattahi, A., et al. 2016, MNRAS, 457, 1931

Schäfer, B. M. 2009, International Journal of Modern Physics D, 18, 173

Schaye, J., Crain, R. A., Bower, R. G., et al. 2015, MNRAS, 446, 521

Schlegel, D. J., Finkbeiner, D. P., & Davis, M. 1998, ApJ, 500, 525

Schombert, J. & Smith, A. K. 2012, PASA, 29, 174

Schombert, J. M. 1986, ApJS, 60, 603

Schombert, J. M. 1988, ApJ, 328, 475

Schuberth, Y., Richtler, T., Hilker, M., et al. 2010, A&A, 513, A52

Schuberth, Y., Richtler, T., Hilker, M., et al. 2012, A&A, 544, A115

Schulze, F., Remus, R.-S., Dolag, K., et al. 2020, MNRAS, 493, 3778

Schulze, F., Remus, R.-S., Dolag, K., et al. 2018, MNRAS, 480, 4636

Schwarzschild, M. 1979, ApJ, 232, 236

Schwarzschild, M. 1993, ApJ, 409, 563

Schweizer, F. 1980, ApJ, 237, 303

Scognamiglio, D., Tortora, C., Spavone, M., et al. 2020, ApJ, 893, 4

Scorza, C. & Bender, R. 1995, A&A, 293, 20

Scorza, C., Bender, R., Winkelmann, C., Capaccioli, M., & Macchetto, D. F. 1998, A&AS, 131, 265

Scott, N., Davies, R. L., Houghton, R. C. W., et al. 2014, MNRAS, 441, 274

Scott, N., Graham, A. W., & Schombert, J. 2013, ApJ, 768, 76

Sengupta, C. & Balasubramanyam, R. 2006, MNRAS, 369, 360

Sikkema, G., Carter, D., Peletier, R. F., et al. 2007, A&A, 467, 1011

Simien, F. & Prugniel, P. 1997a, A&AS, 122, 521

Simien, F. & Prugniel, P. 1997b, A&AS, 126, 15

Simien, F. & Prugniel, P. 1997c, A&AS, 126, 519

Skrutskie, M. F., Cutri, R. M., Stiening, R., et al. 2006, AJ, 131, 1163

Sluis, A. P. N. & Williams, T. B. 2006, AJ, 131, 2089

Smethurst, R. J., Masters, K. L., Lintott, C. J., et al. 2018, MNRAS, 473, 2679

Smith, B., Sigurdsson, S., & Abel, T. 2008, MNRAS, 385, 1443

Somerville, R. S. & Davé, R. 2015, ARA&A, 53, 51

Somerville, R. S., Hopkins, P. F., Cox, T. J., Robertson, B. E., & Hernquist, L. 2008, MNRAS, 391, 481

Sommer-Larsen, J. & Toft, S. 2010, ApJ, 721, 1755

Spavone, M., Capaccioli, M., Napolitano, N. R., et al. 2017, A&A, 603, A38

Spavone, M., Iodice, E., Capaccioli, M., et al. 2018, ApJ, 864, 149

Spiniello, C., Napolitano, N. R., Coccato, L., et al. 2015, MNRAS, 452, 99

Spiniello, C., Tortora, C., D'Ago, G., et al. 2020, arXiv e-prints, arXiv:2011.05347

Springel, V. 2010, MNRAS, 401, 791

Springel, V. & Hernquist, L. 2003, MNRAS, 339, 289

Springel, V., Pakmor, R., Pillepich, A., et al. 2018, MNRAS, 475, 676

Springel, V., Pakmor, R., Zier, O., & Reinecke, M. 2020, arXiv e-prints, arXiv:2010.03567

Stark, A. A. 1977, ApJ, 213, 368

Statler, T. S. 1987, ApJ, 321, 113

Statler, T. S. 1994, ApJ, 425, 500

Statler, T. S. & Smecker-Hane, T. 1999, AJ, 117, 839

Strader, J., Romanowsky, A. J., Brodie, J. P., et al. 2011, ApJS, 197, 33

Strateva, I., Ivezić, Ž., Knapp, G. R., et al. 2001, AJ, 122, 1861

Syer, D. & Tremaine, S. 1996, MNRAS, 282, 223

Tacchella, S., Diemer, B., Hernquist, L., et al. 2019, MNRAS, 487, 5416

Tal, T., van Dokkum, P. G., Nelan, J., & Bezanson, R. . 2009, AJ, 138, 1417

Teklu, A. F., Remus, R.-S., Dolag, K., et al. 2015, ApJ, 812, 29

Tempel, E., Saar, E., Liivamägi, L. J., et al. 2011, A&A, 529, A53

Tenneti, A., Mandelbaum, R., Di Matteo, T., Kiessling, A., & Khandai, N. 2015, MNRAS, 453, 469

Teodorescu, A. M., Méndez, R. H., Bernardi, F., et al. 2011, ApJ, 736, 65

Teodorescu, A. M., Méndez, R. H., Saglia, R. P., et al. 2005, ApJ, 635, 290

Thomas, D., Maraston, C., Bender, R., & Mendes de Oliveira, C. 2005a, ApJ, 621, 673

Thomas, J., Jesseit, R., Saglia, R. P., et al. 2009a, MNRAS, 393, 641

Thomas, J., Saglia, R. P., Bender, R., Erwin, P., & Fabricius, M. 2014, ApJ, 782, 39

Thomas, J., Saglia, R. P., Bender, R., et al. 2005b, MNRAS, 360, 1355

Thomas, J., Saglia, R. P., Bender, R., et al. 2009b, ApJ, 691, 770

Tody, D. 1993, in Astronomical Society of the Pacific Conference Series, Vol. 52, Astronomical Data Analysis Software and Systems II, ed. R. J. Hanisch, R. J. V. Brissenden, & J. Barnes, 173

Tonry, J. L., Dressler, A., Blakeslee, J. P., et al. 2001, ApJ, 546, 681

Tremaine, S. 1987, in Structure and Dynamics of Elliptical Galaxies, ed. P. T. de Zeeuw, Vol. 127, 367–373

Tremmel, M., Karcher, M., Governato, F., et al. 2017, MNRAS, 470, 1121

Tremmel, M., Quinn, T. R., Ricarte, A., et al. 2019, MNRAS, 483, 3336

Treu, T. 2010, ARA&A, 48, 87

Trujillo, I., Conselice, C. J., Bundy, K., et al. 2007, MNRAS, 382, 109

Trujillo, I., Ferré-Mateu, A., Balcells, M., Vazdekis, A., & Sánchez-Blázquez, P. 2014, ApJ, 780, L20

Trujillo, I., Förster Schreiber, N. M., Rudnick, G., et al. 2006, ApJ, 650, 18

Tsatsi, A., Lyubenova, M., van de Ven, G., et al. 2017, A&A, 606, A62

Übler, H., Naab, T., Oser, L., et al. 2014, MNRAS, 443, 2092

van de Sande, J., Bland-Hawthorn, J., Fogarty, L. M. R., et al. 2017, ApJ, 835, 104

van de Sande, J., Lagos, C. D. P., Welker, C., et al. 2019, MNRAS, 484, 869

van de Sande, J., Vaughan, S. P., Cortese, L., et al. 2020, arXiv e-prints, arXiv:2011.08199

van den Bergh, S. 1961, AJ, 66, 562

van den Bergh, S. 2009, ApJ, 702, 1502

van den Bosch, R. C. E. & van de Ven, G. 2009, MNRAS, 398, 1117

van der Marel, R. P. & Franx, M. 1993, ApJ, 407, 525

van der Marel, R. P., Rix, H. W., Carter, D., et al. 1994, MNRAS, 268, 521

van der Wel, A., Franx, M., van Dokkum, P. G., et al. 2014, ApJ, 788, 28

van Dokkum, P. G., Franx, M., Kriek, M., et al. 2008, ApJ, 677, L5

van Dokkum, P. G., Whitaker, K. E., Brammer, G., et al. 2010, ApJ, 709, 1018

van Uitert, E., Hoekstra, H., Schrabback, T., et al. 2012, A&A, 545, A71

Veale, M., Ma, C.-P., Greene, J. E., et al. 2017a, MNRAS, 471, 1428

Veale, M., Ma, C.-P., Greene, J. E., et al. 2018, MNRAS, 473, 5446

Veale, M., Ma, C.-P., Thomas, J., et al. 2017b, MNRAS, 464, 356

Veljanoski, J., Mackey, A. D., Ferguson, A. M. N., et al. 2014, MNRAS, 442, 2929

Viaene, S., Sarzi, M., Baes, M., & Puerari, I. 2018, MNRAS, 474, L47

Vogelsberger, M., Genel, S., Sijacki, D., et al. 2013, MNRAS, 436, 3031

Vogelsberger, M., Genel, S., Springel, V., et al. 2014, MNRAS, 444, 1518

Walo-Martín, D., Falcón-Barroso, J., Dalla Vecchia, C., Pérez, I., & Negri, A. 2020, MNRAS, 494, 5652

Walsh, J. R., Rejkuba, M., & Walton, N. A. 2015, A&A, 574, A109

Wang, B., Cappellari, M., Peng, Y., & Graham, M. 2020, MNRAS, 495, 1958

Wang, L., Dutton, A. A., Stinson, G. S., et al. 2015, MNRAS, 454, 83

Weijmans, A.-M., Cappellari, M., Bacon, R., et al. 2009, MNRAS, 398, 561

Weijmans, A.-M., de Zeeuw, P. T., Emsellem, E., et al. 2014, MNRAS, 444, 3340

Weinberger, R., Springel, V., Hernquist, L., et al. 2017, MNRAS, 465, 3291

Wellons, S., Torrey, P., Ma, C.-P., et al. 2016, MNRAS, 456, 1030

Wellons, S., Torrey, P., Ma, C.-P., et al. 2015, MNRAS, 449, 361

Werner, N., McNamara, B. R., Churazov, E., & Scannapieco, E. 2019, Space Science Reviews, 215, 5

Wetzel, A. R. 2011, MNRAS, 412, 49

White, S. D. M. & Frenk, C. S. 1991, ApJ, 379, 52

White, S. D. M. & Rees, M. J. 1978, MNRAS, 183, 341

Wiersma, R. P. C., Schaye, J., & Smith, B. D. 2009, MNRAS, 393, 99

Wilman, D. J., Oemler, A., J., Mulchaey, J. S., et al. 2009, ApJ, 692, 298

Wu, X., Gerhard, O., Naab, T., et al. 2014, MNRAS, 438, 2701

Wuyts, S., Cox, T. J., Hayward, C. C., et al. 2010, ApJ, 722, 1666

Young, L. M., Rosolowsky, E., van Gorkom, J. H., & Lamb, S. A. 2006, ApJ, 650, 166

Zemp, M., Gnedin, O. Y., Gnedin, N. Y., & Kravtsov, A. V. 2011, ApJS, 197, 30

Zheng, Z., Shang, Z., Su, H., et al. 1999, AJ, 117, 2757

Zhu, L., Long, R. J., Mao, S., et al. 2014, ApJ, 792, 59

Zibetti, S., Gallazzi, A. R., Hirschmann, M., et al. 2020, MNRAS, 491, 3562

Zjupa, J. & Springel, V. 2017, MNRAS, 466, 1625

Zwicky, F. 1937, ApJ, 86, 217

Danksagung

That was fun!
The last six year (...almost seven... oh dear!) were the most life-changing and formative for me. Looking back to when I started this PhD, it is almost incredible to see what an extraordinary journey this was. So it is time now for me to thank all the people that accompanied me during this journey, that guided me, and made all these years such a beautiful experience.

First, there is my supervisor Ortwin. To him I will forever be grateful to have given me the opportunity of doing a PhD at MPE. He believed in me and supported me through all these years, and encouraged me when I needed it most. I am grateful to him and Magda for trusting me to work with such beautiful data and for sharing with me their great expertise. Their enthusiasm and dedication to astronomy are a model for me to look up to.

I am grateful to Florian, my husband and better half. Without his constant support in countless ways, I would have probably not managed to get this thesis done. The last months were hard, as they surely were for anybody else trying to juggle work, household, and kids during a global pandemic. His optimism and love kept me going, and for that I will always be in debt to him. I want to thank Alessandro and Rosalia for their patience when mamma needed to work and for bringing me joy everyday.

I am also grateful to my parents, my brother and sister, my cousins, my aunties, and my family in law for encouraging me from afar and for bearing with me all these years. I know, I am a handful. I want to thank papà and mamma for always being there for me when I needed a wise advise or just to be listened to. I know that they will always have my back no matter what.

I want to thank my colleagues and friends for making my PhD time so much more enjoyable and fun: Chris, Marie, Matthieu, Léonie, Matias, Angeles, Jethro, Corina, Laura, Bhaskar, Johanna, Souradeep, Chiara, Fabrizio, Ximena, Greg, and Sergey. I want like to especially thank my office mates Alessia, Isabella, and Anna for their support since day one and the silly chats, and Shola, Johnny, and Agne for the best morning coffee. I am very grateful that my path crossed with that of these people, even though I get a little heartbroken every time one of them leaves for new adventures.

Finally but not less important, I would like to thank my soul sisters Julia, Letizia, Lorenza, and Manuela. Even though we are far apart, I know I can always count on you.